Structural and functional characterization of nucleoid associated proteins of Deinococcus radiodurans and Deinococcus deserti

Anne-Sophie Banneville

THÈSE

Pour obtenir le grade de

DOCTEUR DE L'UNIVERSITÉ GRENOBLE ALPES

Spécialité : Biologie Structurale et Nanobiologie

Arrêté ministériel : 25 mai 2016

Présentée par

Anne-Sophie BANNEVILLE

Thèse dirigée par **JOANNA TIMMINS**, Université Grenoble Alpes

préparée au sein du **Laboratoire Institut de Biologie Structurale** dans **l'École Doctorale Chimie et Sciences du Vivant**

Caractérisations structurale et fonctionnelle des protéines associées aux nucléoïdes de Deinococcus radiodurans et Deinococcus deserti

Structural and functional characterization of nucleoid associated proteins of Deinococcus radiodurans and Deinococcus deserti

Thèse soutenue publiquement le **14 septembre 2021**, devant le jury composé de :

Madame Joanna TIMMINS
DIRECTRICE DE RECHERCHE, CNRS délégation Alpes, Directrice de thèse
Monsieur Fabrice CONFALONIERI
PROFESSEUR DES UNIVERSITES, Université Paris-Saclay, Rapporteur
Madame Cendrine FAIVRE-MOSKALENKO
MAITRE DE CONFERENCES HDR, Ecole Normale Supérieure de Lyon, Rapporteure
Madame Ingrid TESSMER
PROFESSEUR ASSISTANT, Julius-Maximilians-Universität Würzburg , Examinatrice
Monsieur Sam MEYER
MAITRE DE CONFERENCE, Université Claude Bernard-Lyon 1, Examinateur
Madame Chloé ZUBIETA
DIRECTRICE DE RECHERCHE, CNRS délégation Alpes, Présidente

Remerciements

Je tiens tout d'abord à remercier ma directrice de thèse Joanna Timmins, sans qui cette thèse n'aurait pas eu lieu. Merci de m'avoir confié ce sujet si complexe et intéressant qui m'a permis d'appréhender plusieurs des nombreuses techniques mises en œuvre en biologie structurale intégrative. Je te remercie pour ton encadrement et ton soutien, ainsi que pour ta patience et ta compréhension durant les périodes difficiles de cette thèse. Tes conseils avisés au fil des ans et ton incitation constante à faire preuve de plus d'autonomie et d'esprit d'initiative m'auront permis d'avancer tant sur le plan scientifique que personnel.

Je remercie Mme Cendrine Faivre-Moskalenko et M. Fabrice Confalonieri pour avoir accepté d'être les rapporteurs de mon manuscrit de thèse, ainsi que Mme Cholé Zubieta, Mme Ingrid Tessmer et M. Sam Meyer d'avoir bien voulu évaluer mes travaux de thèse en tant qu'examinateurs.

Je remercie aussi le CEA qui a financé ce sujet de thèse et a bien voulu nous offrir plus de temps en m'accordant deux prolongations pour compléter mes travaux.

Je n'aurais pas eu tant de résultats intéressants dans cette thèse sans l'aide précieuse et l'implication enthousiaste de nos collaborateurs que je souhaite remercier ici. Un grand merci à Jean-Luc Pellequer, Jean-Marie Teulon et Wendy Chen pour m'avoir fait découvrir et aimé la microscopie à force atomique. Nos longues journées devant l'ordinateur et nos discussions sur des sujets plus que variés me manqueront grandement… Merci à Irina Gutsche et Maria Bacia qui ont menés les études par microscopie électronique pour votre enthousiasme devant les échantillons et l'attention que vous avez portée à ce projet malgré les écueils parfois rencontrés. Je vous souhaite une belle réussite pour la poursuite des études de HU dans les pains-aux-raisins et les pelotes de laine ! Un merci également à nos collaborateurs en dynamique moléculaire, François Dehez, Antonio Monari et Cécilia Hognon, qui se sont investis sur ce projet et nous ont permis de lever un peu plus le voile sur le mystère de ma chère DdrC. Mon intérêt pour cette dernière n'aurait pu se développer sans l'aide de nos collaborateurs parisiens de l'I2BC, pionniers de l'étude de DdrC, Claire Bouthier de la Tour, Pascale Servant, Suzanne Sommer et Fabrice Confalonieri. Enfin, je tiens à remercier Aline Le Roy et Christine Ebel pour les expériences de SEC-MALLS et d'ultracentrifugation analytique conduites sur la plateforme PAOL de l'IBS.

Un merci tout particulier aux membres de mon comité de thèse, Irina Gutsche, Jean-Luc Pellequer et William Nasser qui rendaient cet exercice annuel agréable et riche de discussions. Merci encore pour votre humanité et votre empathie, votre soutien m'aura été plus qu'utile pour avancer dans la thèse.

À toute l'équipe GenOM et l'équipe EPIGEN, merci pour votre accueil chaleureux et bienveillant dans ce petit coin du 4ème étage. Merci à Isabel Garcia-Saez, Fabienne Hans, Marjolaine Noirclerc-Savoye, Laura Belot, Pierre Vauclare, Carlo Petosa, Rose-Laure Indorato et Salvatore De Bonis pour leur aide et leur bonne humeur au laboratoire comme au coin café.

Une pensée spéciale pour mes colocataires du bureau des étudiants, Anna Seck, Kaiyao Wei et Hasan Dawi, merci pour tous ces bons moments passés ensemble ! Anna, cette thèse n'aurait pas été aussi agréable sans ta bonne humeur constante, ton sourire et ton amitié ! Merci à Kaiyao pour nos discussions en toute franchise et à Hasan pour nos échanges divers et variés sur la gastronomie, les mangas, la famille (parfois la thèse) et tant d'autres choses.

Je souhaite terminer ces remerciements en exprimant toute ma reconnaissance à mes proches, qui m'ont assuré un soutien sans faille durant les 3 années (et demie) du long chemin de la thèse. Merci à ma mère, mon père, ma Chachou et Tiftif, qui m'ont toujours entouré de leur amour et de leur confiance quelles que soient les difficultés rencontrées et m'ont remonté le moral (et parfois les bretelles…) lorsque je perdais mon chemin.

Enfin, je remercie mon compagnon Jacques-Philippe pour m'avoir d'abord amené sur le chemin de la thèse (que je n'aurais pas envisagé sans lui) et pour m'avoir continuellement poussé à donner le meilleur de moi-même et à me dépasser face aux obstacles rencontrés, fusse dans le travail ou dans notre vie quotidienne. Je suis heureuse de partager ma vie et de construire notre futur avec toi, merci pour toutes ces années d'aventure et pour toutes celles à venir !

Pour finir en beauté (et en douceur), mille mercis à ma petite Alexandra qui m'a appris que les grasses matinées étaient un concept abstrait et désuet, et à qui je dédie cette thèse. Tu m'auras montré que le plus grand et le plus simple des bonheurs est de voir sourire ceux qu'on aime.

Alors, sans avoir rien que la force d'aimer,

Nous aurons dans nos mains, Amie,

Le monde entier !

Jacques Brel - Quand on n'a que l'amour

Table of Contents

List of abbreviations

4WJ	Four-way junction
AFM	Atomic force microscopy
ATP	Adenosine triphosphate
AUC	Analytical ultracentrifugation
BER	Base excision repair
BS3	bis-sulfosuccinimidyl suberate
BSA	bovine serum albumin
CET	cryo-electron tomography
CID	Chromosomal interaction domains
CRP	Cyclic AMP receptor protein
cryo-EM	Cryo-electron microscopy
CTD	C-terminal domain
CTP	Cytosine triphosphate
CV	column volume
Ddr	DNA-damage response
DNA	Deoxyribonucleic acid
Dps	DNA protection during starvation
ds	Double-stranded
DSBR	Double-strand break repair
DTT	dithiothreitol
EDTA	Ethylene diamine tetra-acetic acid
EM	Electron microscopy
EMSA	electrophoretic mobility shift assays
ESDSA	Extended synthesis-dependent strand-annealing
Fis	Factor for inversion stimulation
FP	Fluorescence polarization
FRET	Fluorescence resonance energy transfer
G-segment	Gate-segment
GHKL	Gyrb-Hsp90-histidine kinase-mutl
H-NS	Histone-like nucleoid-structuring protein
HDR	High-density chromosomal regions
HTH	Helix-turn-helix motif
HU	Heat-stable protein from *E. Coli* strain U93
IHF	Integration host factor
IrrE	Ionizing radiation-sensitive protein E
L	Linear
LB	Luria broth

MALLS	multi-angle laser light scattering
MD	Molecular dynamic
MMR	Mismatch repair
NAPs	Nucleoid associated proteins
NER	Nucleotide excision repair
NMR	nuclear magnetic resonance
NTD	N-terminal domain
PAGE	polyacrylamide gel electrophoresis
Par	Partitioning protein
PCR	polymerase chain reaction
PDB	Protein data bank
PEG	Polyethylene glycol
pI	Isoelectric point
Pol	DNA polymerase
R	Relaxed
RDR	Radiation-desiccation response
RDRM	Radiation-desiccation response motif
Rec	Recombinase
ROS	Reactive oxygen species
sbNAP	Small basic nucleoid associated proteins
SC	Supercoiled
Scp	Segregation and condensation protein
SDS	sodium dodecyl sulfate
SEC	Size-exclusion chromatography
SeMet	selenomethionine
Smc	Structural maintenance of chromosomes
ss	Single-stranded
SSB	Single-stranded DNA-binding protein
StpA	Suppressor of *td*$^{-}$ phenotype A
T-segment	Transported-segment
TEM	transmission-EM
TEV	tobacco etch virus
Topo	Topoisomerase
TOPRIM	Topoisomerase-primase
UTR	5' untranslated region
UV	Ultraviolet
WHD	Winged-helix domain
XRE	Xenobiotic response element
β-ME	β-mercaptoethanol

List of figures

Introduction

Materials and Methods

Results

List of tables

Introduction

I. *Deinococcus radiodurans* and *Deinococcus deserti*

I.1. The *Deinococcus* genus

Bacteria belonging to the *Deinococcus* genus are mostly well-known for their outstanding resistance to DNA-damaging agents such as ionizing radiation, UV-light or desiccation. As of today, according to the list of validly published names from the List of Prokaryotic names with Standing in Nomenclature (https://lpsn.dsmz.de/genus/deinococcus) more than 80 species of *Deinococcus* have been isolated (Table 1). This large family includes mesophilic, thermophilic and cryophilic bacteria that were discovered all over the world in various natural habitats like air, river water and sediments, hot springs, soil from mountains, deserts, radiation-polluted area and even Antarctica. Some species have also been found in animal meat, intestines, feces or skin, while others were discovered in unexpected places such as the air-conditioning system of a car or textiles and air from laboratory cleanrooms. All species of *Deinococcus* are aerobic, non-spore-forming and non-motile, with the exception of the motile species *Deinococcus multiflagellatus* (Kim et al., 2018). These bacteria mostly stain as gram-positive, with only one-third of the species that stains as gram-negative. As for the cell shape, there are nearly as many cocci as there are rod-shaped cells, and all species display a pink, red or orange pigmentation when grown as colonies on solid media, except for *Deinococcus deserti* whose colonies are whitish (de Groot et al., 2005).

Table 1. Diversity of the *Deinococcus* genus. List of some of the validly published species of the genus *Deinococcus* based on the LSPN database (https://lpsn.dsmz.de/genus/deinococcus) and their physical characteristics. The complete list of the validly published *Deinococcus* species is presented in Table S1.

***Deinococcus* species (reference)**	**(First) Site(s) of Isolation**	**Gram**	**Cell shape**	**Pigmentation**
Deinococcus aetherius (Yang et al. 2010)	Stratosphere, Japan	+	coccus	pink to red
Deinococcus apachensis (Rainey and da Costa 2005)	Irradiated Sonoran desert soil, AZ, USA	+	coccus	pink
Deinococcus arenae (Lee et al. 2016)	Sand, South Korea	-	rod	red
Deinococcus citri (Ahmed et al. 2014)	Citrus canker lesions, Islamabad, Pakistan	+	coccus	pink to red
Deinococcus deserti (de Groot et al. 2005)	Sahara desert sand	-	rod	whitish
Deinococcus geothermalis (Ferreira et al. 1997)	Hot spring, Italy and Portugal	+	coccus	orange
Deinococcus hopiensis (Rainey and da Costa 2005)	Irradiated Sonoran desert soil, AZ, USA	+	coccus	pink
Deinococcus koreensis (Baek et al. 2018)	Freshwater, Seomjin River, South Korea	-	rod	pink
Deinococcus murrayi (Ferreira et al. 1997)	Hot springs, Portugal	+	coccus	orange
Deinococcus petrolearius (Xi et al. 2017)	Crude oil recovery water, China	+	coccus	red
Deinococcus swuensis (Lee et al. 2013)	Mountain soil, South Korea	+	coccus	pink
Deinococcus taklimakanensis (Liu et al. 2017)	Taklimakan desert in Xinjiang, China	-	rod	light-pink
Deinococcus yavapaiensis (Rainey and da Costa 2005)	Irradiated Sonoran desert soil, AZ, USA	+	rod	red
Deinococcus yunweiensis (Zhang et al. 2007)	Contaminant on an agar plate, China	-	rod	red

I.2. Principal features of *D. radiodurans* and *D. deserti*

Deinococcus radiodurans was the first of the *Deinococcus* species to be discovered and is therefore the most well-known and has been the most extensively studied. It was discovered in 1956, when food microbiologists in Oregon submitted a can of meat to a supposedly sterilizing dose of radiation. Much to their surprise, the food was spoiled and from the remains they were able to isolate a new bacterial species, which was named *Micrococcus radiodurans* (Anderson et al., 1956). In 1981, *M. radiodurans* was excluded from the genus *Micrococcus* and reassigned to a new family, the *Deinococcaceae* based on the structures of its cell wall, its lipid constituents and radiation resistance properties, along with 16S ribosomal RNA analysis (Brooks & Murray, 1981). The bacterium was thus renamed *Deinococcus radiodurans*, meaning "strange berry that endures radiation". In addition to its high resistance to γ-radiation, *D. radiodurans* is also able to withstand UV-light or desiccation (Battista, 1997; Cox & Battista, 2005). Since its first discovery, *D. radiodurans* has been found worldwide in more or less hostile environments such as ground meat, hides and hair of live cows, creek water, sawdust, air from laboratory cleanrooms and even clothes (Christensen & Kristensen, 1981; Ito, 1977; Krabbenhoft et al., 1965; Kristensen & Christensen, 1981).

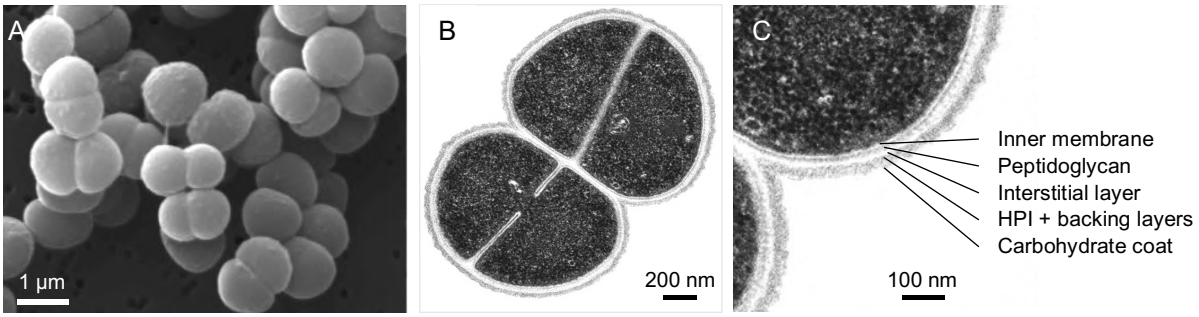

Figure 1. Morphology of *D. radiodurans* cells and their peculiar cell wall. A) Dyads and tetrads of *D. radiodurans* observed by scanning electron microscopy. **B**) Transmission electron micrograph of a slice through a *D. radiodurans* tetrad and **C**) magnification of (B) highlighting the different layers of the cell wall. Adapted from (Ott et al., 2020; Rothfuss et al., 2006).

D. radiodurans is a non-motile, non-pathogenic, spherical bacterium that grows as tetrads or dyads (Fig. 1A-B), with a mean size of 2 µm in diameter (Floc'h et al., 2019). *D. radiodurans* is an aerobic mesophile with an optimal growth temperature at 30°C, although it can survive to temperatures ranging from 4°C to 45°C. The colonies display a pink to red color due to the presence of several carotenoids (in particular deinoxanthin) in the cell wall (Carbonneau et al., 1989). Although it stains as gram-positive, *D. radiodurans* possesses a

complex cell wall reminiscent of gram-negative bacteria (Farci et al., 2014; Lancy & Murray, 1978; Work & Griffiths, 1968). Its envelope is composed of five layers, for a total thickness of 75 nm (Fig. 1C).

During exponential growth, cell division occurs by the formation of a new septum (S_2) in an orthogonal plane with respect to the pre-existing septum (S_1). Thus, dyads of *D. radiodurans* progressively divide into tetrads through six phases (Floc'h et al., 2019). At the beginning of the cell cycle, an elliptical dyad (Phase 1) undergoes cell growth along with a slight invagination of the cell wall contiguous to S_1 (Phase 2). Phase 3 is characterized by the start of S_2 growth, which continues (Phase 4) until it is almost closed (Phase 5). At phase 6, the new S_2 septum is completely closed and the cell now forms a tetrad, that will separate into two dyads to continue a new cycle. In their study of *D. radiodurans*' cell cycle, Floc'h et al. observed that the increase of cell volume is constant during the 6 phases. When *D. radiodurans* cells shift to stationary phase, the newly formed tetrad does not separate into dyads. Moreover, some of the tetrads initiate the growth of new septa leading to the formation of octads, which explain the presence of both tetrads and octads in stationary phase cell cultures.

The genomic DNA of *D. radiodurans* is composed of two chromosomes of respectively 2,648.6 kbp and 412.4 kbp, a mega-plasmid of 177.5 kbp, and a smaller plasmid of 45.7 kbp for a total of 3.28 Mbp (White et al., 1999). The genome encodes for 3,187 proteins and displays a high GC content of 66.8%, characteristic of deinococcal genomes for which the GC content varies from 60% to 70% (Battista, 2016; White et al., 1999). Depending on the growth phase and the culture medium, it is present in 4 to 10 copies per cell (Driedger, 1970; Hansen, 1978; Harsojo et al., 1981). *D. radiodurans*' genome is highly compact, yet it remains dynamic and adopts different conformations in exponential growth phase as the cells progress through their cell cycle (Fig. 2A), adopting a ring-like structure in the early phases and more elongated and branched-shaped structures at the later stages preceding cytokinesis (Floc'h et al., 2019; Levin-Zaidman et al., 2003). Despite its complexity and multiplicity, the DNA of *D. radiodurans* is so tightly compacted that it only occupies 30% to 35% of the cell volume in exponentially growing cells and only 20% in stationary cells (Fig. 2B), whereas in the model bacterium *Escherichia coli* (Fig. 2C), the genomic DNA occupies typically 65% of the cell volume (Floc'h et al., 2019).

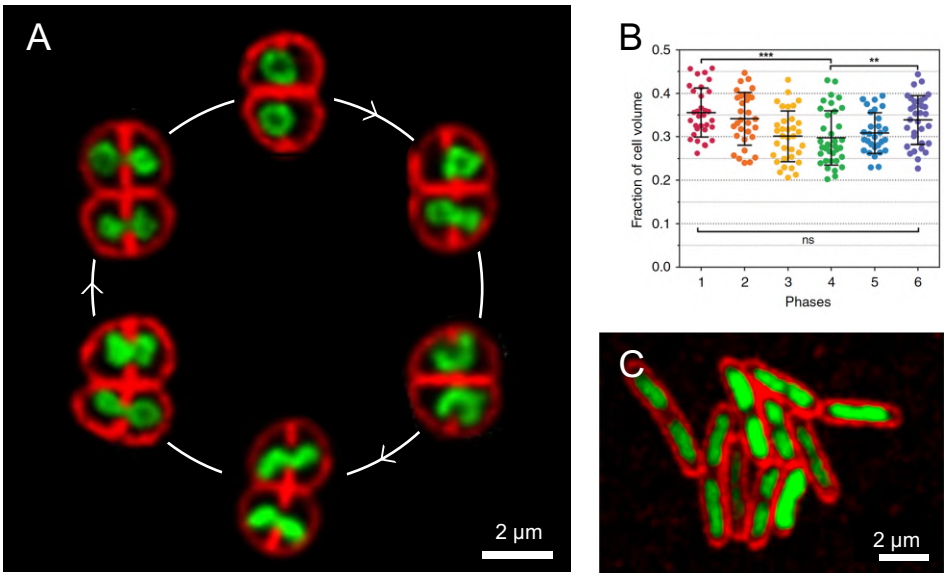

Figure 2. The nucleoid of *D. radiodurans* is dynamic and adopts various yet highly compact shapes throughout the cell cycle. A) Representation of the cell cycle of *D. radiodurans*, during which the nucleoid remains compact despite adopting a diversity of shapes (toroid, square, crescent, rod, branched and double rings). Cells used in this representation are unrelated and were placed in this order based on the phase of their cell cycle. **B**) Fraction of cell volume occupied by the nucleoid of *D. radiodurans* along the different phases of the cell cycle. Data are shown as mean with standard deviations, and dots represents individual values. **C**) *E. coli* cells growing in exponential phase displaying a diffuse nucleoid that occupies a large fraction of the cell. In panels A and C, membranes (in red) and DNA (in green) were stained with Nile Red and Syto9, respectively. Adapted from (Floc'h et al., 2019).

Almost fifty years after the discovery of *D. radiodurans*, *Deinococcus deserti* was isolated from gamma-irradiated sand samples from the Sahara desert (de Groot et al., 2005). Unlike *D. radiodurans, D. deserti* is a gram-negative non-pigmented rod-shaped bacterium that usually grows as dyads (Table 2). It grows at temperatures ranging from 23°C to 37°C but not on rich media (de Groot et al., 2005). The genome of *D. deserti* presents some similarities with that of *D. radiodurans*: it is present in at least two copies per cell and is composed of four replicons (Table 2). This comprises a chromosome of 2,819.8 kbp and three plasmids (P1, P2 and P3) of 324.7 kbp, 314.3 kbp, and 396.5 kbp respectively, for a total of 3.85 Mbp (de Groot et al., 2009). The genome contains 3,455 open reading frames and the GC content of the DNA is of 63%, close to that of *D. radiodurans.*

Table 2. General features of *D. radiodurans* and *D. deserti*. Comparison of *D. radiodurans* and *D. deserti* based on their environmental and physiological characteristics. Adapted from (Brooks & Murray, 1981; de Groot et al., 2005, 2009; White et al., 1999).

Species	***D. radiodurans***	***D. deserti***
Habitat(s)	Gamma-irradiated canned meat	Sahara Desert sand
	Ground meat	
	Hides and hair of live beefs	
	Creek water	
	Sawdust	
	Air from cleanroom	
	Textiles	
Morphology		
Gram-staining	+	-
Cell shape	coccus	rod
Pigmentation	pink	whitish
Mn/Fe ratio in 10-TSB	0.16	0.54
Genome characteristics		
Number of copies per cell	4 to 10	2
Genome size		
Replicon 1 (kbp)	2,648.6	2,819.8
Replicon 2 (kbp)	412.4	324.7
Replicon 3 (kbp)	177.5	314.3
Replicon 4 (kbp)	45.7	396.5
Total (kbp)	3,284.2	3,855.3
GC content	66.8%	63.0%
Open reading frames	3,187	3,455

Little is known regarding the extent of compaction of genomic DNA in *D. deserti*. In their proteomic and genomic study published in 2009, De Groot *et al.* stated that "*D. deserti* (results not shown), like other radioresistant bacteria, has a highly condensed nucleoid" (de Groot et al., 2009). However, this observation could not be reproduced in our lab, where we observed a relatively diffuse nucleoid in *D. deserti* when using confocal fluorescence microscopy (Fig. 3).

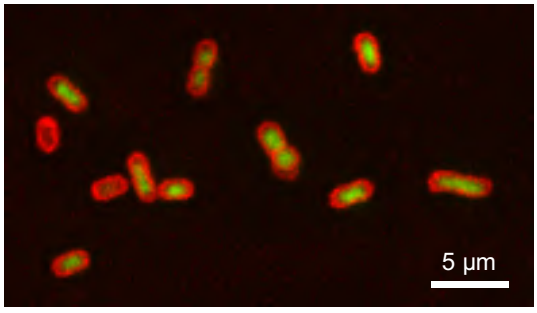

Figure 3. The nucleoid of *D. deserti* does not adopt a compact organization. *D. deserti* cells observed by spinning-disk confocal microscopy. Cell membranes stained with Nile Red appear in red and DNA stained with Syto9 appears in green. Image acquired in our laboratory by my colleague, Françoise Lacroix.

I.3. Resistance to DNA-damaging agents

The most distinctive feature of *D. radiodurans* is its outstanding resistance to several DNA-damaging agents such as ionizing radiation, UV-light and desiccation (Fig. 4A). These conditions greatly damage DNA causing the genome to be shattered into thousands of fragments due to single- or double-strand breaks and to accumulate thousands of base damages. However, when exposed to a dose of 7 kGy of gamma radiation, *D. radiodurans* is able to completely reconstitute its fragmented genome (Fig. 4B) in only 4.5 hours (Slade & Radman, 2011; Zahradka et al., 2006). This extreme resistance most likely results from several mechanisms, which together maintain proteome and DNA integrity, including (i) a remarkable antioxidant system based on both enzymatic and non-enzymatic scavengers of reactive oxygen species (ROS), (ii) a conserved yet highly efficient DNA repair system and (iii) a highly compact nucleoid composed of multiple copies of the genome that provide a template for homologous recombination while preventing dispersion of DNA fragments, thus easing DNA repair processes.

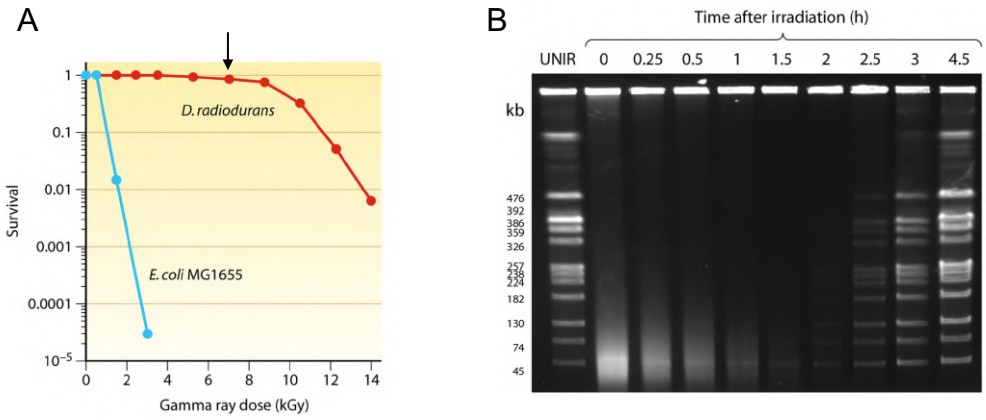

Figure 4. *D. radiodurans* is resistant to ionizing radiation and able to reconstitute its shattered genome in less than 5 hours. A) Survival rate of *D. radiodurans* and *E. coli* strain MG1655 exposed to increasing doses of gamma radiation. The dose corresponding to a 10% survival rate (D_{10}) is close to 12 kGy for *D. radiodurans* whereas that of the radio-sensitive *E. coli* is ~1 kGy. The arrow highlights the survival rate of *D. radiodurans* at a dose of 7 kGy. **B**) DNA was extracted from *D. radiodurans* cells before (lane "UNIR") and after (lanes "0" to "4.5") irradiation with a dose of 7 kGy and digested with the NotI restriction enzyme. The unirradiated digested DNA yields 12 characteristic DNA fragments that were completely reconstituted 4.5 hours after irradiation. Adapted from (Slade & Radman, 2011).

Desiccation and ionizing radiation produce ROS, which in addition to being harmful for DNA can also damage proteins and cellular membranes (Du & Gebicki, 2004; Mitchel, 1975, 1976). The antioxidant defense system of *D. radiodurans* relies mostly on its high intracellular manganese/iron (Mn/Fe) ratio of 0.24, that seems to be a common trait shared by several radio-

resistant bacteria. For instance, the radio-resistant species *Lactobacillus plantarum*, *Kineococcus radiotolerans*, *Enterococcus faecium*, *Rubrobacter xylanophilus* and *Rubrobacter radiotolerans* (Archibald, 1986; Bagwell et al., 2008; Daly et al., 2004; Webb & DiRuggiero, 2012) have a high intracellular Mn/Fe ratio compared to radio-sensitive bacteria like *Escherichia coli*, *Shewanella oneidensis* or *Pseudomonas putida* (Daly et al., 2004, 2010). In cells, iron ions are a liability when it comes to ROS. Superoxide radicals (O_2^-•) and hydrogen peroxide (H_2O_2) mostly affect proteins containing iron-sulfur clusters (Flint et al., 1993; Imlay, 2008), subsequently releasing free Fe^{2+} ions in the cytosol (Imlay, 2006). These released Fe^{2+} ions can interact with H_2O_2 in the Fenton reaction to produce •OH hydroxyl radicals, which are the most deleterious ROS since they react strongly with all proteins, but also with DNA and lipids. Unlike Fe^{2+}, manganese ions (Mn^{2+}) do not engage in the Fenton reaction. Moreover, Mn^{2+} in complex with small molecules such as orthophosphate, nucleosides or peptides, are great scavengers of H_2O_2, •OH and O_2^-• (Archibald & Fridovich, 1982; Barnese et al., 2008; Berlett et al., 1990; Daly et al., 2010). Hence an increased intracellular Mn/Fe ratio contributes to a more antioxidant environment inside the cell. The various carotenoids of *D. radiodurans* also actively take part in the scavenging of ROS, as they are active against the three primary species, H_2O_2, •OH and O_2^-• (Xu et al., 2007; Zhang et al., 2007). Notably, among the carotenoids produced by *D. radiodurans*, the *Deinococcus* specific deinoxanthin is an extremely efficient scavenger of ROS, even more so than other carotenoids such as lycopene and β-carotene (Tian et al., 2007). The antioxidant activity of *D. radiodurans* is also sustained by the expression of several variants of enzymes involved in antioxidant activity. The cell produces three catalases, four superoxide dismutases and two peroxidases (Lipton et al., 2002; Makarova et al., 2001; Markillie et al., 1999). The superoxide dismutase removes O_2^-• thereby producing oxygen and H_2O_2, which is then reduced to H_2O and oxygen by the catalase and peroxidase enzymes. When compared to the model bacterium *E. coli*, the constitutive enzymatic activity of catalase and superoxide dismutase in *D. radiodurans* are ~15 and ~4 times higher respectively (Tian et al., 2004).

By scavenging ROS efficiently by both enzymatic and non-enzymatic means, the cell is able to protect its proteome when exposed to environmental stresses. More specifically, the integrity of the proteins involved in the DNA repair system is of utmost importance to survive the DNA damaging conditions. The DNA repair machinery of *D. radiodurans* consists of the conserved and classical repair pathways found in most bacteria: the base excision repair (BER), nucleotide excision repair (NER), mismatch repair (MMR) and double-strand break repair

(DSBR) pathways. In *D. radiodurans*, the reassembly of broken DNA is mediated by the Extended Synthesis-Dependent Strand-Annealing (ESDSA) pathway. This pathway is initiated by the processing of the broken dsDNA ends by the helicase UvrD and the 5' → 3' exonuclease RecJ to produce ssDNA, onto which RecA is loaded via the RecFOR system. After a RecA-mediated search for an intact homologous template, the RecA-bound ssDNA induces the formation of a D-loop due to strand invasion of the intact dsDNA. The next step relies on the DNA polymerases PolIII and PolI for the synthesis of new DNA fragments, initiated by PolIII and elongated by PolIII and/or PolI. This process produces long ssDNA fragments (hence the term "extended"), which after dissociation from the template can anneal with complementary strands. Finally, the remaining gaps are filled by PolI and joined by the DNA ligase. Interestingly, the DNA repair system of *D. radiodurans* lacks widespread DNA repair proteins such as photolyases, translesion polymerases or recombinases RecB and RecC. Photolyases (PhrB in *E. coli*) are enzymes using photoreactivation to process pyrimidine dimers induced by UV-light. In the absence of a photolyase, pyrimidine dimers are repaired via the NER and/or the UvsE-dependent excision repair pathways in *D. radiodurans*.

The efficiency of the DNA repair machinery of *D. radiodurans* lies both at a genomic level, with the expression of multiple variants, and at the protein level with enhanced enzymatic activities, and broader substrate specificities (Leiros et al., 2005; Pedersen et al., 2015; Timmins & Moe, 2016). The proteins involved in the BER pathway are quite representative of this strategy, since the genome of *D. radiodurans* encodes for eleven DNA glycosylases, among which three Endonuclease III variants, two uracil-DNA glycosylases and two 3-methyladenine DNA glycosylase II, drAlkA1 and drAlkA2 (Makarova et al., 2001). The latter displays a broader substrate specificity that might compensate for the absence of a DNA dioxygenase (Moe et al., 2012). Furthermore, some proteins have different functions or properties compared to their homologues in model bacteria. The DNA helicase UvrD from *D. radiodurans* (drUvrD) is involved in NER along with the UvrABC system as in other bacteria, but is also involved in MMR and in DSBR where it is responsible for processing double-strand break ends. Interestingly, contrary to its homologue in *E. coli*, drUvrD displays a bipolar DNA helicase activity and is thus able to unwind DNA duplexes in both directions 5' → 3' and 3' → 5', which may explain its pleiotropic functions (Stelter et al., 2013).

In response to DNA damage, *D. radiodurans* also increases its DNA degradation activity to eliminate the DNA fragments produced by the processing of DSB DNA ends by exonucleases like RecJ and the removal of damaged bases by the BER pathway (Hariharan &

Cerutti, 1971; Hariharan & Cerutti, 1972). This damaged DNA is further exported outside the cell to prevent its reintegration in the newly synthesized DNA, thus reducing mutagenesis after DNA repair (Vukovic-Nagy et al., 1974).

The processing of damaged DNA in *D. radiodurans* is thus performed by an efficient DNA repair system, which is protected from ROS by a robust antioxidant environment. But it is also facilitated by two characteristics of its genome, which are (i) multiplicity and (ii) compactness. This is particularly true for the processing of DSB, which are repaired via homologous recombination and therefore require a non-damaged DNA template with sequence homology. Having 4 to 10 copies of the genome per cell ensures that there is always at least one non-damaged homologous DNA fragment to serve as a template for DNA synthesis. The second important feature of *D. radiodurans'* genomic DNA is its compact organization maintained in both stationary and exponential growth phases (Floc'h et al., 2019; Levin-Zaidman et al., 2003). This high degree of compaction could limit the diffusion of DNA fragments generated by DSB and protect DNA bases and nucleotides from oxidation by ROS produced by radiation (Levin-Zaidman et al., 2003). It was also proposed that the specific toroid shape of the genome might be linked to radio-resistance (Eltsov & Dubochet, 2005). However, in a study published in 2005, Zimmerman and Battista observed that several radio-resistant *Deinococcus* species such as *D. radiopugnans* and *D. geothermalis* do not exhibit ring-shaped genomes (Zimmerman & Battista, 2005). Despite their lack of a defined ring-shaped structure, the nucleoids of these two bacteria yet appeared more condensed than that of the radio-sensitive *E. coli*. These results thus suggest that the level of compaction of the genome in species from the *Deinococcus* genus has a greater impact on their extreme radio-resistance than the specific toroid shape observed for some of them.

As a member of the *Deinococcus* genus, *D. deserti* is also highly resistant to gamma (Fig. 5A) and UV radiation and to desiccation (de Groot et al., 2005, 2009). When exposed to 6.8 kGy of gamma radiation (Fig. 5B) or 27 days of desiccation, it is able to reconstitute its genome in 8h and 6h respectively (de Groot et al., 2009). Compared to *D. radiodurans*, *D. deserti* is less resistant to UV and gamma radiation, but more resistant to desiccation (de Groot et al., 2009). Its resistance to DNA-damaging agents most likely relies on similar mechanisms as described for *D. radiodurans*, namely the scavenging of ROS to protect the proteome, a classic yet efficient DNA repair system and multiple copies of its genome.

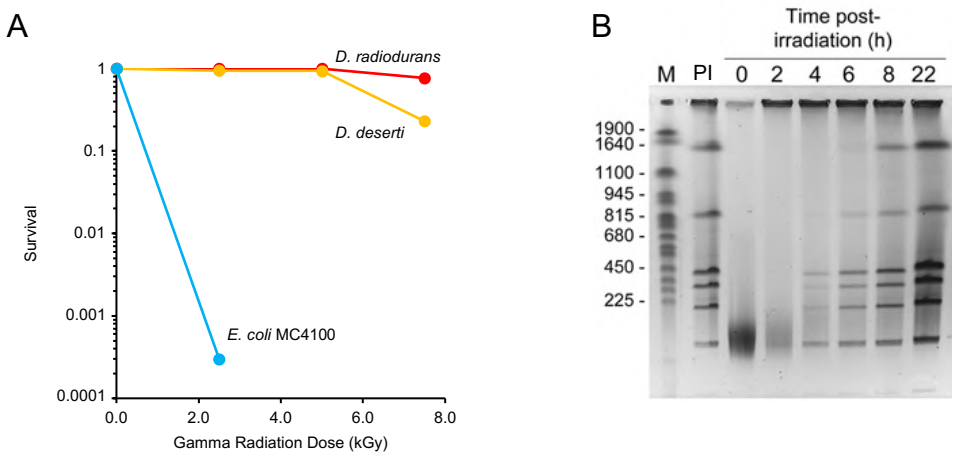

Figure 5. *D. deserti* is resistant to ionizing radiation and able to reconstitute its shattered genome in 8 hours. **A**) Survival rate of *D. deserti*, *D. radiodurans* and *E. coli* strain MC4100 exposed to increasing doses of gamma radiation. The D_{10} has a value above 7.5 kGy for *D. deserti* whereas that of the radio-sensitive bacteria *E. coli* has a value of ~1 kGy. **B**) DNA was extracted from *D. deserti* cells before (lane "PI") and after (lanes "0" to "22") irradiation with a dose of 6.8 kGy and digested with the PmeI and SwaI restriction enzymes. The unirradiated digested DNA yielded 8 fragments that were completely reconstituted 8 hours after irradiation. Adapted from (de Groot et al., 2009)**.**

Regarding scavenging of ROS, *D. deserti* has a higher Mn/Fe ratio than *D. radiodurans*, which could result from the expression of more manganese ABC transporters (Baudet et al., 2009). Their DNA repair systems are quite similar, as they both express several variants of certain DNA repair proteins, although with notable differences between the two species. *D. deserti* produces two recombinase A proteins ($RecA_p$ and $RecA_c$) and two ε-subunits of the DNA polymerase III (DnaQ, coded by Deide_17790 and Deide_05970 genes), contrary to *D. radiodurans* that only expresses one variant of each of these proteins (de Groot et al., 2009). Furthermore, *D. deserti* expresses three error-prone translesion synthesis polymerases (PolB, ImuY and DnaE2) and a putative DNA-repair photolyase (Deide_3p02150 gene), which are completely absent from *D. radiodurans*' genome (de Groot et al., 2009; Dulermo et al., 2009). At the genomic level, as previously observed (Fig. 3), the genome of *D. deserti* is not as condensed as that of *D. radiodurans*, and it has only been reported to be found in two copies, compared to at least 4 in *D. radiodurans*. The genome organization may thus contribute less to the radio-resistance phenotype in *D. deserti* than in *D. radiodurans*.

I.4. The Radiation-Desiccation Response

In response to DNA damage, many bacteria activate an SOS response system that upregulates genes involved in DNA repair pathways. This SOS response system is widely spread among various phylogenetic groups and can be found in several gram-negative and gram-positive bacteria (Erill et al., 2007). It involves a transcriptional repressor, LexA, which binds to a specific DNA sequence, the LexA-box, upstream of the regulated genes (Walker, 1984). The LexA-mediated repression is countered by the activated ATP-bound RecA, which lowers LexA affinity for DNA and promotes the self-cleavage of LexA (Walker, 1984). The recruitment of RecA is triggered by the accumulation of ssDNA caused by DNA damage, that serve as nucleation sites for the formation of ATP-bound RecA filaments (Alekseev et al., 2020).

However, *D. radiodurans* and *D. deserti* lack a SOS system and possess instead a different stress response mechanism called the radiation-desiccation response (RDR) system (Fig. 6C) that induces an increased expression of several DNA repair and *Deinococcus*-specific proteins (Blanchard et al., 2017; de Groot et al., 2019). The components of the RDR system are similar to those of the SOS system, with a transcriptional repressor (DdrO) bound to a conserved RDR motif (RDRM) in the promoter region of the regulated genes and a counteracting protein (the metalloprotease IrrE) that cleaves DdrO in response to stress thereby relieving the repression of transcription (Devigne et al., 2015; Ludanyi et al., 2014). The repressor DdrO, its binding site RDRM, and the protease IrrE are well conserved among the *Deinococcus* species, according to genomics studies (Blanchard et al., 2017; de Groot et al., 2009; Lim et al., 2019; Makarova et al., 2007). The set of genes regulated by the RDR system differs among the *Deinococcus* species, as a regulated gene could either be absent from another species or not possess a RDRM in its promoter region (Blanchard et al., 2017). However, according to a genomic analysis comparing seven completely assembled *Deinococcus* genomes, a set of conserved genes preceded by a RDRM could be defined (Blanchard et al., 2017). The consensus RDR regulon includes ten genes: *ddrO*, *ddrB*, *ddrC*, *recA*, *ssb*, *gyrA*, *gyrB*, *ruvB*, *uvrA* and *uvrB*. In addition to this conserved RDR regulon, *D. radiodurans* and *D. deserti* share additional RDR regulated genes: the *Deinococcus*-specific genes *ddrA*, *ddrD*, *ddrR* and *pprA*, along with the helicases *recD*, *recQ* and *uvrD* (Blanchard et al., 2017). Interestingly, the transcriptional repressor DdrO is also under control of the RDR system. This implies that under activation of the RDR system, DdrO accumulates in the cell so that, when

the stress is alleviated and IrrE is no longer active, the protein can once again repress the RDR regulon.

The RDRM found upstream of the RDR-regulated genes is a 17 bp palindromic motif whose sequence is not entirely conserved: TT($^{A}/_{C}$)($^{T}/_{C}$)G($^{T}/_{C}$)NN($^{T}/_{A}$)N($^{A}/_{G}$)($^{A}/_{G}$)C($^{G}/_{A}$)($^{T}/_{G}$)AA. The most conserved nucleotides are the thymine and adenine base pairs at the 5' and 3' ends of the sequence, as well as the guanine and cytosine bases in 5th and 13th position, respectively (Makarova et al., 2007). In their recent study of the RDRM, Anaganti et al. constructed several variants to dissect the role of the sequence conservation. It appeared that the 5th guanine and 13th cytosine are essential for binding of DdrO to the motif and, surprisingly, that the 5 bp at the 5' end possess the ability to enhance promoter activity in the absence of DdrO (Anaganti et al., 2017). In an earlier study on the genome of *D. deserti*, it was shown that the RDRM position in the promoter region ranges from 50 bp upstream to 20 bp downstream of the transcription start site (TSS) of the regulated genes (de Groot et al., 2014). Since this region corresponds to the binding site of the RNA polymerase, it was proposed that the RDRM-bound DdrO creates a steric hindrance that prevents the fixation of the RNA polymerase leading to the repression of transcription. This hypothesis was confirmed in the work by Anaganti et al., who designed RDRM position-variants located either 170 bp upstream or 22 bp downstream of the TSS in the promoter region of a reporter gene (Anaganti et al., 2017). Despite conservation of a consensus RDRM sequence (**TT**CT**G**TAAGAGA**C**GT**AA**), DdrO was unable to repress the transcription of the reporter gene (Anaganti et al., 2017).

The transcriptional repressor DdrO is a small DNA-binding protein of nearly 15 kDa expressed as a dimer, whose sequence is highly conserved among *Deinococcus* species (de Groot et al., 2019; Lim et al., 2019; Lu et al., 2019). Some *Deinococcus* species such as *D. deserti*, *D. gobiensis* and *D. peraridilitoris* express two DdrO proteins (Blanchard et al., 2017; de Groot et al., 2014; Lim et al., 2019). This protein is essential for cell viability, at least in *D. radiodurans* and *D. deserti* (Devigne et al., 2015; Ludanyi et al., 2014). DdrO belongs to the xenobiotic response element (XRE) family. The various members of this large family are involved in the regulation of gene expression, in response to stress such as temperature or ROS (Hu et al., 2018; Martínez-Salazar et al., 2009; Panyakampol et al., 2015). Although proteins of the XRE family display low sequence similarity and variable lengths, they are usually expressed as dimers and share a common helix-turn-helix fold (HTH) involved in DNA binding as well as dimerization (Brown et al., 2011; Talavera et al., 2019; Wen et al., 2014). The structures of DdrO from *D. deserti* and *D. geothermalis* were solved by two independent

research groups, yielding similar results (de Groot et al., 2019; Lu et al., 2019). DdrO is exclusively composed of α-helices, organized in two distinct domains connected by a flexible linker (Fig. 6A). The N-terminal domain (NTD) contains the conserved HTH DNA-binding motif of the XRE family, while the three α-helices of the C-terminal domain (CTD) adopt a new fold. Integrity of the CTD is essential for DdrO dimerization, as it was shown that cleavage by IrrE impedes dimer formation by severing the loop connecting the last two α-helices (α7 and α8) of the CTD (de Groot et al., 2019; Lu et al., 2019). The loss of α8 along with part of the α7-α8 loop destabilizes the dimer interface to which they both contribute greatly through hydrogen bonds and salt bridges. Since DdrO monomers are unable to bind the RDRM, the transcriptional repression mediated by DdrO is thus alleviated upon cleavage by IrrE (de Groot et al., 2019).

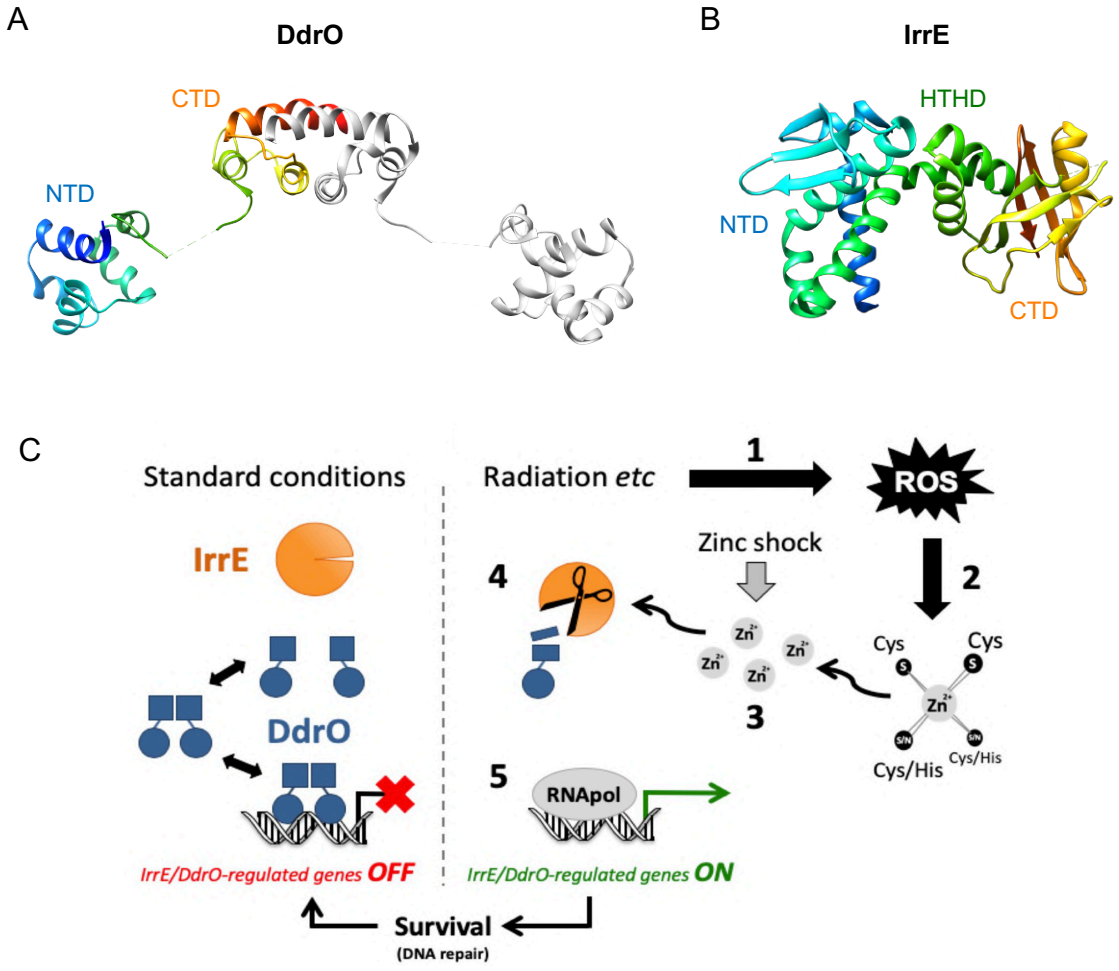

Figure 6. The radiation-desiccation response system is triggered by a zinc shock. A) Structure of the transcriptional repressor DdrO from *D. deserti* (PDB: 6RNX (de Groot et al., 2019)), composed of a N-terminal domain (NTD) and a C-terminal domain (CTD). The first monomer is colored from blue (N-terminus) to red (C-terminus), and the second monomer is colored in gray. **B**) Structure of the metallopeptidase IrrE from *D. deserti* (PDB: 3DTE (Vujičić-Žagar et al., 2009)), organized into three domains: the N-terminal domain (NTD), the helix-turn-helix domain (HTHD) and the C-terminal domain (CTD). The structure is colored from blue (N-terminus) to

red (C-terminus). **C**) A proposed model for the regulation of the radiation-desiccation response system. In standard conditions, DdrO monomers associate as a dimer to bind the RDRM in the promoter region of regulated genes and act as a transcriptional repressor. Due to a lack of available zinc ions (Zn^{2+}), the majority of IrrE is inactive. In response to stress, such as radiation or desiccation, the formation of ROS leads to the release of protein-bound Zn^{2+} ions. These ions are then free to bind to and activate IrrE, which in turn cleaves the CTD of DdrO thereby preventing its dimerization and subsequent binding to the RDRM. Adapted from (de Groot et al., 2019; Magerand et al., 2021; Vujičić-Žagar et al., 2009).

IrrE is a 30 kDa monomeric metalloprotease (Fig. 6B) composed of a N-terminal COG2856 (cluster of orthologous group) zinc-peptidase domain (NTD) fused to a central HTH domain (HTHD) and a C-terminal GAF-like domain (CTD) (Vujičić-Žagar et al., 2009). COG2856 proteins usually form a two component system with XRE family proteins to regulate gene expression in response to various sources of stress, as it is the case for the ImmA/ImmR system in *Bacillus subtilis* (Bose et al., 2008). The NTD of IrrE contains an extended Zn binding motif highly conserved among metallopeptidases of the MA clan: Xaa-Xbb-Xcc-His-Glu-Xbb-Xbb-His-Xbb-Xdd, where Xaa is hydrophobic or a threonine, Xbb is uncharged, Xcc is any amino acid except proline and Xdd is hydrophobic (Jongeneel et al., 1989). The sequence of *D. radiodurans* IrrE contains the motif TLAHEIGHAI, while that of *D. deserti* contains a slightly different motif (TLAHEISHAL). Accordingly, the protease activity of IrrE is greatly induced by Zn^{2+} ions and moderately induced by Mn^{2+} and Fe^{2+} ions (Blanchard et al., 2017; Magerand et al., 2021; Vujičić-Žagar et al., 2009). IrrE is able to cleave DdrO in a loop located between its last two α-helices, as observed in various *in vivo* and *in vitro* experiments (de Groot et al., 2019; Devigne et al., 2015; Lu et al., 2019; Ludanyi et al., 2014). Due to its peculiar location between the NTD and CTD, it was hypothesized that the HTHD of IrrE may not act as a DNA-binding domain (Vujičić-Žagar et al., 2009). In agreement with this theory, gel shift assays confirmed that IrrE from *D. deserti* does not bind to RDRM-containing DNA (Blanchard et al., 2017). The CTD of IrrE contains a GAF domain, named after three proteins containing this putative sensor domain: cGMP-specific phosphodiesterase, adenylyl cyclase and transcription factor FhlA (Ho et al., 2000). Very recently, Magerand et al. investigated the role of the CTD of IrrE regarding the cleavage of DdrO, either by co-expressing a truncated IrrE with DdrO in *E. coli* or by expressing the truncated IrrE in a *D. deserti irrE* deletion mutant. In both *in vivo* experiments, DdrO cleavage was observed yet it was less efficient compared to the full-length IrrE (Magerand et al., 2021). These results suggest that the GAF-like domain is not essential for cleavage of DdrO by IrrE, although it could participate in the interaction with DdrO or contribute to stabilize the structure of IrrE.

II. General organization of the nucleoid

II.1. Structure and composition of bacterial chromatin

II.1.1. The nucleoid is hierarchically organized

In eukaryotes, the genomic material is constrained by means of histone proteins in the form of highly compact chromatin fibers, which are enclosed in the nucleus. Although such a cellular compartment is not present in prokaryotic cells, their genomic DNA remains highly organized as a nucleoid (Valkenburg & Woldringh, 1984). The term nucleoid encompasses the genomic DNA associated with RNA and nucleoid associated proteins (NAPs). The dynamic structure of the nucleoid has been extensively studied and was found to be hierarchically organized in domains of different scales (Fig. 7), namely (i) macrodomains, (ii) high-density chromosomal regions (HDR) and chromosomal interaction domains (CID) and (iii) microdomains.

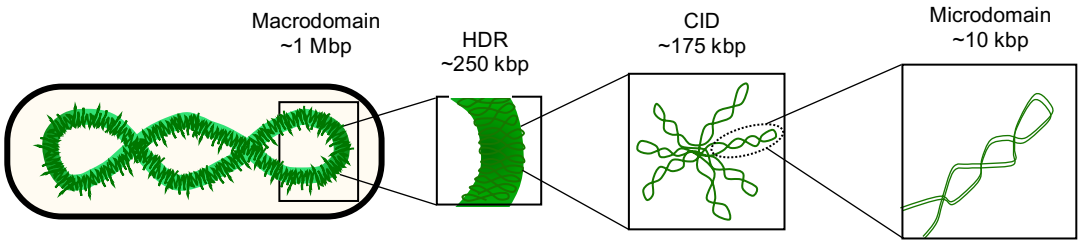

Figure 7. The bacterial chromatin adopts a hierarchical organization. Schematic representation of genomic DNA (represented as green lines) within a bacterial cell. The larger structured DNA-region in the nucleoid is the macrodomain, which contains several high-density chromosomal regions (HDRs). These domains are subdivided into chromosomal interaction domains (CIDs), composed of multiple microdomains. Adapted from (Dame & Tark-Dame, 2016).

Macrodomains were defined as large structured regions that do not interact with each other. This organization of genomic DNA was first observed in the nucleoid of *E. coli* through the analysis of spatial proximity and interaction between different segments of the genome, based on a site-specific recombination system. This genetic approach revealed the arrangement of *E. coli* nucleoid into four macrodomains of nearly 1 Mbp, named Ori, Ter, Left and Right (Valens et al., 2004). The presence of macrodomains were also confirmed in the nucleoid of *B. subtilis*, via the chromosome-conformation capture (Hi-C) technique that revealed genomic contacts and interactions. Based on this study, the nucleoid of *B. subtilis* was found to be organized into three macrodomains of strikingly different sizes. The Ori and Left-Right

macrodomains were ~1.4 Mbp and ~2.5 Mbp in size, respectively, whereas the Ter macrodomain spanned only ~0.5 Mbp (Marbouty et al., 2015).

In their study of the nucleoid of *Caulobacter crescentus*, Le et al. also relied on the Hi-C technique to study the organization of the genomic DNA. Their result highlighted highly self-interacting regions of 30 to 420 kbp, designated as chromosomal interaction domains (CID). These regions seem to be composed of plectonemes, which are loop-structures formed by supercoiled DNA. The boundaries between two CIDs, i.e. the regions with no detected contacts, were found to coincide with highly-expressed genes that correspond to plectoneme-free regions of ~2 kbp (Le et al., 2013). Therefore, the hierarchical organization of the nucleoid in *Caulobacter crescentus* could be linked to the supercoiling of genomic DNA. Similarly, the large macrodomains of *B. subtilis*' nucleoid are further organized into CIDs, as demonstrated by Hi-C experiments (Marbouty et al., 2015). In this species, the size of CIDs ranges from 50 to 300 kbp, with a mean size of ~175 kbp, in good agreement with the previous analysis in *C. crescentus*. The barriers or boundaries between two CIDs all corresponded to plectoneme-free regions although some of them did not contain highly-expressed genes. Instead, one third of the barriers were composed of DNA displaying a low GC content compared to the rest of genomic DNA and bound by Rok, a transcriptional activator (Marbouty et al., 2015). Moreover, an additional higher level of nucleoid organization was described as high-density chromosomal regions (HDR) in *B. subtilis* (Marbouty et al., 2015). Using 3D structured illumination microscopy in combination with high-density whole-chromosome labeling, Marbouty et al. proved that the Ori macrodomain in the nucleoid of *B. subtilis* contains a region of high DNA density with a size of nearly 230 kbp, larger than that observed for CIDs. It was thus proposed that the HDRs might encompass several CIDs.

The smallest structural units in the hierarchical organization of bacterial nucleoid are the microdomains, composed of plectonemes. Postow and colleagues estimated the average size of microdomains in the nucleoid of *E. coli* through two independent methods (Postow et al., 2004). First, they analyzed the diffusion of supercoiling after introduction of double-strand breaks in the genomic DNA, using supercoiling-sensitive gene. Then, they calculated the length of individual plectonemes from isolated chromosomes imaged with electron microscopy. Results obtained via the two methods were similar and converged to a microdomain size of approximately 10 kbp (Postow et al., 2004). These observations were later confirmed in the work of Stein et al., in which the nucleoids of *E. coli* and *Salmonella typhimurium* were analyzed with a site-specific resolution system (Stein et al., 2005). This method is used to

measure the diffusion of supercoiling, like the one previously employed by Postow et al.. Based on the analysis of supercoil diffusion, microdomain size varies from 9 kbp to 13 kbp in *Salmonella typhimurium*, similar to the sizes observed in *E. coli*'s nucleoid.

II.1.2. Macromolecular crowding and nucleoid compaction

In bacteria, the structural organization and compaction of the nucleoid are maintained by the nucleoid associated proteins (NAPs), whose architectural function alter the path of DNA (see *Chapter II.2*), and by macromolecular crowding in the cytoplasm that limits the dispersion of the genome in the cell.

The term "macromolecular crowding" refers to the crowded environment in the cytoplasm of a bacterial cell, in which macromolecules such as RNA and proteins are present at a high concentration of nearly 0.4 g/ml and occupy up to 17% of the cytoplasmic volume (Valkenburg & Woldringh, 1984; Zimmerman & Trach, 1991). The high concentration of these macromolecules, combined with their small size in comparison to DNA, lead to the production of a depletion force that constrains the genomic DNA to adopt a compact conformation. This model of chromosome compaction led by macromolecular crowding was confirmed in an experiment by Pelletier et al., performed on isolated bacterial chromosomes confined in microchannels (Pelletier et al., 2012). To mimic the conditions of macromolecular crowding naturally occurring in the cytoplasm of *E. coli*, the authors used different concentrations of a high molecular weight polyethylene glycol (PEG 20,000). When PEG 20,000 was added to the microchannel buffer, the spread-out chromosome instantly adopted a compact conformation. In contrast, when PEG 20,000 was removed from the microchannel buffer, the chromosome went back to its previous expanded conformation. Interestingly, the compaction of chromosome was only observed at concentrations of PEG 20,000 similar to that of cytoplasmic proteins, *i.e.* corresponding to 12% to 17% of the volume fraction. Moreover, the extent of chromosome compaction was comparable to that observed *in vivo* in *E. coli* cells. This hypothesis is further supported by molecular dynamics simulations in which a supercoiled DNA represented as a chain of beads was immersed in a solution of smaller proteins modelized as smaller beads (Shendruk et al., 2015). Each bead of the supercoiled DNA molecule was defined as a structural monomer of about 300 kbp (approximately the size of a HDR domain), while the small proteins constituted the crowding agents. The simulations were performed for three size ratios of protein radius to structural monomers radius, each time with increasing fractions of the cell volume

occupied by proteins up to 45%. In agreement with Pelletier et al., when the fraction of the cell volume occupied by proteins increases, the modelled chromosome collapses onto itself yielding a highly compact conformation. Altogether, the results of these studies suggest that macromolecular crowding is a major mechanism in nucleoid compaction.

II.2. Diversity and functions of the Nucleoid Associated Proteins

The nucleoid associated proteins (NAPs) are essential to maintain the nucleoid compaction and hierarchical organization. They directly interact with genomic DNA to alter its conformation and topology, thereby preserving its organization into distinct domains.

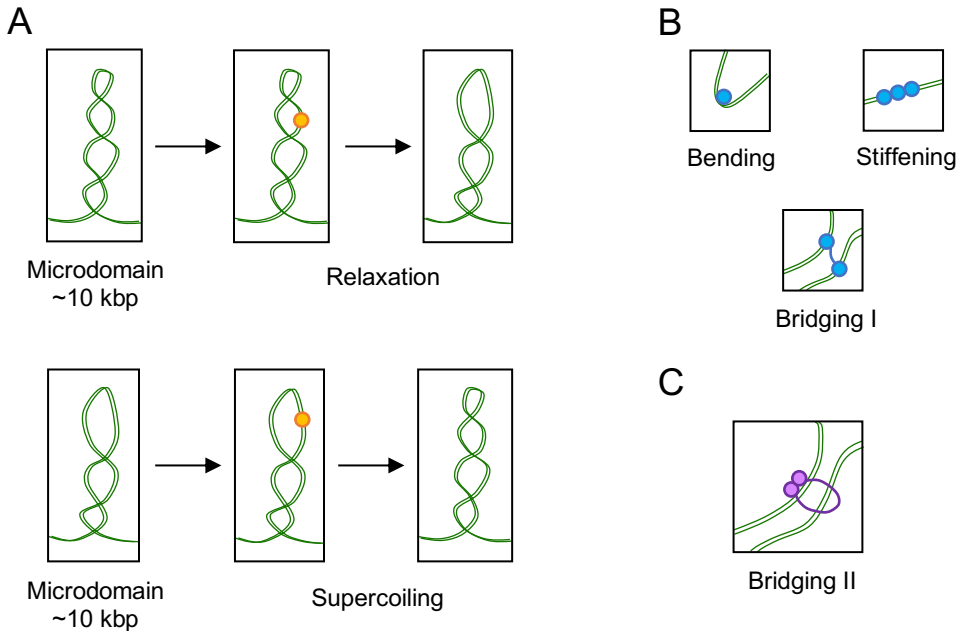

Figure 8. Nucleoid Associated Proteins (NAPs) alter the conformation and topology of DNA through distinct mechanisms. Schematic representation of the various architectural properties of NAPs involved in the nucleoid organization. The genomic DNA is represented as green lines while the NAPs are represented as orange, blue and purple circles. **A**) The topoisomerases (orange) directly affect the compaction of DNA by performing relaxation and/or supercoiling of DNA. **B**) The small basic NAPs (sbNAPs; blue) change the trajectory of DNA via bending, stiffening or bridging of two distinct DNA segments. **C**) The Smc-ScpAB complex and its homologue MukBEF (purple) form a ring-like structure able to bridge two distant DNA domains. Adapted from (Dame & Tark-Dame, 2016).

These proteins may be classified into five categories: (i) the Dps protein family that has been shown to protect DNA during starvation in a number of bacteria, (ii) the parABS system involved in chromosome segregation, (iii) the SMC-ScpAB complex that bridges distant DNA fragments (Fig. 8C), (iv) the topoisomerases, which modify DNA conformation via strand

cleavage (Fig. 8A) and (v) the small basic NAPs (sbNAPs) that affect DNA topology through bridging, bending or stiffening (Fig. 8B).

II.2.1. Dps, DNA protection during starvation

The DNA protection during starvation (Dps) proteins represent one of the three subfamilies of the ferritin-fold protein family expressed in bacteria. Dps proteins have the capacity to protect DNA in stationary phase cells during starvation and other stress conditions such as oxidative stress or exposure to UV radiation (Karas et al., 2015; Nair & Finkel, 2004). Dps is overexpressed during stationary phase and displays low level of expression during exponential phase. In *E. coli*, the promoter activity of Dps is enhanced by the sbNAP IHF, but repressed in the presence of two other sbNAPs, Fis and H-NS (Altuvia et al., 1994). The mechanism by which Dps protects DNA relies on two specific functions: (i) a ferroxidase activity allows Dps to oxidize and store free iron ions, and (ii) the ability to co-crystallize with DNA offers a physical protection against DNA damaging agents. Dps monomers of nearly 20 kDa adopt a ferritin-like fold composed of a four helix bundle with a N-terminal extension of variable length (Fig. 9A), sometimes involved in DNA binding or Dps oligomerization (Bhattacharyya & Grove, 2007; Stillman et al., 2005). Indeed, this protein is able to assemble as a dodecamer (Fig. 9A) forming a large hollow spherical complex of ~ 8 nm in external diameter (Dadinova et al., 2019; Grant et al., 1998). Oligomeric forms of Dps possess a highly conserved ferroxidase center located at the interface between two monomers (Grant et al., 1998; Ilari et al., 2000, 2005). Upon binding to a ferroxidase center, ferrous iron ions (Fe^{2+}) are oxidized into ferric iron ions (Fe^{3+}) using H_2O_2 as an oxygen source, followed by the storage of Fe^{3+} ions in the dodecamer cavity. This reaction therefore reduces oxidative damages caused by hydrogen peroxide while avoiding the formation of hydroxyl radicals via the Fenton chemistry (Zhao et al., 2002). Thanks to the numerous metal binding sites of its dodecameric structure, Dps binds approximately 500 ferric iron ions per dodecamer (Yamamoto et al., 2002; Zhao et al., 2002).

The second mechanism of protection is the co-crystallization of Dps with DNA that was first highlighted *in vitro* and *in vivo* in 1999 by Wolf et al. (Wolf et al., 1999). In their study, they combined *in vitro* incubation of Dps with circular DNA and *in vivo* observation of Dps over-producing *E. coli* cells or starved wild-type *E. coli* cells (Fig. 9B-C). In both experiments, they could see the formation of highly ordered Dps-DNA complexes (Wolf et al., 1999). Since it has a loose sequence specificity for DNA, Dps occupies almost all the nucleoid in stationary

phase *E. coli* cells (Azam & Ishihama, 1999; Talukder & Ishihama, 2015). The dodecameric assemblies are able to crystallize without DNA into a pattern that contains ~ 2 nm gaps, corresponding to the diameter of a double-stranded DNA helix (Grant et al., 1998; Wolf et al., 1999). This highly structured Dps-DNA complex protects the DNA from DNase or restriction enzymes, although it remains dynamic and able to rearrange rapidly, as it was shown to accommodate the binding of RNA polymerase (Janissen et al., 2018).

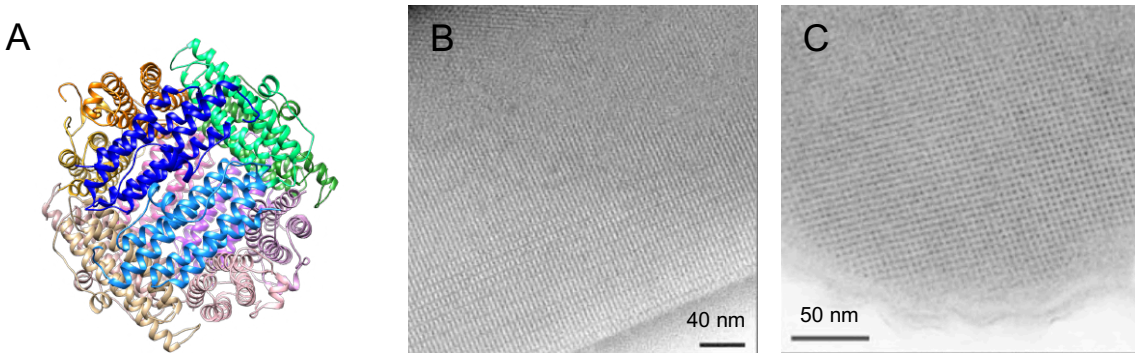

Figure 9. Dps assembles as a dodecamer able to co-crystallize with DNA *in vitro* and *in vivo*. A) Structure of the dodecameric assembly of Dps from *E. coli* (PDB: 1DPS (Grant et al., 1998)), composed of twelve four-helix bundle monomers, each colored differently. **B-C**) Electron microscopy images of Dps-DNA complexes observed *in vitro* (**B**) and *in vivo* (**C**). **B**) Purified Dps incubated for 15s with closed circular DNA at a Dps:DNA ratio of 1:5. **C**) Dps-over-producing *E. coli* cell induced at mid-logarithmic phase and then incubated for 48 h. Adapted from (Grant et al., 1998; Wolf et al., 1999).

Deinococcus species typically express one protein of the Dps family, as it is the case for *D. deserti* (de Groot et al., 2009; Lim et al., 2019). However, among the eleven *Deinococcus* species whose genome was completely assembled, *D. radiodurans* and *D. gobiensis* express two members of the Dps family (Lim et al., 2019; White et al., 1999). In *D. radiodurans*, the chromosome-encoded Dps1 only shares 16% sequence identity with the mega-plasmid-encoded Dps2 (White et al., 1999). The N-terminal extensions of *D. radiodurans* Dps1 and Dps2 are quite long compared to those of Dps proteins from other bacteria, with an extra 32 and 49 amino acids for Dps1 and Dps2 compared to their *E. coli* homologue. The N-terminal extension of Dps1 possesses a unique metal-binding site and is essential for DNA binding and assembly of the dodecamer (Bhattacharyya & Grove, 2007; Nguyen & Grove, 2012; Santos et al., 2017). The oligomeric state of Dps1 depends on salt concentration, as dimers are formed at low salt concentrations and dodecamers are only found at higher salt concentration. Notably, the dimer is able to protect DNA from hydroxyl radicals and DNase although it binds with lower affinity than the dodecamer suggesting a potentially different function *in vivo* (Grove & Wilkinson, 2005). In a more recent study, dimers, trimers and dodecamers of Dps1 were

directly identified in cell extracts of *D. radiodurans*, suggesting that all the oligomers co-exist *in vivo* (Santos et al., 2015). It was proposed that each oligomeric state of Dps1 plays a specific function in the cell. Under physiological conditions, Dps1 would be mostly dimeric and loosely bind to DNA. In the presence of a high concentration of manganese ions (Mn^{2+}), the protein would dissociate from DNA and shift to a trimeric form in complex with Mn^{2+} and participate in the scavenging of ROS (see Chapter I.3). Upon increasing iron concentration, Dps1 would gradually assemble into a dodecamer and act as a ferritin by storing and oxidizing Fe^{2+} (Santos et al., 2015, 2019).

Regarding the plasmid-encoded Dps2 of *D. radiodurans*, its C-terminal extension seems to provide the same function as that of the N-terminal extension in Dps1. Indeed, it is essential for assembly of the Dps2 dodecamer and harbors a metal binding site that might stabilize the C-terminal structure when occupied, favoring DNA binding (Cuypers et al., 2007; Reon et al., 2012). Contrary to Dps1, the promoter activity of Dps2 seems to be enhanced in the presence of hydrogen peroxide and its basal expression is low even in stationary phase compared to that of Dps1 (Reon et al., 2012; Santos et al., 2015). The first 30 residues of the N-terminal extension of Dps2 contain a signal-peptide that targets Dps2 outside the cytoplasm (Reon et al., 2012). Accordingly, Dps2 was only found in the membrane fraction of *D. radiodurans* cell extracts in agreement with *in vivo* studies highlighting a particular localization at the cell periphery, in the septum between cells in tetrads (Reon et al., 2012; Santos et al., 2017, 2019). Additionally, while Dps1 adopts three different oligomeric forms depending on growth phase and metal concentrations, Dps2 is a stable dodecamer in solution regardless of salt and iron concentrations or the presence of DNA (Reon et al., 2012; Santos et al., 2015). The Dps2 dodecamer is able to bind and protect DNA, yet the Dps-DNA complexes seem less stable than those formed with Dps1 (Reon et al., 2012; Santos et al., 2015). Based on these specific properties, Dps2 might be involved in the maintenance of iron homeostasis in *D. radiodurans* more than in the direct protection of DNA.

II.2.2. ParABS partitioning system

The parABS nucleoprotein complex is a well-conserved tripartite system involved in chromosome and plasmid segregation following replication in bacterial cells. It is composed of a Walker-type ATPase partitioning protein A (ParA) that binds DNA non-specifically, and a DNA-binding partitioning protein B (ParB, Fig. 10A) that binds to a specific DNA sequence, named *parS*, to form a nucleoprotein complex and stimulates the ATPase activity of ParA (Chen

et al., 2015; Funnell, 1991; Schumacher & Funnell, 2005). Briefly, ParB proteins assemble as large partition complexes upon binding to *parS* sites. These complexes are subsequently dragged towards the opposite cell pole via a Brownian diffusion ratchet mechanism along a gradient of ATP-bound ParA (Fig. 10B), thereby segregating newly replicated chromosomes or plasmids into their respective daughter cells (Hu et al., 2015; Le Gall et al., 2016; Lim et al., 2014).

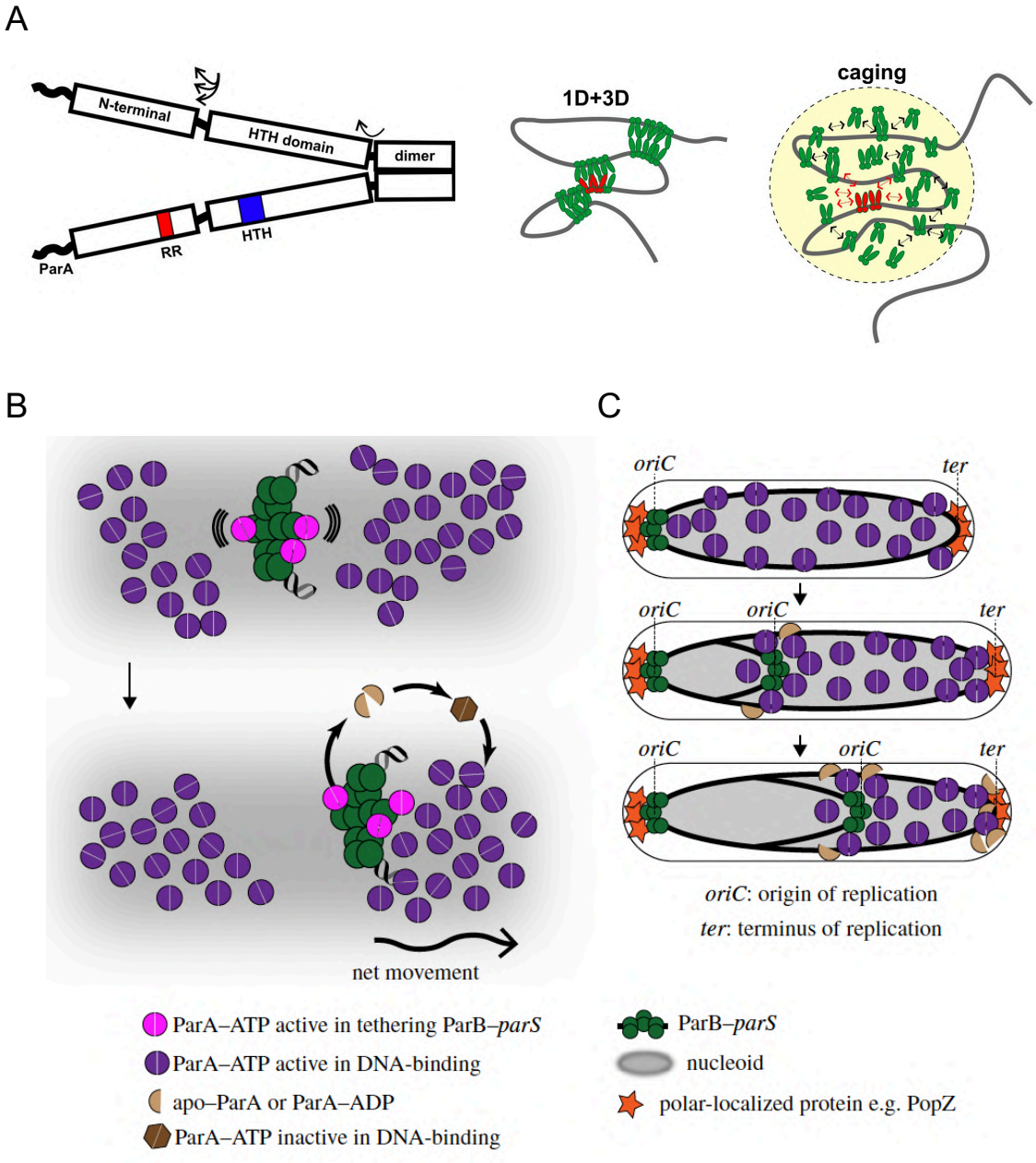

Figure 10. The ParABS partitioning system is based on a Brownian diffusion ratchet mechanism. A) The left panel represents the domain organization of ParB. The helix-turn-helix motif of the DNA-binding domain and the highly-conserved arginine-rich motif of the N-terminal domain are shown as red and blue boxes respectively. Arrows represent the flexibility of linkers between the three domains. The middle and right panels are a schematic

representation of the two models proposed for the formation of the partition complex. The first model (1D+3D) is based on a combination of sliding (1D) and bridging (3D) between ParB dimers (in green). In the caging model, *parS*-bound ParB dimers (in red) act as nucleation sites to create a locally high concentration of ParB. **B**) Schematic representation of the general principle of the Brownian diffusion ratchet mechanism. The ParB-*parS* complex (green) is tethered to the nucleoid (grey background) via non-specifically bound ParA-ATP dimers (purple). Upon ParB-stimulated ATP hydrolysis, ParA dissociates into monomers (light brown) that rebind ATP, but do not engage in DNA binding (dark brown). This creates a ParA-ATP depletion zone around the ParB-*parS* complex, which moves by thermal fluctuation (wavy lines) to rebind ParA-ATP. **C**) Illustration of the mechanism leading to the segregation of a newly replicated chromosome in a bacterial cell. One ParB-*parS* complex remains at the pole after chromosome replication, while the other moves along the gradient of ParA-ATP to the opposite cell pole. Polarly localized proteins such as PopZ (orange) contribute to maintaining the ParA-ATP gradient by sequestering ParA monomers away from the nucleoid. Adapted from (Funnell, 2016; Jalal & Le, 2020).

The *parA* and *parB* genes are usually located close to each other in the genome and near a *parS* site and are encoded by either plasmid or chromosomal DNA. However, according to phylogenetic analyses, chromosome-encoded and plasmid-encoded ParA and ParB proteins belong to distinct groups (Dubarry et al., 2006; Gerdes et al., 2000). Although *parS* sites are found in both plasmid and chromosomal DNA, only the chromosomal *parS* sequences are well conserved. They are usually 16 bp in length and contain an inverted repeat, with a conserved TGTTNCACGTGAAACA motif. The parABS system is expressed by a majority of prokaryotes, as showed by Livny and colleagues in their genomic study. Analysis of sequenced bacterial genomes from 400 different species revealed that 69 % of the sequenced strains possess one or more putative *parS* sites, that are mostly located in the region near the replication origin of the chromosome (Livny et al., 2007). *parS* sequences are highly conserved and found in species from all prokaryotic phyla, with the exception of gamma-proteobacteria such as the model organism *E. coli* (Livny et al., 2007).

The amino acid sequence of chromosomal DNA-binding ParB varies within bacterial species, however they all share a similar domain organization (Fig. 10A). ParB proteins are expressed as homo-dimers composed of 20 to 40 kDa monomers organized into three domains connected via flexible linkers: (i) a N-terminal domain with a highly conserved GERRxRA motif involved in cytosine tri-phosphate (CTP) hydrolysis and interaction with other ParB dimers or ParA, (ii) a central DNA-binding domain containing a helix-turn-helix motif that binds to *parS* and (iii) a C-terminal domain involved in ParB dimerization through a conserved leucine-zipper motif (Chen et al., 2015; Leonard et al., 2004; Schumacher & Funnell, 2005). The formation of a ParB-*parS* partition complex starts with the binding of a ParB dimer on a *parS* site, followed by the oligomerization of a *parS*-bound ParB with other dimers bound to

adjacent non-specific DNA, in a process termed spreading. The *parS* binding and spreading process of ParB may require the binding of CTP, as observed in *B. subtilis* and *Myxococcus xanthus* (Osorio-Valeriano et al., 2019; Soh et al., 2019). Recently, two different models were proposed to explain the assembly of the large nucleoprotein complex (Fig. 10A). The first model states that the partition complex arises from the formation of ParB filaments on DNA through lateral contacts, combined with bridging of distant DNA molecules via oligomerization of ParB mediated by their NTDs (Broedersz et al., 2014; Graham et al., 2014). In the second model, termed caging, the *parS*-bound ParB complexes act as nucleation sites that recruit other dimers, leading to a local high concentration of ParB that would be maintained via weak interactions with non-specific DNA and other ParB dimers (Sanchez et al., 2015).

Once the partition complex is formed, the ParB dimers in the partition complex interact with DNA-bound ParA. Chromosome-encoded ParA are small proteins of ~25 kDa that form dimers and bind DNA non-specifically upon ATP binding through a Walker-box motif (Gerdes et al., 2000; Leonard et al., 2005; Scholefield et al., 2011). Structural studies of ParA dimers in complex with either ATP (or its non-hydrolysable analog), ATP and DNA, or ATP and ParB, highlighted a change of conformation upon DNA binding (Chu et al., 2019; Zhang & Schumacher, 2017). The ATP-bound ParA dimer adopts a conformation called the nucleotide sandwich dimer, which is more favorable for ATP binding and hydrolysis. When ParA dimer binds to non-specific DNA sequences in the nucleoid, it shifts to a new conformation that exposes more of its basic residues, thereby favoring DNA binding. The interaction of the NTD of ParB with ParA stabilizes the nucleotide sandwich dimer conformation, stimulating ATP hydrolysis and triggering the dissociation of the ParA dimer into monomers, with the subsequent release of ParA from the DNA. The ParB-mediated dissociation of ParA from the DNA creates a gradient of ATP-bound ParA dimers along the nucleoid followed by the partition complex (Fig. 10C). This lateral movement leaves a ParA-depleted zone that prevents the nucleoprotein complex from moving backward, hence the term ratchet to describe the diffusion mechanism of the partition system.

ParB dimers are also able to interact with proteins outside the partitioning system, such as the polarly localized PopZ in *C. crescentus* (Fig. 10C), involved in chromosome segregation by its anchoring of a partition complex at one of the cell poles (Bowman et al., 2008). Moreover, ParB dimers were found to recruit another complex, the structural maintenance of chromosomes (SMC), to the origin region (Gruber & Errington, 2009; Sullivan et al., 2009). The SMC complex promotes chromosome condensation, thereby easing the segregation process by

preventing the entanglement of the newly replicated chromosomes (Gruber & Errington, 2009; Sullivan et al., 2009).

II.2.3. SMC, Structural maintenance of chromosomes complex

The SMC complex is highly conserved among bacteria, although it is missing in *E. coli* and other γ-proteobacteria, which instead express an analogous MukBEF complex, which exerts the same function as the SMC complex in the maintenance of nucleoid organization (Niki et al., 1991). This complex is formed by the association of three proteins: the large Smc and the comparably smaller ScpA and ScpB (Fig. 11A).

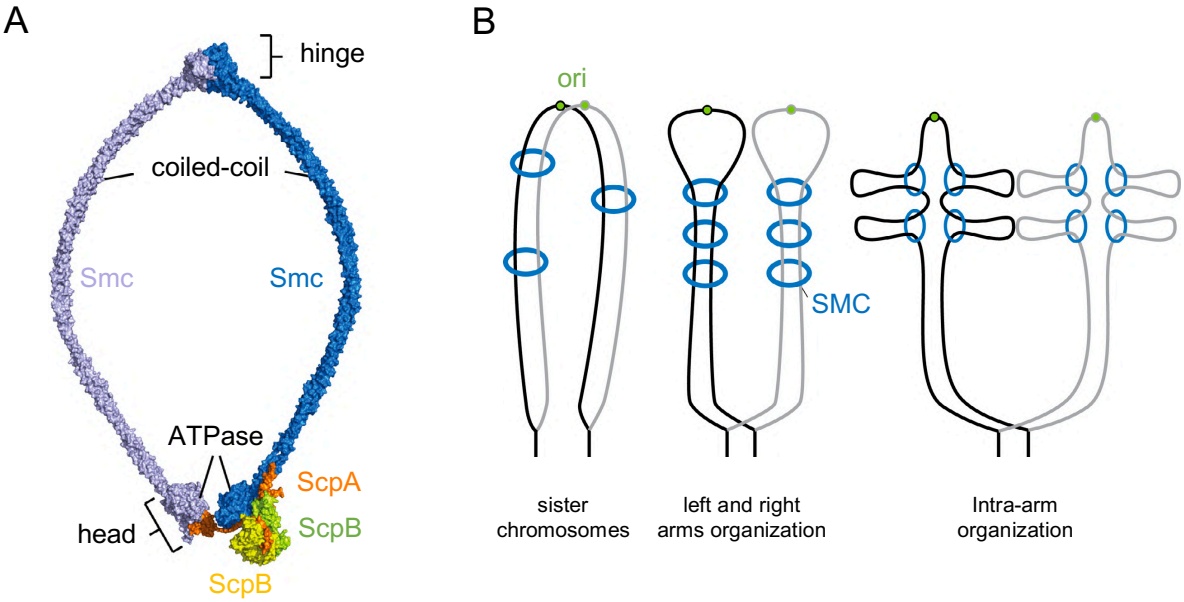

Figure 11. The ring-like Smc_2-$ScpAB_2$ complex is involved in chromosome segregation and compaction. A) Hypothetical model for the overall architecture of the Smc_2-$ScpAB_2$ complex based on several separate crystal structures. Smc monomers are colored in light and dark blue, ScpA is colored orange and the two ScpB monomers are colored in green and yellow. **B**) Models for the bridging and looping of chromosomal DNA by Smc-ScpAB rings, specific for sister DNA, left and right arm of the chromosome and intra-arm DNA (from left to right). Chromosomes are represented as black and gray lines, with their respective origins of replication (*ori*) indicated by a green circle. Adapted from (Gruber, 2014).

The structural maintenance of chromosome (Smc) protein is a long protein of more than 125 kDa, homologous to eukaryotic cohesin and condensin complexes (Britton et al., 1998; Bürmann et al., 2013). It is organized as a long coiled-coil domain framed by a hinge domain at one end and an ATPase head domain at the other end (Bürmann et al., 2013; Lammens et al., 2004; Melby et al., 1998). Upon dimerization via its hinge domain, Smc forms a ring-like

structure, whose closing and opening is controlled by ATP binding and hydrolysis at the head domain (Lammens et al., 2004). The Smc dimer further associates with a complex of regulatory subunits formed by the segregation and condensation proteins (Scp) A and B that each have a distinct function in the Smc_2-$ScpAB_2$ (or SMC) complex. ScpA has the ability to link the coiled-coil of a Smc monomer to the head domain of the other Smc monomer, and also enhances the ATPase activity of Smc (Bürmann et al., 2013; Kamada et al., 2013). Despite a lack of direct interaction between ScpB and Smc, this small dimeric protein is essential for the formation of the SMC complex and might trigger a conformational change in ScpA, responsible for its ability to increase ATP hydrolysis (Kamada et al., 2013).

Due to its specific ring-like structure, the SMC complex and the analogous MukBEF complex are able to bridge DNA segments from distinct chromosomal domains, thus aiding compaction (Fig. 11B). They are also involved in proper positioning of chromosomal *ori* domains when associated with *ori*-proximal regions in *B. subtilis* and *E. coli*, through their interaction with ParB (Danilova et al., 2007; Gruber & Errington, 2009; Sullivan et al., 2009). Moreover, the SMC and MukBEF complexes are essential for proper chromosome segregation in *B. subtilis* and *E. coli*, since cells lacking these complexes displayed an abnormal nucleoid organization or were even anucleate (Britton et al., 1998; Danilova et al., 2007; Gruber & Errington, 2009; Sullivan et al., 2009). The mechanisms by which these complexes participate in chromosome segregation differ between MukBEF and SMC. In *E. coli*, the dimerization domain of MukB directly interacts with the ParC subunits of the Topo IV topoisomerase, which is notably responsible for the disentanglement of sister chromosomes (Li et al., 2010). Through this interaction, the MukBEF recruits Topo IV to the *ori*-region of *E. coli* nucleoid and enhances the relaxation and decatenation activities of Topo IV, thus ensuring a proper segregation of the sister chromosomes (Li et al., 2010; Nicolas et al., 2014; Zawadzki et al., 2015). In contrast, the SMC complex expressed in *B. subtilis* does not interact with Topo IV, but may instead promote chromosome segregation by condensing the DNA at the replication sites thereby preventing the entanglement of sister chromosomes (Gruber, 2014; Wang et al., 2014).

Interestingly, the genome of *D. radiodurans* only encodes for homologues of two components of the SMC complex, Smc (DR_1471) and ScpB (DR_1861), but lacks a ScpA homologue (White et al., 1999). The absence of ScpA might affect the function of Smc as it is required for Smc dimerization and ATPase activity in other bacteria. Accordingly, *D. radiodurans* mutants devoid of Smc showed no growth defect nor abnormal nucleoids, suggesting that Smc is not essential for chromosome segregation in *D. radiodurans* (Bouthier

de la Tour et al., 2009). Regarding *D. deserti*, as of today no studies were performed on the putative SMC complex, although its genome encodes for homologues of the three components: Smc (Deide_08800), ScpA (Deide_07090) and ScpB (Deide_08600) (de Groot et al., 2009).

II.2.4. Topoisomerases

The topoisomerases are essential to manage the topological constraints induced by the many cellular processes involving circular genomic DNA, such as nucleoid compaction, DNA repair, transcription and replication. These enzymes possess the ability to modulate the compaction level of dsDNA by performing either relaxation or supercoiling via the cleavage of one or two strands of DNA. Some topoisomerases are also able to resolve catenated DNA structures that arise after DNA replication in dividing bacterial cells.

Table 3. **Classification of the type I and type II topoisomerases.** The topoisomerase families are well distributed among the three cellular domains of life (bacteria, eukaryotes and archaea), and affect DNA topology through relaxation, supercoiling or decatenation (ATP-dependent activities are indicated as "x^{ATP}").

Family	Subfamilies	Bacteria	Eukaryotes	Archaea	Relaxation	Supercoiling	Decatenation
Type IA	**Topo IA**	x			x		x
	Topo III	x	x		x		x
	Reverse gyrase	x		x	x	x^{ATP}	
Type IB	**Topo IB**	x	x		x		
Type IC	**Topo V**			x	x		
Type IIA	**Topo II**		x		x^{ATP}		x^{ATP}
	Topo IV	x			x^{ATP}		x^{ATP}
	DNA Gyrase	x	x	x	x	x^{ATP}	x^{ATP}
Type IIB	**Topo VI**	x	x	x	x^{ATP}		x^{ATP}
	Topo VIII	x		x	x^{ATP}		x^{ATP}

Topoisomerases are classified into two types, depending on whether they cut one (type I) or two (type II) strands of DNA (Table 3). An important feature conserved among the topoisomerase families is the tyrosine of their active site involved in the formation of the single- or double-strand DNA break. This residue forms a specific phosphotyrosyl link with the phosphate group of the DNA backbone, through a nucleophilic attack either on the 5'- or 3'-phosphate of the DNA strand. The type I and type II categories are further subdivided into five families, namely type IA, IB, IC and type IIA and IIB, according to their structure and mechanism of action (Table 3). A majority of bacteria express different topoisomerases corresponding to several of these subfamilies in order to cover all the activities pertaining to

genome maintenance, which requires a combination of relaxation, supercoiling and decatenation functions (Table 4). The Topo IA (type I topoisomerase) and the DNA gyrase (type II topoisomerase) are the most widespread enzymes.

Table 4. Topoisomerases are expressed in a variety of combinations in different bacteria. Topoisomerases expressed in the model bacteria *E. coli*, *B. subtilis*, *Staphylococcus aureus* and *Streptococcus pneumoniae*, in the two *Deinococcus* species *D. radiodurans* and *D. deserti*, and in the thermophile *Thermus thermophilus* (a close relative of *D. radiodurans*).

Family	Subfamilies	*E. coli*	*B. subtilis*	*S. aureus*	*S. pneumoniae*	*T. thermophilus*	*D. radiodurans*	*D. deserti*
Type IA	Topo IA	x	x	x	x	x	x	x
	Topo III	x	x	x				
	Reverse Gyrase					x		
Type IB	Topo IB						x	x
Type IIA	Topo IV	x	x	x	x			
	DNA Gyrase	x	x	x	x	x	x	x

II.2.4.1. Type I topoisomerases

Type I topoisomerases are large monomeric proteins of nearly 100 kDa that cleave only one DNA strand (Bush et al., 2015; Champoux, 2001; McKie et al., 2021). The type I classification includes three families of DNA topoisomerases, (i) type IA, (ii) type IB and (iii) type IC. The type IA topoisomerases share a ring-like monomeric structure whose function is based on a strand passage mechanism (Fig. 12A). Briefly, an intact single DNA strand referred to as the transported-segment (or T-segment) is translocated through a cleaved single DNA strand, called the gate-segment (or G-segment), followed by the ligation of the DNA strand break (Tan et al., 2015). The nucleophilic attack of the phosphate group by the topoisomerase tyrosine occurs at the 5' end of the DNA strand. The relaxation and decatenation activities of type IA topoisomerases do not require any ATP-hydrolysis, but they are Mg^{2+}-dependent. The type IA topoisomerase family comprises three subfamilies with distinct *in vivo* functions: the bacterial DNA topoisomerase I (Topo IA), the bacterial and eukaryotic DNA topoisomerase III (Topo III) and the bacterial and archaeal reverse gyrase, a topoisomerase specific to thermophiles (Table 3).The main function of Topo IA *in vivo* is to relax the transcription-induced negative supercoils of the genomic DNA to prevent their deleterious accumulation (Massé & Drolet, 1999). The function of Topo III in *E. coli* is essential for chromosome segregation, as it disentangles DNA catenanes produced by the replication of genomic DNA via its decatenation activities (Li et al., 2000; Nurse et al., 2003). Unlike Topo IA and Topo III,

the reverse gyrase is able to perform positive supercoiling in an ATP-dependent process. This particularity arises from the combination of two domains, a helicase-like N-terminal domain (h-NTD) and a Topo IA-like C-terminal domain (t-CTD), coordinated by a latch domain (Confalonieri et al., 1993; Ganguly et al., 2013; Rudolph et al., 2013). When only the t-CTD is expressed, the reverse gyrase relaxes negatively supercoiled DNA in an ATP-independent manner similar to Topo IA function. This activity combined with the unwinding of dsDNA by the h-NTD likely enables the positive supercoiling function of the reverse gyrase (Déclais et al., 2000).

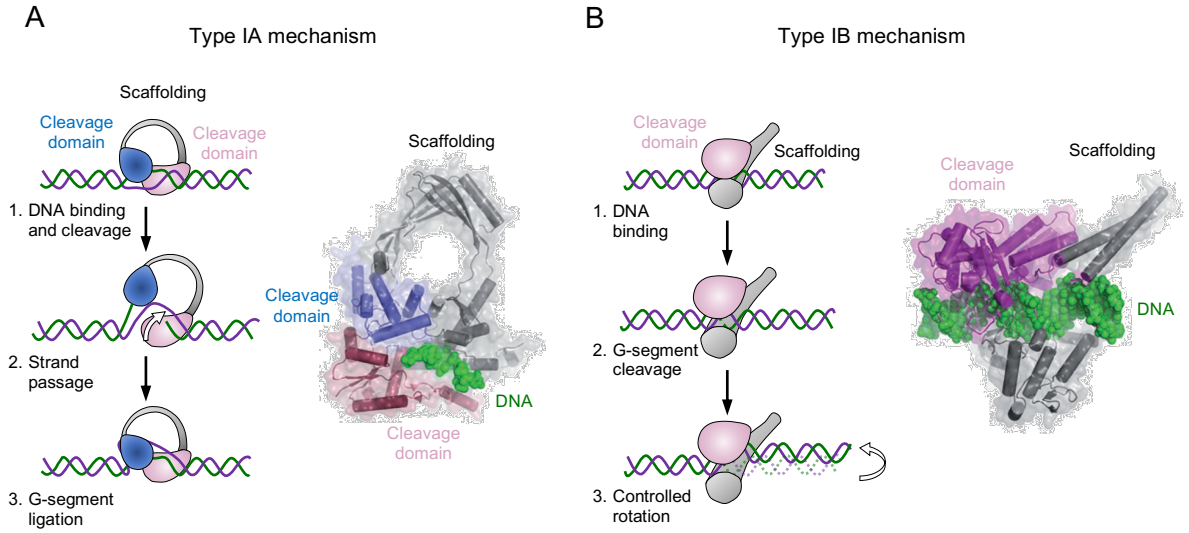

Figure 12. General mechanisms of type IA and type IB topoisomerases. A) The type IA topoisomerases bind a dsDNA segment and cleave one DNA strand called the G-segment (step 1). The uncleaved DNA strand (called the T-segment) is translocated through the gap of the cleaved G-segment, via a strand passage mechanism (step 2). Finally, the G-segment is re-ligated and the dsDNA is released (step 3). On the right, the structure of *E. coli* Topo III bound to ssDNA (PDB: 2O5C (Changela et al., 2007)) is colored like its schematic representation, with cleavage domains in blue and pink and scaffolding in grey. **B**) The type IB topoisomerases follow similar steps, as they also bind a dsDNA and cleave only one strand (steps 1 and 2). However, their mechanism is based on a controlled rotation, where the free dsDNA end rotates around the cleaved G-segment (step 3). On the right, the structure of human Topo IB bound to dsDNA (PDB: 1A36 (Stewart et al., 1998)) is colored like its schematic representation, with cleavage domain in pink and scaffolding in grey. Adapted from (Vos et al., 2011).

As part of the type I topoisomerases, members of the type IB and type IC families also cleave only one DNA-strand yet their structure and mechanism differ from the type IA family (Stewart et al., 1998; Stivers et al., 1997). Type IB and type IC topoisomerases break the DNA backbone via a covalent link with the phosphate group at the 3' end of the DNA single strand and function by a controlled rotation rather than by a strand passage mechanism, that does not require the presence of magnesium ions (Fig. 12B). In the controlled rotation mechanism, the

G-segment is the moving strand instead of the T-segment. After cleavage of the G-segment, the free end of the cleaved DNA (i.e. the one that is not involved in a phosphotyrosyl link) rotates around the intact strand at a regulated speed, due to friction with the enzyme cavity, after which the DNA break is ligated (Koster et al., 2005). The structures of type IB topoisomerases resemble more a clamp, with no similarities to the structures of type IA topoisomerases (Fig. 12). The type IB family only includes one sub-family, the DNA topoisomerases IB (Topo IB), but its members are represented in the three cellular domains of life (Table 3). In contrast, the only representative of the type IC family, DNA topoisomerase V (Topo V), is only found in the hyperthermophillic archaeon *Methanopyrus kandleri*. Topo IB and Topo V both perform relaxation of supercoiled DNA, however the structure and active site of Topo V is quite different from the other type I topoisomerases (Taneja et al., 2006).

II.2.4.2. Type II topoisomerases

Topoisomerases of the type IIA and type IIB families display some common characteristics in terms of structure and function (Bush et al., 2015; Champoux, 2001; McKie et al., 2021). The two families of type II topoisomerases share a 2-fold structural symmetry and are functional either as hetero-tetramers or homo-dimers, depending on the subfamilies considered (Table 5). This symmetry produces two to three protein-protein interfaces, which are referred to as N-gate, DNA-gate and C-gate (the latter being absent from type IIB topoisomerases).

Table 5. Structural symmetry among the five subfamilies of type II topoisomerases. For each type IIA and type IIB topoisomerase subfamilies, the subunit(s) forming the homo-dimer or hetero-tetramer are indicated, with a schematic representation of the overall oligomeric structure. Dimers of Top2, ParE, GyrB, Top6B and Top8 are represented in light and dark blue, and dimers of ParC, GyrB and Top6B are represented in orange and yellow.

Family	**Type IIA**			**Type IIB**	
Subfamily	Topo II	Topo IV	DNA Gyrase	Topo VI	Topo VIII
Subunit(s)	Top2	ParE, ParC	GyrB, GyrA	Top6B, Top6A	Top8
Oligomeric state	homo-dimer	hetero-tetramer	hetero-tetramer	hetero-tetramer	homo-dimer
Overall structure	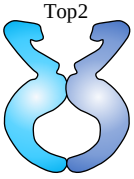	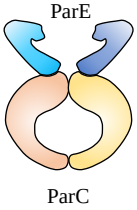	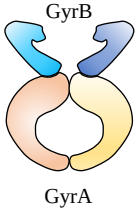	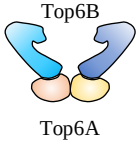	

As suggested by their denomination, the type II topoisomerases modify DNA topology by producing a double-strand break in the DNA backbone, via the formation of covalent links with the phosphate group at the 5' end of each DNA strand. Their activity is based on a double-strand passage mechanism, where a double-stranded T-segment is translocated through a cleaved double-stranded G-segment (Fig. 13A), in an ATP- and Mg^{2+}-dependent manner (Schoeffler & Berger, 2005; Wang, 1998).

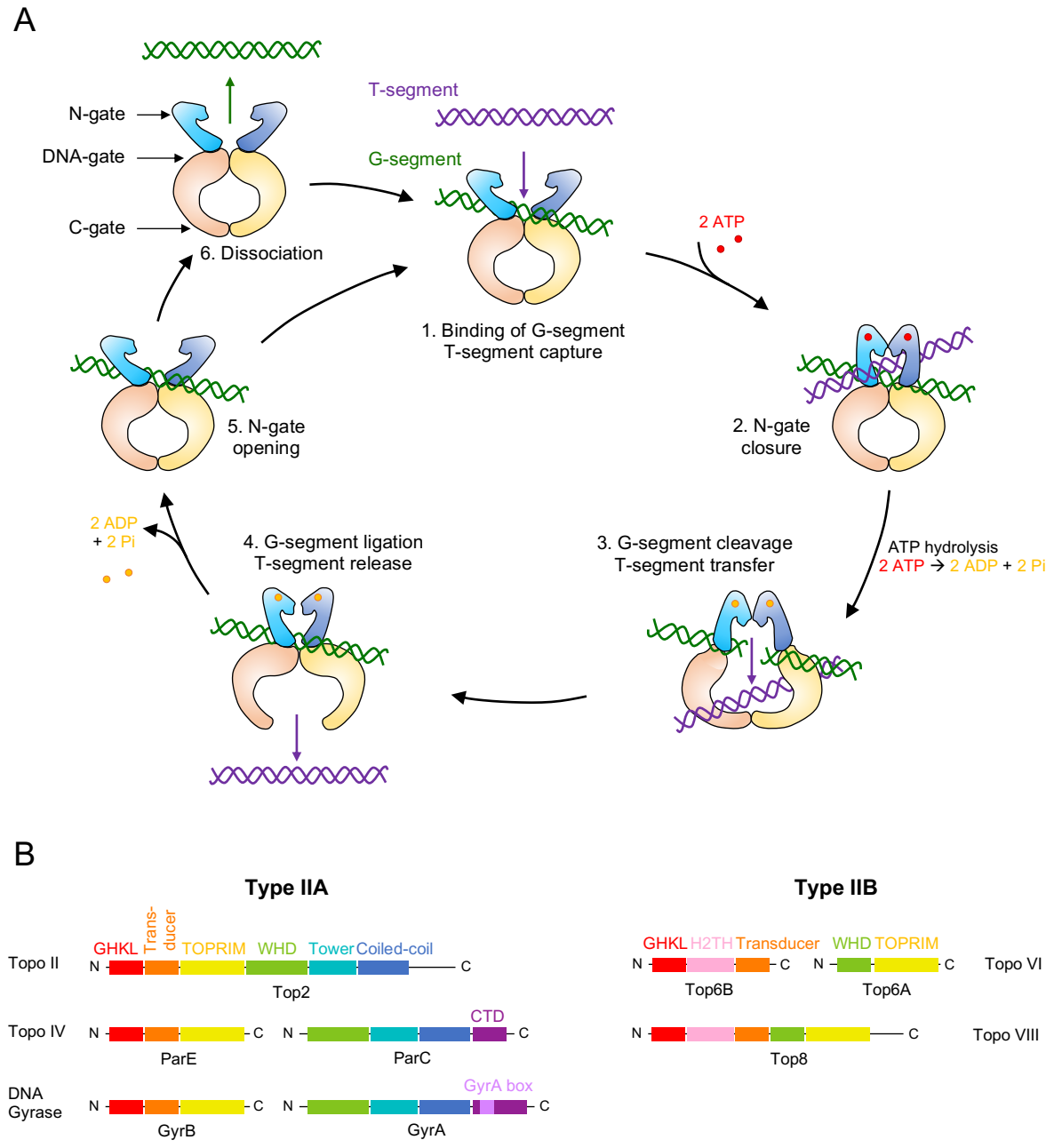

Figure 13. Type II topoisomerases rely on a double-strand passage mechanism, through the coordination of their conserved domains. A) Double-strand passage mechanism of type II topoisomerases. The enzyme binds a dsDNA segment (G-segment) at the DNA-gate while a second dsDNA segment (T-segment) is captured in the cavity between the N-gate and DNA-gate (step1). Following the binding of ATP to the GHKL domain, the N-gate

closes and the G-segment is cleaved by the combined actions of the WHD and TOPRIM domains (step 2). ATP hydrolysis triggers the opening of the DNA-gate, allowing the translocation of the T-segment through the gap of the cleaved G-segment (step 3). While the T-segment is released through the opening of the C-gate, the DNA-gate returns to a closed conformation for the ligation of the G-segment (step 4). The dissociation of the ADP molecules from the GHKL domain induces the opening of the N-gate (step 5), either to release the G-segment (step 6) or to capture a new T-segment (step 1 of a new cycle). **B**) The ATPase and cleavage domains are conserved among the type II subfamilies, but some domains are specific of a family (H2TH domain in type IIB topoisomerases) or a subfamily (GyrA-box in the DNA Gyrases). Adapted from (McKie et al., 2021).

Before DNA binding, the N-gate at the top of the enzyme is opened whereas the central DNA-gate and the lower C-gate are closed. The first step of the mechanism consists in the binding of a dsDNA G-segment to the DNA-gate, while a dsDNA T-segment is trapped by the closing of the N-gate triggered by ATP binding. Next, the G-segment is cleaved by the two tyrosines of the active site, and the ATP hydrolysis into ADP + Pi promotes the opening of the DNA-gate. This allows the passage of the T-segment through the double-strand break of the G-segment. Subsequently, the G-segment is re-ligated and the T-segment is released through opening of the C-gate or directly exits the enzyme in the case of type IIB topoisomerases that lack the C-gate. After dissociation of the ADP + Pi, the N-gate returns to an open conformation either releasing the G-segment or engaging in a new cycle with the capture of a new T-segment (Fig. 13A).

The type IIA family is composed of three sub-families, the eukaryotic topoisomerase II (Topo II), the bacterial topoisomerase IV (Topo IV) and the DNA Gyrase, which is mostly found in bacteria, but also in archaea and some plants (Table 3). Although all type IIA topoisomerases are able to perform decatenation and relaxation, DNA Gyrases are the only topoisomerases with a negative supercoiling activity. Members of the three subfamilies share conserved domains, although the eukaryotic Topo II is expressed as a unique polypeptide chain that assembles as a homo-dimer contrary to Topo IV and DNA Gyrase whose two subunits form a hetero-tetramer (Table 5). The conserved regions are the ATPase domain of the GHKL (GyrB-Hsp90-histidine kinase-MutL) family, the transducer domain, the Topoisomerase-Primase (TOPRIM) domain, the winged-helix domain (WHD), and in the C-terminal part, the tower and coiled-coil domains. Since topoisomerases of the Topo II subfamily are expressed as homo-dimers, all these domains are found on the same monomer. In the case of the hetero-tetrameric Topo IV and DNA gyrase, the ParE and GyrB subunits hold the GHKL, transducer and TOPRIM domains, while the ParC and GyrA subunits contain the WHD, tower and coiled-coil domains, along with a specific C-terminal domain (CTD) absent from Topo II (Fig. 13B).

The GHKL domain holds a Bergerat-fold motif containing three conserved sequences responsible for ATP-binding and hydrolysis, called the N, G1 and G2-boxes. The binding of ATP to the GHKL domain of each subunit induces their dimerization, leading to closure of the N-gate (Fig. 13A). The GHKL domain is connected to the TOPRIM domain via the transducer domain, which contains a highly-conserved "switch" lysine able to interact with bound ATP and act as a sensor. Upon binding and hydrolysis of ATP, the transducer domain rotates from 11° to 18° with respect to the GHKL domain, thereby promoting the opening of the DNA-gate and the passage of the T-segment (Corbett & Berger, 2003, 2005). The two domains involved in cleavage and ligation of the G-segment are the TOPRIM and WHD domains, that form the DNA-gate of type IIA topoisomerases. The TOPRIM domain participates in cleavage and ligation through the binding of magnesium ions to a DxD motif and the presence of a glutamate residue acting as a proton donor or acceptor during cleavage or ligation (Aravind et al., 1998; Sissi & Palumbo, 2009). It also possesses two highly conserved motifs, EGDSA and PLRGK, that facilitate DNA binding of the G-segment (Laponogov et al., 2009). The WHD contains the active site tyrosine responsible for DNA cleavage, as well as an isoleucine that promotes this function by producing a 150° bend in the G-segment (Dong & Berger, 2007). This bend is also partly maintained by the Tower domain, which forms the second cavity of the type IIA topoisomerases along with the coiled-coil domain.

Compared to eukaryotic Topo II, the Topo IV and DNA Gyrase possess a 30-35 kDa C-terminal extension termed the CTD, that is variable in terms of structure and sequence. The structure and composition of the CTD is highly conserved among bacterial DNA Gyrases, with six beta-sheets (referred to as blades) that adopt an unusual β-pinwheel fold (Bouige et al., 2013; Corbett et al., 2004; Hsieh et al., 2010; Ruthenburg et al., 2005; Sachdeva et al., 2020). In contrast, the CTD of topoisomerases from the Topo IV subfamily are not well conserved, as they can be composed of 3 to 8 β-sheets depending on the bacterial phylum considered, and therefore adopt either an open spiral fold or a β-pinwheel fold (Corbett et al., 2005; Hsieh et al., 2004; Vos et al., 2013). Due to their mostly basic outer surface and their cylindrical fold, the CTDs of bacterial DNA Gyrase and Topo IV are involved in DNA binding and are both able to induce a ~180° bend in the G-segment, as demonstrated by Corbett, Shultzaberger and Berger in their fluorescence resonance energy transfer (FRET) experiments with isolated CTDs of GyrA from *Borrelia burgdorferi* and ParC from *E. coli* (Corbett et al., 2004).

Strikingly, despite the similarities of their CTDs, topoisomerases of the Topo IV subfamily are unable to perform negative supercoiling. This is due to a specific sequence

(QRRGGKG) in the CTD of the GyrA subunit, the GyrA-box, which is a hallmark feature of DNA Gyrases (Ward & Newton, 1997). This sequence, located on a loop in the first blade of the β-pinwheel, is essential for the supercoiling activity of DNA Gyrases (Kramlinger & Hiasa, 2006; Lanz & Klostermeier, 2012; Vanden Broeck et al., 2019). When the GyrA-box of *E. coli* GyrA was deleted or replaced by alanine residues, the DNA Gyrase was unable to perform negative supercoiling, although it retains its decatenation and relaxation activities (Kramlinger & Hiasa, 2006). Lanz and Klostermeier also performed a mutagenic analysis on the GyrA-box of *B. subtilis* DNA Gyrase and obtained the same results with an abolition of the supercoiling activity upon deletion or mutation of the sequence. To further elucidate the role of the GyrA-box, they used FRET experiments and showed that this specific motif had an impact on the bending of the G-segment wrapped around the CTDs of GyrA (Lanz & Klostermeier, 2012). The precise mechanism by which the GyrA-box participates in bending of the G-segment was unraveled in 2019, with the first complete structure of *E. coli* DNA Gyrase bound to a DNA fragment of 180 bp, solved by cryo-electron microscopy (Vanden Broeck et al., 2019). This structure revealed that the first contact of the DNA with the β-pinwheel occurs at blade 3, followed by a wrapping around blades 4 to 6 before exiting the CTD through a contact with blade 1 (Fig. 14). Since the GyrA-box is precisely located in the portion of blade 1 that contacts the wrapped DNA, this suggests that the GyrA-box acts as a clamp at the end of the DNA, stabilizing the energetically unfavorable bent conformation (Vanden Broeck et al., 2019).

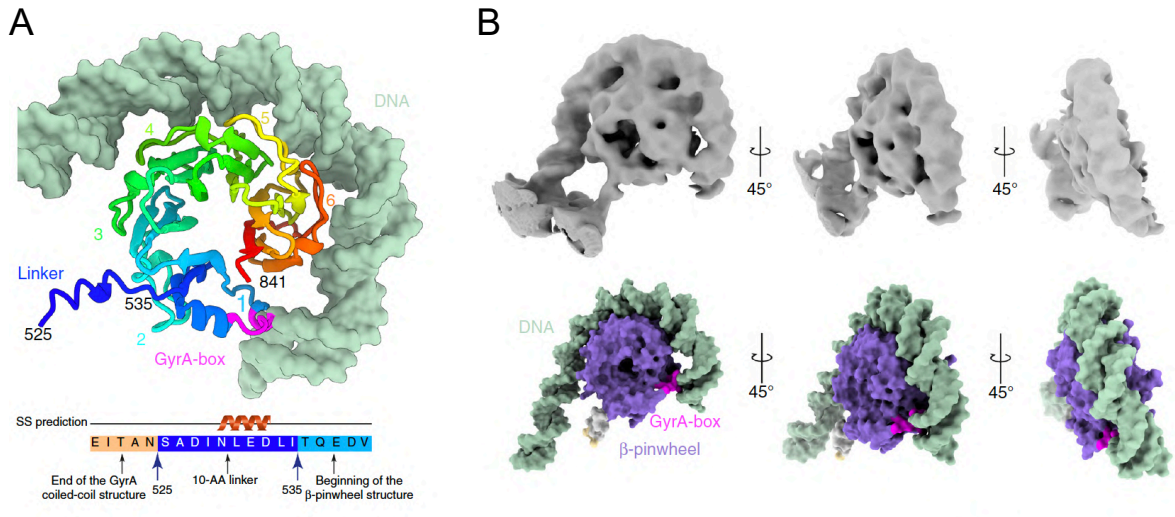

Figure 14. DNA Wrapping around the GyrA CTD β-pinwheel and GyrA-box structure in *E. coli* DNA Gyrase. A) Cartoon representation of the molecular structure of the GyrA β-pinwheel, rainbow colored from the N-terminal end in blue, to the C-terminal end in red. The GyrA-box (QRRGGKG) is colored in magenta and DNA in pale green. The β-pinwheel blades are numbered from 1 to 6. The first contact between DNA and the β-pinwheel occurs at blade 3, wraps around the disk by contacting blade 4, 5, 6 and exits the β-pinwheel through contact with

blade 1. **B**) Different views of the 6.3 Å cryo-EM map (in grey) zoomed on the β-pinwheel wrapped with DNA and the corresponding molecular models in surface representation. The GyrA-box is colored in magenta, the DNA in pale green and the β-pinwheel in dark green. The slight superhelical structure of the pinwheel is clearly visible on the side view. Adapted from (Vanden Broeck et al., 2019).

II.2.5. Small basic NAPs

Small basic NAPs (sbNAPs) are basic and highly abundant DNA-binding proteins of less than 30 kDa that change DNA topology through bending, bridging or stiffening of DNA filaments (Fig. 8B). They are usually distributed all across the nucleoid and bind non-specifically to DNA (no sequence specificity), although some of them show a preference for AT-rich sequences or a specific topology such as nicked DNA or four-way junctions (Lee et al., 2011; Wang et al., 2011). In the study by Azam and Ishihama, 12 proteins were isolated from the nucleoid of *E. coli*, among which five abundant sbNAPs: the histone-like nucleoid-structuring protein (H-NS) and its paralogue the suppressor of *td*$^{-}$ phenotype A (StpA), the heat-stable protein from *E. coli* strain U93 (HU), the integration host factor (IHF) and the factor for inversion stimulation (Fis) (Azam & Ishihama, 1999). Among these five sbNAPs, only HU homologues are encoded by the genomes of *D. radiodurans* and *D. deserti* (White 1999, Groot 2009). The low diversity of sbNAPs expressed in these two species is nonetheless not uncommon among bacteria, considering that well studied species also lack several of the sbNAPs present in *E. coli* (Table 6). Fis, H-NS and StpA are specific to γ-proteobacteria such as *E. coli* and therefore absent from species of other phyla such as *B. subtilis, S. aureus* or *S. pneumoniae* (Ohniwa et al., 2011). This is also the case of IHF, which is mostly expressed in α- and γ-proteobacteria (Dey et al., 2017; Kamashev et al., 2017). Contrastingly, HU homologues are widely conserved among the different prokaryotic phyla (Dey et al., 2017; Grove, 2011; Kamashev et al., 2017; Swinger & Rice, 2004).

Table 6. The five major sbNAPs of *E. coli* are absent from other model bacteria. Expression of the sbNAPs HU, H-NS, StpA, IHF and Fis in the model bacteria *E. coli*, *B. subtilis*, *S. aureus* and *S. pneumoniae*, in the two *Deinococcus* species *D. radiodurans* and *D. deserti*, and in the closely related thermophile *T. thermophilus*.

sbNAP	*E. coli*	*B. subtilis*	*S. aureus*	*S. pneumoniae*	*T. thermophilus*	*D. radiodurans*	*D. deserti*
HU	x	x	x	x	x	x	x
H-NS	x						
StpA	x						
IHF	x						
Fis	x						

II.2.5.1. Bridging sbNAPs

H-NS is a sbNAP of 15 kDa assembled as a dimer in solution, with the dual ability to either stiffen dsDNA or bridge two distant dsDNA fragments (Spurio et al., 1997). This double mechanism is directly linked to the peculiar structure and oligomerization of H-NS. The monomer is composed of a N-terminal oligomerization domain (NTD) and a C-terminal DNA binding domain (CTD), joined by a flexible linker (Fig. 15A).

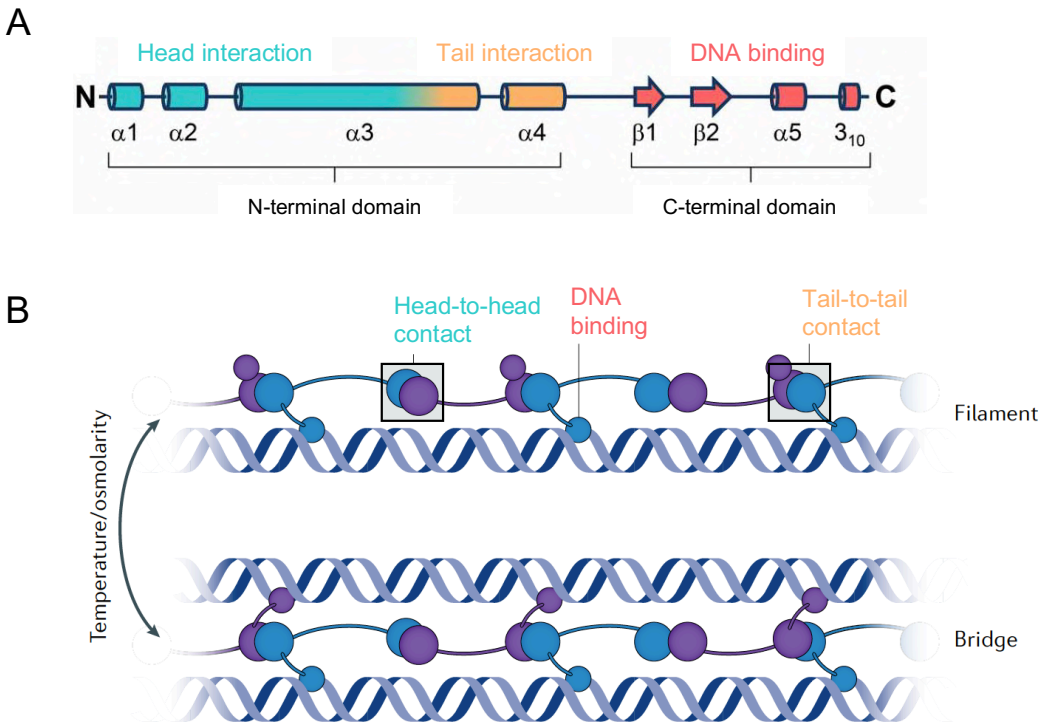

Figure 15. The histone-like nucleoid structuring protein H-NS displays a dual DNA-binding mechanism regulated by temperature and osmolarity. A) Secondary structure and domain organization of H-NS. The N-terminal domain contains the head and tail interaction regions (in blue and orange respectively), while the C-terminal domain (in red) encloses the conserved AT-hook motif responsible for DNA binding. **B**) Schematic representation of the two DNA-binding mechanisms of H-NS in a "daisy chaining" fashion. When the head-to-head dimers are in "folded" conformation, only one DNA-binding site is available leading to the formation of a H-NS filament and DNA stiffening (top). In the presence of Mg^{2+} or at lower temperature, the H-NS dimers adopt an "open" conformation with two DNA-binding sites, forming bridged structures between two DNA fragments (bottom). H-NS monomers are represented in blue or purple, so that a head-to-head dimer consists of one monomer of each color (one blue plus one purple). Adapted from (Dame et al., 2020; Grainger, 2016).

The NTD of H-NS includes two different dimerization interfaces, the head-to-head and tail-to-tail interaction regions, each of them requiring the involvement of the α-helix α3 (Arold et al., 2010). Since dimerization can occur on both interfaces simultaneously, the protein is able to oligomerize in a "daisy chaining" fashion (Arold et al., 2010). The CTD harbors a highly

conserved TGQGRTP sequence folded as an AT-hook motif responsible for specifically binding in the minor-groove of DNA (Gordon et al., 2011). AT-rich DNA sequences display a narrower minor-groove, hence H-NS shows a preference for binding to such sequences (Gordon et al., 2011).

The regulation between the two DNA-binding modes of H-NS directly derives from its structure (Fig. 15B). The functional unit of H-NS is a dimer formed by the head-to-head interaction; therefore it should have two DNA binding sites, yet the long α3 helix is unstable. This causes buckling of the said helix that folds the CTD onto the protein structure thereby hindering one DNA-binding domain of the dimer (van der Valk et al., 2017). When the H-NS dimer is in a "folded" conformation, it first binds to an AT-rich DNA sequence then multimerizes laterally along the DNA, forming a filament that stiffens the DNA (Amit et al., 2003; Dame et al., 2000; Liu et al., 2010). A concentration of Mg^{2+} ions superior to 5 mM or a growth temperature inferior to 30°C induce a conformational change that stabilizes the H-NS dimer in an "open" conformation (Kotlajich et al., 2015; Liu et al., 2010; van der Valk et al., 2017). In this configuration, the second DNA-binding site is now available for the formation of bridged DNA-H-NS-DNA filaments, creating DNA loops (Dame et al., 2006; Liu et al., 2010; van der Valk et al., 2017). The loops maintained via H-NS bridging could correspond to the smallest organizational units of the nucleoid, i.e. the 10 kbp microdomains (Noom et al., 2007). Apart from its architectural role in nucleoid organization, H-NS is involved in the transcription of several genes in proteobacteria (Ali et al., 2014; Dorman, 2014; Ono et al., 2005; Singh et al., 2014). It appears that the dual binding mode of H-NS could explain how this sbNAP regulates gene expression by stalling the progression of RNA polymerase (Kotlajich et al., 2015). When RNA polymerase binds to a H-NS-coated DNA, it displaces the H-NS filament and transcription occurs. Conversely, if the transcription starts on a H-NS-bridged DNA, the RNA polymerase is trapped by the looped conformation of DNA and transcription elongation is impeded (Kotlajich et al., 2015).

II.2.5.2. Bending sbNAPs

HU, the histone-like protein

HU is the most ubiquitous sbNAP as it is expressed in bacteria from all prokaryotic phyla (Dey et al., 2017; Grove, 2011; Kamashev et al., 2017; Swinger & Rice, 2004). HU are usually expressed as homodimers, with the exception of HU from Proteobacteria. Notably, *E.*

coli produces two HU subunits, HUα and HUβ, able to form heterodimers as well as homodimers depending on the different phases of the cell cycle (Claret & Rouviere-Yaniv, 1997). HU is a small basic protein (pI ≈ 10) with a conserved core of 90 residues, sometimes completed by N- or C-terminal extensions (also called tails) of up to 13 kDa depending on species (Fig. 16A). C-terminal extensions are mostly found in HU from Actinobacteria such as species from the genera *Streptomyces* and *Mycobacterium*, whereas N-terminal extensions are almost exclusively found in HU from the *Deinococcus* genus, along with a few proteobacteria like *Xanthomonas campestris* and *Xylella fastidiosa* (Bouthier de la Tour et al., 2015; Dey et al., 2017; Yee et al., 2011). Interestingly, in the bacteria *Gemmata obscuriglobus* and *Methylacidiphilum infernorum* from the Planctomycetes and Verrumicrobia phyla respectively, two HU homologues are expressed: one protein has an N-terminal extension and the other one has a C-terminal extension (Yee et al., 2011). Most of the N- or C-tails from HU proteins of *Deinococcus* and Actinobacterial species contain several repeats of a PAKKA motif, reminiscent of the ($^{S}/_{T}$)PKK motif repeated in the 100 residue-long C-terminal extension of eukaryotic linker histone H1 (Bharath et al., 2002). Similar to the role of these eukaryotic C-tails in DNA compaction and protein-protein interaction, bacterial HU extensions have been shown to be involved in DNA binding as well as in the interaction with other sbNAPs in the cell (Datta et al., 2019; Hołówka et al., 2017; Mukherjee et al., 2008).

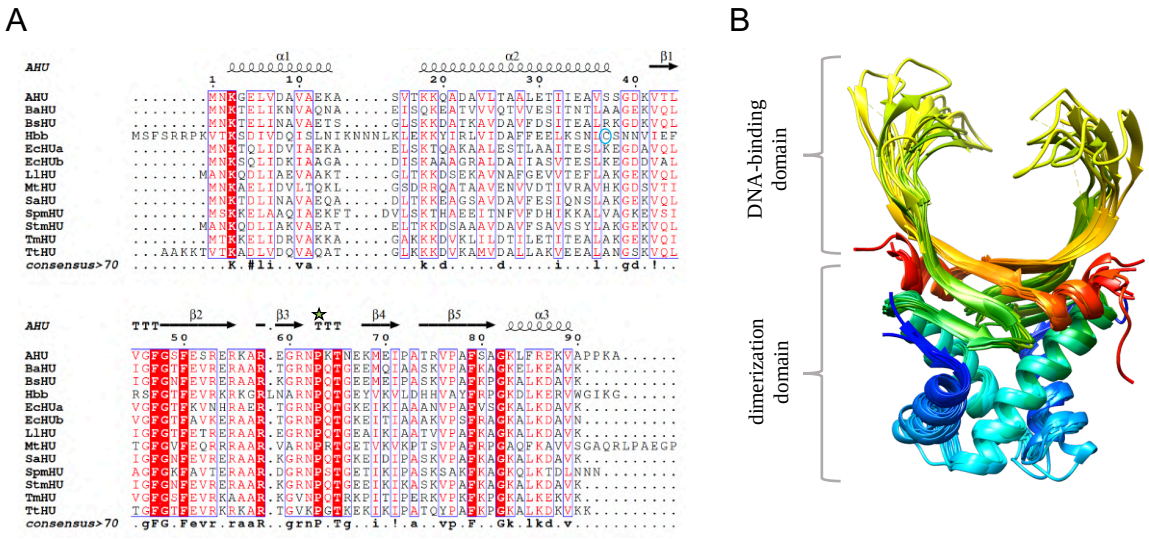

Figure 16. Despite sequence variability, the structure of HU is highly conserved among bacteria. A) Multiple sequence alignment of thirteen HU proteins from various species, whose structures were solved by X-ray crystallography. Aligned HU proteins are respectively from *Anabaena* (AHU), *Bacillus anthracis* (BaHU), *Bacillus stearothermophilus* (BsHU), *Borrelia burgdorferi* (Hbb), *Escherichia coli* (EcHUa and EcHUb), *Lactococcus lactis* (LlHU), *Mycobacterium tuberculosis* (MtHU), *Staphylococcus aureus* (SaHU), *Spiroplasma melliferum* (SpmHU), *Streptococcus mutans* (StmHU), *Thermotoga maritima* (TmHU) and *Thermus thermophilus*

(TtHU). The strictly conserved DNA-intercalating proline is indicated by a green star. The unique cysteine residue of Hbb is highlighted by a blue circle. **B**) The conserved HU-fold is composed of a DNA-binding domain and a dimerization domain. Structure alignment of HU from twelve bacterial species: AHU (PDB: 1P51 (Swinger et al., 2003)), BaHU (PDB: 3RHI (Osipiuk et al., 2011, to be published), BsHU (PDB: 1HUU (White et al., 1989)), Hbb (PDB: 2NP2 (Mouw & Rice, 2007)), EcHUαα (PDB: 6O6K (Remesh et al., 2020)), EcHUαβ (PDB: 4YEW (Hammel et al., 2016)), EcHUββ (PDB: 4P3V (Le Meur et al., 2015, to be published)), LlHU (PDB: 5LVT (Le Meur et al., 2017, to be published)), MtHU (PDB: 4DKY (Bhowmick et al., 2014)), SaHU (PDB: 4QJN (Kim et al., 2014)), SpmHU (PDB: 5L8Z (Boyko et al., 2016)), StmHU (PDB: 5FBM (O'Neil et al., 2016)), TmHU (PDB: 1B8Z (Christodoulou & Vorgias, 1998)) and TtHU (PDB: 5EKA (Papageorgiou et al., 2016)). In each of the aligned structures, monomers are colored from blue (N-terminus) to red (C-terminus).

Strikingly, despite a great variability among the sequences, structures of HU proteins from various bacteria are highly similar (Fig. 16B). The structure of the conserved core consists of a compact hydrophobic α-helical body from which two flexible β-arms protrude (Fig. 16B). The specific fold of the HU proteins is thus composed of a dimerization domain, i.e. the α-helical body, and a DNA-binding domain formed by the two β-arms (Fig. 16B). The three α-helices of the hydrophobic core are strictly conserved and only vary in length, with two α-helices contributed by the N-terminal part and one contributed by the C-terminal part of the sequence. The β-sheet content of the HU fold varies from three to five, as the β-arms are structured as either two long or four short β-strands. This is well exemplified by the long β-strands in the HU from *Borrelia burgdorferi* (Hbb) compared to those visible in HU from *Mycobacterium tuberculosis* (MtHU) (Bhowmick et al., 2014; Mouw & Rice, 2007). The N- or C-terminal extensions are expected to be highly disordered, hence they are rarely modeled in crystal structures owing to a lack of electronic density. In the structure of MtHU, the 114 residues of the C-terminal tail are missing as they degraded during crystallization of the protein (Bhowmick et al., 2014). Moreover, due to its flexibility, the loops at the tip of the β-arms are missing from 8 out of the 15 HU structures solved by crystallography, suggesting that HU are relatively flexible proteins. These residues are missing in the structures of HU from *Burkholderia ambifaria*, *E. coli* (EcHUαα, EcHUαβ and EcHUββ), *Streptomyces mutans*, *Thermotoga maritima* and *Thermus thermophilus* (Abendroth et al., 2018, to be published; Christodoulou & Vorgias, 1998; Hammel et al., 2016; Le Meur et al., 2015, to be published; O'Neil et al., 2016; Papageorgiou et al., 2016; Remesh et al., 2020).

This disordered loop contains a strictly conserved proline at position 63 of the core sequence, essential for the DNA binding and bending properties of the HU proteins (Figs. 16 and 17). Upon DNA binding, the proline residue from each β-arm is inserted between base pairs, thereby inducing a bend of nearly 140° in the DNA (Swinger et al., 2003). As this is an

energetically unfavorable conformation for DNA, the bend is maintained by several arginine and lysine residues (Fig. 17A). These positively charged amino acids form hydrogen bonds and/or Van der Waals contacts with the phosphate backbone, the sugar moieties and sometimes directly with a nucleotide, which stabilize the DNA-protein interface (DeRouchey et al., 2013; Luscombe, 2001). Moreover, a patch of positively charged residues on the side of HU proteins might provide contacts to DNA more distant to the binding site, thus enhancing the bending effect as illustrated by the structure of *Anabaena* HU bound to a 19 bp dsDNA fragment (Fig. 17B).

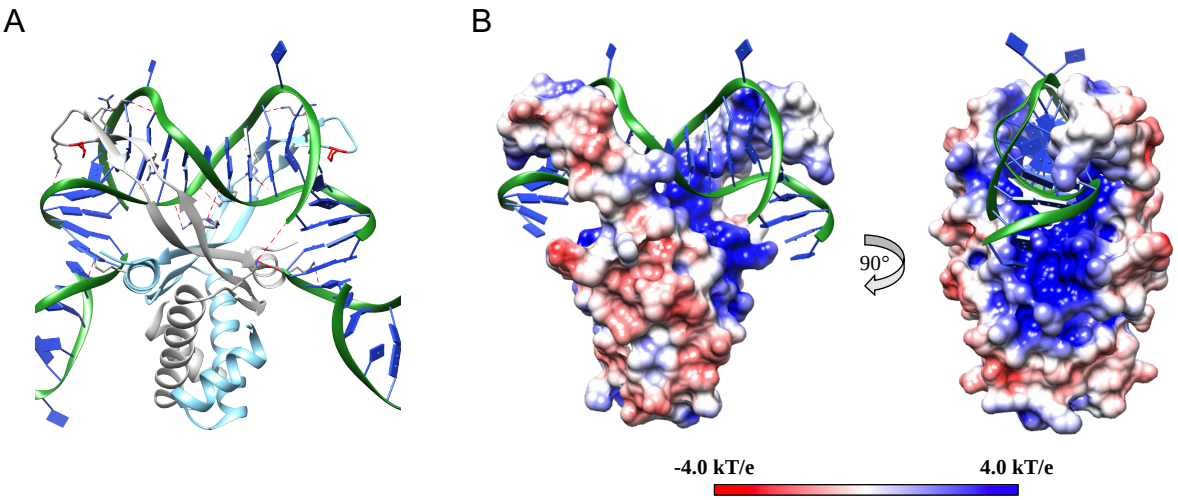

Figure 17. Proline-mediated DNA bending by *Anabaena* HU is stabilized by positively-charged lysine and arginine residues. A) Structure of HU from *Anabaena* (AHU) in complex with a 19 bp dsDNA (PDB: 1P51 (Swinger et al., 2003)). The DNA backbone and base pairs are depicted in green and dark blue respectively. The two monomers of AHU are colored in sky blue and gray, with the intercalating proline residues represented in red. Lysine and arginine residues involved in DNA binding are shown as sticks, in which nitrogen atoms are colored in blue. Van der Walls contacts and hydrogen bonds were selected based on inter-atom distances of less than 3.9 Å and 2.7 Å respectively, and are shown as red dashed lines. **B**) Electrostatic surface properties of AHU bound to DNA (PDB: 1P51 (Swinger et al., 2003)), calculated with the APBS software and displayed in Chimera. The color scale refers to electrostatic charges of the protein surface (red indicates negative charges while blue indicates positive charges). The trajectory of the DNA backbone is clearly correlated with the location of positively charged surfaces on the HU protein.

This contribution of positively charged residues from the compact α-helical body to DNA binding and bending was also evidenced in a recent study of the HU protein from *B. burgdorferi* (Hbb) using molecular dynamic (MD) simulations. In this study, Hognon et al. demonstrated that the 160° bend imposed on the 35 bp oligonucleotide bound by Hbb required to overcome a free-energy barrier of nearly 40 kcal/mol (Hognon et al., 2019). The results of their MD simulations on Hbb point-mutants hinted toward a coupled mechanistic constraint

exerted by the interaction of the β-arms with the minor groove of DNA and the electrostatic interactions of several arginine and lysine residues from the α-helical body with the DNA phosphate backbone (Hognon et al., 2019). Moreover, they ran a 1.5 µs equilibrium MD simulation on a straight DNA placed in close proximity to Hbb, starting with a model in which the β-arms of Hbb were out of the DNA minor grooves. This relatively long simulation showed that (i) Hbb alone is able to induce a major bend in the DNA, (ii) the flexibility of the β-arms is crucial in the first step of DNA binding for a correct positioning in the DNA minor grooves and (iii) the positively charged N-terminal residues undergo a partial unfolding during the first step of DNA bending as they extend out to capture the DNA molecule (Hognon et al., 2019).

Based on DNA-bound HU structures currently available in the PDB database, it seems that the interaction of HU proteins with dsDNA, as well as the residues involved, might differ in some species. In the DNA-bound structures of HU from *Anabaena*, *B. burgdorferi* and *S. aureus*, the dsDNA sits on top of the DNA binding domain between the two β-arms (Fig. 17) and is clearly bent through this interaction (Kim et al., 2014; Mouw & Rice, 2007; Swinger et al., 2003). Quite contrastingly, in the structures of DNA-bound HU from *E. coli* both the homodimer EcHUαα and heterodimer EcHUαβ lie almost parallel to the DNA backbone (Hammel et al., 2016; Remesh et al., 2020). More importantly, no DNA bending was observed in these structures, therefore Hammel and colleagues hypothesized that these two dimers of EcHU could multimerize along the DNA to form spiral filaments that might straighten it (Hammel et al., 2016; Remesh et al., 2020).

Generally, HU proteins bind to double-stranded DNA with little to no specificity as illustrated by the well-studied HU proteins from *E. coli*. Depending on the considered homo- or heterodimer, the affinity for linear dsDNA in salt concentrations similar to that observed *in vivo* varies from 2.5 mM to 66 mM for EcHUαα and EcHUββ respectively (Pinson et al., 1999). However, the three EcHU proteins all seem to favor binding to structurally distorted dsDNA such as cruciform dsDNA or dsDNA with nicks or gaps as shown by their increased affinities for a gapped dsDNA of 8 nM and 400 nM for EcHUαα and EcHUββ respectively (Pinson et al., 1999). This could be explained by the lower energy required to bend such conformations, as they tend to be more flexible. In *E. coli*, alteration of DNA topology upon HU binding depends on protein concentration. At low abundance, EcHU increases the compaction of DNA, while at high concentration corresponding to one EcHU dimer per 9 bp, it stiffens DNA (Dame & Goosen, 2002; Luijsterburg et al., 2008; Sagi et al., 2004; Skoko et al., 2004; van Noort et al., 2004). In other species like *M. tuberculosis*, HU displays a different mechanism of DNA

compaction *in vitro*. In an AFM study conducted by Datta and colleagues, the incubation of MtHU with a linearized plasmid DNA yielded condensed ball-like structures (Datta et al., 2019).

HU proteins were shown to be associated with a variety of cell functions. In *M. tuberculosis*, MtHU interacts with TopoI to stimulate relaxation of supercoiled DNA and associates preferentially with *Ori* region of the genomic DNA where it promotes chromosome segregation (Ghosh et al., 2014; Hołówka et al., 2017). Specific mutations in the sequence of HU from *Streptococcus intermedius* perturb nucleoid segregation and cell division, besides altering cell surface (Liu et al., 2008). In the related species *S. pneumoniae*, HU is essential for cell viability and is required to maintain supercoiling of genomic DNA *in vivo* (Ferrándiz et al., 2018). In addition, in the bacteria *E. coli* and *Salmonella typhimurium* we note the presence of a HU regulon in which gene transcription is controlled by the HU proteins by means of DNA supercoiling (Mangan et al., 2011; Oberto et al., 2009).

IHF, the integration host factor

Another important DNA-bender is the integration host factor (IHF) that shares the conserved fold of HU proteins along with a sequence similarity of nearly 40%. Despite these resemblances, IHF has many features that differ compared to HU. IHF is exclusively expressed by Proteobacteria, as heterodimers of α and β subunits. Unlike HU, IHF binds with a high affinity of 1.5 nM to a specific DNA sequence characterized by the consensus WATCARNNNNTTR, where W is adenine or thymine, R is adenine or guanine and N is any nucleotide (Hales et al., 1994; Wang et al., 1995). The structure of IHF from *E. coli* in complex with a 36 bp dsDNA revealed a bending of the DNA backbone of more than 160°, superior to that caused by HU binding to DNA (Rice et al., 1996). In a thorough study published in 2017, Dey and colleagues used phylogenetic and structural analyses to unravel the specificities that differentiate HU and IHF (Dey et al., 2017). Regarding the sequences, they noted some specific positions in the dimerization and DNA-binding domains that could discriminate between the two protein families (Table 7).

Table 7. Residues that discriminate between proteins of the HU, IHFα and IHFβ families. The position of residues refers to the sequence of MtHU. Conserved residues are designated by their three-letter codes and variable positions are indicated by a "Δ" sign. Adapted from (Dey et al., 2017).

Residue Position (MtHU)	HU	IHFα	IHFβ
11	Ala / Ser	Δ	Δ
21	Ala / Val	Δ	Δ
22	Δ	Ala / Ser	Ala / Ile / Val
24	Ala / Val	Δ	Δ
26	Δ	Ala / Ile / Val	Ala / Ile / Val
27	Ala / Ser / Thr	Glu / Asp	Δ
40	Δ	Δ	Arg
43	Δ	Lys	Glu
45	Δ	Arg	Arg
55	Arg	Lys	Arg / His / Tyr
74	Δ	Arg	Arg / Lys

The authors also highlighted family-specific features when comparing the structures of HU and IHF proteins. The dimer interface of IHF is mostly maintained by two aromatic clusters, whereas there is only one aromatic cluster in HU proteins. Furthermore, the dimerization domain of IHF is enriched in charged residues such as Arg and Glu, which form salt bridges tethering the two monomers together. As for the DNA-binding site, IHF is richer in arginine residues, whereas the DNA binding domain of HU contains more lysine residues. Arginines are more prone to interact with DNA bases bringing specificity to the interaction, while lysines tend to bind to the DNA backbone, thereby reinforcing the stability of protein-DNA interactions (DeRouchey et al., 2013; Luscombe, 2001). Alike HU, IHF has been shown to affect important cellular processes like transcription, chromosome replication through competing interactions with DnaA at the *Ori* site, and recombination (Andrade et al., 2021; Hołówka et al., 2018; Macchi et al., 2003; Mumm et al., 2006; Siam et al., 2003; Taniguchi et al., 2019).

Fis, factor for inversion stimulation

Fis or factor for inversion stimulation is also a DNA-bending sbNAP, although it is quite different from HU and IHF, both in terms of sequence and structure (Fig. 18). This small basic protein of 11 kDa is expressed as a homodimer that folds into two β-sheets and four α-helices, with a specific helix-turn-helix (HTH) motif on the C-terminal part of the sequence. Upon binding dsDNA through the two HTH motifs of the dimer, Fis induces a bend of 50° to 90° to the DNA backbone (Hancock et al., 2016; Pan et al., 1996). This protein usually binds to an

AT-rich DNA sequence of 15 bp containing a G or C nucleotide at position 1 and 15 respectively, although it mostly recognizes the narrow minor grooves rather than the sequence itself (Cho et al., 2008; Stella et al., 2010). Fis is a sbNAP specific to γ-proteobacteria, mostly expressed at the beginning of the exponential growth phase (Azam & Ishihama, 1999; Browning et al., 2010). It is involved in the regulation of more than four hundred genes in *E. coli*, as exemplified by its regulation of the expression of another NAP, Dps, through an interaction with the RNA polymerase (Gawade et al., 2020; Grainger et al., 2008; Opel et al., 2004). Fis also participates in the maintenance of genome supercoiling, by stabilizing plectonemes of supercoiled DNA through its binding at the intercross of two dsDNA (Schneider et al., 2001). Moreover, this sbNAP interferes with the supercoiling activity of DNA gyrase indirectly as it acts as a transcriptional repressor of the *gyrA* and *gyrB* genes (Schneider et al., 1999).

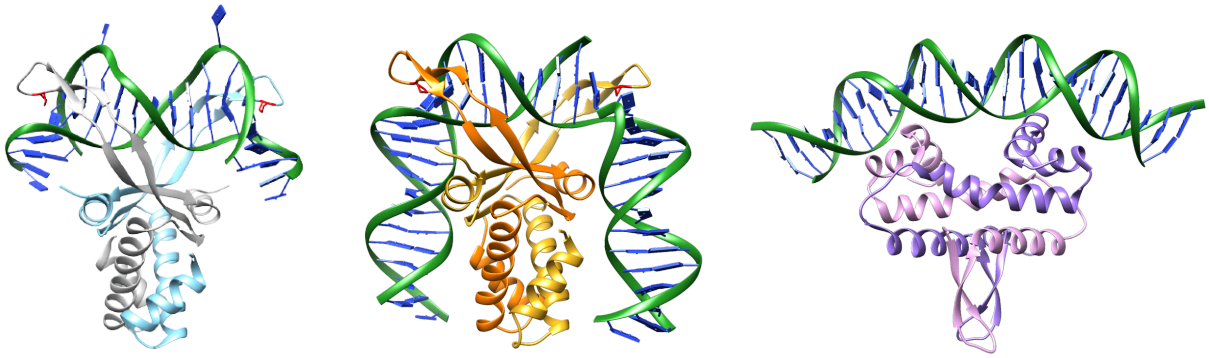

AHU EcIHF EcFis

Figure 18. The sbNAPS HU, IHF and Fis bend DNA to different extents. Structures of *Anabaena* HU (PDB: 1P51 (Swinger et al., 2003)), *E. coli* IHF (PDB: 1IHF (Rice et al., 1996)) and *E. coli* Fis (PDB: 3JRA (Stella et al., 2010)) in complex with dsDNA, highlighting the variability of bending imposed on DNA by these three sbNAPs. The DNA backbone and base pairs are colored in green and dark blue respectively. HU is colored in blue and gray, IHF is in orange and gold, Fis is in purple and plum. Intercalating proline residues in HU and IHF are represented in red.

III. Nucleoid associated proteins of *D. radiodurans* and *D. deserti*

According to shotgun proteomics experiments, the most abundant proteins associated with the nucleoids of *D. radiodurans* and *D. deserti* are the DNA Gyrase and the histone-like protein HU (Toueille et al., 2012).

III.1. *D. radiodurans* and *D. deserti* HU proteins

III.1.1 Specific features of deinococcal HU proteins

Deinococcus' HU proteins are expressed as homodimers that possess the same conserved core domain as other bacterial HUs. According to the genome annotations available in the UniProtKB database (https://www.uniprot.org/), 27 of the 84 *Deinococcus* species contain at least one gene annotated as HU. More than 75% of these 27 *Deinococcus* bacteria have at least two genes coding for HU homologues (with up to 9 genes for *D. hopiensis*), while the genome of only a few species seem to encode for a single HU as it the case for *D. radiodurans*. The alignment of HU proteins translated from the afore mentioned annotated loci highlights some common features, notably regarding the nature of their N-terminal extensions (Fig. 19A). At least one HU homologue with an N-terminal extension longer than 15 residues is encoded in the genome of all 27 of these species, with the exception of *D. cellulosilyticus* and *D. radiophilus* that bear potential HU genes with a short N-tail of less than 6 residues.

Regarding the amino acid composition of these long N-terminal extensions (> 15 residues), they appear to be enriched in lysine, alanine and proline residues compared to the core sequence (Fig. 19B). The N-tails of deinococcal HU are indeed composed of 20-25% lysine, 25-35% alanine and 8-13% proline on average, and contain a PAKKPA motif that bears resemblance with the motif repeated in the C-tail of eukaryotic histone H1. As a comparison, the sequence of the C-terminal extension of linker histone H1 is composed of 40% lysine, 20–35% alanine and 15% proline residues.

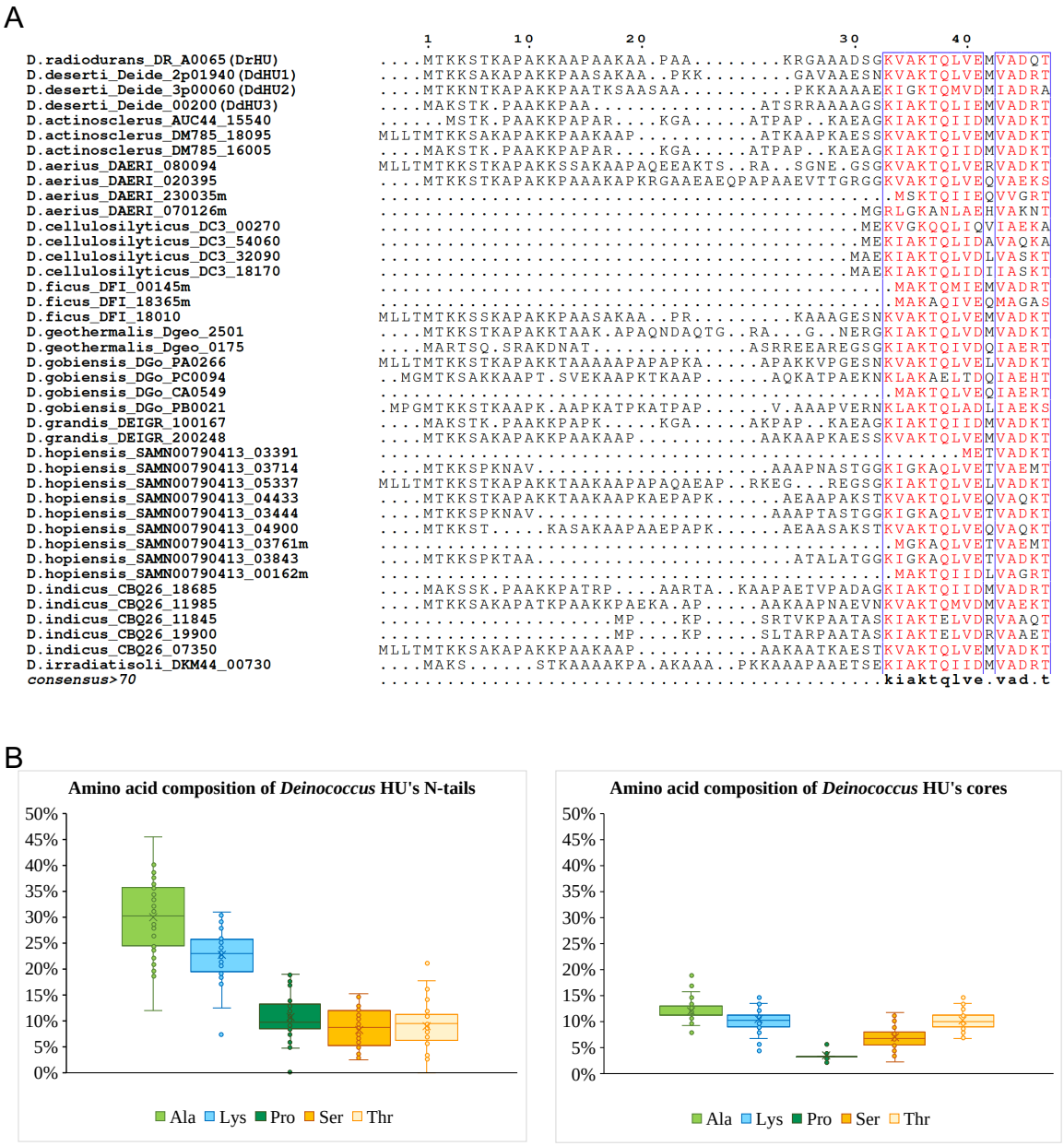

Figure 19. Most of the *Deinococcus* HU proteins possess a long N-terminal extension enriched in lysine and alanine. A) Multiple sequence alignment of HU proteins from 12 *Deinococcus* species, based on annotated genome loci deposited in the UniprotKB database. Each HU is identified by the Deinococcus species to which it belongs, followed by the gene locus. Residue numbering refers to the sequence of DrHU, and a consensus sequence is shown at the bottom of the alignment. **B**) Proportion of alanine (Ala, in light green), lysine (Lys, in blue), proline (Pro, in dark green), serine (Ser, in dark orange) and threonine (Thr, in light orange) residues present in the N-terminal extension of at least 15 residues (left panel, N=50) and in the core of HU proteins from *Deinococcus* (right panel, N=50).

III.1.2 The single HU of *D. radiodurans*

DrHU is the only HU variant expressed in *D. radiodurans*, which seems quite rare among *Deinococcaceae* since only five other species (*D. irradiatisoli*, *D. puniceus*, *D. reticulitermitis*, *D. soli* and *D. swuensis*) possess only one HU variant. In the absence of other sbNAPs such as H-NS, IHF or Fis in *D. radiodurans*, DrHU is essential for the cell viability (Nguyen et al., 2009). As most of the Deinococcal HU proteins, DrHU possesses a long N-terminal extension of 33 residues enriched in lysines, alanines and prolines (Fig. 19A). DrHU's N-tail is involved in DNA binding, as suggested by the study of Ghosh and Grove using a truncated DrHU devoid of its 33 residue-long extension (Ghosh & Grove, 2006). Contrary to the full-length protein, the truncated DrHU was able to bind shorter dsDNA oligonucleotides and displayed a preference for gap or nicked DNA. A homology model of DrHU computed with the structure prediction server Robetta (https://robetta.bakerlab.org/) clearly highlights the length of this extension compared to the core folding and how it may interact with DNA (Fig. 20). It is plausible that this disordered N-terminal extension may become partially folded as α-helices upon DNA binding, alike the C-terminal tail of histone H1 (Roque et al., 2005).

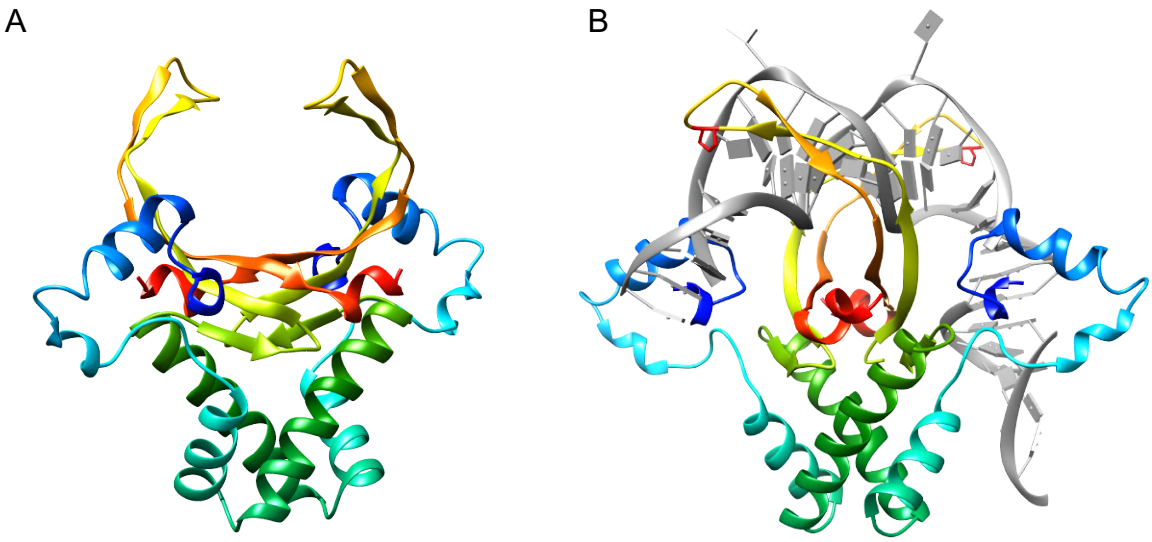

Figure 20. The lysine-rich N-terminal extension of DrHU involved in DNA binding could be partially folded into one or more α-helices. A) Homology model of the structure of DrHU, calculated by the structure prediction server Robetta (https://robetta.bakerlab.org/), with one of the energetically plausible configuration of the N-terminal extensions. Each monomer is colored from blue (N-terminus) to red (C-terminus). The long N-terminal extension could be highly flexible and composed of α-helices. The core of the protein would retain the characteristic of the conserved HU-fold, with two β-arms protruding from a compact hydrophobic α-helical body. **B**) Possible configuration of DrHU upon DNA-binding, inferred by structure overlay with DNA bound *Anabaena* HU (PDB: 1P51 (Swinger et al., 2003)). DNA from the AHU structure is represented in gray and intercalating proline residues of DrHU are colored in red.

Surprisingly, studies on the DNA-bending properties of DrHU concluded that it was unable to bend double-stranded oligonucleotides and thus did not play a role in nucleoid compaction (Ghosh & Grove, 2004, 2006). Instead, it was proposed that the major function of DrHU is to stabilize a specific DNA conformation named the four-way junction (4WJ) for which the highest affinity was observed. The 4WJ, also called Holliday junction, is a peculiar DNA structure made of four DNA strands associated in a cross-like or "X" shape, thought to be an intermediate structure formed during homologous recombination events, arising during DNA repair (Holliday, 1974). Nonetheless, a recent study revealed that the original DrHU gene had been misannotated in the databank and that these earlier experiments had been performed with an irrelevant 15 amino-acid extension at the N-terminus of DrHU (Bouthier de la Tour et al., 2015). These additional residues could have had an impact on DNA binding and bending properties of DrHU.

III.1.3 The three HU variants of *D. deserti*

The genome of *D. deserti* contains four genes coding for HU homologues, yet a proteomic analysis performed on cell extracts of *D. deserti* demonstrated that only three HU proteins are expressed (Toueille et al., 2012). These sbNAPs were named DdHU1 (Deide_2p01940), DdHU2 (Deide_3p00060) and DdHU3 (Deide_00200) based on their sequence similarity compared to DrHU (Fig. 21). Among the three HU proteins of *D. deserti*, DdHU1 is the predominant HU homologue *in vivo* as it is 5 and 10 times more abundant in the nucleoid than DdHU2 and DdHU3 respectively (Toueille et al., 2012). It has been shown that expression of either DdHU1 or DdHU2 alone is sufficient for *D. deserti* cell survival, implying that these two variants may have overlapping functions *in vivo* and that DdHU3 is dispensable (Bouthier de la Tour et al., 2015). Furthermore, in *D. radiodurans*, DrHU can be replaced with either DdHU1 or DdHU2, but not with DdHU3 (Bouthier de la Tour et al., 2015). Thus, it seems that DdHU3 is not essential for *D. deserti* survival and that it cannot fulfill the functions of the other two variants or DrHU. As of today, no biochemical studies were performed with HU proteins from *D. deserti* to further characterize their DNA binding ability and their role in DNA compaction.

The three HU variants of *D. deserti* all possess N-terminal extensions similar to DrHU, but their lengths and sequences differ, with the N-tail of DdHU3 being markedly shorter than that of DdHU1 and DdHU2 by six residues (Fig. 21). Compared to the other two variants, the

core sequence of DdHU3 has three main differences located in the DNA binding domain and the dimerization domain (Fig. 21). In the DNA binding domain, the positively charged residue 86 is replaced by an alanine, whereas the position 111 is occupied by an arginine instead of an alanine (residue numbering refers to the sequence of DrHU, as in Fig. 20). The last particularity of DdHU3 is the presence of a cysteine, located at position 64 on one of the long α-helices in the dimerization domain. Based on the DrHU model computed by Robetta (Fig. 20), this cysteine that is also present in DrHU would be located on the surface of the protein. Since it might be exposed to solvent, this single cysteine could be involved in scavenging of ROS via its thiol functional group or in oligomerization of HU (Requejo et al., 2010).

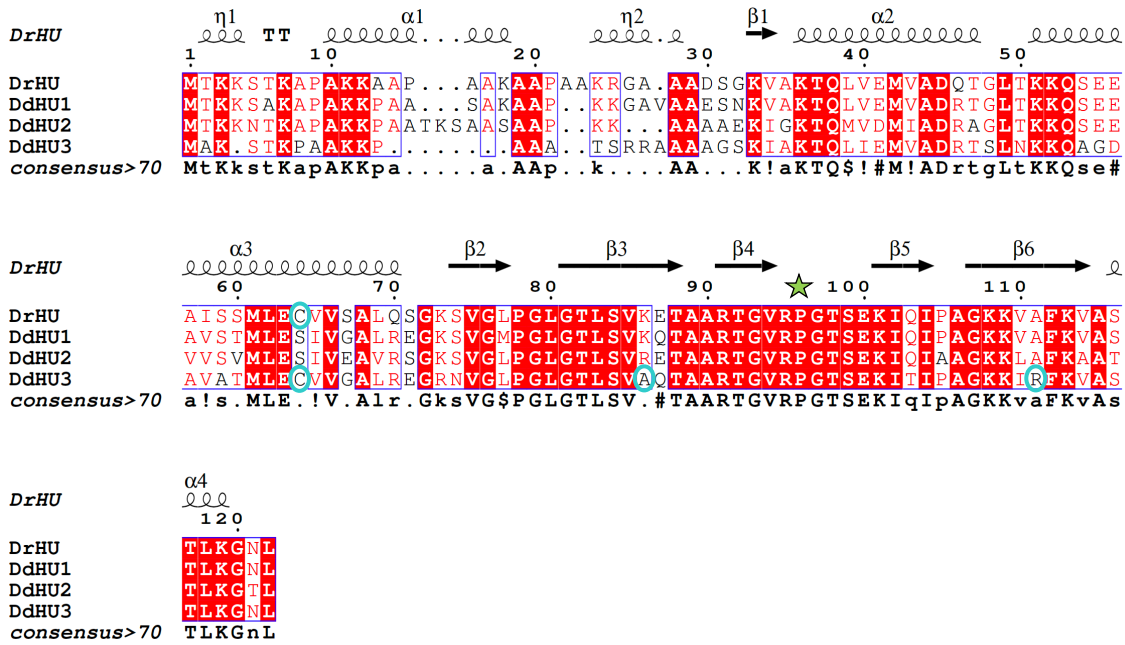

Figure 21. Residues of the DNA-binding domain of HU from *D. radiodurans* and *D. deserti* are highly conserved. Multiple sequence alignment of DrHU from *D. radiodurans* and DdHU1, DdHU2, DdHU3 from *D. deserti*. The strictly conserved DNA-intercalating proline is indicated by a green star. The unique cysteine residues of DrHU and DdHU3, as well as the alanine and arginine residues in positions 86 and 111 of DdHU3 are highlighted by blue circles. The secondary structure of DrHU displayed on top of the alignment is that of the homology model predicted by the Robetta server (https://robetta.bakerlab.org/).

III.2. *D. radiodurans* DNA gyrase

The second most abundant DNA-binding protein in the nucleoid of *D. radiodurans* is the DNA Gyrase, a type IIA topoisomerase essential for cell viability (Toueille et al., 2012). In addition to DNA gyrase, many bacteria encode a second topoisomerase of the type IIA family, namely topoisomerase IV (Topo IV), whose function is to resolve catenation events arising

after replication (Wang et al., 2008). However, some species like *D. radiodurans* or *Mycobacterium tuberculosis* lack a Topo IV, and in these cases, the DNA gyrase takes over the function of decatenation (Tomb et al., 1997; Fraser et al., 1998; Cole et al., 1998; Bouige et al., 2013). Accordingly, it was shown that the DNA gyrase from *D. radiodurans* (DrGyr) induces negative-supercoiling or relaxation, while also acting as a Topo IV by performing decatenation of intertwined duplicated circular chromosomes (Kota et al., 2016). Through biochemical and structural characterization, Bouige and colleagues proved that the decatenation activity of *M. tuberculosis* DNA gyrase was directly linked to the presence of a second GyrA-box motif (QGRGGKG), called GyrA-box-1, in the β-pinwheels formed by the C-terminal domain of the GyrA subunit (Bouige et al., 2013). Alignment of the GyrA subunits of *D. radiodurans* (DrGyrA) and *M. tuberculosis* (MtGyrA) reveals the presence of a similar GyrA-box-1 motif (KGRGGLG) in the sequence of DrGyrA at position 731 to 737, that could exert the same function as in MtGyrA (Fig. 22).

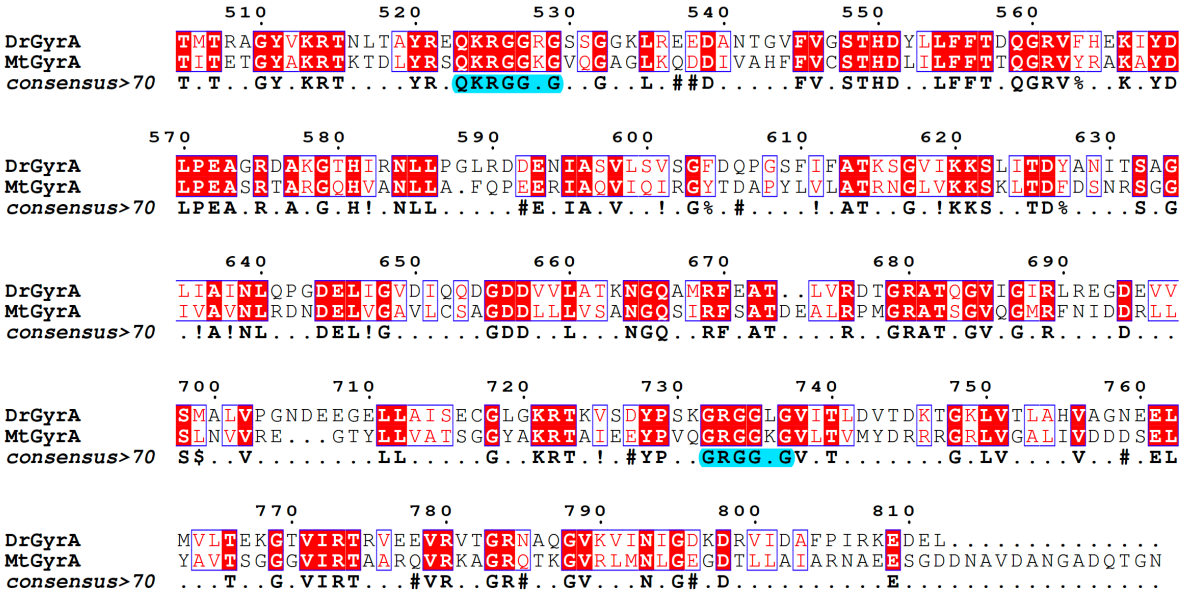

Figure 22. The GyrA subunit of *D. radiodurans* possesses a second GyrA-box motif similar to that of the GyrA subunit of *M. tuberculosis*. Sequence alignment of the GyrA subunits of *D. radiodurans* (DrGyrA) and *M. tuberculosis* (MtGyrA). Only the C-terminal domains corresponding to the β-pinwheel fold are shown. The consensus sequence for the canonical GyrA-box (residues 523 to 529) and the GyrA-box-1 (residues 731 to 737) are highlighted in blue. Residue numbering refers to the sequence of DrGyrA.

Upon radiation or desiccation, the *gyrA* and *gyrB* genes are up-regulated as they are part of the radiation-desiccation response regulon controlled by DdrO and IrrE (Bouthier de la Tour et al., 2013; Tanaka et al., 2004). Two independent studies demonstrated that in these stress conditions the two subunits of DrGyr interact with PprA, another radiation-induced protein

(Devigne et al., 2016; Kota et al., 2016). *In vitro*, the *Deinococcus*-specific PprA stimulates the decatenation and relaxation activity of DrGyr, while inhibiting its supercoiling activity, thereby easing chromosome decatenation after exposure to ionizing radiation or desiccation (Devigne et al., 2016; Kota et al., 2016). Additionally, it was shown that the 5' untranslated region (UTR) of the *gyrA* gene further activates gene expression under the same stress conditions (Villa et al., 2017). The 5' UTRs are non-coding RNAs frequently associated with gene regulation as they can modify the conformation of the ribosome binding site, control mRNA degradation, and even serve as a binding site for other molecules involved in gene regulation (Arthur et al., 2011; Papenfort & Vanderpool, 2015; Tay et al., 2013; Vazquez-Anderson & Contreras, 2013).

III.3. DdrC, a *Deinococcus* specific NAP

III.1.1 The *Deinococcus*-specific DNA damage response proteins

The DNA damage response (Ddr) proteins are *Deinococcus* specific proteins of unknown function, whose expression is induced following exposure to ionizing radiation, UV light or desiccation suggesting that they might be important for the extreme resistance of *Deinococcus* species to DNA damaging agents. The Ddr proteins A to P were first identified in the study conducted by Tanaka and colleagues on *D. radiodurans* cells exposed to ionizing radiation and desiccation (Tanaka et al., 2004). A more recent transcriptomic study on irradiated cells of *D. deserti* revealed the expression of eight new Ddr proteins, coined DdrQ to X (Blanchard et al., 2017). Of the numerous Ddr proteins discovered as of today, only six are encoded in all of the eleven *Deinococcus* species whose genomes have been completely annotated and assembled: DdrB, DdrC, DdrH, DdrI, DdrN and DdrO (Lim et al., 2019).

As presented in Chapter I.4. of the present manuscript, DdrO is a transcriptional repressor that controls the radiation-desiccation response regulon through its interaction with IrrE, another protein present in all *Deinococcaceae*. DdrI, encoded by the DR_0997 gene in *D. radiodurans*, is a putative cyclic AMP receptor protein (CRP) whose deletion induced an increased sensitivity to hydrogen peroxide, ionizing radiation and UV light (Yang et al., 2016). As a member of the CRP family, DdrI is a transcriptional regulator that controls the expression of several genes in *D. radiodurans*, similar to the function of its homologue in *E. coli* (Geng & Jiang, 2015; Yang et al., 2016). The putative CRP regulon was identified by Yang and colleagues, who discovered DNA sequences with a similarity to the binding site of *E. coli* CRP

upstream of 18 genes in *D. radiodurans* and demonstrated that DdrI could bind to these sequences *in vitro* (Yang et al., 2016).

While no structural or biochemical data are available yet for DdrH and DdrN, DdrB was studied during the past decade leading to its identification as a single-strand binding (SSB) protein (Bouthier de la Tour et al., 2011; Norais et al., 2009; Quevillon-Cheruel & Servant, 2020; Sugiman-Marangos & Junop, 2010; Sugiman-Marangos et al., 2013, 2016; Xu et al., 2010). DdrB is expressed as a pentameric ring of nearly 100 kDa that binds exclusively to ssDNA and is able to coat ssDNA similarly to RecA or SSB (Norais et al., 2009; Sugiman-Marangos & Junop, 2010; Xu et al., 2010). This protein contains a specific ssDNA-binding fold that differs from the canonical oligonucleotide-binding domain of other SSB proteins (Sugiman-Marangos & Junop, 2010). To coat ssDNA, two DdrB pentamers assemble into an higher order assembly, which promotes high-fidelity DNA annealing, by partially restricting access to unpaired nucleotides (Sugiman-Marangos et al., 2013, 2016; Xu et al., 2010). Due to its specific properties, DdrB is involved in double-strand break repair after exposure to DNA damaging agents, while also affecting the transformation of *D. radiodurans* by plasmid DNA (Bouthier de la Tour et al., 2011; Quevillon-Cheruel & Servant, 2020).

III.1.2 The DNA damage response protein DdrC

In *D. radiodurans* and *D. deserti*, DdrC is one of the five genes whose expression is the most up-regulated following irradiation or desiccation (Blanchard et al., 2017; Tanaka et al., 2004). After irradiation, DdrC is rapidly recruited to the nucleoid of *D. radiodurans* where it binds homogenously throughout the genome (Bouthier de la Tour et al., 2017). However, after 2 to 3h post-irradiation, the protein distribution changes drastically as it gathers into foci positioned between the two segregating nucleoids of a dyad. The DNA-binding properties of DdrC were characterized *in vitro* by Bouthier de la Tour and colleagues, highlighting a capacity to bind both ds- and ssDNA with a preference for the latter (Bouthier de la Tour et al., 2017). Strikingly, DdrC is able to perform a variety of processes upon DNA-binding. Regardless of the substrate conformation (circular or linear) or composition (ss- or dsDNA), DdrC protects DNA from degradation by DNaseI and Mung Bean endonucleases or exonuclease III. In the presence of ssDNA, DdrC was shown to be able to stimulate annealing of complementary oligonucleotides and to induce a strong compaction of circular ssDNA. DdrC also impacted the conformation of circular dsDNA, although bridge structures were observed instead of the

compact conformation previously obtained with circular ssDNA. Last, after incubation with linear dsDNA the protein was shown to promote circularization of DNA molecules containing either cohesive or blunt ends.

Objectives of the thesis

The main goal of my thesis project was to better understand the organization and assembly of the nucleoid in *D. radiodurans*. Which features allow the genome of this extremely resistant *Deinococcus* species to be so compact, yet remarkably dynamic capable of changing its shape along the cell cycle? To tackle this question, I focused my work on the two major NAPs of *D. radiodurans*, the HU protein and the DNA Gyrase, and also on DdrC, the *Deinococcus*-specific NAP with pleiotropic activities. In order to compare DrHU with other deinococcal HU proteins, I also studied the three HU variants of *D. deserti*, DdHU1, DdHU2 and DdHU3. The long-term goal of this work is to reconstitute a minimal chromatin *in vitro*, which could be used for instance to study DNA repair mechanisms in the context of chromatin instead of naked DNA.

In this context, the project was divided into three main parts to achieve both structural and functional characterization of these proteins. The first goal was to use either X-ray crystallography or cryo-electron microscopy (cryo-EM) to elucidate the structures of the basic elements of *D. radiodurans* nucleoid, namely the DNA Gyrase and the HU proteins, and DdrC. One can note that at the beginning of my thesis, several DNA Gyrase structures with sequences similar to that of *D. radiodurans* (DrGyr) had already been determined, however they were all incomplete lacking residues at either the N- or C-termini of the GyrA and/or GyrB subunits (Chan et al., 2017; Germe et al., 2018; Papillon et al., 2013; Petrella et al., 2019; Schoeffler et al., 2010). Thus, obtaining a complete structure of *D. radiodurans* DNA Gyrase would help us apprehend the versatility of its functions. Regarding the HU proteins, solving the structure of their N-terminal extensions would allow us to better understand their DNA-binding specificity. As for the *Deinococcus* specific NAP DdrC, it has no known structural homologs, thus its structure could potentially enlighten us on its particular functions in irradiated *Deinococcus* cells.

The second part of the project was to characterize the interaction of these NAPs with ss- or dsDNA of different length and topology to determine the substrate preference, affinity and binding site length. To do so, the proteins were subjected to gel shift assays, fluorescence polarization experiments and supercoiling or relaxation activity assays in the case of DNA Gyrase. Such DNA binding properties had already been characterized *in vitro* for DdrC, so my work focused mostly on the HU proteins and the DNA gyrase for this part.

The third and last part of the thesis project was to study the effects of the HU proteins, DNA Gyrase and DdrC on the conformation and compaction of DNA, by means of atomic force microscopy, electron microscopy and cryo-electron tomography, with the aim to observe specific DNA-protein complexes and determine their architectures. We chose to perform our experiments on plasmid DNA, as its properties are closer to those of circular genomic DNA than that of an oligonucleotide.

Materials and Methods

I. Cloning, expression and purification of proteins

I.1. Molecular Biology

I.1.1. The DNA Gyrase of *D. radiodurans*

To express the heterotetrameric DrGyr complex, I relied on two distinct strategies that consisted either in (i) the separate expression and purification of DrGyrA and DrGyrB subunits, followed by the reconstitution of the full complex ($DrGyrA_2B_2$), or (ii) the direct expression and purification of a fusion of the two subunits (DrGyrBAfus) with a 3-amino acid linker (Gly-Asp-Leu) between DrGyrB and DrGyrA to stabilize the complex. For the first approach, the *gyrA* and *gyrB* genes were amplified from the genomic DNA of *D. radiodurans* and inserted into pET21D and pProExHTB plasmids respectively (maps are presented in Appendices). The constructs were designed so that DrGyrA is expressed with a non-cleavable C-terminal His-tag, while DrGyrB is expressed with a cleavable N-terminal His-tag (Table 8). For the pProExHTB_DrGyrBAfus construct, the amplified *gyrA* and *gyrB* genes from *D. radiodurans* were both inserted in the pProExHTB plasmid downstream of the cleavable N-terminal His-tag (Table 8).

Table 8. Characteristics of the constructs used to express DrGyrA, DrGyrB and DrGyrBAfus in *E. coli*. "His_6" denotes the presence of a hexa-histidine purification tag, "Tcs" refers to the tobacco etch virus (TEV) protease recognition and cleavage site (ENLYFQG, cleaved between Q and G), and "GDL" is the 3-amino acid linker between the C-terminus of DrGyrB and the N-terminus of DrGyrA in the fusion. The His_6 and Tcs in pProExHTB are linked by 7 amino acids (DYDIPTT).

Construct	pET21D_DrGyrA	pProExHTB_DrGyrB	pProExHTB_DrGyrBAfus
Protein	DrGyrA-His_6	His_6-Tcs-DrGyrB	His_6-Tcs-DrGyrB-GDL-DrGyrA
Plasmid	pET21D	pProExHTB	pProExHTB
Promoter	T7	T7	T7
Inducer	IPTG	IPTG	IPTG
Purification tag	6-His	6-His	6-His
Position	C-terminus	N-terminus	N-terminus
Cleavage	No	Tev digestion	Tev digestion

The three constructs were produced by means of Gibson assembly, which relies on a combination of three enzymes in one reaction: an exonuclease, a DNA polymerase and a DNA ligase. After addition of overlapping regions to both the DNA to be inserted and the receiving vector, the exonuclease digests the 5' ends of the DNA to create 3' overhangs. Due to their complementarity, the DNA fragments anneal allowing the DNA polymerase to extend the 3'

ends leaving nicks that are sealed by the DNA ligase. Following this approach, the genes and vectors were amplified by polymerase chain reaction (PCR) to produce dsDNA fragments with overlapping ends (Table 9). To enhance the efficiency of Gibson assembly, the PCR amplified plasmids were digested by DpnI, a restriction enzyme that only digests methylated DNA thereby removing the plasmid template. Then, the vectors and the inserted genes were mixed at a molar ratio of 1 to 3 (vector to inserted gene) with a fixed vector quantity of 0.05 pmol, followed by addition of NEBuilder HiFi DNA Assembly Master Mix (New England Biolabs) for a final reaction volume of 20 µl. After a 15 min incubation at 50°C, the reactions were stored on ice. The constructs were amplified in DH5α *E. coli* cells (New England Biolabs) grown in LB with 100 µg/ml ampicillin and extracted from 5 ml of overnight cell cultures using the NucleoSpin Plasmid QuickPure kit (Macherey-Nagel). Correct insertion of the *gyrA* and/or *gyrB* genes was assessed by restriction enzymes digestion followed by Sanger sequencing of the positive constructs (GENEWIZ).

Table 9. List of the primers used to insert *gyrA* and/or *gyrB* into pET21D or pProExHTB. Sequences of the primers used in the PCR to amplify the *gyrA* and *gyrB* genes, as well as the pET21D and pProExHTB vectors for Gibson assembly. The nucleotides in bold in the sequences of GyrB_Fus_Rev and GyrA_Fus_For correspond to the 3-amino acid linker inserted between DrGyrB and DrGyrA for the fusion (GGC GAT CTC → Gly Asp Leu).

Construct	Sequence (5' to 3')
pET21D_DrGyrA	
GyrA_For	5'-TACCATGGGAATGACCGGAATTCAACCTG-3'
GyrA_Rev	5'-TGGTGCTCGAGCAGCTCGTCTTCCTTGCG-3'
pET21_For	5'-AAGACGAGCTGCTCGAGCACCACCACCAC-3'
pET21_Rev	5'-TTCCGGTCATTCCCATGGTATATCTCCTTC-3'
pProExHTB_DrGyrB	
GyrB_For	5'-CGCCATGGGAATGAGCTTTTCCCATGCG-3'
GyrB_Rev	5'-ATGCCTCGAGTCAGACGCTGATTTCAGC-3'
pPro_For	5'-CAGCGTCTGACTCGAGGCATGCGGTACC-3'
pPro_Rev	5'-AAAAGCTCATTCCCATGGCGCCCTGAAA-3'
pProExHTB_DrGyrBAfus	
GyrB_For	5'-CGCCATGGGAATGAGCTTTTCCCATGCG-3'
GyrB_Fus_Rev	5'-GTCAT**GAGATCGCC**GACGCTGATTTCAG-3'
GyrA_Fus_For	5'-AGCGTC**GGCGATCTC**ATGACCGGAATTC-3'
GyrA_Fus_Rev	5'-ATGCCTCGAGTTACAGCTCGTCTTCCTTG-3'
pPro_Fus_For	5'-CGAGCTGTAACTCGAGGCATGCGGTACC-3'
pPro_Rev	5'-AAAAGCTCATTCCCATGGCGCCCTGAAA-3'

I.1.2. The HU proteins of *D. radiodurans*, *D. deserti*, *B. burgdorferi* and *T. thermophilus*

The constructs designed for the expression of the HU proteins from *D. radiodurans* and *D. deserti* were already produced when I started my thesis project. Briefly, the *hu* gene (DR_A0065) from *D. radiodurans* was amplified from the genomic DNA of *D. radiodurans* by PCR amplification and inserted after a cleavable His-tag in the pProExHTB plasmid by restriction-ligation using the NcoI-HF and HindIII-HF restriction enzymes (New England Biolabs). The *hu1* (Deide_2p01940), *hu2* (Deide_3p00060) and *hu3* (Deide_00200) genes from *D. deserti* were amplified from plasmids pTOPO_DdHU1, p11559_DdHU2 and p11559_DdHU3 provided by our collaborators (L. Blanchard and A. De Groot from CEA Cadarache). The PCR amplified genes were then inserted into the pProExHTB plasmid as described for DrHU.

For the HU proteins of *B. burgdorferi* and *T. thermophilus*, synthetic *hup* (BB_0232) and *hutth* (TTHA1349) genes were ordered from Eurofins Genomics with insertion of restriction sites for the NcoI and HindIII restriction enzymes at their 5' and 3' end respectively. The genes were extracted from the pEX-A128_Hbb and pEX-A128_TtHU plasmids provided by Eurofins Genomics by digestion with the NcoI-HF and HindIII-HF restriction enzymes and inserted by ligation into the pProExHTB vector previously digested with the same restriction enzymes. The constructs were amplified in E. cloni *E. coli* cells (Lucigen) grown in LB with 100 µg/ml ampicillin and extracted from 5 ml of overnight cell cultures using the NucleoSpin Plasmid QuickPure kit. Correct insertion of the genes was assessed by restriction enzymes digestion followed by Sanger sequencing of the positive constructs (GENEWIZ).

I.1.3. DdrC of *D. radiodurans*

The construct designed for the expression of DdrC was already produced when I started my thesis project. The *ddrc* (DR_0003) gene of *D. radiodurans* was amplified from the pET26b_DdrC plasmid kindly provided by our collaborators (P. Servant from I2BC, Orsay). The PCR amplified gene was subsequently inserted into the pProExHTB plasmid with the restriction-ligation method using the NcoI-HF and HindIII-HF restriction enzymes.

I.2. Expression & Purification

I.2.1. The DNA Gyrase of *D. radiodurans*

Production of the reconstituted complex

To produce $DrGyrA_2B_2$, the two subunits were expressed and purified separately, prior to reconstitute the heterotetrameric complex. DrGyrA and DrGyrB were expressed in BL21 (DE3) *E. coli* cells grown at 37°C in 1 L of LB with 100 µg/ml ampicillin. Once the optical density at 600 nm (OD_{600}) reached 1.0 to 1.2, the temperature was lowered to 20°C and expression was induced with 1 mM of isopropyl β-d-1-thiogalactopyranoside (IPTG) overnight. After centrifugation of the cell cultures, each pellet was resuspended in 20 ml of a lysis buffer composed of 50 mM Tris-HCl pH 8.0, 500 mM NaCl, 0.5 mM phenylmethylsulphonyl fluoride (PMSF), 1 mM $MgCl_2$, 10 µg/ml DNaseI, 10 µg/ml lysozyme, 5 % glycerol and a tablet of complete EDTA-free Protease Inhibitor Cocktail (Roche). Cells were lysed by sonication on ice for 3 min with 10s pulses (10s ON for 30s OFF) at 50 % amplitude and centrifuged at 48,000 g for 30 min. For each subunit, the cleared cell lysate was loaded on 2 ml of Ni-Sepharose 6 Fast Flow resin (GE Healthcare) pre-equilibrated with buffer Gr-A (50 mM Tris-HCl pH 8.0, 250 mM NaCl, 1 mM β-mercaptoethanol (β-ME), 5 % glycerol). After washing the column with 10 column volumes (CV) of buffer Gr-A, 12 CV of buffer Gr-A supplemented with 25 mM imidazole and 12 CV of buffer Gr-A supplemented with 50 mM imidazole, DrGyrA or DrGyrB were eluted in a single step with 6 CV of buffer Gr-A supplemented with 250 mM imidazole. The fractions containing DrGyrB were pooled and submitted to digestion by tobacco etch virus (TEV) protease to cleave the N-terminal His-tag. The protein was mixed with TEV protease at a mass ratio of 1:20 (TEV protease to DrGyrB), and incubated at room temperature for 30 min to activate the protease followed by an overnight incubation at 4°C to complete the digestion. DrGyrA and the cleaved DrGyrB were then diluted with buffer Gr-B (50 mM Tris-HCl pH 8.0, 50 mM NaCl, 1 mM β-ME, 5 % glycerol) to lower NaCl concentration to 100 mM prior to loading on 5 ml HiTrap Heparin HP columns (GE Healthcare) previously equilibrated with buffer Gr-C (50 mM Tris-HCl pH 8.0, 100 mM NaCl, 1 mM β-ME, 5 % glycerol) to eliminate nucleic acid contaminations. After washing the column with 5 CV of buffer Gr-C, the subunits were eluted by a step gradient of NaCl from 250 mM to 1 M NaCl in buffer Gr-C, using 5 CV for each step of the elution (250 mM, 500 mM, 750 mM and 1 M of NaCl). The cleaved DrGyrB was eluted at 250 mM NaCl while DrGyrA was eluted at 500 mM NaCl. The fractions were pooled and concentrated on Amicon Ultra-15 Centrifugal Filter Units with a cut-

off of 30 kDa (Millipore) before a final purification step on a Superdex S200 10/300 column (GE Healthcare) pre-equilibrated with buffer Gr-C. DrGyrA and DrGyrB were concentrated to a final concentration of 2.5 and 6 mg/ml respectively and stored at -80°C before reconstitution of the complex. To obtain the heterotetrameric complex $DrGyrA_2B_2$, the two subunits DrGyrA and DrGyrB were mixed at a molar ratio of 1:1.2 (DrGyrA to DrGyrB) in a 350 µl reaction and incubated for 15 min on ice. To confirm the oligomeric state of the complex and remove the slight excess of DrGyrB, the reaction was loaded on a Superdex S200 10/300 column pre-equilibrated with buffer Gr-C. The fractions containing $DrGyrA_2B_2$ were pooled and directly stored at -80°C, at a final concentration of 0.3 mg/ml corresponding to a molar concentration of 1 µM.

Production of the fusion

DrGyrBAfus was expressed in BL21 (DE3) *E. coli* cells grown at 37°C in 2 L of LB with 100 µg/ml ampicillin. Once the OD_{600} reached 0.8 to 1.0, expression was induced with 1 mM of IPTG for 5h at 25°C. After centrifugation of the cell culture, the pellet was resuspended in 20 ml of a lysis buffer composed of 50 mM Tris-HCl pH 8.0, 500 mM NaCl, 2 mM $MgCl_2$, 10 µg/ml DNaseI, 10 µg/ml lysozyme, 5 % glycerol and a tablet of protease inhibitors. Cells were lysed by sonication on ice for 3 min with 10s pulses (10s ON for 30s OFF) at 50 % amplitude and centrifuged at 48,000 g for 30 min. The cleared cell lysate was loaded on 2 ml of Ni-Sepharose 6 Fast Flow resin pre-equilibrated with buffer Gf-A (50 mM Tris-HCl pH 8.0, 250 mM NaCl, 5 % glycerol). After washing the column with 3 CV of buffer Gf-A, 7.5 CV of buffer Gf-A supplemented with 25 mM imidazole and 7.5 CV of buffer Gf-A supplemented with 50 mM imidazole, DrGyrBAfus was eluted in a single step with 10 CV of buffer Gf-A supplemented with 250 mM imidazole. The fractions containing the protein were pooled and diluted with buffer Gf-B (50 mM Tris-HCl pH 8.0, 50 mM NaCl, 5 % glycerol) to lower NaCl concentration down to 100 mM before loading on a 5 ml HiTrap Heparin HP column pre-equilibrated with buffer Gf-C (50 mM Tris-HCl pH 8.0, 100 mM NaCl, 5 % glycerol). After washing the column with 8 CV of buffer Gf-C, the protein was eluted by a linear gradient of NaCl from 100 mM to 1 M NaCl in buffer Gf-C over 12 CV. The fusion eluted in a single peak around 500 mM NaCl and the pooled fractions were digested by TEV protease as described previously for DrGyrB. The cleaved DrGyrBAfus was then concentrated on an Amicon Ultra-15 Centrifugal Filter Unit with a cut-off of 50 kDa, for further purification on a Superdex S200

10/300 column pre-equilibrated with buffer Gf-C. The purified DrGyrBAfus was concentrated to a final concentration of 7.2 mg/ml and stored at -80°C.

I.2.2. The HU proteins of *D. radiodurans*, *D. deserti* and *B. burgdorferi*

General process for the production of HU proteins

As variants of the same protein family, the HU proteins of *D. radiodurans*, *D. deserti* and *B. burgdorferi* were expressed and purified following the same protocol (Fig 23), with slight variations in the composition of the buffers for Hbb compared to the *Deinococcus* HUs.

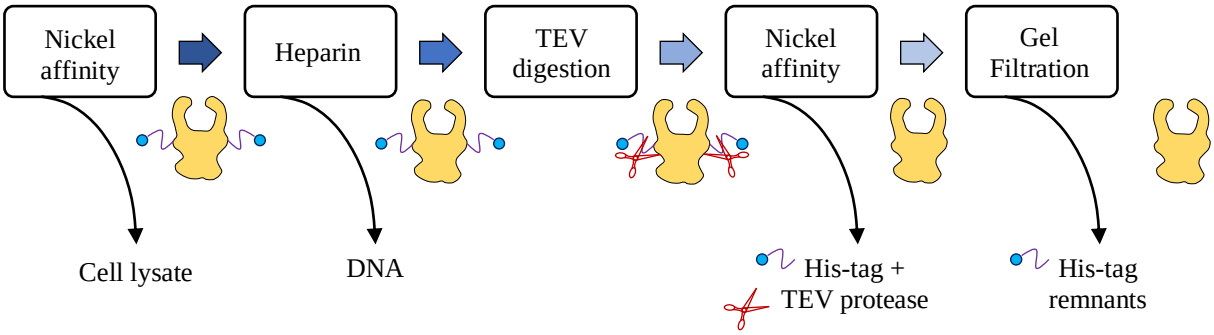

Figure 23. Overview of the HU proteins purification process. Schematic representation of the successive purification steps performed to obtain a pure HU protein devoid of its N-terminal His-tag. The yellow shape represents a HU protein dimer with a His-tag (blue circle) linked to its N-terminal extremity via a cleavable TEV site (purple line). This N-terminal His-tag is removed during the purification process upon digestion by the TEV protease (red scissors).

Briefly, after an overnight expression in *E. coli* the cells were lysed by sonication and the lysate was cleared by centrifugation. Then the soluble fraction of the cell lysate was loaded on a nickel affinity column to bind the HU proteins that were expressed with a cleavable N-terminal His-tag. After a dilution to lower the salt concentration, the HU proteins were loaded on a Heparin column to remove the DNA that could have been co-purified with these DNA-binding proteins. To remove the His-tag, the purified HU proteins were incubated overnight with the TEV protease. The cleaved HU proteins were separated from the enzyme and the cleaved His-tag by a second nickel affinity chromatography. Since the proteins lost their His-tag, they no longer bind to the resin and were recovered in the flow through and the first washes, while the cleaved His-tag and the TEV protease remained bound to the column. Finally, the cleaved HU proteins were purified by size exclusion chromatography before being concentrated and flash-cooled in liquid nitrogen for storage at -80°C.

Detailed process for the production of DrHU, DdHU1, DdHU2 and DdHU3

The HU proteins of *D. radiodurans* and *D. deserti* were expressed in BL21 (DE3) *E. coli* cells grown at 37°C in 2 L of LB supplemented with 100 µg/ml ampicillin. Once the OD_{600} reached 1.0 to 1.4, the expression was induced overnight at 20°C by addition of 1 mM IPTG. Cells were harvested by centrifugation at 9,000 g for 30 min and resuspended in 80 ml of lysis buffer (50 mM Tris-HCl pH 8.0, 500 mM NaCl, 2 mM $MgCl_2$, 10 µg/ml DNaseI, 10 µg/ml lysozyme and a tablet of protease inhibitors). Cells were lysed by sonication on ice for 3 min with 10s pulses (10s ON for 30s OFF) at 70 % amplitude and centrifuged at 48,000 g for 30 min. The cleared cell lysate was loaded on a 5 ml HisTrap FF nickel affinity column, pre-equilibrated with buffer HU-A (50 mM Tris-HCl pH 8.0, 500 mM NaCl). After washing the column with 7 column volumes (CV) of buffer HU-A, two additional washes were performed with 5 CV of buffer HU-A supplemented with 25 mM imidazole followed by 11 CV of buffer HU-A supplemented with 50 mM imidazole. Then the HU protein was eluted by a linear gradient of imidazole from 50 to 500 mM imidazole in buffer HU-A over 12 CV. The four HU proteins were all eluted around 250 mM of imidazole. The fractions were pooled and diluted with buffer HU-B (50 mM Tris-HCl pH 8.0, 50 mM NaCl). The diluted pool was loaded on a 5 ml HiTrap Heparin HP column pre-equilibrated with buffer HU-C (50 mM Tris-HCl pH 8.0, 250 mM NaCl). The column was washed with 5 CV of buffer HU-C, followed by elution with a linear gradient of NaCl from 250 mM to 2 M NaCl in buffer HU-C over 12 CV. To remove the cleavable N-terminal His-tag, fractions corresponding to the purified HU protein were pooled, mixed with TEV protease at a mass ratio of 1:20 and incubated overnight at 4°C after a short incubation at room temperature to start the digestion. The cleaved HU protein was loaded on 1 ml of Ni-Sepharose 6 Fast Flow resin equilibrated with buffer HU-A. The resin was washed with 6 CV of 25 mM imidazole in buffer HU-A and 6 CV of 50 mM imidazole in buffer HU-A. The TEV protease was eluted in a single step with 12 CV of 250 mM imidazole in buffer HU-A. The cleaved HU protein was typically present in the flow through and the first wash (at 25 mM imidazole). After concentration by successive centrifugations at 3,200 g on a Amicon Ultra-15 Centrifugal Filter Unit with a cut-off of 10 kDa, the cleaved HU protein was loaded on an ENrich SEC 650 column (Biorad) equilibrated with buffer HU-D (20 mM Tris-HCl pH 8.0, 200 mM NaCl, 5% glycerol). For each of the four variants, the purified HU protein eluted in a single peak around 15 ml. After a final concentration step, the proteins were flash-cooled in liquid nitrogen and stored at -80°C until further use.

Adaptation of the process for the production of Hbb

The HU protein of *B. burgdorferi* was expressed in BL21 (DE3) *E. coli* cells as previously described. Cell lysis and protein purification were performed following the same protocol used for the production of DrHU, DdHU1, DdHU2 and DdHU3, with minor adjustments. First, to account for the presence of a cysteine in the sequence of Hbb, 1 mM of dithiothreitol (DTT) was added in all the lysis and purification buffers. Secondly, the concentration of NaCl in the buffer used for equilibration of the Heparin column was lowered from 250 mM to 100 mM of NaCl and thus the elution was performed with a linear gradient from 100 mM to 1 M of NaCl instead of 250 mM to 2 M of NaCl.

I.2.3. DdrC of *D. radiodurans* and its selenomethionine variant

The DNA damage response protein C (DdrC) of *D. radiodurans* was expressed in BL21 (DE3) *E. coli* cells grown at 37°C in 2 L of LB supplemented with 100 µg/ml ampicillin. Once the OD_{600} reached 1.0 to 1.2, the expression was induced for 4 hours at 28°C by addition of 1 mM IPTG. Cells were harvested by centrifugation at 9,000 g for 15 min and resuspended in 40 ml of lysis buffer (50 mM Tris-HCl pH 7.5, 800 mM NaCl, 5 mM $MgCl_2$, 10% sucrose, 0.01% triton X-100, 1 µg/ml DNaseI, 1 µg/ml lysozyme and a tablet of protease inhibitors). Cells were lysed by sonication on ice for 3 min with 15s pulses (15s ON for 30s OFF) at 70 % amplitude and centrifuged at 48,000 g for 30 min. The cleared cell lysate was loaded on a 5 ml HisTrap FF nickel affinity column, pre-equilibrated with buffer Dd-A (50 mM Tris-HCl pH 7.5, 800 mM NaCl, 1 mM $MgCl_2$). After washing the column with 10 CV of buffer Dd-A, two additional washes were performed with 6 CV of buffer Dd-A supplemented with 25 mM imidazole followed by 5 CV of buffer Dd-A supplemented with 50 mM imidazole. Then DdrC was eluted with a linear gradient of imidazole from 50 to 500 mM imidazole in buffer Dd-A over 8 CV. The fractions corresponding to DdrC were pooled and, after addition of TEV protease at a mass ratio of 1:20 to cleave the His-tag, they were transferred in a dialysis tubing with a 10 kDa cut-off and dialyzed overnight at 4°C against 1 L of buffer Dd-A with 5% glycerol. To remove the His-tag and traces of uncleaved protein, the cleaved DdrC was loaded on 1 ml of Ni-Sepharose 6 Fast Flow resin equilibrated with buffer Dd-A. The resin was washed with 5 CV of buffer Dd-A, then 6 CV of 25 mM imidazole in buffer Dd-A and 6 CV of 50 mM imidazole in buffer Dd-A. The TEV protease was eluted in a single step with 6 CV of 500 mM imidazole in buffer Dd-A. The cleaved DdrC was recovered in the flow-through and in the 25 mM imidazole wash.

After concentration by successive centrifugations at 5,000 g on a Amicon Ultra-15 Centrifugal Filter Unit with a cut-off of 10 kDa, DdrC was loaded on a Superdex S75 10/300 GL column (GE Healthcare) pre-equilibrated with buffer Dd-B (20 mM Tris-HCl pH 7.5, 200 mM NaCl, 5% glycerol). Finally, DdrC was concentrated to a final concentration of 24 mg/ml, flash-cooled in liquid nitrogen and stored at -80°C until further use.

For the AFM experiments, a batch of DdrC was produced following the protocol described previously, but without glycerol in the purification buffers. Therefore, the final size exclusion chromatography was performed with buffer Dd-C (20 mM Tris-HCl pH 7.5, 500 mM NaCl). This 'glycerol-free' batch was stored at a final concentration of 16 mg/ml at -80°C.

The selenomethionine-substituted DdrC (SeMet-DdrC) was produced in BL21 (DE3) *E. coli* cells grown at 37°C in minimal M9 medium supplemented with 100 µg/ml ampicillin using a modified version of the metabolic inhibition protocol described previously (Doublie, 1997; Timmins et al., 2005). Expression was induced overnight with 1 mM IPTG at 28°C. The SeMet-DdrC protein was then purified as described for native DdrC and was stored at 20 mg/ml in buffer Dd-B at -80°C.

I.2.4. Monitoring protein purity by polyacrylamide gel electrophoresis

The successive purification steps of each protein were analyzed by polyacrylamide gel electrophoresis (PAGE) under denaturing conditions in the presence of sodium dodecyl sulfate (SDS) according to the protocol described by Laemmli (Laemmli, 1970). Before loading on SDS-PAGE gels, samples were mixed with 4X denaturing protein loading dye (62.5 mM Tris-HCl pH 6.8, 20 % SDS, 100 mM β-ME, 5 % bromophenol blue, 10 % glycerol) and heated for 5 min at 95°C. To monitor the production of $DrGyrA_2B_2$, DrGyrBAfus and DdrC, the samples were loaded on handcast TGX Stain-Free polyacrylamide gels (Biorad). These gels contain a fluorescent compound that forms a covalent bond with tryptophan residues, enhancing their fluorescence under UV-light. After a short activation under UV-light, protein fluorescence is then directly detected using a ChemiDoc MP imager, thereby suppressing the need for staining after migration. Since none of our HU proteins contain tryptophan residues, their purification was monitored on "traditional" handcast polyacrylamide gels that were stained with Coomassie blue or InstantBlue (Expedeon) after migration, and visualized with the ChemiDoc MP imager. After loading of the denatured samples, the gels were run either at 250 V for 30 min (Stain-Free gels) or 200 V for 45 min ("traditional" gels) in TGS buffer (25 mM Tris-HCl pH 8.0, 192

mM glycine, 0.1 % SDS) at room temperature. The percentage of polyacrylamide in the gels was adjusted to the molecular weight of the protein of interest (Table 10).

Table 10. Percentage of polyacrylamide gels used to monitor protein production. For each protein produced during the thesis, the molecular weight is given, along with the corresponding percentage of bisacrylamide in the gels used for SDS-PAGE. The type of gel (Stain-Free or classic) is also mentioned. *In the case of HU proteins, the indicated molecular weight is an average value of that of the 6 proteins (DrHU, DdHU1, DdHU2, DdHU3, Hbb and TtHU).

Protein	Molecular weight (kDa)	Percentage of polyacrylamide	Stain-Free or classic
DrGyrA	89.8	10 %	Stain-Free
DrGyrB	73.1	10 %	Stain-Free
DrGyrBAfus	163.6	7.5 %	Stain-Free
DdrC	25.1	12 %	Stain-Free
HU proteins	*12.0	15 %	Classic

II. Biophysical characterization

II.1. Size-exclusion chromatography coupled to multi-angle laser light scattering

Size-exclusion chromatography (SEC) coupled to multi-angle laser light scattering (SEC-MALLS) is a combined technique that allows the determination of the molecular weight, the size and the distribution of these parameters (i.e. the homogeneity) in a protein sample in solution. In a standard MALLS experiment, a solution of macromolecules such as proteins or polymers is exposed to a well-focused polarized light beam usually produced by a laser source (Fig. 24A). Interaction of the polarized light with the macromolecules in solution leads to light scattering in multiple directions. The intensity of the scattered light at different angles is recorded by up to 18 photodiode detectors positioned in a horizontal plane, which is orthogonal to the polarization plane (typically vertical by convention). The molar mass of the molecule is inferred from the scattered light function $R(\theta)$ that expresses the scattered light intensity as a function of the scattering angle θ and from the protein concentration. The size of the protein has a direct influence on the intensity of scattered light as a function of the scattering angle (Fig. 24B-C). A small molecule with a size comparable to that of the light beam will produce

an isotropic scattering meaning that the intensity of the scattered light will not vary as a function of the scattering angle. However, larger molecules produce an anisotropic scattering in which the intensity of scattered light varies depending on the scattering angle and this effect increases proportionally to the molecule size (Fig. 24B-C). This phenomenon is referred to as the angular dependence of the scattered light, or $P(\theta)$ function, and is used to determine the size of the protein in solution.

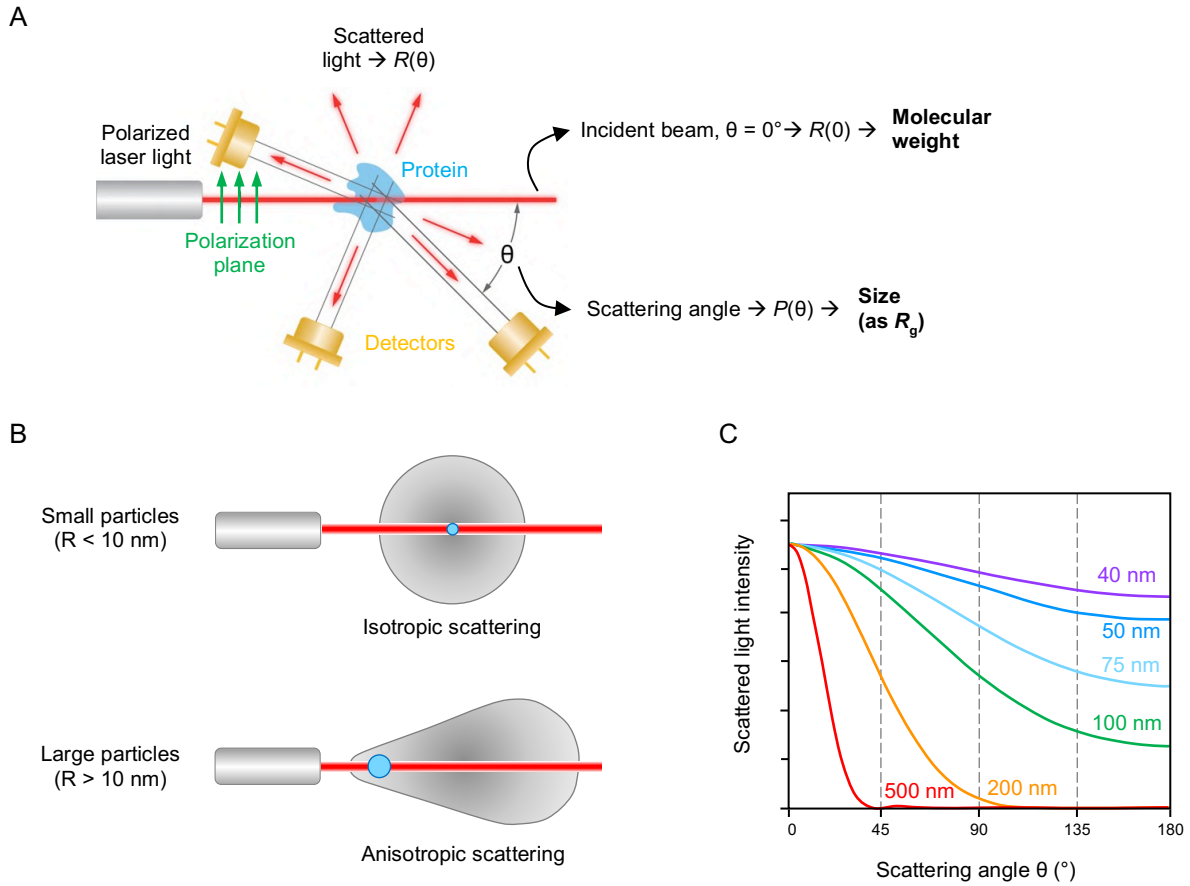

Figure 24. Principle of multi-angle laser light scattering. A) Schematic illustration of a MALLS experiment, where a polarized laser light (red line) is scattered (red arrows) by a protein in solution (blue shape). The intensity of scattered light at different angles is measured by several detectors (in yellow). **B**) Illustration of the isotropic (top) and anisotropic (bottom) light scattering (represented by a grey cloud) due to the size of the molecule (blue circle). **C**) The scattered light intensity function $R(\theta)$ of nanoparticles of various size is shown, illustrating the increased anisotropy of light scattering for the larger molecules. Adapted from the Wyatt Technology website.

Loading of a potentially heterogenous protein sample on a SEC column prior to MALLS measurement allows the separation of the various protein conformations based on their hydrodynamic radius and their interaction with the column. By the combination of the two techniques, one can therefore assign a precise molecular weight and size to each elution peak so as to characterize the oligomerisation profile and/or size distribution of a protein sample.

The SEC-MALLS analysis of DdrC was performed on a purified protein solution at a concentration of 16 mg/ml in a buffer composed of 20 mM Tris pH 7.5 and 200 mM NaCl, using 2 mg/ml BSA as a control. For a more detailed protocol, please see the "Materials and Methods" section of the article presented in *Chapter III* of the *Results* section of this manuscript. The measurements and data analysis were performed by our collaborators from the protein analysis online (PAOL) platform, which is part of the Integrated Structural Biology Grenoble (ISBG) Biophysics platform.

II.2. Analytical ultracentrifugation

Analytical ultracentrifugation (AUC) is based on the real-time monitoring through absorbance and interference optics of the sedimentation over time of a molecule in solution when subjected to a high centrifugal force (Fig. 25). A typical sedimentation velocity experiment by AUC is performed in a specific analytical ultracentrifuge designed to accommodate integrated optic systems that measure absorbance and interference along the radius of a double-sector cell at several time-points during the experiment (Fig. 25A).

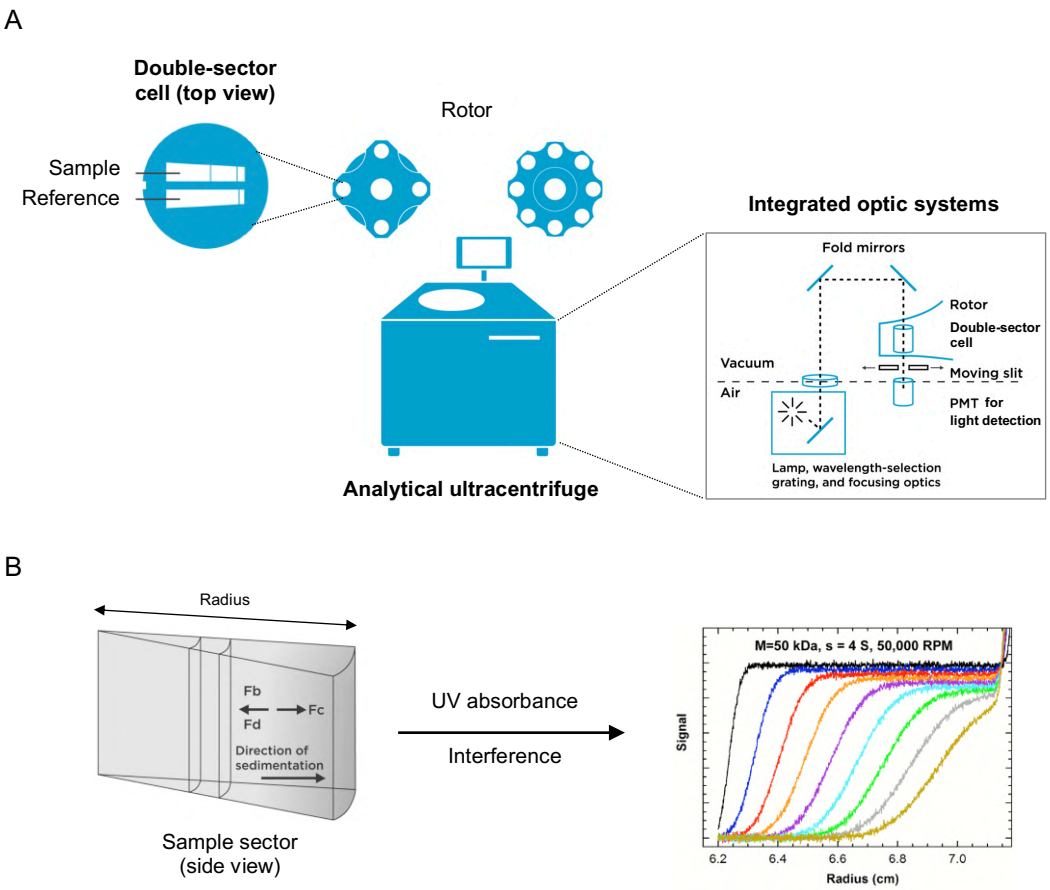

Figure 25. Principle and experimental setup of analytical ultracentrifugation. A) Schematic illustration of an AUC setup, where the analytical ultracentrifuge, with the rotors, the two-sector cell and the integrated optic systems are represented as simplified diagrams. In the close-up on the integrated optic systems, PMT indicates the photomultiplier tube used for light detection by photon counting. **B**) On the left, illustration of the various forces applied to the protein sample in the sample sector during ultracentrifugation: the buoyant force (Fb), the diffusion force (Fd) and the centrifugal force (Fc) that determines the direction of sedimentation. On the right, simulation of absorbance scans displayed at 20-minute intervals, obtained during a sedimentation velocity AUC experiment. The simulation was run for a protein of 50 kDa with a sedimentation coefficient of 4 S, at a rotor speed of 50,000 rpm. Adapted from the Beckman Coulter Life Sciences website and the review by (Cole et al., 2008).

By plotting the absorbance or interference as a function of cell sector radius for each measured timepoint (Fig. 25B), an AUC software like SEDFIT then determines the sedimentation coefficient S and the diffusion coefficient D of the protein. Using these parameters, it is possible to calculate the precise molecular weight and the global shape of the protein as globular or elongated and more or less compact. Accordingly, sedimentation velocity AUC experiments were performed to evaluate the mass and global shape of DdrC at 1, 4 and 8 mg/ml protein concentration, using the protein buffer as a reference (20 mM Tris pH 7.5 and 200 mM NaCl). The measurements and data analysis were performed by our collaborators from the PAOL platform, which belongs to ISBG Biophysics platform.

II.3. Chemical crosslinking

The oligomerisation profile of the deinococcal HU proteins in solution or bound to dsDNA was determined by chemical crosslinking using bis-sulfosuccinimidyl suberate (BS3; Sigma), a bifunctional N-hydroxysuccinimide ester that reacts with the primary amines of lysine residues and the N-terminus of proteins. As the commonly used buffering compound Tris contains a primary amine, it is used to quench the crosslinking reaction and must therefore be removed from the composition of the protein buffer prior crosslinking. To do so, we exchanged the Tris-containing buffer of our purified HU proteins with a phosphate buffer (20 mM phosphate pH 8, 100 mM NaCl) by means of size-exclusion chromatography. DrHU, DdHU1 and DdHU3 remained stable in the phosphate buffer and were subsequently used for crosslinking assays.

The crosslinking of DrHU, DdHU1 and DdHU3 in solution was performed by incubation of 0.6 mg/ml HU with 0 to 1 mM (or 0 to 0.5 mM for DdHU1) BS3 in a reaction

volume of 10 µl. After a 30 min incubation at room temperature, the crosslinking reaction was quenched by addition of 0.1 M Tris pH 8. Following the addition of 4 µl 4X denaturing SDS protein loading dye, the reactions were heated for 5 min at 95°C before loading on 12% acrylamide gels run in denaturing conditions for SDS-PAGE analysis. Crosslinking assays with DrHU and DdHU3 were also performed in the presence of dsDNA using either a 30 bp dsDNA oligonucleotide (dsU30) or supercoiled pUC19 plasmid (pUC19sc). For these assays, we set the final protein concentration to 0.6 mg/ml and the final BS3 concentration to 1 mM. DrHU or DdHU3 were mixed with 0 to 100 µM dsU30 or 0 to 0.5 µM pUC19sc in a final volume of 9 µl and incubated for 15 min at room temperature to allow formation of the nucleoprotein complexes. The samples were then crosslinked by addition of 1 mM BS3 and incubation at room temperature for 30 minutes as described previously, and were subsequently analysed by SDS-PAGE on either a 12% (dsU30) or a 8-15% gradient polyacrylamide SDS (pUC19sc) gel.

III. Crystallization, X-ray data collection and structure determination

III.1. Basic principles of X-ray protein crystallography

The three main methods to unravel the three-dimensional structure of a protein are cryo-electron microscopy (cryo-EM), nuclear magnetic resonance (NMR) and X-ray crystallography. Based on the number of released PDB structures per year, X-ray crystallography is still the most used approach to this day, although there is a net increase in structures solved by cryo-EM.

III.1.1 Crystallogenesis and cryo-protection of a protein crystal

The first step (and major bottleneck) of X-ray crystallography is the crystallization of the protein. A protein crystal is an ordered arrangement of proteins linked by non-covalent interactions, like hydrogen bonds or Van der Waals contacts, forming a crystal lattice repeated through the three directions of space. The crystal lattice is defined by the unit cell, which is the smallest array of proteins that is repeated to generate the full crystal by repeated translations

only. The unit cell is characterized by the length of its three axes (a, b, c) and the angles between these axes (α, β, γ). Protein crystallization can be seen as a phase transition from a disordered undersaturated liquid state to an ordered supersaturated solid state (Fig. 26A). Changes in the stable environment of a soluble protein (Fig. 26Aa) lead to a metastable state in which non-specific aggregates can form and turn into a nucleus (Fig. 26Ab), i.e. a small ordered aggregate. As the nucleus grows, it draws more and more proteins from the solution leading to a decrease in protein concentration in the solution. This triggers a phase transition towards a second metastable zone, which favors crystal growth (Fig. 26Ac).

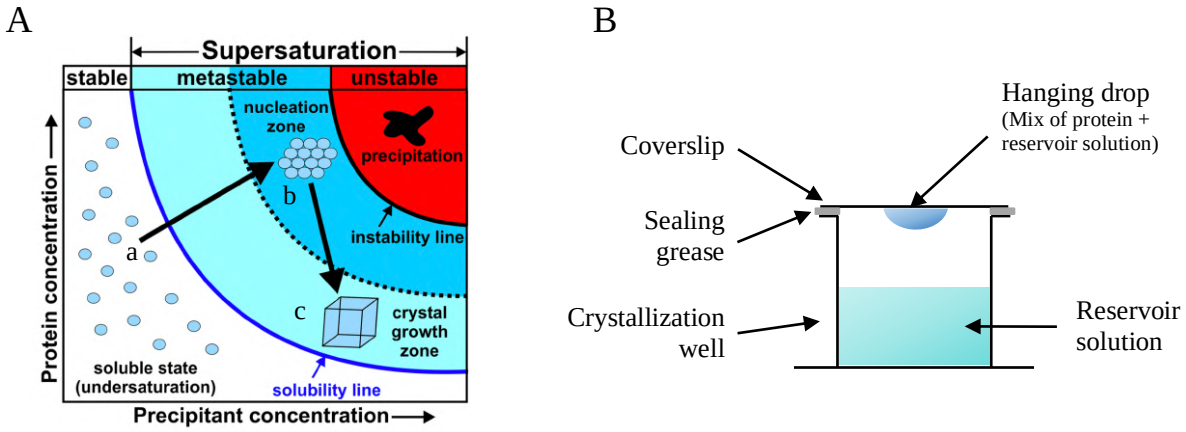

Figure 26. Protein crystallization is a complex process that can be achieved by the vapor diffusion technique. **A**) Phase diagram of protein crystallization. The stable (white background), metastable (blue background) and unstable (red background) zones of the protein solution are represented as a function of protein and precipitant concentrations. Upon addition of precipitant or increase in the protein concentration, proteins (blue circles) leave the soluble state (a) to enter the nucleation zone of the metastable state (b). In this state, proteins form an ordered aggregate called the nucleus, whose growth causes a decrease in protein concentration in the solution, allowing the formation of crystals and the transition to the crystal growth zone (c). **B**) Crystallization setup for hanging-drop vapor diffusion. A well containing a reservoir solution composed of precipitating agent is closed by a coverslip and hermetically sealed with grease. The crystallization drop hangs from the coverslip above the reservoir solution and contains a mix of protein and reservoir solution, usually at a 1:1 volume ratio. Adapted from (Bijelic & Rompel, 2018).

The initial transition from the stable soluble state to the metastable nucleation zone is achieved through the variation of multiple factors such as the protein concentration, the buffer composition, different temperatures to regulate the kinetics of crystal formation or the addition of a precipitating agent. The role of the precipitating agent (or precipitant) is to promote the aggregation of proteins by altering the ionic strength, polarity or viscosity of the solution. Salts like ammonium sulfate or NaCl affect protein solubility by competing for water molecules, while organic solvents such as ethanol or isopropanol alter the dielectric constant of the

solution, meaning its polarity. Polymers, such as the commonly used polyethylene glycol (PEG), are another type of precipitant that increase the viscosity of the solution, excluding protein from the solvent thereby favoring their aggregation.

Several methods are available for protein crystallization, namely micro-dialysis, batch crystallization, liquid–liquid free-interface diffusion or vapor-diffusion. The latter was used for crystallization of our proteins, more specifically the hanging-drop setup (Fig. 26B). In this approach, a drop of the protein mixed with a mother liquor solution containing a precipitant is placed above a reservoir filled with the same mother liquor, in a sealed crystallization well. The protein and the mother liquor are usually mixed at 1:1 volume ratio, so that the concentration of the latter is half that of the reservoir mother liquor. Due to the sealed environment and difference in mother liquor concentration between the drop and the reservoir, water is exchanged through the vapor phase to achieve an equilibrium of the two compartments. Since water diffuses from the drop to the reservoir, the volume decrease leads to a slow increase of both the protein and precipitant concentrations, shifting the protein state to the supersaturation zone where a nucleus can form.

The protein crystal must be protected from radiation damage caused by the intense X-ray beam used for X-ray data collection. To slow down radiation damage, the diffraction data are collected at cryogenic temperature at 100 K (equivalent to -173°C) by keeping the protein crystal under a continuous stream of nitrogen gas. However, most protein crystals are composed of 20 to 90 % solvent that resides in solvent channels located between the proteins inside the crystal. At such a low temperature, the formation of ice in the solvent channels can affect the diffraction or even break the crystal lattice. To avoid this, the crystal is soaked in a cryo-protecting solution before being flash-cooled in liquid nitrogen. Instead of forming ice crystals at cryogenic temperatures, the cryo-protectant molecules form an amorphous material whose structure is that of a frozen liquid, thereby preserving the integrity of the crystal lattice and the quality of the diffraction data. Commonly used cryo-protectants include glycerol, ethylene glycol, low molecular weight PEGs or sucrose.

III.1.2. X-ray diffraction data collection and data processing

To solve a protein structure, X-ray crystallography relies on the interaction between a crystal of the protein and a beam of X-rays (Fig. 27). When the protein crystal is subjected to an incident X-ray beam, all the electrons of the proteins in the crystal contribute to diffuse the

X-rays. The crystal lattice can be defined as an infinite set of lattice planes, some of which are parallel. If the X-rays diffused by atoms from parallel lattice planes are in phase, it creates constructive interferences between the scattered X-rays leading to diffraction. These requirements for X-ray diffraction are expressed by Bragg's law:

$$n\lambda = 2d \sin\theta$$

Here, "n" is an integer, "λ" is the wavelength of the X-rays, "d" is the spacing between two parallel lattice planes, and "θ" is the angle between the direction of the incident X-ray beam and the lattice plane that contains the diffracting atoms.

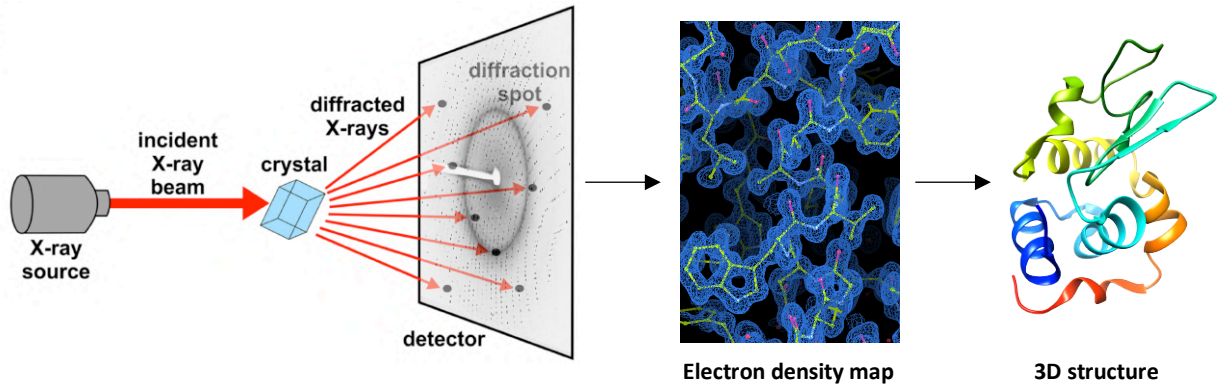

Figure 27. Principle of X-ray crystallography. Schematic representation of the three-dimensional structure determination process using X-ray crystallography. The diffraction pattern, electron density map and 3D-structure are those of the hen egg white lysozyme, from the PDB structure 7AFV (Ramos et al., 2021). Adapted from (Bijelic & Rompel, 2018).

The diffraction of X-rays by the crystal is recorded on a detector where it forms a diffraction pattern consisting of several diffraction spots, also called reflections (Fig. 27). To gather the structural information from the different sets of parallel lattice planes, diffraction data are recorded for various orientations of the crystal with respect to the incident X-ray beam, yielding thousands of diffraction patterns, which together constitute a dataset. Each reflection of a diffraction pattern corresponds to the diffraction of X-rays by a specific set of parallel lattice planes and is assigned to Miller indices (h, k, l) that characterize these lattice planes in the reciprocal space. The reciprocal lattice is a mathematical construction obtained by applying a Fourier Transform to the crystal lattice. It only exists in the reciprocal space and is centro-symmetric with the coordinates 0, 0, 0 (h, k, l) corresponding to the center of the crystal.

Hence, the first step of data processing is to extract the reflections from the background of each image recorded by the detector for every orientation of the crystal. The reflections are

then assigned to Miller indices (h, k, l) in a process termed "indexing" that also computes the unit cell parameters (a, b, c and α, β, γ) and the symmetry operators forming the crystal lattice (also called "space group"). The intensity of each reflection is extracted during the following "integration" step. Since the reciprocal lattice is centro-symmetric, some reflections correspond to equivalent lattice planes, as stated by Friedel's law. "Merging" consists in calculating the average intensity and associated standard deviation for every equivalent reflection. Then the data are corrected based on experimental parameters such as the distance between the crystal and the detector, beam position, crystal orientation and radiation damage. These first steps of data processing are often performed with the X-ray detector software (XDS) program (Kabsch, 2010). Regarding the main function of XDS, COLSPOT finds the strong reflections to be indexed in the background of images, IDXREF performs the indexing, INTEGRATE extracts the intensity of the reflections and CORRECT (and sometimes XSCALE) applies the corrections due to the experimental conditions and radiation damage. Additionally, XDSCONV is used to produce a file compatible with other programs such as CCP4 or Phenix that are used for the following steps of structure determination.

A reflection of indices (h, k, l) can be described by a structure factor ($\vec{F}_{hkl}$), which is a complex number defined by an amplitude ($|F_{hkl}|$) and a phase (α_{hkl}). The amplitude is related to the scattering power of atoms, which is correlated with the number of electrons, while the phase is linked to the position of these atoms in the lattice plane. Therefore, the electron density at coordinates (x, y, z), in a crystal defined by a unit cell of volume V, is expressed as a function of the amplitude and phase of the structure factor of coordinates (h, k, l) in the reciprocal space, using the inverse Fourier transform:

$$\rho(x, y, z) = \frac{1}{V}\sum_h \sum_k \sum_l |F_{hkl}| \exp[-2\pi i(hx + ky + lz) - \alpha_{hkl}]$$

To derive the electron density map (and thus the protein structure) from the set of collected reflections, one needs both the amplitude and the phase of the diffracted X-rays. While the amplitude is directly related to the measured intensities of each reflection recorded during the experiment ($|F_{hkl}| \approx \sqrt{I_{hkl}}$), the corresponding phase is unknown leading to the well-known "phase problem". There are several methods to calculate the phase of the structure factors, namely molecular replacement, multiple or single isomorphous replacement, and multiple- or single-wavelength anomalous dispersion. In this project, we used the molecular replacement (MR) and single-wavelength anomalous dispersion (SAD) phasing methods.

In MR, a protein with a known structure is used as a search model to generate a set of structure factors with amplitude and phase data, based on the unit cell and space group determined during the first steps of data processing. The model protein must be similar to the target protein in terms of sequence and cover a large part if not all the sequence of the target protein. To assess the agreement between the model and the target, MR relies on the Patterson function, which is a vector map of the interatomic distances in the structure calculated only with the intensities. The method proceeds by comparison of the calculated (model) and observed (target) Patterson functions with the aim to minimize the discrepancy between the two. To do so, the model is fitted in the given unit cell by successive rotation and translation operations to refine its orientation and position it correctly in the unit cell.

SAD method relies on an anomalous difference in diffraction to solve the substructure of a heavy atom introduced in the protein and use this to build a first model of the protein structure. When the wavelength of X-rays is close to the absorption edge of a heavy atom, its electrons can absorb the X-ray energy and release it by emitting fluorescence. This specific interaction modifies the structure factors so that Friedel's law is no longer obeyed ($\vec{F}_{\mathrm{hkl}} \neq \vec{F}_{\overline{hkl}}$) leading to an anomalous difference expressed as:

$$\Delta F_{ano} = ||\vec{F}_{\mathrm{hkl}}| - |\vec{F}_{\overline{hkl}}||$$

Selenium is one of the most commonly used heavy atoms since it can substitute for the sulfur atom in methionine residues of a protein. Once a selenomethionine variant of the protein is produced and crystallized, the diffraction data are collected with X-rays at a wavelength close to the absorption edge of selenium. Then, the position of the selenium atom is determined with the Patterson function using $|\Delta F_{ano}|^2$ instead of intensity. The location of the heavy atom is then used to initiate phase calculation.

Once the phase problem is solved, the atoms of the crystallized protein are placed into the computed electron density thereby building a first model of its three-dimensional structure. The electron density map, also called 2Fo-Fc map, is generated from the observed (Fo) and calculated (Fc) structure factors, based on the observed and calculated amplitudes combined with the calculated phases. The 2Fo-Fc map appears as an electron density around the protein residues and can be displayed in specific programs such as the Crystallographic Object-Oriented Toolkit (Coot) program (Emsley et al., 2010). To account for a plausible bias in the model due to the calculated phases, a second map is generated. This difference density map, or Fo-Fc map, highlights the differences between the model of the structure and the experimental

data. Negative density (red in Coot) will appear on the elements present in the model, but which should not be present according to the experimental data, while positive density (green in Coot) will appear where something is missing from the model to explain this density. Refinement of a protein structure consists in minimizing the difference between the observed and calculated structure factors by repeated iteration of two steps:

- (i) reconstruction of the model in the real space, meaning manually adjusting the position of the atoms so that they fit in the electron density while maintaining a proper geometry (usually with Coot)
- (ii) reciprocal space refinement based on the difference between Fo and Fc, performed by programs such as Refmac (Murshudov et al., 1997) or Phenix Refine (Adams et al., 2010).

The progression of the refinement and the overall quality of the final structure are monitored by an R factor (R_{work}) expressed as a percentage of disagreement between Fo and Fc. The lower this factor is, the more the model can be considered valid. To prevent "over-refinement", a fraction of the reflections (usually 5 %) are removed from the refinement process, typically before generating the electron density map. These reflections are used to calculate a R factor "free" of refinement biases, called R_{free}. Monitoring the difference between the R_{work} and R_{free} factors throughout the refinement process acts as a safety net to avoid over-refinement, as this difference should not increase during refinement.

III.2. The DNA Gyrase of *D. radiodurans*

III.2.1. Crystallization trials of DrGyrA_2B_2 and DrGyrBAfus

The reconstituted DrGyrA_2B_2 complex and the fusion DrGyrBAfus were used for crystallization trials by the vapor-diffusion method at 20°C. The protein was set to a concentration of 7 ± 1 mg/ml, in buffer Gf-C (50 mM Tris-HCl pH 8.0, 100 mM NaCl, 5 % glycerol). To stabilize the DrGyrA_2B_2 complex, crystallization trials were performed in the presence of 2 mM $MgCl_2$ and 2 mM AMP-PNP (Jena Biosciences), a non-hydrolysable analog of ATP.

Initial crystallization hits were obtained for the DrGyrA_2B_2 complex by robotic screening at the HTX lab (high throughput crystallization facility of EMBL) using the sitting

drop vapor-diffusion method with nanoliter drops at 20°C (Dimasi et al., 2007). The following crystallization screens were tested: Wizard I and II (Rigaku Reagents), Classics Suite and PEGs I (Qiagen), PACT and JCSG+ (Molecular Dimensions) and a salt screen composed of the Salt-Grid screen, Quick Screen Sodium/Potassium Phosphate, Grid Screen Ammonium Sulfate and Grid Screen Sodium Malonate from Hampton Research, along with a home-made (HTX lab) grid screen of Sodium Formate. Regarding the fusion DrGyrBAfus, no crystals were obtained in any condition. Crystals of the reconstituted $DrGyrA_2B_2$ ± AMP-PNP appeared within one week in the following conditions: (i) 0.1 M Tris-HCl pH 7.0, 10 % PEG 8,000, 0.2 M $MgCl_2 \cdot 6H_2O$ and (ii) 0.1 M imidazole pH 8.0, 10 % PEG 8,000, 0.2 M $Ca(CH_3COO)_2$.

These conditions were optimized by manual crystallization screens performed using the hanging-drop crystallization setup (Fig. 26B) in 24-well plates at 20°C. The conditions were first refined using 0.1 M Tris-HCl pH 7.0 to pH 8.5 over 8 to 18 % PEG 8,000 and 0.2 M of either $MgCl_2$ or calcium acetate. A second screening was performed using 6 to 16 % PEG 3,350, 6,000, 8,000 or 10,000 with 0.1 M Tris-HCl pH 8.0 and 0.2 M $MgCl_2$. The crystallization drops were made by mixing 0.5 µl of protein solution with 0.5 µl of mother liquor solution (or 1 µl of each in the case of DrGyrBAfus) and equilibrated against 500 µl of mother liquor solution (or 1 ml for the second screening). In the first screening, hexagonal bipyramidal crystals of $DrGyrA_2B_2$ ± AMP-PNP appeared after one week in conditions containing 8 to 14 % PEG 8000 and 0.1 M Tris pH 8.0 or pH 8.5 with 0.2 M $MgCl_2$. In the second screening, hexagonal bipyramidal crystals of $DrGyrA_2B_2$ were obtained in conditions containing 8 to 10 % PEG (or 10 to 12 % in the presence of AMP-PNP), regardless of the PEG's molecular weight (3,350, 6,000, 8,000 or 10,000). Crystals were fished with a cryo-loop, transferred into a drop of mother liquor solution supplemented with 18 % glycerol as a cryoprotectant and directly flash-cooled in liquid nitrogen. X-ray diffraction of the cryoprotected crystals was assessed on the automated beamline ID30A1 at the European Synchrotron Radiation Facility (ESRF), yielding diffraction up to 7 Å resolution.

To enhance the diffraction quality of the crystals, the crystallization conditions of the apo-$DrGyrA_2B_2$ were further optimized using additives from the screening kits HR2-420, HR2-422 and HR2-430 (Hampton Research). The starting condition was set as 0.1 M Tris-HCl pH 8.0, 0.2 M $MgCl_2$, 10 % PEG 8,000. Crystallization drops were made by mixing 1 µl of $DrGyrA_2B_2$ with 0.8 µl of mother liquor solution (starting condition) supplemented with 0.2 µl of additive. These 2 µl drops were equilibrated against 1 ml of mother liquor solution. After 4 days, a myriad of tiny crystals appeared in the crystallization drops of about 60 % of the

conditions in each of the three additive screens. Larger hexagonal bipyramidal crystals were obtained only in a few conditions that contained either 100 mM Glycine, 3 % dimethyl sulfoxide (DMSO), 0.1 M phenol, 4 % ter-butanol or 0.2 M sodium thiocyanate. Crystals were fished with a cryo-loop, transferred into a drop of mother liquor solution containing 18 % glycerol as a cryoprotectant and directly flash-cooled in liquid nitrogen.

III.2.2. Data collection and data processing

Diffraction data of the optimized $DrGyrA_2B_2$ crystals were collected at 100 K on beamline Proxima-2A (SOLEIL), on a Eiger 9 M detector (Dectris). A total of 3,600 images were collected at a wavelength of 0.980 Å with 25 ms exposure at a transmission of 15 to 25 % and an oscillation angle of 0.1° per frame. Several crystals yielded diffraction data at a low resolution around 7 Å, and one crystal obtained with 0.2 M Sodium Thiocyanate as additive yielded diffraction up to 4 Å resolution. Data were indexed, integrated and scaled with XDS, XSCALE and XDSCONV. The space group of the three processed $DrGyrA_2B_2$ datasets was P622, with unit cell parameters of a = 160.5 Å, b = 160.5 Å, c = 150.9 Å and $\alpha = 90°$, $\beta = 90°$, $\gamma = 120°$. To select the most appropriate search model for molecular replacement, the crystal content was verified by SDS-PAGE analysis. Crystals from the same condition as that of the diffracting crystals were fished with a cryo-loop and directly deposited into 4X denaturing protein loading dye, heated for 5 min at 95°C and loaded on a 10 % poly-acrylamide TGX Stain-Free gel run for 30 min at 250 V in 1X TGS. After direct visualization on the ChemiDoc MP imager, it appeared that only the DrGyrA subunit was present in the crystals. The structure of DrGyrA was therefore solved by molecular replacement using the structure of *Staphylococcus aureus* GyrA subunit as a search model (PDB 2XCT (Bax et al., 2010)), with the Phaser MR program (McCoy et al., 2007). The structure was solved at 3.5 Å resolution and the electron density of this first model was improved using the density modification program Parrot (Cowtan, 2010). The values of the initial R_{work} and R_{free} of the phased DrGyrA model were 51.95 % and 54.93 % respectively. Refinement of this structure is ongoing.

III.3. Crystallization trials of the HU proteins of *D. radiodurans* and *D. deserti*

Initial crystallization trials with DrHU were performed by robotic screening at the HTX lab (EMBL) using the vapor-diffusion method with nanoliter sitting drops at 20°C (Dimasi et al., 2007). The protein concentration was set to 12 mg/ml in a buffer composed of 20 mM Tris-HCl pH8, 100 mM NaCl, 5% glycerol. Screening was performed with the following crystallization screening kits: Wizard I and II (Rigaku Reagents), Classics Suite and PEGs I (Qiagen), PACT and JCSG+ (Molecular Dimensions) and the combined Salt-Grid_hampton (Hampton Research and HTX lab).

Since no crystals were obtained in these conditions, manual crystallization trials of DrHU, DdHU1, DdHU2 and DdHU3 were also performed using the hanging-drop crystallization setup in 24-well plates at 20°C. The crystallization drops were made by mixing 0.5 or 1 µl of protein solution with 0.5 or 1 µl of mother liquor solution (always at a 1:1 volume ratio) and equilibrated against 500 µl or 1 ml of mother liquor solution. Manual screening was performed with crystallization screening kits: Crystal screen HR2-110, Grid screen Ammonium sulfate HR2-211, PEGRx-1 HR2-082 (Hampton Research) and the conditions 1 to 48 of MIDAS MD1-59 (Molecular Dimensions). The table below illustrates the different screens and setup parameters used for the crystallization assays of each HU proteins (Table 11).

Table 11. Manual crystallization assays of DrHU, DdHU1, DdHU2 and DdHU3. For each HU protein, the screening kit used for crystallization trials is given as HR2-110 (Crystal screen HR2-110), HR2-211 (Grid screen Ammonium sulfate HR2-211), HR2-082 (PEGRx-1 HR2-082) or MD1-59 (conditions 1 to 48 of MIDAS MD1-59). The protein concentration and composition of the protein buffer are calculated before mixing with the mother liquor solution. Reservoir and drop volumes refer to the volume of mother liquor solution in the reservoir and the total volume of the crystallization drop ($V_{protein}$ + $V_{mother\ liquor}$). All crystallization drops were made with a protein to mother liquor volume ratio of 1:1.

Protein	Screen	Concentration (mg/ml)	Buffer composition	Reservoir (ml)	Drop (µl)
DrHU	HR2-110	30 49	50 mM Tris-HCl pH8 250 mM NaCl	0.5	2
	HR2-211	49	50 mM Tris-HCl pH8 250 mM NaCl	0.5	1
	HR2-082	29.5 17.5	50 mM Tris-HCl pH8 250 mM NaCl	0.5	2
	MD1-59	25	20 mM Tris-HCl pH8 200 mM NaCl	1	2
DdHU1	HR2-110	34 68	50 mM Tris-HCl pH8 250 mM NaCl	0.5	2

	HR2-211	68	50 mM Tris-HCl pH8 250 mM NaCl	0.5	1
	MD1-59	18	20 mM Tris-HCl pH8 100 mM NaCl 5% glycerol	1	2
DdHU2	MD1-59	18	20 mM Tris-HCl pH8 100 mM NaCl 5% glycerol	1	2
DdHU3	MD1-59	22	20 mM Tris-HCl pH8 100 mM NaCl 5% glycerol	1	2

III.4. DdrC of *D. radiodurans* and its selenomethionine variant DdrC-SeMet

III.4.1. Crystallization of DdrC and DdrC-SeMet

Initial crystallization trials of DdrC were performed by robotic screening at the HTX lab (EMBL) using the vapor-diffusion method with nanoliter sitting drops at 20°C (Dimasi et al., 2007). Two protein concentrations were used: 11 and 24 mg/ml in Dd-B buffer. Screening was performed with the following crystallization screening kits: Wizard I and II (Rigaku Reagents), Classics Suite and PEGs I (Qiagen), PACT and JCSG+ (Molecular Dimensions) and the combined Salt-Grid_hampton (Hampton Research and HTX lab). Crystals grew after 2 to 3 months in conditions containing 1.6 M ammonium sulfate and 0.1 M Tris pH 8.0 or Bicine pH 9.0. These conditions were optimized by manual crystallization screens performed using the hanging-drop crystallization setup in 24-well plates at 20°C. The conditions were refined using 0.1 M Tris pH 8.0 to pH 8.5 or Bicine pH 9.0 to pH 9.5 and 1.0 M to 2.1 M ammonium sulfate, with 24 mg/ml of DdrC. The crystallization drops were made by mixing 1 µl of protein solution with 1 µl of mother liquor solution and equilibrated against 500 µl of mother liquor solution. Hexagonal bipyramidal or triangular prism-shaped crystals appeared after three months in all conditions with ammonium sulfate below 1.9 M (Fig. 28A). Crystals were transferred to a drop of mother liquor supplemented with 20% glycerol as a cryoprotectant and flash-cooled in liquid nitrogen before data collection (Fig. 28B-C). Crystal quality (in terms of diffracting power) was assessed by collecting diffraction data on the automated beamline ID30A1 (ESRF), yielding diffraction up to a resolution of 2.2 Å (Fig. 28D).

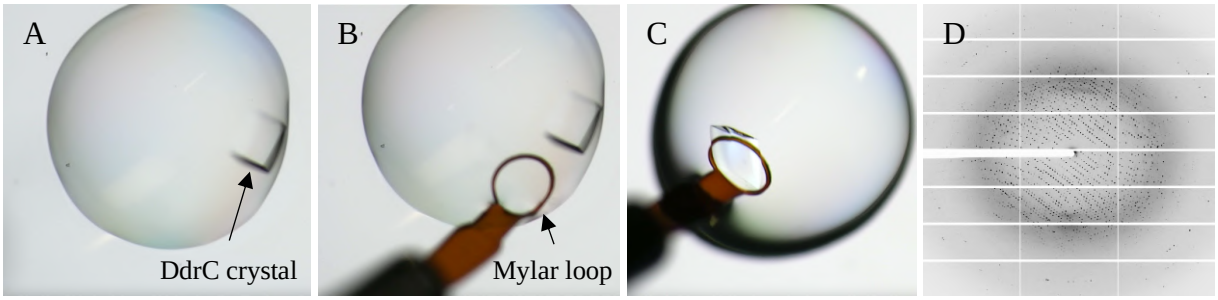

Figure 28. Harvesting of a DdrC crystal and its corresponding diffraction pattern. DdrC crystallized as a triangular prism-shaped crystal in a condition composed of 0.1 M Bicine pH 9.5, 1.6 M ammonium sulfate at 20°C in a hanging-drop vapor diffusion setup (**A**). The crystal was harvested with a mylar loop (**B**) and transferred into a cryo-protecting solution of mother liquor supplemented with 20 % glycerol (**C**). The diffraction data of the cryo-protected crystal were collected on the automated beamline ID30A-1 (ESRF), with a resolution of up to 2.2 Å (**D**).

To solve the phase problem by means of single-wavelength anomalous diffraction (SAD), a selenomethionine variant of DdrC was produced and crystallized at a concentration of 20 mg/ml in the Dd-B buffer. Crystals were obtained by the hanging-drop vapor diffusion method using the same manual screening conditions as those used to obtain DdrC crystals. Hexagonal bipyramidal or triangular prism-shaped crystals of DdrC-SeMet appeared in all conditions with ammonium sulfate below 1.9 M in less than one month. The crystals were cryoprotected and flash-cooled as previously described for DdrC.

III.4.2. Data collection and data processing of DdrC and DdrC-SeMet

The crystallographic data collection and processing of the DdrC-SeMet and native DdrC datasets are described in detail in the article presented in the Results section of this manuscript.

IV. Preparation of DNA samples

IV.1. Oligonucleotides

To perform gel shift and fluorescence polarization assays, several oligonucleotides with different features were purchased from Eurofins Genomics (Table 12). These oligonucleotides, which differed in terms of length, were labelled at their 5' ends with a fluorescein dye (FAM) or comprised a fluorescein-conjugated thymine in the middle of their sequence. To obtain

double-stranded DNA, the single-stranded oligonucleotides were annealed with their reverse complementary counterpart. Briefly, 50 µM of an unlabeled oligonucleotide was mixed with 50 µM of the complementary fluorescein-labeled oligonucleotide at a 1:1 volume and molar ratio, in a final reaction volume of 100 µl. After placing the oligonucleotides (protected from light) in a water bath (1L) at 95°C for 5 min, the heating block was turned off and the water was left to cool progressively for 3 to 4 hours until reaching room temperature. The stock solution of annealed oligonucleotide was then stored at -20°C until further use.

Table 12. List of the oligonucleotides used in this study. Sequences of the oligonucleotides used during the project. The name of a given oligonucleotide is based on its characteristics in terms of length of the sequence (12 to 50 nucleotides), whether it is a single- or double-stranded DNA ("s" or "d"), and the presence of a fluorophore ("5'F" or "F15-26"). Regarding the fluorophore, "5'F" indicates the addition of a 6-FAM fluorescein moiety (**F**) at the 5' end of the oligonucleotide, while "F15-26" signals the presence of a thymine conjugated to fluorescein (**X**) at position 15, 22 or 26 of the sequence.

Name	Oligonucleotide sequence
20s5'F 20d5'F	5'-**F** GAC TAC GTA CTG TTA CGT CT-3' 3'-CTG ATG CAT GAC AAT GCA GA-5'
43d5'F	5'-**F** GAC TAC GTA CTG TTA CGG CTC TAT CGC TAC CGC AAT CAG GCC A-3' 3'-CTG ATG CAT GAC AAT GCC GAG ATA GAG ATG GCG TTA GTC CGG T-5'
50s5'F 50d5'F	5'-**F** GAC TAC GTA CTG TTA CGG CTC CAT CTC TAC CGC AAT CAG GCC AGA TCT GC-3' 3'-CTG ATG CAT GAC AAT GCC GAG GTA GAG ATG GCG TTA GTC CGG TCT AGA CG-5'
30dF15	5'-AGG TCT CTT CTT CT**X** TGC ACT TCT TCC TCC-3' 3'-TCC AGA GAA GAA GAA ACG TGA AGA AGG AGG-5'
43dF22	5'-GAC TAC GTA CTG TTA CGG CTC **X**AT CGC TAC CGC AAT CAG GCC A-3' 3'-CTG ATG CAT GAC AAT GCC GAG ATA GAG ATG GCG TTA GTC CGG T-5'
50dF26	5'-GAC TAC GTA CTG TTA CGG CTC CAT C**X**C TAC CGC AAT CAG GCC AGA TCT GC-3' 3'-CTG ATG CAT GAC AAT GCC GAG GTA GAG ATG GCG TTA GTC CGG TCT AGA CG-5'

IV.2. Plasmid DNA

pUC19 is a widely used double-stranded circular plasmid DNA of 2,686 bp with a GC content of 51 %, containing a gene for ampicillin resistance. To further characterize protein-DNA interactions and protein-induced DNA compaction, three different conformations of pUC19 (Fig. 29) were prepared: (i) circular pUC19 either in a supercoiled (pUC19-S) or (ii) relaxed (pUC19-R) conformation, and (iii) linear pUC19 (pUC19-L). Plasmid DNA amplified and extracted from *E. coli* cells is mostly supercoiled, so the production of relaxed and linear pUC19 required further treatment with either a type I topoisomerase or a restriction enzyme.

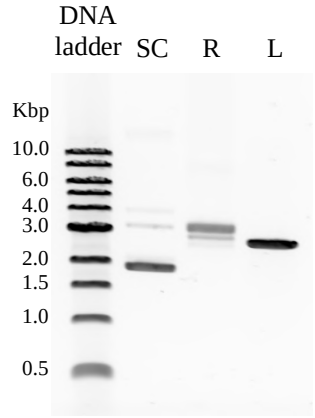

Figure 29. The supercoiled, relaxed and linearized conformations of pUC19. The three purified plasmid DNA conformations were analysed by electrophoresis on a 1% (w/v) agarose gel, ran for 1 h at 100 V in a Tris-Borate-EDTA (TBE) buffer and stained with Gel Red (1:10,000 dilution). The first well corresponds to the DNA ladder, followed by the supercoiled (SC), relaxed (R) and linearized (L) pUC19. The expected size of the plasmid DNA is 2,686 bp, as illustrated when pUC19 is digested by EcoRI-HF (pUC19-L^E). The supercoiled pUC19-SC migrated more rapidly due to its compact conformation, whereas the extended loose conformation of the relaxed pUC19-R delayed its migration.

Supercoiled pUC19 was amplified by transformation of competent DH5α *E. coli* cells grown overnight at 37°C in 100 ml Luria broth (LB) supplemented with 100 µg/ml ampicillin. After harvesting the cell culture by centrifugation, pUC19-SC was extracted from the cells using the NucleoBond Xtra Midi kit (Macherey-Nagel) following manufacturer's instructions. After cell lysis by a combined NaOH-SDS treatment containing RNase A, the basic pH of the solution is neutralized by addition of potassium acetate. This triggers the precipitation of SDS, along with proteins, genomic DNA and other cellular debris. The latter are discarded upon loading of the cell lysate onto a specifically designed filter. To retrieve the plasmid DNA, the flow through is transferred into a column holding an anion exchange resin that binds the negatively charged DNA under acidic pH conditions. Following elution at high salt concentration, the DNA is further purified by precipitation and successive steps of washes to remove the salt. The final solution of pUC19-SC is resuspended in 50 µl of Milli-Q water, yielding a concentration of 3.5 µg/µl (i.e. 2 µM) DNA. The purity of pUC19-SC was analyzed by electrophoresis on a 1 % (w/v) agarose gel run for 1 h at 100 V in 1X TBE buffer (89 mM Tris, 89 mM Boric acid, 2 mM EDTA) stained with Gel Red (Interchim) and visualized with a ChemiDoc MP imager (BioRad). Since the solution appeared to be contaminated by residual RNA, pUC19-SC was further treated with RNase I (Sigma). 20 µl of pUC19-SC at 1.5 µg/µl were mixed with 6 µl of RNase I at 20 µg/µl in a buffer composed of 20 mM Tris pH 8, 100 mM NaCl in a final reaction volume of 500 µl. After overnight incubation at 37°C, the treated

pUC19-SC was purified by phase separation upon addition of phenol-chloroform at 1:1 volume ratio. The aqueous phase was retrieved and washed against 500 µl of chloroform. After a brief centrifugation for 30s at 20,000 g, the DNA was precipitated by addition of 50 µl of 5 M NaCl and 1.1 ml of 100 % (v/v) ethanol. Successive washes by centrifugation for 15 min at 20,000 g and resuspension of the precipitated DNA in 1 ml of 70 % (v/v) ethanol were used to remove the salt, after which the DNA was resuspended in 20 µl of sterile Milli-Q water. The final pUC19-SC solution appeared purer after the RNase I treatment, as shown by electrophoresis on a 1 % (w/v) agarose gel (Fig. 29).

To obtain the relaxed conformation of pUC19, the purified pUC19-SC was treated with a recombinantly expressed truncated form of human topoisomerase I (hTopoI-70) produced in our team by a former PhD student, Müge Senarisoy. To relax the plasmid DNA, four reactions containing 7.9 µl of pUC19-SC at 1.8 µg/µl and 1.5 µl of hTopoI-70 at 4.5 µg/µl in a final reaction volume of 30 µl, were prepared. The buffer was composed of 20 mM Tris pH 8, 72 mM KCl, 5 mM $MgCl_2$, 0.2 mg/ml bovine serum albumin (BSA). After incubation at 37°C for 30 min, hTopoI-70 was inactivated by incubation at 65°C for 20 min and the relaxed plasmid DNA was purified using the NucleoSpin Gel and PCR Clean Up kit (Macherey-Nagel) following manufacturer's instructions. This purification kit uses a silica membrane onto which the DNA binds in the presence of a chaotropic salt. After two washes with a buffer containing ethanol, the DNA is eluted by a low salt buffer or Milli-Q water. The four reactions of pUC19-R were purified together in a single filter and eluted in 50 µl of a sterile buffer composed of 5 mM Tris pH 8.5, 0.5 mM EDTA (TE buffer) at a final concentration of 356 ng/µl. The purity and relaxed conformation of the plasmid DNA was controlled by electrophoresis on a 1 % (w/v) agarose gel, as described for pUC19-SC (Fig. 29).

The linear plasmid DNA pUC19-L was produced by digestion of pUC19-SC with the restriction enzyme EcoRI-HF or HindIII-HF (New England Biolab). These two restriction enzymes only cut pUC19 at one site, yielding a full-length linearized plasmid DNA. 4.5 µl of pUC19-SC at 3.2 µg/µl was mixed with 0.75 µl of EcoRI-HF (pUC19-L^E) or HindIII-HF (pUC19-L^H) at 20 units/µl in a final reaction volume of 15 µl in the provided CutSmart Buffer (20 mM Tris-acetate pH 7.9, 50 mM Potassium acetate, 10 mM Magnesium acetate, 100 µg/ml BSA). The reaction was first incubated for 1 h at 37°C, followed by a second addition of 0.75 µl of EcoRI-HF or HindIII-HF at 20 units/µl and a second incubation step for 1 h at 37°C. The enzyme was then inactivated by incubation at 65°C for 20 min. The linearized plasmid DNA was purified as described earlier for pUC19-R with the NucleoSpin Gel and PCR Clean Up kit

(Macherey-Nagel). Elution was performed with 30 µl of sterile TE buffer, yielding a final concentration of 334 ng/µl for pUC19-L^E and 255 ng/µl for pUC19-L^H. Purity and complete digestion of the plasmid DNA was assessed by electrophoresis on a 1 % (w/v) agarose gel, as described for pUC19-SC (Fig. 29).

V. DNA-protein interactions

V.1. Electrophoretic mobility shift assays

The interaction of HU proteins with DNA was first evaluated by means of electrophoretic mobility shift assays (EMSA). This method is based on the difference between the migration profiles of unbound DNA and DNA in complex with a protein. The formation of DNA-protein complexes alters the migration profile of DNA due to the added mass, volume and electrostatic charges of the bound protein(s), resulting in a so-called band-shift (Fig. 30).

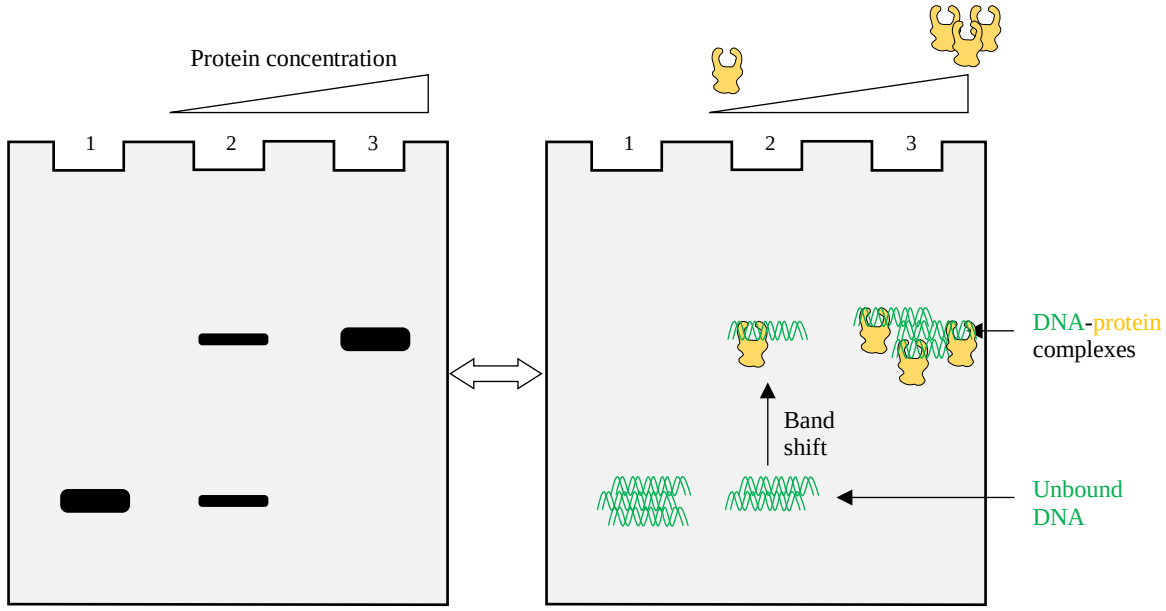

Figure 30. Basic principle of electrophoretic mobility shift assay, also called gel shift assay. The left panel is a schematic representation of a gel shift assay while the right panel explains the principle of this method. **Lane 1.** Upon electrophoresis on an agarose or polyacrylamide gel, an oligonucleotide (green) migrates down to a specific position in the gel. **Lanes 2 and 3.** Addition of a DNA-binding protein (yellow) will trigger the formation of DNA-protein complexes. Due to the additional mass and charges brought by the DNA-binding protein, the protein-bound

oligonucleotide will display a delayed migration (band-shift). **Lane 2.** At low protein concentration, the band-shift might be incomplete if not all oligonucleotides are bound, and thus two bands might be visible on the gel. **Lane 3.** When the protein concentration is higher, all the oligonucleotides form a complex with the protein and migrate as a single shifted band.

V.1.1. DNA binding of HU proteins

A fixed concentration of oligonucleotide or plasmid DNA diluted in EMSA buffer was incubated with increasing concentrations of HU proteins in a reaction volume of 10 µl (see Table 13 for details). As a negative control, DNA alone was incubated with an equivalent amount of HU dilution buffer (20 mM Tris pH 8, 200 mM NaCl). After incubation at 30°C for 15 min, non-denaturing loading dye (0.2 % bromophenol blue, 5X TBE, 12.5 % glycerol) was added and the reactions were loaded on a 7.5% acrylamide gel (or on a 1% agarose gel in the case of plasmids) run at 4°C for 1 h at 100 V. In the case of unlabeled oligonucleotides or plasmid DNA, the gel was stained with Gel Red for 30 min after migration before visualization with a ChemiDoc MP imager (BioRad). Gel shift assays performed with fluorescein-labelled oligonucleotides were directly visualized with the ChemiDoc MP imager by excitation of the fluorescein (λexc 482-16 nm, λem 530-40 nm). To optimize the formation of protein-DNA complexes between HU and the plasmid DNA, different buffer compositions were tested by using $MgSO_4$ or $MnSO_4$ instead of $MgCl_2$, or both $MgSO_4$ and $MnSO_4$ at different ratios (4:1, 1:1, 1:4). The effect of NaCl was also estimated by varying its concentration from 100 mM to 200 mM or by diluting the HU-DNA mixes directly in Milli-Q water.

Table 13. Concentrations of DNA and HU proteins in the EMSA reactions depending on the nature of DNA and corresponding buffer composition. The final concentrations of DNA and HU proteins in the reaction mix (volume = 10 µl) are given as a function of the nature of the DNA used in the binding assay, along with the corresponding buffer composition.

Nature of DNA	[DNA] in nM	[HU] in µM	Buffer composition
fluorescein-labelled oligonucleotide	50	0.25 to 5	20 mM Tris pH 8, 100 mM NaCl, 1 mM $MgCl_2$
unlabeled oligonucleotide	50	0.25 to 4	20 mM Tris pH 8, 150 mM NaCl, 1 mM $MgSO_4$, 0.1 mg/ml BSA
plasmid DNA	3	0.15 to 9.6	20 mM Tris pH 8, 150 mM NaCl, 1 mM $MgCl_2$, 0.1 mg/ml BSA

V.1.2. DNA binding of DNA Gyrase

The binding of DNA Gyrase to pUC19-SC was assessed either alone or in the presence of DrHU. To do so, 3 nM of pUC19-SC was incubated with increasing concentrations of DNA Gyrase (1.25 nM to 320 nM) with or without 4.8 µM of DrHU in a reaction volume of 10 µl, in the binding buffer (20 mM Tris pH 8, 150 mM NaCl, 1 mM $MgCl_2$, 0.1 mg/ml BSA). As a negative control, DNA alone was incubated with an equivalent amount of protein dilution buffer (20 mM Tris pH 8, 200 mM NaCl). After incubation at 30°C for 30 min, non-denaturing loading dye was added and the reactions were loaded on a 1% agarose gel and run at 4°C for 1 h at 100 V. The gel was stained with Gel Red for 20 min before visualization with a ChemiDoc MP imager (BioRad).

V.2. Fluorescence polarization

Fluorescence polarization is used to monitor the binding of a non-fluorescent molecule such as a DNA-binding protein to a smaller fluorescent molecule like fluorescein-labelled oligonucleotides. This approach relies on the difference in polarization of the light emitted by a fluorophore between its free and bound states (Fig. 31).

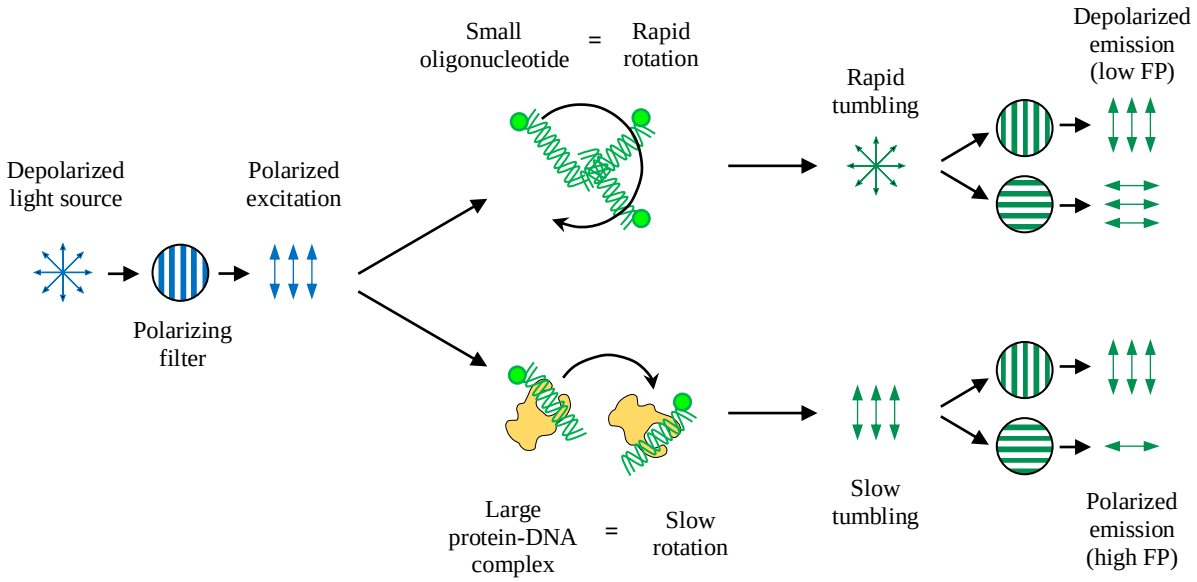

Figure 31. General principle of fluorescence polarization. A depolarized light source is polarized into one direction upon going through a polarizer. In solution, the free fluorescein-labelled oligonucleotide (green) rotates rapidly so that when the polarized light excites the fluorescein, the rapid tumbling leads to a depolarized emission.

Upon addition of a DNA-binding protein (yellow), a protein-DNA complex is formed and the bound oligonucleotide undergoes a slower rotation due to the larger volume of the complex. The tumbling is thus slowed down, which allows for a more polarized emission of fluorescence. Since the measure of fluorescence polarization (FP) corresponds to the ratio between the light emitted in the parallel plane and that emitted in the orthogonal plane, the FP is higher when the emitted light is polarized.

In solution, a free fluorescein-labelled oligonucleotide rotates rapidly causing the polarized excitation light to be emitted as a depolarized light due to its rapid tumbling. However, when the protein binds the DNA, it forms a larger complex whose rotation is slower compared to the unbound DNA. The slower tumbling retains the polarization of the excitation light, and thus the emitted light is also polarized leading to a higher measurement of fluorescence polarization.

Reactions were performed in triplicates in black 386-well medium-binding plates (Greiner) in a reaction volume of 40 µl. A fluorescein-labelled dsDNA oligonucleotide was incubated at room temperature with increasing concentrations of HU proteins or DdrC in a reaction buffer composed of 20 mM Tris pH 8, 100 mM NaCl, 1 mM $MgCl_2$, 0.02 mg/ml BSA. The fluorescence polarization was measured on a Clariostar microplate reader (BMG Labtech), fitted with polarization filters using an excitation wavelength of 482-16 nm and an emission of 530-40 nm. The DNA-binding ability of DrHU, DdHU1, DdHU2 and DdHU3 were evaluated on 1 nM 43-mer dsDNA (43d5'F) at a protein concentration ranging from 0 to 10 µM. For DdrC, 20-mer and 50-mer dsDNA oligonucleotides were used (20d5'F and 50d5'F) at a concentration of 10 nM, with an increasing concentration of DdrC from 0 to 400 µM.

After subtracting the polarization values obtained for DNA alone, the mean data from at least three independent measurements were fitted to one of the following equations using GraphPad Prism 8: (a) a simple one-site specific binding model ($y = \frac{B_{max} \times X}{K_D + X}$), (b) a one-site specific binding model with Hill coefficient ($y = \frac{B_{max} \times X^h}{K_D^h \times X^h}$), or (c) a two-site specific binding model ($y = \frac{B_{max(Hi)} \times X}{K_D(Hi) + X} + \frac{B_{max(Lo)} \times X}{K_D(Lo) + X}$), where "y" is the difference between the anisotropy (i.e. polarization) of completely bound and completely free oligo, "B_{max}" is the maximal polarization signal, "x" is the protein concentration, "K_D" is the equilibrium dissociation constant and "h" is the Hill coefficient that accounts for a potential cooperativity in DNA binding.

VI. Supercoiling and relaxation assays

To compare the correct folding and activity of the two DNA Gyrase constructs, viz. $DrGyrA_2B_2$ and DrGyrBAfus, supercoiling and relaxation assays were performed with and without ATP on the relaxed or supercoiled conformation of pUC19. For each DNA Gyrase construct, 50 ng of pUC19-R or pUC19-SC was incubated with increasing concentrations of DNA Gyrase from 0 to 250 nM in a buffer composed of 20 mM Tris pH 8, 72 mM KCl, 5 mM $MgCl_2$, 0.2 mg/ml BSA ± 1 mM of ATP. After a first 30 min incubation at 30°C to allow supercoiling or relaxation of the plasmid DNA, the DNA Gyrase was denatured by addition of 0.2% SDS and 0.5 mg/ml Proteinase K followed by a 15 min incubation at 30°C. Denaturing DNA loading dye 10X (0.1 M EDTA, 0.5 % SDS, 0.1% bromophenol blue, 25 % glycerol) was then added and the reaction was again incubated for 10 min at 65°C before separation by gel electrophoresis for 1h at 100V on a 1% agarose gel at 4°C. The gel was then stained with Gel Red and visualized on a Chemidoc MP imager (BioRad).

VII. Study of DNA compaction by microscopy

VII.1. Atomic force microscopy

VII.1.1. Three-dimensional imaging at the single-molecule level

Atomic force microscopy (AFM) is a single-molecule scanning probe microscopy (SPM) technique, which relies on a physical probe to analyze a sample through interactions between the tip of the probe and the surface of the sample (Binnig, Quate &Gerber, 1986). AFM makes use of a cantilever, whose sharp tip serves as the physical probe interacting with the sample surface. When the cantilever tip contacts the surface of the sample, it is deflected by interaction forces. While it scans the surface of the sample, the fluctuations of the cantilever deflection are monitored through a laser focused on the cantilever end, which reflects the light into a photodiode that converts the deflection into mV (Fig. 32). To obtain the topographic data, the cantilever either gently scrapes (Contact mode) or taps (Tapping mode) the surface of the sample while keeping a constant deflection (in Contact mode) or amplitude (in Tapping mode) through an electronic feedback. This feedback is received by the cantilever-holding piezo that

finely adjusts the height of the cantilever with respect to the sample to maintain the constant value of deflection or amplitude.

The PeakForce mode is a third AFM imaging technique more commonly used in the study of biological samples as it causes less damage. In PeakForce, the piezo adjusts the cantilever height so that it presses slightly on the surface for a given deflection and then it gently taps the surface. To study biological samples, it is also important to choose the right cantilever. Cantilevers vary in length and shorter cantilevers are less sensitive to variations in the sample surface, due to a higher rigidity reflected by a higher force constant (named k and expressed in N/m). In our case, it is thus better to use a cantilever with more flexibility and sensitivity, i.e. with a force constant below 1 N/m.

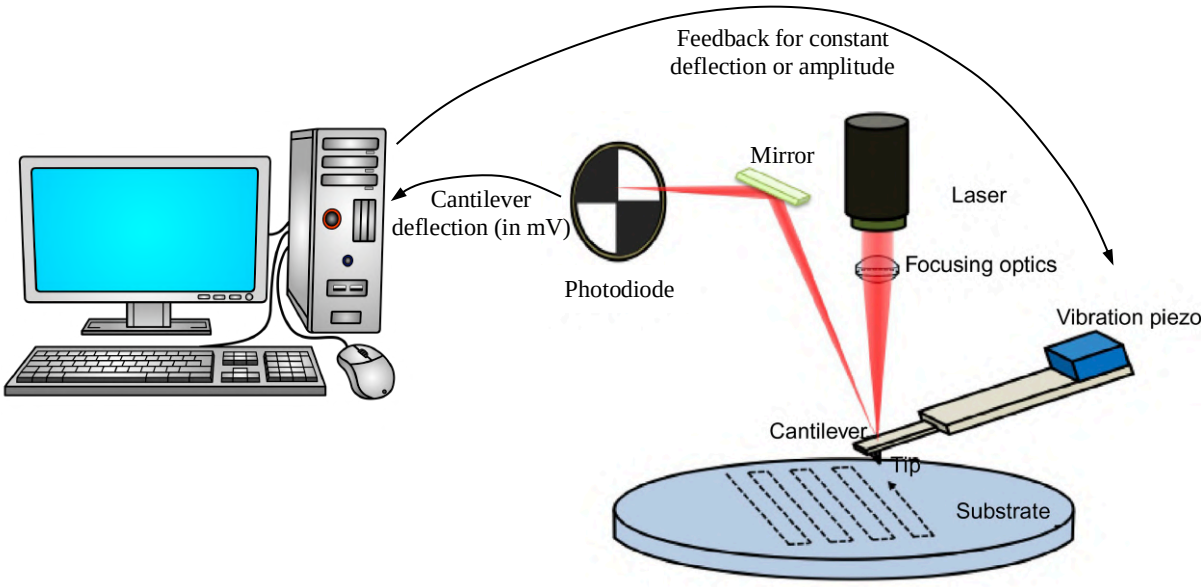

Figure 32. General principle of imaging by atomic force microscopy. The tip of the cantilever scans the surface of the sample, which results in a deflection of the cantilever due to interaction forces. The variation of this deflection, caused by the topography of the sample, are monitored by a laser reflected on to a photodiode and converted into mV. By means of electronics, a constant deflection is maintained through the movement of the piezo holding the cantilever. Adapted from (LeBlanc et al., 2017).

One prerequisite for AFM imaging is the need for a perfectly flat surface for sample deposition to avoid any bias on height measurement. Muscovite mica is the typical substrate for AFM sample deposition, as its surface has an atomic flatness upon cleavage and it can be functionalized to adapt surface properties to optimize sample deposition. Muscovite mica is a natural mineral composed of several layers of aluminum hydroxide silicate maintained together by weak ionic interactions through an interlayer of potassium ions (Fig. 33). The aluminum hydroxide silicate layer is made of two tetrahedral sheets of silicon or aluminum oxide

($(Al,Si)O_4$) surrounding an octahedral sheet of aluminum oxyhydroxide ($Al_2O_2(OH)_2$). The tetrahedral and octahedral sheets share some of their oxygen atoms, which provides a strong bond between the sheets. When a scotch tape is used to cleave the mica surface, the weak bond between two aluminum hydroxide silicate layers is broken, resulting in a surface with atomic flatness perfectly suitable for AFM imaging (Fig. 33).

The cleaved mica surface is mainly negatively charged due to the loss of half of the interstitial K^+ ions that remained bound to the removed upper layers (Müller & Chang, 1969). This can be a problem when negatively charged molecules are studied, such as DNA whose backbone is negatively charged due to the phosphate groups. To overcome this drawback, the mica surface is functionalized by addition of either positively charged silanes like APTES or divalent cations such as Ni^{2+}, Mg^{2+} or Ca^{2+}.

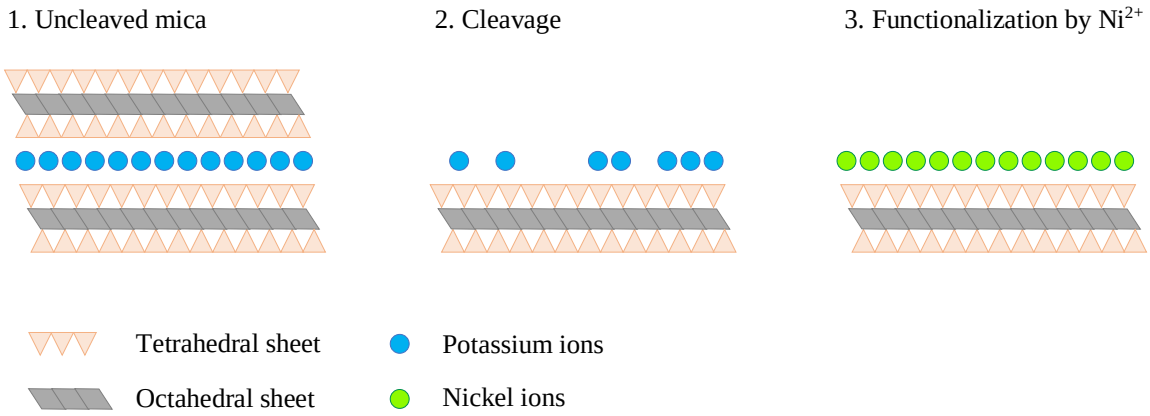

Figure 33. Mica composition ensures an atomic flatness suitable for AFM. Before cleavage (**1**), muscovite mica is naturally organized as a superposition of TOT-arranged layers, which are composed of an octahedral (O) sheet of aluminum oxyhydroxide (gray rhombuses) between two tetrahedral (T) sheets of silicon or aluminum oxide (orange triangles) in a TOT manner. These layers are held together by weak ionic interactions through a thin interlayer of K^+ ions (blue circles). Upon cleavage using scotch tape (**2**), the upper TOT layer is removed with around half of the interlayer K^+ ions. Then, the atomically flat mica surface can be functionalized (**3**) by addition of Ni^{2+} ions (green circles) to neutralize the residual negative charges of the surface and allow binding of the negatively charged DNA.

VII.1.2. Sample preparation and instrumental setup

Plasmid DNA pUC19 (either supercoiled, relaxed or linear) was diluted in Milli-Q water to a final concentration of 0.5 nM and incubated with increasing concentrations of proteins (DrHU, DdHU1, DdHU3 or DdrC) for 1h on ice or 30 min at 30°C in the case of DdrC. To

evaluate the effect of protein concentration on plasmid compaction, different plasmid to protein ratios were analyzed (Table 14). The proteins were diluted in Milli-Q water to various concentrations corresponding to plasmid-to-protein molar ratios of 1:1 to 1:40.

Table 14. Effect of the sbNAPs on DNA compaction was assessed for various plasmid-to-protein molar ratios. The four sbNAPs studied by AFM were DrHU, DdHU1, DdHU3 and DdrC. For each protein, the "x" indicates which ratios were evaluated, taking into account the three plasmid conformations (supercoiled, relaxed and linear).

plasmid : protein molar ratio	1:1	1:2	1:4	1:5	1:10	1:20	1:40
DrHU	x	x		x	x	x	
DdHU1	x	x		x	x		
DdHU3		x		x	x		
DdrC			x		x	x	x

For AFM measurements, a freshly cleaved V-1 grade muscovite mica disk of 12.7 mm in diameter (Nanoandmore, Wetzlar, Germany) was functionalized by addition of 10 µl of 5 mM $NiCl_2$, dried under a gentle stream of nitrogen gas. 5 µl of sample were then deposited on the functionalized mica surface and left to adsorb for 2 min before being dried under a stream of nitrogen gas (Fig. 34).

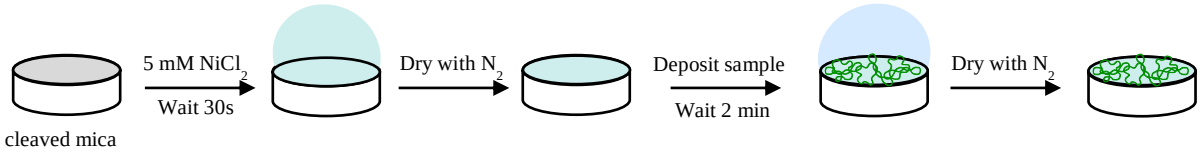

Figure 34. Preparation of an AFM sample. Schematic representation of the protocol to prepare an AFM sample. A freshly cleaved mica is functionalized by addition of NiCl2, then dried under a stream of nitrogen gas. The sample is then added and incubated on the mica surface for 2 min before drying under a stream of nitrogen gas.

VII.1.3. Instrumental setup

Topographic data were acquired on a multimode 8 microscope equipped with a Nanoscope V controller (Bruker, Santa Barbara, USA). All imaging was conducted with the PeakForce Tapping mode and ScanAsyst mode at a rate of ~1.0 Hz with a resolution set to either 512 or 1024 pixels per scan line. The sample surface was scanned either with a ScanAsyst-Air cantilever or a ScanAsyst-Air-HR cantilever, both characterized by a force constant of 0.4 N/m and a tip radius of 2 nm, along with respective resonance frequency of 70

kHz and 130 kHz (Bruker probes, Camarillo, CA, USA). They can also be distinguished by their shape and length (Fig. 35). Whenever the ScanAsyst mode was applied, a semi-manual control was maintained during the imaging procedure to manually adjust the set point and gain in order to reduce the tip-sample interactions to the minimum. The ramp size was kept constant at 150 nm.

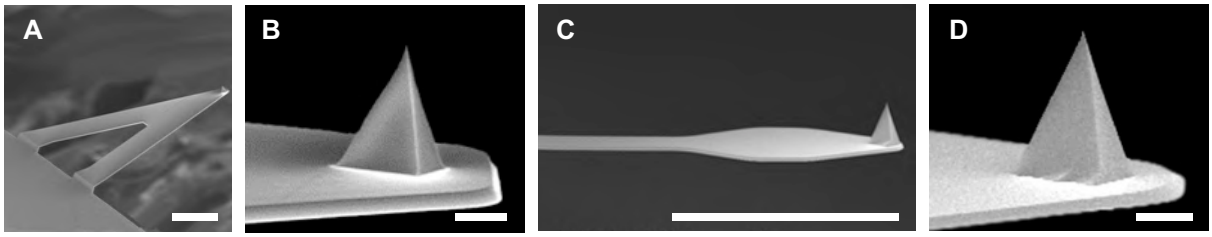

Figure 35. Two AFM cantilevers observed by scanning electron microscopy. A-C) Overall view of the ScanAsyst-Air (**A**) and ScanAsyst-Air-HR (**C**) cantilevers highlighting their different shapes and size. The scale bar in **A** and **C** represents 30 µm. **B-D**) Close-up view of the tip of the ScanAsyst-Air (**B**) and ScanAsyst-Air-HR (**D**) cantilevers, which both display a tip radius of 2 nm. The scale bar in **B** and **D** represents 2 µm. Images were taken from the Bruker Probes website (https://www.brukerafmprobes.com).

VII.1.4. Image processing

Processing of raw AFM images was systematically performed using the Gwyddion software version 2.53 (Nečas & Klapetek, 2012). As illustrated in Figure 36, raw AFM images were treated with the "Plane Level" tool of Gwyddion to remove possible tilt that happens when the sample is not exactly orthogonal to the cantilever. Then, images were flattened using a plan fit to the first order with the "Align Rows" tool of Gwyddion. After exclusion of all imaged objects whose height values exceeded the given threshold, flattening effect was enhanced by a second correction algorithm applied with the "Align Rows" tool using a polynomial of order 3. When necessary, stripe noises were reduced using the "Remove Scars" function in Gwyddion.

To extract the Laplacian volume and projected surface area of individual plasmids or plasmid-protein complexes, a mask was applied to the treated images to exclude objects smaller than DNA. Then, a second cut-off was applied with the "Grain Filtering" function to discard DNA fragments, proteins or protein aggregates by removing objects for which the projected surface area was considered too low. The Laplacian volume and projected surface area of each individual object were then extracted and exported in text format through the "Grain Distributions" tool. The data were then exported to GraphPad Prism 8 software for further analysis.

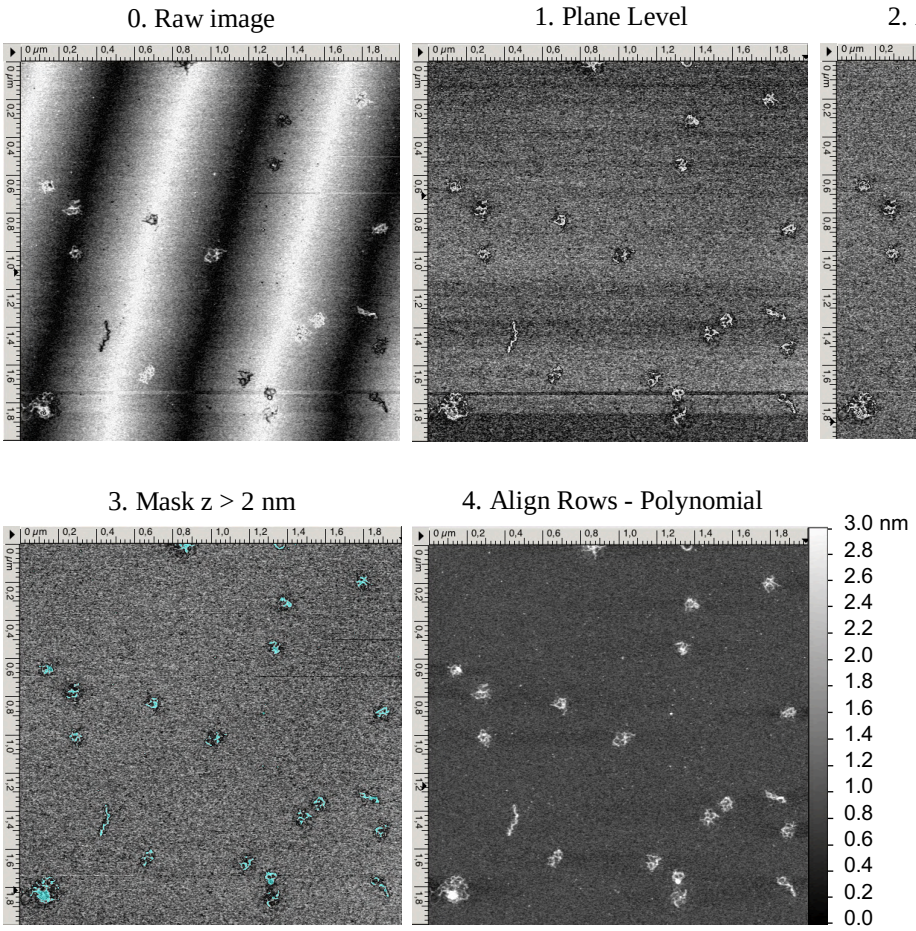

Figure 36. Processing of a raw AFM image. The raw image (**0**) is first treated by plane levelling (**1**) to remove possible biases due to the orientation of the sample in relation to the microscope. Then the background is flattened by applying a "median" plan fit (**2**), followed by exclusion of plasmids via a mask selecting objects higher than 2 nm (**3**). The final processing consists of a second plan fit using a 3rd order polynomial (**4**), excluding the masked objects from the process. The scale bar of image **4** (0 to 3 nm) represents the height of the sample in nm along the z axis, with a zero-value based on the pixel with the lowest z value.

VII.2. Electron microscopy

VII.2.1. Basic principle of transmission-EM, cryo-EM and cryo-electron tomography

Electron microscopy (EM) relies on the interaction of a beam of accelerated electrons with a sample to analyze its composition, morphology and structure. In our case, the samples were either proteins, DNA or proteins bound to DNA. In this section, I will briefly describe the

principles of transmission-EM (TEM) and the related cryo-EM and cryo-electron tomography (CET) imaging techniques that were used during my thesis.

To acquire an image by TEM (Fig. 37), electrons generated by an electron gun are focused into a beam by condensers while being accelerated by a high voltage, usually between 100 kV and 300 kV, applied between the electron gun and the anode. To avoid any interactions of the electrons with air, the microscope is operated under vacuum. TEM samples, in our case biomolecules in solution, are specifically prepared to be thin (less than 50 nm). Owing to the thinness of the sample, the accelerated electrons go through the sample and are scattered upon interacting with its atoms. Regions of the sample that are thicker compared to the background or where heavy metal atoms such as tungsten or uranium are present (due to staining) will have a greater scattering power, leading to a decreased transmission of the electron beam. The transmitted electrons then pass through an objective lens, forming an intermediate magnified image that is further magnified by a final projector lens. The final image is projected on an electron detector and recorded for visualization on a computer.

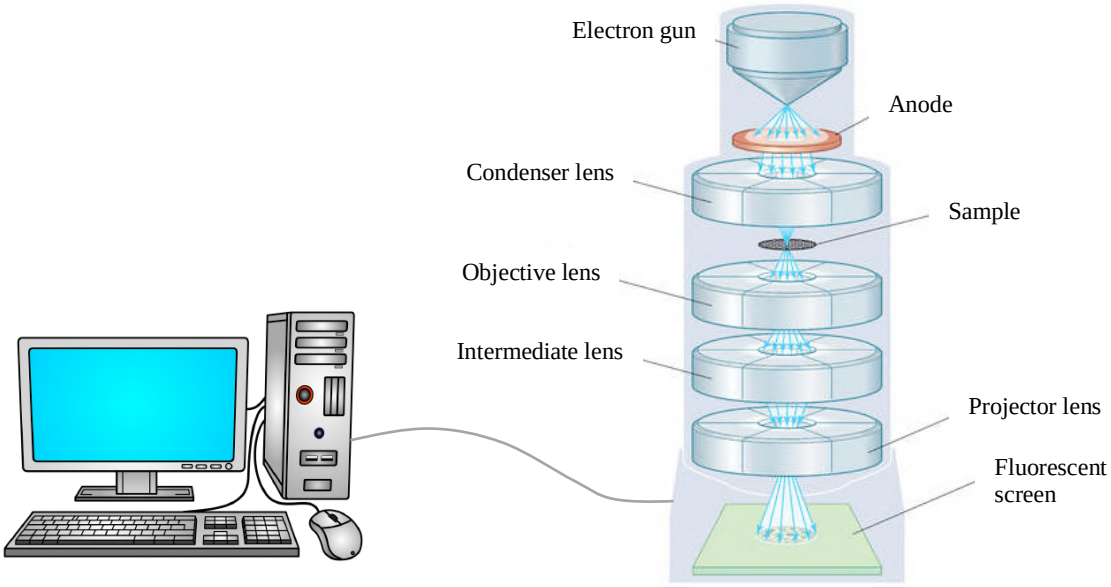

Figure 37. Schematic representation of a transmission electron microscope. The electrons (blue arrows) produced by the electron gun are accelerated by a high voltage and focused into a beam through a condenser lens. After passing through the sample, the transmitted electron beam forms an intermediate magnified image by going through the objective lens. This first image is then further magnified by an intermediate lens and a projector lens before being visualized on a fluorescent screen or recorded on an electron detector coupled to an electronic device. Adapted from Encyclopedia Britannica, 2008.

Negative-staining TEM consists in enhancing the contrast between the biological sample and the background. When accelerated electrons interact with the atoms of a biological

sample, their transmission is lower than that of electrons going through the solvent surrounding the sample (i.e. the background). Thus, on an electron micrograph, biomolecules usually appear as dark objects on a light background. However, since biomolecules like proteins and DNA are mostly composed of atoms with low atomic numbers such as hydrogen, carbon, oxygen, nitrogen or phosphorus, their weak scattering power leads to a poor signal-to-noise ratio. To overcome this problem, negative staining embeds the biological sample in a solution containing heavy-metal salts such as silico-tungstate or uranyl acetate. By doing so, the high scattering power of these heavy metals will yield a low electron transmission hence a dark background, onto which the poorly scattering biomolecules will appear as bright objects with a higher contrast.

Negative-staining starts by depositing the sample on a carbon-coated meshed metal grid. The thin carbon film on the surface of the metal grid serves as a low electron-interacting support for the sample to minimize the background. Few microliters of the sample are deposited on the carbon-coated grid and allowed to settle for one or two minutes for a correct adsorption to the surface. Then the drop is blotted dry and a drop of staining solution such as silico-tungstate or uranyl acetate is deposited on the sample-covered grid. After a short incubation time, the excess of staining solution is removed by blotting with a filter paper and the grid is ready for TEM imaging.

The major drawback of negative-staining TEM is that the sample needs to be dried and stained. The removal of the solvent could be damaging for protein and DNA, altering their shape or integrity. As for the staining, it could spread unevenly onto the grid giving rise to artifacts that would locally lower the contrast. To bypass these issues, one can use a complementary approach termed cryo-EM. The main advantage of cryo-EM is that the sample is observed in a close-to-native condition, more precisely in a thin layer of solvent frozen as an amorphous ice, without resorting to staining. To acquire cryo-EM images, the sample is deposited on a holey carbon-coated grid maintained by tweezers. As the sample spreads on the grid, it binds to the carbon surface but also fills the array of holes in the grid. Then, the grid is briefly blotted with filter paper to leave only a thin layer of sample solution covering these holes while avoiding interactions between the filter paper and the sample. To freeze the sample solution without producing ice crystals that could damage the sample and interact with electrons, the grid is plunged very rapidly in liquid ethane at a temperature of -188°C to form amorphous ice in a process termed plunge-freezing. The frozen grid is then transferred to an

electron microscope specifically designed for cryo-EM, operated at cryogenic temperature using liquid nitrogen.

As a complement to cryo-EM, cryo-electron tomography (cryo-ET) is a method that allows the visualization of the inner structure of a sample. Samples for cryo-ET are prepared as those imaged by cryo-EM, with the addition of nanometer-sized gold beads (5 to 25 nm in diameter) to the sample before vitrification. To construct a 3D representation of the sample (also called tomogram), the sample stage is gradually tilted from -60° to 60° so that multiple images are acquired at different angles. Using the high-contrast gold beads as position markers, the multiple tilt-images can subsequently be aligned and merged by software computations to yield a final 3D tomogram.

VII.2.2. Sample, grid preparation and instrument setup

DNA Gyrase sample preparation

The integrity of the two DNA gyrase complexes was assessed by TEM. The $DrGyrA_2B_2$ and DrGyrBAfus samples at 9 mg/ml were diluted 100 times in 20 mM Tris-HCl pH 8.0, 100 mM NaCl. For the preparation of TEM grids, a thin carbon film (5 to 10 nm) was deposited on a freshly-cleaved mica sheet using a carbon evaporator. 4 µl $DrGyrA_2B_2$ or 4 µl DrGyrBAfus was subsequently adsorbed to the carbon-coated mica sheet. After blotting with a filter paper, the carbon-coated mica sheet was deposited at the surface of a 200 µl drop of negative-staining solution. In our case, the staining solution was uranyl acetate. The heavy mica sheet sank into the solution while the lighter carbon film floated on the surface. A clean EM grid was carefully placed beneath the floating carbon film and gently raised to the surface so that the carbon film laid onto it. After blotting the excessive negative-staining solution with filter paper, the grid was transferred to a Tecnai T12 electron microscope for imaging.

DrHU sample preparation

The complexes formed by DrHU bound to a relaxed or supercoiled pUC19 plasmid DNA were analyzed by negative-staining TEM, cryo-EM or cryo-ET. Regardless of the DNA, the samples were prepared by incubating the protein with the DNA for 30-60 minutes at 20°C before grid preparation. For negative-staining EM, 10 nM relaxed or supercoiled pUC19 was incubated with 30 nM to 1 µM DrHU in distilled water. The samples were then stained with

2% uranyl acetate. Grids were prepared as described above for the DNA gyrase and were visualized on a Tecnai T12 electron microscope.

For the most promising plasmid:DrHU ratios, additional samples were prepared for cryo-EM. These samples were prepared at higher protein and DNA concentrations, typically 4 to 20 times more, to achieve a high density of molecules on the carbon grids. For relaxed pUC19, 40 nM pUC19-R was mixed with DrHU at ratios of 1:3, 1:6, 1:9, 1:20, 1:60 and 1:100 in either distilled water or in 12.5 mM NaCl. Gold beads were added to these samples to perform cryo-ET experiments with these grids. For supercoiled pUC19, 200 nM pUC19-SC was mixed with DrHU at ratios of 1:10, 1:25 and 1:100 in 10 mM Tris-HCl pH 8.0 and 1 mM $MgCl_2$. To prepare cryo-EM and cryo-ET grids, 4 µl of sample was applied to a holey carbon-coated grid placed in a Vitrobot (FEI). The grid was blotted for 2.5 s to remove the excess liquid and quickly frozen in liquid ethane by plunge-freezing. The images were then acquired on a Glacios microscope. TEM, cryo-EM and cryo-ET data acquisition and processing were performed by our collaborators, I. Gutsche and M. Bacia (IBS, Grenoble).

Results

I. The DNA Gyrase of *D. radiodurans*

I.1. DNA gyrase production: the reconstitution vs fusion strategy

The DNA gyrase is a heterotetrameric complex formed by the two subunits DrGyrA and DrGyrB, so we designed two distinct production strategies. The first approach consisted in the separate expression and purification of DrGyrA and DrGyrB, followed by reconstitution of the full complex ($DrGyrA_2B_2$). The second strategy aimed at the direct expression and purification of a fusion of the two subunits (DrGyrBAfus) with a 3-amino acid linker with the sequence glycine-aspartate-leucine (GDL) between DrGyrB and DrGyrA to stabilize the complex as has been reported previously (Papillon et al., 2013). We chose to fuse the C-terminus of DrGyrB to the N-terminus of DrGyrA based on the overall conserved structure of DNA gyrases among bacteria (Fig. 38). The TOPRIM domains at the C-termini of the GyrB subunits make contact with the WHD domains at the N-termini of the GyrA subunits to form the DNA-gate. Therefore the linker should stabilize this interface between the C-terminus of DrGyrB and the N-terminus of DrGyrA (Fig. 38). The size and sequence of the linker were chosen based on previous work by Papillon et al. on the DNA Gyrase of *T. thermophilus* (Papillon et al., 2013). The author used a three amino-acid linker with the sequence GDL to fuse the C-terminus of GyrB to the N-terminus of GyrA. Their GyrBA-fus construct was successfully expressed and purified as a stable heterotetrameric complex whose supercoiling activity was similar to that of the native reconstituted DNA gyrase. It was further used to solve the structure of *T. thermophilus* DNA gyrase by cryo-electron microscopy in complex with a 155 bp double-stranded DNA.

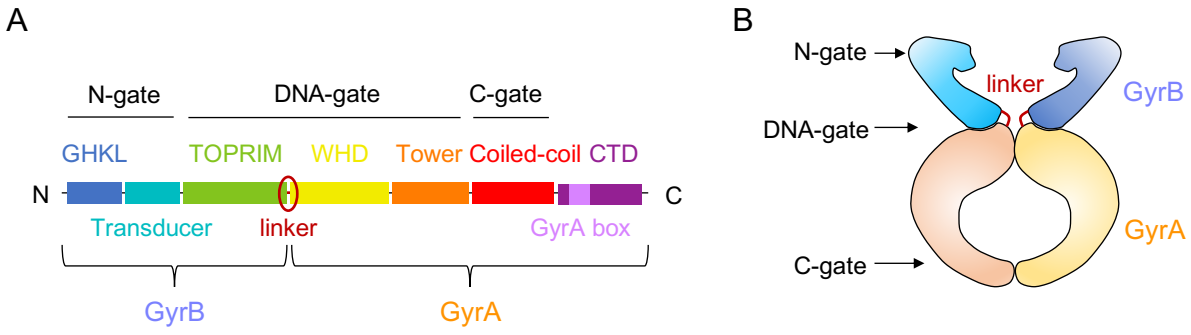

Figure 38. DrGyrBAfus is a fusion of DrGyrB and DrGyrA at the DNA-gate interface. A) Domain organization of the DNA gyrase fusion DrGyrBAfus based on that of bacterial DNA gyrase. The three protein-protein interfaces (the N-, C-, and DNA-gates) of the GyrA and GyrB subunits are indicated above the sequence. The DNA-gate involves domains of the two subunits. The linker is represented as a red line highlighted by a red circle, between the GyrA and GyrB subunits. **B**) Schematic representation of the DNA gyrase structure showing the three gates formed by the heterotetrameric complex. The GyrB subunits are represented in blue, the GyrA

subunits are coloured in yellow and orange, and the linkers between the C-terminus of GyrB and the N-terminus of GyrA are represented as red lines.

I.1.1. Expression and purification of DrGyrA$_2$B$_2$

In the context of the reconstitution strategy, the *gyrA* and *gyrB* genes were PCR amplified from the genomic DNA of *D. radiodurans* and cloned into pET21D and pProExHTB plasmids respectively, by means of Gibson's assembly. To overcome difficulties in obtaining the pET21D_DrGyrA construct, the amplification of pET21D by PCR was optimised by increasing the annealing temperature from 55°C to 66°C. Two different DNA polymerases were also evaluated, the Phusion or the Q5 high-fidelity DNA polymerases (New England Biolabs). The Q5 DNA polymerase was more efficient and specific when amplifying the inserts and plasmids, except for *gyrA* whose amplification was more specific when using the Phusion DNA polymerase. The two subunits were expressed separately as recombinant proteins in *E. coli* cells with poly-histidine purification tags (His-tag). In the case of DrGyrA, a non-cleavable His-tag was fused to the C-terminus, whereas for DrGyrB the His-tag was added to its N-terminus and was cleavable by the tobacco etch virus (TEV) protease. The different steps of the production process of DrGyrA$_2$B$_2$ are presented in Figure 39.

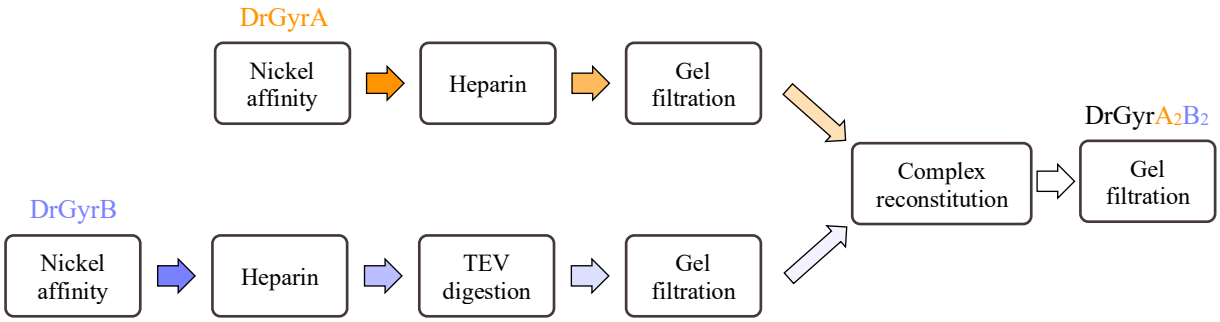

Figure 39. Production process of DrGyrA$_2$B$_2$. Graphic representation of the successive purification steps performed to obtained the DrGyrA (orange arrows) and DrGyrB (blue arrows) subunits before the final reconstitution and purification of the DrGyrA$_2$B$_2$ complex.

Each subunit was first purified by affinity on a nickel column before a second purification step on a heparin column to remove possible DNA contaminants (Fig. 40). As seen by the presence of large bands at 90 kDa (DrGyrA) and 73 kDa (DrGyrB) on the SDS-PAGE analysis of the nickel affinity chromatography, the two constructs are over-expressed and soluble (Fig. 40A). After this first purification step that removed the majority of impurities, the

yield was of 18 mg of DrGyrA and 33 mg of DrGyrB starting from pellets of 1 L of cell culture. To cleave the His-tag of DrGyrB, the protein was incubated overnight with TEV protease. There was some protein loss during the second purification step and the His-tag cleavage, so that only 10 mg of DrGyrA and 16 mg of DrGyrB remained. The two constructs were subsequently purified on a size exclusion chromatography before reconstitution of the $DrGyrA_2B_2$ complex. As seen on Fig. 40B-C, the two subunits eluted as single peaks with no aggregates and we recovered 6 mg of each after a final concentration step.

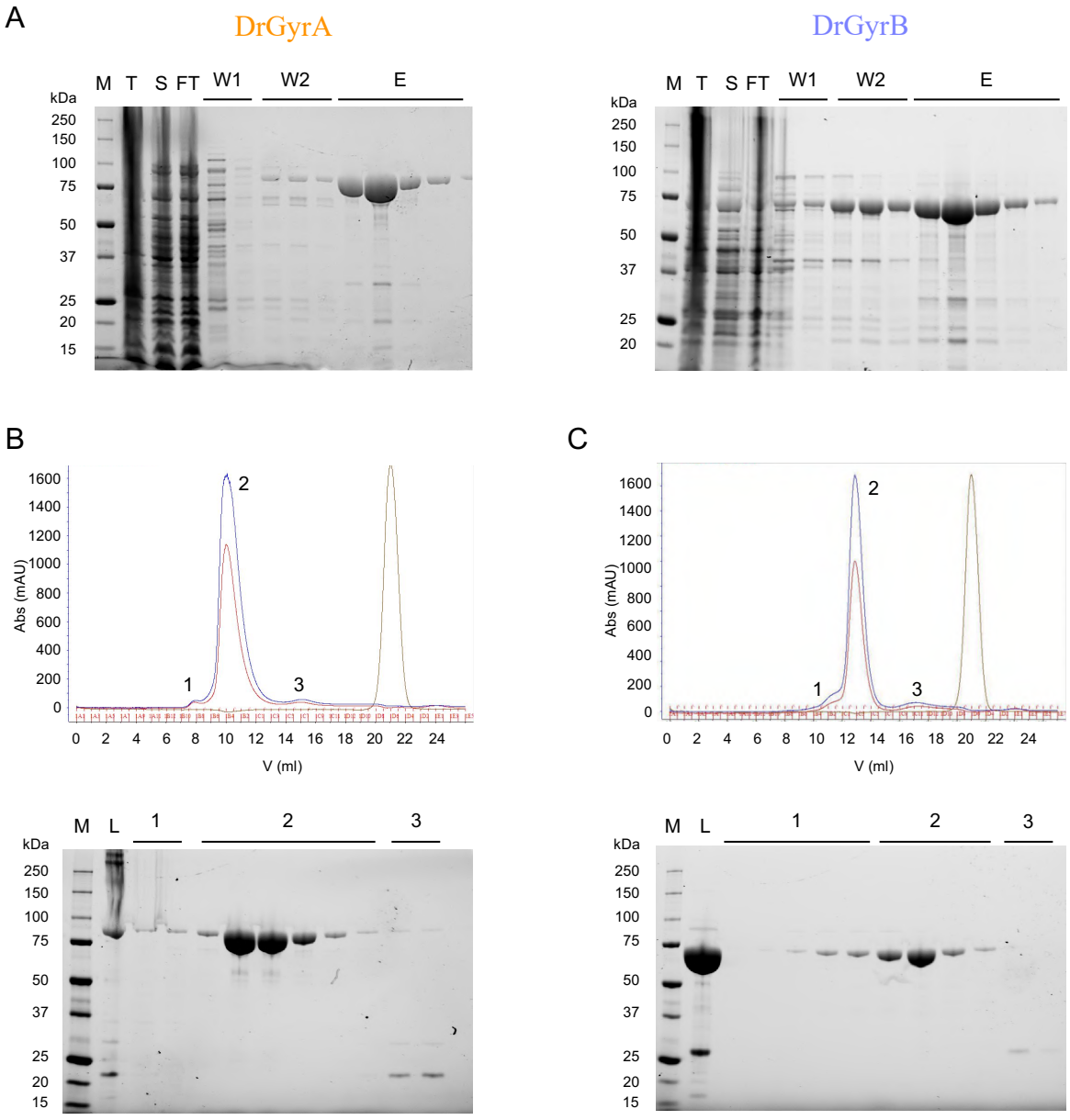

Figure 40. Purification of DrGyrA and DrGyrB. A) SDS-PAGE analysis of the first purification step of DrGyrA (left gel) and DrGyrB (right gel) performed on 2 ml of Ni-Sepharose 6 Fast Flow resin. Lanes are annotated as follows: M: Marker (protein ladder), T and S: Total and Soluble fractions of cell lysis, FT: column flow-through, W1 and W2: first and second washes, E: elution. **B-C**) Elution profiles of DrGyrA (**B**) and DrGyrB (**C**) on a

Superdex S200 10/300 gel filtration column, with corresponding SDS-PAGE analysis. Numbers 1 to 3 correspond to the three peaks on the elution profiles (by order of elution) and their corresponding fractions on the gel, while L refers to the protein sample loaded onto the column. On the elution profiles, the blue and red lines correspond to the absorbance at 280 nm and 260 nm respectively, and the brown line indicates the conductivity.

To reconstitute the DNA gyrase, the purified DrGyrA and DrGyrB were incubated together for 15 min on ice with a slight excess of DrGyrB, at a final molar ratio of 1 to 1.2 (DrGyrA to DrGyrB). The reconstituted $DrGyrA_2B_2$ complex isolated via size exclusion chromatography eluted as a single peak clearly separated from the excess of DrGyrB (Fig. 41). The purified $DrGyrA_2B_2$ was concentrated to 1 µM (equivalent to 0.3 mg/ml). Two additional batches of $DrGyrA_2B_2$ were prepared following the same protocol and further concentrated to 7 mg/ml for use in crystallization assays. To stabilize the complex for crystallisation, 2 mM of AMP-PNP was added to one of the concentrated batches. The three stock solutions of $DrGyrA_2B_2$ were flash-cooled in liquid nitrogen and stored at -80°C.

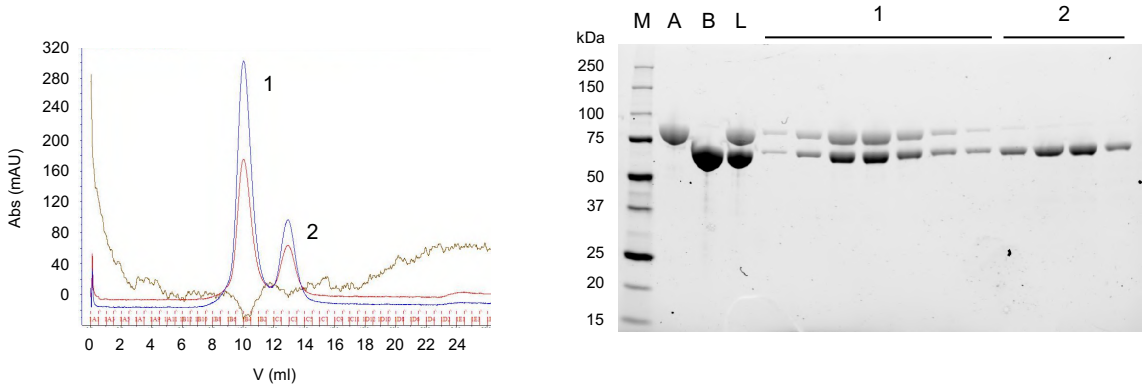

Figure 41. Purification of the reconstituted complex by size exclusion chromatography. Elution profile and corresponding SDS-PAGE analysis of the purification of $DrGyrA_2B_2$ on a Superdex S200 10/300 gel filtration column. On the elution profile, the blue and red lines correspond to the absorbance at 280 nm and 260 nm respectively, and the brown line indicates the conductivity. The lanes of the gel are annotated as follows: M: Marker for molecular weight, A: purified DrGyrA, B: purified DrGyrB, L: protein sample loaded on the column (i.e. $DrGyrA_2B_2$). Numbers 1 and 2 correspond to the two peaks on the elution profile (by order of elution) and their corresponding fractions on the gel.

I.1.2. Expression and purification of DrGyrBAfus

The DNA gyrase fusion was produced by simultaneous insertion of *gyrB* and *gyrA* into the pProExHTB plasmid by means of Gibson's assembly. Some issues due to recurrent mutations in *gyrA* following amplification were solved by increasing the annealing temperature

and using the Q5 DNA polymerase instead of the Phusion DNA polymerase. The fusion protein was then expressed in *E. coli* as a recombinant protein with a cleavable N-terminal His-tag and purified as described previously for DrGyrB (Fig. 42). After nickel affinity and heparin purification steps to remove impurities and contaminating DNA, the His-tag of DrGyrBAfus was cleaved by overnight incubation with the TEV protease. The cleaved DrGyrBAfus was further purified by gel filtration before storage at -80°C.

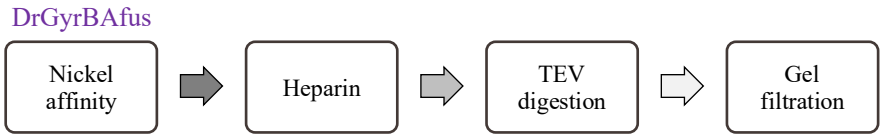

Figure 42. Successive purification steps for DrGyrBAfus production. Graphic representation of the successive purification steps of DrGyrBAfus.

While analysing the production of DrGyrBAfus by SDS-PAGE analysis, we expected a band at 163 kDa corresponding to the molecular weight of the fusion protein. According to SDS-PAGE analysis of the first purification step, DrGyrBAfus was over-expressed and purified as a stable soluble construct, yielding 22.5 mg of protein from 2L of cell culture (Fig. 43A).

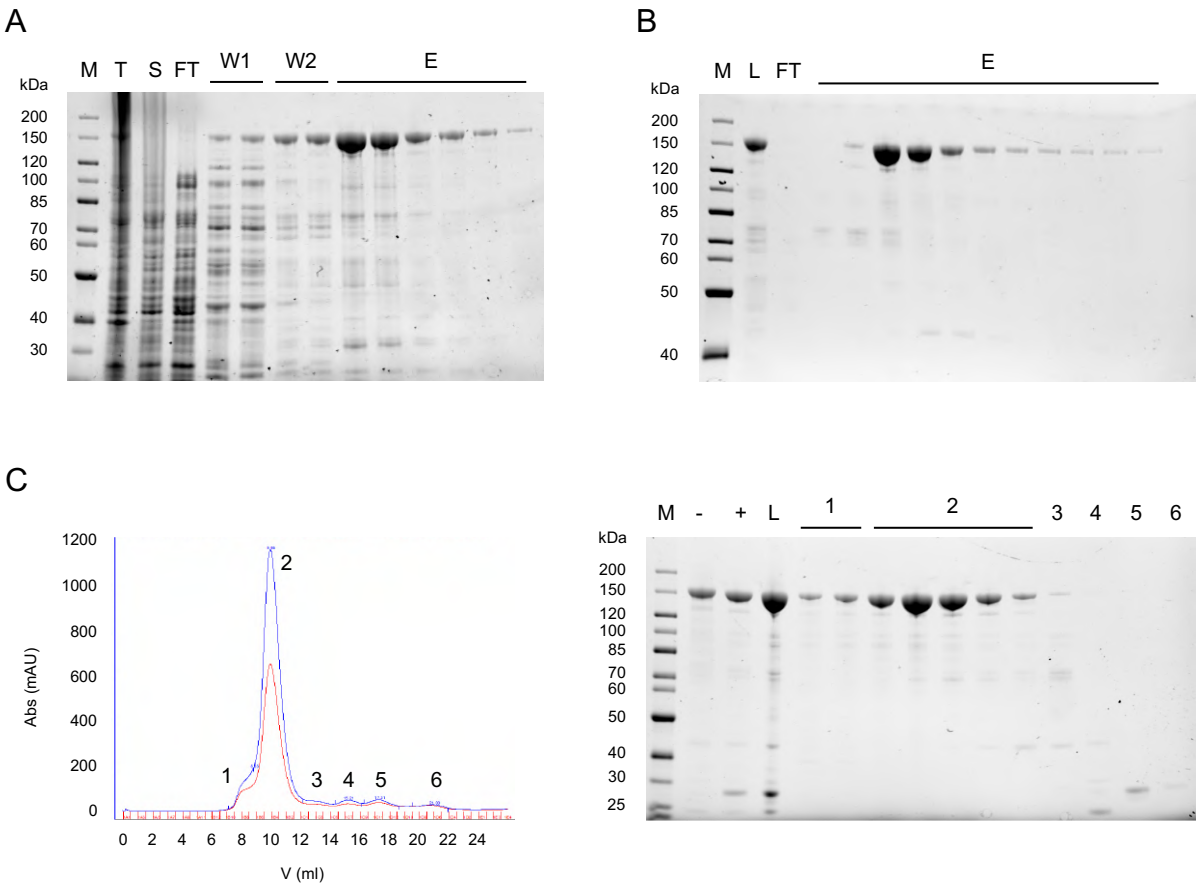

Figure 43. Purification of DrGyrBAfus. A) SDS-PAGE analysis of the first purification step of DrGyrBAfus on 2 ml of Ni-Sepharose 6 Fast Flow resin. **B**) SDS-PAGE analysis of the second purification step on a 5 ml Heparin column. C) Elution profile and corresponding SDS-PAGE analysis of the final purification step on a Superdex S200 10/300 gel filtration column. On the elution profile, the blue and red lines correspond to the absorbance at 280 nm and 260 nm respectively, and the brown line indicates the conductivity. In the three gels, lanes are annotated as follows: M: Marker (protein ladder), T and S: Total and Soluble fractions of cell lysis, FT: column flow-through, W1 and W2: first and second washes, E: elution, L: protein sample loaded on the column (i.e. DrGyrBAfus), - and +: before and after TEV cleavage, 1 to 6: peaks on the elution profile and corresponding fractions on the gel.

After a second purification on a Heparin column (Fig. 43B), the remaining 13 mg of protein were digested by TEV to cleave the His-tag on its N-terminus before a last purification step by size exclusion chromatography (Fig. 43C). The purification by size exclusion chromatography successfully eliminated the TEV protease and cleaved His-tag from our protein sample, as they eluted in separate peaks due to their much lower molecular weight compared to DrGyrBAfus (Fig. 43C). With a final yield of 7 mg, the purified DrGyrBAfus was concentrated to 4.3 µM (equivalent to 1.4 mg/ml) and frozen in liquid nitrogen to be stored at -80°C. For crystallization assays, a fraction of the purified DrGyrBAfus was further concentrated to 7 mg/ml and stored at -80°C after flash-cooling in liquid nitrogen.

I.2. Supercoiling and relaxation activity of the two constructs

In order to ensure that the recombinant DNA gyrases were functional, their supercoiling activity was evaluated by using 50 ng of relaxed pUC19 plasmid as a substrate, in presence of 1 mM ATP (Fig. 44). Both the reconstituted complex $DrGyrA_2B_2$ and the fusion DrGyrBAfus were active and able to negatively supercoil pUC19, as bands corresponding to relaxed states of pUC19 were shifted down toward a single band of supercoiled pUC19. When using $DrGyrA_2B_2$, a broad band of supercoiled pUC19 was observed for a protein concentration above 25 nM. However, with DrGyrBAfus this band of supercoiled plasmid was only clearly observed at protein concentration higher than 100 nM. Thus, the reconstituted complex appeared to be slightly more active, which could be caused by the presence of the linker at the interface forming the DNA-gate. The reduced flexibility of this interface due to the fusion of the two subunits might hinder either the cleavage or the strand passage of the double-stranded DNA thereby decreasing the supercoiling activity of DrGyrBAfus.

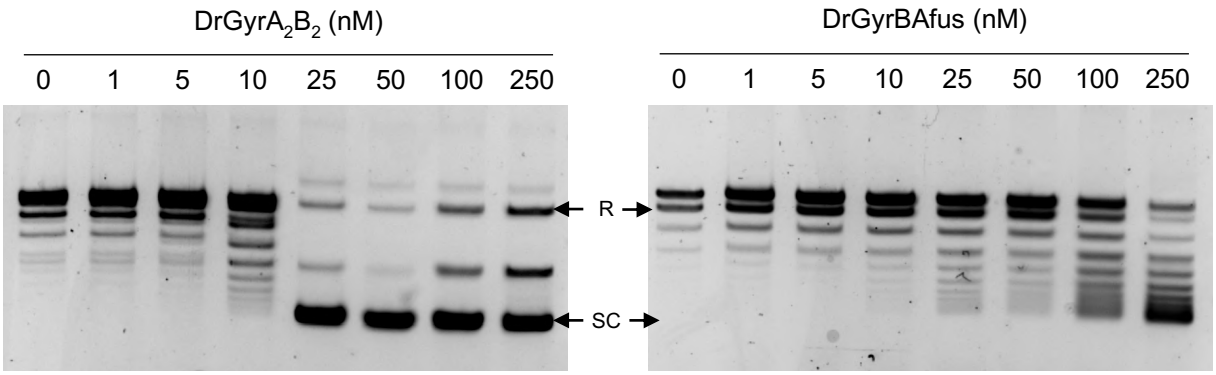

Figure 44. DrGyrA$_2$B$_2$ is more efficient at supercoiling than DrGyrBAfus. DNA supercoiling assays were performed by incubating 50 ng of relaxed pUC19 with increasing concentrations of DrGyrA$_2$B$_2$ (left gel) or DrGyrBAfus (right gel) from 1 nM to 250 nM, in presence of 1mM ATP and 5 mM MgCl$_2$. After addition of SDS and proteinase K to denature the DNA gyrase, reactions were analysed on 1% agarose gels run for 1h at 100 V in TBE 1X and stained with Gel Red for visualisation. The arrows pointing from R and SC indicate the bands corresponding to the relaxed (R) or supercoiled (SC) conformations of the pUC19 plasmid on the agarose gels.

We also characterized the relaxation activity of the two constructs and confirmed the effect of ATP on the two activities of the DNA Gyrase. Briefly, 50 ng of relaxed (Fig. 45A) or supercoiled plasmid (Fig. 45B) was incubated with 10 or 250 nM of either DrGyrA$_2$B$_2$ or DrGyrBAfus, with or without 1 mM of ATP. As expected, supercoiling of the relaxed plasmid was only observed in the presence of ATP for the two constructs. In agreement with our previous supercoiling assay, a mostly supercoiled plasmid was obtained with only 10 nM of DrGyrA$_2$B$_2$ whereas some relaxed topoisomers of the plasmid were observed even at 250 nM of DrGyrBAfus. Upon incubation with a supercoiled plasmid, DrGyrA$_2$B$_2$ displayed a relaxation activity as several bands corresponding to more or less relaxed topoisomers were observed. However this relaxation activity appeared less efficient than its supercoiling activity, since no relaxation of the plasmid was observed at 10 nM of DrGyrA$_2$B$_2$. When ATP was added in the reaction buffer, not relaxation was observed even at the highest protein concentration, which confirmed that ATP acts as a switch between the supercoiling and relaxation activities of gyrase. Compared to DrGyrA$_2$B$_2$, the DNA gyrase fusion seemed unable to perform relaxation even at the highest DrGyrBAfus concentration of 250 nM, regardless of the presence of ATP.

Taken together, these results suggest that the activity of the DNA gyrase fusion might be impeded by the reduced flexibility caused by linker. It is also possible that this construct is somehow less stable or more aggregated compared to the reconstituted complex.

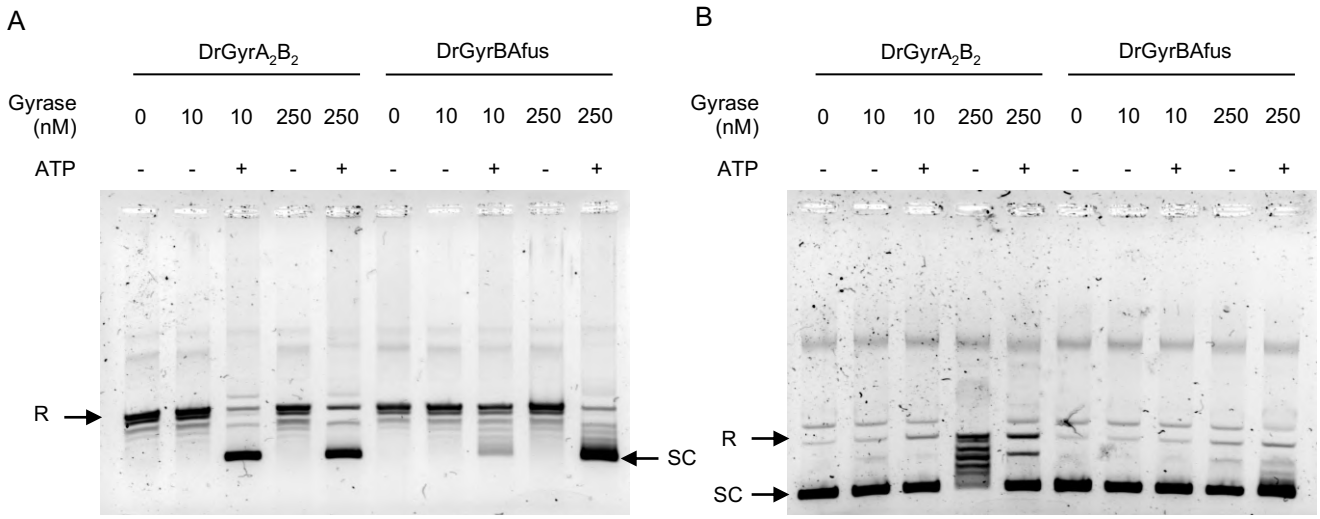

Figure 45. DrGyrBAfus is unable to perform relaxation. DNA supercoiling (**A**) and relaxation (**B**) assays were performed by incubating 50 ng of relaxed or supercoiled pUC19 with 10 or 250 nM of DNA gyrase, with or without 1mM ATP. After addition of SDS and proteinase K to denature the DNA gyrase, reactions were analysed on 1% agarose gels run for 1h at 100 V in TBE 1X and stained with Gel Red for visualisation. The arrows pointing from R and SC indicate the bands corresponding to the relaxed (R) or supercoiled (SC) conformations of the pUC19 plasmid on the agarose gels.

I.3. Toward the structural characterization of *D. radiodurans* DNA Gyrase

I.3.1. Crystallization assays of the two constructs

To gain insight into the structure of the DNA gyrase of *D. radiodurans*, we aimed at producing crystals of $DrGyrA_2B_2$ or DrGyrBAfus for X-ray crystallography. We started our crystallization assays by screening a large number of conditions (576 in total) thanks to the high-throughput crystallisation platform of EMBL (the HTX lab). The purified reconstituted and fusion proteins previously concentrated to 7 mg/ml were sent to the HTX lab for crystallization at 20°C using the sitting-drop vapour diffusion method with nanoliter drops. For the $DrGyrA_2B_2$ reconstituted complex, we compared crystallization trials in the absence and presence of a non-hydrolysable ATP analogue (AMP-PNP) that can trap the DrGyrB subunits in a closed conformation by closure of the N-gate (see Fig. 13 in the *Chapter Introduction* of this manuscript). After a week, micro-crystals of $DrGyrA_2B_2$ alone and in complex with AMP-PNP were obtained in conditions that contained 10% PEG 8000 and 0.2 M $MgCl_2$ or 0.2 M

calcium acetate, at pH 7.0 or 8.0 (Fig. 46). In contrast, no crystals of DrGyrBAfus could be obtained regardless of the screened conditions. The $DrGyrA_2B_2$ crystals were manually reproduced and optimised using the hanging-drop vapour diffusion setup with microliter drops at 20°C. Variations of the following parameters were tested:

- Precipitant concentration and molecular weight: 8 % to 18 % of PEG 8,000 and later on, 6 % to 16 % of PEG 3,350, 6,000, 8,000 or 10,000.
- Salt: 0.2 M of magnesium chloride or calcium acetate
- pH of the solution: 0.1 M Tris pH 7.0 to pH 8.5.

After one week, large hexagonal bipyramidal crystals were obtained in conditions containing 10 % ± 2 % of any tested PEG, 0.2 M $MgCl_2$ and 0.1 M Tris-HCl pH8 or pH 8.5 (Fig. 46). In average, the crystals dimensions were ~100 x 50 x 50 μm^3. Crystals of $DrGyrA_2B_2$ alone or in complex with AMP-PNP were collected and subsequently frozen in liquid nitrogen with a suitable amount of cryoprotectant. X-ray diffraction data were then collected on the automated beamline ID30A1 (ESRF), yielding diffraction up to 7 Å resolution (Fig. 46).

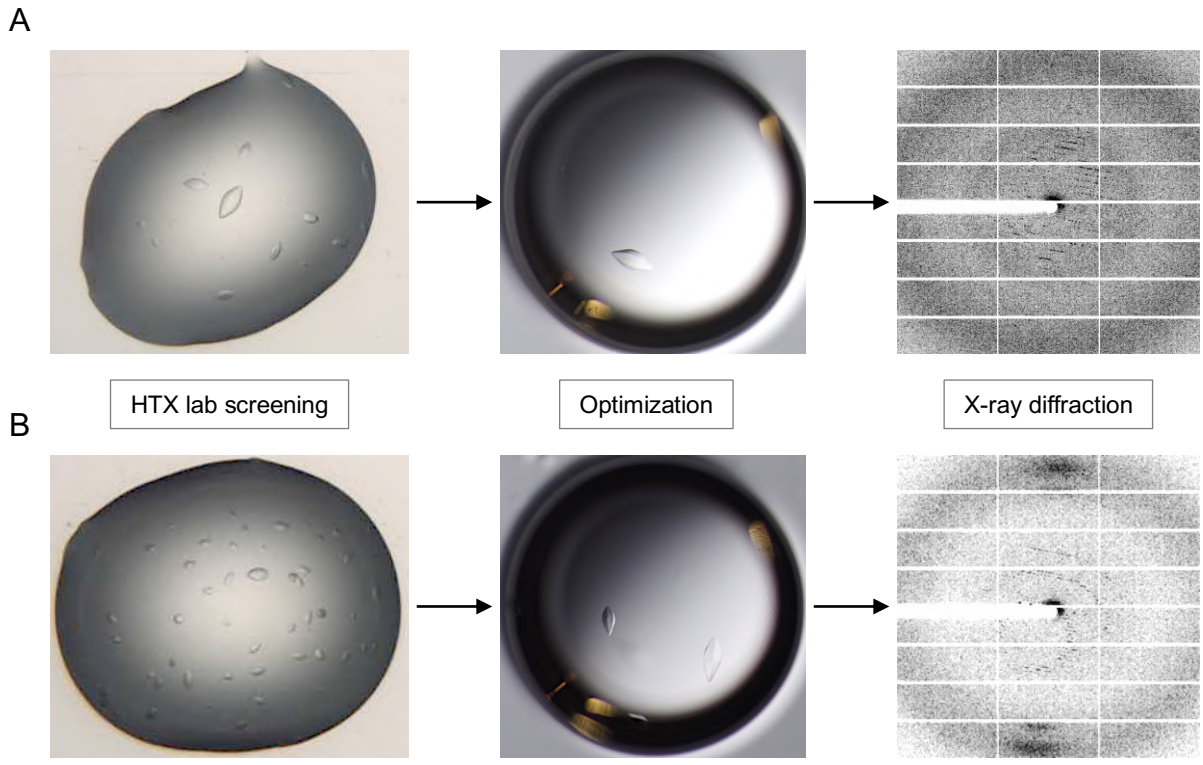

Figure 46. Optimized $DrGyrA_2B_2$ crystals diffracted up to 7 Å resolution. The condition composed of 10 % PEG 8,000, 0.2 M $MgCl_2$, 0.1 M Tris pH 7.0, yielding crystals of $DrGyrA_2B_2$ alone (**A**) or in complex with AMP-PNP (**B**) was determined by screening at the HTX lab (left panels). It was optimized by manual screening to produce large crystals suitable for X-ray diffraction (middle panels). These optimized crystals produced diffraction

patterns with diffraction spots up to 7 Å resolution (right panels) when brought to the ID30A1 beamline at ESRF for data collection (0.966 Å energy, 100% transmission, 50 µm, 100 ms exposition).

Given the low resolution at which the X-rays were diffracted by these crystals (7 Å), we optimized again the crystallization conditions with different salts, detergents, and amino acids, using additive screens 1 (HR2-420), 2 (HR2-430) and 3 (HR2-422) from Hampton Research. The additives were added to a starting condition composed of 10 % PEG 8,000, 0.2 M $MgCl_2$, 0.1 M Tris pH 8.0. The majority of the additives (about 60 %) only produced a myriad of micro-crystals not suitable for X-ray diffraction at the synchrotron due to their submicron size. Nonetheless, regular, well-formed crystals of larger dimensions were obtained in the presence of the following additives: 100 mM Glycine, 3 % dimethyl sulfoxide (DMSO), 0.1 M phenol, 4 % ter-butanol or 0.2 M sodium thiocyanate (Fig. 47). Crystals from these conditions were cryo-protected with 18 % glycerol and frozen in liquid nitrogen for diffraction data collection on Proxima-2A beamline at SOLEIL.

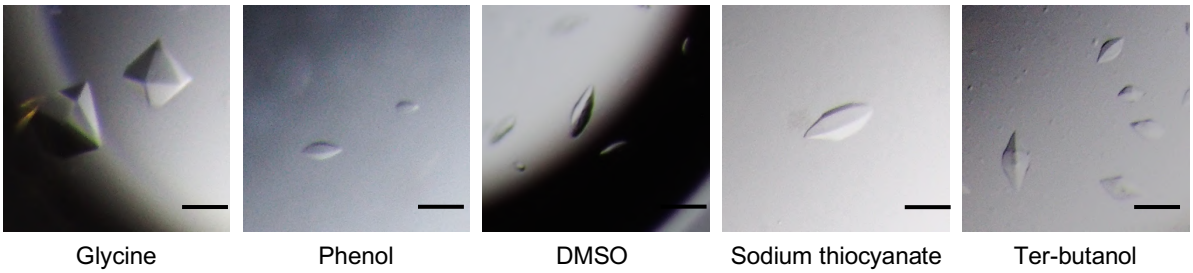

Figure 47. Crystals of DrGyrA$_2$B$_2$ optimized with various additives. Crystals seemingly suitable for X-ray crystallography were obtained when the starting crystallization condition composed of 10 % PEG 8,000, 0.2 M $MgCl_2$, 0.1 M Tris pH 8.0, was supplemented with either 100 mM Glycine, 0.1 M phenol, 3 % DMSO, 0.2 M sodium thiocyanate or 4 % ter-butanol (from left to right). The scale bar at the bottom right of each picture corresponds to 100 µm.

The only diffracting crystals were those obtained with 0.2 M sodium thiocyanate. The best dataset with a maximal resolution of 3.5 Å was processed with the XDS software and indexed in P622 space group with the unit cell parameters: a = b = 160.5 Å, c = 150.9 Å and α = β = 90°, γ = 120°. Several structures of DNA gyrase subunits or truncated complexes from other bacteria such as *S. aureus*, *M. tuberculosis*, or *T. thermophilus* are available in the Protein Data Bank (PDB), so we tried to solve the phase problem by molecular replacement (MR) using one of these structures as a search model (Table 15). The first attempt at MR was performed with mrBUMP, an automated molecular replacement program that uses homologous structures from the PDB (Keegan & Winn, 2008). Since no solutions were found, we turned to another MR program called Phaser MR, which relies on a user-given homologous structure (McCoy et

al., 2007). We chose the *S. aureus* DNA Gyrase structure (PDB: 2XCT (Bax et al., 2010)) as a search model, since it has 70% sequence similarity with $DrGyrA_2B_2$, but then again no solutions were found.

Table 15. List of the cryo-EM or crystal structures of DNA gyrase or Topo IV deposited on the PDB. Note that the complete structure of E. coli DNA gyrase was not available yet when we first tried to solve the phase problem.

PDB	Species	Protein	Ligand	Method	Resolution (Å)	DrGyr sequence coverage	Fusion
4DDQ	*Bacillus subtilis*	Gyrase - A	-	X-ray	3.3	1-502 over 812	-
3NUH	*Escherichia coli*	Gyrase - AB	-	X-ray	3.1	408-1353 over 1482	Yes
4TMA	*Escherichia coli*	Gyrase - AB	Inhibitor	X-ray	3.3	408-1353 over 1482	Yes
6RKW	*Escherichia coli*	Gyrase - AB	DNA + antibiotic	CryoEM	6.6	Complete	No
1ZVU	*Escherichia coli*	Topo IV - A	-	X-ray	3.0	25-716 over 812	-
2Y3P	*Escherichia coli*	Gyrase - A	DNA + antibiotic	X-ray	2.6	1-522 over 812	-
1EI1	*Escherichia coli*	Gyrase - B	AMP-PNP	X-ray	2.3	10-411 over 663	-
4XTJ	*Escherichia coli*	Gyrase - B	AMP-PNP	X-ray	1.9	10-411 over 663	-
4PRV	*Escherichia coli*	Gyrase - B	ADP	X-ray	2.0	10-411 over 663	-
1S16	*Escherichia coli*	Topo IV - B	AMP-PNP	X-ray	2.1	9-415 over 663	-
4PRX	*Escherichia coli*	Gyrase - B	ADP+Pi	X-ray	1.8	10-411 over 663	-
6GAV	*Mycobacterium tuberculosis*	Gyrase - AB	-	X-ray	2.6	5-1179 over 1482	Yes
5BS8	*Mycobacterium tuberculosis*	Gyrase - AB	DNA + antibiotic	X-ray	2.4	410-1166 over 1482	Yes
3IFZ	*Mycobacterium tuberculosis*	Gyrase - A	-	X-ray	2.7	1-502 over 812	-
3ZKB	*Mycobacterium tuberculosis*	Gyrase - B	AMP-PNP	X-ray	2.9	1-411 over 663	-
3ZM7	*Mycobacterium tuberculosis*	Gyrase - B	AMP-PCP	X-ray	3.3	1-411 over 663	-
5NPP	*Staphylococcus aureus*	Gyrase - AB	DNA + antibiotic	X-ray	2.2	420-1112 over 1482	Yes
2XCQ	*Staphylococcus aureus*	Gyrase - AB	-	X-ray	3.0	420-1146 over 1482	Yes
5CDP	*Staphylococcus aureus*	Gyrase - AB	DNA + antibiotic	X-ray	2.5	428-1101 over 1482	Yes
6FQV	*Staphylococcus aureus*	Gyrase - AB	DNA	X-ray	2.6	428-1101 over 1482	Yes
5IWI	*Staphylococcus aureus*	Gyrase - AB	DNA + antibiotic	X-ray	2.0	428-1101 over 1482	Yes
2INR	*Staphylococcus aureus*	Topo IV - A	-	X-ray	2.8	1-514 over 812	-
4URL	*Staphylococcus aureus*	Topo IV - B	Antibiotic	X-ray	2.3	5-419 over 663	-
4I3H	*Streptococcus pneumoniae*	Topo IV - AB	DNA + antibiotic	X-ray	3.7	7-1145 over 1482	Yes
4JUO	*Streptococcus pneumoniae*	Topo IV - AB	DNA + antibiotic	X-ray	6.5	5-1162 over 1482	Yes
4KPE	*Streptococcus pneumoniae*	Topo IV - AB	DNA + antibiotic	X-ray	3.4	415-1179 over 1482	No
3RAF	*Streptococcus pneumoniae*	Topo IV - AB	DNA + antibiotic	X-ray	3.2	415-1179 over 1482	No
3KSA	*Streptococcus pneumoniae*	Topo IV - AB	DNA	X-ray	3.3	415-1179 over 1482	No
3FOE	*Streptococcus pneumoniae*	Topo IV - AB	DNA + antibiotic	X-ray	4.0	415-1179 over 1482	No
4Z2C	*Streptococcus pneumoniae*	Gyrase - AB	DNA + antibiotic	X-ray	3.2	415-1183 over 1482	No
6N1P	*Streptococcus pneumoniae*	Gyrase - A	DNA	CryoEM	6.4	1-511 over 812	-
6N1R	*Streptococcus pneumoniae*	Gyrase - A	-	CryoEM	4.0	1-511 over 812	-
2NOV	*Streptococcus pneumoniae*	Topo IV - A	-	X-ray	2.7	1-490 over 812	-
5J5P	*Streptococcus pneumoniae*	Topo IV - B	AMP-PNP	X-ray	2.0	1-420 over 663	-
1KIJ	*Thermus thermophilus*	Gyrase - B	antibiotic	X-ray	2.3	11-412 over 663	-
6ENH	*Thermus thermophilus*	Gyrase - B	antibiotic	X-ray	1.9	8-412 over 663	-
3LNU	*Xanthomonas oryzae*	Topo IV - B	-	X-ray	2.2	1-414 over 663	-

To understand the cause of our struggle to solve the phase problem, we verified the presence of a full DNA Gyrase complex in the crystals, by loading several of these on a SDS-PAGE gel. Unfortunately, we found that only DrGyrA was present in the crystals since no band corresponding to DrGyrB (73 kDa) was detected on the gel (Fig. 48A). Based on this result, another molecular replacement was performed with Phaser MR using only the GyrA subunit of *S. aureus* (SaGyrA) as a search model (Fig. 48B). One plausible solution was found with initial R values of 0.52 and 0.55 for the R_{work} and R_{free} respectively. The crystal packing seemed correct with a solvent content of 60.9 % and no visible steric clashes between the symmetry mates (Fig. 48C). Using the "mutate and align" command in Coot, the sequence of SaGyrA was replaced with the sequence of DrGyrA. This updated structure was used for a first cycle of refinement using the Refmac 5 program, which lowered the R values to R_{work} = 0.46 and R_{free} = 0.52 (Fig. 48D). Further refinement of this dataset is still ongoing.

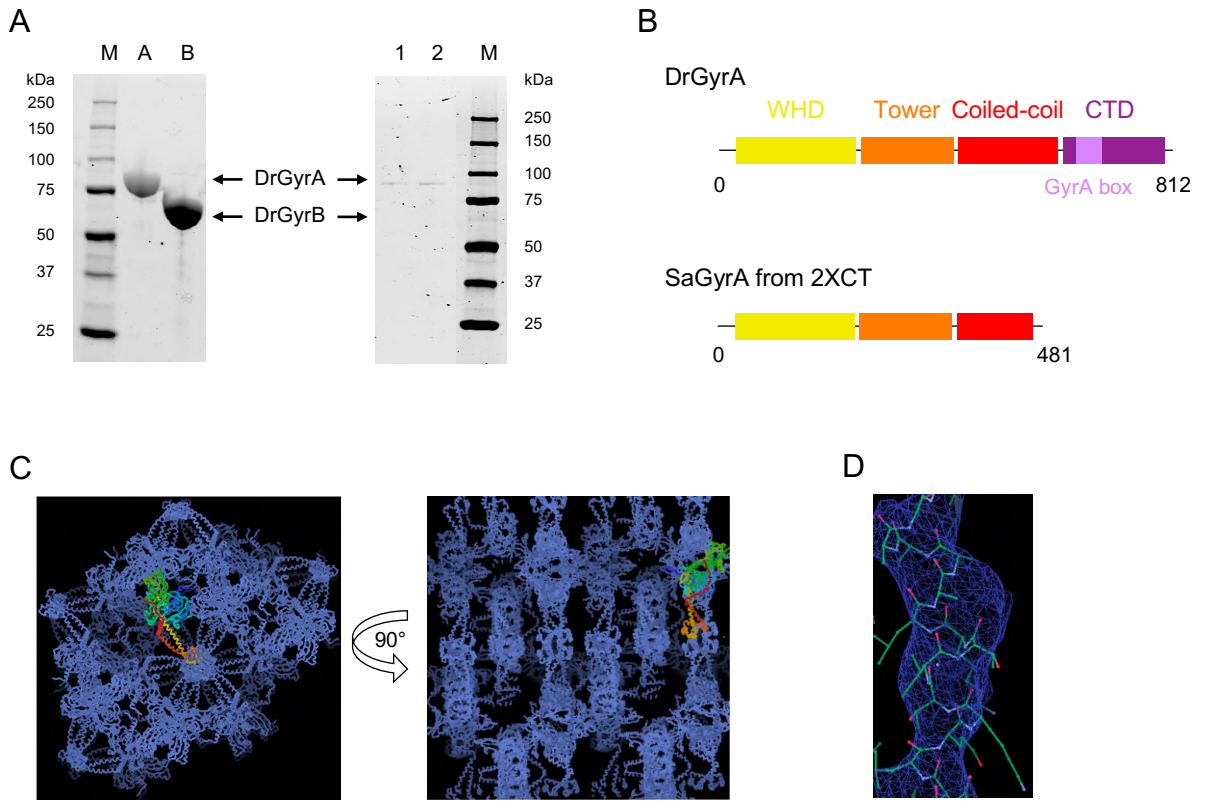

Figure 48. A first look at the structure of DrGyrA. A) SDS-PAGE analysis of purified DrGyrA (lane A), DrGyrB (lane B) and $DrGyrA_2B_2$ crystals (lanes 1 and 2) dissolved in denaturing loading dye and heated at 95°C. **B**) Sequence coverage of the different domains of DrGyrA by SaGyrA from the PDB 2XCT (Bax et al., 2010), showing that only the N-terminal part is covered. C) Crystal packing of the plausible model phased by Phaser MR showing the solvent channels in the crystal. One SaGyrA subunit is rainbow-coloured from its N-terminus (blue) to its C-terminus (red), while its symmetry mates are represented as blue ribbons. **D**) First manual refinement of

the model in Coot using the refined 2Fo-Fc map from Refmac5. The protein appears as green sticks with oxygen in red and nitrogen in blue. The electron density contoured at 1 σ is represented as a blue mesh around the protein.

I.4. Electron microscopy of the reconstituted complex and the fusion

Taking into account the reduced supercoiling activity and difficulty to obtain crystals of the fusion, one could question the stability and homogeneity of the produced DrGyrBAfus. The same could be asked for the reconstituted complex, in light of the crystallization of the GyrA subunit alone. To assess the quality of our two purified constructs, we resorted to negative-staining electron microscopy (EM). Considering that the DNA gyrase is a large heterotetramer of nearly 320 kDa, we should be able to visualize the complex by EM. Samples of purified $DrGyrA_2B_2$ and DrGyrBAfus prepared by J. Timmins and S. De Bonis were imaged by negative staining EM, in collaboration with I. Gutsche and M. Bacia (Fig. 49). The reconstituted complex was not homogenous, and we even observed some aggregates (Fig. 49A-B). In contrast, the DrGyrBAfus sample appeared more stable and homogenous, and no aggregates were detected with negative staining EM (Fig. 49C-D). These preliminary results were intriguing as we could obtained crystals of DrGyrA from the reconstituted complex while the fusion did not crystallize at all. Moreover, the non-homogenous partially aggregated $DrGyrA_2B_2$ was more efficient in the supercoiling assays than the homogenous DrGyrBAfus, which was also puzzling.

Based on these negative stain EM images, we decided to freeze several grids of DrGyrBAfus to perform cryo-EM in collaboration with I. Gutsche and M. Bacia. The advantages of cryo-EM over negative-staining is that the sample is in a more native environment since no staining agents are used and the sample resides in a thin layer of amorphous ice formed by flash-cooling in liquid ethane. The cryo-EM imaging of the purified DrGyrBAfus construct revealed that the sample was homogeneous, but the protein chains appeared to be partially denatured and thus the collected images were not suitable for single-particle image reconstruction. Further experiments will be needed to optimize the sample preparation so as to obtain exploitable data for 3D structure determination.

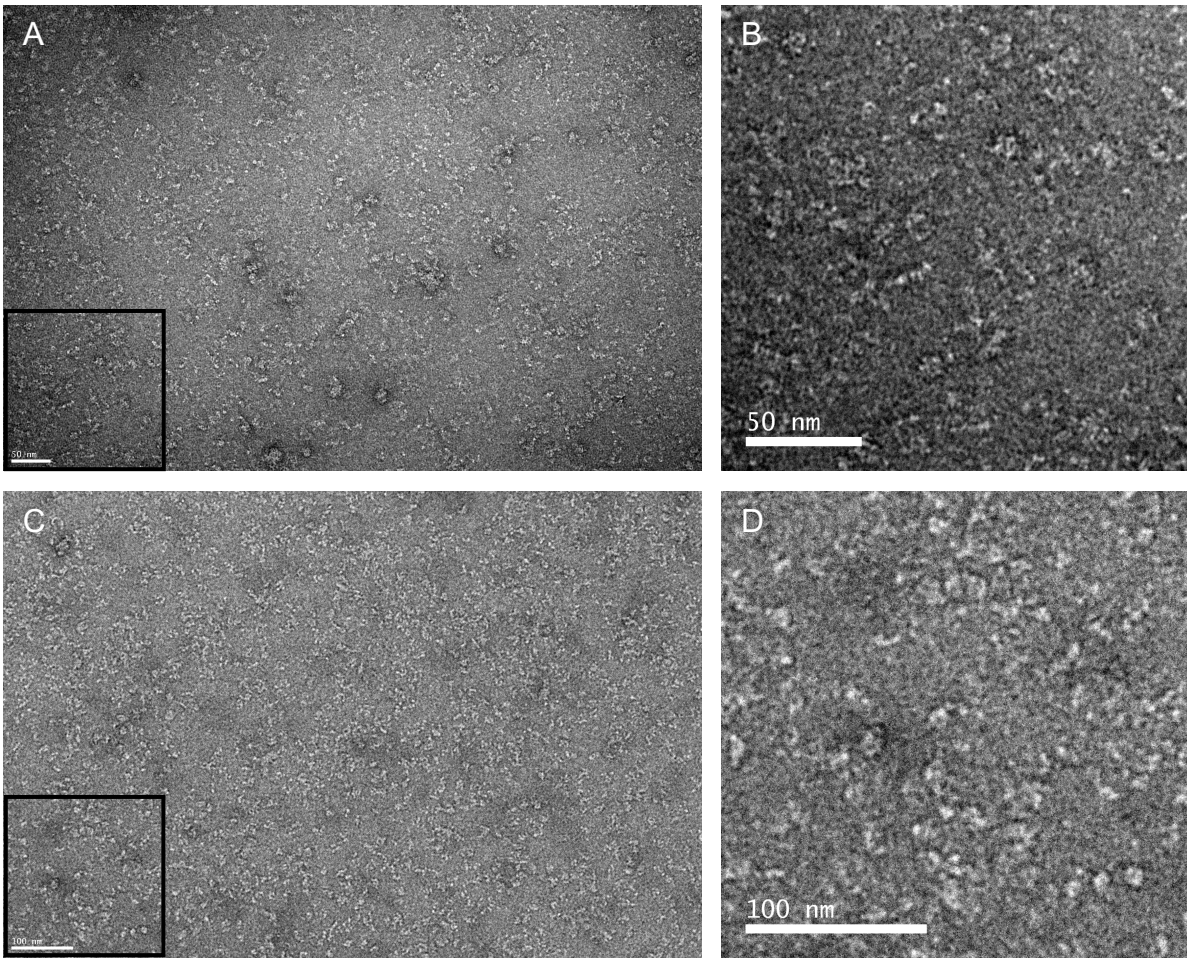

Figure 49. DrGyrBAfus appears to be more homogenous and stable than DrGyrA$_2$B$_2$. Images of DrGyrA$_2$B$_2$ (**A-B**) and DrGyrBAfus (**C-D**) obtained by negative-stain EM. Due to the negative-staining solution in the background, the proteins appear as white objects on a darker background. The **B** and **D** panels are numerically enlarged images of the area delimited by black squares in panel **A** and **C**. The scale bars represent 50 nm in **A** and **B** and 100 nm in **C** and **D**.

II. The HU proteins of *D. radiodurans* and *D. deserti*

II.1. Production of the HU proteins

II.1.1. Expression and purification of the deinococcal HU proteins

The four HU proteins of *D. radiodurans* and *D. deserti* were expressed in *E. coli* cells as recombinant proteins with a cleavable N-terminal hexa-histidine tag (His-tag). After an overnight induction the proteins were extracted by cell lysis and purified through successive purification steps (Fig. 50). The HU proteins were first purified on a nickel affinity column to remove the majority of impurities from the cell lysis (Fig. 50A). After a second purification step on a Heparin column to remove DNA, the His-tag was cleaved by an overnight incubation with an His-tagged TEV protease. To separate the cleaved HU proteins from the protease and the His-tag, the reaction was loaded onto a nickel affinity resin (Fig. 50B). Since the His-tag was cleaved, the HU proteins did not bind to the resin contrary to the TEV protease and the cleaved His-tag. Thus, we retrieved our HU proteins from the column flow-through and the first washes. Lastly, the HU proteins were purified on a size-exclusion chromatography column, concentrated and flash-cooled in liquid nitrogen for storage at -80°C (Fig. 50C). The average final yield for DrHU, DdHU1, DdHU2 and DdHU3 ranged from 4 to 8 mg of protein per liter of cell culture.

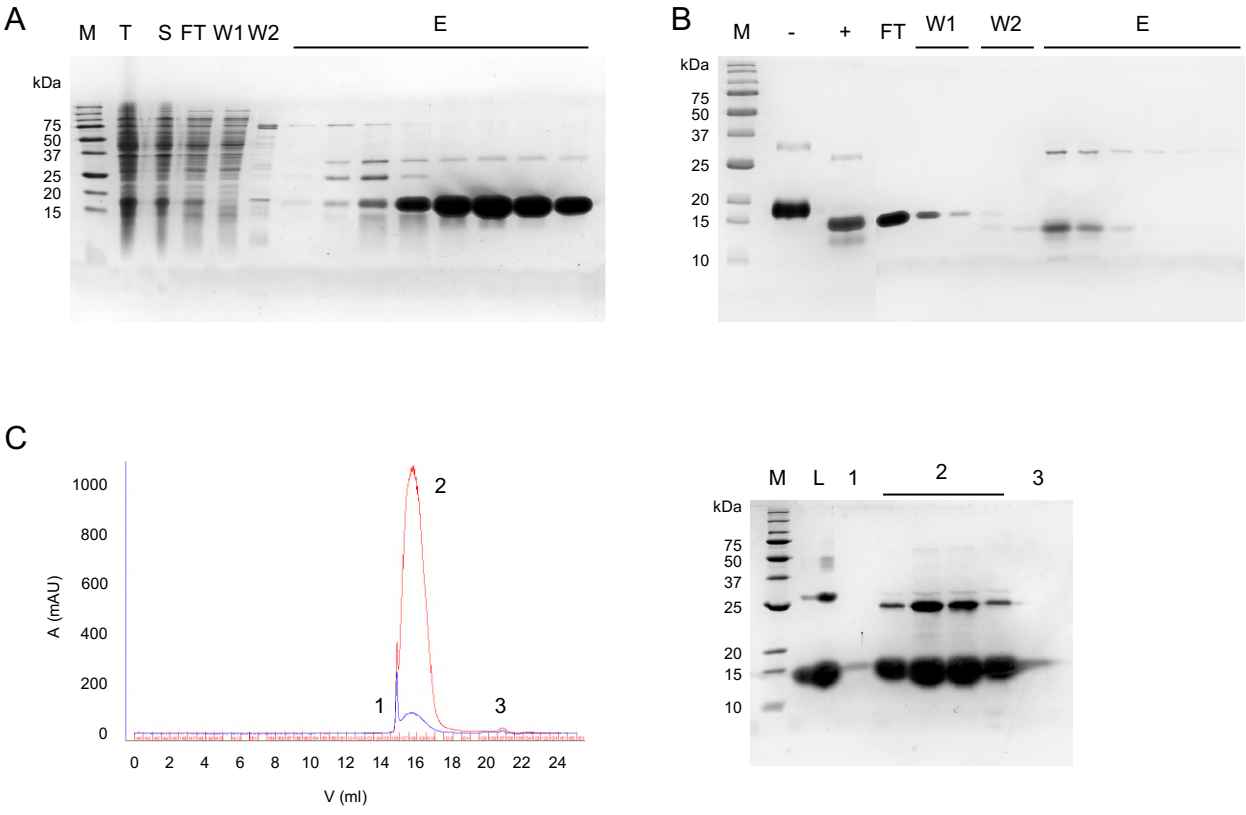

Figure 50. Purification process of DdHU1. A) SDS-PAGE analysis of the first purification step of DdHU1 on a 5 ml HisTrap FF column. Lanes are annotated as follows: M: Marker, T and S: Total and Soluble fractions of cell lysis, FT: column flow-through, W1 and W2: first and second washes, E: elution. **B**) SDS-PAGE analysis of the third purification step of DdHU1 on 2 ml of Ni-Sepharose 6 FF resin. Lanes are annotated as follows: M: Marker, - and +: before and after TEV cleavage, FT: flow-through, W1 and W2: first and second washes, E: elution. **C**) Elution profile of DdHU1 purified on a ENrich SEC650 gel filtration column, with the corresponding SDS-PAGE analysis. Numbers 1 to 3 correspond to the three peaks on the elution profile (by order of elution) and their corresponding fractions on the gel, while L refers to the protein sample loaded onto the column. On the chromatogram, the blue and red lines correspond to the absorbance at 280 nm and 260 nm respectively.

As exemplified by the chromatogram of the size exclusion chromatography (Fig. 50C), the HU proteins of *D. radiodurans* and *D. deserti* do not absorb much at 280 nm. Owing to their complete lack of tyrosine or tryptophan residues, after cleavage of the His-tag their molar extinction coefficients (ε) at 280 nm dropped from 1490 $M^{-1}.cm^{-1}$ to 0 $M^{-1}.cm^{-1}$. Because of this shared peculiarity, we had to resort to other methods to follow the DrHU, DdHU1, DdHU2 or DdHU3 proteins and determine their concentrations along the different steps of their production. At first, to evaluate HU concentrations, we relied on direct comparison of band intensities on a SDS-PAGE gel quantified with the Image Lab software using a range of lysozyme concentrations as a reference. Using the ImageLab software to quantify the bands on gel, we could produce a standard curve of the band intensity as a function of lysozyme concentration. The mass and resulting concentration of the HU proteins would be obtained by calculating the band intensity produced by migration of different volumes of our sample. Nonetheless, this approach was expensive and particularly time-consuming as for each concentration measurement we needed to make a new SDS-PAGE analysis. For this reason, we decided to measure the concentration of DrHU, DdHU1, DdHU2 and DdHU3 by means of their sequence-specific absorbance at 205 nm. At this wavelength, most of the absorbance comes from the peptide backbone. Nevertheless, Anthis and Clore showed that individual side chains also still contribute to the overall absorbance at 205 nm, so that one could calculate a sequence-specific $\varepsilon_{205\ nm}$ and use it to more accurately determine protein concentration (Anthis & Clore, 2013). Phenylalanine, methionine, arginine and cysteine are among the seven most absorbing amino acids at 205 nm with molar extinction coefficients of 8,600, 1,830, 1,350 and 690 $M^{-1}.cm^{-1}$ respectively (Goldfarb et al., 1951). Interestingly, these residues make up to 11% of the sequence of our deinococcal HU proteins hence the molar extinction coefficients of DrHU, DdHU1, DdHU2 and DdHU3 at 205 nm are quite high. This approach is much faster and easier to implement than the SDS-PAGE lysozyme range, as it only requires three measurements on a spectrophotometer.

II.1.2. Expression and purification of the HU protein of *B. burgdorferi*

We wanted to produce the HU protein of *B. burgdorferi* (Hbb) to compare its biochemical and DNA-binding properties with those of DrHU, since molecular dynamics simulations of Hbb binding to DNA had been performed by our laboratory in collaboration with F. Dehez and A. Monari from Nancy (Hognon et al., 2019). To do so, the *hup* gene from the genomic DNA of *B. burgdorferi* was amplified and inserted into a pProExHTB plasmid to express Hbb as recombinant protein with a cleavable N-terminal His-tag. Expression was induced overnight at 20°C in 2 L cell cultures of *E. coli* strain BL21. After cell lysis, we attempted to purify the protein following the same purification protocol as that of the deinococcal HU proteins (Fig. 51). However, Hbb turned out to be more difficult to produce than DrHU as the majority of the protein was found in the insoluble fraction after cell lysis (Fig. 51A). The purification process was yet carried out up to the gel filtration step, with the hope to purify a sufficient amount of Hbb (at least 1 mg) for DNA-binding assays with oligonucleotides. After purification on a nickel affinity column and a Heparin column, we could gather only 260 µg of Hbb. Although the amount of protein was still of 200 µg after cleavage of the His-tag (Fig. 51B), the quantity of Hbb dropped to 10 µg after the last purification step by size exclusion chromatography (Fig. 51C). After three failed attempts to produce Hbb, we decided to focus on the deinococcal HU proteins.

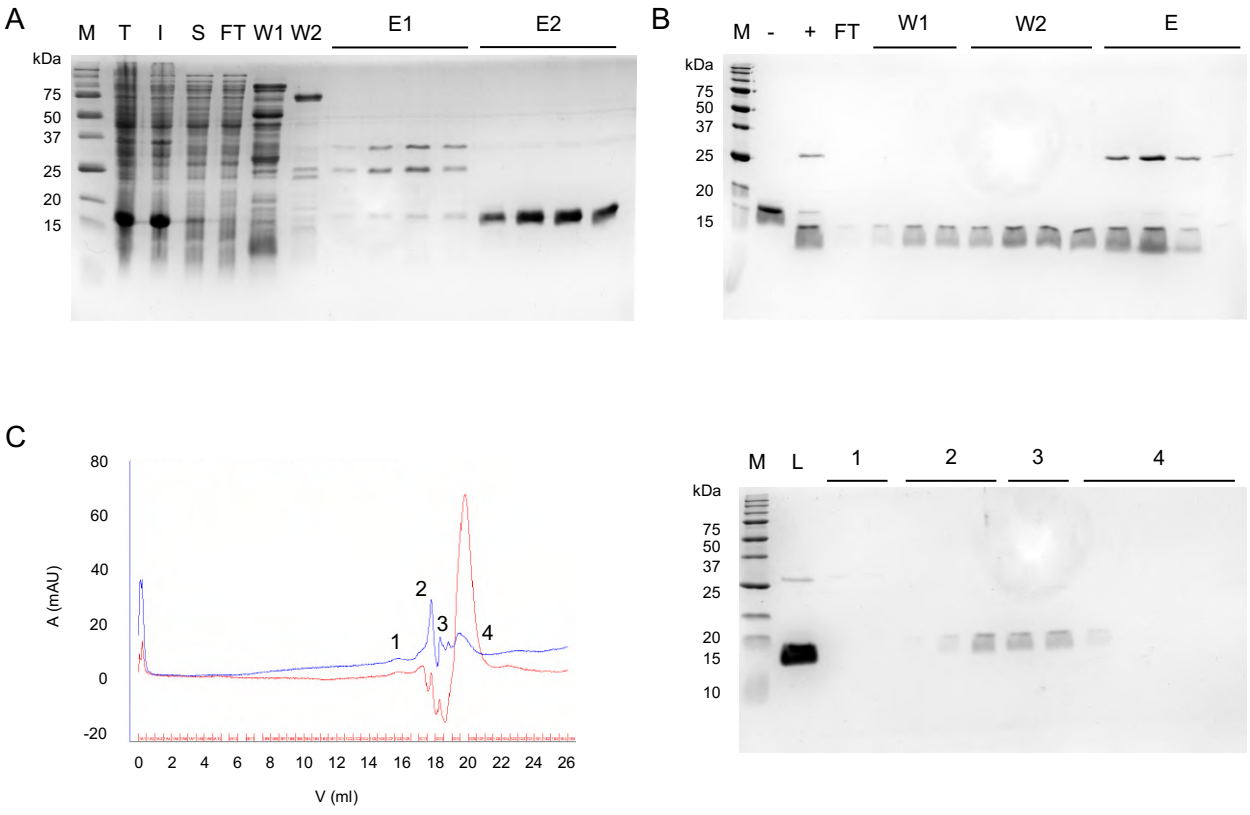

Figure 51. Purification of Hbb from 2L of cell culture. A) SDS-PAGE analysis of the first purification step of Hbb on a 5 ml HisTrap FF column. Lanes are annotated as follows: M: marker, T, I and S: total, insoluble and soluble fractions of cell lysis, FT: column flow-through, W1 and W2: first and second washes, E1 and E2: first and second step of elution. **B**) SDS-PAGE analysis of the third purification step on 2 ml of Ni-Sepharose 6 FF resin. Lanes are annotated as follows: M: marker, - and +: before and after TEV cleavage, FT: flow-through, W1 and W2: first and second washes, E: elution. **C**) Elution profile of Hbb purified on a ENrich SEC650 gel filtration column, with the corresponding SDS-PAGE analysis. Numbers 1 to 4 correspond to the four elution peaks (by order of elution) and their corresponding fractions on the gel, while L refers to the protein sample loaded onto the column. On the chromatogram, the blue and red lines correspond to the absorbance at 280 nm and 260 nm respectively.

II.2. Crystallization trials of DrHU, DdHU1, DdHU2 and DdHU3

The four HU proteins were sent to the HTX lab (EMBL), to test crystallisation screening kits from diverse suppliers (Qiagen, Molecular Dimensions, Hampton Research and Rigaku Reagents). Crystallization trials were done at 20°C by the sitting-drop vapour diffusion method using small volumes (hundreds of nanoliters) of proteins at concentrations ranging from 12 to 23 mg/ml. No crystals were obtained regardless of the many tested conditions.

The next attempts at crystallising DrHU, DdHU1, DdHU2 and DdHU3 were performed by manual screening at 20°C, using the hanging-drop vapour method with a protein concentration around 18 mg/ml. We tried different crystallisation screening kits from Hampton Research (HR2-211, HR2-082, HR2-110) and Molecular Dimensions (MD1-59):

- HR2-211 is made of several concentrations of ammonium sulfate screened against a range of pH,
- HR2-082 proposes several concentrations of PEG with different molecular weights against a range of pH,
- HR2-110 and MD1-59 explore a variety of salts and precipitants at different pH.

These conditions did not promote the crystallization of any of the four HU proteins. To shift the solution equilibrium towards supersaturation and potential nucleus formation, we reproduced the experiment with higher concentrations of DrHU and DdHU1, at 49 mg/ml and 68 mg/ml respectively. Surprisingly, the two proteins remain quite stable despite the high concentration as we could observe clear drops in some conditions. Once again, no crystals were formed and the drops were either clear or contained precipitated protein or phase separation.

II.3. Study of the DNA binding properties of DrHU, DdHU1, DdHU2 and DdHU3

II.3.1 Interaction of the HU proteins with oligonucleotides

To characterize the DNA binding ability of our proteins, we performed electrophoretic mobility shift assays (EMSA) for which fluorescein-labelled ss- or dsDNA oligonucleotides were incubated with increasing concentrations of DrHU, DdHU1, DdHU2 or DdHU3. DNA-protein complexes were then separated by electrophoresis on acrylamide native gels and visualized by excitation of the fluorescein. In other bacteria such as *E. coli*, HU does not possess an N-terminal extension and has a very short 9 bp binding site. To determine the minimal binding site of DrHU, DdHU1, DdHU2 and DdHU3, we performed EMSA with dsDNA oligonucleotides ranging from 20 bp to 50 bp in length. After incubation with dsDNA oligonucleotides, HU proteins were able to form distinct stable DNA-protein complexes (Fig. 52). All four HU proteins bound efficiently to a 20-mer dsDNA oligonucleotide, meaning that a 20 bp stretch of DNA is sufficient for stable binding by the HU proteins (Fig. 52A). Shorter DNA fragments were not tested. We observed that *D. deserti* DdHU2 and DdHU3 bound significantly more tightly to 20 bp DNA than their DrHU and DdHU1 homologues, with the DNA shifting at 2 to 5 times lower protein concentrations in the case of DdHU2 and DdHU3.

We also evaluated the binding of the four HU proteins to 30, 43 and 50 bp oligonucleotides. The data for the 30 and 50 bp DNA is not presented, but was very similar to that observed with the 43 bp fragments (Fig. 52B). With these longer oligonucleotides, all four HU proteins shifted the DNA, but multiple shifted bands could be seen in the EMSA gels, which may be induced by HU oligomerization on the dsDNA oligonucleotides or multiple binding sites. In agreement with the finding that *Deinococcal* HUs can bind a 20 bp DNA fragment, it would be expected that at least two HU dimers could assemble on each 43 or 50 bp DNA oligonucleotides. With ssDNA, DNA-protein complexes were observed regardless of the oligonucleotide length, but appeared to be less stable than with dsDNA, as seen by the smearing on the gel for the highest concentrations, thereby hinting at a clear preference for dsDNA (Fig. 52C). Interestingly, the affinity of HU for dsDNA increased when a fluorescein-conjugated thymine was introduced in the middle of the sequence, thereby altering the DNA backbone (Fig. 52B). This suggests that the HU proteins of *D. radiodurans* and *D. deserti* might favour binding to distorted and more flexible dsDNA, possibly due to lower required energy in such case.

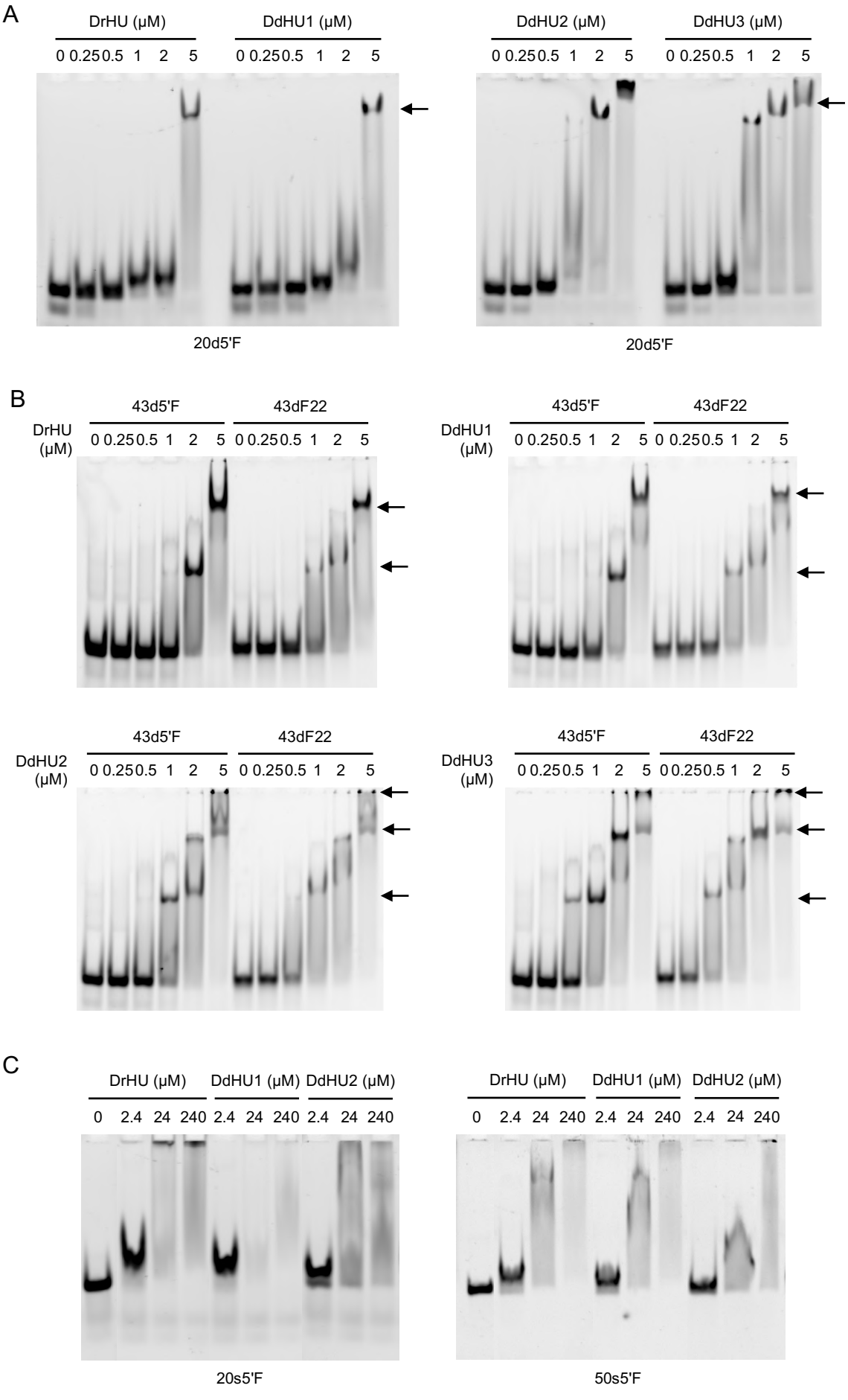
A
DrHU (μM)
0 0.25 0.5 1 2 5
DdHU1 (μM)
0 0.25 0.5 1 2 5
20d5'F
DdHU2 (μM)
0 0.25 0.5 1 2 5
DdHU3 (μM)
0 0.25 0.5 1 2 5
20d5'F
B
DrHU (μM)
43d5'F
43dF22
0 0.25 0.5 1 2 5 0 0.25 0.5 1 2 5
DdHU1 (μM)
43d5'F
43dF22
0 0.25 0.5 1 2 5 0 0.25 0.5 1 2 5
DdHU2 (μM)
43d5'F
43dF22
0 0.25 0.5 1 2 5 0 0.25 0.5 1 2 5
DdHU3 (μM)
43d5'F
43dF22
0 0.25 0.5 1 2 5 0 0.25 0.5 1 2 5
C
DrHU (μM)
DdHU1 (μM)
DdHU2 (μM)
0 2.4 24 240 2.4 24 240 2.4 24 240
20s5'F
DrHU (μM)
DdHU1 (μM)
DdHU2 (μM)
0 2.4 24 240 2.4 24 240 2.4 24 240
50s5'F

Figure 52. Binding of DrHU, DdHU1, DdHU2 and DdHU3 to single- or double-stranded DNA oligonucleotides. The DNA binding ability of the deinococcal HU proteins was assessed with single- or double-stranded oligonucleotides of 20 to 50 bp in length. A fluorescein was either fused at the 5' end of the oligonucleotides (20d5'F, 20s5'F, 43d5'F, 50s5'F) or inserted in the middle of the sequence as a modified thymine (43dF22). Increasing concentrations of HU proteins were incubated with 50 nM of 20d5'F (**A**), 43d5'F, 43dF22 (**B**), 20s5'F or 50s5'F (**C**). The formation of the protein-DNA complexes were studied by EMSA through migration on 7.5% acrylamide native gels. In panels A and B, arrows indicate the stable protein-DNA complexes.

All HU variants displayed the same preferences for dsDNA and more flexible oligonucleotides, but as for the shorter 20 bp DNA, *D. deserti* DdHU2 and DdHU3 displayed tighter binding to 30, 43 or 50 bp DNA than DrHU and DdHU1. When incubated with a 43-mer dans oligonucleotide (43d5'F), the band shift was equally induced by 2 µM DrHU or 2 µM DdHU1. However, DdHU2 and DdHU3 displayed a higher affinity for this dsDNA compared to DrHU and DdHU1, as an equivalent band shift was observed for concentrations as low as 1 µM of DdHU2 and 0.5 µM of DdHU3 (Fig. 52B).

To better evaluate the affinity of HU proteins for dsDNA, we relied on fluorescence polarization (FP). FP assays were carried out by incubation of 1 nM of 43d5'F with 0 to 10 µM of either DrHU, DdHU1, DdHU2 or DdHU3 (Fig. 53). When the fluorescent oligonucleotide is free in solution, it rotates rapidly which yields a low FP value but when the DNA is bound to the HU proteins the rotation is slower, which produces a higher FP value. Our results confirmed that DdHU3 has the highest affinity for dsDNA, with a K_d of 0.16 µM, while DdHU2 and DdHU1 have K_d values of 0.25 µM and 0.24 µM respectively. Of the four deinococcal HU proteins, DrHU displayed the lowest affinity with a K_d of 0.30 µM.

A

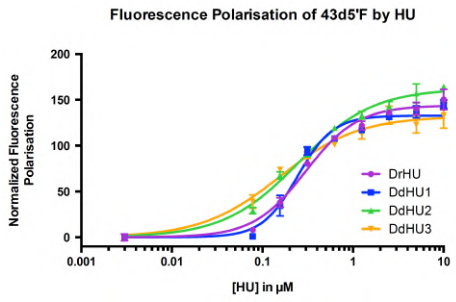

B

Protein	Kd (µM)	Hill coefficient	R^2
DrHU	0.30 ± 0.02	1.5 ± 0.1	0.99
DdHU1	0.24 ± 0.02	2.2 ± 0.3	0.97
DdHU2	0.25 ± 0.02	1.1 ± 0.1	0.99
DdHU3	0.16 ± 0.02	1.0 ± 0.1	0.97

Figure 53. Binding of the deinococcal HU proteins to a 43mer double-stranded oligonucleotide. The affinity of the deinococcal HU proteins for the fluorescein-labelled dsDNA 43d5'F was assessed by fluorescence polarization by incubation of 1 nM of 43d5'F with increasing concentrations of HU proteins. The fluorescence polarisation value was measured on a CLARIOstar microplate reader. The data were treated with GraphPad Prism and mean values were fitted to a one-site specific binding with Hill slope to account for possible cooperativity (**A**). The binding parameters (Kd and Hill coefficient) for each HU proteins were derived from the fitting model (**B**).

To account for a potential cooperativity upon binding to DNA, the FP values were fitted to a model that includes Hill coefficient. Hill coefficient, determined as the slope of a binding curve in logarithmic scale, gives an indication about the cooperativity between proteins when binding to a ligand (in our case the DNA). Binding to a ligand is considered to be cooperative when the binding of a first protein lowers the energy required for the binding of a second protein. A Hill coefficient greater than 1 suggests that the binding is cooperative and higher values indicates a higher cooperativity upon binding. Accordingly, the four HU proteins could be classified into two groups based on the apparent slope of the binding curve and the value of the Hill coefficient. The slopes of the binding curves of DrHU and DdHU1 appeared steeper than those of DdHU2 and DdHU3. These two HU proteins displayed Hill coefficient values of 1.1 and 1.0, which denoted the lack of cooperativity upon binding to the 43 bp oligonucleotide. On the other hand, the Hill coefficient values of DrHU and DdHU1 were greater than 1, suggesting a cooperativity in their binding mechanism. This cooperative effect seemed even stronger in the case of DdHU1, for which the Hill coefficient had a value of 2.2 ± 0.3.

Taken together, our results suggest that HU variants from *D. radiodurans* and *D. deserti* all bind preferentially to dsDNA, with a binding site of 20 base pairs or less. In all cases, we observed a slightly stronger binding to DNA substrates containing a modified base in central position, which may be a little distorted or less stable, which may lower the energy required for DNA bending. The DrHU and DdHU1 showed similar DNA binding profiles and cooperative binding, whereas DdHU2 was more similar to DdHU3 without any cooperativity upon binding. It is interesting to note that DdHU3, which has the highest affinity for dsDNA, is also the most divergent regarding sequence homology with a shorter N-terminal extension and therefore might have a complementary or distinct function compared to the other HUs in *D. deserti*.

II.3.2 Interaction of the HU proteins with pUC19 plasmid

To characterize the DNA-binding properties of the deinococcal HU proteins with a substrate closer to genomic DNA, we decided to work with plasmid DNA, namely pUC19 (2686 bp). Like bacterial genomic DNA, pUC19 is double-stranded, circular and its length enables for a variety of conformations including supercoiled, linear or relaxed states. The binding of DrHU, DdHU1, DdHU2 and DdHU3 to different conformations of pUC19 were

assessed by the EMSA method. To do so, we incubated 3 nM of pUC19, either supercoiled, relaxed or linearized, with 0 to 9.6 µM of HU proteins and analysed their interaction by electrophoresis on 1% agarose gels (Fig. 54). The supercoiled plasmid (pUC19-SC) was extracted and purified from *E. coli* cells without further treatment. The relaxed (pUC19-R) and linearized (pUC19-L) conformations required an additional step to alter the native supercoiled state. The relaxed conformation was obtained by incubation of the supercoiled plasmid with the human topoisomerase I while the linearized plasmid was produced by digestion with the restriction enzyme HindIII.

In the first assays, we only used the supercoiled conformation to compare the affinity of the various HU proteins for plasmid DNA (Fig. 54A). While incubating pUC19-SC with DrHU, DdHU1 or DdHU2, a band shift was visible for protein concentrations of 2.4 µM and higher. The same band shift was detected with DdHU3 at lower concentrations starting from 1.2 µM of protein. These results are in agreement with those obtained with oligonucleotides, as DdHU3 seemed to display the highest affinity for plasmid DNA compared to DrHU, DdHU1 or DdHU2. We then compared the binding of DrHU to supercoiled, relaxed or linearized pUC19 to assess a possible effect of the plasmid conformation (Fig. 54B). Band shifts were observed at protein concentrations of 2.4 µM or higher for the three plasmid conformations, implying that DrHU has no preference regarding the conformation of plasmid DNA. Interestingly, our results highlighted the formation of distinct protein-DNA complexes with plasmid DNA when increasing the concentration of HU protein. While this could suggest multiple binding events or different level of plasmid compaction, it could also hint at a possible alternative binding mode at higher concentrations with a possible rearrangement of the protein-DNA assembly.

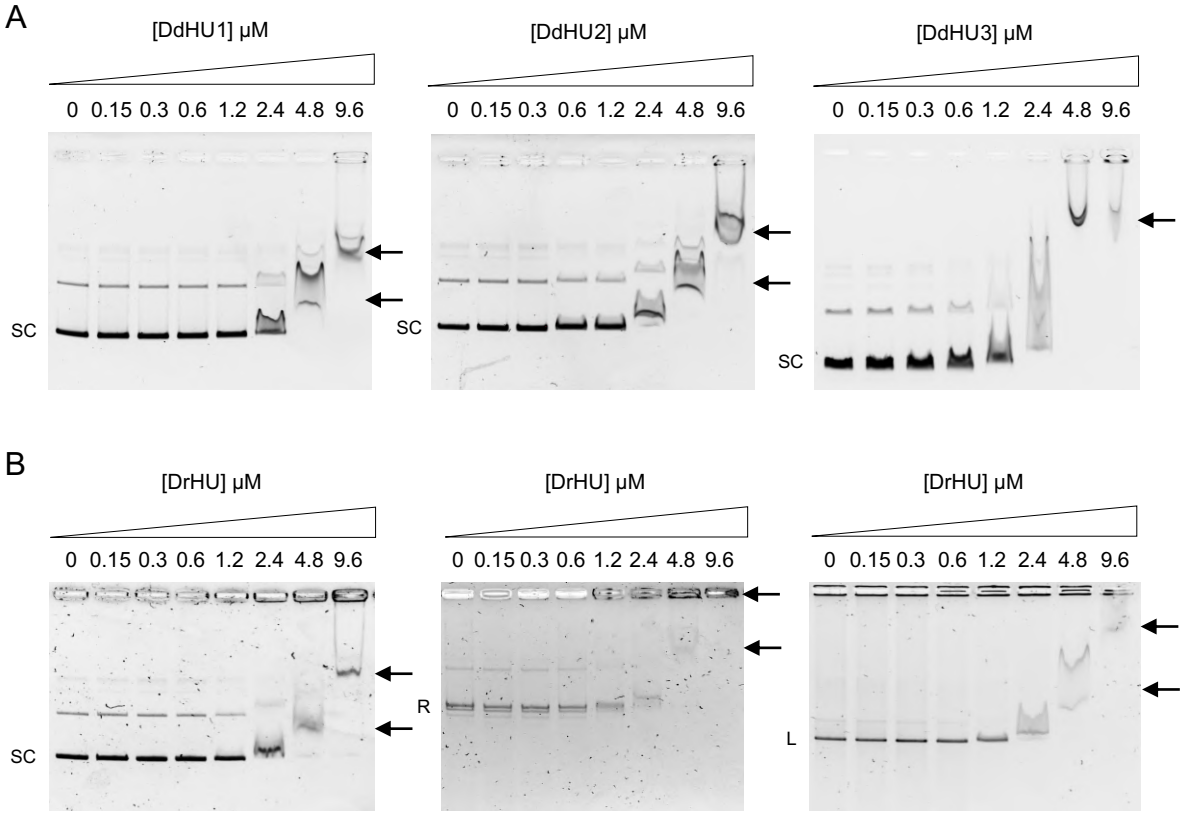

Figure 54. Binding of DrHU, DdHU1, DdHU2 and DdHU3 to plasmid DNA analysed by EMSA. A) 3 nM of supercoiled pUC19 (SC) was incubated with 0 to 9.6 µM of DdHU1, DdHU2 or DdHU3, after which the protein-DNA complexes were separated on 1% agarose gels. **B**) 3 nM of supercoiled (SC), relaxed (R) or linearized (L) pUC19 (from left to right) was incubated with 0 to 9.6 µM of of DrHU and their interaction was analysed by migration on 1% agarose gels. In panels A and B, arrows indicate the protein-DNA complexes.

II.4. The oligomeric state of DrHU, DdHU1 and DdHU3

While testing the DNA-binding ability of the four HU proteins with the 43mer dans oligonucleotides, we noticed the formation of two stable protein-DNA complexes. The first complex was observed in the presence of 0.5 to 2 µM of protein whereas the second complex appeared at higher concentrations of 2 to 5 µM depending on the protein. These results suggest that the deinococcal HU proteins might be able to form higher order oligomers or to polymerise in the presence of dsDNA, as it was shown for the HU protein of *E. coli* (Guo & Adhya, 2007; Hammel et al., 2016; Remesh et al., 2020). In order to evaluate the ability of DrHU, DdHU1 and DdHU3 to form oligomers in their apo- or DNA-bound states, we relied on crosslinking

assays with bis-sulfosuccinimidyl suberate (BS3), a bifunctional amine-to-amine crosslinking agent with a 11.4 Å spacer arm (Fig. 55).

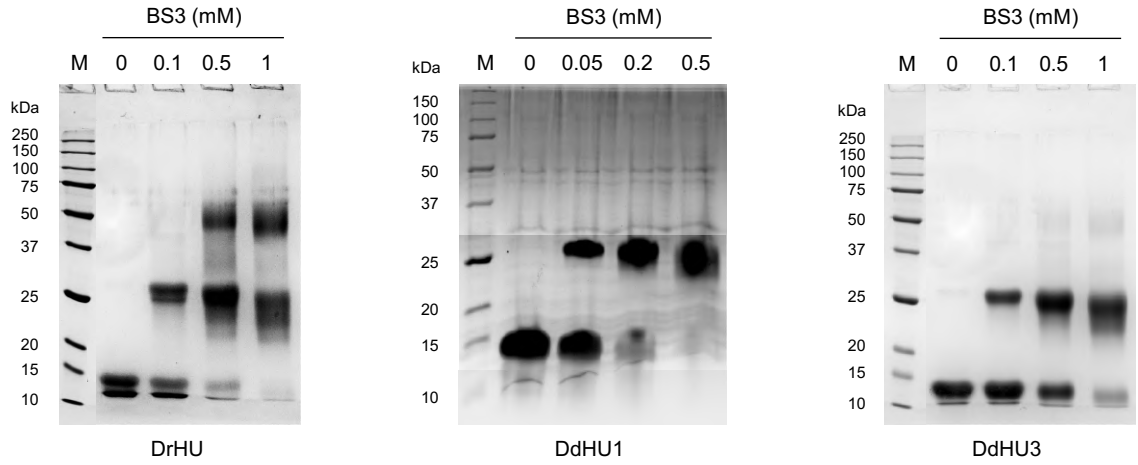

Figure 55. DrHU, DdHU1 and DdHU3 are mostly present as dimers in solution. 0.6 mg/ml of DrHU, DdHU1 or DdHU3 (left to right) was incubated with 0 to 1 mM (or 0 to 0.5 mM for DdHU1) of BS3 as a crosslinking agent. The reactions were incubated for 30 min at room temperature and stopped by addition of 1 M Tris pH 8. The oligomerisation profiles of the three HU proteins were analysed in denaturing conditions on 12% acrylamide SDS-PAGE gels stained with InstantBlue.

In the presence of 0.05 or 0.1 mM of BS3, the three HU proteins migrated as two bands: an intense band around 25 kDa (corresponding to an HU dimer) and another band around 12 kDa (corresponding to the monomer). Interestingly, the crosslinking assay of DrHU also revealed the presence of tetramers that migrated as a band around 50 kDa, observed at higher concentrations of BS3 from 0.5 to 1 mM (Fig. 55). In contrast, for the same concentrations of BS3, the crosslinking of DdHU1 did not reveal any tetramers and only a very small fraction of tetramers could be detected for DdHU3 (Fig. 55). These results thus confirm that DrHU, DdHU1 and DdHU3 are mainly present as dimers in solution, in agreement with well-conserved structures of HU proteins from other bacteria. But in addition, *D. radiodurans* HU is able to form tetramers in solution.

To assess the possible effect of DNA-binding on the oligomerization ability of DrHU and DdHU3, crosslinking assays were reproduced in the presence of either a 30 mer dsDNA oligonucleotide (dsU30) or a supercoiled plasmid DNA (pUC19-SC). To do so, 0.6 mg/ml of DrHU or DdHU3 was incubated with increasing concentrations of oligonucleotide or plasmid DNA. The crosslinking reaction was then performed as described previously with 1 mM of BS3 and analysed on 12% acrylamide or 8 to 15% acrylamide gradient SDS-PAGE gels, for the oligonucleotide and plasmid respectively (Fig. 56).

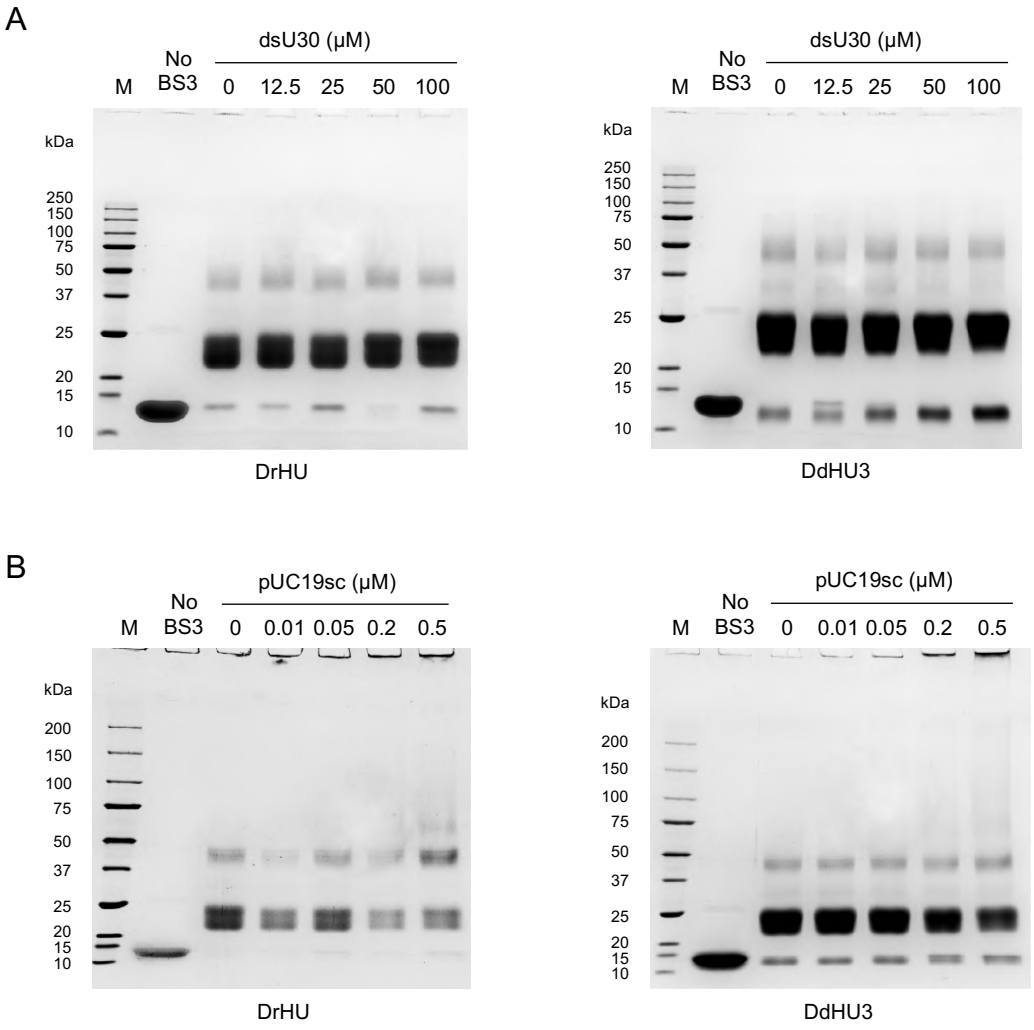

Figure 56. Oligomerisation profile of DrHU and DdHU3 in the presence of DNA. 0.6 mg/ml of DrHU or DdHU3 (left to right) was incubated with increasing concentrations of a 30mer dsDNA (**A**) or supercoiled plasmid DNA (**B**), in the presence of 1 mM of BS3 as a crosslinking agent. The reactions were incubated for 30 min at room temperature and stopped by addition of 1 M Tris pH 8. The oligomerisation profiles were analysed in denaturing conditions on 8% acrylamide (**A**) or 8 to 15% acrylamide gradient (**B**) SDS-PAGE gels stained with InstantBlue.

Binding to dsU30 seemed to have no visible effect on the oligomerisation profile of DrHU and DdHU3, as we observed a majority of dimers and a small fraction of tetramers and monomers regardless of the DNA concentration (Fig. 56A). In the presence of pUC19-SC, higher order oligomers were formed resulting in a smearing effect observed at plasmid DNA concentrations of 0.2 to 0.5 μM, with some oligomers too large to enter the gel (Fig. 56B). Thus, our crosslinking assays suggest that DrHU and DdHU3 may form larger oligomeric complexes with plasmid DNA that might be different from those formed with shorter DNA molecules such as 20mer or 43mer oligonucleotides.

II.5. Study of DNA conformation in the presence of HU proteins

II.5.1. Characterization of the complexes formed by binding of DrHU to plasmid DNA

II.5.1.1 Effect of DrHU on the topology of plasmid DNA analyzed by AFM

To better characterize the complexes formed by DrHU bound to plasmid DNA, we studied DrHU and the protein-DNA complexes formed by DrHU binding to plasmid DNA using atomic force microscopy (AFM), as it has already been applied to the study of DNA-binding of HU proteins from other bacteria such as *E. coli* or *Mycobacterium tuberculosis* (Datta et al., 2019; Japaridze et al., 2017; Kundukad et al., 2013; Maurer et al., 2009; van Noort et al., 2004). AFM is a three-dimensional imaging technique that allows the visualization of molecules down to a nanometer resolution by measurement of the height of a sample surface. This approach can also be used to gather quantitative values such as the volume or the height of individual molecules.

The following article, published in the journal Nanoscale, reports the results of our AFM study of DrHU alone or bound to relaxed or linearized pUC19 plasmid DNA. AFM images were treated by a Laplacian-weight filter developed by our collaborators that enhances the structural features of the imaged molecules while reducing the background noise (Chen et al., 2016). Processed images of DrHU revealed different orientations of the dimer deposited on the mica surface, with a size in good agreement with the structure of other HU proteins. Naked pUC19 displayed a smooth surface on which we could distinguish the super-helical turns of DNA. When DrHU was added, the Laplacian weight filter revealed the presence of distinct substructures on the DNA surface, that provided evidence for the presence of bound DrHU molecules. The binding of DrHU to DNA induced different conformational changes that depended on the protein concentration. At high concentration, DrHU multimerized along the DNA filament, forming a higher order structure that covered DNA. This specific architecture stiffened DNA filaments, and exerted a de-condensation effect on the plasmid. On the contrary, at low concentration, DrHU condensed DNA by stabilizing or increasing the compact conformation of pUC19. This dual property could allow DrHU to modulate the dynamics of the nucleoid *in vivo*, by condensing the genomic DNA of *D. radiodurans* during cell division and stiffening it to provide an easier access during gene expression.

For this work, I prepared the protein and DNA samples and deposited them on mica for AFM imaging. I also participated in the acquisition of AFM images together with J.-M. Teulon.

The processing of AFM images and their analysis with the Laplacian weight filter were done by J.-L. Pellequer and S. W. Chen.

Nanoscale

ROYAL SOCIETY OF CHEMISTRY

PAPER

View Article Online
View Journal | View Issue

Cite this: *Nanoscale*, 2020, **12**, 22628

Nanoscale surface structures of DNA bound to *Deinococcus radiodurans* HU unveiled by atomic force microscopy†

Shu-wen W. Chen,*‡[a,b] Anne-Sophie Banneville,‡[a] Jean-Marie Teulon,[a] Joanna Timmins *[a] and Jean-Luc Pellequer *[a]

The *Deinococcus radiodurans* protein HU (DrHU) was shown to be critical for nucleoid activities, yet its functional and structural properties remain largely unexplored. We have applied atomic force microscopy (AFM) imaging to study DrHU binding to pUC19-DNA *in vitro* and analyzed the topographic structures formed at the nanoscale. At the single-molecule level, AFM imaging allows visualization of super-helical turns on naked DNA surfaces and characterization of free DrHU molecules observed as homodimers. When enhancing the molecular surface structures of AFM images by the Laplacian weight filter, the distribution of bound DrHUs was visibly varied as a function of the DrHU/DNA molar ratio. At a low molar ratio, DrHU binding was found to reduce the volume of condensed DNA configuration by about 50%. We also show that DrHU is capable of bridging distinct DNA segments. Moreover, at a low molar ratio, the binding orientation of individual DrHU dimers could be perceived on partially "open" DNA configuration. At a high molar ratio, DrHU stiffened the DNA molecule and enlarged the spread of the open DNA configuration. Furthermore, a lattice-like pattern could be seen on the surface of DrHU–DNA complex, indicating that DrHU multimerization had occurred leading to the formation of a higher order architecture. Together, our results show that the functional plasticity of DrHU in mediating DNA organization is subject to both the conformational dynamics of DNA molecules and protein abundance.

Received 16th July 2020,
Accepted 28th October 2020

DOI: 10.1039/d0nr05320a

rsc.li/nanoscale

Introduction

A wide range of biophysical approaches can be used to probe the conformation of isolated DNA molecules and DNA–protein assemblies, including single-molecule techniques such as molecular tweezers,[1] electron microscopy (EM),[2] atomic force microscopy (AFM),[3] and ensemble measurements such as electrophoresis[4] or Förster resonance energy transfer (FRET) for example.[5]

AFM imaging has been widely applied to many DNA-based systems. It has successfully revealed configurations of free DNAs,[6,7] supercoiled plasmids,[8,9] and that of DNA–protein and DNA–polymer assemblies.[10–14] In particular, AFM has been successfully used to investigate the interactions of bacterial nucleoid-associated proteins (NAPs), the various roles of which have been reviewed elsewhere,[15] with DNA, an essential step for chromosome packaging in bacteria. AFM has supplied a direct visualization of NAPs binding to plasmid[16–21] and linearized DNAs,[22–25] as well as the formation of higher order structure gradually induced by NAPs from the protein-free state of DNA.[26]

Among bacterial species, NAPs from *E. coli* have been most extensively studied. Of the top five abundant nucleoproteins (Fis, HU, H-NS, IHF, and Dps) of *E. coli*, HU has the highest DNA-binding affinity,[27] despite its binding being apparently nonspecific to DNA sequence. Because of its high abundance and high affinity for DNA, HU was believed to be a major player in nucleoid organization and DNA stabilization.[28] HU proteins consist of about 90 residues with a high prevalence of basic amino acids.[29] The first three-dimensional (3D) structure determined for an HU protein is the one from *Bacillus stearothermophilus* (HUBst), which exists in dimeric form.[30] The dimeric form is now widely accepted as the biologically active unit for HU.[15] The common structural features of various HU dimers include two β-arms connected *via* several β-strands to a α-helical body formed of two tightly packed hydrophobic cores. The β-arms are quite flexible; their disorder has been illustrated by NMR-determined structural models.[31]

[a]*Univ. Grenoble Alpes, CEA, CNRS, Institut de Biologie Structurale (IBS), F-38000 Grenoble, France. E-mail: jean-luc.pellequer@ibs.fr, joanna.timmins@ibs.fr, cmft551@yahoo.com*
[b]*Rue Cyprien Jullin, Vinay, 38470, France*

†Electronic supplementary information (ESI) available. See DOI: 10.1039/d0nr05320a

‡Their contributions are equally significant to the work.

E. coli strains lacking HU are more sensitive to γ-irradiation and UV,[32,33] but broadly speaking, *E. coli* strains deficient in HU or expressing a mutant of HU exhibit only a subtle variation in cell phenotypes.[34,35] This suggests that *in vivo* either the individual contribution of HU is modest or its function can be fulfilled by another nucleoprotein.[36] In contrast, the depletion of HU from the radiation-resistant bacterium *Deinococcus radiodurans* (DrHU) was found to lead to fractionation of the nucleoid and the failure to obtain viable bacteria, indicating that *D. radiodurans* does not have a backup for its HU protein.[37] These findings demonstrate the essential role of DrHU in the cellular machinery of *D. radiodurans*.

Regarding HU–DNA binding mechanisms, 3D structures of DNA complexed with HU proteins from *Anabaena*[38] and *Staphylococcus aureus*[39] have revealed that the two β-arms of HU dimers insert into the minor grooves of an aberrant DNA site, where the nucleotide bases are mismatched, to form a specific H-bonding pattern. With a regular base pairing in the binding site of DNA, the crystal structure of *Borrelia burgdorferi* HU–DNA complex revealed a DNA conformation which was largely bent by almost 180°, leading to a partial opening of the two DNA strands.[40] In another X-ray diffraction study, the *E. coli* HU dimer does not bind DNA in the same mode as described above, but through electrostatic interactions between DNA phosphate moieties and HU peptide amides.[41] In this study, the β-arms of HU were shown to be involved in forming an interaction network in the HU–DNA assembly, which promotes protein multimerization and multiple DNA alignments.

From a structural point of view, very little is known regarding the DNA-binding properties of DrHU. Compared to *E. coli*, one major difference is that DrHU possesses a ~30 amino acid lysine-rich extension appended to its N-terminus.[42] This long N-terminal tail is a unique feature of HU proteins from *Deinococcus* bacteria, and has been shown to significantly modulate DNA binding.[43] Besides, the primary sequence of DrHU reveals that it possesses a high proportion of Ala residues up to 18%, while lacking aromatic Trp and Tyr amino acids.

In the above crystallographic studies of HU–DNA binding, the DNA molecules used were limited to short DNAs (≤35 base pairs). In order to investigate HU binding effects on DNA molecules of longer length (>1000 bps), the use of an imaging strategy is a suitable alternative which provides a means to visualize a wide scope of DNA–protein assemblies and organizations. EM was used in earlier studies to visualize the configurations adopted by DNAs upon HU binding.[44] In one EM study of *E. coli* HU–DNA binding, a beaded form was observed that was reminiscent of nucleosome-like structures, leading to a corollary that DNA coils around HU.[44] However, the natural supercoiling of naked DNAs has been shown to be able to closely mimic the condensing behavior of DNA complexed with histones *in vivo*.[45] Parallel to EM, AFM imaging technique has shown that *E. coli* HU protein plays a dual architectural role on fragmented DNAs as both a flexible hinge and a stiffener of DNA filaments.[46] Moreover, AFM also allowed identification of two fibered forms with diameters of 40 and 80 nm from nucleoid materials extracted from *E. coli* cells.[47]

In many studies of ligand–receptor interactions using AFM imaging, a comparative strategy is commonly adopted to verify the presence of bound ligands by an increased height, width or size of the receptor. This analysis approach can be exemplified by one study of HU–DNA binding,[46] in which the thickening of DNA filaments was used as an indicator of HU proteins bound to DNA. In the AFM imaging experiments described below, we have studied the influence of DrHU concentration on the configuration of double-stranded DNA. In addition to classical geometric measures, we have analyzed the topographic structures of free DrHU proteins, naked DNA molecules and their complexed forms. We have applied our previously developed processing tool, the Laplacian weight filter, to enhance the surface features of these imaged molecules.[48] The enhancement of AFM images has allowed us to observe arrangements of bound DrHUs on the DNA at a molecular level. For the first time, the full-length DrHU protein is imaged at the single-molecule level, different oriented surfaces of free DrHUs can be seen, and variations in distributions of bound DrHUs at different protein concentrations can be detected by visual inspection. The present research provides a structural basis for deciphering the binding effects of DrHU, a long N-terminal tailed HU protein, on the configuration of circular and linear DNA.

Experimental

DrHU production

The *hu* (DR_A0065) gene from *D. radiodurans* was cloned and expressed in BL21 (DE3) cells grown in LB supplemented with 100 μg mL^{-1} ampicillin. Expression was induced with 1 mM IPTG at 20 °C for 16 hours. Cells were pelleted by centrifugation and resuspended in 40 mL lysis buffer [50 mM Tris-HCl, pH 8.0, 500 mM NaCl, 2 mM $MgCl_2$, 1 μg mL^{-1} DNaseI, 1 μg mL^{-1} lysozyme, and a tablet of complete EDTA-free Protease Inhibitor Cocktail]. Resuspended cells were lysed by sonication on ice for 3 min. The cleared supernatant was loaded on a 5 mL HisTrap FF nickel affinity column (GE Healthcare), pre-equilibrated with buffer A [50 mM Tris-HCl, pH 8.0, 250 mM NaCl]. After the column was thoroughly washed, the recombinant His-DrHU was eluted with a linear gradient of imidazole (75–500 mM) in Buffer A. The purified His-tagged protein eluted at ~250 mM imidazole. The fractions were pooled and diluted with a buffer B [50 mM Tris-HCl, pH 8.0, 50 mM NaCl] to lower the NaCl concentration to 100 mM.

To further purify His-DrHU, the protein was loaded on a 5 mL heparin HiTrap HP column (GE Healthcare), pre-equilibrated with buffer C [50 mM Tris-HCl, pH 8.0, 100 mM NaCl]. After washing with buffer B, the elution was carried out by a gradient from 0.1 to 2 M NaCl in buffer B. The eluate at ~1 M NaCl was collected. In the absence of aromatic residues, the concentration of His-DrHU was determined by measuring the absorbance at 205 nm and with the help of the online algor-

ithm (http://spin.niddk.nih.gov/clore)[49] allowing to compute the sequence-specific molar extinction coefficient at 205 nm. The His-tag was removed by TEV digestion (1 : 20 ratio) at 4 °C overnight; its full removal was assessed by electrophoresis on 15% denaturing polyacrylamide gel. The His-tag itself and traces of uncleaved protein were subsequently removed by Ni-affinity chromatography on a 1 mL Ni-Sepharose 6 FF resin (GE Healthcare) pre-equilibrated in buffer A. The cleaved DrHU was recovered from the flow-through and washes of the Ni-Sepharose column, pooled and concentrated prior to size exclusion chromatography on an ENrich SEC 650 column (Biorad) pre-equilibrated with buffer D [20 mM Tris-HCl, pH 8.0, 100 mM NaCl]. Finally, DrHU was concentrated to a final monomeric concentration of 2.36 mM and stored at −80 °C.

Preparation of circular and linearized DNAs

In this study, circular DNA denotes uncleaved natively supercoiled pUC19 plasmid DNA (2686 bp), where "circular" is termed as opposed to "linearized" DNA to be described later. Plasmid pUC19 DNA was amplified in DH5α *E. coli* cells grown in LB with 100 μg mL^{-1} ampicillin. The plasmid DNA was extracted from 100 mL overnight cultures using the NucleoBond Xtra Midi kit (Macherey-Nagel) following manufacturer's instructions. The final DNA resuspension was performed in 50 μL of Milli-Q water, yielding a concentration of 3.5 μg μL^{-1} (equivalent to 2 μM) of pUC19. The stock solution of circular DNA was aliquoted and stored at −20 °C.

Linearized DNA, here, refers to the products obtained after linearization of natively supercoiled plasmid pUC19. For this, *E. coli* pUC19 was digested with HindIII-HF (New England Biolabs) for 1 hour at 37 °C, and subsequently purified using the Gel and PCR Clean Up kit (Macherey-Nagel) following manufacturer's instructions. The conformation and purity of the linearized DNA were assessed by electrophoresis on a 1% agarose gel followed by staining with Gel Red (Interchim) and visualization using a ChemiDoc MP imager (BioRad).

AFM protein samples were prepared by diluting the stock solution of DrHU in Milli-Q water to a desired concentration prior to imaging experiments. The molar ratio of a sample solution was represented by the concentration of DrHU monomer relative to that of the DNA. Unless otherwise noted, the final concentration of DNA was set to 0.8 nM and the concentration of DrHU was consistently adapted to reach the target DrHU/DNA ratio.

AFM instrumental setup

Topographic data were acquired by a multimode 8 microscope equipped with a Nanoscope V controller (Bruker, Santa Barbara, USA). Before use, a freshly cleaved V-1 grade muscovite mica (Nanoandmore, Wetzlar, Germany) sheet was pretreated with 10 μL of $NiCl_2$ (2–10 mM) and dried under the nitrogen gas. A 2 μL aliquot of a sample solution was deposited on the mica, after which the mica was incubated for 3 min, then dried under a gentle stream of nitrogen gas.

All imaging was conducted with the PeakForce Tapping mode and ScanAsyst mode at a rate of ~1.0 Hz; the resolution was set to either 512 or 1024 pixels per scan line. The SCANASYST-AIR-HR cantilever was employed with nominal values of k = 0.4 N m^{-1}, F_q = 130 kHz and tip radius = 2 nm (Bruker probes, Camarillo, CA, USA). Whenever the ScanAsyst mode was applied, a semi-manual control was on during the imaging procedure to manually adjust the set point and gain in order to reduce the tip–sample interactions to the minimum. The ramp size was kept constant at 150 nm.

Pre-treatment, post-processing and analysis of topographic data

Pre-treatments of raw AFM images were systematically performed using the Gwyddion software.[50] First, raw AFM images were flattened using a plan fit to the first order. Flattening effect was further enhanced by applying the "line flattening" tool of Gwyddion with a polynomial of order 3, after excluding all the imaged objects whose height value exceeds the given threshold (usually 0.1–0.5 nm). When necessary, stripe noises were reduced using the Destripe program.[51] The minimal intensity was set to zero for all AFM images.

In order to better observe imaged molecules, one may magnify the image by either theoretical computations or AFM magnification. AFM magnified image was specified for an image which was acquired by scanning a smaller region of its parent image at the same scan rate. Different from AFM magnified image, numerically magnified image is made of intensities calculated with the B-spline interpolation of the Gwyddion software. To enhance AFM molecular topography, the Laplacian weight (L-weight) filter, which was first introduced for revealing detailed surface structures of protein assemblies,[48] was routinely applied. Basically, this filter computes the Laplacian function value as a weighting factor for the intensity values of the pixels in the image. For validation, we compared the size of single DrHU particles in the AFM image with that derived from the 3D structural information; therefore, it required the construction of an *in silico* image based on known 3D molecular structures.[52] We used the Adepth program to generate molecular surfaces of the 3D structure,[53] and then projected the molecular surfaces onto the image plane. The entire protocol of our own-made software is designated as "3D to 2D". It should be noted that a z-scale color bar, in the unit of nanometer, is shown beside each AFM image with a color gradient to indicate the height distribution of the image. Because the intensity values of processed images using the L-weight filter do not represent height values there is no scale bar present on these filtered images.

In the geometric analysis of image objects, the variables: height, size and volume were estimated using the "grain" option of Gwyddion. First of all, we visually marked the foreground pixels (the objects of interest) with an intensity threshold such that the background pixels could be separately treated. The height of a marked pixel was measured as the intensity of the pixel subtracting the average intensity of background pixels. The size of an object (called a grain in Gwyddion) was estimated using the moment fitting function in the "measure individual grain" tool. The fitting result was

View Article Online
Nanoscale Paper

represented by ($a \times b$), where "a" and "b" are the lengths of the object corresponding to the doubled size of the major and minor radii determined. The volume of an object is represented by the value of "Laplacian background basis volume", in which the object base was determined by the intensity values of its neighboring background pixels.

Results

AFM imaging of free DrHU

AFM imaging was first performed on isolated DrHU molecules. Throughout our figures, a scale bar (z-scale) is always associated with AFM topographic images but not with the L-weight filter processed ones whose height values have been modified and become physically irrelevant. Fig. 1A displays the full-sized image from which four sub-images containing isolated protein particles were cropped and numerically magnified. The resulting images are presented in Fig. 1B on the left and their respective processed images by the L-weight filter on the right. In effect, the L-weight filter enhances the structural characteristics of molecular topography while making the structureless part fade away. From Fig. 1A, 13 particles could be selected using a threshold greater than 2 nm in height (and an area greater than 41 px) for which the average size is 8.5 ± 1.5 × 5.6 ± 0.8 nm^2. For the four selected particles processed with the L-weight filter and shown in Fig. 1B, the size of DrHU particles were measured as 8.2 × 5.0, 8.0 × 5.2, 7.6 × 5.0 and 7.8 × 6.0 nm^2 for the molecules labelled 1 to 4, respectively. Thus, the mean size of free DrHU post-L-weight filter is 7.9 ± 0.3 × 5.3 ± 0.5 nm^2.

Since dimeric HU is widely accepted as the biologically functional unit, its size is of great concern for image analysis. To validate the size of an HU dimer in our AFM images, we superimposed multiple crystal structures of dimeric HU orthologs with the sup3d program.[54] The atomic coordinates of the reference structure for superposition were taken from PDB code 5EKA, corresponding to the HU protein from *Thermus thermophilus*,[55] the closest ortholog of DrHU. With more than 80% of the backbone atoms (N, CA, C) of the protein structures used in the superposition, the root mean square deviations (RMSDs) of each superimposed crystal structure were below 1 Å from the reference (Fig. 2A). We used the set of superimposed structures as a composite structure to construct an *in silico* image of an HU dimer (Fig. 2B); the size of this HU dimer was measured as 6.7 × 5.0 nm^2 in good agreement with our AFM-measured particles.

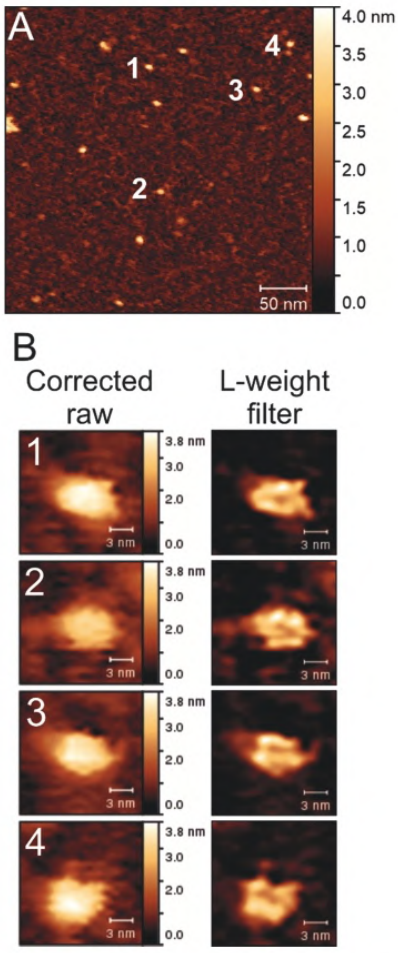

Fig. 1 AFM images of isolated single DrHU molecules. (A) Full-sized AFM image of single free DrHU molecules at a protein concentration of 8 nM. The size of the image is of 330 × 330 nm^2 with 512 × 512 pixels. (B) On the left, numerical magnification (×4) of cropped sub-images from (A). All sub-images contain 25 × 25 pixels; each presented image is therefore composed of 100 × 100 pixels with a physical size of 16.11 × 16.11 nm^2. The number in the top-left corner of each image addresses the location of the cropped object in (A). On the right, the corresponding processed images by the L-weight filter.

AFM imaging of circular DNA

Fig. 3 shows AFM topographies of circular natively supercoiled DNA at different DrHU concentrations, where the left column displays the topographic data, and the right presents the corresponding images processed with the L-weight filter. Fig. 3A and B show the conformations and structural features observed for naked circular DNAs (among a total of six independent images). The two images were cropped respectively from ESI Fig. S1A and S1B.†

In the full-sized images, we observed that most DNAs are highly compact, while some are partially open consistent with the presence of a small fraction of open circular form of the plasmid extracted from *E. coli*. Despite the variation in DNA topology, the average volume of single circular DNA molecules (N = 36) is 4045 ± 849 nm^3. The high similarity in structural feature between the AFM topography (Fig. 3A) and the processed image (Fig. 3B) indicates that the L-weight filter hardly

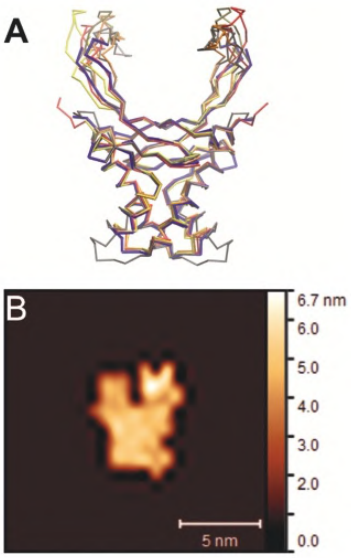

Fig. 2 Superposition of the Cα traces of five crystal structures of HU proteins from various species. (A) The reference structure used for superposition is PDB code 5EKA (in blue), corresponding to *Thermus thermophilus* HU. The other superimposed structures are colored in red for *Anabaena* (1P71), gray for *Borrelia burgdorferi* (2NP2), orange for *Staphylococcus aureus* (4QJU), and yellow for *Escherichia coli* (4YF0). (B) *In silico* image of HU dimer. The 3D structure used to make the image contains the five HU crystal structures described in (A). The image was constructed at the same pixel resolution as that of the AFM image shown in Fig. 1A and subsequently magnified the same way as those in Fig. 1B with most spread projection of molecular surfaces of the composite structure. The y axis of the image plane can be used to indicate the protein-body axis of HU dimer. The *z*-scale bar, in the unit of nanometer, is shown beside with a color gradient to indicate the height distribution of the image.

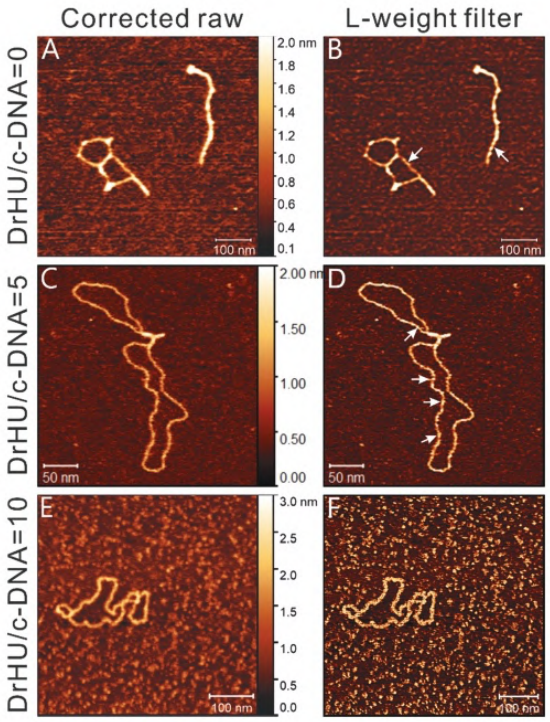

Fig. 3 Visualization of circular DNA (c-DNA) configurations in the absence and presence of DrHUs at a DNA concentration of 0.8 nM. The left column presents the AFM images of the molecular system while the corresponding processed images are shown on the right. (A and B) Circular DNA in the absence of DrHUs. Images (A) and (B) were obtained by numerically magnifying (×4) the cropped sub-images indicated by a white box in Fig. S1A and S1B,† respectively. Both images contain 640 × 640 pixels with a physical size of 625 × 625 nm^2. White arrows in image (B) indicate super-helical turns of naked circular DNAs. (C) Circular DNA in the presence of DrHUs at a DrHU/DNA molar ratio of 5. The AFM image consists of 512 × 512 pixels with a physical size of 325 × 325 nm^2 cropped from Fig. S2A† with magnification (×2). (D) The image was acquired by processing image (C) with the L-weight filter, the resulting image consists of 512 × 512 pixels with a physical size of 325 × 325 nm^2. White arrows indicate DrHU molecules in various shapes along the DNA filament. (E and F) Circular DNA in the presence of DrHUs at DrHU/DNA molar ratio of 10. The AFM image (E) is composed of 512 × 512 pixels with a physical size of 281 × 281 nm^2 cropped from Fig. S2B† with magnification (×2); (F) is the processed image of (E) by the L-weight filter.

manifests any other structural feature than the super-helical turns on the surfaces of naked circular DNAs (arrows in Fig. 3B).

The AFM images of circular DNA in the presence of DrHUs are presented in Fig. 3C–F. The middle and bottom rows illustrate the circular DNAs at DrHU/DNA molar ratio of 5 and 10, respectively. Fig. 3C and E present AFM magnified images corresponding to the white-lined sub-images of Fig. S2A and B.† Fig. S2A† displays two kinds of DrHU–DNA complexes of contrasting compactness; one is condensed (on the left) while the other is quite loose. The average volume of the condensed configurations is about 2071 ± 1028 nm^3 (N = 29), much smaller than that of a naked circular DNA described previously.

Since a high level of compactness of the DNA hinders the visualization of DrHU distribution on the DNA, we found it to be more instructive to observe DNA molecules displaying an open configuration rather than a condensed one. Thus, we focused our image processing on relatively open structures like the one present in Fig. 3C. However, it should be noted that such a structure is not very common, despite the presence of a second partially open molecule at the top of Fig. S2A.† After applying the L-weight filter and numerical magnification to Fig. 3C, the sub-image containing the open complex is shown in Fig. 3D, while that of a condensed one is presented in Fig. 5C. The processed image in Fig. 3D reveals some substructures rather different from the simple super-helical turns observed on naked DNA (Fig. 3B). These new substructures protrude out of the DNA filament, and provide evidence for the presence of bound DrHU molecules. We found that these

bound DrHUs are scattered along the DNA double helix and their shapes differ (white arrows in Fig. 3D). When doubling the concentration of DrHU, the DNA filament becomes uniformly thicker and wider. In Fig. 3E, the average width of the DNA filament is ~13 nm *versus* ~6 nm for the open complex in Fig. 3C. The processed image in Fig. 3F shows a lattice-like pattern on the surface of the DrHU–DNA complex, indicating a more ordered structure formed by the bound DrHUs on the DNA.

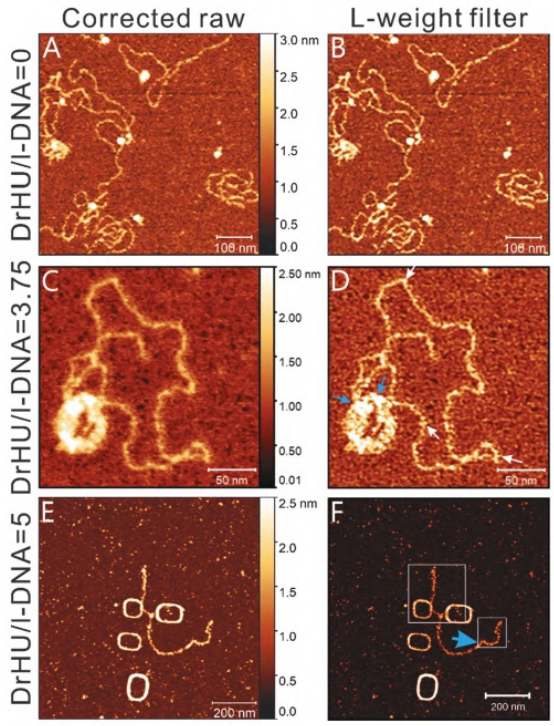

Fig. 4 Visualization of linearized DNA (l-DNA) configurations in the absence and presence of DrHU proteins. The left column presents AFM images of probed molecules while the corresponding processed images are shown on the right. (A and B) Naked linearized DNA at 8.0 nM. The images were obtained by numerical magnification (×4) with respect to the white-lined sub-images of Fig. S1C and D,† containing 640 × 640 pixels with a physical size of 625 × 625 nm^2. (C) Linearized DNA in the presence of DrHUs at a DrHU/DNA molar ratio of 3.75, where the concentration is 7.5 nM for DrHU and 2 nM for DNA cropped from Fig. S2C† with magnification (×2). The AFM image (C) contains 512 × 512 pixels with a physical size of 332 × 332 nm^2. (D) Processed image of (C) using the L-weight filter. White arrows indicate isolated DrHU dimers, whereas blue arrows specify the regions of higher DrHU abundance. (E and F) AFM and processed images of linearized DNA in presence of DrHU at a DrHU/DNA molar ratio of 5, where the concentrations of DrHU and DNA are 4.0 nM and 0.8 nM, respectively. Images (E and F) are composed of 1024 × 1024 pixels with a physical size of 1 × 1 μm^2. In image (F), a small and a large white box indicate the position of the sub-images presented in Fig. 5A and B, respectively; the former consists of 128 × 128 pixels while the latter of 256 × 256 pixels. The thick blue arrow labels the DrHU packing resembling a piece of ribbon.

AFM imaging of linearized DNA

To investigate the effects of DrHU binding to DNA released from topological constraints, we performed AFM imaging on linearized pUC19 plasmid DNA (Fig. 4A and B). The images in Fig. 4A and B correspond to the sub-images in Fig. S1C and S1D.† In Fig. S1C,† naked linearized DNAs adopt various conformations such as random coils, folded structures and aggregates of compact and extended DNA filaments. The size of isolated extended DNA filaments was estimated as the average height of open DNA filaments in the image, a value of 0.74 ± 0.14 nm, a typical size of duplex DNA obtained by AFM imaging in air on a bare mica. In the processed image of Fig. 4B, no particular protruding substructures were found on the DNA surfaces. The only structural feature observed is the super-helical turns, similar to that seen on naked circular DNAs (Fig. 3B).

Fig. 4C and D present the AFM and processed images of linearized DNA in the presence of DrHUs at a DrHU/DNA molar ratio of 3.75. The image of Fig. 4C is an AFM magnified image of the white-lined sub-image in Fig. S2C;† it contains a DrHU–DNA complex of both condensed and open structures. The condensed structure presents a toroidal shape. After post-processing of the image presented in Fig. 4C, the complex of mixed toroidal and open DNA configurations is shown in Fig. 4D. The L-weight filter processing of a single toroidal shape of condensed DNA, as observed in the second white square of Fig. S2C† is shown in Fig. 5D. Substructures with prominently protruding shapes can be seen in both toroid structures. The protruding substructures are, as mentioned earlier, indicative of bound DrHUs in the complex. In both figures, some individual DrHU molecules indicated by white arrows are distinguishable, while others are clustered (blue arrows). Along the open DNA filaments of the complex in Fig. 4D, the bound DrHUs exhibit a variety of molecular shapes (exemplified by white arrows in the image). The shape of a bound DrHU dimer most likely reflects the binding orientation of the protein relative to the DNA filament.

Fig. 4E–F show the AFM and processed images for four complexes of linearized DNA and DrHU at a DrHU/DNA molar ratio of 5. Three of them adopt an intriguing large oblong configuration, with a much larger central hole than the two encountered in Fig. 4C and 5D. The fourth complex is composed of an oblong structure from which two open filaments extend in opposite direction. The apparent widths of the open filaments are varied with the local abundance of bound DrHUs. With high levels of bound DrHU, the DNA segment (around the smaller white square in Fig. 4F) has a width ranging from ~10 to 14 nm, while that measured for stacked filaments of oblong structures is ~10 nm. Fig. 5A and B present magnification results of two sub-images of Fig. 4F. From the structural details revealed in Fig. 5A, the two open filaments seem to twine with the oblong body, suggesting a shared folding mechanism and the presence of multiple turns of DNA filaments within the oblong body. Height measurements of these oblong structures indicate that the estimated

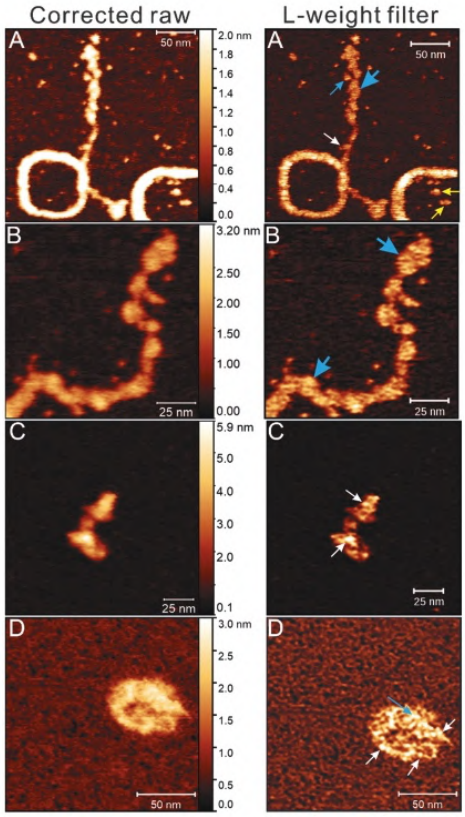

Fig. 5 Close-up views of structural details of DrHU–DNA complexes with raw processed and L-weight filter images shown on the left and right, respectively. (A) Intertwined connection between stacked oblong shapes and linear filaments. The image consists of 512 × 512 pixels with a physical size of 250 × 250 nm^2, a sub-image from the large white box in Fig. 4E and F by numerical magnification (×2). Yellow arrows indicate free DrHU dimers with likely β-arms like a fish tail, while the white arrow points to a bound DrHU dimer also with putative β-arms. The thin blue arrow points at a single dimer with β-arms hidden by certain protein orientation, while the other two blue arrows indicate paired DrHU dimers. (B) DrHU multimerization on linear filaments of linearized DNA complex. The image consists of 512 × 512 pixels with a physical size of 125 × 125 nm^2, and was processed by the following procedures: sub-image cropped from the small white box in Fig. 4F, with numerical magnification (×4). The thick blue arrows illustrate bound DrHU dimers in a paired form. (C) Condensed configuration of circular DNA upon DrHU binding. The image contains 512 × 512 pixels and a physical size of 162.5 × 162.5 nm^2, obtained by performing the L-weight filter on image Fig. S2A,† cropping the target object in the processed image with an application of numerical magnification (×4). The white arrows indicate the presence of bound DrHUs on the supercoiled DNA. (D) Condensed configuration of linearized DNA upon DrHU binding. Image (D) was acquired as follows: processing image Fig. S2C† by the L-weight filter and performing numerical magnification (×4) on the cropped sub-image. The image consists of 512 × 512 pixels and a physical size of 166 × 166 nm^2. The white arrows point out the presence of bound DrHUs, while the blue arrow highlights the higher abundance of DrHU in the region of crossed DNA filaments.

number of bound DrHU molecules was lower in the oblong structure than in the thickened segment of the open DNA filament. It is important to point out that these intriguing oblong structures were not frequently observed (only in three AFM images out of a total of 16 images). Among the three images, one was obtained on a naked linearized DNA which indicates that they are likely composed largely of stacked DNA filaments (Fig. S3†). However, condensed and toroid shapes (as in Fig. 5D) are more commonly found as displayed in Fig. S2C.†

In Fig. 4F, bound DrHUs appear to distribute over the open filaments unevenly, speaking in terms of abundance and spatial arrangement. According to size measurements, we found that several DrHU dimers are clustered on the DNA segment of higher DrHU abundance. Some DrHUs, in the form of one or two dimer-dimer pairs, are packed in the direction transverse to the DNA axis (thick blue arrows in Fig. 4F and 5A, B), while a single-dimer binding can be found in the area of low DrHU abundance (the white arrow in Fig. 5A). Moreover, DrHUs were found in Fig. 5A to bind to the DNA filament obliquely with different tilt angles, as indicated by the thin blue arrow, a DrHU dimer, and the thick blue arrow, paired DrHU dimers.

Discussion

Size and shape of free DrHU

Despite some variations in protein sequences of HU proteins from different organisms, their 3D structures are well conserved,[56] as evidenced by the excellent structural superposition (Fig. 2A). This implies that any HU crystal structure is eligible to be used as a structure template,[54] or to construct the *in silico* image as a reference for comparison. The dimensions of free DrHU were estimated to be on average ~7.9 × 5.3 nm^2 by AFM using the L-weight filter, while that of the HU composite structure are 6.7 × 5.0 nm^2. Thus, the AFM imaging result is in good agreement with that derived from X-ray crystallography with a discrepancy of only about 1 nm, confirming that the isolated DrHU particles imaged are protein dimers. The slightly longer length of DrHU dimers could be attributed to their extended N-terminal tails, which are absent in the crystal structures used to prepare the *in silico* model (Fig. 2B). The successful determination of the oligomeric state of isolated DrHU particles validates AFM imaging as a technique to adequately derive the quaternary structure of a protein molecule.

In addition to size measurements of DrHU, AFM imaging also allows the visualization of various shapes of isolated DrHU dimers. One should be aware that in solution the protein conformation is largely susceptible to thermal motion and distortion[57] which affect the shape of the protein, and accordingly its size displayed in the image. In Fig. 1B, three out of the four DrHU dimers most likely align their protein-body axis on the mica surface, while the last one (object 4) orients its protein-body axis in an oblique direction relative to the mica surface. Each shape with different structural details represents a different conformation or orientation of DrHU

dimers, where the surface features reflect the arrangement of secondary structure elements of the protein.

One can find different shapes of DrHU dimers in Fig. 5A, where two isolated DrHU dimers (indicated by yellow arrows) adopt a fish-like shape, in which the tail most likely corresponds to the β-arms of the DrHU dimer. According to the superimposed structures, the length of the β-arms extending out of the helical body is slightly greater than 3 nm.

Shape and orientation of bound DrHU

At low DrHU concentrations, it is challenging to detect the presence of bound DrHUs based on the thickness or width measurement of DNA filaments (Fig. 3C and 4C). Nevertheless, this limitation can be waived by examining the topographic substructures of protein–DNA assemblies enhanced by the L-weight filter. Provided with the known structure of HU dimers, it becomes possible to deduce the binding orientation of a DrHU dimer from AFM images. In the processed images of Fig. 3D and 4D, the bound DrHUs appear in different shapes along the open DNA filament, highlighting individual arrangements of bound DrHU dimers. That makes each DrHU molecule discernible and its shape apprehensible (see white arrows in Fig. 3D and 4D). In particular, the binding orientations of some DrHU dimers can be determined by the positioning of their β-arms, which are deduced from the elongated conformation of DrHU (Fig. 2). Moreover, we were able to distinguish some regions in the complex (blue arrows in Fig. 4D) from others by their denser binding of DrHU. Our images suggest a structural preference of DrHU for binding on stacked DNA filaments. This propensity is consistent with a previous finding that the full-length DrHU has a higher affinity for the arms of four-way DNA junctions than for a simple DNA duplex.[58] Besides, our AFM images reveal that DrHU possesses the bridging ability to tether distinct DNA filaments or promote long-ranged DNA contacts.

On the open DNA filaments shown in Fig. 4F and 5A, B, a couple of paired DrHU dimers is observed to bind alternately on one side and the other of the DNA duplex, which could be attributed to the helical distribution of DNA binding sites. As observed in Fig. 5A, the two extended DNA filaments may gradually integrate into the more condensed oblong component. The DNA segments close to the merging region exhibit a low DrHU binding density, even down to a single protein dimer (the white arrow in Fig. 5A). This configuration implies that an exclusion of some DrHU molecules is likely required to integrate DNA filaments into the condensed DNA of the oblong body. This image thus suggests that reorganization of DNA configuration is probably accompanied by a change in the distribution of bound DrHUs. The dynamic nature of DrHU binding to DNA may result from the relatively low affinity of HU binding to double-stranded DNA in general[58–60] including a weak-strength characteristic of electrostatic interactions[41,61] between the protein and DNA.

Multimerization of DrHU

As the concentration of DrHU was increased to a DrHU/DNA molar ratio of 10, we observed a global thickening of the DNA filament (Fig. 3E). Similar thickening of DNA filaments by a large amount of bound *E. coli* HU heterodimers has also been reported.[46] From the processed image in Fig. 3F, we found that many indiscernible copies of DrHU protein cover the DNA filament. Beyond the thickening effect, the high-density binding of DrHU yields a lattice-like pattern on the molecular surface of the DrHU–DNA complex. This pattern reflects the formation of a structured interaction network that governs multimerization of DrHU over the DNA surface, thus resulting in a higher order architecture. This hallmark feature can be used to distinguish DNA surfaces bound by a very high density of DrHUs, that form ordered structures on the DNA. The formation of higher order architectures has been proposed to be a prerequisite for a cooperative behavior of HU binding to DNA.[62–64] Our results show structural evidence of cooperativity for DrHU–DNA binding. On the contrary, DrHU binding to 50- and 89-mer DNA duplexes did not exhibit such cooperativity.[43] The difference may come from the different lengths and topology of the DNA molecules used in the two studies, 50–89 *vs.* 2686 bps. In our case, the long DNA provides a structured template for building up an effective higher order structure for DrHUs.

As shown in Fig. 4E and F, the thickening of DNA filaments was also observed in DrHU linearized–DNA complexes. The shape of the DNA segment thickened by bound DrHUs resembles a piece of ribbon. A similar structural pattern has been revealed by EM imaging of DNA fragments bound to *Bacillus* SASP protein.[65] The ribbon-shaped DNA segment results from a tight arrangement of bound DrHUs along the DNA filament thereby facilitating protein multimerization. By examining the substructures revealed in Fig. 4F and 5A, B, we found that DrHU multimerization occurred preferentially on relatively straight DNA segments. DrHU dimers align themselves in the transverse direction of the DNA filament leading to an increase in the width of the DNA filament, and in the direction of the DNA main axis. In the latter case, DrHU multimerization continues to grow along the DNA filament. The protein multimerization of *E. coli* HU has been proposed to promote straightening but not bending of the DNA axis.[41] In DrHU–DNA complexes, the DNA molecule, however, is not totally straightened out to the end, instead it tends to integrate within the condensed DNA structure. Nevertheless, local DrHU multimerization makes finite pseudo-straight DNA segments straightened or stiffened temporarily. Taken together, the formation of an effective higher order structure, which promotes cooperative binding of DrHU, requires a long enough DNA and sufficient amount of DrHUs.

Condensation and de-condensation effects of DrHU

A caveat of imaging single molecules is the lack of repeatability of their individual shapes. Beyond the problem known as "operational aspects", fully described for AFM imaging of nanoparticles,[66] a critical step is the adsorption of sample molecules onto a flat and globally charged mica substrate. All the data of this work has been obtained from four independent experiments. The more than one hundred AFM images collected over this period did not display twice the same con-

figuration of DNA or DrHU–DNA complexes. A good example of this is provided by our AFM images of natively supercoiled pUC19, which in most cases adopts a compact configuration, but is occasionally seen in a partially open configuration. Under different AFM imaging conditions such as in liquid and/or using a chemical modification of the mica surface, pUC19 supercoiled plasmids have been observed to adopt different configurations,[67] although compact configurations were also observed when imaging pUC19 in air.[68] In this work, special attention has been given to particular configurations of DNA and DrHU–DNA complexes with two objectives: describe the condensation of DNA upon DrHU binding and select the configurations for which image processing will most efficiently decipher the conformation of bound molecules.

For circular supercoiled DNAs in the presence of a low concentration of DrHU (DrHU/DNA ≤5), the measured volumes of condensed DNA complexes are about half of that for naked circular supercoiled DNAs (2071 ± 1028 nm^3 *vs.* 4045 ± 849). The volume reduction indicates that DrHU binding leads to increased DNA compactness. This provides a possibility for resolving a previous puzzle in the analysis of gel retardation assays that the increasing mobility of the supercoiled DNA in the low range of HU/DNA ratio cannot be interpreted by further super-helical turns introduced by HU–DNA binding.[61] Such a condensation resulting from DrHU binding was also observed with linearized DNAs (Fig. S2C *vs.* S1C†).

In the processed image of Fig. 5C, DrHUs are visibly distributed on supercoiled surfaces of the circular DNA. In the configuration of linearized DNA shown in Fig. 5D, bound DrHUs are visible almost throughout the entire DNA chain. It is likely that the circular DNA molecule has self-twisted and preformed a compact configuration, which was further stabilized and constrained by incoming DrHUs. However, as inferred by the configuration of DrHU–DNA complex in Fig. 4D, where the open complexed filaments tend to associate with a condensed, toroid component, the condensed configuration of DrHU bound to linear DNA as seen in Fig. 5D could be initially in an open form and subsequently condensed into the compact structure. The above elucidates two possible mechanisms for DNA condensation. As described previously, the binding of DNA and HU protein is highly dynamic, leading to a rapid exchange between free and HU–bound states of DNA[61,69] and between open and supercoiled configurations.[63,70] The two condensation mechanisms may happen to DNA in a combinatory manner by changing alternately the DNA topology and the distribution of bound DrHUs.

In the open DNA configuration at high DrHU concentration, the DrHU–circular DNA complex, as seen in Fig. 3F, is neither twisted like naked circular DNAs nor condensed as the compact DrHU–bound DNAs at a lower DrHU/DNA molar ratio (Fig. S2A†). Further comparison made with the DrHU–bound DNA in Fig. 3D reveals that the DNA complex in Fig. 3F is not only more open but also globally thickened. The thickening of the DNA filament upon HU binding has been suggested to symbolize the stiffening of the DNA,[46,71] which as a result becomes too rigid to fold. The enlargement of DNA spreading upon more DrHU binding reflects a de-condensation effect. Essentially, one can regard the apparently opposite effects of DrHU binding as a stabilization result for the DrHU–DNA complex. Taken together, the interplay between the dynamic behavior of DNA molecules and the level of DrHU plays a crucial role in the functional plasticity of the protein.

Conclusions

This study has shown that the AFM imaging combined with the L-weight filter allows us to study the topography of biological molecules represented in a wide spectrum of sizes and forms. For example, we managed to distinguish different conformations of a small protein, the free DrHU protein dimer (~25 kDa). In DrHU–DNA complexes, the orientation of DrHU dimers bound to the DNA can be determined from their distinctive shapes in the image. The L-weight filter was shown to significantly alleviate AFM tip-convolution effects so that the structural features of the imaged molecule can be greatly enhanced. The revelation of detailed structures gives us the confidence to comprehend and interpret the molecular behavior of DrHU protein upon DNA-binding from AFM images. From the present results, DrHU was shown to possess the ability to bridge and tether flexible DNA molecules. The topographic structures of DrHU–DNA complexes clearly demonstrate that DrHUs can multimerize over the surface of the DNA filament to form a higher order structure when the protein concentration is high. The building of a higher order architecture promotes cooperative binding of DrHU to DNA. By combining geometric analyses with L-weight filtering, AFM imaging reveals that DrHU binding may exert both condensation and de-condensation effects; this dual functionality of DrHU depends on naked DNA configuration and the protein concentration. The condensation effect of DrHU binding is observed by stabilizing the compact conformation of naked DNA or by increasing the compactness of condensed DNA configuration. The de-condensation effect stiffens DNA filaments, and expands the width of open DNA configuration. They also provide valuable information regarding the DNA-binding properties of HU proteins, especially the one from *D. radiodurans*, DrHU, and its close orthologues from the genus *Deinococcus*.

Conflicts of interest

There are no conflicts to declare.

Acknowledgements

IBS acknowledges integration into the Interdisciplinary Research Institute of Grenoble (IRIG, CEA). This work acknowledges the AFM platform at the IBS. This work was supported in part by the Grenoble Alliance for Integrated Structural Cell Biology [ANR-10-LABX-49-01] and by the Commissariat à

l'Energie Atomique et aux Energies Alternatives [CFR fellowship to A. S. B.] and [Radiobiology grant].

Notes and references

1 L. Springall, A. V. Inchingolo and N. M. Kad, *Methods Mol. Biol.*, 2016, **1431**, 141–150.
2 D. I. Cherny and T. M. Jovin, *J. Mol. Biol.*, 2001, **313**, 295–307.
3 V. Cassina, D. Seruggia, G. L. Beretta, D. Salerno, D. Brogioli, S. Manzini, F. Zunino and F. Mantegazza, *Eur. Biophys. J.*, 2011, **40**, 59–68.
4 L. Li, R. An, J. Tang, Z. Sui, G. Wang, M. Komiyama and X. Liang, *Biophys. J.*, 2020, **118**, 1702–1708.
5 S. Blouin, T. D. Craggs, D. A. Lafontaine and J. C. Penedo, *Methods Mol. Biol.*, 2015, **1334**, 115–141.
6 H. G. Hansma, R. L. Sinsheimer, M. Q. Li and P. K. Hansma, *Nucleic Acids Res.*, 1992, **20**, 3585–3590.
7 H. G. Hansma, D. E. Laney, M. Bezanilla, R. L. Sinsheimer and P. K. Hansma, *Biophys. J.*, 1995, **68**, 1672–1677.
8 N. K. Lee, T. Schmatko, P. Muller, M. Maaloum and A. Johner, *Phys. Rev. E: Stat., Nonlinear, Soft Matter Phys.*, 2012, **85**, 051804.
9 G. Witz, K. Rechendorff, J. Adamcik and G. Dietler, *Phys. Rev. Lett.*, 2008, **101**, 148103.
10 Y. L. Lyubchenko, L. S. Shlyakhtenko, T. Aki and S. Adhya, *Nucleic Acids Res.*, 1997, **25**, 873–876.
11 B. J. Rackstraw, A. L. Martin, S. Stolnik, C. J. Roberts, M. C. Garnett, M. C. Davies and S. J. B. Tendler, *Langmuir*, 2001, **17**, 3185–3193.
12 D. D. Dunlap, A. Maggi, M. R. Soria and L. Monaco, *Nucleic Acids Res.*, 1997, **25**, 3095–3101.
13 S. Cosgriff, K. Chintakayala, Y. T. A. Chim, X. Y. Chen, S. Allen, A. L. Lovering and D. C. Grainger, *Mol. Microbiol.*, 2010, **77**, 1289–1300.
14 Y. L. Lyubchenko and L. S. Shlyakhtenko, *Methods*, 2009, **47**, 206–213.
15 S. C. Dillon and C. J. Dorman, *Nat. Rev. Microbiol.*, 2010, **8**, 185–195.
16 P. Ghatak, K. Karmakar, S. Kasetty and D. Chatterji, *PLoS One*, 2011, **6**, e16019.
17 V. V. Melekhov, U. S. Shvyreva, A. A. Timchenko, M. N. Tutukina, E. V. Preobrazhenskaya, D. V. Burkova, V. G. Artiukhov, O. N. Ozoline and S. S. Antipov, *PLoS One*, 2015, **10**, e0126504.
18 A. Japaridze, S. Renevey, P. Sobetzko, L. Stoliar, W. Nasser, G. Dietler and G. Muskhelishvili, *J. Biol. Chem.*, 2017, **292**, 7607–7618.
19 N. T. Odermatt, M. Lelli, T. Herrmann, L. A. Abriata, A. Japaridze, H. Voilquin, R. Singh, J. Piton, L. Emsley, G. Dietler and S. T. Cole, *J. Struct. Biol.*, 2020, **209**, 107434.
20 A. Mishra, M. Vij, D. Kumar, V. Taneja, A. K. Mondal, A. Bothra, V. Rao, M. Ganguli and B. Taneja, *PLoS One*, 2013, **8**, e69985.
21 R. T. Dame, M. S. Luijsterburg, E. Krin, P. N. Bertin, R. Wagner and G. J. L. Wuite, *J. Bacteriol.*, 2005, **187**, 1845–1848.
22 S. Maurer, J. Fritz and G. Muskhelishvili, *J. Mol. Biol.*, 2009, **387**, 1261–1276.
23 C. J. Lim, S. Y. Lee, L. J. Kenney and J. Yan, *Sci. Rep.*, 2012, **2**, 509.
24 J. Lin, H. Chen, P. Droge and J. Yan, *PLoS One*, 2012, **7**, e49885.
25 Y. F. Gao, Y. H. Foo, R. S. Winardhi, Q. N. Tang, J. Yan and L. J. Kenney, *Proc. Natl. Acad. Sci. U. S. A.*, 2017, **114**, 12560–12565.
26 R. L. Ohniwa, H. Muchaku, S. Saito, C. Wada and K. Morikawa, *PLoS One*, 2013, **8**, e72954.
27 T. A. Azam and A. Ishihama, *J. Biol. Chem.*, 1999, **274**, 33105–33113.
28 T. A. Azam, A. Iwata, A. Nishimura, S. Ueda and A. Ishihama, *J. Bacteriol.*, 1999, **181**, 6361–6370.
29 P. Stojkova, P. Spidlova and J. Stulik, *Front. Cell. Infect. Microbiol.*, 2019, **9**, 159.
30 I. Tanaka, K. Appelt, J. Dijk, S. W. White and K. S. Wilson, *Nature*, 1984, **310**, 376–381.
31 H. Vis, M. Mariani, C. E. Vorgias, K. S. Wilson, R. Kaptein and R. Boelens, *J. Mol. Biol.*, 1995, **254**, 692–703.
32 F. Boubrik and J. Rouviere-Yaniv, *Proc. Natl. Acad. Sci. U. S. A.*, 1995, **92**, 3958–3962.
33 S. Li and R. Waters, *J. Bacteriol.*, 1998, **180**, 3750–3756.
34 D. R. Storts and A. Markovitz, *J. Bacteriol.*, 1988, **170**, 1541–1547.
35 S. Kar, R. Edgar and S. Adhya, *Proc. Natl. Acad. Sci. U. S. A.*, 2005, **102**, 16397–16402.
36 R. T. Dame, *Mol. Microbiol.*, 2005, **56**, 858–870.
37 H. H. Nguyen, C. B. de la Tour, M. Toueille, F. Vannier, S. Sommer and P. Servant, *Mol. Microbiol.*, 2009, **73**, 240–252.
38 K. K. Swinger, K. M. Lemberg, Y. Zhang and P. A. Rice, *EMBO J.*, 2003, **22**, 3749–3760.
39 D. H. Kim, H. Im, J. G. Jee, S. B. Jang, H. J. Yoon, A. R. Kwon, S. M. Kang and B. J. Lee, *Acta Crystallogr., Sect. D: Biol. Crystallogr.*, 2014, **70**, 3273–3289.
40 K. W. Mouw and P. A. Rice, *Mol. Microbiol.*, 2007, **63**, 1319–1330.
41 M. Hammel, D. Amlanjyoti, F. E. Reyes, J. H. Chen, R. Parpana, H. Y. Tang, C. A. Larabell, J. A. Tainer and S. Adhya, *Sci. Adv.*, 2016, **2**, e1600650.
42 C. B. de la Tour, L. Blanchard, R. Dulermo, M. Ludanyi, A. Devigne, J. Armengaud, S. Sommer and A. de Groot, *Microbiology*, 2015, **161**, 2410–2422.
43 S. Ghosh and A. Grove, *Biochemistry*, 2006, **45**, 1723–1733.
44 J. Rouviere-Yaniv, M. Yaniv and J. E. Germond, *Cell*, 1979, **17**, 265–274.
45 T. H. Eickbush and E. N. Moudrianakis, *Cell*, 1978, **13**, 295–306.
46 J. van Noort, S. Verbrugge, N. Goosen, C. Dekker and R. T. Dame, *Proc. Natl. Acad. Sci. U. S. A.*, 2004, **101**, 6969–6974.

47 J. Kim, S. H. Yoshimura, K. Hizume, R. L. Ohniwa, A. Ishihama and K. Takeyasu, *Nucleic Acids Res.*, 2004, **32**, 1982–1992.
48 S. W. Chen, J. M. Teulon, C. Godon and J. L. Pellequer, *J. Mol. Recognit.*, 2016, **29**, 51–55.
49 N. J. Anthis and G. M. Clore, *Protein Sci.*, 2013, **22**, 851–858.
50 D. Nečas and P. Klapetek, *Cent. Eur. J. Phys.*, 2012, **10**, 181–188.
51 S.-w. W. Chen and J. L. Pellequer, *BMC Struct. Biol.*, 2011, **11**, 7.
52 S.-w. W. Chen, M. Odorico, M. Meillan, L. Vellutini, J.-M. Teulon, P. Parot, B. Bennetau and J.-L. Pellequer, *Nanoscale*, 2013, **22**, 10877–10886.
53 S.-w. W. Chen and J.-L. Pellequer, *Nucleic Acids Res.*, 2013, **41**, W412–W416.
54 S.-w. W. Chen and J.-L. Pellequer, *Curr. Med. Chem.*, 2004, **11**, 595–605.
55 A. C. Papageorgiou, P. S. Adam, P. Stavros, G. Nounesis, R. Meijers, K. Petratos and C. E. Vorgias, *Extremophiles*, 2016, **20**, 695–709.
56 D. Kamashev, Y. Agapova, S. Rastorguev, A. A. Talyzina, K. M. Boyko, D. A. Korzhenevskiy, A. Vlaskina, R. Vasilov, V. I. Timofeev and T. V. Rakitina, *PLoS One*, 2017, **12**, e0188037.
57 J. Ramstein, N. Hervouet, F. Coste, C. Zelwer, J. Oberto and B. Castaing, *J. Mol. Biol.*, 2003, **331**, 101–121.
58 S. Ghosh and A. Grove, *J. Mol. Biol.*, 2004, **337**, 561–571.
59 V. Berthold and K. Geider, *Eur. J. Biochem.*, 1976, **71**, 443–449.
60 A. Balandina, D. Kamashev and J. Rouviere-Yaniv, *J. Biol. Chem.*, 2002, **277**, 27622–27628.
61 H. Shindo, A. Furubayashi, M. Shimizu, M. Miyake and F. Imamoto, *Nucleic Acids Res.*, 1992, **20**, 1553–1558.
62 J. D. McGhee and P. H. von Hippel, *J. Mol. Biol.*, 1974, **86**, 469–489.
63 Y. Flashner and J. D. Gralla, *Cell*, 1988, **54**, 713–721.
64 A. M. Segall, S. D. Goodman and H. A. Nash, *EMBO J.*, 1994, **13**, 4536–4548.
65 J. Griffith, A. Makhov, L. Santiago-Lara and P. Setlow, *Proc. Natl. Acad. Sci. U. S. A.*, 1994, **91**, 8224–8228.
66 J.-M. Teulon, C. Godon, L. Chantalat, C. Moriscot, J. Cambedouzou, M. Odorico, J. Ravaux, R. Podor, A. Gerdil, A. Habert, N. Herlin-Boime, S.-w. W. Chen and J.-L. Pellequer, *Nanomaterials*, 2019, **9**, 18.
67 J. Adamcik, J. H. Jeon, K. J. Karczewski, R. Metzler and G. Dietler, *Soft Matter*, 2012, **8**, 8651–8658.
68 J. Adamcik, V. Viglasky, F. Valle, M. Antalik, D. Podhradsky and G. Dietler, *Electrophoresis*, 2002, **23**, 3300–3309.
69 K. Floc'h, F. Lacroix, P. Servant, Y. S. Wong, J. P. Kleman, D. Bourgeois and J. Timmins, *Nat. Commun.*, 2019, **10**, 3815.
70 S. S. Broyles and D. E. Pettijohn, *J. Mol. Biol.*, 1986, **187**, 47–60.
71 J. Rouviere-Yaniv and F. Gros, *Proc. Natl. Acad. Sci. U. S. A.*, 1975, **72**, 3428–3432.

Figure S1

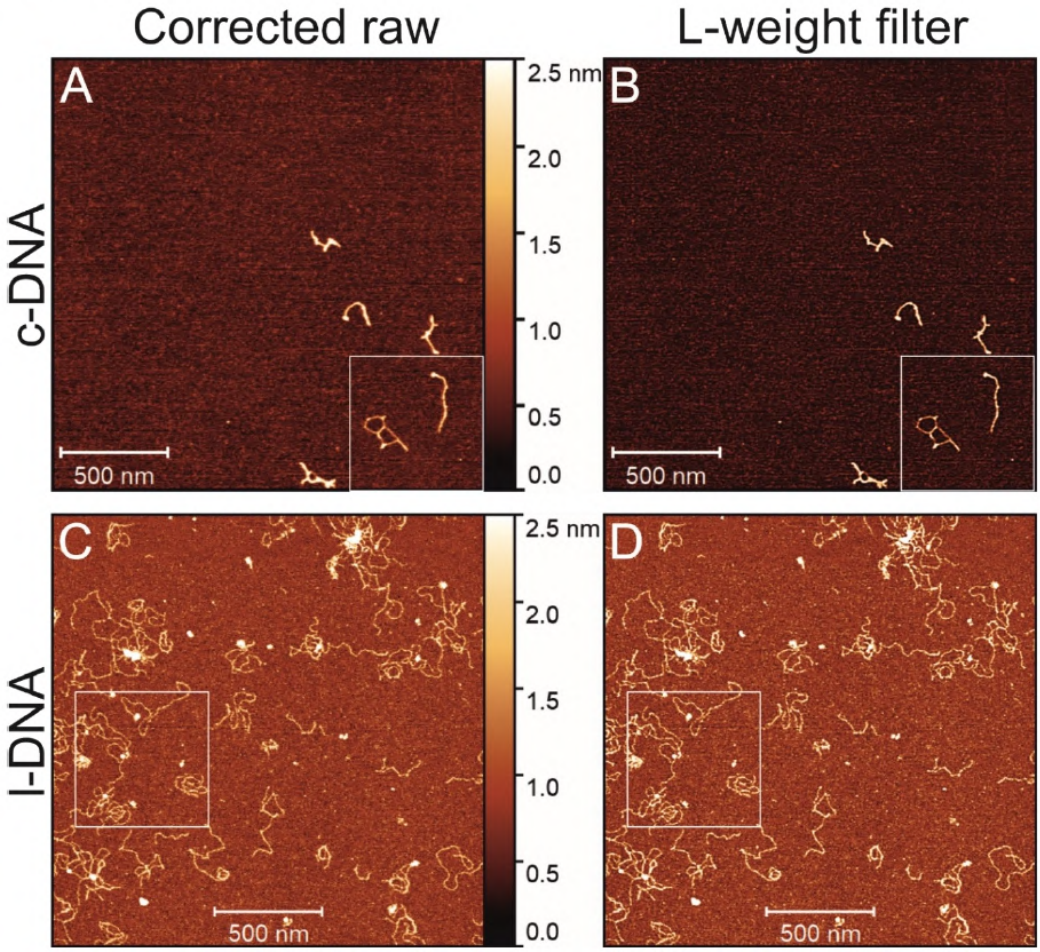

Figure S1: Visualization of naked DNA molecules. The left column presents the AFM image of the molecular system and while the right column corresponds to the L-weight filter processed images. All images contain 512 x 512 pixels with a physical dimension of 2 x 2 μm². **(A-B)** Naked circular, supercoiled DNAs (c-DNAs) at a concentration of 0.8 nM. Subimages indicated with white boxes contain 160 x 160 pixels and were cropped for use in **Figs. 3A-B**. **(C-D)** Naked linearized DNAs (l-DNAs) at a concentration of 0.8 nM. Boxed subimages are composed of 160 x 160 pixels, and were used in **Figs. 4A-B**; see details in the main text.

In this work, natively supercoiled DNA extracted and purified from bacteria was used either without further treatment or after linearization. The following terminology is used throughout the text: "partially open" DNA conformation describes a non-compact DNA where a couple of twists or cross-overs are visible; "compact" DNA conformation describes a DNA with a low appearance of DNA duplex sections; "condensed" DNA conformation describes a further compacted DNA due to binding of DrHU.

Figure S2

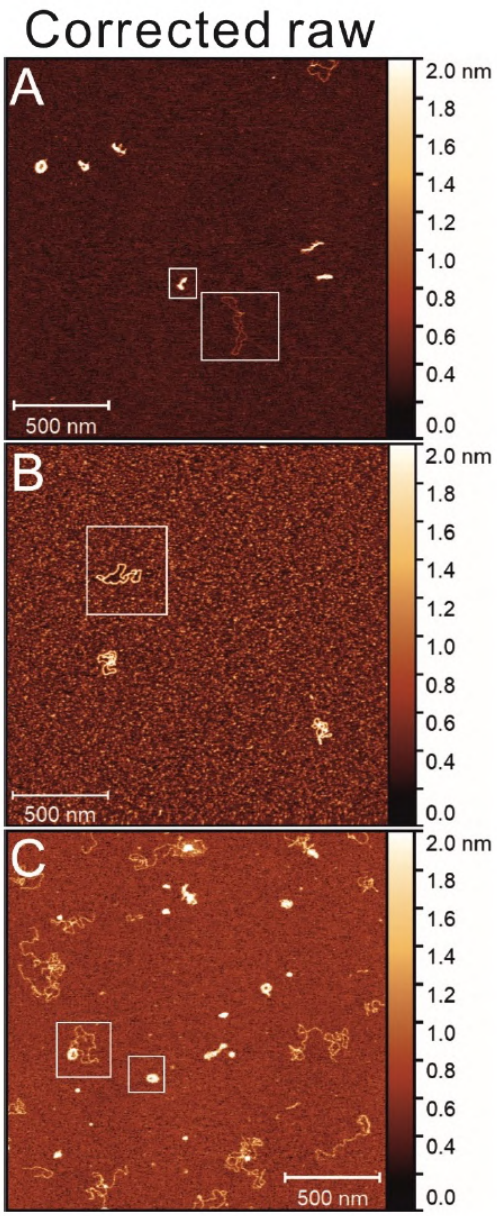

Figure S2: AFM images of DrHU-DNA complexes at a lower scan resolution. All images have a physical size of 2 x 2 μm² with 512 x 512 pixels. The boxed regions were imaged by AFM at a higher scan resolution, and the resulting images are presented in the main text; see details in the main text. **(A)** The parent image of image 5C and 3C, from left to right, respectively. **(B)** The parent image of image **3E**. **(C)** The parent image of images **4C** and **5D**.

Figure S3

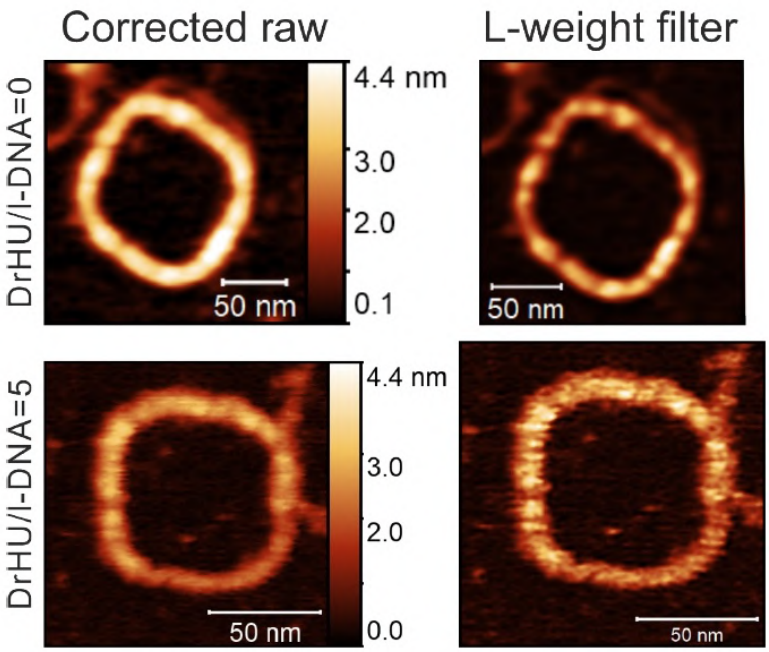

Figure S3: Comparison of AFM images of naked linearized DNA and DrHU-linearized DNA oblong complexes demonstrating the common DNA origin of these intriguing shapes but some noticeable differences when observing the rough surface of DrHU bound complexes versus the smooth surface of bare DNA. The left column presents the AFM image of the molecular system while the right column corresponds to the L-weight filter processed images. **(A)** The image was cropped from a larger scan size of bare linearized DNA and has a final size of 204 x 204 pixels with a magnification of (x4) and a physical size of 200 x 200 nm². **(B)** Cropped image from **Fig. 5A** that contains DrHU bound to linearized DNA at a molar ratio of 5. The image has a final size of 128 x 128 pixels with a magnification of (x2) and a physical size of 125 x 125 nm². Note that the two structures have different sizes where the diameter of A) is about 155 nm whereas that in B) is about 90 nm.

II.5.1.2 DrHU forms bead-like or spiral-shaped complexes on plasmid DNA

In parallel to our AFM study, we used transmission electron microscopy (TEM) to analyze the structures produced by the binding of DrHU to relaxed pUC19 plasmid DNA. TEM is an imaging technique that relies on the interaction of an accelerated electron beam with the molecules present in the sample to achieve a high spatial resolution comparable to that of AFM. The main advantages of the different TEM techniques used during my thesis were (i) the rapid image acquisition by negative-staining TEM compared to AFM, (ii) the possibility to image the sample in more native-like conditions with cryo-EM and (iii) the ability to observe the inner structure of the protein-DNA complexes by means of cryo-electron tomography (cryo-ET). The images were acquired and processed by our collaborators, I. Gutsche and M. Bacia (IBS, Grenoble).

We first evaluated several plasmid-to-DrHU molar ratios by means of negative-staining TEM, by incubating 60 nM to 1 µM of DrHU with 10 nM of relaxed pUC19 in distilled water. After a 1-hour incubation on ice, the samples were stained with uranyl acetate and deposited on EM grids for imaging (Fig. 57). We observed the formation of compact bead-like protein-DNA complexes that were even visible in the sample with the lowest plasmid-to-DrHU molar ratio of 1:6 (Fig. 57A). At this molar ratio, most of the DNA formed random coils as in the plasmid alone sample, but several spherical complexes could already be observed with diameters in the range of 50 to 75 nm. When the molar ratio increased to 1:60, more bead-like complexes were detected although their average diameter remained unchanged. At the highest plasmid-to-DrHU molar ratio of 1:100, it seemed that most of the relaxed plasmid was arranged as highly condensed spherical complexes induced by DrHU binding. Moreover, the diameter of the protein-DNA complexes formed at this 1:100 molar ratio varied from less than 50 nm up to more than 100 nm. These results suggest that the highly compact bead-like structures might gradually grow as the concentration of DrHU increases. At low DrHU concentration corresponding to a molar ratio of 1:6, a small protein-DNA complex of less than 50 nm in diameter would form. Then, as the DrHU concentration increases, the proteins might oligomerize with DNA-bound proteins of the already formed complex. These newly bound DrHU could in turn recruit other DNA molecules to the protein-DNA complex, leading to the observed increase of its diameter up to more than 100 nm at the highest plasmid-to-DrHU molar ratio. As we incubated the relaxed pUC19 with DrHU in distilled water corresponding to a final NaCl concentration of 85 µM for the molar ratio of 1:100, we wanted to assess the effect of NaCl on the already formed protein-DNA complexes by adding NaCl to a final concentration

of 12.5 mM in the sample of 1:100 molar ratio (Fig. 57B). In this condition, no compact protein-DNA complexes were observed and it seemed that the previously formed bead-like structures were decondensed by the addition of NaCl even at low concentration. As expected, the presence of salts hindered the electrostatic interactions between the negatively charged plasmid DNA and the positively charged DrHU.

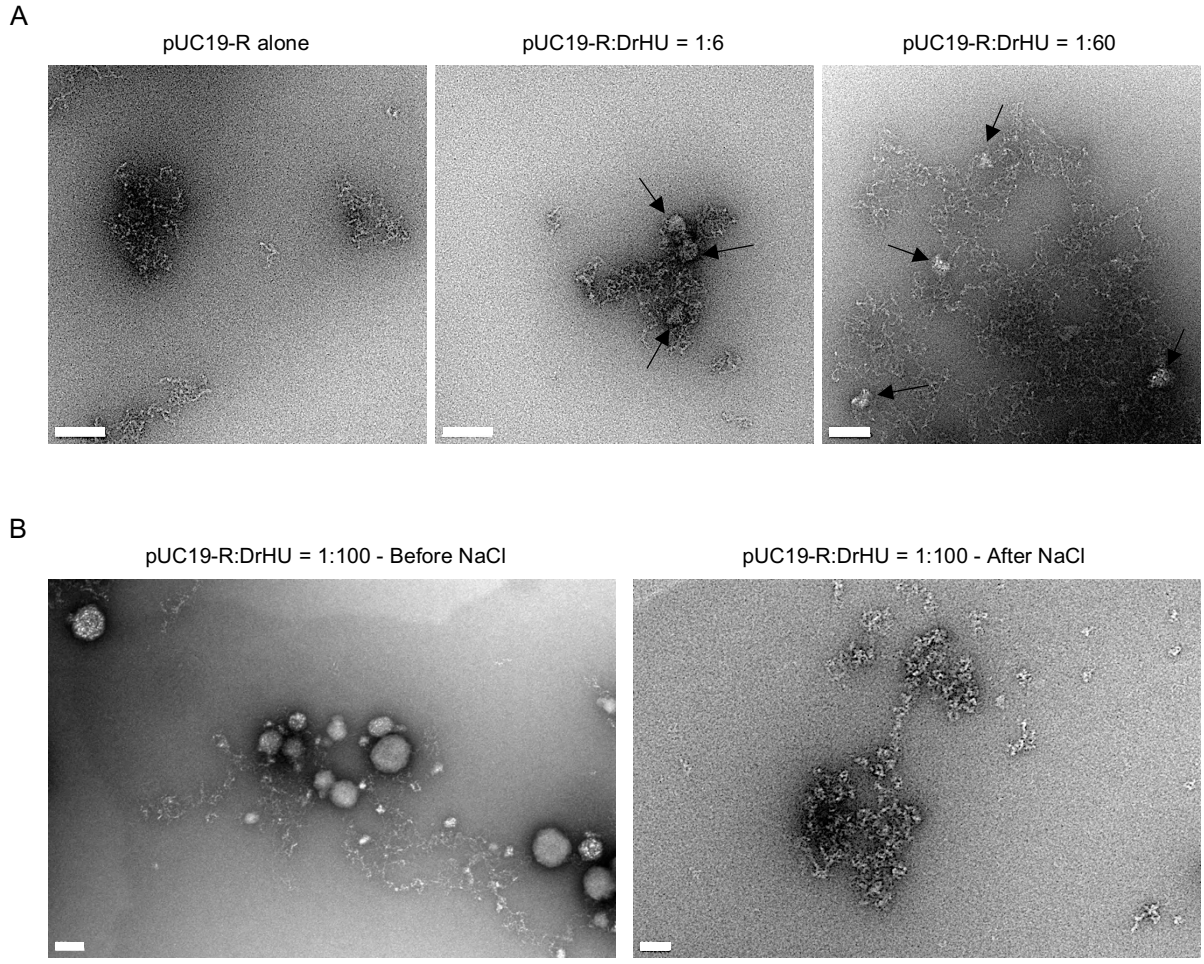

Figure 57. DrHU in complex with relaxed plasmid DNA forms highly condensed bead-like structures. Relaxed pUC19 (pUC19-R) at 10 nM was incubated with increasing concentrations of DrHU for a pUC19-R to DrHU molar ratio of 1:6 or 1:60 in distilled water (**A**). The protein-DNA complexes were analyzed by negative-staining TEM using 2% uranyl acetate. An additional molar ratio of 1:100 was imaged once in distilled water and a second time after addition of 12.5 mM NaCl (**B**). The white scale bar represents 100 nm in all five images. The arrows in the middle and right panels of (**A**) indicate the bead-like structures form upon DrHU binding to DNA.

Next, we imaged the condensed structures formed by the binding of DrHU to relaxed pUC19 plasmid DNA by cryo-EM and cryo-ET. The two imaging methods were used to acquire high resolution images of our complexes and gain some insights into their internal structure, while eliminating a potential bias caused by the negative-staining solution and the withdrawal of solvent from the sample. We chose to focus on the relaxed pUC19-to-DrHU molar ratio of

1:6 because it was the best compromise between (i) a ratio high enough to potentially observe the formation of the condensed protein-DNA complexes and (ii) a low ratio that could be reproduced with higher concentrations of relaxed pUC19 and DrHU needed for cryo-EM. After incubation of DrHU with the plasmid in distilled water, gold beads were added to serve as position markers during processing of cryo-ET images. After sample deposition on cryo-EM grids, the grids were rapidly plunged in liquid ethane to form a thin layer of frozen sample solution in which our molecules remained trapped. The cryo-EM images and the cryo-ET tomogram were acquired on the Glacios transmission electron microscope operating at cryogenic temperature (Fig. 58).

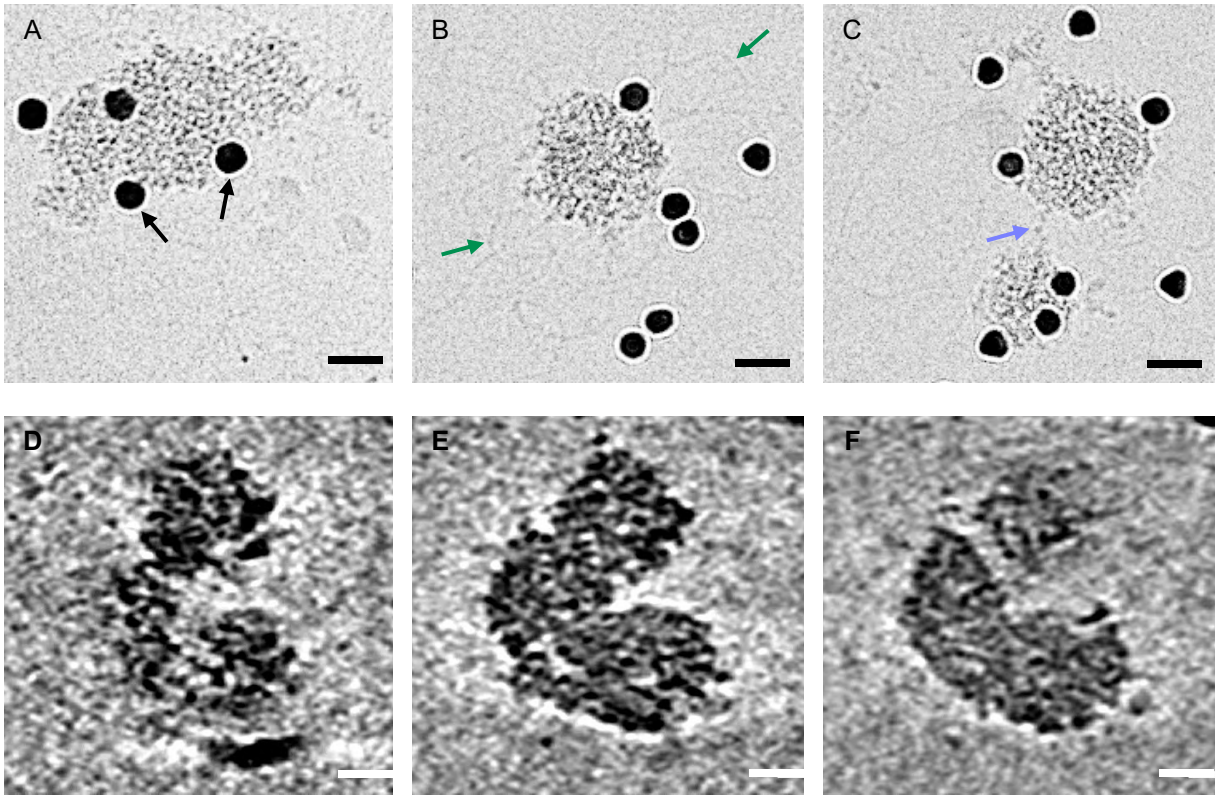

Figure 58. DrHU in complex with relaxed plasmid DNA was imaged by cryo-EM and cryo-ET. Relaxed pUC19 at 44 nM was incubated with DrHU at 283 nM for a molar ratio of 1:6. The protein-DNA complexes were analyzed by cryo-EM (**A-C**) and cryo-ET (**D-F**). In the cryo-EM images, the gold beads are indicated with a black arrow, bare DNA filaments are highlighted by green arrows and the blue arrow shows the supposedly DrHU-bound DNA between two protein-DNA complexes. The black scale bar in the three images represents 20 nm. The panels D to F are consecutive slices of the tomogram and the white scale bar represents 20 nm.

As previously observed by negative-staining TEM, relaxed plasmid DNA bound by DrHU was condensed into ball-like structures although at this ratio only a fraction of the DNA was recruited into the formation of well-structured protein-DNA complexes (Fig. 58A). The

structures were either isolated or close to one another (Fig. 58B-C). A close look at an isolated DrHU-plasmid complex revealed the presence of DrHU-free DNA filaments that seemed to come out of the ball-like structure (Fig. 58B). However, these filaments of bare DNA were quite hard to detect within the thin ice layer because dsDNA alone is only 2 nm in diameter. In Figure 58C, two spherical complexes were imaged next to each other showing a thin thread that appeared to connect the two structures. This could be a DNA filament covered in DrHU as it appears to be thicker than the bare DNA filaments observed in Figure 58B. A common feature of the DrHU-plasmid complexes imaged by cryo-EM is that an inner organization of the structures is discernible. The core of the complexes was filled with small black objects that might be DrHU, which were more or less regularly arranged. According to preliminary results acquired by cryo-ET on a sample of relaxed pUC19 incubated with DrHU, the compaction of plasmid DNA is maintained throughout the structure making it very challenging to trace the DNA filament through this compact structure (Fig. 58D-F).

We next sought to evaluate the effect of DrHU on the conformation of supercoiled plasmid and to characterize the structure of such complexes using cryo-EM. Samples were prepared by incubation of 200 nM of supercoiled pUC19 with increasing concentrations of DrHU to test plasmid-to-DrHU molar ratios of 1:10, 1:25 and 1:100. The samples were deposited on cryo-EM grids that were subsequently frozen by rapid plunge-freezing in liquid ethane and imaged by cryo-EM (Fig. 59). At plasmid-to-DrHU molar ratios of 1:10 and 1:25 (Fig. 59B-C), no particular structures were visible and the DNA conformation remained similar to that of the plasmid alone (Fig. 59A). However, when shifting to a higher molar ratio of 1:100 the protein-DNA complexes formed by DrHU binding to the supercoiled plasmid adopted a surprising regular spiral shape, and in some cases two spirals were connected by a linear DNA fragment (Fig. 59D-E). Alternatively, the DrHU-bound supercoiled pUC19 was assembled as a seemingly more disorganised structure resembling fingerprints, although some spirals were still visible in those samples (Fig. 59F). These spiral-shaped and fingerprint-like complexes were never observed in plasmid alone samples. They are largely two-dimensional, as determined by cryo-ET acquisitions (data not shown) and both displayed a rather regular spacing between DNA double-strands inside their structure. These results suggest that DrHU can induce the formation of ordered protein-DNA complexes upon binding to supercoiled plasmid DNA. They also reveal that the conformation of the plasmid DNA (either supercoiled or relaxed) strongly affects the shape and level of compaction of these structures. The regular

spacing observed between dsDNA filaments inside the structures could be maintained by DrHU proteins that might have polymerized along the DNA. Researchers in I. Gutsche's team are now trying to develop computational tools to process these images to locate the bound HU molecules – a very challenging task considering the small size of HU dimers for cryo-EM data analysis.

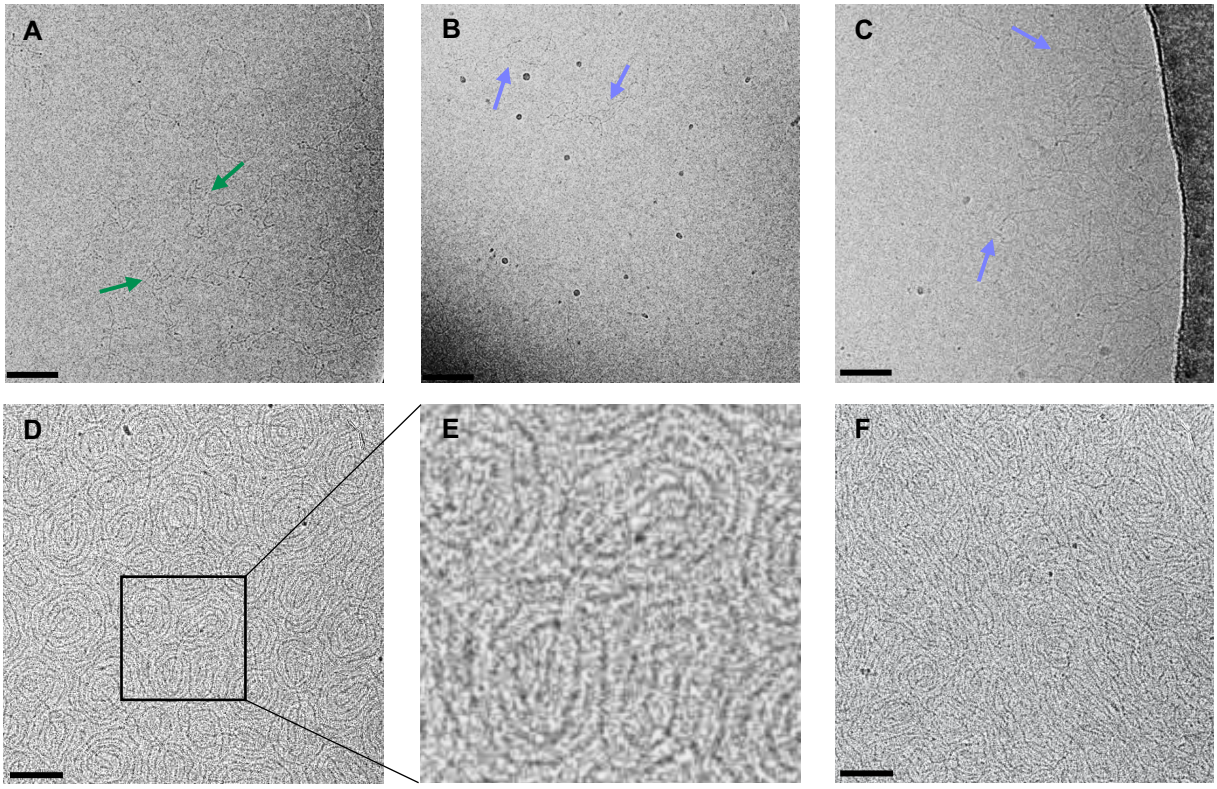

Figure 59. Binding of DrHU to supercoiled pUC19 plasmid yields spiral-shaped or fingerprint-like complexes. Supercoiled pUC19 at 200 nM (**A**) was incubated with increasing concentrations of DrHU for a plasmid-to-DrHU molar ratio of 1:10 (**B**), 1:25 (**C**) or 1:100 (**D-F**) and observed by cryo-EM. In panel A, the green arrows highlight the bare DNA molecules, while in panel B and C the blue arrows indicate DrHU-bound DNA. Panel E is a numerical magnification of the area delimited by a black square in panel D. The scale bars represent 100 nm.

II.5.2. Comparative studies of the protein-DNA complexes formed by deinococcal HU proteins

II.5.2.1. Comparison of the DNA compaction induced by DrHU and DdHU1

To verify if the previously observed compaction of DNA into ordered protein-DNA structures induced by DrHU is specific to this protein or a common trait of deinococcal HU proteins, we analyzed and compared the compaction and topology of supercoiled plasmid DNA

(pUC19-SC) in the presence of either DrHU or DdHU1, by means of AFM. Samples of pUC19-SC at 500 pM incubated with increasing concentrations of HU proteins were deposited on a nickel-coated mica, dried under nitrogen gas flow and imaged by AFM in air using the Peak Force mode. For these experiments, the AFM acquisitions were performed by J.-M. Teulon, and then I performed image processing and analysis, i.e. extracted the surface and volume of each bare plasmid or HU-bound plasmid for the plasmid to HU protein molar ratios of 1:1, 1:5,

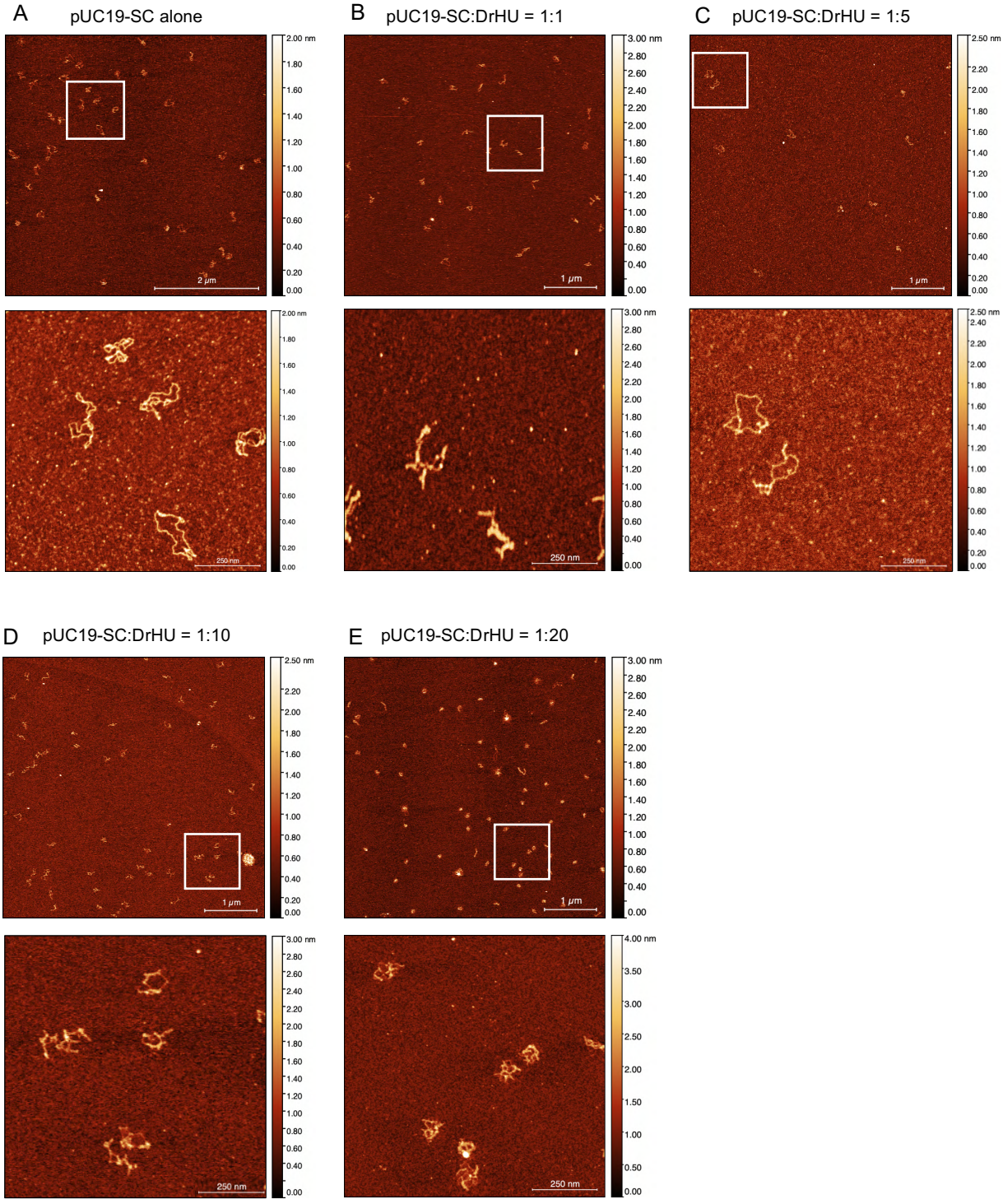

1:10 and 1:20.

Figure 60. Supercoiled plasmid DNA forms compact structures in the presence of DrHU. AFM images of 0.5 nM of supercoiled pUC19 (**A**) incubated with increasing concentrations of DrHU for plasmid-to-DrHU molar ratios of 1:1 (**B**), 1:5 (**C**), 1:10 (**D**) and 1:20 (**E**). Upper panels correspond to 5 μm^2 areas, in which a zone of 1 μm^2 area is delimited by a white square. Lower panels correspond to the physical magnification of the white boxed 1 μm^2 areas in the upper panels. The z-scale bar is shown as a colour gradient to indicate the distribution of height in the images. Scale bar corresponds to 1 µm in the upper panels (or 2 µm in upper panel A) and to 250 nm in the lower panels.

The supercoiled plasmid alone showed diverse supercoiling levels with more or less open pUC19 molecules observed in the large 5 μm^2 scan zone (Fig. 60A). At low plasmid-to-DrHU molar ratios such as 1:1 and 1:5, the protein did not appear to condense the supercoiled plasmid and plasmid molecules with a more open conformation could still be observed (Fig. 60B-C). At a molar ration of 1:10, the supercoiled plasmids were not highly condensed, but the proportion of open conformations visibly decreased, as illustrated in Figure 60D. When the highest concentration of DrHU was used, the majority of supercoiled pUC19 molecules formed condensed protein-DNA complexes onto which the binding of DrHU could be detected through the visible thickening of the dsDNA filament. These complexes were mostly arranged into spherical structures of approximately 70 nm in diameter although some rod-shaped condensed structures of ~200 nm in length were also observed (Fig. 60D). To quantify the extent of the compaction induced by the binding of DrHU, surface and volume values of each individual protein-DNA complex were extracted from the images acquired at the various molar ratios (Fig. 61).

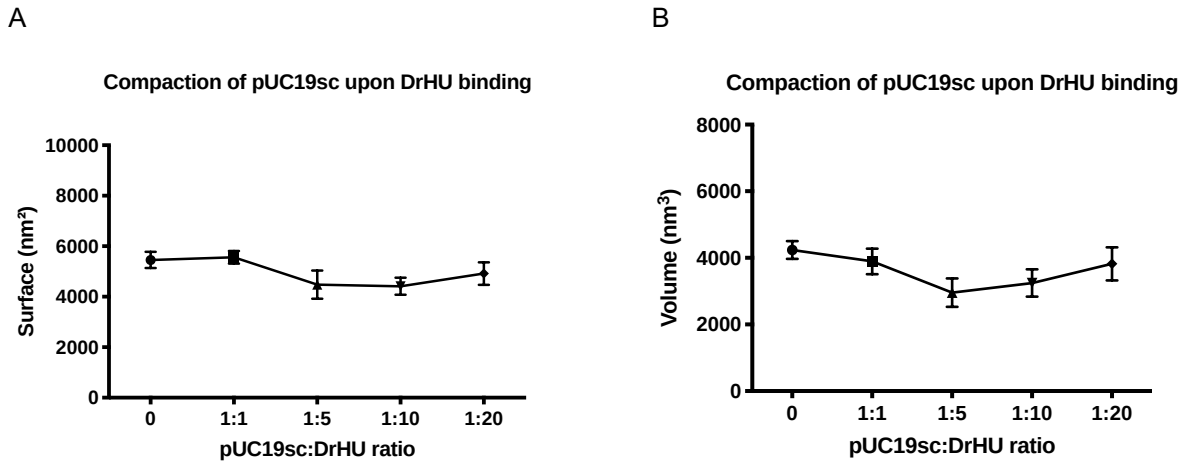

Figure 61. Effect of DrHU on the surface and volume of DrHU-bound supercoiled plasmid DNA. Graphs illustrating the mean surface (**A**) and the mean volume (**B**) of individual DrHU-pUC19-SC complexes (N>50 for each plasmid-to-DrHU molar ratio) as a function of the plasmid-to-DrHU molar ratio. Each data point represent the mean value for a given protein concentration and the error bars correspond to the 95% confidence interval.

The quantitative measurements of surface and volume of the DrHU-pUC19 complexes demonstrated that the supercoiled plasmid was condensed even at a 1:5 molar ratio, with a simultaneous decrease in surface and volume. The surface occupied by the protein-DNA assemblies remained quite stable at higher ratios, despite the visible compaction in our AFM images. This trend was also observed when quantifying the volume of the complexes, as the mean volume decreased at molar ratios 1:1 and 1:5, while it increased at higher molar ratios of 1:10 and 1:20. This could be explained by the added volume and surface brought by the DrHU proteins upon binding to supercoiled plasmid to form the complexes. At low ratios, the binding of DrHU induces a compaction leading to a decrease in surface and volume of the protein-DNA complexes. Nonetheless, as more DrHU binds to the supercoiled plasmid DNA, the additional surface and volume of the proteins compensate for the condensation effect leading to a net increase in surface and volume of the protein-DNA structures at higher molar ratios.

Complexes formed by the binding of DdHU1 to the supercoiled plasmid were imaged in the same conditions and with the same molar ratios as used for DrHU (Fig. 62). At the lowest plasmid-to-DdHU1 molar ratio, the binding of DdHU1 did not seem to affect the structure or compaction of supercoiled DNA (Fig. 62B). Interestingly, at a 1:5 molar ratio DdHU1 completely covered some plasmids, while other plasmids remained completely free of any protein (Fig. 62C). A high-resolution image of this sample showed that in the case of DdHU1-bound supercoiled pUC19 assemblies, the DNA was fully coated with DdHU1 leaving no bare DNA. When reaching a 1:10 molar ratio, the majority of the imaged supercoiled pUC19 molecules were completely covered in DdHU1 that appeared to be stacked upon the DNA as highlighted by the increased height of the protein-DNA complexes compared to the 1:5 molar ratio (Fig. 62D). At these two molar ratios, DdHU1-bound supercoiled pUC19 did not appear to be more condensed than the bare plasmid DNA. However, at the highest molar ratio of 1:20 the DdHU1-pUC19 complexes formed either small bead-like structures or rod-shaped structures and were more compact, with a high amount of DdHU1 still covering the DNA.

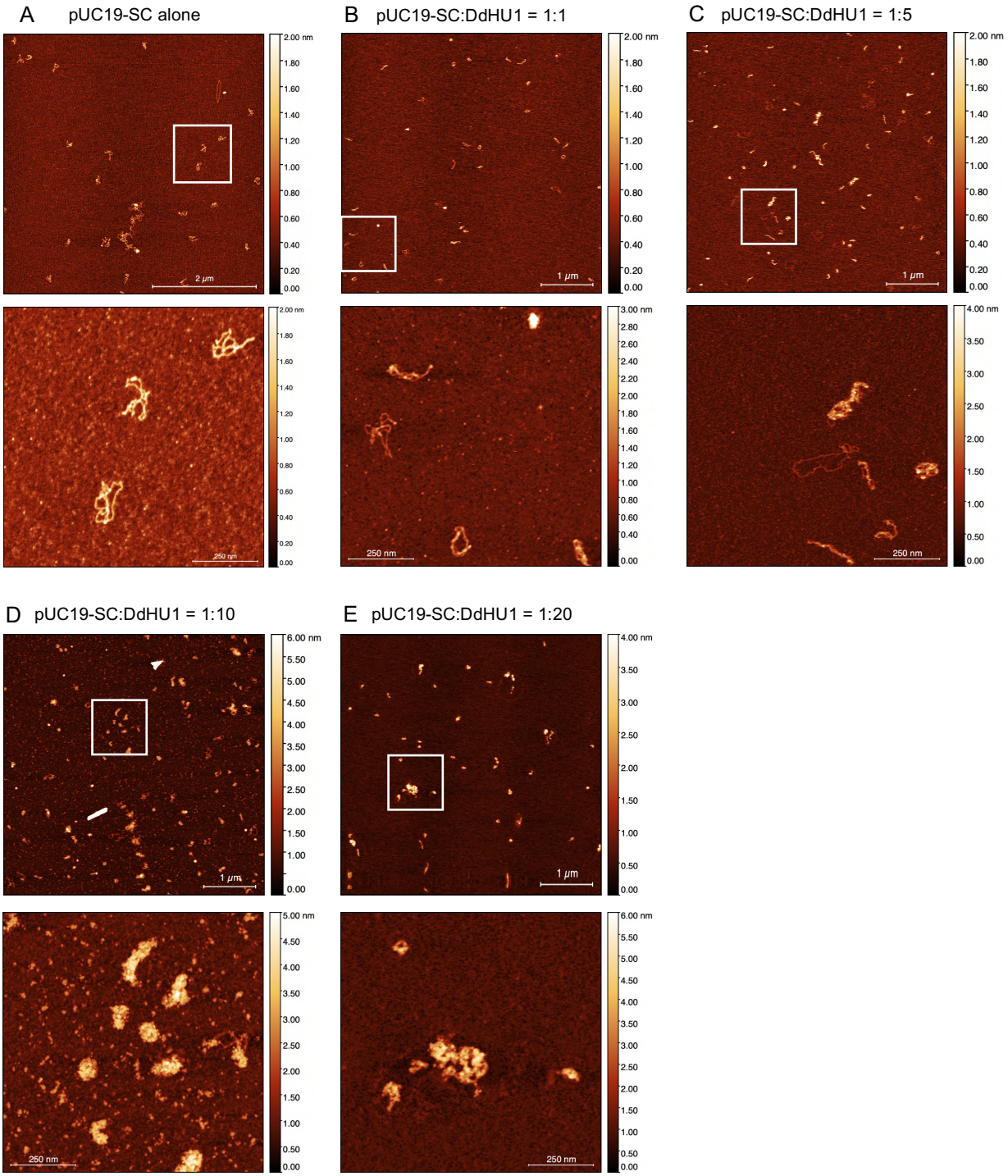

Figure 62. Complexes of DdHU1 bound to supercoiled plasmid DNA differ from that formed by DrHU. AFM images of 0.5 nM of supercoiled pUC19 (**A**) incubated with increasing concentrations of DdHU1 for plasmid-to-DdHU1 molar ratios of 1:1 (**B**), 1:5 (**C**), 1:10 (**D**) and 1:20 (**E**). Upper panels correspond to 5 μm^2 areas, in which a zone of 1 μm^2 area is delimited by a white square. Lower panels correspond to the physical magnification of the white boxed 1 μm^2 areas in the upper panels. The z-scale bar is shown as a colour gradient to indicate the distribution of height in the images. Scale bar corresponds to 1 µm in the upper panels (or 2 µm in upper panel A) and to 250 nm in the lower panels.

To better understand the intriguing effect of DdHU1 on supercoiled pUC19, the surface and volume of each protein-DNA complexes were extracted as previously described for DrHU and compared to the values obtained with the same concentrations of DrHU (Fig. 63).

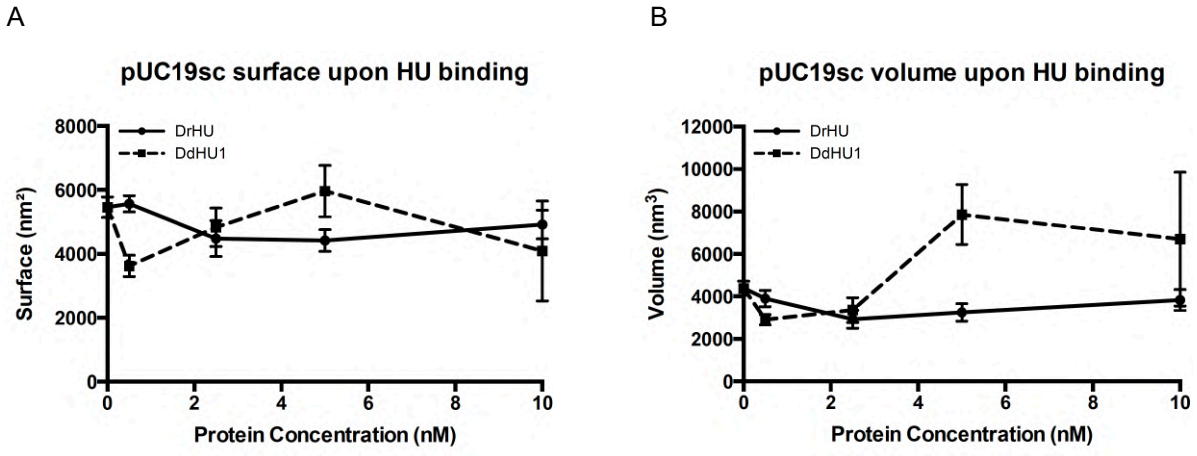

Figure 63. DrHU and DdHU1 display different behaviors upon binding to supercoiled plasmid DNA. Graphs illustrating the mean surface (**A**) and the mean volume (**B**) of individual DrHU-pUC19-SC (solid line) or DdHU1-pUC19-SC (dashed-line) complexes (N>50 for each HU protein concentration) as a function of the protein concentration. Each data point represent the mean value for a given protein concentration and the error bars correspond to the 95% confidence interval.

The measurement of surface and volume of the DdHU1-DNA complexes revealed that the lowest concentration of DdHU1 at 0.5 nM (corresponding to a plasmid-to-DdHU1 molar ratio of 1:1) induced a significant compaction by decreasing the surface and volume of the complexes (Fig. 63). However, these values steadily increased at higher concentrations of DdHU1 to reach a peak at 5 nM DdHU1 (molar ratio of 1:10). The highest concentration of DdHU1 at 10 nM (molar ratio of 1:20) induced a condensation of the protein-DNA complexes whose surface and volume decreased as observed in the AFM images.

Taken together, our results indicate that DrHU and DdHU1 may use two distinct strategies to induce DNA compaction of supercoiled plasmid DNA (Fig. 64). When a low amount of DrHU is bound to supercoiled plasmid DNA, it may start to condense the DNA molecule by bringing together distant DNA fragments without the formation of a structured protein-DNA complex. As more DrHU binds to the supercoiled plasmid, the DNA condensation would increase with the formation of compact round or rod-shaped complexes. In these conditions, the DNA-bound DrHU may polymerize along the DNA in a way that favours protein-DNA contacts over protein-protein contacts. Accordingly, at molar ratios of 1:10 and 1:20, we observed a thickening of the DNA filaments compared to lower ratios while

the height of the DrHU-bound plasmid remained stable around 3 nm suggesting that the bound DrHU do not lie on top of each other. The DNA binding and compaction mechanisms of DdHU1 on supercoiled plasmid DNA differ from those of DrHU. We hypothesize that a small amount of DdHU1 may first bind to a few supercoiled plasmids, inducing a condensation without the formation of a distinct structure. When more DdHU1 is available, a strong cooperative binding would cause all the DdHU1 proteins to bind preferentially to the DdHU1-bound plasmids rather than to the bare plasmid DNA, explaining the repartition of bound DdHU1 observed at molar ratio 1:5. In contrast with DrHU, DdHU1 would not polymerize along the DNA but would rather stack onto the DNA and the already bound DdHU1. The oligomerization of bound DdHU1 onto supercoiled plasmid DNA might therefore be based on the promotion of protein-protein contacts over protein-DNA contacts, which could be the exact opposite of the DNA compaction mechanism of DrHU. The "protein- protein" oligomerization mode of DdHU1 is supported by the increased height of DdHU1-pUC19 complexes at higher DdHU1 concentrations, as the average height of such complexes was of 3 nm at molar ratios of 1:1 and 1:5 but increased up to 6 nm at the higher molar ratios of 1:10 and 1:20. When the amount of bound DdHU1 reaches a critical concentration, the structure of the protein-DNA complexes would reorganize to adopt a more compact organization thereby explaining the decreased surface and volume as well as the highly condensed DdHU1-pUC19 complexes observed at a molar ratio of 1:20.

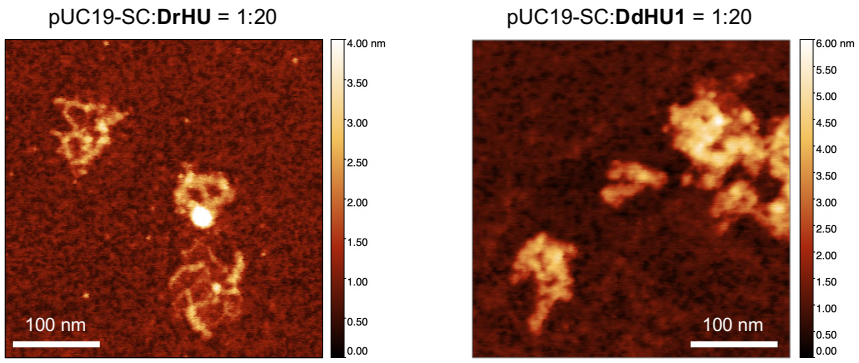

Figure 64. Different DNA-binding mode of DrHU and DdHU1 in complex with supercoiled plasmid DNA. Numerical magnification of the AFM images of the protein-DNA complexes formed at the highest plasmid-to-HU ratio of 1:20. Left panel: DrHU, right panel: DdHU1.

II.5.2.2. Comparison of two HU proteins of *D. deserti*

To complete our analysis of the DNA-binding and DNA-compaction mechanisms of the deinococcal HU proteins, we used AFM to analyze the complexes formed by DdHU3 upon binding to supercoiled plasmid pUC19-SC. The plasmid concentration was set to 2 nM and the final DdHU3 concentration was adjusted to reach a plasmid-to-DdHU3 molar ratio of 1:2, 1:5 or 1:10 (Fig. 65A-C). The surface and volume values of individual DdHU3-pUC19 complexes were extracted as described previously for DrHU and DdHU1 (Fig. 65D-E).

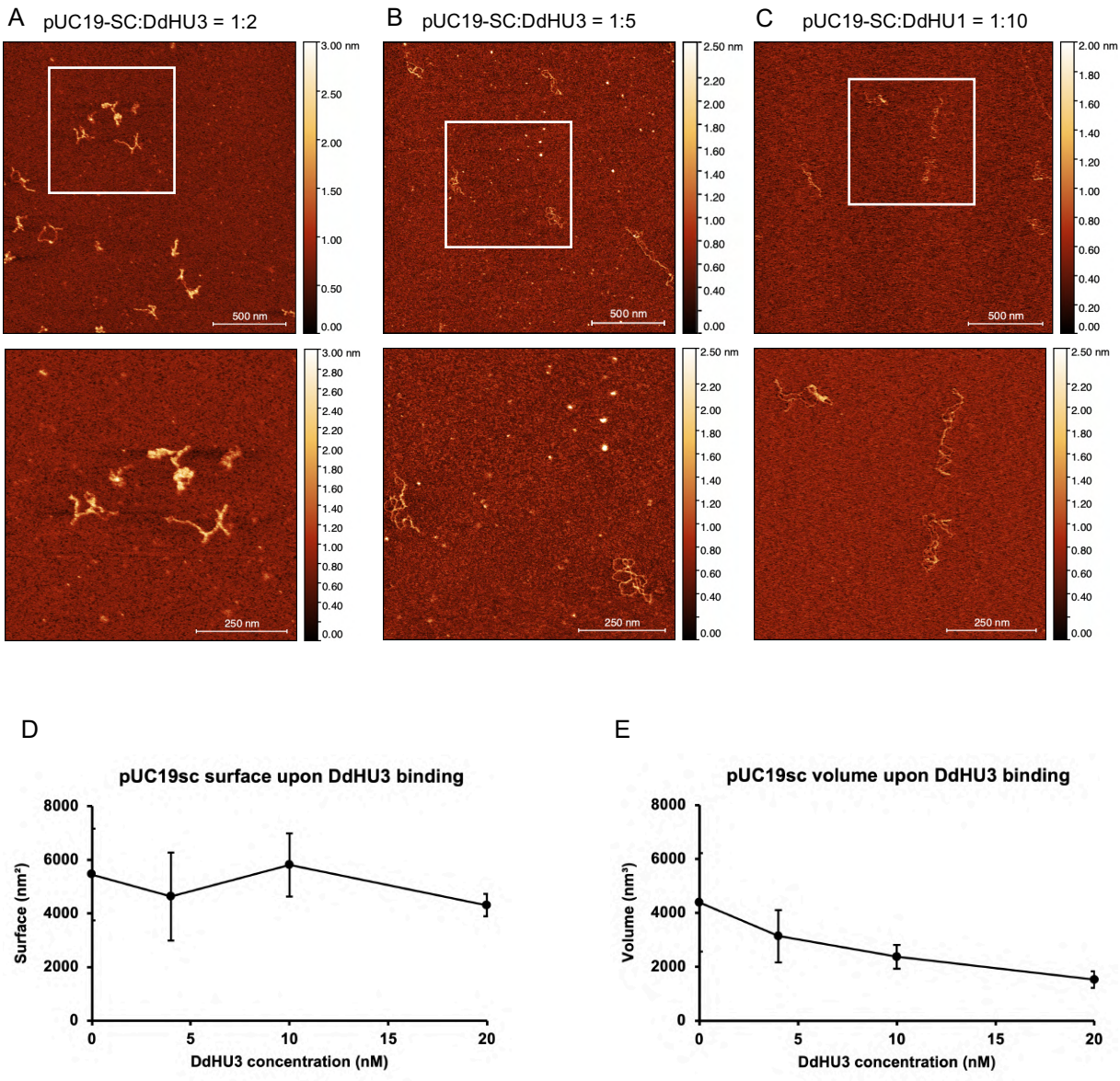

Figure 65. AFM imaging of DdHU3 bound to supercoiled pUC19 plasmid DNA. A-C) AFM images of 2 nM of supercoiled pUC19 incubated with increasing concentrations of DdHU3 for a plasmid-to-DdHU3 molar ratio of 1:2 (**A**), 1:5 (**B**) or 1:10 (**C**). Upper panels correspond to 2 µm^2 areas, in which a zone of 1 µm^2 area is delimited by a white square. Lower panels correspond to the physical magnification of the white boxed 1 µm^2 areas in the

upper panels. The z-scale bar is shown as a colour gradient to indicate the distribution of height in the images. Scale bar corresponds to 500 nm in the upper panels and to 250 nm in the lower panels. **D-E**) Graphs illustrating the mean surface (**D**) and the mean volume (**E**) of individual DdHU3-pUC19-SC complexes as a function of the protein concentration. Each data point represent the mean value for a given protein concentration and the error bars correspond to the 95% confidence interval, with n=37 for 5 nM of DdHU3, n=14 for 10 nM of DdHU3 and n=5 for 20 nM of DdHU3.

In contrast with DrHU and DdHU1, even at high concentrations of DdHU3, it was difficult to clearly asses the presence of bound protein on the supercoiled pUC19 molecules. Although DdHU3-bound pUC19 seemed condensed at a low molar ratio of 1:2, this effect was not perceived at higher molar ratios of 1:5 and 1:10. Based on these first images, DdHU3 does not seem to be able to polymerize along DNA like DrHU or to completely cover the supercoiled plasmid like DdHU1. Moreover, no specific well-ordered DdHU3-pUC19 assemblies were observed regardless of the protein concentration. Despite these qualitative visual observations, the surface and volume values extracted from this limited set of AFM images suggest that DdHU3 may have an effect on plasmid compaction, as we measured a steady decrease in the mean volume of the protein-DNA complexes when increasing DdHU3 concentration. Additional experiments will have to be performed to confirm these preliminary results, which unlike the DrHU and DdHU1 have not been repeated several times.

III. Structure and DNA-binding properties of *D. radiodurans* DdrC

In *D. radiodurans*, the response to DNA damaging agents such as ionizing radiation, UV-light or desiccation is mediated by the radiation-desiccation response mechanism that induces the over-expression of several genes involved in DNA repair (Blanchard et al., 2017; de Groot et al., 2019; Tanaka et al., 2004). Four of the five most up-regulated genes in response to such stress are *Deinococcus*-specific DNA-binding proteins called the DNA-damage response (Ddr) proteins DdrA, DdrB, DdrC, DdrD (Tanaka et al., 2004). While DdrA and DdrB were identified as parts of the ssDNA end-protection system, the function of DdrC in irradiated *D. radiodurans* cells remains elusive, mostly because of its pleiotropic activities upon DNA binding (Bouthier de la Tour et al., 2011, 2017; Harris et al., 2004). Moreover, DdrC is quickly recruited to the nucleoid following irradiation and could thus be involved in the genome organization in this specific context (Bouthier de la Tour et al., 2017).

To gain insight into the functions that DdrC may exert in *D. radiodurans* after irradiation, we aimed to solve its three-dimensional structure by X-ray crystallography and characterize its binding to DNA as well as its possible effect on plasmid DNA conformation by means of diverse methods such as fluorescence polarization (FP), molecular dynamics (MD) simulations and atomic force microscopy (AFM). The following article, which will be submitted to a peer-reviewed journal in the near future, describes our results and notably the structure of DdrC solved *de novo* by single-wavelength anomalous dispersion (SAD) and the biochemical and biophysical studies of the DNA binding properties of DdrC.

The native and SeMet-derivatized DdrC were purified and crystallized (Fig 66) by myself and J. Timmins, respectively. I collected the Se-SAD and native diffraction datasets that were initially processed by J.-P. Colletier, who assisted me in structure determination. A Se-SAD dataset collected on crystals of DdrC-SeMet allowed the determination of the selenomethionine-variant structure at 2.5 Å resolution. This structure was later used as a search model to elucidate the structure of the native DdrC by molecular replacement, which gave a final model of the structure at 2.8 Å resolution. I then refined this structure using Coot and Refmac5.

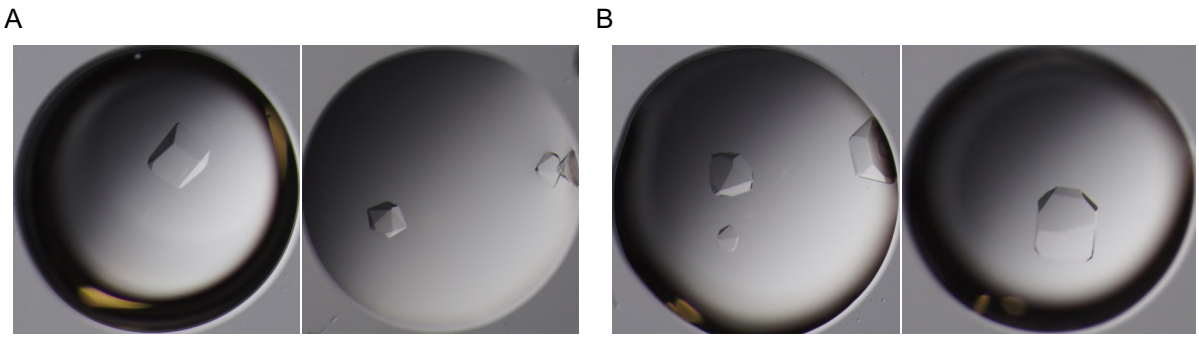

Figure 66. Crystals of DdrC-SeMet and DdrC obtained by the hanging-drop vapor diffusion method. A) DdrC-SeMet crystals in 2 µl crystallization drops, grown at 20°C in 0.1 M Tris pH 8.5, 1.4 ammonium sulfate (left) or in 0.1 M Bicine pH 9.5, 1.6 ammonium sulfate (right). **B**) DdrC crystals in 2 µl crystallization drops, grown at 20°C in 0.1 M Tris pH 8.0, 1.4 (left) or 1.6 M (right) ammonium sulfate.

The study of DdrC oligomeric state in solution by SEC-MALLS and AUC was carried out in collaboration with the PAOL platform, which is part of the ISBG Biophysics platform. To characterize the DNA binding properties of DdrC, I performed the FP assays and built the model of DdrC binding two dsDNA duplexes that was later used for MD simulations. J. Timmins designed DdrC mutants that were produced and characterized by S. De Bonis using FP assays. I acquired the atomic force microscopy images with the help of J.-M. Teulon, after which I extracted the surface and volume values of each individual DdrC-plasmid assemblies from the 2 µm² images. The MD simulations were performed by our collaborators in Nancy (C. Hognon, F. Dehez and A. Monari) and the topoisomerase assay to study the effect of DdrC on the plasmid topology was performed by our collaborator in Paris, C. Bouthier de la Tour.

Structural and functional characterization of DdrC, a novel DNA damage-induced nucleoid associated protein involved in DNA compaction

Anne-Sophie Banneville[1], Claire Bouthier de la Tour[2], Salvatore De Bonis[1], Cécilia Hognon[3], Jacques-Philippe Colletier[1], Jean-Marie Teulon[1], Aline Le Roy[1], Jean-Luc Pellequer[1], Antonio Monari[3,4], François Dehez[3], Fabrice Confalonieri[2], Pascale Servant[2] and Joanna Timmins[1*]

[1] Univ. Grenoble Alpes, CEA, CNRS, IBS, F-38000 Grenoble, France
[2] Université Paris-Saclay, CEA, CNRS, Institute for Integrative Biology of the Cell (I2BC), 91198, Gif-sur-Yvette, France
[3] LPCT, UMR 7019, Université de Lorraine, CNRS, Vandœuvre-lès-Nancy, France
[4] Université de Paris, CNRS, Itodys, F 75006 Paris, France

* To whom correspondence should be addressed. Tel: +33 (0)4 57 42 86 78; Email: joanna.timmins@ibs.fr

ABSTRACT

Deinococcus radiodurans is a spherical bacterium well-known for its outstanding resistance to DNA-damaging agents. Exposure to such agents leads to drastic changes in the transcriptome of *D. radiodurans*. In particular, four *Deinococcus*-specific genes, known as DNA Damage Response genes, are strongly up-regulated and have been shown to contribute to the resistance phenotype of *D. radiodurans*. One of these, DdrC, is expressed shortly after exposure to g-radiation and is rapidly recruited to the nucleoid. *In vitro*, DdrC has been shown to compact circular DNA, circularize linear DNA, anneal complementary DNA strands and protect DNA from nucleases. To shed light on the possible functions of DdrC in *D. radiodurans*, we determined the crystal structure of the domain-swapped DdrC dimer at a resolution of 2.8 Å and further characterized its DNA binding and compaction properties. Notably, we show that DdrC bears two asymmetric DNA binding sites located on either side of the dimer and can modulate the topology and level of compaction of circular DNA. These findings suggest that DdrC may be a DNA damage-induced nucleoid-associated protein that enhances nucleoid compaction to limit the dispersion of the fragmented genome and facilitate DNA repair after exposure to severe DNA damaging conditions.

INTRODUCTION

Deinococcus radiodurans is a gram-positive spherical bacterium, highly resistant to DNA-damaging agents including ionizing radiation, UV-light, desiccation and reactive oxygen species (1). Several mechanisms have been proposed to contribute to the maintenance of proteome and genome integrity in this bacterium: (i) multiple anti-oxidant strategies including a high intracellular Mn/Fe ratio (2), (ii) efficient DNA repair systems (3, 4) and (iii) a highly compact nucleoid (5–7), which may limit dispersion of DNA fragments, thus easing DNA repair processes. Following exposure to ionizing radiation or desiccation, the transcriptome of *D. radiodurans* undergoes a drastic change with the up-regulation of many genes, several of which are involved in DNA repair (8). Interestingly, in *D.*

radiodurans, this up-regulation has been shown to involve an SOS-independent response system, the radiation-desiccation response (RDR) regulon that is negatively regulated at the transcriptional level under normal growth conditions by the transcriptional repressor, DdrO (9–13). DdrO binds to a conserved 17 bp palindromic sequence named the radiation-desiccation response motif (RDRM), located in the promoter regions of regulated genes (10, 14–16). Exposure of cells to radiation or desiccation leads to the activation of IrrE, a constitutively expressed metalloprotease, that cleaves DdrO leading to its inactivation, thereby relieving its negative control over gene expression (10, 16–20).

After exposure to radiation or desiccation, four of the most up-regulated genes in the RDR regulon are *ddrA*, *ddrB*, *ddrC* and *ddrD* (21). These DNA damage response proteins (Ddr) are DNA-binding proteins specific to *Deinococcus* species. After exposure to ionizing radiation, these proteins are rapidly recruited to the nucleoid where they perform distinct functions (8, 22). DdrA preferentially binds *in vitro* to 3' single-stranded DNA (ssDNA) ends, protecting them from degradation by exonucleases and has thus been proposed to be part of an end-protection system (23, 24). DdrB is an ssDNA-binding (SSB)-like protein that promotes single-strand annealing (SSA), thereby playing an important role in the assembly of small chromosomal fragments produced by exposure to high doses of g-radiation (25, 26). DdrB is also involved in plasmid transformation, through its SSA activity that enables the reconstitution of double-stranded DNA (dsDNA) plasmid after its internalization (26, 27). Recent studies have showed that DdrD is a ssDNA binding protein that likely contributes to genome reconstitution following exposure to irradiation (28).

DdrC is a 25 kDa DNA-binding protein that is highly overexpressed shortly after irradiation and is rapidly recruited to the nucleoid, where it has been proposed to interact with damaged DNA (8, 29). Interestingly, DdrC is distributed all over the nucleoid shortly after irradiation, but after 2 to 3 hours, it forms discrete foci located at the sites of septal closure in between the newly segregated chromosomes of *D. radiodurans* (29). *In vitro* assays have shown that DdrC binds both ss- and dsDNA, with a preference for ssDNA. This protein exerts many activities upon DNA-binding, such as compaction of circular DNA, circularization of linear DNA, annealing of complementary DNA strands and protection of DNA from nucleases. These pleiotropic activities suggest that DdrC may play a role in the repair of radiation-induced DNA damage by preventing the dispersion of DNA fragments and participating in single-strand annealing.

To shed further light on the possible functions of *D. radiodurans* DdrC in the response to DNA damage, we here focused on elucidating its three-dimensional crystal structure and on characterizing its DNA binding properties using a combination of biochemical, biophysical and computational approaches. In the absence of any structures of DdrC homologues, we solved its structure *de novo* by use of the single-wavelength anomalous dispersion method (SAD). The structure reveals that DdrC is a largely a-helical protein, composed of an N-terminal winged helix-turn-helix (wHTH) motif and a C-terminal four-helix bundle, that folds as a domain-swapped dimer. We reveal that DdrC possesses two asymmetric DNA binding sites, one on either side of the dimer formed by motifs from both its N- and C-terminal domains.

We also demonstrate that DdrC can modify the topology and induce a strong compaction of circular plasmid DNA in a concentration-dependent manner. Together these findings indicate that DdrC may be a novel DNA damage-induced nucleoid-associated protein (NAP) that is recruited to the nucleoid in response to irradiation to modulate the extent of compaction of the genome and facilitate DNA repair processes.

MATERIAL AND METHODS

Expression and purification of DdrC, DdrC-SeMet and mutant DdrCs

The *ddrC* gene (A2G07_003810) was amplified from *D. radiodurans* genomic DNA by PCR and cloned into pProExHtB (EMBL) expression vector for expression with a cleavable N-terminal His-tag. DdrC was expressed in *E. coli* BL21(DE3) cells grown in LB supplemented with 100 $\mu g.ml^{-1}$ ampicillin. DdrC point mutants M1 to M9 were prepared by site-directed mutagenesis using the Agilent QuickChange mutagenesis protocol, the wild-type DdrC clone in pProexHtB as a template and the oligonucleotides listed in Supp. Table S1. Mutant M10 corresponding to the N-terminally truncated DdrC missing residues 1 to 16 was PCR amplified and cloned by restriction digestion into pProexHtB (Supp. Table S1). Expression of wild-type (WT) and mutant DdrC was induced with 1 mM IPTG at 28°C for 4 hours. Cells were pelleted by centrifugation and resuspended in 40 ml lysis buffer composed of 50 mM Tris-HCl pH 7.5, 0.8 M NaCl, 5 mM $MgCl_2$, 10% (w/v) sucrose, 0.01% (v/v) triton X-100, 1 $\mu g.ml^{-1}$ DNaseI, 1 $\mu g.ml^{-1}$ lysozyme and a tablet of complete EDTA-free Protease Inhibitor Cocktail (Roche). Cells were lysed by sonication on ice for 3 min and centrifuged at 48,300 x g for 30 min. The cleared supernatant was loaded on a 5 ml HisTrap FF nickel affinity column (GE Healthcare), pre-equilibrated with buffer A (50 mM Tris-HCl pH 7.5, 0.8 M NaCl, 1 mM $MgCl_2$). After washing the column with buffer A, buffer A supplemented with 25 mM imidazole and buffer A supplemented with 50 mM imidazole, DdrC was eluted with a linear gradient of imidazole from 50 to 500 mM imidazole in buffer A. The fractions containing DdrC were pooled and dialyzed overnight at 4°C against buffer A supplemented with 5% (v/v) glycerol in the presence of 1:20 (w/w) TEV protease to cleave the His-tag. The His-tag itself and traces of uncleaved protein were subsequently removed by nickel affinity chromatography on 1 ml Ni-Sepharose 6 FF resin (GE Healthcare) pre-equilibrated in buffer A. The cleaved DdrC was recovered in the flow-through and in a 25 mM imidazole wash, and was concentrated prior to size exclusion chromatography on a Superdex 75 10/300 GL column (GE Healthcare) pre-equilibrated with buffer B (20 mM Tris-HCl pH 7.5, 200 mM NaCl, 5% (v/v) glycerol). Finally, DdrC was concentrated and stored at -80°C. WT DdrC was concentrated to a final concentration of 24 $mg.ml^{-1}$, while mutants were concentrated to 2 to 16 $mg.ml^{-1}$. For the AFM experiments, a batch of DdrC was produced following the protocol described previously, but without glycerol in the purification buffers. This 'glycerol-free' batch was stored at a concentration of 16 $mg.ml^{-1}$ at -80° C. The selenomethionine substituted DdrC (SeMet-DdrC) was produced in *E. coli* BL21(DE3) cells grown at 37°C in minimal M9 medium

supplemented with 100 µg.ml^{-1} ampicillin using a modified version of the metabolic inhibition protocol described previously (30, 31). Expression was induced overnight with 1 mM IPTG at 28°C. The SeMet-DdrC protein was then purified as described for native DdrC and was stored at 20 mg.ml^{-1} in buffer B at -80°C.

Crystallization of DdrC and SeMet-DdrC

Initial crystallization hits were obtained by robotic screening at the HTX lab (EMBL) using nanoliter sitting drops at 20°C (32). Crystals grew after 2 to 3 months in conditions containing 1.6 M ammonium sulfate and 0.1 M Tris pH 8.0 or Bicine pH 9.0. Manual crystallization screens were then performed using the hanging-drop vapor-diffusion method in 24-well plates at 20°C. Briefly, 1 µl protein solution (at 24 mg.ml^{-1} for native DdrC or 20 mg.ml^{-1} for SeMet-DdrC) was mixed with 1 µl mother liquor solution and equilibrated against 500 µl mother liquor solution. Crystallization conditions were refined using 0.1 M Tris pH 8.0 to pH 8.5 or Bicine pH 9.0 to pH 9.5 and 1.0 M to 2.1 M ammonium sulfate. Hexagonal bipyramidal or triangular prism-shaped crystals of DdrC and SeMet-DdrC appeared after 3-4 weeks in all conditions with ammonium sulfate below 1.9 M. Crystals were transferred to mother liquor containing 20% (v/v) glycerol as a cryoprotectant and flash-cooled in liquid nitrogen before data collection. The best diffracting crystals were obtained in 0.1 M Tris pH 8.0, 1.2 M ammonium sulfate for native DdrC and 0.1 M Tris pH 8.5, 1.9 M ammonium sulfate for SeMet-DdrC.

Data collection and structure determination

A selenium single-wavelength anomalous diffraction (Se-SAD) dataset was collected on a SeMet-DdrC crystal at 100 K on beamline ID23-1 at the European Synchrotron Radiation Facility (Grenoble, France), on a Pilatus 6M detector (Dectris). A total of 500 images were collected at a wavelength of 0.978 Å with 100 ms exposure and an oscillation angle of 0.15° per frame. For the native DdrC, data collection was performed at 100 K on beamline Proxima-2A at the SOLEIL (Paris, France), on a Eiger 9 M detector (Dectris). A total of 3600 images were collected at a wavelength of 0.980 Å with 25 ms exposure and an oscillation angle of 0.1° per frame. Data were integrated, indexed and scaled with XDS (33). The space group was $P3_221$ for both the SeMet variant and the native DdrC, with unit cell parameters of a = 111.36 Å, b = 111.36 Å, c = 104.88 Å and a = 111.28 Å, b = 111.28 Å, c = 104.71 Å respectively (Table 1). The Se-SAD dataset was processed with the CRANK2 suite (34). Briefly, SHELXC (35) was used to calculate structure factor estimates from merged intensities, after what heavy-atom search was performed using SHELXD (35) and a resolution cutoff of 3.69 Å. Two selenium sites were found. The substructure refinement and phasing were performed with REFMAC5 (36), then experimental phases were improved using density modification with PARROT (37), which enabled automatic determination of the correct hand. Automatic model building and structure refinement were performed with Buccaneer (38, 39) and REFMAC5. Refinement converged at an R_{work} and R_{free} of 34.3 % and 40.0 %, respectively. The native DdrC structure was solved by molecular replacement with Phaser MR (40) using the SeMet-

DdrC structure as a search model to a resolution of 2.8 Å (Table 1). The DdrC structure was then refined using iterative cycles of manual building in Coot (41) and refinement in PHENIX (42). The final R_{work} and R_{free} are 26.1 % and 31.1 % respectively. The structure of DdrC was validated in MolProbity (43) with only 3 residues in the outliers region of the Ramachandran plot (Table 1) and deposited in the Protein Data Bank with accession number ####. Analysis of dimerization interface and crystal contacts was carried out using PISA (44). Electrostatic surfaces (at pH 7.5 and 200 mM NaCl) were produced by APBS (45) from structures protonated by PDB2PQR (46) after structure-based titration of protonatable residues using PROPKA (47).

DdrC structure prediction

The sequence of DdrC was submitted to AlphaFold2 (48) via the Colaboratory service from Google Research(https://colab.research.google.com/github/sokrypton/ColabFold/blob/main/beta/AlphaFold2_advanced.ipynb) and to RosettaFold (49) (https://robetta.bakerlab.org). Of note, the mmseq2 method (50, 51) was employed for the multiple-sequence alignment. The first five models predicted by each program were overlaid using the *align* tool in PyMOL (52) with overall root mean square deviation (rmsd) values of 0.312 to 0.498 Å for RosettaFold and of 0.266 to 0.735 Å for AlphaFold2. Nonetheless, attempts to phase the native crystallographic data by molecular replacement with Phaser (40) using the best-ranked model from AlphaFold2 in its entirety as a search model, and looking for either one or two copies of the protein, failed. Similar results were obtained when using isolated N- and C-terminal domains as search models, asking for placement of either one or two copies of each, or just one or two copies of the more correctly predicted C-terminal domain. Regardless of the strategy, no solution was obtained that yielded R_{free}/R_{work} values indicative of success after reciprocal space refinement using Refmac5 (10 cycles) (53). We furthermore subjected the top three molecular replacement solutions in each case to the buccaneer pipeline in CCP4 (38) with the aim to verify if automatic model-building and refinement would have been possible based on these, but once again this was unsuccessful. Thus, neither the prediction from AlphaFold2 nor that from RosettaFold would have allowed successful phasing by molecular replacement. Finally, we attempted to predict the dimer structure of DdrC using AlphaFold2, yet none of the predicted dimer models came close to the experimentally determined structure of DdrC, likely due to the bias induced by prediction of the same monomeric structure for the two monomers in the dimer.

Preparation of supercoiled plasmid DNA

Plasmid pUC19 DNA was amplified in DH5α *E. coli* cells grown in LB with 100 $\mu g.ml^{-1}$ ampicillin. The supercoiled pUC19 (pUC19sc) was extracted from 100 ml overnight cultures using the NucleoBond Xtra Midi kit (Macherey-Nagel) following manufacturer's instructions. The final DNA resuspension was performed in 50 µl milli-Q water, yielding pUC19sc at a concentration of 1.5 $\mu g.\mu l^{-1}$ (equivalent to 900 nM). The stock solution was stored at -20°C.

Atomic Force Microscopy

pUC19sc was diluted in milli-Q water to a final concentration of 0.5 nM for all samples. 'Glycerol-free' DdrC was diluted in milli-Q water to a final concentration of either 2 nM, 5 nM, 10 nM or 20 nM. For the protein-DNA samples, pUC19sc was incubated with DdrC for 30 min at 30°C before sample deposition on the mica sheet. Topographic data were acquired by a multimode 8 microscope equipped with a Nanoscope V controller (Bruker, Santa Barbara, USA). Before use, a freshly cleaved V-1 grade muscovite mica (Nanoandmore, Wetzlar, Germany) sheet was pre-treated with 10 µl 5 mM $NiCl_2$ and dried under nitrogen gas. 5 µl of each sample solution was deposited on the mica, after which the mica was incubated for 2 min, then dried under a gentle stream of nitrogen gas. All imaging was conducted with the PeakForce Tapping mode and ScanAsyst mode at a rate of ~1.0 Hz; the resolution was set to either 512 or 1024 pixels per scan line. The SCANASYST-AIRHR cantilever was employed with nominal values of k = 0.4 N m^{-1}, Fq = 130 kHz and tip radius = 2 nm (Bruker probes, Camarillo, CA, USA). Whenever the ScanAsyst mode was applied, a semi-manual control was on during the imaging procedure to manually adjust the set point and gain in order to reduce the tip-sample interactions to the minimum. The ramp size was kept constant at 150 nm. Processing of raw AFM images was systematically performed using the Gwyddion software (54). First, raw AFM images were flattened using a plane fit to the first order, then the flattening effect was further enhanced by applying the "line flattening" tool of Gwyddion with a polynomial of order 3, followed by exclusion of all imaged objects whose height values exceeded the given threshold (usually 0.1 – 0.5 nm). When necessary, stripe noises were reduced using the 'Remove Scars' function in Gwyddion. Measurements of the surface areas of individual assemblies were performed on these processed AFM images corresponding to 2 µm² or 1 µm² areas. A classical height threshold was applied on the image to select as many individual assemblies as possible. Assemblies that either touched the border of the image or were not clearly identifiable due to unresolved overlapping (three or more plasmids in a single selection) were excluded from the statistical analysis. The surface areas of the selected assemblies were extracted using the grain distribution function in Gwyddion. To discriminate between the condensed or more opened assemblies, a surface area threshold of 6000 nm² to 9500 nm² was applied to each image depending on their respective height threshold used for selection. Histograms and scatter-plots representing the fraction of condensed assemblies as a function of DdrC concentration were then plotted using the GraphPad Prism 8 software.

Fluorescence polarization

Equilibrium fluorescence polarization DNA binding assays were performed on a Clariostar (BMG Labtech) microplate reader, fitted with polarization filters. Reactions were performed in black 386-well medium-binding plates (Greiner). 0 to 100 µM DdrC (dimer) were titrated into 10 nM 5'-FAM labelled dsDNA 20 mer or 50 mer substrates (Table S2) in binding buffer composed of 20 mM Tris pH 8.0, 100

mM NaCl, 1 mM $MgCl_2$ and 0.2 $mg.ml^{-1}$ BSA. Reactions were performed in a final volume of 40 µl at room temperature. After subtracting the polarization values obtained for DNA alone, the mean data from at least three independent measurements were fitted to one of the following equations using GraphPad Prism 8: (a) a one-site specific binding model with Hill coefficient ($Y = \frac{B_{max} \times X}{K_D + X}$), or (b) a two-site specific binding model ($Y = \frac{B_{max(Hi)} \times X}{K_{D(Hi)} + X} + \frac{B_{max(Lo)} \times X}{K_{D(Lo)} + X}$), where Y is the difference between the anisotropy of completely bound and completely free oligo, B_{max} is the maximal polarization signal, X is the DdrC concentration, K_D is the equilibrium dissociation constant and h is the Hill slope.

Analysis of plasmid topology by 1D and 2D gel electrophoresis

200 ng of relaxed DNA (relaxed pHOT-1 DNA, 2.4 kb) (Topogen) was incubated for 15 min at 4°C in the absence or presence of increasing concentrations of DdrC in 25 µl of buffer composed of 40 mM Tris-HCl pH7.8, 5 mM $MgCl_2$, 1.5 mM DTT, 50 mM NaCl, 12% (v/v) glycerol. 10 U of topoisomerase I from wheat germ (Sigma) was then added and the samples were incubated 30 min at 30°C. Reactions were stopped by addition of a mix of 1 $mg.ml^{-1}$ Proteinase K and 0.5% (w/v) SDS followed by an incubation at 37°C for 10 min. 7 µl 6X DNA Loading Dye were then added to the reactions and 10 µl of the reaction mixtures were separated by gel electrophoresis at 4°C on 1.2% agarose gels in TEP buffer (36 mM Tris-HCl pH 7.8, 30 mM NaH_2PO4, 1 mM EDTA) at 4.3V/cm for 4h. DNA topoisomers were revealed after ethidium bromide staining. For 2D gel electrophoresis, 20 µl of the remaining reaction mixtures were loaded on a 1.2% agarose gel. The first dimension was performed as described above. The second dimension was run in a perpendicular direction at 1V/cm for 16h at room temperature in TEP buffer containing 3 $\mu g.ml^{-1}$ chloroquine, a DNA intercalator that unwinds the double helix of a closed circular DNA, resulting in a loss of negative supercoils and formation of positive supercoils. The chloroquine was then eliminated from the gel by incubation in H_2O for 3h and the distribution of topoisomers was visualized after ethidium bromide staining.

Size-exclusion chromatography coupled to multi-angle laser light scattering

Size exclusion chromatography (SEC) combined with multi-angle laser light scattering (MALLS), dynamic light scattering (DLS) and refractometry (RI) experiments were performed with a Superdex 200 10/300 GL size exclusion column equilibrated with Buffer C (20 mM Tris pH 7.5 and 200 mM NaCl) at room temperature. 20 µl DdrC at 16 $mg.ml^{-1}$ was injected onto the column at 0.5 ml min^{-1}. On-line MALLS detection was performed with a miniDAWN-TREOS detector (Wyatt), DLS was recorded with a DynaPro Nanostar and RI measurements were performed with an Optilab eEX system (Wyatt).

Analytical ultracentrifugation

Sedimentation velocity experiments were performed at 42,000 rpm and 4°C, on a Beckman XLI analytical ultracentrifuge using a AN-60 Ti rotor (Beckman Coulter, Brea, USA) and double-sector cells

with optical path lengths of 12 and 1.5 mm equipped with sapphire windows (Nanolytics, Potsdam, DE). Buffer C was used as a reference. Measurements were made on 1 $mg.ml^{-1}$, 4 $mg.ml^{-1}$ and 8 $mg.ml^{-1}$ DdrC using absorbance at 280 nm and interference optics. Data were processed with the REDATE software (https://www.utsouthwestern.edu/labs/mbr/software/) and the parameters were determined with SEDNTERP and SEDFIT (55). Analysis of sedimentation coefficients and molecular weights were performed using SEDFIT (55) and GUSSI (56).

Molecular dynamics simulations

The domain-swapped DdrC dimer from the asymmetric unit was used as a starting model for all-atoms MD simulations after building the missing loops between helices α7 and α8 in chains A and B using the loop modelling tool in Modeller (57). Two MD simulations were performed on the apo-DdrC structure to verify the stability of the dimer and evaluate the overall dynamics of DdrC. For protein-DNA assemblies, two 25 bp DNA duplexes of random sequence were manually positioned on either side of the DdrC dimer following the positively charged grooves so as to minimize steric clashes between the DNA and protein side chains. DdrC-bound to two DNA duplexes were then used for five independent MD simulations to enhance the statistical sampling. All the macromolecular systems were explicitly hydrated in boxes of 42,000 water molecules containing 22 sodium ions to ensure the overall electrical neutrality of the unit cells. Water was represented by means of the TIP3P water model (58), whereas protein, DNA and ions were described using the amberf99 force field (59) including the bsc1 corrections for DNA (60). All setups were generated using the tleap facility of Amber Tools (61, 62). Molecular rendering and analyses were done using VMD (63). MD simulations were performed using the massively parallel code NAMD (64). All trajectories were generated in the isobaric-isothermal ensemble, at 300 K under 1 atm using Langevin dynamics (65) (damping coefficient 1 ps^{-1}) and the Langevin piston method (66), respectively. Long-range electrostatic interactions were accounted for by means of the Particle Mesh Ewald (PME) algorithm (67). The rattle algorithm was used to constrain lengths of covalent bonds involving hydrogen atoms to their equilibrium value (68). The classical equations of motion were integrated through a time step of 4 fs using the hydrogen mass repartition strategy (69). Each molecular assay was thermalized during 15 ns, followed by 500 ns of production.

RESULTS

***De novo* phasing of the structure of DdrC - an unusual asymmetric domain-swapped dimer**

DdrC is a protein for which no known structural homologues have been identified. We therefore solved the structure of *D. radiodurans* DdrC *de novo* by use of the single-wavelength anomalous dispersion method (SAD). We determined the structure of a selenomethionine variant of DdrC (SeMet-DdrC) by SAD to a resolution of 2.5 Å, and then solved the structure of native DdrC by molecular replacement using the SeMet-DdrC as a search model and refined it to 2.8 Å resolution (Table 1). The asymmetric

unit contains a DdrC dimer composed of chains A and B. Almost all residues are visible in the electron density, notwithstanding 3 terminal residues missing at both the N- (residues 1 to 3) and C-termini (residues 229 to 231) and a highly disordered loop between helices α7 and α8 (Fig. 1A and B), corresponding to residues 167-173 and 161-169 in chains A and B, respectively.

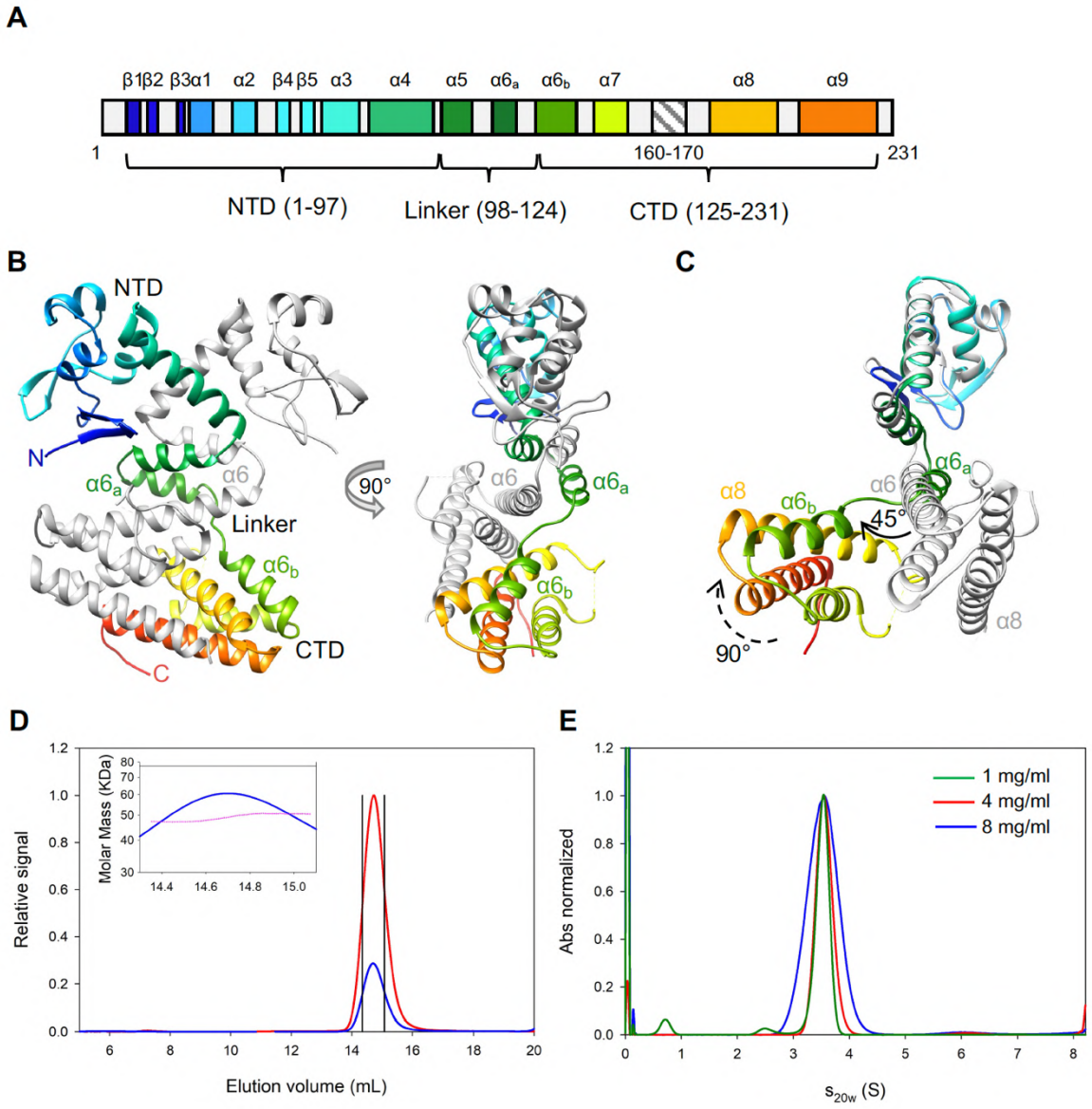

Figure 1. DdrC is an unusual domain-swapped dimer composed of two domains. (**A**) Secondary structure organization of DdrC (chain B), colored from blue (N-terminus) to orange (C-terminus). Residues 160 to 170 were not visible in the structure and are thus expected to form a disordered loop. NTD: N-terminal domain, CTD: C-terminal domain. (**B**) Front and side views of the DdrC dimer, with monomer A colored in gray and monomer B colored in rainbow colors from blue (N-terminus) to red (C-terminus). The side view of DdrC highlights the asymmetry between the two faces of the dimer. (**C**) Side view of the overlay of the two DdrC chains using the NTD as a reference. Chains A and B are colored as in (B). The $\alpha6_a$ and $\alpha6_b$ helices in chain B correspond to a distorted conformation of the long α6 helix of chain A, probably to accommodate the domain swapping of the two monomers. (**D**) Size-exclusion chromatogram obtained from SEC-MALLS analysis of DdrC. The blue line corresponds to the refractive index and the red line to the light scattering. The inset represents a close-up view of

the DdrC refractive index peak (defined by black lines), illustrating molar mass points in pink obtained along the peak. The mean mass of DdrC derived from this data was 49.1 kDa, corresponding to a dimer. (**E**) Distribution of sedimentation coefficients obtained by analytical ultracentrifugation analysis of DdrC at three concentrations: 1 $mg.ml^{-1}$ (green), 4 $mg.ml^{-1}$ (red) and 8 $mg.ml^{-1}$ (blue). The normalized absorption is plotted versus $S_{20,w}$, the sedimentation coefficient corrected to 20°C in pure water. A majority of the sample (94 ± 4%) was found in a peak at a $S_{20,w}$ value of 3.55S with a mean mass of 43.5 ± 3.5 kDa from Non-Interacting Species analysis, corresponding here again to a dimer.

Recently, it was shown that use of artificial intelligence in programs such as AlphaFold2 (48) or RosettaFold (49) could enable prediction of protein structures to an accuracy high enough to allow phasing of crystallographic data by molecular replacement. To determine whether this would have been possible in the case of DdrC, we submitted the sequence of DdrC to the two programs and then attempted phasing of the native crystallographic data by molecular replacement using the best-ranked model from AlphaFold2 in its entirety or as isolated N- and C-terminal domains as a search model (see Materials and Methods for details; Supp. Table S3 and Fig. S1). Regardless of the strategy, no solution was obtained that yielded R_{free}/R_{work} values indicative of success and when these putative molecular replacement solutions were submitted to automatic model-building and refinement programs, there again, they failed to produce a reliable solution. In the case of DdrC at least, experimental phasing thus turned out to be the only route towards structure elucidation.

The asymmetric unit contains a domain-swapped homo-dimer of DdrC, in which each monomer buries on average 3214 ± 24 $Å^2$, corresponding to 36% of its surface area, within the dimer interface that is stabilized by 16 H-bonds and 16 salt bridges (44). Each monomer of DdrC is composed of two domains connected by a linker region (Fig. 1A and B). The N-terminal domain (NTD; residues 1-97) comprises five β-strands and four α-helices adopting a classic winged-helix-turn-helix (wHTH) motif (β3 to β5 and α1 to α3) preceded by a β-hairpin (β1 and β2) and followed by an α-helix (α4) that provides the first contacts for dimerization. The C-terminal domain (CTD; residues 125-231), which is domain-swapped between the two monomers, is composed of four α-helices organized in a four-helix bundle motif ($\alpha6_b$ to α9). The two domains are connected by a linker region comprising residues 98-124 that encompass helix α5 and the N-terminal region of α6 ($\alpha6_a$).

Although DdrC is homo-dimeric, there is a remarkable asymmetry between the two chains, which is rarely observed in domain-swapped dimers (Fig. 1C and Supp. Table S3). The two monomers of DdrC display distinct conformations that do not overlay when the full polypeptide is considered (rmsd = 7.412 Å, Supp. Table S3, Fig. 1C). Yet, the folding of each of the two domains is conserved with the NTD, CTD and linker domains overlaying with rmsd values of 0.536, 0.870 and 4.569 Å, respectively (Supp. Table S3). In chain A, however, the first helix of the CTD (α6) is a long uninterrupted helix ranging from residues 110 to 136, while in chain B this helix is fragmented into two shorter helices ($\alpha6_a$ and $\alpha6_b$) separated by a 6-residue coil that positions $\alpha6_b$ at a 45° angle relative to $\alpha6_a$ helix, causing the CTD to adopt a very different orientation relative to the NTD. This disruption of the α6 helix in chain B is

essential to accommodate the constraints of the domain-swapping. Moreover, in chain B, the CTD undergoes a further 90° rotation along the longitudinal axis of $\alpha 6_b$ that positions the helical bundle on the opposite side of the α6 helix compared to chain A (Fig. 1C) and thereby allows chain B to wrap tightly around chain A, making contacts via the NTD, the linker region and the CTD (Fig. 1B). As a result, the two monomers adopt very distinct conformations and this asymmetry creates a marked difference in the two faces of the dimer (Fig. 1B).

A dimer of dimers was also observed by crystallographic symmetry in which two dimers face each other at a 93° angle (Supp. Fig. S2), thereby forming a putative tetramer, with a dimer-dimer interface covering 1044 $Å^2$, with 10 H-bonds and 10 salt bridges. We used size-exclusion chromatography coupled to multi-angle laser light scattering (SEC-MALLS) and analytical ultracentrifugation (AUC) to further characterize the quaternary structure of DdrC. Both techniques revealed that a large majority (>90%) of DdrC protein is in the form of dimers with a mass around 45 kDa (Fig. 1D and E). These measurements are in agreement with earlier chemical crosslinking studies that indicated that DdrC could indeed form dimers (29). No tetramers of DdrC were detected by SEC-MALLS and AUC, suggesting that the observed tetramers most likely result from crystal packing. The biological unit thus appears to be the domain-swapped homo-dimer observed in our crystal structure.

All-atom MD simulations of the DdrC homo-dimer confirmed that the dimer was stable throughout the simulation and that the asymmetry of the dimer was also maintained, indicating that this asymmetry observed in our crystal structure does not result from crystal contacts (Supp. Fig. S3). The CTD region, with the exception of the loop linking helices α7 and α8, and the dimer interface of DdrC are particularly stable. In the NTD, the loops and the wHTH motif exhibit some flexibility. Significant movements of the NTD with respect to the CTD were also observed allowing the wHTH of one monomer to come very close and even interact with the C-terminal four-helix bundle of the second monomer (Supp. Fig. S3).

DdrC-NTD contains a negatively charged wHTH motif

To gain insight into the potential function of DdrC, we performed a search for structural homologues of DdrC using the DALI server. The four-helix bundle in the CTD of DdrC is a very common structural motif found in diverse protein families and is thus not indicative of a particular function. The wHTH motif found in the NTD, on the other hand, has been identified as a DNA-binding motif in several proteins (70–72). The classic wHTH is a positively charged HTH motif followed by a β-hairpin, the "wing", and preceded by a short β-strand. The conserved motif is usually folded as "β-α-'turn'-α-β-'wing'-β". In most wHTH proteins, additional α-helices are packed next to the wHTH motif, usually preceding it in the sequence. In the usual DNA binding mechanism, the HTH part is inserted into the major groove of DNA while the "wing" of the β-hairpin inserts into the minor groove.

The NTD of DdrC exhibits a classic wHTH motif (β3-α1-α2-β4-β5), although the additional α-helix (α3) is located downstream of the wHTH motif in the sequence (Fig. 2A). The wHTH motif of DdrC is also preceded by a hairpin structure composed of β1 and β2. Surprisingly, the electrostatic surface potential of the NTD, calculated with the APBS program (45), indicates that the surface is mainly negatively charged, which would likely prevent DNA binding to this motif (Fig. 2B). A DALI search with the NTD alone confirmed the structural homology of DdrC NTD with other wHTH-containing proteins. The proteins with the highest Z-scores were the human Dachshund protein (PDB code 1L8R, Z score 7.0), the Dachshund-homology domain of human SKI protein (SKI-DHD, PDB code 1SBX, Z score 5.5) and *Bacillus subtilis* RacA (BsRacA, PDB code 5I44, Z score 4.9).

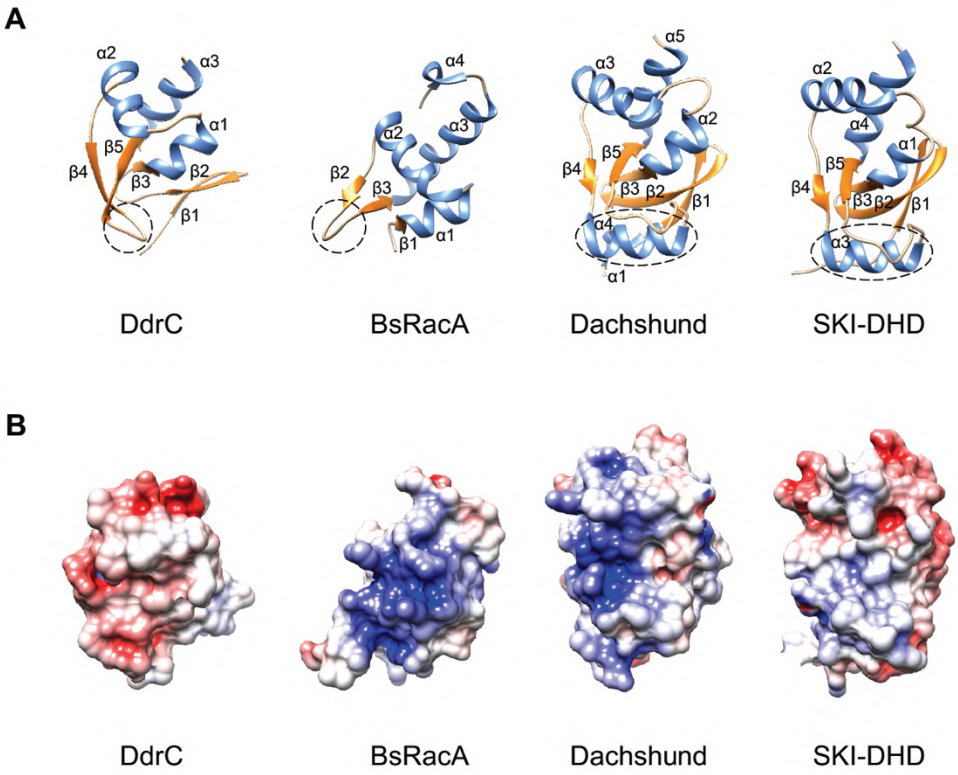

Figure 2. DdrC exhibits a classic yet negatively charged wHTH motif. (**A**) wHTH motifs of DdrC and structurally similar proteins, BsRacA (PDB code 5I44), Dachshund (PDB code 1L8R) and SKI-DHD (PDB code 1SBX). The proteins are colored based on their secondary structure, with α-helices in blue and β-sheets in orange. (**B**) DdrC, BsRacA, Dachshund and SKI-DHD are colored by electrostatic surface potential, as calculated by APBS. The color scale is the same for all proteins, ranging from -5 to +5 kT/e, with negative charges in red and positive charges in blue.

The human Dachshund protein (73) and the SKI-DHD domain (74) both of which are involved in transcriptional regulation are very similar to each other and display an unusual wHTH motif, which contains an α-helix inserted in the β-hairpin "wing" between β4 and β5 (β3-α2-α3-β4-**α4**-β5) with the adjacent α-helix located downstream in the sequence (Fig. 2A). As in the case of DdrC, their wHTH motifs are preceded by a β-hairpin structure composed of the two N-terminal β-strands. However,

contrary to DdrC, the wHTH motif of the Dachshund protein displays a positively charged surface, which could constitute a DNA-binding interface (73). BsRacA is a kinetochore-like chromosome-anchoring protein that possesses a more classic wHTH motif (β1-α1-α2-β2-β3) and is also positively charged (Fig. 2A and B). The crystal structure of BsRacA in complex with DNA showed that the positively charged wHTH motif is directly involved in DNA binding (75). Unlike Dachshund and BsRacA, the surface of the wHTH motif of SKI-DHD is rather neutral with some electronegative patches (Fig. 2B), and has been proposed to play a role in protein binding rather than in DNA binding (74). These observations suggest that the function of wHTH motifs as DNA-binding sites is more likely associated with their electrostatic surface potential than with their fold. Since the wHTH motif of DdrC exhibits a largely negatively charged surface, it is unlikely to play a direct role in DNA binding.

DdrC dimer possesses two distinct DNA binding sites

To identify a potential DNA binding site on DdrC, we analyzed the charges displayed at the surface of the DdrC dimer with the APBS program (Fig. 3A). A large positive groove involving mostly arginine residues contributed by the four α-helices of the CTD and α4-α5 of the NTD is present on both sides of the dimer, suggesting that DdrC could possess two distinct DNA binding sites. To test this hypothesis, we performed fluorescence polarization assays with fluorescein-labelled dsDNA oligonucleotides of either 20 (20d5'F) or 50 (50d5'F) base-pairs. DdrC was able to bind efficiently to both DNA substrates and in both cases, the best fit was obtained using the two-sites specific binding model (Fig. 3B and C). For the 20 mer DNA, 48% of the DNA was bound to the high affinity site with a K_D(Hi) of 59 nM and 52% of the DNA was bound to a second low affinity site with a K_D(Lo) of 5.43 µM (Table 2). In contrast, with the longer DNA substrate (50 mer), 60% of the DNA was bound to the high affinity site with a K_D(Hi) of 81 nM and 40% was bound to the lower affinity site with a K_D(Lo) of 22.23 µM (Table 2). These data clearly indicate that DdrC dimers possess two distinct DNA binding sites with different affinities for the DNA that can equally accommodate short DNA strands between 20 and 50 nucleotides long. However, binding of longer DNA fragments to the low affinity site appears to be less favorable.

Table 2. DNA binding constants of DdrC derived from fluorescence polarization measurements after fitting to a two-sites specific model.

DNA	Kd (Hi) µM (+SEM)	Kd (Lo) µM (+SEM)	% Hi affinity	R^2
20d5'F	0.059 ± 0.009	5.435 ± 0.906	48.01 ± 2.33	0.995
50d5'F	0.081 ± 0.014	22.232 ± 9.454	60.51 ± 2.97	0.982

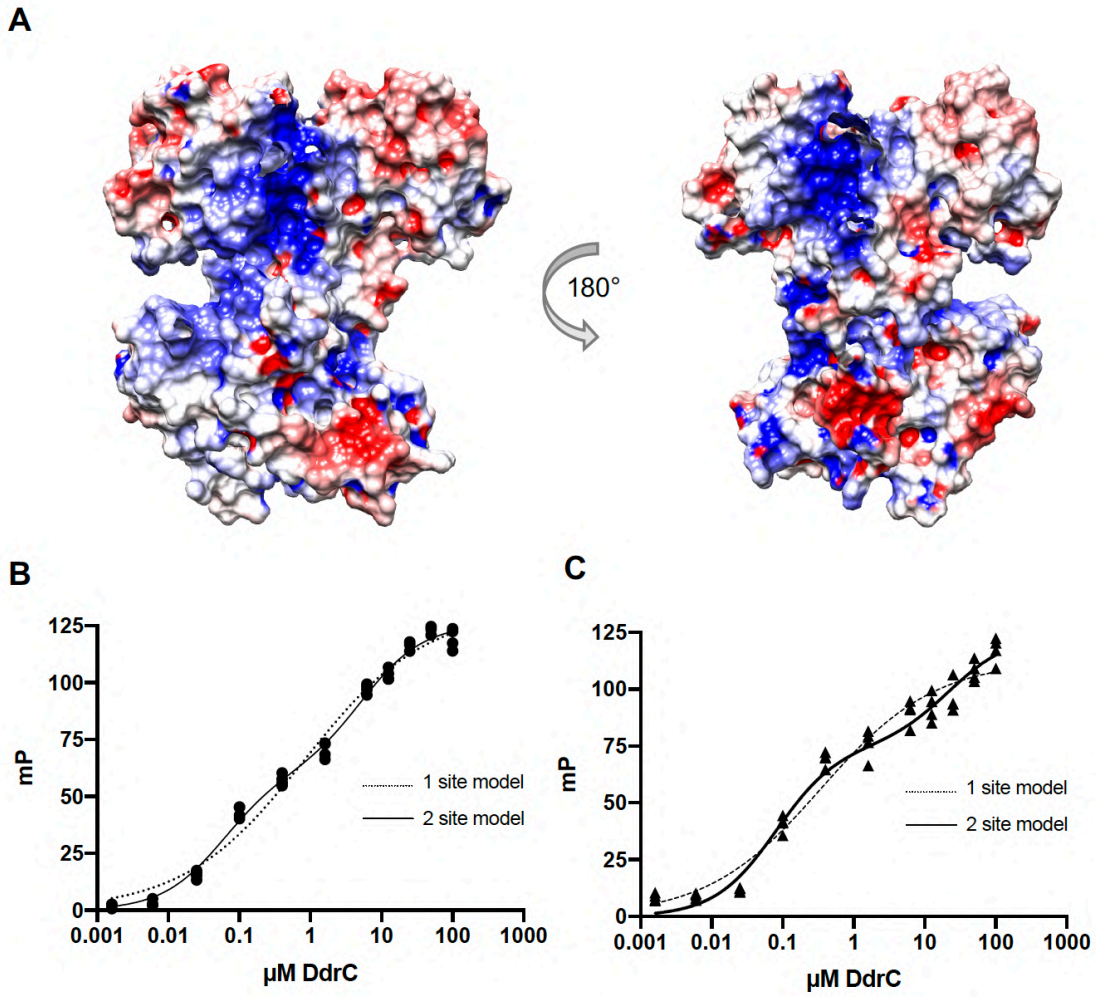

Figure 3. DdrC dimer bears two DNA-binding sites. (**A**) Depiction of the electrostatic surface potential of the DdrC dimer, as calculated by APBS. Positive and negative charges are colored in blue and red, respectively from -5 to +5 kT/e. (**B-C**) Fluorescence polarization measurements of 0 to 100 µM DdrC binding to 10 nM 5'-FAM-labelled dsDNA oligonucleotides of 20 bp (B) or 50 bp (C). The mean of the three individual polarization values recorded at each DdrC concentration, shown respectively as black spheres (B) or black triangles (C), were fitted to one of two models using Prism 8: one-site specific binding with Hill coefficient (dashed line) and two-sites specific binding (solid line).

Based on these observations, we built a model in which two 25 bp dsDNA fragments were bound to either face of the DdrC dimer (Fig. 4A). The DNA duplexes were positioned manually along the positively charged grooves of DdrC so as to minimize steric clashes and maintain good geometry. It is interesting to note that the 25 bp dsDNA stretches all the way across these grooves, but adopts a straight conformation on one side and a more bent conformation on the other side of the DdrC dimer where the four-helix bundle of monomer A creates a bulge on the DdrC surface (Fig. 4A). The robustness of this model was then verified by running five independent all-atoms MD simulations over a timescale of 500 ns each (Fig. 4B and Supp. Fig. S4 and S5 and Table S4). As in the case of DdrC alone, only minor changes in the protein conformation were observed during these simulations most of which were

restricted to loop regions (Supp. Fig. S4), whereas the two DNA molecules on either side of the DdrC dimer moved substantially to adapt to the protein surface (Supp. Fig. S4 and S5). These movements of the DNA duplex include twisting, bending, sliding along the groove and rotation of the duplex to establish more favorable contacts between the minor grooves of the DNA molecules and the protein.

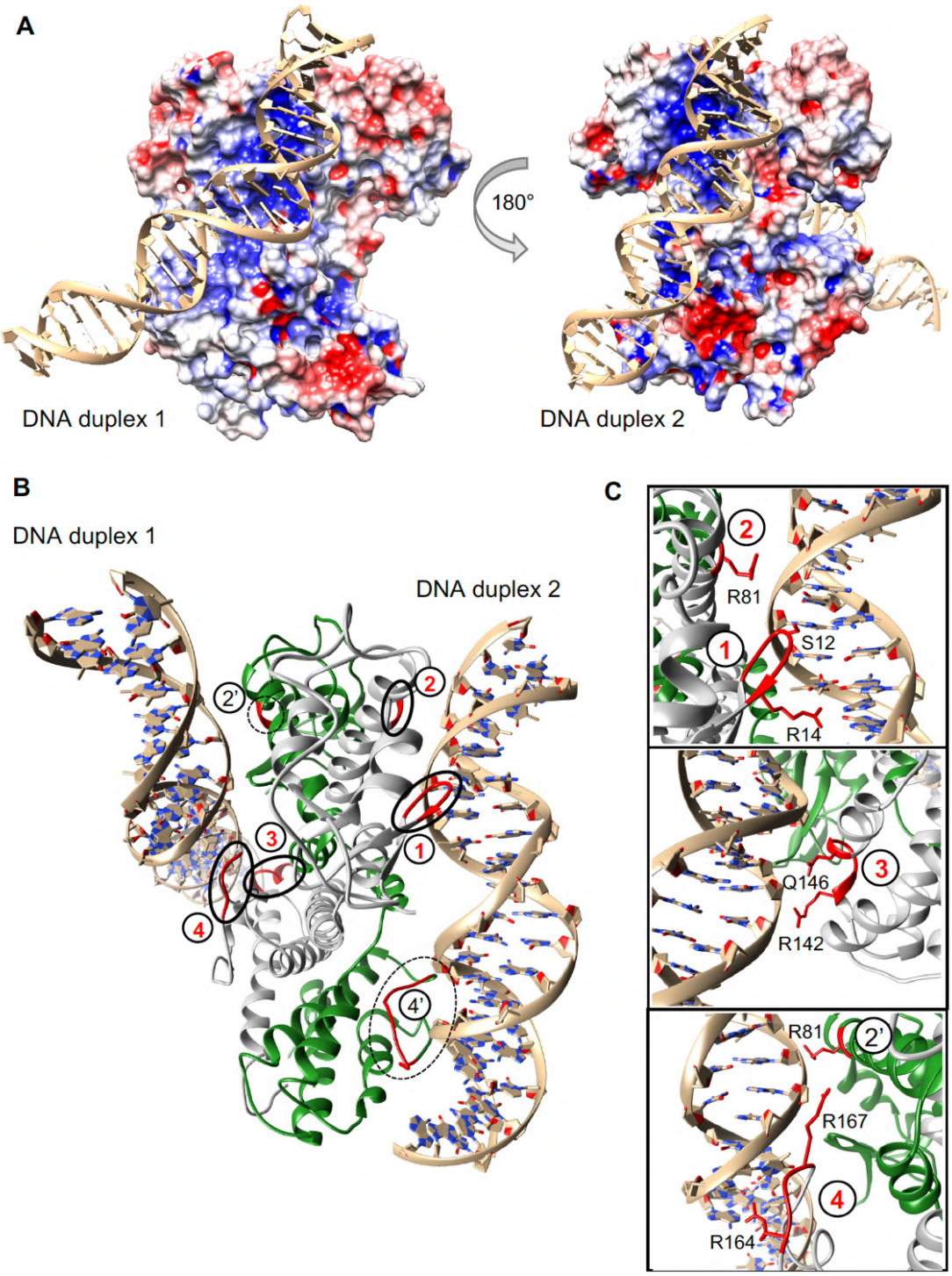

Figure 4. DdrC-dsDNA models derived from MD simulations. (**A**) Model of DNA-bound DdrC dimer used for MD simulations. Two 25 bp dsDNA fragments were manually positioned along the two positively charged grooves lining each side of the DdrC dimer. (**B**) Model of DNA-bound DdrC dimer (monomer A in grey and monomer B

in green) at the end of MD simulation run3, illustrating the four major contact points (labelled 1-4 in red) and two additional contact points (labelled 2' and 4' in black) between the DNA duplexes and the DdrC protein. The regions of DdrC in contact with the DNA are highlighted in red. (**C**) Close-up views of the major DdrC-DNA contact sites illustrated in (B). The main residues involved in the interactions with the DNA are shown as sticks and are labelled.

Four major contact sites between the DdrC dimer and the DNA duplexes were observed in at least four out of five MD runs (Fig. 4B and 4C, Supp. Table S4 and Fig. S6). Interestingly, the four major contact points are all located in chain A of DdrC that interacts significantly more with the two DNA duplexes than chain B (Supp. Table S4 and Fig. S6). Both the NTD and the CTD domains of DdrC contact the DNA (Fig. 4B and C). The first major contact point involves the N-terminal β-hairpin that precedes the wHTH motif located in the NTD. The second site is located in helix α4 and involves mostly Arg81. The third and fourth contact sites are located in the CTD and involve respectively Arg142 and Gln146 from helix α7 and three positively charged residues (Lys158, Arg164 and Arg167) situated in the flexible linker between α7 and α8. The second (Arg81) and fourth (Lys158, Arg164 and Arg167) DNA contact regions were also seen for chain B in at least three out of the five MD runs (Fig. 4B and C; contact points 2' and 4'). Each face of the DdrC dimer thus contacts a DNA duplex through at least three interaction sites, but as a result of the intrinsic asymmetry of the DdrC dimer, the contact surfaces are quite distinct (Fig. 4B). The interactions between DdrC and DNA are predominantly electrostatic, between the phosphate backbone and positively charged residues, notably arginines, although additional contacts between either protein side chains or the peptide backbone and bases located in the minor groove of the DNA duplexes are also seen (Fig. 4C).

To validate these findings, we evaluated the DNA binding properties of several mutants of DdrC, listed in Supp. Table S1. Point mutants, DdrC^{R14E}, DdrC^{R81E}, DdrC^{R142E}, DdrC^{K158E}, DdrC^{R164E}, DdrC^{R167E} and the double mutant DdrC$^{R164E/R167E}$, were prepared to exchange positively charged residues identified in our MD simulations as contacting DNA with negatively charged glutamates. In DdrC$^{R164A/R167A}$, the two arginines were mutated instead to alanine, and two N-terminally deleted constructs were also prepared to either delete entirely residues 1 to 16 (DdrC^{delN}) or to shorten the N-terminal β-hairpin by removing residues 9 to 14 and replacing them with a serine (DdrC$^{del9\text{-}14S}$). Fluorescence polarization experiments were then performed with each of these mutants to assess their binding to the fluorescein-labelled 50 mer dsDNA and the experimental data was fitted to either a single or a two-sites specific model (Supp. Fig. S7 and Table 3). Three classes of mutants could be distinguished. The first class includes DdrC$^{del9\text{-}14S}$, DdrC^{R81E} and DdrC^{R142E} mutants. These three mutants retain two distinct DNA binding sites similar to WT DdrC, with a high and a low affinity site (Table 3). DdrC$^{del9\text{-}14S}$ shows no impaired DNA binding, indicating that the tip of the N-terminal β-hairpin is not needed for DNA binding, while DdrC^{R81E} and DdrC^{R142E} exhibit a 3 to 5-fold reduced high affinity DNA binding site compared to WT DdrC. These two arginines are thus likely involved in DNA binding by the high affinity site of DdrC, but are not key players in this process. The second class of mutants includes the N-terminally deleted DdrC, DdrC^{delN},

and the point mutant DdrC^{R14E}. These two mutants, in contrast to WT and class 1 mutants, exhibit only one DNA binding site, with a Kd value around 1 µM, *i.e.,* one order of magnitude higher than the high affinity site of WT DdrC (Table 3). Class 2 mutants thus no longer exhibit a low affinity site and show reduced binding to their high affinity site. This suggests that the N-terminal region, and more specifically R14 (since the single point mutant recapitulates the effect of deleting residues 1 to 16), is probably implicated in both the high and the low affinity binding sites. It is absolutely needed for the low affinity site, whereas the high affinity site remains in its absence with a reduced DNA binding ability. Finally, the third class of mutants involves mutations in the C-terminal flexible loop connecting α7 and α8 (Supp. Fig. S7 and Table 3). In these mutants (DdrC^{K158E}, DdrC^{R164E}, DdrC^{R167E}, DdrC$^{R164E/R167E}$ and DdrC$^{R164A/R167A}$), DNA binding is largely disrupted. Data were fitted to single specific binding models and the derived Kd values were over 200 µM. For the double DdrC$^{R164E/R167E}$ mutant, no reliable fit was obtained, since the binding signal was too low. This C-terminal loop thus clearly constitutes the major DNA binding motif of DdrC, contributing to both the high and low affinity sites. The high affinity site of DdrC thus likely corresponds to the tight interaction of this loop, bearing Lys158, Arg164 and Arg167, from chain A with the DNA major groove of duplex 1 (contact site 4 in Fig. 4B and C), with further stabilization of this contact by Arg14 and Arg81 from chain B and Arg142 from chain A (corresponding respectively to contact points 2' and 3 in Fig. 4B and C). In contrast, the interaction of duplex 2 with the 'flat' surface of the DdrC dimer, notably via contact points 1 and 4' (Fig. 4B and C), likely represents the low affinity binding site.

Table 3. DNA binding constants of DdrC mutants derived from fluorescence polarization measurements after fitting to either a single site or a two-sites specific model.

Mutant	Best binding model	Kd (Hi) µM (+SEM)	Kd (Lo) µM (+SEM)	% Hi affinity	R^2
WT	2 sites	0.081 ± 0.014	22.232 ± 9.454	60.51 ± 2.97	0.982
DdrC^{R142E}	2 sites	0.257 ± 0.074	61.265 ± 20.448	27.98 ± 2.22	0.981
DdrC^{K158E}	1 site	-	224.125 ± 246.998	N/A	0.991
DdrC^{R164E}	1 site	-	312.844 ± 361.794	N/A	0.981
DdrC^{R167E}	1 site	-	305.272 ± 300.850	N/A	0.988
DdrC$^{R164E/R167E}$	1 site	-	N/A (Kd>1500)	N/A	0.885
DdrC$^{R164A/R167A}$	1 site	-	212.398 ± 341.420	N/A	0.980
DdrC^{R14E}	1 site	0.725 ± 0.101	-	N/A	0.988
DdrC^{R81E}	2 sites	0.347 ± 0.034	52.713 ± 36.977	73.56 ± 3.78	0.995
DdrC$^{del9-14S}$	2 sites	0.086 ± 0.015	12.604 ± 3.576	46.66 ± 2.52	0.992
DdrC^{delN}	1 site	1.317 ± 0.320	-	N/A	0.982

DdrC alters the topology of plasmid DNA

A previous study based on transmission electron microscopy showed that DdrC was able to condense circular DNA at a high concentration (29). To further investigate the effects of DdrC on plasmid conformation, we incubated supercoiled pUC19 plasmid DNA with increasing concentrations of DdrC and analyzed the resulting DNA-protein complexes by atomic force microscopy (AFM) (Fig. 5 and Supp. Fig. S8). Figure 5 presents representative fields of view obtained at 0, 2, 5, 10 and 20 nM DdrC. To compare the different DNA topologies, we extracted the projected surface areas of individual plasmid-DdrC assemblies (Fig. 5A-E and Supp. Fig. S8) and determined for each field of view the fraction of plasmid molecules that exhibit a condensed conformation (Fig. 5F). At the highest DdrC concentration, almost all the plasmids adopted a highly condensed configuration (93% ± 13%; Fig. 5E and F), which was strikingly different from the 7.5% ± 13% of condensed pUC19sc plasmid molecules in the absence of DdrC (Fig. 5A and F). The fraction of condensed plasmid molecules was clearly seen to increase significantly in a DdrC concentration-dependent manner, suggesting that DdrC may be able to maintain circular plasmid DNA in a condensed conformation.

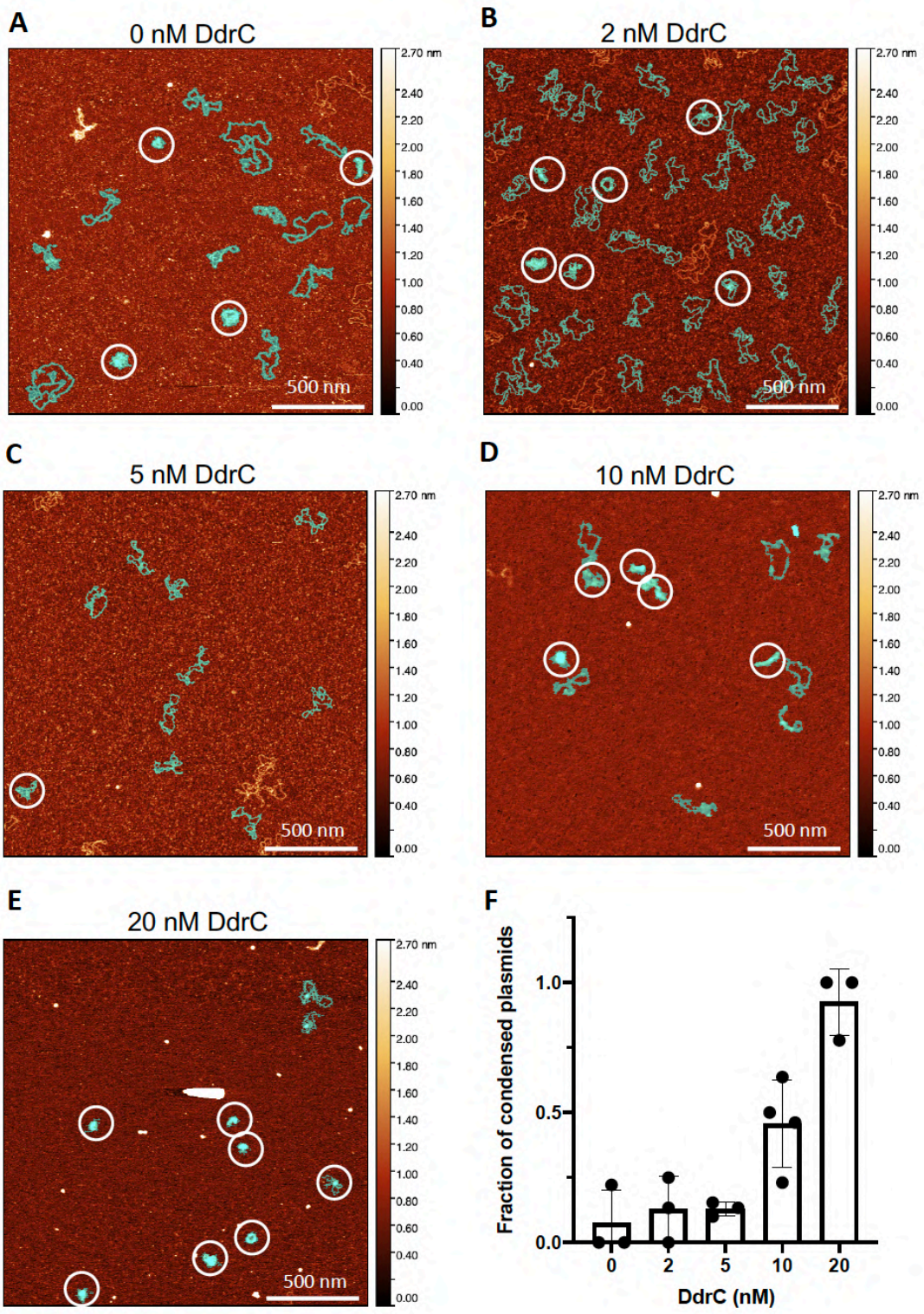

Figure 5. DdrC maintains circular plasmid in a condensed conformation. (**A-E**) Representative AFM images of 0.5 nM of pUC19sc incubated with 0 (A), 2 (B), 5 (C), 10 (D) and 20 nM (E) DdrC. Additional images are presented in Supp. Fig.S7. All images correspond to 4 μm^2 areas, in which the assemblies displaying a more condensed conformation are indicated by white circles. The light-blue mask highlights assemblies that have been used in the statistical analysis presented in (F). Assemblies that touch the border of the image or were not clearly identifiable due to unresolved overlapping were excluded from the statistical analysis. The z-scale bar is shown as

a color gradient to indicate the distribution of height in the images. Scale bar corresponds to 500 nm. (**F**) Histogram and scatter plot illustrating the mean fraction of condensed pUC19sc-DdrC assemblies as a function of DdrC concentration. The error bars represent the standard deviation of at least three replicates. Individual data points correspond to the fraction of condensed assemblies derived from a single AFM image after estimation of the projected surface area of individual assemblies.

To further explore this property of DdrC, we evaluated whether DdrC could change the topology of circular plasmid DNA by introducing either positive or negative supercoils into relaxed plasmid. For this purpose, we incubated DdrC with a relaxed circular pHOT DNA plasmid, prior to treatment with wheat germ topoisomerase I (TopoI) to relax positive or negative supercoils that might have been introduced by DdrC (Fig. 6). Incubation of TopoI with the relaxed form of the plasmid had no effect on DNA topology in the absence of DdrC (Fig. 6A). In contrast, when the relaxed plasmid was preincubated with DdrC prior to addition of TopoI, several additional topoisomers exhibiting increased supercoiling (faster migration) were observed indicating that DdrC is indeed able to constrain closed circular DNA in a more supercoiled conformation. To distinguish between positive and negative supercoiled topoisomers, plasmid DNA incubated with TopoI alone or with DdrC followed by TopoI were further separated by two-dimensional gel electrophoresis in the presence of chloroquine, a DNA intercalator that unwinds closed circular DNA in the second dimension (Fig. 6B and C). Interestingly, while the starting relaxed pHOT-DNA substrate migrated as slightly positively supercoiled, as expected for relaxed circular plasmid in the presence of chloroquine (76), the incubation of the substrate with increasing concentrations of DdrC generated negatively supercoiled DNA (Fig. 6B and C). DdrC is thus capable of modifying the topology of duplex DNA *in vitro* by generating negative DNA supercoils.

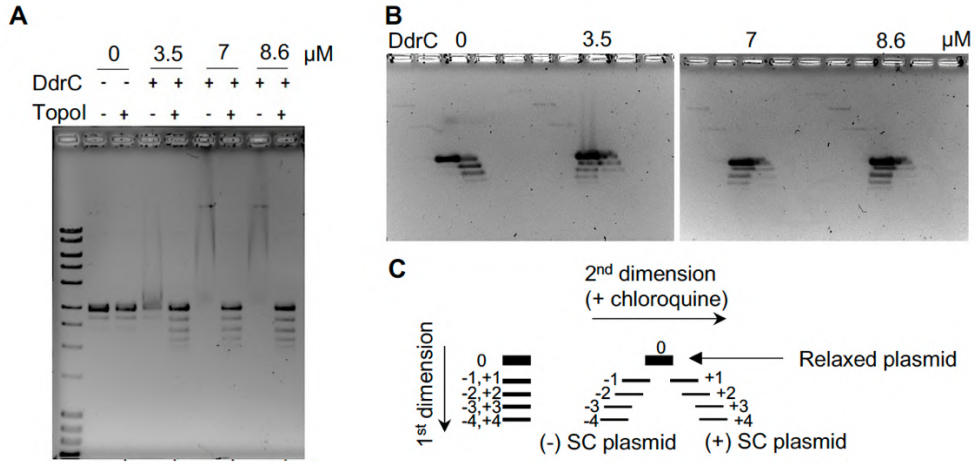

Figure 6. DdrC changes the topology of plasmid DNA by constraining DNA supercoils. (**A**) Relaxed pHOT plasmid DNA (250 ng) incubated with 0, 3.5, 7 and 8.6 µM DdrC was then treated or not with topoisomerase I (TopoI) from wheat germ. After deproteinization, reaction products were separated by electrophoresis on a 1.2 % agarose gel to resolve topoisomers. Treating relaxed plasmid DNA with TopoI has no effect, whereas treating relaxed plasmid DNA pre-incubated with 3.5-8.6 µM DdrC prior to the TopoI treatment results in a ladder like pattern. (**B**) The topoisomers resulting from DdrC and TopoI treatment were further separated by bidimensional

gel with 3 µg/mL chloroquine included in the gel and buffer in the second dimension. Under these conditions, positively supercoiled ((+)-SC) topoisomers migrated towards the right and negatively supercoiled ((-)-SC) topoisomers towards the left, as illustrated in the schematic diagram shown in (**C**).

DISCUSSION

Our crystallographic data reveal that DdrC is composed of two domains, an unusual N-terminal wHTH motif and a more classical four-helix bundle at its C-terminus, which is domain swapped in the DdrC homo-dimer. This domain swapping is facilitated by the rearrangement of a long α-helix, α6 in chain A, into two shorter α-helices, $\alpha6_a$ and $\alpha6_b$, connected by a 6-residue linker in chain B. This break in the helix creates a highly unusual asymmetric homo-dimer, which was not predicted by current artificial intelligence programs. AlphaFold2 correctly predicted the structure of monomer A, but not of monomer B with the disrupted helix, suggesting that the monomer A conformation is likely more stable. The conformation of monomer B may only be elicited upon protein dimerization. If true, this would mean that interaction of monomer A with monomer B changes the equilibrium conformational energy landscape of monomer B, leading to adoption of a new structure through inducement of a helix break and change in the relative orientation of the two domains — an impressive illustration of structural moonlighting. Alternatively, both structures may exist in solution, even though the conformation of monomer B was not predicted by the machine learning algorithms. Improvements of these algorithms in the future may allow to favor one or the other of the two hypotheses. Regardless, the DdrC dimer structure exemplifies that *de novo* phasing of crystallographic data will in some cases remain the surest pathway towards structure determination.

In DdrC, the domain swapping creates an asymmetric dimer exhibiting two distinct DNA binding surfaces. Our DdrC-DNA models suggest, however, that the conserved wHTH motif that is found in numerous DNA binding proteins is not involved in DNA binding in the case of DdrC (70–72). The electrostatic surface potential of DdrC's wHTH motif is indeed largely electronegative, precluding a direct involvement in DNA binding. The closest structural homologues of this wHTH motif of DdrC are found in the Dachsund protein (73) and the SKI-DHD domain (74), which also possess unusual wHTH motifs preceded by a N-terminal β-hairpin structure. The Dachshund protein, however, exhibits a positively charged wHTH, while the electrostatic surface potential of the SKI-DHD domain is more similar to that of DdrC and has been shown to be the site of protein-protein interactions (74). The negatively charged wHTH of DdrC may thus also constitute a binding site for a partner protein rather than for DNA.

Taken together, our fluorescence polarization and MD simulations data clearly indicate that DdrC can simultaneously bind two DNA duplexes via its two sides. Six DNA interaction sites were identified on DdrC with elements from both the NTD and the CTD taking part in DNA binding. Interestingly, monomer A contributes significantly more than monomer B to direct contacts with the DNA (four out of the six contact points). Although each side of DdrC contacts the DNA in three different regions, the

two DNA binding surfaces of DdrC are remarkably different. Our mutational study clearly shows that the high and the low affinity binding sites identified in our fluorescence polarization experiments correspond to either side of the DdrC dimer. The flexible C-terminal linker connecting helices α7 and α8 from monomer A, in which the CTD forms a bulge on the surface, constitutes the major DNA binding motif and largely contributes to the high affinity DNA binding site of DdrC reinforced by several additional electrostatic interactions involving both the NTD and CTD of DdrC. The low affinity site is instead formed by the flat side of the DdrC dimer and involves the N-terminal β-hairpin together with the flexible CTD loop.

These findings indicate that DdrC may function by bridging DNA duplexes bound on either side of the dimer. This could explain its previously reported DNA circularization and single-strand annealing activities (29), but also its ability to maintain circular plasmid DNA in a condensed conformation as shown in our AFM images. This may be achieved in part at least by neutralizing the negatively charged DNA backbone to allow the close packing of DNA duplexes. DNA compaction by DdrC may also be facilitated by its ability to modify the topology of circular DNA as revealed by our experiments with DdrC coupled to TopoI relaxation activity. DdrC can indeed modify the topology of DNA *in vitro* by constraining DNA supercoils that are subsequently transformed into negative supercoils by TopoI in our assay. This additional function of DdrC may be needed for the reorganization of the nucleoid in response to genotoxic stress.

These features of DdrC are reminiscent of those of NAPs, which play key roles in the organization and tight packaging of genomic DNA in bacterial cells through DNA bending, wrapping and bridging (77–79). The genome of *D. radiodurans* only encodes for a small number of NAPs, with HU and the DNA gyrase complex being the most abundant NAPs associated with *Deinococcus* nucleoids (22, 80, 81). Unlike other bacterial species, the genome of *D. radiodurans* does not encode for a classical DNA bridging NAP such as the nucleoid-structuring protein H-NS. Under normal growth conditions, the HU and DNA gyrase are thus largely responsible for maintaining the high level of compaction of *D. radiodurans* nucleoids, whilst providing sufficient plasticity to allow for the necessary rearrangements associated with cellular activity and cell cycle progression (5). Interestingly, fluorescence microscopy studies have revealed that exposure of *D. radiodurans* to high doses of g-irradiation induces increased nucleoid compaction (29, 82). Since DdrC is rapidly recruited to the nucleoid following irradiation, we propose that DdrC may function as a DNA damage-induced NAP that contributes to the enhanced level of compaction of the nucleoid after irradiation by bridging DNA duplexes, thereby limiting the dispersion of the fragmented genome immediately after irradiation to facilitate subsequent DNA repair. The DNA gyrase is also over-expressed after irradiation, and may thus also contribute to the increased nucleoid compaction observed following irradiation by modulating the extent of supercoiling of the genomic DNA, a function that may be further enhanced by the binding of DdrC to DNA and its ability to constrain DNA supercoils.

Three hours post-irradiation, once the DNA repair process is almost complete (83), the abundance of DdrC decreases and the cellular distribution of DdrC changes drastically (29). DdrC which was so far evenly distributed throughout the nucleoid relocalizes to foci located near the closing septum between two *D. radiodurans* cells (29). This site corresponds to the location of the *Ter* regions of the chromosomes, where final chromosome segregation occurs, including DNA decatenation of replicated chromosomes (5, 82). At this stage, the nucleoids also progressively recover their original less compacted conformation, perhaps as a result of the changes in the abundance and distribution of DdrC. This intriguing relocalization of DdrC suggests that DdrC may play a second, distinct function at the late stages of the response to DNA damage to ensure that chromosome segregation and cell division do not resume before DNA repair is complete (5, 82). Further studies will be needed to explore the molecular mechanisms underlying this second putative role of DdrC in the response of *D. radiodurans* to severe radiation-induced DNA damage.

DATA AVAILABILITY

Atomic coordinates and structure factors for the reported crystal structures have been deposited with the Protein Data bank under accession number XXXX.

ACKNOWLEDGEMENT

IBS acknowledges integration into the Interdisciplinary Research Institute of Grenoble (IRIG, CEA). This work used the platforms of the Grenoble Instruct-ERIC center (ISBG; UMS 3518 CNRS-CEA-UGA-EMBL) within the Grenoble Partnership for Structural Biology (PSB), supported by FRISBI (ANR-10-INBS-0005-02) and GRAL, financed within the University Grenoble Alpes graduate school (Ecoles Universitaires de Recherche) CBH-EUR-GS (ANR-17-EURE-0003). We thank Christine Ebel for access to the AUC and SEC-MALLS platforms. This work acknowledges the AFM platform at the IBS. All the calculations were performed on the local LPCT computing cluster.

FUNDING

This work was supported by the Commissariat à l'énergie atomique et aux énergies renouvelables (CEA) through a CFR PhD grant to ASB and a radiobiology grant. The ANR (Agence Nationale de la Recherche) and CGI (Commissariat à l'Investissement d'Avenir) are gratefully acknowledged for their financial support of this work through Labex SEAM (Science and Engineering for Advanced Materials and devices): ANR 11 LABX 086 and ANR 11 IDEX 05 02. Funding for open access charge: CEA Radiobiology.

CONFLICT OF INTEREST

There are no conflicts to declare.

Table 1. Crystallographic data collection and refinement statistics

Values in parentheses are for the highest resolution shell.

Dataset	SeMet-DdrC	Native DdrC
Data collection parameters		
Beamline, facility	ID23-1, ESRF	PX2-A, SOLEIL
Space group	$P32_21$	$P32_21$
Cell dimensions		
a, b, c (Å)	111.4, 111.4, 104.9	111.5, 111.5, 105.4
α, β, γ (°)	90, 90, 120	90, 90, 120
Wavelength (Å)	0.979	0.979
Resolution range (Å)	36.50 - 2.52 (2.61 - 2.52)	48.29 - 2.80 (2.90 - 2.80)
Unique reflections	24129 (1476)	19052 (1876)
(I)/σ(I)	6.0 (0.3)	16.9 (0.7)
R_{merge} **(%)**	9.3 (394.6)	8.1 (129.6)
$Cc_{1/2}$ **(%)**	99.7 (9.8)	100 (87.4)
Completeness (%)	93.1 (58.0)	99.9 (100.0)
Refinement statistics		
Reflections used in refinement	24129 (1477)	19052 (1876)
Reflections used for R_{free}	1212 (79)	952 (94)
R_{work} / R_{free}	0.35 (0.46) / 0.36 (0.44)	0.26 (0.38) / 0.31 (0.43)
Number of atoms	3250	3641
Protein	3250	3393
Ligands/ions	0	158
Water	0	90
Average b-factor	88.1	103.60
Protein	88.1	102.31
Ligands/ions	N/A	132.89
Water	N/A	100.82
Ramachandran		
Favored (%)	-	96.97
Allowed (%)	-	2.56
Outliers (%)	-	0.47
Rotamer outliers (%)	-	1.19
Clashscore	-	11.34
R.m.s. Deviations		
Bond lengths	-	0.006
Bond angles	-	1.11
PDB accession code	-	XXXX

REFERENCES

1. Battista,J.R. (1997) Against all odds: the survival strategies of Deinococcus radiodurans. *Annu. Rev. Microbiol.*, **51**, 203–224.
2. Daly,M.J. (2004) Accumulation of Mn(II) in Deinococcus radiodurans Facilitates Gamma-Radiation Resistance. *Science*, **306**, 1025–1028.
3. Cox,M.M. and Battista,J.R. (2005) Deinococcus radiodurans - the consummate survivor. *Nat. Rev. Microbiol.*, **3**, 882–892.
4. Timmins,J. and Moe,E. (2016) A decade of biochemical and structural studies of the DNA repair machinery of Deinococcus radiodurans. *Computational and Structural Biotechnology Journal*, **14**, 168–176.
5. Floc'h,K., Lacroix,F., Servant,P., Wong,Y.-S., Kleman,J.-P., Bourgeois,D. and Timmins,J. (2019) Cell morphology and nucleoid dynamics in dividing Deinococcus radiodurans. *Nature Communications*, **10**, 3815.
6. Levin-Zaidman,S., Englander,J., Shimoni,E., Sharma,A.K., Minton,K.W. and Minsky,A. (2003) Ringlike structure of the Deinococcus radiodurans genome: a key to radioresistance? *Science*, **299**, 254–6.
7. Zimmerman,J.M. and Battista,R.J. (2005) A ring-like nucleoid is not necessary for radioresistance in the Deinococcaceae. *BMC Microbiology*, **5**.
8. Tanaka,M., Earl,A.M., Howell,H.A., Park,M.J., Eisen,J.A., Peterson,S.N. and Battista,J.R. (2004) Analysis of Deinococcus radiodurans's transcriptional response to ionizing radiation and desiccation reveals novel proteins that contribute to extreme radioresistance. *Genetics*, **168**, 21–33.
9. Blanchard,L., Guérin,P., Roche,D., Cruveiller,S., Pignol,D., Vallenet,D., Armengaud,J. and de Groot,A. (2017) Conservation and diversity of the IrrE/DdrO-controlled radiation response in radiation-resistant Deinococcus bacteria. *Microbiologyopen*, **6**, e00477.
10. de Groot,A., Siponen,M.I., Magerand,R., Eugénie,N., Martin-Arevalillo,R., Doloy,J., Lemaire,D., Brandelet,G., Parcy,F., Dumas,R., *et al.* (2019) Crystal structure of the transcriptional repressor DdrO: insight into the metalloprotease/repressor-controlled radiation response in Deinococcus. *Nucleic Acids Res*, **47**, 11403–11417.
11. Devigne,A., Ithurbide,S., Bouthier de la Tour,C., Passot,F., Mathieu,M., Sommer,S. and Servant,P. (2015) DdrO is an essential protein that regulates the radiation desiccation response and the apoptotic-like cell death in the radioresistant Deinococcus radiodurans bacterium. *Mol Microbiol*, **96**, 1069–84.
12. Blanchard,L. and de Groot,A. (2021) Coexistence of SOS-Dependent and SOS-Independent Regulation of DNA Repair Genes in Radiation-Resistant Deinococcus Bacteria. *Cells*, **10**.
13. Radman,M. (1975) SOS repair hypothesis: phenomenology of an inducible DNA repair which is accompanied by mutagenesis. *Basic Life Sci*, **5A**, 355–367.
14. Makarova,K.S., Omelchenko,M.V., Gaidamakova,E.K., Matrosova,V.Y., Vasilenko,A., Zhai,M., Lapidus,A., Copeland,A., Kim,E., Land,M., *et al.* (2007) Deinococcus geothermalis: the pool of extreme radiation resistance genes shrinks. *PLoS One*, **2**, e955.
15. Wang,Y., Xu,Q., Lu,H., Lin,L., Wang,L., Xu,H., Cui,X., Zhang,H., Li,T. and Hua,Y. (2015) Protease Activity of PprI Facilitates DNA Damage Response: Mn(2+)-Dependence and Substrate Sequence-Specificity of the Proteolytic Reaction. *PLOS ONE*, **10**, e0122071.
16. Eugénie,N., Zivanovic,Y., Lelandais,G., Coste,G., Bouthier de la Tour,C., Bentchikou,E., Servant,P. and Confalonieri,F. (2021) Characterization of the Radiation Desiccation Response Regulon of the Radioresistant Bacterium Deinococcus radiodurans by Integrative Genomic Analyses. *Cells*, **10**.
17. Vujičić-Žagar,A., Dulermo,R., Le Gorrec,M., Vannier,F., Servant,P., Sommer,S., de Groot,A. and Serre,L. (2009) Crystal Structure of the IrrE Protein, a Central Regulator of DNA Damage Repair in Deinococcaceae. *Journal of Molecular Biology*, **386**, 704–716.
18. Ludanyi,M., Blanchard,L., Dulermo,R., Brandelet,G., Bellanger,L., Pignol,D., Lemaire,D. and de Groot,A. (2014) Radiation response in Deinococcus deserti : IrrE is a metalloprotease that cleaves repressor protein DdrO. *Molecular Microbiology*, **94**, 434–449.
19. Magerand,R., Rey,P., Blanchard,L. and de Groot,A. (2021) Redox signaling through zinc activates the radiation response in Deinococcus bacteria. *Scientific Reports*, **11**, 4528.
20. Narasimha,A. and Basu,B. (2021) New insights into the activation of Radiation Desiccation Response regulon in Deinococcus radiodurans. *Journal of Biosciences*, **46**, 10.

21. Tanaka,M., Earl,A.M., Howell,H.A., Park,M.-J., Eisen,J.A., Peterson,S.N. and Battista,J.R. (2004) Analysis of *Deinococcus radiodurans* 's Transcriptional Response to Ionizing Radiation and Desiccation Reveals Novel Proteins That Contribute to Extreme Radioresistance. *Genetics*, **168**, 21–33.
22. Bouthier de la Tour,C., Passot,F.M., Toueille,M., Mirabella,B., Guérin,P., Blanchard,L., Servant,P., de Groot,A., Sommer,S. and Armengaud,J. (2013) Comparative proteomics reveals key proteins recruited at the nucleoid of Deinococcus after irradiation-induced DNA damage. *Proteomics*, **13**, 3457–3469.
23. Harris,D.R., Tanaka,M., Saveliev,S.V., Jolivet,E., Earl,A.M., Cox,M.M. and Battista,J.R. (2004) Preserving genome integrity: the DdrA protein of Deinococcus radiodurans R1. *PLoS Biol*, **2**, e304.
24. Gutsche,I., Vujicic-Zagar,A., Siebert,X., Servant,P., Vannier,F., Castaing,B., Gallet,B., Heulin,T., de Groot,A., Sommer,S., *et al.* (2008) Complex oligomeric structure of a truncated form of DdrA: a protein required for the extreme radiotolerance of Deinococcus. *Biochim Biophys Acta*, **1784**, 1050–8.
25. Xu,G., Lu,H., Wang,L., Chen,H., Xu,Z., Hu,Y., Tian,B. and Hua,Y. (2010) DdrB stimulates single-stranded DNA annealing and facilitates RecA-independent DNA repair in Deinococcus radiodurans. *DNA Repair (Amst)*, **9**, 805–812.
26. Bouthier de la Tour,C., Boisnard,S., Norais,C., Toueille,M., Bentchikou,E., Vannier,F., Cox,M.M., Sommer,S. and Servant,P. (2011) The deinococcal DdrB protein is involved in an early step of DNA double strand break repair and in plasmid transformation through its single-strand annealing activity. *DNA Repair*, **10**, 1223–1231.
27. Ithurbide,S., Coste,G., Lisboa,J., Eugénie,N., Bentchikou,E., Bouthier de la Tour,C., Liger,D., Confalonieri,F., Sommer,S., Quevillon-Cheruel,S., *et al.* (2020) Natural Transformation in Deinococcus radiodurans: A Genetic Analysis Reveals the Major Roles of DprA, DdrB, RecA, RecF, and RecO Proteins. *Front Microbiol*, **11**, 1253.
28. Bouthier de la Tour,C., Mathieu,M., Servant,P., Coste,G., Norais,C. and Confalonieri,F. (2021) Characterization of the DdrD protein from the extremely radioresistant bacterium Deinococcus radiodurans. *Extremophiles*, **25**, 343–355.
29. Bouthier de la Tour,C., Mathieu,M., Meyer,L., Dupaigne,P., Passot,F., Servant,P., Sommer,S., Le Cam,E. and Confalonieri,F. (2017) In vivo and in vitro characterization of DdrC, a DNA damage response protein in Deinococcus radiodurans bacterium. *PLoS One*, **12**, e0177751.
30. Doublie,S. (1997) Preparation of selenomethionyl proteins for phase determination. *Methods enzymol*, **276**, 523–30.
31. Timmins,J., Leiros,H.K., Leonard,G., Leiros,I. and McSweeney,S. (2005) Crystal structure of maltooligosyltrehalose trehalohydrolase from Deinococcus radiodurans in complex with disaccharides. *J Mol Biol.*, **347**, 949–63.
32. Dimasi,N., Flot,D., Dupeux,F. and Marquez,J.A. (2007) Expression, crystallization and X-ray data collection from microcrystals of the extracellular domain of the human inhibitory receptor expressed on myeloid cells IREM-1. *Acta Crystallogr Sect F Struct Biol Cryst Commun*, **63**, 204–8.
33. Kabsch,W. (2010) Integration, scaling, space-group assignment and post-refinement. *Acta Crystallogr D Biol Crystallogr*, **66**, 133–144.
34. Skubák,P. and Pannu,N.S. (2013) Automatic protein structure solution from weak X-ray data. *Nat Commun*, **4**, 2777.
35. Sheldrick,G.M. (2010) Experimental phasing with SHELXC/D/E: combining chain tracing with density modification. *Acta Crystallogr D Biol Crystallogr*, **66**, 479–485.
36. Murshudov,G.N., Vagin,A.A. and Dodson,E.J. (1997) Refinement of macromolecular structures by the maximum-likelihood method. *Acta Crystallogr D Biol Crystallogr*, **53**, 240–255.
37. Cowtan,K. (2010) Recent developments in classical density modification. *Acta Crystallogr D Biol Crystallogr*, **66**, 470–478.
38. Cowtan,K. (2006) The Buccaneer software for automated model building. 1. Tracing protein chains. *Acta Crystallogr D Biol Crystallogr*, **62**, 1002–1011.
39. Cowtan,K. (2008) Fitting molecular fragments into electron density. *Acta Crystallogr D Biol Crystallogr*, **64**, 83–89.
40. McCoy,A.J., Grosse-Kunstleve,R.W., Adams,P.D., Winn,M.D., Storoni,L.C. and Read,R.J. (2007) Phaser crystallographic software. *J Appl Crystallogr*, **40**, 658–674.
41. Emsley,P., Lohkamp,B., Scott,W.G. and Cowtan,K. (2010) Features and development of Coot. *Acta Crystallogr D Biol Crystallogr*, **66**, 486–501.

42. Adams,P.D., Afonine,P.V., Bunkóczi,G., Chen,V.B., Davis,I.W., Echols,N., Headd,J.J., Hung,L.-W., Kapral,G.J., Grosse-Kunstleve,R.W., *et al.* (2010) PHENIX: a comprehensive Python-based system for macromolecular structure solution. *Acta Crystallogr D Biol Crystallogr*, **66**, 213–221.
43. Chen,V.B., Arendall,W.B., Headd,J.J., Keedy,D.A., Immormino,R.M., Kapral,G.J., Murray,L.W., Richardson,J.S. and Richardson,D.C. (2010) MolProbity: all-atom structure validation for macromolecular crystallography. *Acta Crystallogr D Biol Crystallogr*, **66**, 12–21.
44. Krissinel,E. and Henrick,K. (2007) Inference of macromolecular assemblies from crystalline state. *J Mol Biol*, **372**, 774–797.
45. Baker,N.A., Sept,D., Joseph,S., Holst,M.J. and McCammon,J.A. (2001) Electrostatics of nanosystems: Application to microtubules and the ribosome. *P Natl Acad Sci USA*, **98**, 10037–10041.
46. Dolinsky,T.J., Czodrowski,P., Li,H., Nielsen,J.E., Jensen,J.H., Klebe,G. and Baker,N.A. (2007) PDB2PQR: expanding and upgrading automated preparation of biomolecular structures for molecular simulations. *Nucleic Acids Res*, **35**, W522–W525.
47. Olsson,M.H.M., Søndergaard,C.R., Rostkowski,M. and Jensen,J.H. (2011) PROPKA3: Consistent Treatment of Internal and Surface Residues in Empirical pKa Predictions. *J. Chem. Theory Comput.*, **7**, 525–537.
48. Jumper,J., Evans,R., Pritzel,A., Green,T., Figurnov,M., Ronneberger,O., Tunyasuvunakool,K., Bates,R., Žídek,A., Potapenko,A., *et al.* (2021) Highly accurate protein structure prediction with AlphaFold. *Nature*, **596**, 583–589.
49. Baek Minkyung, DiMaio Frank, Anishchenko Ivan, Dauparas Justas, Ovchinnikov Sergey, Lee Gyu Rie, Wang Jue, Cong Qian, Kinch Lisa N., Schaeffer R. Dustin, *et al.* (2021) Accurate prediction of protein structures and interactions using a three-track neural network. *Science*, **373**, 871–876.
50. Steinegger,M. and Söding,J. (2017) MMseqs2 enables sensitive protein sequence searching for the analysis of massive data sets. *Nature Biotechnology*, **35**, 1026–1028.
51. Mirdita,M., Steinegger,M., Breitwieser,F., Söding,J. and Levy Karin,E. (2021) Fast and sensitive taxonomic assignment to metagenomic contigs. *Bioinformatics*, **37**, 3029–3031.
52. DeLano,W.L. (2002) The PyMOL Molecular Graphics System.
53. Murshudov,G.N., Skubak,P., Lebedev,A.A., Pannu,N.S., Steiner,R.A., Nicholls,R.A., Winn,M.D., Long,F. and Vagin,A.A. (2011) REFMAC5 for the refinement of macromolecular crystal structures. *Acta Crystallogr D Biol Crystallogr*, **67**, 355–67.
54. Nečas,D. and Klapetek,P. (2012) Gwyddion: an open-source software for SPM data analysis. *Open Physics*, **10**.
55. Schuck,P. (2000) Size-distribution analysis of macromolecules by sedimentation velocity ultracentrifugation and lamm equation modeling. *Biophys J*, **78**, 1606–1619.
56. Brautigam,C.A. (2015) Calculations and Publication-Quality Illustrations for Analytical Ultracentrifugation Data. *Methods Enzymol*, **562**, 109–133.
57. Webb,B. and Sali,A. (2016) Comparative Protein Structure Modeling Using MODELLER. *Curr Protoc Bioinformatics*, **54**, 5.6.1-5.6.37.
58. Jorgensen,W.L., Chandrasekhar,J., Madura,J.D., Impey,R.W. and Klein,M.L. (1983) Comparison of simple potential functions for simulating liquid water. *J. Chem. Phys.*, **79**, 926–935.
59. Perez,A., Marchán,I., Svozil,D., Sponer,J., Cheatham,T.E., Laughton,C.A. and Orozco,M. (2007) Refinement of the AMBER Force Field for Nucleic Acids: Improving the Description of alphaγConformers. *Biophysical Journal*, **92**, 3817–3829.
60. Ivani,I., Dans,P.D., Noy,A., Pérez,A., Faustino,I., Hospital,A., Walther,J., Andrio,P., Goñi,R., Balaceanu,A., *et al.* (2015) Parmbsc1: A refined force field for DNA simulations. *Nature Methods*, **13**, 55–58.
61. Case,D.A., Berryman,J.T., Betz,R.M., Cerutti,D.S., T. E. Cheatham,I.I.I., Darden,T.A., Duke,R.E., Giese,T.J., Gohlke,H., Goetz,A.W., *et al.* (2015) AMBER 2015. *AMBER 15, Universiyt of California San Francisco*.
62. Case,D.A., Cheatham,T.E., Darden,T., Gohlke,H., Luo,R., Merz,K.M., Onufriev,A., Simmerling,C., Wang,B. and Woods,R.J. (2005) The Amber biomolecular simulation programs. *Journal of Computational Chemistry*, **26**, 1668–1688.
63. Humphrey,W., Dalke,A. and Schulten,K. (1996) VMD: Visual molecular dynamics. *Journal of Molecular Graphics*, **14**, 33–38.

64. Phillips,J.C., Braun,R., Wang,W., Gumbart,J., Tajkhorshid,E., Villa,E., Chipot,C., Skeel,R.D., Kalé,L. and Schulten,K. (2005) Scalable molecular dynamics with NAMD. *Journal of Computational Chemistry*, **26**, 1781–1802.
65. Feller,S.E., Zhang,Y., Pastor,R.W. and Brooks,B.R. (1995) Constant pressure molecular dynamics simulation: The Langevin piston method. *The Journal of Chemical Physics*, **103**, 4613–4621.
66. Martyna,G.J., Tobias,D.J. and Klein,M.L. (1994) Constant pressure molecular dynamics algorithms. *The Journal of Chemical Physics*, **101**, 4177–4189.
67. Darden,T., York,D. and Pedersen,L. (1993) Particle mesh Ewald: An N·log(N) method for Ewald sums in large systems. *The Journal of Chemical Physics*, **98**, 10089–10092.
68. Andersen,H.C. (1983) Rattle: A 'velocity' version of the shake algorithm for molecular dynamics calculations. *Journal of Computational Physics*, **52**, 24–34.
69. Tuckerman,M., Berne,B.J. and Martyna,G.J. (1992) Reversible multiple time scale molecular dynamics. *The Journal of Chemical Physics*, **97**, 1990–2001.
70. Gajiwala,K.S. and Burley,S.K. (2000) Winged helix proteins. *Current Opinion in Structural Biology*, **10**, 110–116.
71. Aravind,L., Anantharaman,V., Balaji,S., Babu,M.M. and Iyer,L.M. (2005) The many faces of the helix-turn-helix domain: Transcription regulation and beyond⋆. *FEMS Microbiology Reviews*, **29**, 231–262.
72. Teichmann,M., Dumay-Odelot,H. and Fribourg,S. (2012) Structural and functional aspects of winged-helix domains at the core of transcription initiation complexes. *Transcription*, **3**, 2–7.
73. Kim,S.-S., Zhang,R., Braunstein,S.E., Joachimiak,A., Cvekl,A. and Hegde,R.S. (2002) Structure of the retinal determination protein Dachshund reveals a DNA binding motif. *Structure*, **10**, 787–795.
74. Wilson,J.J., Malakhova,M., Zhang,R., Joachimiak,A. and Hegde,R.S. (2004) Crystal structure of the dachshund homology domain of human SKI. *Structure*, **12**, 785–792.
75. Schumacher,M.A., Lee,J. and Zeng,W. (2016) Molecular insights into DNA binding and anchoring by the *Bacillus subtilis* sporulation kinetochore-like RacA protein. *Nucleic Acids Res*, **44**, 5438–5449.
76. Gibson,E.G., Oviatt,A.A. and Osheroff,N. (2020) Two-Dimensional Gel Electrophoresis to Resolve DNA Topoisomers. *Methods Mol Biol*, **2119**, 15–24.
77. Dame,R.T. and Tark-Dame,M. (2016) Bacterial chromatin: converging views at different scales. *Curr Opin Cell Biol*, **40**, 60–5.
78. Gruber,S. (2014) Multilayer chromosome organization through DNA bending, bridging and extrusion. *Curr Opin Microbiol*, **22**, 102–10.
79. Hołówka,J. and Zakrzewska-Czerwińska,J. (2020) Nucleoid Associated Proteins: The Small Organizers That Help to Cope With Stress. *Frontiers in Microbiology*, **11**, 590.
80. Bouthier de la Tour,C., Blanchard,L., Dulermo,R., Ludanyi,M., Devigne,A., Armengaud,J., Sommer,S. and de Groot,A. (2015) The abundant and essential HU proteins in Deinococcus deserti and Deinococcus radiodurans are translated from leaderless mRNA. *Microbiology*, **161**, 2410–22.
81. Chen,S.W., Banneville,A.-S., Teulon,J.-M., Timmins,J. and Pellequer,J.-L. (2020) Nanoscale surface structures of DNA bound to Deinococcus radiodurans HU unveiled by atomic force microscopy. *Nanoscale*, **12**, 22628–22638.
82. Passot,F.M., Nguyen,H.H., Dard-Dascot,C., Thermes,C., Servant,P., Espéli,O. and Sommer,S. (2015) Nucleoid organization in the radioresistant bacterium Deinococcus radiodurans. *Molecular Microbiology*, **97**, 759–774.
83. Zahradka,K., Slade,D., Bailone,A., Sommer,S., Averbeck,D., Petranovic,M., Lindner,A.B. and Radman,M. (2006) Reassembly of shattered chromosomes in Deinococcus radiodurans. *Nature*, **443**, 569–73.

Supplementary Data:

Tables S1-S4

Supplementary Figures S1-S8

Table S1: List of primers used in this study to construct the DdrC mutants

Mutant	Oligonucleotide name and sequence
$DdrC^{R142E}$	**DdrC_R142E_F** 5'-CGGTGGCGAGGGCGAGGTCTACGGTCAG-3' **DdrC_R142E_R** 5'-CTGACCGTAGACCTCGCCCTCGCCACCG-3'
$DdrC^{K158E}$	**DdrC_K158E_F** 5'-CACCGTCCTTGGCGAGGACAGCGCGTC-3' **DdrC_K158E_R** 5'-GACGCGCTGTCCTCGCCAAGGACGGTG-3'
$DdrC^{R164E}$	**DdrC_R164E_F** 5'-AGGACAGCGCGTCGGTAGAGCAGGAACGCGGCG-3' **DdrC_R164E_R** 5'-CGCCGCGTTCCTGCTCTACCGACGCGCTGTCCT-3'
$DdrC^{R167E}$	**DdrC_R167E_F** 5'-AGCGCGTCGGTACGTCAGGAAGAGGGCGTCAAGGC-3' **DdrC_R167E_R** 5'-GCCTTGACGCCCTCTTCCTGACGTACCGACGCGCT-3'
$DdrC^{R164E/R167E}$	**DdrC_R164E167E_F** 5'-AGGACAGCGCGTCGGTAGAGCAGGAAGAGGGCGTCAAGGCACC-3' **DdrC_R164E167E_R** 5'-GGTGCCTTGACGCCCTCTTCCTGCTCTACCGACGCGCTGTCCT-3'
$DdrC^{R164A/R167A}$	**DdrC_R164A167A_F** 5'-GACAGCGCGTCGGTAGCTCAGGAAGCCGGCGTCAAGGC-3' **DdrC_R164A167A_R** 5'-GCCTTGACGCCGGCTTCCTGAGCTACCGACGCGCTGTC-3'
$DdrC^{R14E}$	**DdrC_R14E_F** 5'-ATTTCGGCTCCGTGGAGCTGCCTGTCAGCG-3' **DdrC_R14E_R** 5'-CGCTGACAGGCAGCTCCACGGAGCCGAAAT-3'
$DdrC^{R81E}$	**DdrC_R81E_F** 5'-CCCCGAAGCCCGGGAGTGGCAGAAGCGGG-3' **DdrC_R81E_R** 5'-CCCGCTTCTGCCACTCCCGGGCTTCGGGG-3'
$DdrC^{del9-14S}$	**DdrC_del9-14S_F** 5'- CTCCGCTGACCCTCAGCCTGCCTGTCAGCGC-3' **DdrC_ del9-14S_R** 5'- GCGCTGACAGGCAGGCTGAGGGTCAGCGGAG-3'
$DdrC^{delN}$	**For_DdrCdelN** 5'- AACCATGGGAGTCAGCGCGGACGGTTTGCTTCAC -3' (*NcoI*) **Rev_DdrC** 5'- TTCTCGAGTCAGCCTACGCGCTGCACCTGGC -3' (*XhoI*)

Table S2: List of DNA oligonucleotides used in this study for fluorescence polarization

dsDNA	Oligonucleotide name, sequence and label
50d5'F	**50mer_F_FAM** 5'- [FAM] GACTACGTACTGTTACGGCTCCATCTCTACCGCAATCAGGCCAGATCTGC -3' **50mer_R** 5'-GCAGATCTGGCCTGATTGCGGTAGAGATGGAGCCGTAACAGTACGTAGTC -3'
20d5'F	**20mer_F_FAM** 5'- [FAM] GACTACGTACTGTTACGTCT-3' **20mer_R** 5'-AGACGTAACAGTACGTAGTC-3'

Table S3: Comparison of the *de novo* DdrC crystal structure with the top five predicted DdrC models obtained with RosettaFold and AlphaFold2. The table lists the rmsd values for the overlays of either the whole structure or separate domains (NTD, residues 1-97; Linker, residues 98-138; CTD, residues 139-231).

Alignment to chain A											
Rmsd (Å)	X-ray structure	RosettaFold					AlphaFold2				
	Chain B	Model 1	Model 2	Model 3	Model 4	Model 5	Model 1	Model 2	Model 3	Model 4	Model 5
all atoms	7.412	7.677	7.692	7.799	7.622	7.676	2.439	2.439	2.439	2.439	2.439
residues 1-97	0.536	2.430	2.555	2.656	2.559	2.954	0.813	0.856	0.907	0.872	0.874
residues 98-138	4.569	1.858	2.101	2.348	2.093	2.414	1.084	1.129	1.096	1.092	1.229
residues 139-231	0.870	0.807	0.762	0.761	0.792	0.796	0.736	0.740	0.783	0.757	0.661
Alignment to chain B											
Rmsd (Å)	X-ray structure	RosettaFold					AlphaFold2				
	Chain A	Model 1	Model 2	Model 3	Model 4	Model 5	Model 1	Model 2	Model 3	Model 4	Model 5
all atoms	7.412	11.231	11.231	11.231	11.231	11.231	6.870	6.870	6.870	6.870	6.870
residues 1-97	0.536	2.467	2.682	2.730	2.488	3.439	0.881	0.936	0.998	0.984	0.973
residues 98-138	4.569	4.151	4.200	4.433	4.061	4.451	4.282	4.430	4.270	4.272	4.272
residues 139-231	0.870	1.065	1.040	1.145	0.959	1.100	0.767	0.781	0.722	0.719	0.724

Table S4: List of residues of DdrC that contact DNA in at least 3 of the five independent runs of MD simulations (500 ns).

Residue	Chain ID	Min. dist. ± SD (Å)	Mean dist. ± SD (Å)	Run1	Run2	Run3	Run4	Run5
S12	A	2.29 ± 0.16	4.01 ± 0.56	X	X	X	X	X
R81	A	2.37 ± 0.11	3.59 ± 0.24	X	X	X	X	X
R167	A	2.40 ± 0.12	5.24 ± 1.94	X	X	X	X	X
R14	A	2.42 ± 0.12	5.05 ± 0.73	X	X	X		X
R81	B	2.40 ± 0.21	4.48 ± 0.89		X	X	X	X
Q103	A	2.32 ± 0.49	4.80 ± 0.85	X	X	X		X
R142	A	2.56 ± 0.05	4.28 ± 0.69		X	X	X	X
Q146	A	2.53 ± 0.10	3.82 ± 0.38		X	X	X	X
R164	A	2.40 ± 0.09	5.56 ± 0.96	X	X	X		X
R164	B	2.56 ± 0.11	5.67 ± 1.00	X			X	X
R167	B	2.43 ± 0.21	4.24 ± 0.88	X		X		X
R173	B	2.48 ± 0.13	4.33 ± 0.75			X	X	X

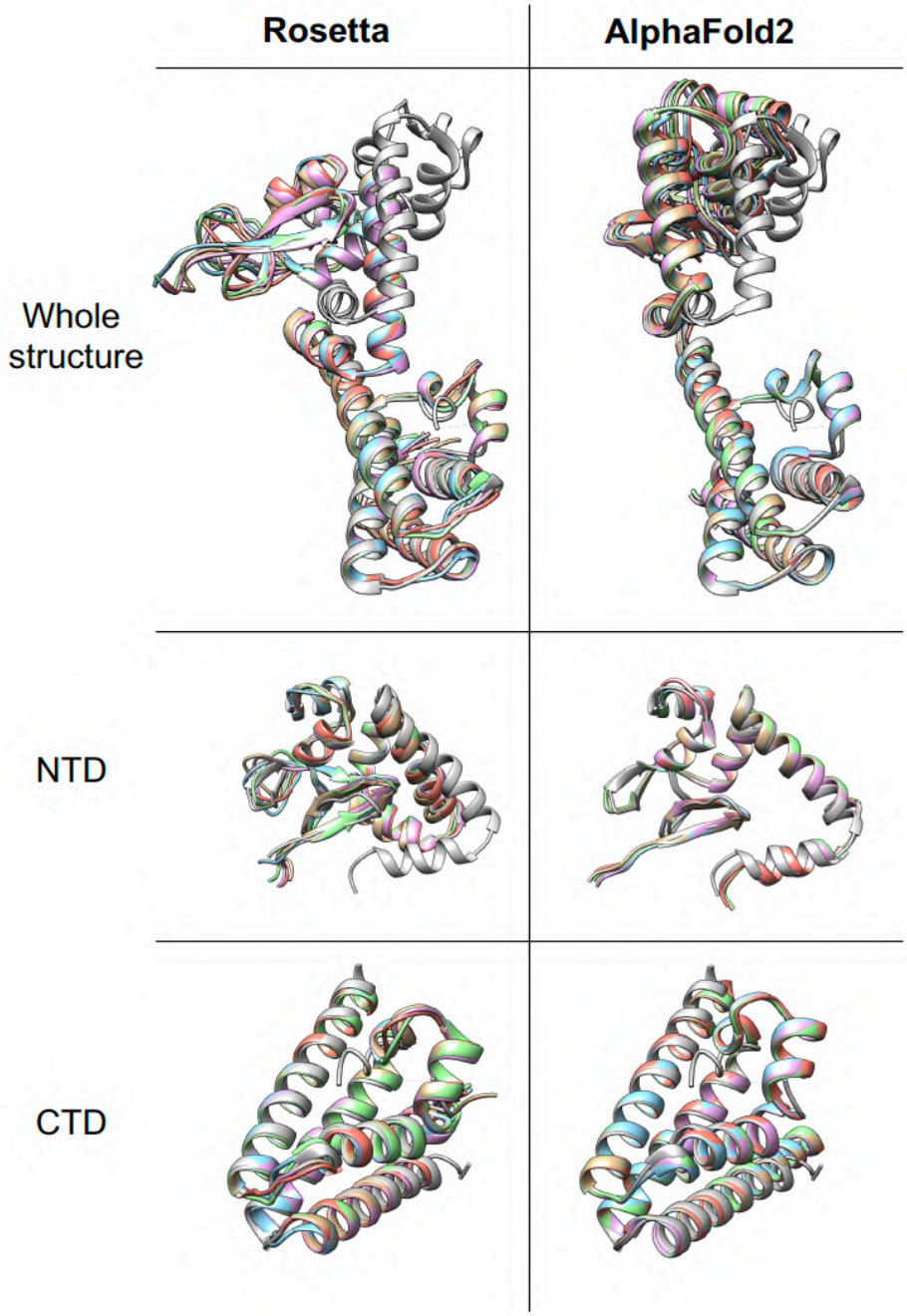

Figure S1: Overlay of DdrC crystal structure and predicted DdrC models. Overlay of the NTD (middle) and CTD (bottom) regions of DdrC and overlay of the entire structures (top) after fitting the CTDs. The top five predicted models of DdrC obtained with RosettaFold (left) and with AlphaFold2 (right) are depicted in color (gold, blue, pink, green and red), while the monomer A of the crystal structure of DdrC is colored grey. The CTDs were correctly predicted in both cases, while the NTD was only correctly predicted with AlphaFold2. Nonetheless, the relative orientation of the NTD with respect to the CTD was incorrect in both cases as can be seen in the overlay of the whole structure.

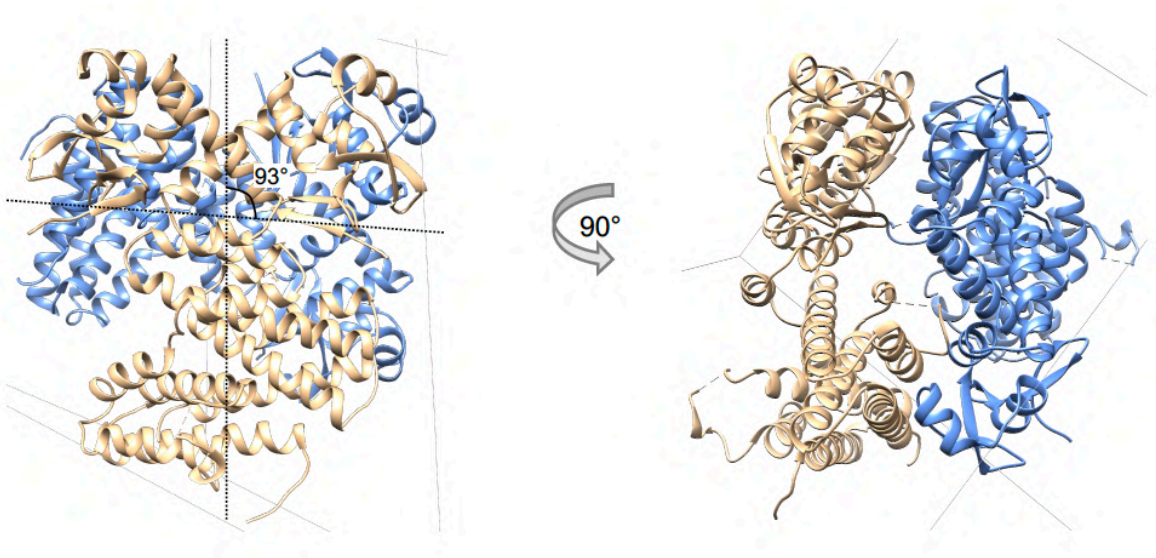

Figure S2: View of the crystallographic tetramer interface. Front and side views of a DdrC tetramer, with one dimer colored in beige and the other dimer colored in blue. In the crystal, DdrC forms a tetramer in which one of the dimers is rotated 93 with respect to the other, so that both the chain A and B of each dimer are involved in the interaction.

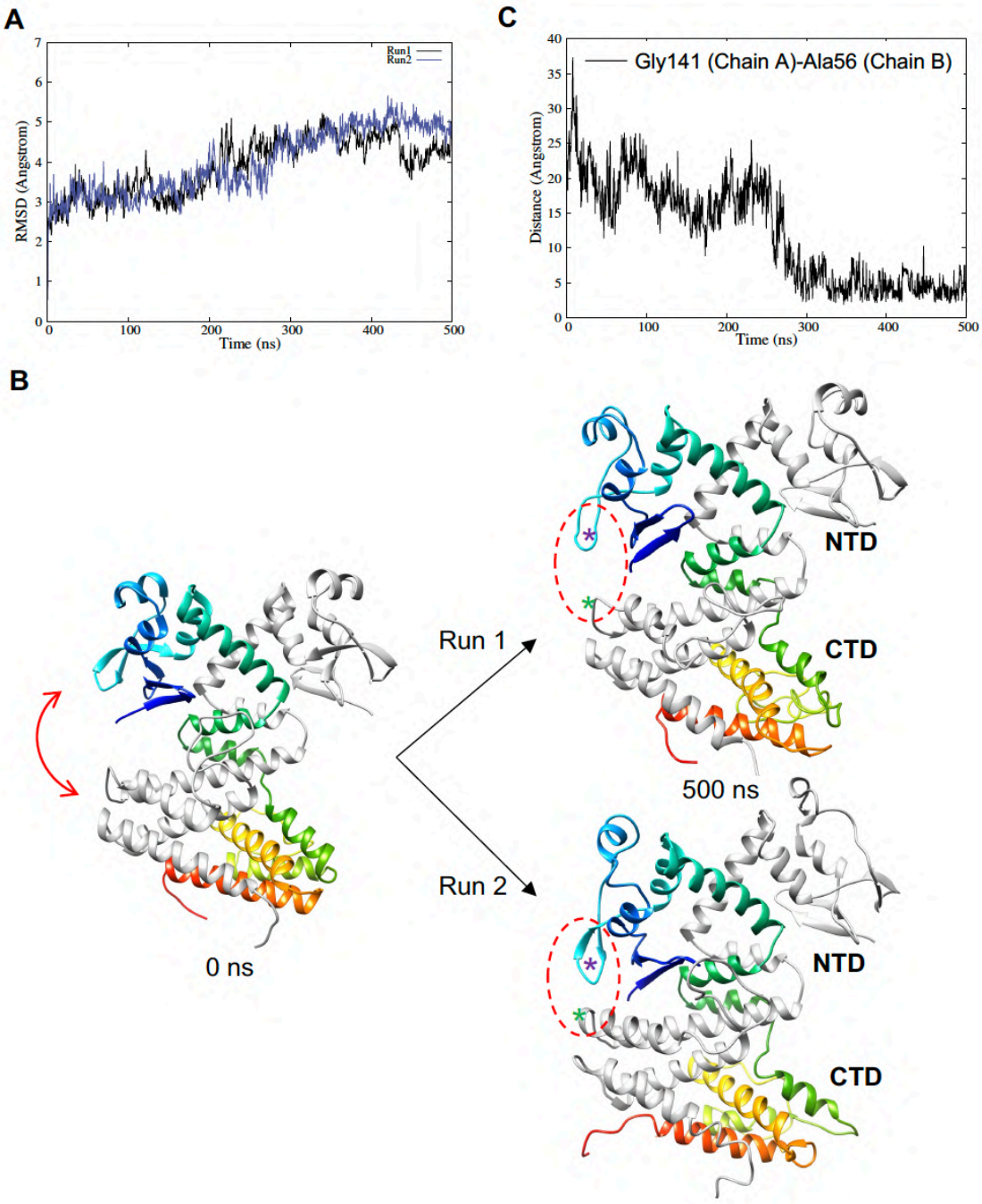

Figure S3: Molecular dynamics (MD) simulations of DdrC alone. (**A**) Time series of the rmsd of DdrC extracted from two 500 ns MD simulation runs of DdrC dimer alone. (**B**) Comparison of the conformations of dimeric DdrC at the start of the MD simulations (left) and at the end of the two 500ns runs (right). The dimer is very stable as are all the secondary structure elements, but movements between the NTD and CTD domains (red arrow) are observed, bringing the N-terminal wHTH of monomer B (colored in rainbow colors) in close proximity to the C-terminal four-helix bundle of the monomer A (grey). A red circle with a dashed line indicates this flexible region of DdrC. (**C**) Time series of the distance between Ala56 located in the bhairpin structure of the wHTH motif of DdrC chain B (purple star in (B)) and Gly141 of DdrC chain A (green star in (B)) extracted from the 500 ns MD simulation run 2 of DdrC dimer alone.

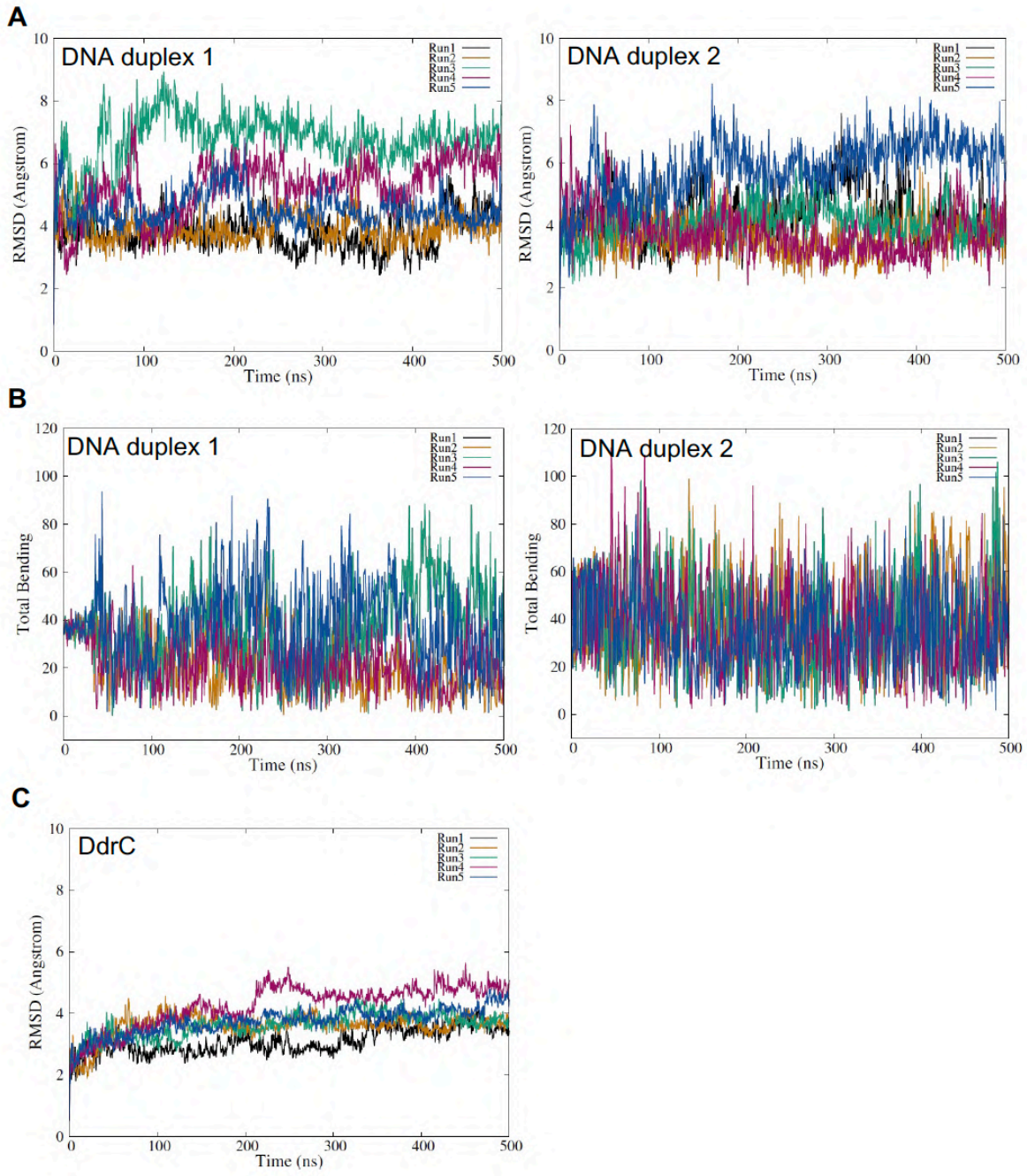

Figure S4: Molecular dynamics (MD) simulations of DdrC in complex with DNA. (**A-B**) Time series of the RMSD (A) and the total bending (B) of the two DNA duplexes (duplex 1, left and duplex 2, right) extracted from the five 500 ns MD simulation runs of DNA-bound DdrC dimer. (**C**) Time series of the RMSD of DdrC extracted from the five 500 ns MD simulation runs of DNA-bound DdrC dimer.

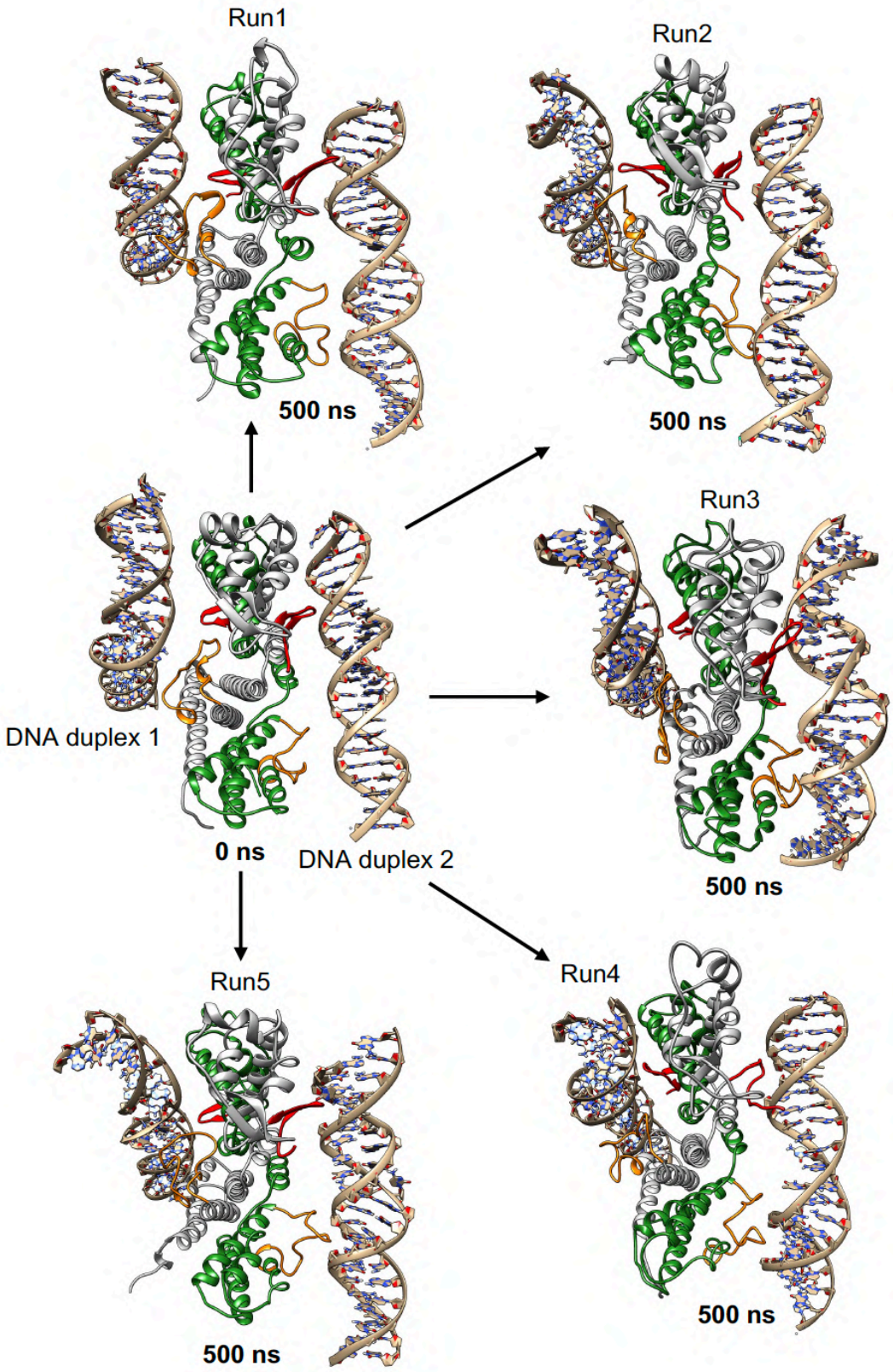

Figure S5: Molecular dynamics (MD) simulations of DdrC in complex with DNA. Comparison of the conformations of DNA-bound dimeric DdrC at the start of the MD simulations (left, middle) and at the end of the five independent 500ns runs. The monomers of DdrC are colored in grey (chain A) and green (chain B) and the elements involved in DNA binding are highlighted in red (NTD) and in orange (CTD).

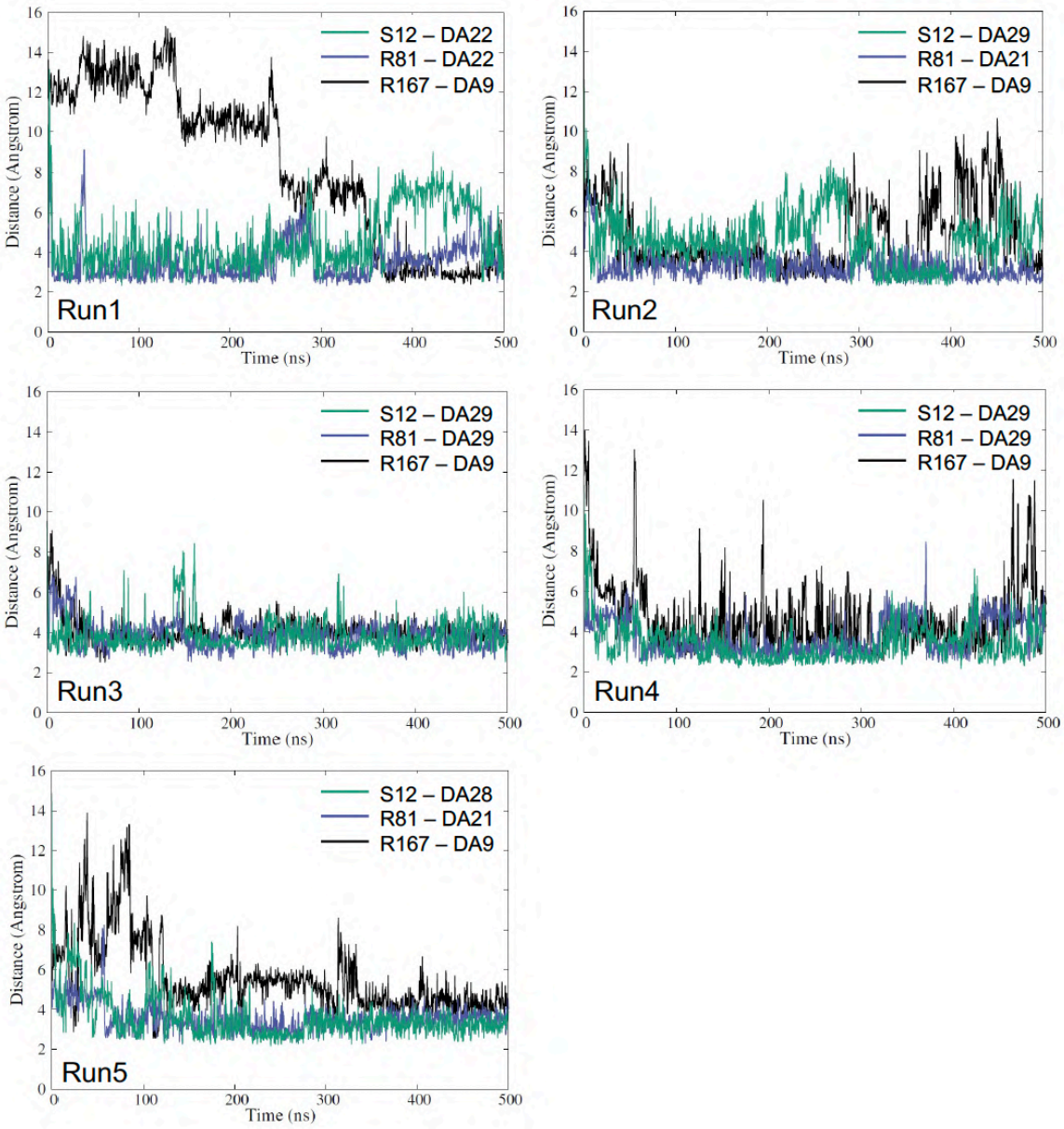

Figure S6: Evolution of the distances between the three major DNA-interacting residues of DdrC and DNA along the five MD runs. Time series of the distance between Ser12 (turquoise), Arg81 (blue) and Arg167 (black) of DdrC chain A and the closest DNA atom extracted from the five 500 ns MD simulation runs of DNA-bound DdrC dimer.

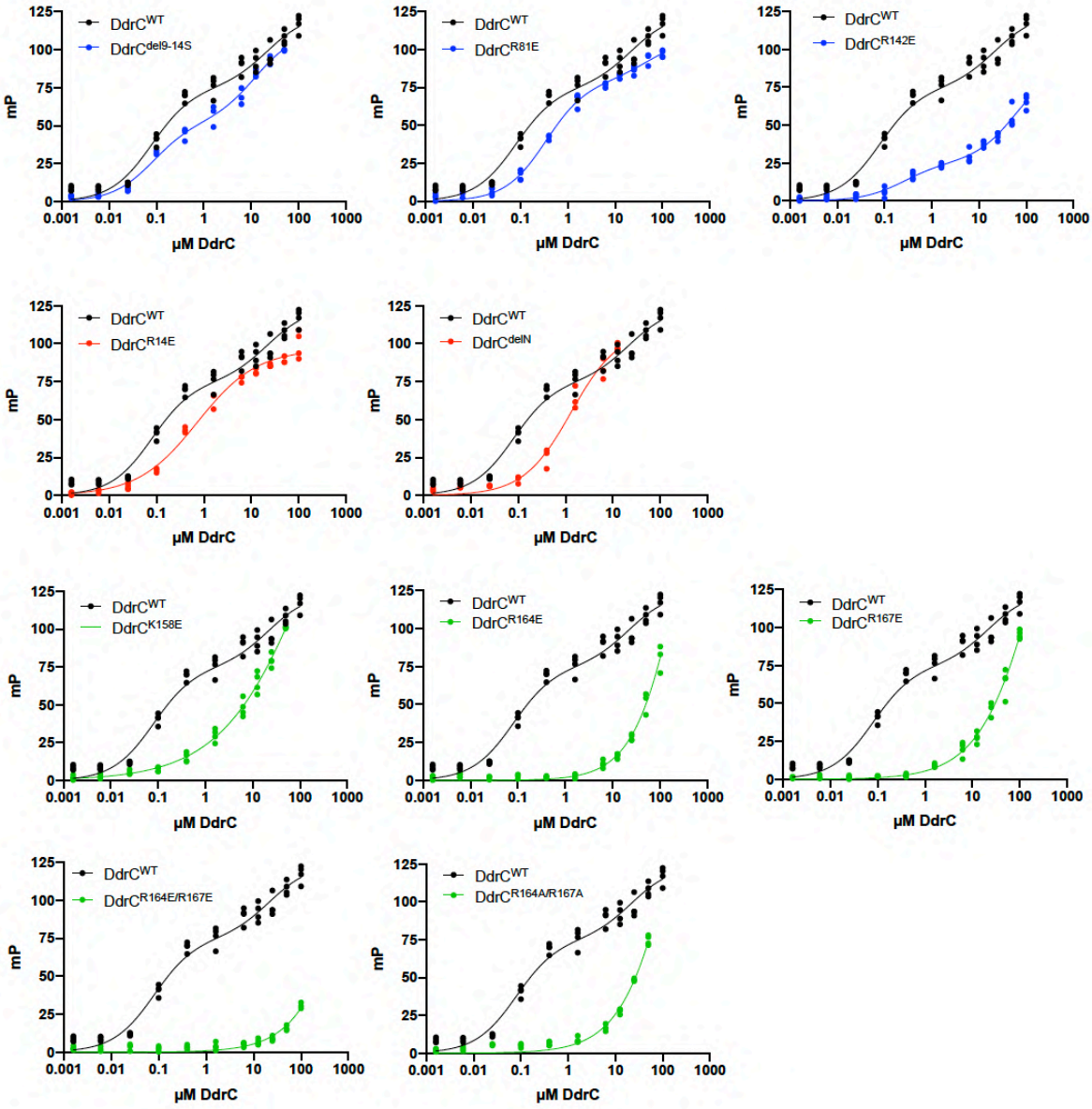

Figure S7: DNA binding curves derived from the fluorescence polarization (FP) measurements of wild-type (WT) and mutant DdrC binding to 50mer dsDNA. The binding curve of WT DdrC is shown in black in all graphs for comparison. For the DdrC mutants, three classes of mutants could be distinguished. Blue curves correspond to DdrC mutants retaining two distinct DNA binding sites. Red curves correspond to DdrC mutants having lost the second, low affinity binding site and exhibiting reduced affinity for their high affinity site. Finally, green curves correspond to DdrC mutants having severely impaired DNA binding properties. DNA binding constants derived from these curves are presented in Table 3. The graphs present individual FP measurements from at least three independent measurements, and the best fits.

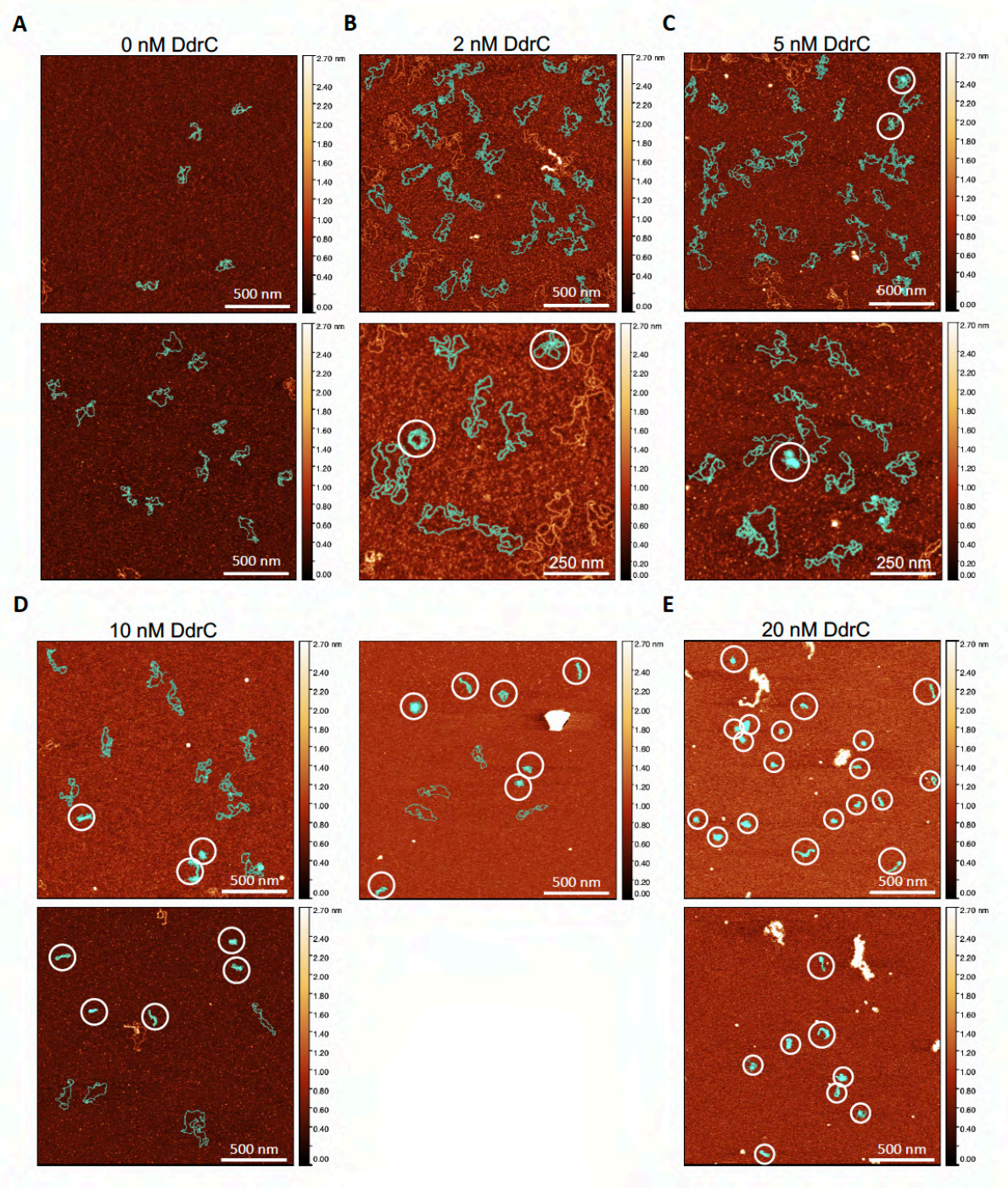

Figure S8. DdrC maintains circular plasmid in a condensed conformation. (**A-E**) AFM images of 0.5 nM of pUC19sc incubated with 0 (A), 2 (B), 5 (C), 10 (D) and 20 nM (E) DdrC. The light-blue mask highlights assemblies that have been used in the statistical analysis presented in Fig. 5F. Assemblies displaying a more condensed conformation are indicated by white circles. The z-scale bar is shown as a color gradient to indicate the distribution of height in the images.

Discussion and Perspectives

Deinococcus radiodurans is a gram-positive spherical bacterium that displays a high resistance to DNA-damaging agents such as ionizing radiation, UV-light, desiccation and reactive oxygen species (Slade & Radman, 2011; Zahradka et al., 2006). Several mechanisms appear to be at play to maintain proteome and DNA integrity, such as a high intracellular Mn/Fe ratio that protects proteome from oxidative damage, an efficient DNA double-stand break repair system, which allows the reconstitution of a functional genome from hundreds of DNA fragments generated by radiation or desiccation as well as the expression of *Deinococcus*-specific proteins such as the DNA-damage response proteins in response to irradiation or desiccation. Moreover, despite a high amount of genomic material, the nucleoid of *D. radiodurans* is extremely compact, which may limit dispersion of such DNA fragments, thus easing DNA repair processes (Floc'h et al., 2019; Levin-Zaidman et al., 2003). Despite being compact, the nucleoid of *D. radiodurans* yet remains highly dynamic as illustrated by the variety of shapes and the different compaction levels it adopts along the cell cycle or in reaction to stressful conditions (Floc'h et al., 2019).

In this context, the objective of my thesis project was to expand our knowledge on the organisation and dynamics of the nucleoid of *D. radiodurans*, through the study of the two most abundant NAPs in *D. radiodurans* nucleoid, namely DrHU and the DNA Gyrase, and a *Deinococcus*-specific NAP expressed in response to DNA-damaging conditions, DdrC. Additionally, the three HU proteins of *D. deserti*, namely DdHU1, DdHU2 and DdHU3, were also studied to compare DrHU with other Deinococcal HU proteins. We investigated the structure and function of these proteins and characterized their interaction with DNA and their effect on DNA conformation, in view to ultimately assemble a minimal chromatin *in vitro* for the study of DNA related processes.

DrHU is characterized by a binding site of 20 bp or less and a moderate affinity for dsDNA

My thesis project started with the production and characterization of the DNA binding properties of DrHU, which we expect to be the main architect of the nucleoid organisation due to its abundance and to the fact that no other DNA-bending or bridging NAPs such as IHF or H-NS are expressed in *D. radiodurans*. Our results showed that DrHU binds preferentially to dsDNA with a binding site of 20 bp or less in a cooperative manner, displaying an affinity of 300 ± 20 nM with a Hill coefficient of 1.5 ± 0.1 for a 43 bp dsDNA. Our estimation of the

length of the binding site is in contradiction with results previously obtained by Ghosh and Grove, showing that DrHU did not form stable complexes with oligonucleotides less than 50 bp in length (Ghosh & Grove, 2004). However, the more recent correction of the start codon position of DrHU removed 15 amino-acids wrongly assigned to its N-terminal extension, which might explain the longer binding site observed in their experiments (Bouthier de la Tour et al., 2015). A binding site of 20 bp or less would be in agreement with the length of the binding sites determined for HU proteins of other bacterial species. While the binding sites of the HU proteins of *E. coli* (EcHU) and *Bacillus subtilis* (BsHU) were estimated to be 9 to 13 bp in length, those of the HU proteins of *Anabaena* (AHU)*, Helicobacter pylori* (HpHU) and *Mycobacterium tuberculosis* (MtHU) are about 17 to 20 bp long and the even longer binding site of the HU protein of *Thermotoga maritima* (TmHU) spans 37 bp (Bhowmick et al., 2014; Chen et al., 2004; Grove & Lim, 2001; Kamashev & Rouviere-Yaniv, 2000; Kamau et al., 2005; Swinger et al., 2003).

The affinity of DrHU for the intact dsDNA oligonucleotide is comparable to that of EcHU or the HU proteins of *Bacillus stearothermophilus* (BstHU) and *Mycobacterium galliseptum*, for which the Kd values range from 293 nM to 440 nM indicating a moderate affinity (Benevides et al., 2008; Kamashev et al., 2017). It is worth noting that such a moderate affinity for dsDNA is not a feature common to the entire HU protein family, as BsHU, MtHU and TmHU all have a strong affinity for dsDNA with hundred times lower Kd values ranging from 5 to 16 nM (Bhowmick et al., 2014; Grove & Lim, 2001; Kamau et al., 2005). Nevertheless, one should be cautious when comparing Kd values originating from different studies as they may have been determined using different methods, like gel shift assays, microscale thermophoresis, isothermal titration calorimetry or fluorescence polarization, or under different experimental conditions such as different buffer compositions.

DrHU might modulate the compaction of the genomic DNA of D. radiodurans by keeping a balance between its compacting and stiffening effects on DNA

Having characterized the DNA-binding properties of DrHU, our next step was to evaluate its effect on DNA compaction and topology, using a dsDNA template that would be closer to the genomic DNA in terms of length and mechanical constraints such as plasmid DNA. Our analysis of DrHU in complex with relaxed or supercoiled plasmid DNA using atomic force microscopy (AFM) and electron microscopy (EM) revealed that this HU protein could form both highly compact and ordered assemblies with plasmid DNA and locally stiffen the DNA

maintaining it in a more open conformation depending on the amount of DrHU. This dual effect of DrHU on plasmid conformation as well as the structure of the protein-DNA complexes depend both on DrHU concentration and the initial plasmid conformation. A proposed model for the bimodal DNA binding mechanism of DrHU is summarized in Figure 67.

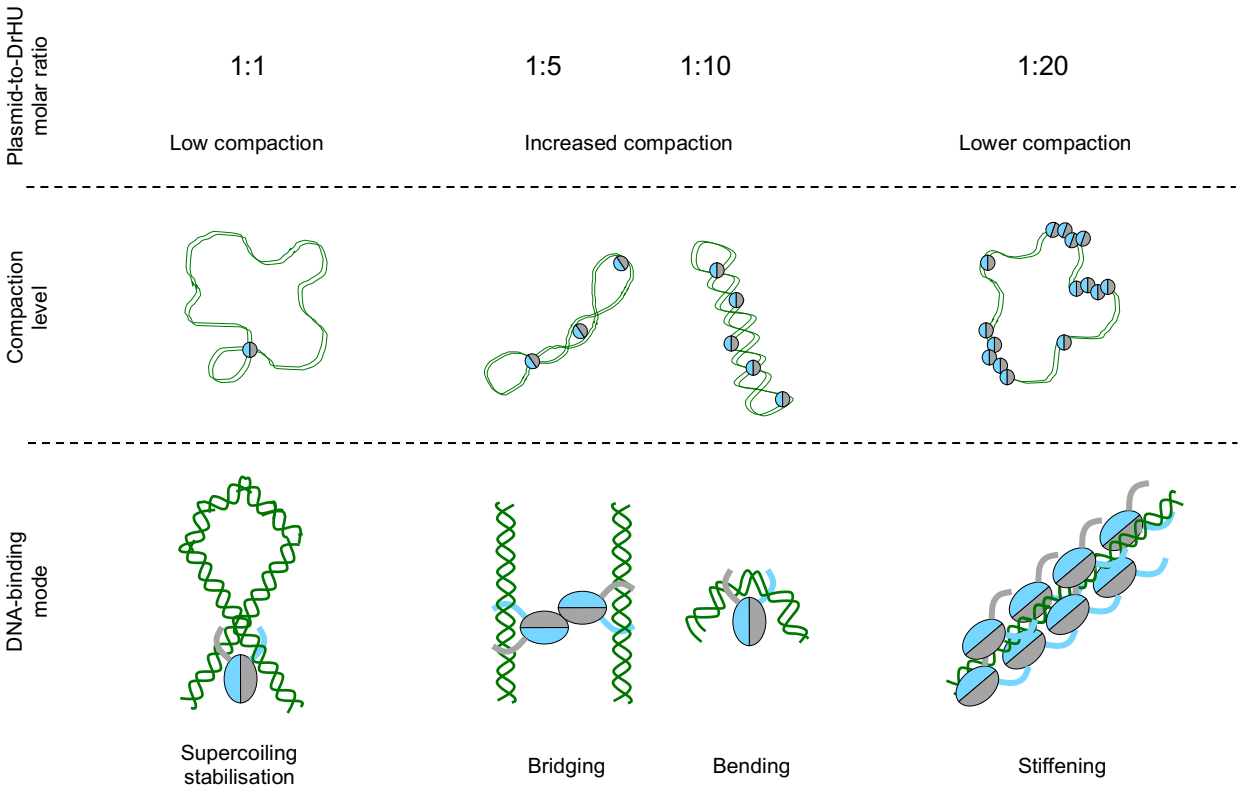

Figure 67. The dual effect of DrHU on supercoiled plasmid DNA conformation depends on DrHU concentration and cooperativity upon DNA-binding. This diagram illustrates the proposed model for the DNA binding mechanism of DrHU at different plasmid-to-DrHU molar ratios (increasing DrHU concentration from left to right). The dsDNA fragments and plasmid DNA are represented as green lines while the DrHU dimer is depicted as a grey and blue ellipse with two protruding curved lines to represent the DNA-binding β-arms.

In the presence of a supercoiled plasmid, a low amount of bound DrHU seems to maintain the supercoiled conformation, maybe by securing the negative writhes of the DNA molecule by binding at the site where two dsDNA fragments cross one another, as suggested by the study of Ghosh and Grove, which indicated that DrHU showed preferential binding to four-way junctions (Ghosh & Grove, 2004). As the amount of bound DrHU increases, the proteins further compact the supercoiled plasmid DNA, possibly by locally bending the DNA or by bridging distant DNA filaments. However, when reaching a locally high amount of bound DrHU proteins, the latter may re-organize and adopt a different oligomeric structure that would use dsDNA as a scaffold for multimerization, leading to localized stiffening of the DNA. This

binding mechanism would explain the less compacted plasmid conformations observed by AFM and cryo-EM at the highest plasmid-to-DrHU molar ratio.

DrHU might polymerise along DNA by forming nucleoprotein spiral filaments as it was observed for the EcHU, which compacts DNA at low concentration while stiffening it at higher concentration through multimerization (Hammel et al., 2016; Remesh et al., 2020; Skoko et al., 2004; van Noort et al., 2004). A similar dual effect was also proposed for BstHU based on the study of Sagi and colleagues, who used Förster resonance energy transfer (FRET) to measure the bending of 55 bp dsDNA oligonucleotides by BstHU (Sagi et al., 2004). Their results showed that the bending induced by BstHU was abrogated at high concentration, suggesting a bimodal effect depending on the concentration. This hypothesis was further supported by results from the study of Nir and colleagues that used tethered particle motion and AFM to analyse the contour length, persistence length and curvature of a 2.7 kb linear dsDNA fragment incubated with increasing concentration of BstHU (Nir et al., 2011).

The results of our crosslinking experiments suggested that DrHU is able to form tetramers in solution. Upon incubation with high concentrations of plasmid DNA, higher-order oligomers of DrHU were detected such as hexamers and even larger complexes unable to enter the gel. Since this behaviour was not observed in the presence of a shorter 30 bp dsDNA oligonucleotide, we hypothesize that the multimerization of DrHU requires the presence of a DNA molecule long enough to provide a scaffold for the formation of a nucleoprotein filament that would stiffen the DNA. In the future, to strengthen our analysis of DNA-induced oligomerisation profile of DrHU, we could use analytical ultracentrifugation to study the presence of higher-order oligomers as a function of DrHU concentration and dsDNA length, as this method was successfully applied to the study of several protein-DNA complexes as reviewed in (Edwards et al., 2020).

Based on the crystal contacts observed in the crystal structures of HU proteins from other bacteria, we produced some plausible models for the assembly of a DrHU tetramer (Fig. 68). To form a tetramer, two DrHU dimers could make contact through their respective alpha-helical dimerization domains (Fig. 68A and B) or through their DNA-binding β-arms (Fig. 68C) as it was observed in the crystal structures of EcHUαα and EcHUαβ (Hammel et al., 2016; Remesh et al., 2020). Alternatively, DrHU oligomerisation could involve the overall positively charged 30 residue-long N-terminal extension of DrHU containing eight lysine and one arginine residues. A DrHU tetramer might indeed assemble through contacts between the positively charged N-terminus of one dimer and the negatively charged electrostatic surface of the second

α-helix composing the dimerization domain of another DrHU dimer, which contains three of the six glutamate residues present in the sequence of DrHU.

By combining such models of tetrameric DrHU with models of DNA-bound HU, we can propose different ways in which DrHU tetramers might bridge two adjacent dsDNA duplexes, either through interactions with their central alpha-helical core (Fig 68A) or via their extended β-arms (Fig. 68B). In both cases, the DNA duplexes would be maintained between 5 and 10 nm apart, as observed in the spiral assemblies in our cryo-electron micrographs (Fig. 59).

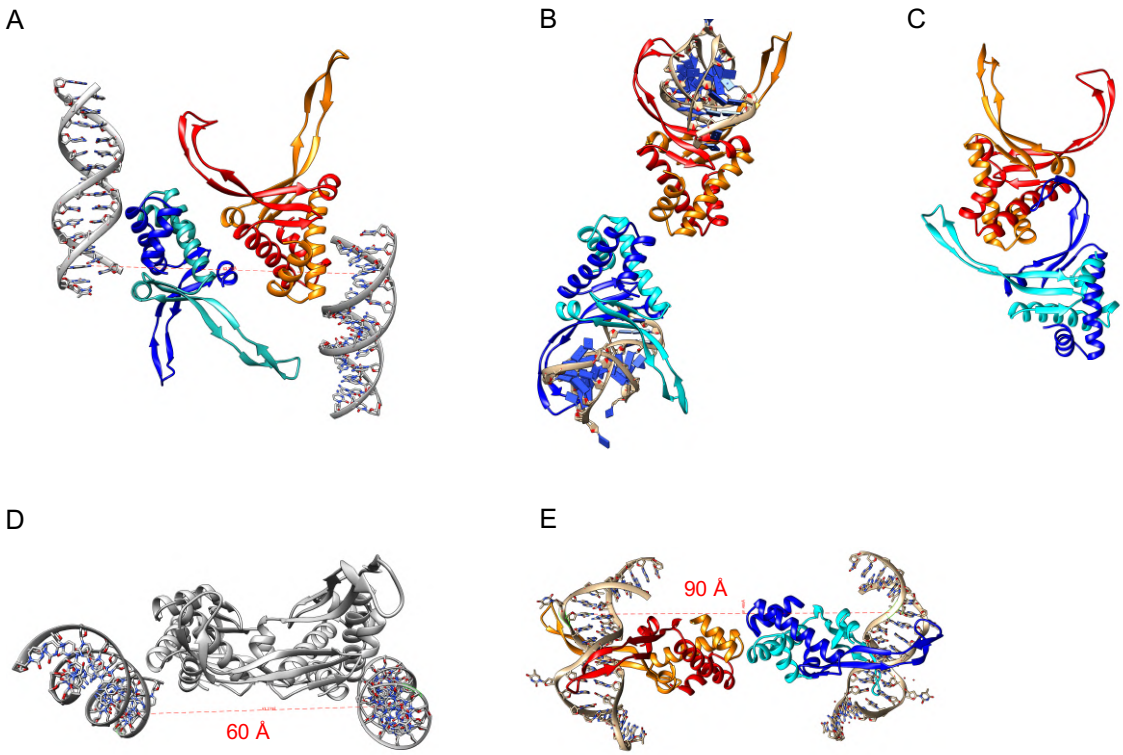

Figure 68. Models of DrHU tetramer based on crystal structures of HU proteins from *E. coli*, *Anabaena* or *Bacillus anthracis*. A model of DrHU tetramer was designed based on the crystal contacts found in the crystal structures of **A**) EcHUαα in complex with a 19 bp dsDNA (PDB code 4YEX (Hammel et al., 2016)), **B**) AHU in complex with a 19 bp dsDNA (PDB code 1P51 (Swinger et al., 2003)) and **C**) *Bacillus anthracis* HU (PDB code 3RHI (Osipiuk et al., 2011, to be published)). For the models based on EcHUαα (**D**) and AHU (**E**), the distance between the two bridged dsDNA fragments is indicated on a side view of the structure. The two chains of the first HU dimer are coloured in light and dark blue while the two chains of the second HU dimer are coloured in red and orange.

AFM and cryo-EM analyses of the protein-DNA assemblies formed at high concentrations of DrHU with supercoiled or relaxed plasmid DNA both highlighted the presence of regions of bare DNA nearby regions covered in DrHU. These converging results

indicate strong cooperative binding properties that were also evidenced by the Hill coefficient of 1.5 ± 0.1 determined from our FP assay with a 43 bp dsDNA oligonucleotide. The spiral-shaped structures observed in our cryo-EM experiments therefore could be explained by an uneven distribution of bound DrHU on plasmid DNA driven by cooperativity, where some stiffened segments of the plasmid DNA covered in bound DrHU would be linked by more flexible and potentially bent segments, onto which the amount of bound DrHU would be too low for multimerization to occur. Such an uneven distribution of bound HU proteins was observed (although not shown) by Van Noort and colleagues in their AFM study of the complexes formed by EcHUαβ bound to 500 to 2,100 bp dsDNA fragments when using low salt concentration in the binding buffer as in our experiments (van Noort et al., 2004).

Although the results of our AFM and cryo-EM experiments on the protein-DNA assemblies formed by DrHU with supercoiled plasmid DNA both suggest a DNA binding mode where an increasing amount of bound DrHU would lead to a shift from DNA compaction to localized DNA stiffening, we observed some differences notably regarding the shape of the protein-DNA complexes. While compacted rod- or globular-shaped complexes were observed with AFM at a plasmid-to-DrHU molar ratio of 1:20, the cryo-EM analysis of the complexes formed at a molar ratio of 1:100 displayed only spiral-shaped or fingerprint-like structures. As summarized in the table below, these differences could arise from various biases inherent to the method used to analyse the DrHU-plasmid assemblies (Table 16).

Table 16. Comparison of the possible biases introduced by atomic force microscopy (AFM) and cryo-electron microscopy (Cryo-EM) for the study of nucleoprotein complexes. For the AFM and cryo-EM technique, the indicated biases refer to the protocols used during the thesis project.

Method	Solvent	Temperature	Support	HU-support interaction	DNA-support interaction
AFM	no (dried)	room temperature	Ni^{2+}-coated mica	low (positively charged HU)	high (phosphate backbone)
Cryo-EM	yes (frozen)	cryogenic temperature	carbon coated grid	protein-DNA complex aggregated at the air-water interface	

While neither AFM nor cryo-EM require to stain the sample, we performed our AFM imaging in air on a dried sample that might have been damaged by the removal of the solvent. Furthermore, when depositing our sample on nickel-coated mica, the negatively charged backbone of the plasmid DNA is expected to strongly interact with the positively charged mica surface, leading to a bias in the observed conformations as protein-DNA assemblies would tend to bind in specific orientations that favour the interaction with the mica. In contrast, the sample

imaged by cryo-EM are kept in solution, but the preparation is frozen in liquid ethane to image the sample at cryogenic temperatures. While the protein and DNA remain hydrated in this method and less prone to favour a specific orientation, the freezing process also introduces a bias, as the molecules tend to gather in a thin layer at the air/solvent interface during cryo-cooling in liquid ethane, which could potentially lead to denaturation or artefacts in the protein-DNA complex (Atherton & Moores, 2021; D'Imprima et al., 2019).

Additionally, we faced some discrepancies between our qualitative assessments of DrHU-DNA assemblies and the quantitative measurements performed on these same assemblies when exploring the effect of the HU proteins on plasmid DNA conformation by AFM. The values of the mean surface or volume of the plasmid molecules or the protein-plasmid complexes derived from our AFM images did not always reflect the apparent compaction observed in these images, indicating that these parameters may not be the best suited for such an analysis. As an alternative, we could follow DNA compaction by measuring the longest distance between two points of a given plasmid molecule (or protein-plasmid complex). This analysis of plasmid compaction through the determination of end-to-end distances was implemented by Maurer and colleagues in their AFM study of the nucleoprotein complexes formed by various NAPs of *E. coli* (Maurer et al., 2009).

Taken together, our results contribute to a better understanding of the function of DrHU in the dynamic organisation of *D. radiodurans* nucleoids. As previously shown by my colleagues, although DrHU colocalizes with the genomic DNA *in vivo*, it is only transiently associated with the DNA as most of the DrHU population was found to be mobile (Floc'h et al., 2019). We thus propose a model in which the moderate affinity for dsDNA and significant mobility of DrHU in the nucleoid would lead to only a small fraction of DrHU molecules bound to DNA at any given time that would compact the genomic DNA by maintaining supercoiling and bridging distant DNA fragments. Through a combination of changes in DrHU mobility and local cooperative binding to DNA, some regions of the genomic DNA may become enriched in bound DrHU and could adopt a more rigid and less compact structure suitable for DNA processes such as transcription, replication or DNA repair.

The dual binding mechanism of DrHU is not a common feature of deinococcal HU proteins, as evidenced by the DNA binding properties of the HU proteins of D. deserti

During this thesis project, the DNA binding properties of DrHU were compared with that of other deinococcal HU proteins, namely DdHU1, DdHU2 and DdHU3, which are the three HU variants expressed in *D. deserti*. Alike DrHU, the three HU variants all showed a clear preference for binding to dsDNA and were able to form stable complexes with dsDNA oligonucleotides as short as 20 bp. Nevertheless, some notable differences between the four HU proteins were observed as DdHU3 appeared to have a 1.5 to 2 times higher affinity for dsDNA than the other *D. deserti* HU proteins and DrHU, respectively. The three HU proteins of *D. deserti* also displayed different levels of cooperativity upon binding to dsDNA when compared to DrHU, with respective Hill coefficients of 2.2 ± 0.3 for DdHU1, 1.1 ± 0.1 for DdHU2 and 1.0 ± 0.1 for DdHU3, indicating a strong binding cooperativity for DdHU1 and almost none for DdHU2 and DdHU3.

As these variations in the DNA binding characteristics among the deinococcal HU proteins are likely to influence their effects on DNA conformation and compaction, we analysed the protein-DNA assemblies formed by DdHU1 and DdHU3 in complex with supercoiled plasmid DNA using AFM. Our results showed that the binding mode and compaction mechanism of DdHU1 is strikingly different from those of DrHU. While we showed that DrHU either condensed or stiffened the DNA in a concentration-dependent manner, DdHU1 induced a slight compaction at the lowest protein concentration before progressively coating the plasmid DNA as the protein concentration increased, up to a point where the bound DdHU1 fully covered the plasmid DNA. At the highest protein concentration, where DrHU was found to locally stiffen the DNA, the bound DdHU1 fully coated plasmid DNA and seemed to re-organize to form highly compact protein-DNA structures that were either globular or rod-shaped. The distinct DNA binding mode of DdHU1 could arise from an inability to multimerize as filaments along DNA compared to DrHU, hinting at an oligomerization profile that differs from DrHU. Based on our crosslinking experiments DdHU1 is indeed only present as dimers in solution since no tetramers were detected on our gels, although crosslinking in the presence of dsDNA was not performed with this HU variant. The most distinctive feature of DdHU1 compared to the other deinococcal HU proteins was its high cooperativity upon DNA binding, as evidenced by its Hill coefficient of 2.2 ± 0.3 determined by FP with a 43 bp dsDNA oligonucleotide. The highly cooperative binding of DdHU1 was confirmed by AFM imaging at intermediate protein concentrations corresponding to plasmid-to-DdHU1 molar ratios of 1:5

and 1:10, where plasmid DNA molecules covered in DdHU1 laid in close vicinity to seemingly bare plasmid DNA molecules.

As we previously suggested, the coating of plasmid DNA by DdHU1 through cooperative binding might be driven by an oligomerisation mechanism that does not involve the formation of a stiffening HU-DNA filament, but rather the stacking of DdHU1 dimers onto each other, possibly through protein-protein interactions. Since no tetramers or higher-order oligomers were observed by crosslinking of DdHU1 in solution, we propose that the oligomerisation of DdHU1 could be driven by a re-arrangement of the structure of DdHU1, possibly involving its N-terminal extension, upon binding to DNA as it was shown for the C-terminal tail of eukaryotic histone H1 (Roque et al., 2005). These major differences between DrHU and DdHU1 were surprising considering that these two HU variants share a sequence similarity of 92%. Based on the DrHU and DdHU1 structures produced by homology modelling using the structure of *S. aureus* HU (PDB code 4QJN (Kim et al., 2014)), the divergent residues located in their conserved core appear to be solvent exposed and localized along the sides of the HU dimers (Fig. 69A-C). Major differences concern Q46 in DrHU which is replaced by an arginine in DdHU1, and the residues Q70 and S71 in DrHU which are replaced respectively by an arginine and a glutamate in DdHU1. It is worth noting also that the unique cysteine in DrHU that is also surface exposed is replaced by a serine in DdHU1. Analysis of the electrostatic surface properties of the modelled structures of DrHU and DdHU1 reveals that these residues induce a slightly more positively charged surface on the side of the DrHU dimer compared to that of DdHU1 (Fig. 69B-D). However, the superposition of the modelled structures of DrHU and DdHU1 on the structure of *S. aureus* HU bound to a 21 bp dsDNA shows that these residues are probably not involved in DNA binding since they are localized on the sides of the HU dimer, orthogonal to the path of the bound dsDNA. They could instead influence protein-protein interactions.

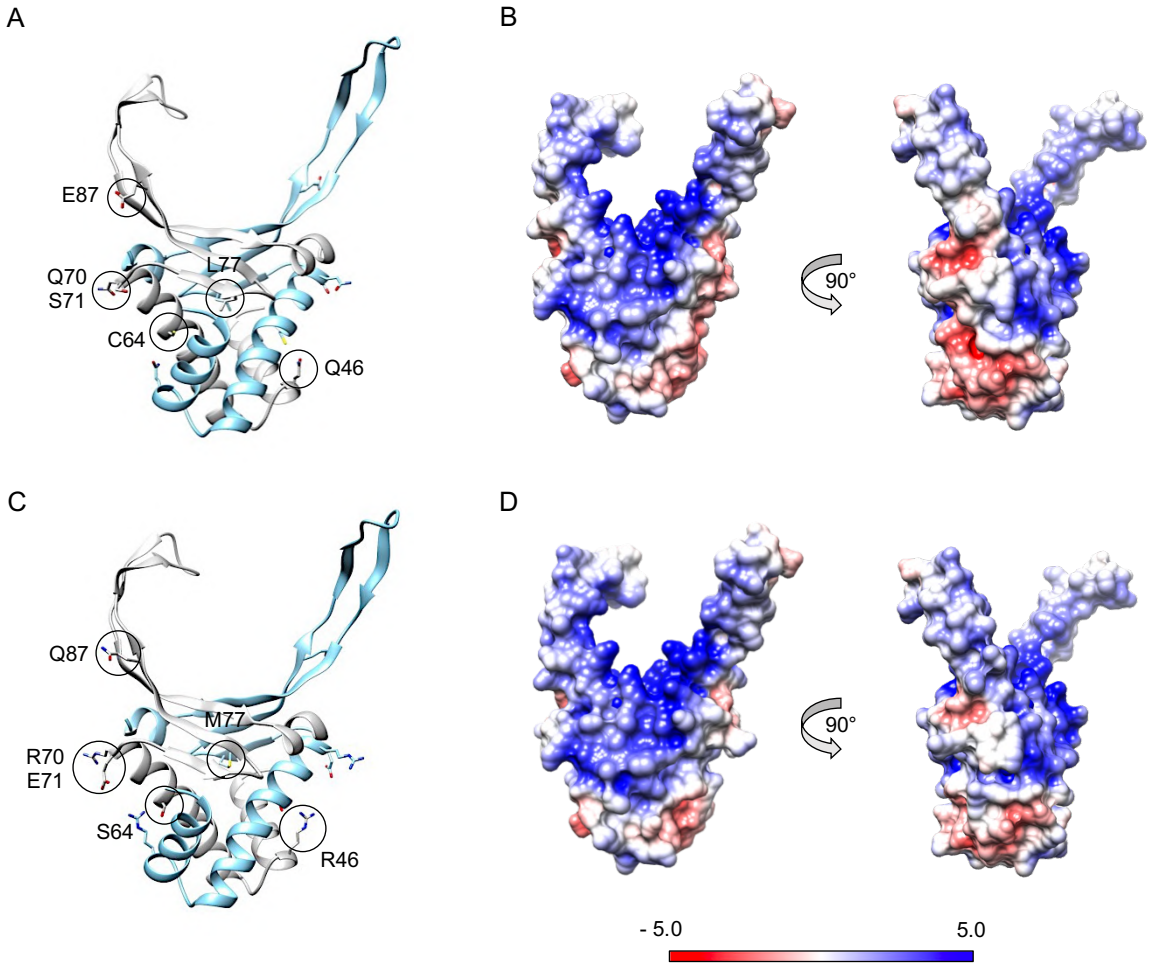

Figure 69. DrHU and DdHU1 only differ by a few residues located on the side of the HU dimers. Modelled structures of DrHU (**A**) and DdHU1 (**C**) were obtained by homology modelling based on the crystal structure of *S. aureus* HU (PDB code 4QJN (Kim et al., 2014)) using the online software SWISS-MODEL (Waterhouse et al., 2018). For each HU dimer, one monomer is coloured in grey and the other in blue. The main residues that differ between DrHU and DdHU1 are represented as sticks with the oxygen atoms in red, the nitrogen atoms in blue, the sulphur atoms in yellow and are identified by their position in the sequence (residue numbering refers to the sequence of DrHU). The electrostatic surface properties of the modeled DrHU (**B**) and DdHU1 (**D**) structures were calculated with the APBS software and displayed in Chimera. The color scale is the same for the two structures and refers to electrostatic charges of the protein surface (red indicates negative charges while blue indicates positive charges).

Although we only gathered preliminary data from our AFM study of DdHU3 in complex with supercoiled plasmid DNA, we observed a higher affinity and lower cooperativity upon binding to dsDNA oligonucleotide compared to DrHU and DdHU1. DdHU3 is the more divergent HU protein of *D. deserti* when compared to DrHU as they only share 69 % of their residues. Notably, the N-terminal extension of DdHU3 is seven residues shorter than that of

DrHU yet it is more positively charged with a pI value of 12.04 instead of 10.82 for that of DrHU. This difference is due to the presence of a second arginine and a lack of negatively charged residues in the N-terminal extension contrary to DrHU, DdHU1 and DdHU2 (Table 17). The enrichment of the N-terminal extension of DdHU3 with positively charged residues compared to the other three HU proteins might explain the higher affinity for dsDNA observed in our DNA binding assays, suggesting the implication of the N-terminal extension in the DNA binding process or the stabilisation of the bound DNA.

Table 17. Composition and pI of the N-terminal extensions of DrHU, DdHU1, DdHU2 and DdHU3. For each of the four HU proteins, the sequence, length, pI and number of charged residues (Arg, Lys, Asp and Glu) of the N-terminal-extension are indicated. For the pI values, the number in brackets correspond to the pI of the total protein sequence. The pI values of the charged residues are indicated in brackets.

Protein	Sequence	Length	pI (total)	Arg (pI 10.76)	Lys (pI 9.47)	Asp (pI 2.87)	Glu (pI 3.08)
DrHU	MTKKSTKAPAKKAAPAA KAAPAAKRGAAADSGK	33	10.82 (10.20)	1	8	1	0
DdHU1	MTKKSAKAPAKKPAASA KAAPKKGAVAAESNK	32	10.54 (10.43)	0	9	0	1
DdHU2	MTKKNTKAPAKKPAATK SAASAAPKKAAAAEK	32	10.54 (10.40)	0	9	0	1
DdHU3	MAKSTKPAAKKPAAATS RRAAAAGSK	26	12.04 (11.12)	2	5	0	0

Some interesting differences in the sequence of DrHU and DdHU3 are found in the more conserved core region of the two HU proteins. Two main sequence variations of DdHU3 compared to DrHU, namely Q46R and Q70R (DrHU residue numbering), seem to be specific to the *D. deserti* HU proteins as they are also present in DdHU1 and DdHU2 (Fig. 70A). Compared to DdHU1, the sequence of DdHU3 presents a double-mutation in the β-strands of the DNA binding domain, K86A and A111R, which according to a superposition of the modelled DdHU3 structure with that of *S. aureus* HU in complex with a 21 bp dsDNA could be involved in DNA binding (Fig. 70B). Arginine residues bind to the DNA backbone more tightly because they are able to form two hydrogen bonds per residue with the phosphate groups of DNA, whereas lysines can only form one hydrogen bond (Luscombe, 2001). The presence of this arginine in the DNA-binding domain along with the shorter but more positively charged N-terminal extension of DdHU3 could explain its 1.5 to 2 times higher affinity for dsDNA compared to the other deinococcal HU variants.

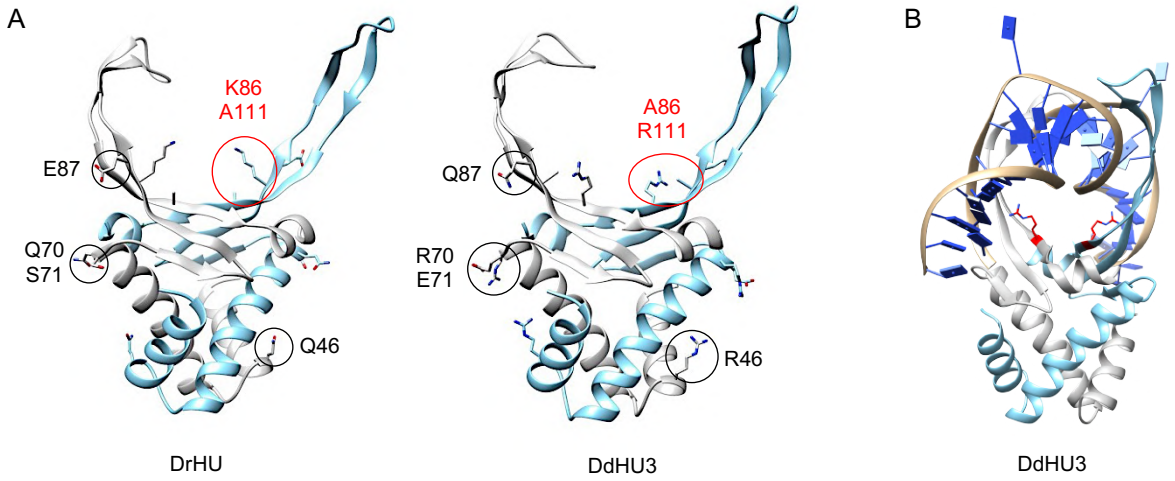

Figure 70. DdHU3 presents a mutation at the base of the β-arms that might enhance its affinity for dsDNA. **A**) Structures of DrHU (left) and DdHU3 (right) were obtained by homology modelling based on the crystal structure of *S. aureus* HU (PDB code 4QJN (Kim et al., 2014)) using the online software SWISS-MODEL (Waterhouse et al., 2018). For each HU dimer, one monomer is coloured in grey and the other in blue. The main residues that differ between DrHU and DdHU3 are represented as sticks with the oxygen atoms in red, the nitrogen atoms in blue and are identified by their position in the sequence (residue numbering refers to the sequence of DrHU). The double-mutation K86A-A111R is highlighted by a red circle on each structure. **B**) Superposition of the modelled DdHU3 structure on the crystal structure of *S. aureus* HU in complex with a 21 bp dsDNA (PDB code 4QJU (Kim et al., 2014)), showing that the arginine residues (represented as red sticks with the nitrogen atoms in blue) could be involved in DNA binding or stabilisation of the bound DNA. For clarity, the *S. aureus* HU used for structure alignment is not shown.

Reflexions on the N-terminal extensions of the HU proteins of D. radiodurans and D. deserti

As previously stated, variations in the sequences of the core regions of DdHU1 and DdHU3 compared to that of DrHU might explain the distinct DNA binding modes of DrHU and DdHU1 as well as the higher affinity of DdHU3. Nevertheless, it is noteworthy that half of the divergent residues of DdHU1 and DdHU3 compared to DrHU reside in their N-terminal extension, which suggest a role either in the first step of DNA binding or in the stabilisation of a possibly bent conformation of the bound DNA. To explore the plausible conformations energetically accessible to the N-terminal extension of DrHU, we used the online structure prediction server Robetta that yielded five potential conformations (Fig 71). Based on these models, the N-terminal extensions are expected to be quite flexible as they can adopt diverse conformations that are more or less folded, either positioned on the sides of the DrHU dimer or in between the DNA-binding β-arms, which could prevent or modulate the binding to DNA. DNA binding or higher order oligomerisation of DrHU is likely to change the flexibility and conformational space of this N-terminal extension.

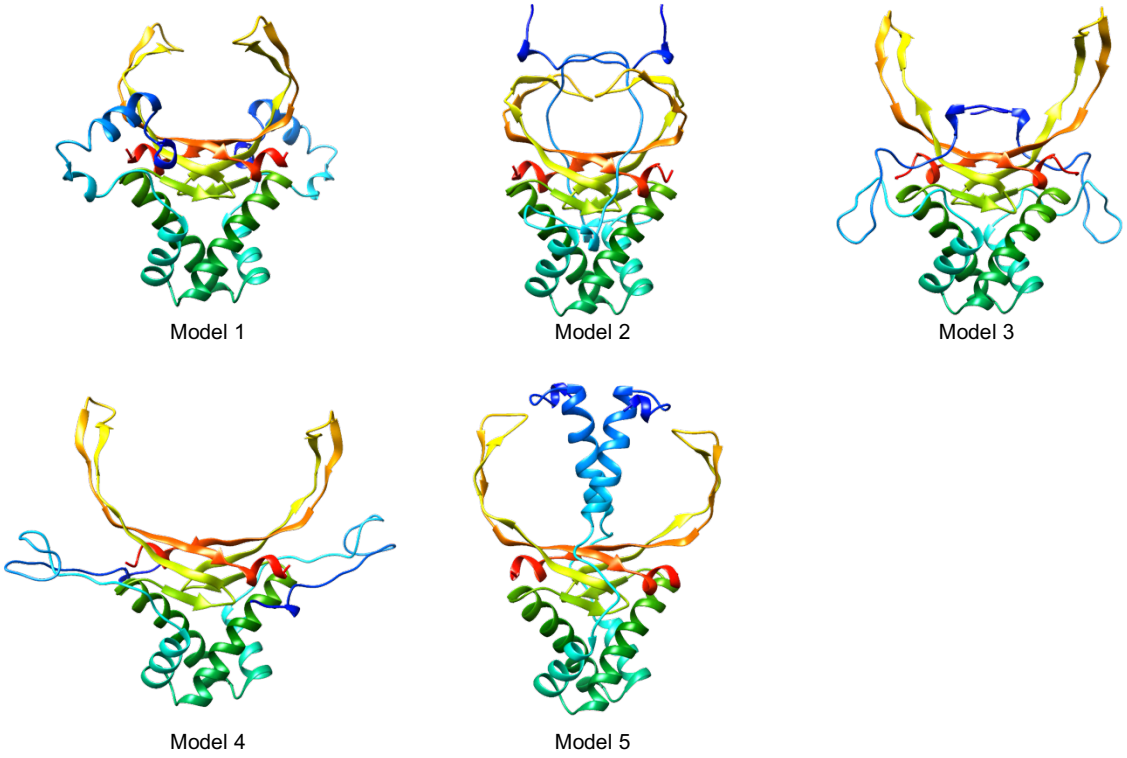

Figure 71. Possible conformations of the N-terminal extensions of DrHU based on energetic landscape. The most energetically favourable conformations of the complete structure of DrHU were modelled with the structure prediction server Robetta. The five predicted models are presented here, with each monomer coloured from blue (N-terminus) to red (C-terminus). The N-terminal extensions are thus depicted in blue and are predicted to adopt either folded (models 1 and 5) or unfolded/partially folded conformations (Models 2-4).

Moreover, the equilibrium between one or the other of these conformations of the N-terminal extensions might be regulated by the introduction of post-translational modifications (PTMs) on the multiple lysine, arginine, serine and threonine residues present in this specific region of the protein, as it was shown that PTMs can alter the protein structure (Xin & Radivojac, 2012). In a recent review on the PTMs of the HU proteins in bacteria, Carabetta listed 21 bacterial species in which the HU protein contains at least one acetylation site (Carabetta, 2021). Moreover, a proteomic study by Yagüe and colleagues found that 40 % of HU homologues from 24 bacterial species contained at least one phosphorylation site (Yagüe et al., 2019). Looking at the conserved 90 residue-long core sequence of the HU proteins, three conserved acetylation sites could be highlighted, namely K36, K51 and K119 (residue numbering based on DrHU sequence). The acetylation of lysine residues in BsHU and MtHU has been proven to reduce the affinity of HUs for dsDNA *in vitro* (up to tenfold in the case of MtHU) and to induce a decompaction of the nucleoid *in vivo* compared to non-acetylated BsHU and MtHU (Anand et al., 2017; Carabetta et al., 2019; Ghosh et al., 2016). Since these lysine residues are highly conserved among HU proteins and therefore present in the sequence of the

four deinococcal HU proteins, it would be of particular interest to perform a proteomic analysis on HU proteins extracted from *D. radiodurans* and *D. deserti* cells to assess the presence of PTMs like acetylation, succinylation or phosphorylation. Should such PTMs be found, we could evaluate their impact on the DNA binding properties of the deinococcal HU proteins by means of AFM and cryo-EM as it was done for the study of acetylated MtHU, using the results presented here as a reference for their non-acetylated counterparts (Ghosh et al., 2016).

The structures of the deinococcal HU proteins remain elusive

To shed light on the function of the N-terminal extensions in deinococcal HU proteins and their distinct DNA-binding properties, we tried to elucidate the structure of the full-length HU proteins of *D. radiodurans* and *D. deserti*, but unfortunately failed to crystallize the four variants. Our goal was to obtain a full-length structure of the deinococcal HU protein and in particular to gain insight into the structure of their unusual N-terminal extensions, since the rest of the protein is highly conserved with that of *T. thermophilus* HU for which a crystal structure is available (Papageorgiou et al., 2016). Based on the diverse conformations accessible to the N-terminal extension of DrHU modelized by structure prediction, it is not so surprising that these proteins did not crystallize; their N-terminal extensions are clearly highly flexible. To stabilize these extensions, we considered performing crystallisation screening in the presence of a bound dsDNA oligonucleotide. For this we designed a set of palindromic oligonucleotides of various length and GC content. However, we encountered numerous difficulties when trying to anneal these oligonucleotides to assemble dsDNA. As a result of their palindromic nature, these oligonucleotides preferentially self-annealed rather than annealing to a second strand. This strategy was thus abandoned.

In the future, as an alternative to X-ray crystallography, the structure of DrHU and the *D. deserti* HU proteins could be determined by nuclear magnetic resonance (NMR). A main advantage of this approach is that the measurements leading to the elucidation of the protein structure are performed in solution without the need to crystallize the protein, which allow to obtain a structure in near-to-physiological conditions. This technique is also particularly well adapted for the study of small proteins comprising disordered regions. After determining the structure of the isolated DrHU by NMR, it would also be of much interest to use NMR to probe the regions of DrHU involved in DNA binding.

The reconstituted DNA gyrase of D. radiodurans is more active than the fused construct

The first requirement to achieve our long-term objective to reconstitute a minimal chromatin *in vitro* was to produce and characterize the DNA-binding properties of the main actors of the nucleoid organisation, namely the HU protein and the DNA gyrase. With this in mind, the DNA gyrase of *D. radiodurans*, which is the second most abundant protein in the nucleoid, was successfully expressed and purified both as a reconstituted complex and as a recombinant fusion. The reconstitution of the heterotetrameric complex $DrGyrA_2B_2$ was performed by mixing the purified GyrA and GyrB subunits at a molar ratio of 1:1.2 (slight excess of GyrB) and purifying this assembly by size-exclusion chromatography. To obtain a more stable complex suitable for structural studies by X-ray crystallography or cryo-EM, the recombinant DNA gyrase fusion, DrGyrBAfus, was produced by insertion of a three residue-long linker between the C-terminal TOPRIM domain of GyrB and the N-terminal WHD of GyrA as previously designed by Papillon and colleagues in their structural study of *T. thermophilus* DNA gyrase (Papillon et al., 2013).

To validate the functionality of the fusion compared to the reconstituted complex, we characterized their respective supercoiling and relaxation activities. The reconstituted $DrGyrA_2B_2$ was able to efficiently supercoil relaxed plasmid DNA in an ATP-dependent fashion and could also partially relax supercoiled plasmid DNA – an activity that in contrast did not require ATP. These results are in agreement with the previous characterisation of the supercoiling and relaxation activities of *D. radiodurans* DNA gyrase by Kota et al. and by Devigne et al., which both used a reconstituted complex in their study (Devigne et al., 2016; Kota et al., 2016). In sharp contrast, the recombinant fusion, DrGyrBAfus, displayed a lower supercoiling activity than the reconstituted complex and was unable to perform relaxation of supercoiled plasmid DNA even in the absence of ATP. This was unexpected as a recombinant fusion of *T. thermophilus* DNA gyrase produced by Papillon and colleagues with the same G-D-L linker displayed the same supercoiling activity as the reconstituted complex. The preserved supercoiling activity of a recombinant DNA gyrase fusion designed with the G-D-L linker was also more recently evidenced in a structural study on the DNA gyrase of *M. tuberculosis* (Petrella et al., 2019). Since the linker is located in the region of the DNA-gate where the dsDNA G-segment binds and is subsequently cleaved to allow the passage of the dsDNA T-segment, a potential decrease in the subunit's flexibility might hinder the binding of the G-segment or its cleavage.

Although due to lack of time, the functional reconstituted DNA gyrase has not yet been tested in our *in vitro* reconstituted chromatin, the purification and functional characterization of these two DNA gyrase constructs have brought us one-step closer to our goal of reconstituting a minimal chromatin *in vitro* using the two most abundant NAPs, the DNA gyrase and DrHU in complex with supercoiled or relaxed plasmid DNA. This will no doubt be the subject of a future study in the laboratory.

A fortuitous preliminary glance at the structure of D. radiodurans GyrA subunit

Since *D. radiodurans* does not express any Topo IV but only produces a DNA gyrase, this topoisomerase has evolved to perform both the supercoiling-relaxation activity of a classical DNA gyrase and the decatenation activity of a Topo IV. This unusual decatenation activity might be linked to specific motifs in *D. radiodurans* DNA gyrase or to a combination of deletions and insertions compared to the sequence and structure of other bacterial DNA gyrases such as that of *E. coli* (see Appendix for alignments of the GyrA and GyrB subunits of *D. radiodurans* with that of *E. coli* and *T. thermophilus*). With the aim of solving the structure of the full-length DNA gyrase heterotetramer by X-ray crystallography, we attempted to crystallize the two DNA gyrase constructs. Although we were not able to obtain crystals of the recombinant fusion, DrGyrBAfus, some crystals suitable for data collection were obtained when using the reconstituted complex. However, SDS-PAGE analysis of the crystals along with some difficulties encountered during phasing by molecular replacement clearly indicated that only the GyrA subunit was present in the crystals, yielding a preliminary structure of DrGyrA at 3.5 Å that still requires several rounds of refinement and manual building before the structure can be validated and further analysed. Although, we would have preferred to obtain crystals of the full complex, determining the structure of the DrGyrA subunit alone is of interest, since it differs from the canonical *E. coli* GyrA in that it is missing two 25-30-residue insertions within its C-terminal half (see Appendix). Efforts will thus be made to finalise this structure in the coming weeks.

The fact that only the GyrA subunit crystallized when using the reconstituted complex $DrGyrA_2B_2$ may be a consequence of either the dissociation of the GyrB subunit from the complex or a partial degradation of GyrB during the crystallization process that was performed at 20°C. It is also possible that the GyrB subunits remained too flexible, even in the recombinant fusion DrGyrBAfus, since they have been reported to adopt either open or closed conformations

(Brino et al., 2000; Hartmann et al., 2017; Wigley et al., 1991). To favour the crystallization of the complete DNA gyrase complex, we could stabilize the GyrB subunits by addition of a non-hydrolysable ATP analogue and/or DNA and cross-link the structure with glutaraldehyde to trap the complex in a given conformation. This strategy was successfully applied to solve the structure of a recombinant fusion of *T. thermophilus* DNA gyrase by cryo-EM at a global resolution of 16.9 Å (Papillon et al., 2013).

Analysis of the stability and homogeneity of the purified DrGyrA_2B_2 and DrGyrBAfus by negative-staining EM revealed that the reconstituted complex was heterogeneous and partially aggregated, while the recombinant fusion appeared more stable and homogeneous. So, although this fusion construct is not suitable for functional studies, it appears to be more promising for structural studies, in which low flexibility is an advantage. The reduced supercoiling activity of DrGyrBAfus is indeed most probably due to a decreased flexibility caused by the presence of the short linker connecting DrGyrB to DrGyrA. Likewise, these EM observations provide a plausible explanation regarding the crystallization of the GyrA subunit to the detriment of the GyrB subunit, since the reconstituted DrGyrA_2B_2 sample seemed to be partially aggregated and unstable even before crystallisation. Based on the stability and homogeneity of DrGyrBAfus observed by negative-staining EM, it would be of great interest to use cryo-EM to solve the structure of the full-length *D. radiodurans* DNA gyrase. Preliminary data were encouraging as the sample still appeared homogenous, but unfortunately the protein appeared to be denatured in the cryo-EM images (loss of secondary structure) most likely as a result of the freezing process, indicating that further optimization of the sample preparation and freezing process would thus be a pre-requisite for the acquisition of data suitable for single-particle reconstruction and structure determination at near atomic resolution. Moreover, as mentioned previously, the complex could be further stabilized before grid preparation by addition of ATP analogues, crosslinking or antibiotics such as the ciprofloxacin or the gepotidacin that trap the DNA gyrase in a specific conformation in the presence of a bound dsDNA. Recently, Vanden Broeck and colleagues solved the full-length structure of *E. coli* DNA gyrase in complex with a 180 bp dsDNA by cryo-EM (Vanden Broeck et al., 2019). In this work, the DNA-bound gyrase was further stabilized by addition of gepotidacin and AMP-PNP and centrifuged at 16,000 g for 2 hours to remove potential aggregates prior to grid preparation. A major drawback of cryo-EM sample preparation is indeed the adsorption of the proteins to the air-water interface during plunge-freezing that can lead to denaturation. To prevent this, Vanden Broeck and colleagues added a fluorinated detergent (CHAPSO) to their

sample prior to grid preparation thereby also avoiding possible orientation bias. Alternatively, one could try different buffer compositions or use graphene oxide as a support instead of carbon to minimize sample-support interactions. Altogether, optimisation of the sample preparation in view of structure determination of the full-length DNA gyrase by cryo-EM is a vast issue that alone could be the subject of a future PhD thesis.

The Deinococcus-specific DdrC could be the main actor of the strong nucleoid compaction following irradiation and could also serve as a checkpoint for the resumption of the cell cycle

In normal growth conditions, the structure of *D. radiodurans* nucleoid is organized and maintained by two major NAPs, the small DrHU protein that compacts or locally stiffens the genomic DNA and the large DNA gyrase complex that introduces negative supercoils and resolves catenation events. Our study of these two principal NAPs involved in nucleoid organization during unperturbed cell growth led us to ponder on the possible expression by *D. radiodurans* of a specific NAP that would affect the nucleoid organization following exposure to harmful conditions like desiccation or irradiation. Among the many proteins whose expression is induced in response to radiation or desiccation, the DNA-binding protein DdrC appeared as a good candidate: it colocalizes with the nucleoid shortly after irradiation and was shown to compact ssDNA and to form bridges on dsDNA plasmid DNA as observed by TEM (Bouthier de la Tour et al., 2017).

Since little was known about the exact function of DdrC in irradiated *D. radiodurans* cells, we first focused on the determination of its three-dimensional structure, for which no known structural homologues exist, before characterizing its DNA-binding mode and effect on plasmid DNA. Using selenium-SAD X-ray crystallography, the structure of DdrC was solved *de novo* at 2.8 Å resolution, revealing that DdrC is a mostly alpha-helical domain-swapped dimer, with each monomer composed of a N-terminal domain (NTD) and a C-terminal domain (CTD). The NTD contains a winged helix-turn-helix (wHTH) motif while the CTD is folded into a four-helix bundle. The domain-swapped dimer observed in our crystal structure is most likely biologically relevant as confirmed by PISA analysis of the dimer interface, whose conclusions were further supported by our SEC-MALLS and AUC experiments. Based on the electrostatic surface potential of the structure and the results of our FP assays, we proposed a model of DdrC binding to dsDNA that was further evaluated by molecular dynamic simulations. Our results confirmed that DdrC has two DNA binding sites on each side of the dimer, involving three major contact sites composed of the N-terminal β-hairpin preceding the

wHTH motif and a disordered loop between the second and third α-helices of the CTD. The effect of DdrC binding on the conformation of supercoiled plasmid DNA was assessed by AFM, showing that DdrC induces a strong compaction of DNA in a concentration-dependent manner, which is in agreement with the strong DNA compaction previously observed in the cryo-EM study of our collaborators. As suggested by the topoisomerase assay, DdrC-induced DNA compaction might rely on the introduction or stabilization of negative supercoils in plasmid DNA, maybe in combination with a bridging mechanism through its two DNA-binding sites.

Based on our results and those of previous studies showing (i) nucleoid reorganization after irradiation (Passot et al., 2015; unpublished data from our laboratory), (ii) DdrC association with the nucleoid after irradiation (Bouthier de la Tour et al., 2017) and (iii) the formation of DdrC foci at specific location in the cell 2 to 3h post-irradiation (Bouthier de la Tour et al., 2017), we propose a model in which DdrC would be a stress-induced *Deinococcus*-specific NAP that contributes to the strong compaction of the nucleoid after irradiation to limit the dispersion of the fragmented genomic DNA and possibly ease the DNA repair process, and would later act as a checkpoint delaying chromosome segregation and cell division that are paused until DNA repair is complete (Fig. 72).

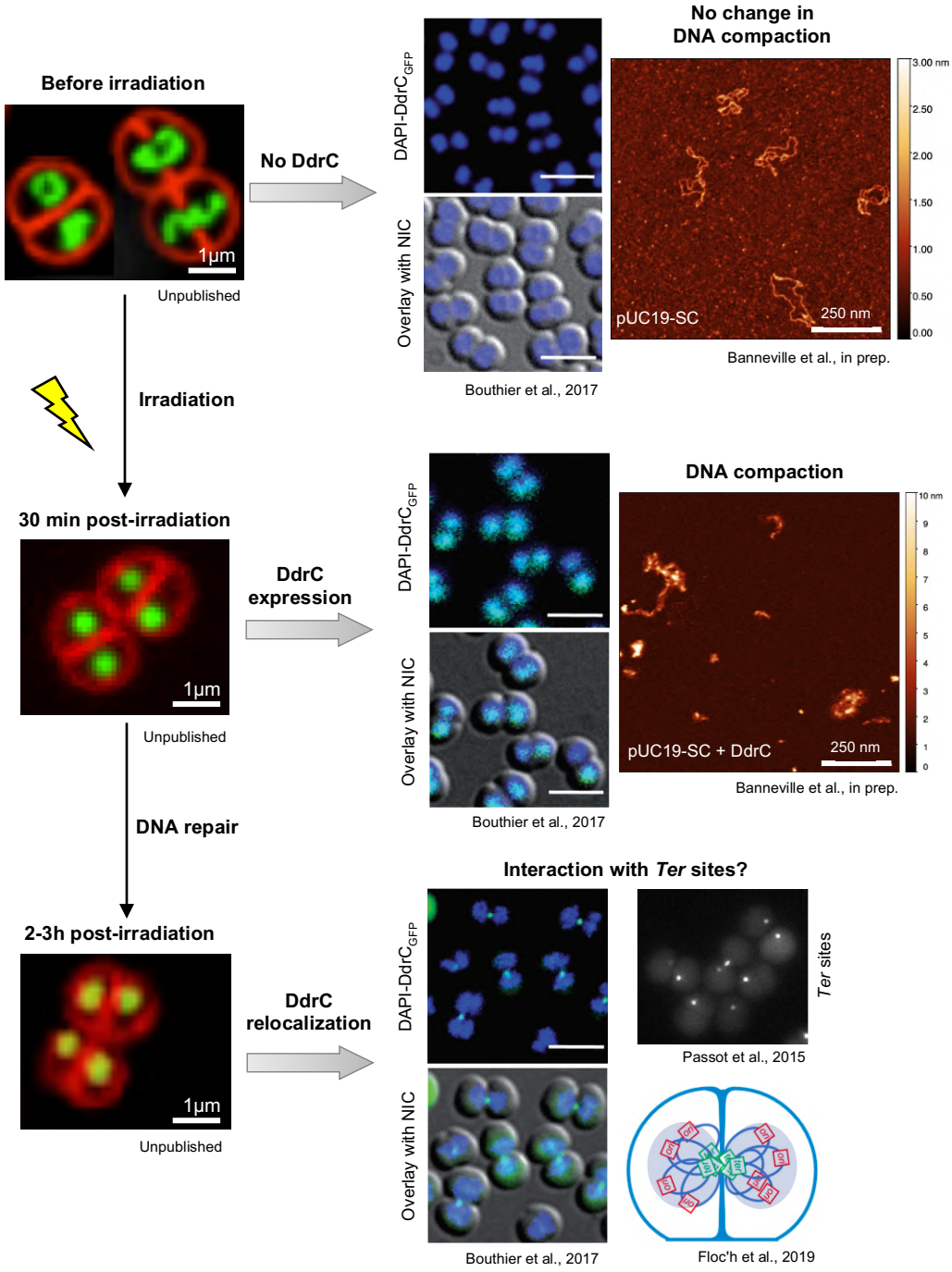

Figure 72. Model for a possible function of DdrC in irradiated cells as a NAP that enhances nucleoid compaction and might participate in pausing chromosome segregation and cell division. Images of *D. radiodurans* cells presented on the left were acquired by fluorescence microscopy (courtesy of P. Vauclare). Cell membranes (in red) and DNA (in green) were stained with Nile Red and Syto9, respectively. The middle images of *D. radiodurans* cells show the localization of a GFP-fused DdrC (in green) in the nucleoid (in blue, stained with DAPI) before and after irradiation. Cell contour is shown by the overlay of DAPI-DdrC$_{GFP}$ images with Nomarski interference contrast (NIC) images (Bouthier de la Tour et al., 2017). Localization of the *Ter* sites (in white) of *D. radiodurans* genomic DNA were acquired by introduction of specific *parS* sequences near the *Ter* site, which were detected by binding of a GFP-fused ParB (Passot et al., 2015). The diagram in the bottom right corner illustrates the distribution of the Ter (in green) and Ori (in red) sites in the nucleoid (light blue shade) of a dividing *D.*

radiodurans cell whose membrane and septum are represented by a thick blue line (Floc'h et al., 2019). The AFM images of pUC19 plasmid DNA with and without DdrC are from our article on DdrC, to be published.

Under normal growth conditions (Fig. 72, top panels), the nucleoid organisation is compact yet it remains highly dynamic through the negative-supercoiling activity of the DNA gyrase and the equilibrium between the compaction and stiffening effects of DrHU mediated by its transient association with genomic DNA. Irradiation of *D. radiodurans* cells (Fig. 72, middle panels) triggers the radiation-desiccation response mechanism (de Groot et al., 2019; Devigne et al., 2015) in which the activation of IrrE leads to cleavage of DdrO thereby suppressing the repression of DdrC transcription, which is quickly recruited and distributed throughout the nucleoid (Bouthier de la Tour et al., 2017). Upon binding to genomic DNA, DdrC would strongly compact the nucleoid that adopts a more condensed organisation preventing the diffusion of dsDNA fragments generated by the irradiation. As the two subunits of DNA gyrase are also over-expressed after irradiation, we posit that the increased nucleoid compaction following irradiation could result from an enhanced negative supercoiling of the genomic DNA that would be maintained by DdrC in addition to its own contribution to DNA compaction. As the DNA repair progresses towards the reconstitution of the genome, which is almost complete within 3 hours after irradiation (Fig. 72, bottom panels), DdrC expression decreases and the protein relocalizes to form foci near the closing septum between two *D. radiodurans* cells (Bouthier de la Tour et al., 2017; Zahradka et al., 2006).

This site corresponds to the location of the *Ter* regions of the chromosomes, where final chromosome segregation occurs, including DNA decatenation of replicated chromosomes (Passot et al., 2015; Floc'h et al., 2019). As DdrC is no longer evenly distributed throughout the nucleoid at this stage, it cannot exert its compaction effect on the genomic DNA, therefore the nucleoid organization progressively returns to its original less compacted conformation. We hypothesize that this intriguing relocalization of DdrC near the septum 2 to 3 hours after irradiation might be associated with a second function of DdrC in the response to DNA damage, i.e. prevention of unwanted chromosome segregation and halting of cell division, acting as a checkpoint that would ensure chromosome segregation and cell division do not resume before DNA repair is complete (Floc'h et al., 2019; Passot et al., 2015).

Perspectives

In this thesis project, I produced and studied the main NAPs involved in the nucleoid organization of *D. radiodurans*, namely DrHU and the DNA gyrase, as well as a stress-induced Deinococcus-specific NAP, DdrC. Based on our characterization of the DNA-binding properties of DrHU and the unravelling of its bimodal DNA compaction and stiffening mechanism, we could propose a model of the function of DrHU in maintaining a structured and yet dynamic nucleoid. Interestingly, the dual DNA-binding mechanism of DrHU is not shared by other deinococcal HU proteins as evidenced by our comparative study of the three HU variants expressed in *D. deserti*, DdHU1, DdHU2 and DdHU3. Seeing that DrHU is the only HU protein produced by *D. radiodurans* and that the three HU variants of *D. deserti* displayed distinct DNA-binding properties like enhanced cooperativity or affinity, DrHU might have evolved as a Swiss Army knife to compensate for the lack of other NAPs that usually perform DNA-bending, bridging or stiffening in other bacteria like IHF, Fis or H-NS. Finally, our work on DdrC reveal that this *Deinococcus*-specific NAP may assist DrHU in maintaining genome structure and organization in response to high levels of DNA damage, to facilitate the DNA repair process and ensure pausing of chromosome segregation and cell division until genome integrity is restored and the cell cycle can resume. Together, our results pave the way towards a better understanding of the nucleoid organization in *D. radiodurans* and how it could relate to its extreme resistance to DNA damaging agents.

Bibliography

Alekseev, A., Cherevatenko, G., Serdakov, M., Pobegalov, G., Yakimov, A., Bakhlanova, I., Baitin, D., & Khodorkovskii, M. (2020). Single-Molecule Insights into ATP-Dependent Conformational Dynamics of Nucleoprotein Filaments of Deinococcus radiodurans RecA. *International Journal of Molecular Sciences*, *21*(19). https://doi.org/10.3390/ijms21197389

Ali, S. S., Soo, J., Rao, C., Leung, A. S., Ngai, D. H.-M., Ensminger, A. W., & Navarre, W. W. (2014). Silencing by H-NS potentiated the evolution of Salmonella. *PLoS Pathogens*, *10*(11), e1004500. https://doi.org/10.1371/journal.ppat.1004500

Altuvia, S., Almirón, M., Huisman, G., Kolter, R., & Storz, G. (1994). The dps promoter is activated by OxyR during growth and by IHF and sigma S in stationary phase. *Molecular Microbiology*, *13*(2), 265-272. https://doi.org/10.1111/j.1365-2958.1994.tb00421.x

Amit, R., Oppenheim, A. B., & Stavans, J. (2003). Increased bending rigidity of single DNA molecules by H-NS, a temperature and osmolarity sensor. *Biophysical Journal*, *84*(4), 2467-2473. https://doi.org/10.1016/S0006-3495(03)75051-6

Anaganti, N., Basu, B., Mukhopadhyaya, R., & Apte, S. K. (2017). Proximity of Radiation Desiccation Response Motif to the core promoter is essential for basal repression as well as gamma radiation-induced gyrB gene expression in Deinococcus radiodurans. *Gene*, *615*, 8-17. https://doi.org/10.1016/j.gene.2017.03.002

Anand, C., Garg, R., Ghosh, S., & Nagaraja, V. (2017). A Sir2 family protein Rv1151c deacetylates HU to alter its DNA binding mode in Mycobacterium tuberculosis. *Biochemical and Biophysical Research Communications*, *493*(3), 1204-1209. https://doi.org/10.1016/j.bbrc.2017.09.087

Anderson, A., Nordon, H., Cain, R. F., Parrish, G., Duggan, D., Nordan, H., Parish, G., & Cullum-Dugan, D. (1956). Studies on a radio-resistant micrococcus. I. Isolation, morphology, cultural characteristics, and resistance to gamma radiation. *Food Technology*, *10*, 575-578.

Andrade, A., Hernández-Eligio, A., Tirado, A. L., Vega-Alvarado, L., Olvera, M., Morett, E., & Juárez, K. (2021). Specialization of the Reiterated Copies of the Heterodimeric Integration Host Factor Genes in Geobacter sulfurreducens. *Frontiers in Microbiology*, *12*, 626443. https://doi.org/10.3389/fmicb.2021.626443

Anthis, N. J., & Clore, G. M. (2013). Sequence-specific determination of protein and peptide concentrations by absorbance at 205 nm : Sequence-Specific Protein Concentration at 205 nm. *Protein Science*, *22*(6), 851-858. https://doi.org/10.1002/pro.2253

Aravind, L., Leipe, D. D., & Koonin, E. V. (1998). Toprim—A conserved catalytic domain in type IA and II topoisomerases, DnaG-type primases, OLD family nucleases and RecR proteins. *Nucleic Acids Research*, *26*(18), 4205-4213. https://doi.org/10.1093/nar/26.18.4205

Archibald, F. (1986). Manganese : Its acquisition by and function in the lactic acid bacteria. *Critical Reviews in Microbiology*, *13*(1), 63-109. https://doi.org/10.3109/10408418609108735

Archibald, F. S., & Fridovich, I. (1982). The scavenging of superoxide radical by manganous complexes : In vitro. *Archives of Biochemistry and Biophysics*, *214*(2), 452-463. https://doi.org/10.1016/0003-9861(82)90049-2

Arold, S. T., Leonard, P. G., Parkinson, G. N., & Ladbury, J. E. (2010). H-NS forms a superhelical protein scaffold for DNA condensation. *Proceedings of the National Academy of Sciences of the United States of America*, *107*(36), 15728-15732. https://doi.org/10.1073/pnas.1006966107

Arthur, D. C., Edwards, R. A., Tsutakawa, S., Tainer, J. A., Frost, L. S., & Glover, J. N. M. (2011). Mapping interactions between the RNA chaperone FinO and its RNA targets. *Nucleic Acids Research*, *39*(10), 4450-4463. https://doi.org/10.1093/nar/gkr025

Atherton, J., & Moores, C. A. (2021). Cryo-EM of kinesin-binding protein : Challenges and opportunities from protein-surface interactions. *Acta Crystallographica. Section D, Structural Biology*, *77*(Pt 4), 411-423. https://doi.org/10.1107/S2059798321001935

Azam, T. A., & Ishihama, A. (1999). Twelve species of the nucleoid-associated protein from Escherichia coli. Sequence recognition specificity and DNA binding affinity. *The Journal of Biological Chemistry*, *274*(46), 33105-33113. https://doi.org/10.1074/jbc.274.46.33105

Bagwell, C. E., Milliken, C. E., Ghoshroy, S., & Blom, D. A. (2008). Intracellular Copper Accumulation Enhances the Growth of Kineococcus radiotolerans during Chronic Irradiation. *Applied and Environmental Microbiology*, *74*(5), 1376-1384. https://doi.org/10.1128/AEM.02175-07

Barnese, K., Gralla, E. B., Cabelli, D. E., & Valentine, J. S. (2008). Manganous phosphate acts as a superoxide dismutase. *Journal of the American Chemical Society*, *130*(14), 4604-4606. https://doi.org/10.1021/ja710162n

Battista, J. R. (1997). Against all odds : The survival strategies of Deinococcus radiodurans. *Annual Review of Microbiology*, *51*, 203-224. https://doi.org/10.1146/annurev.micro.51.1.203

Battista, J. R. (2016). Deinococcus–Thermus Group. In *ELS* (p. 1-12). American Cancer Society. https://doi.org/10.1002/9780470015902.a0021151

Baudet, M., Ortet, P., Gaillard, J.-C., Fernandez, B., Guérin, P., Enjalbal, C., Subra, G., de Groot, A., Barakat, M., Dedieu, A., & Armengaud, J. (2009). Proteomics-based Refinement of Deinococcus deserti Genome Annotation Reveals an Unwonted Use of Non-canonical Translation Initiation Codons. *Molecular & Cellular Proteomics*, *9*(2), 415-426. https://doi.org/10.1074/mcp.M900359-MCP200

Bax, B. D., Chan, P. F., Eggleston, D. S., Fosberry, A., Gentry, D. R., Gorrec, F., Giordano, I., Hann, M. M., Hennessy, A., Hibbs, M., Huang, J., Jones, E., Jones, J., Brown, K. K., Lewis, C. J., May, E. W., Saunders, M. R., Singh, O., Spitzfaden, C. E., … Gwynn, M. N. (2010). Type IIA topoisomerase inhibition by a new class of antibacterial agents. *Nature*, *466*(7309), 935-940. https://doi.org/10.1038/nature09197

Benevides, J. M., Danahy, J., Kawakami, J., & Thomas, G. J. (2008). Mechanisms of Specific and Nonspecific Binding of Architectural Proteins in Prokaryotic Gene Regulation. *Biochemistry*, *47*(12), 3855-3862. https://doi.org/10.1021/bi7009426

Berlett, B. S., Chock, P. B., Yim, M. B., & Stadtman, E. R. (1990). Manganese(II) catalyzes the bicarbonate-dependent oxidation of amino acids by hydrogen peroxide and the amino acid-facilitated dismutation of hydrogen peroxide. *Proceedings of the National Academy of Sciences*, *87*(1), 389-393. https://doi.org/10.1073/pnas.87.1.389

Bharath, M. M. S., Ramesh, S., Chandra, N. R., & Rao, M. R. S. (2002). Identification of a 34 amino acid stretch within the C-terminus of histone H1 as the DNA-condensing domain by site-directed mutagenesis. *Biochemistry*, *41*(24), 7617-7627. https://doi.org/10.1021/bi025773+

Bhattacharyya, G., & Grove, A. (2007). The N-terminal extensions of Deinococcus radiodurans Dps-1 mediate DNA major groove interactions as well as assembly of the dodecamer. *The Journal of Biological Chemistry*, *282*(16), 11921-11930. https://doi.org/10.1074/jbc.M611255200

Bhowmick, T., Ghosh, S., Dixit, K., Ganesan, V., Ramagopal, U. A., Dey, D., Sarma, S. P., Ramakumar, S., & Nagaraja, V. (2014). Targeting Mycobacterium tuberculosis nucleoid-associated protein HU with structure-based inhibitors. *Nature Communications*, *5*, 4124. https://doi.org/10.1038/ncomms5124

Blanchard, Guérin, P., Roche, D., Cruveiller, S., Pignol, D., Vallenet, D., Armengaud, J., & de Groot, A. (2017). Conservation and diversity of the IrrE/DdrO-controlled radiation response in radiation-resistant Deinococcus bacteria. *MicrobiologyOpen*, *6*(4), e00477. https://doi.org/10.1002/mbo3.477

Bose, B., Auchtung, J. M., Lee, C. A., & Grossman, A. D. (2008). A conserved anti-repressor controls horizontal gene transfer by proteolysis. *Molecular Microbiology*, *70*(3), 570-582. https://doi.org/10.1111/j.1365-2958.2008.06414.x

Bouige, A., Darmon, A., Piton, J., Roue, M., Petrella, S., Capton, E., Forterre, P., Aubry, A., & Mayer, C. (2013). Mycobacterium tuberculosis DNA gyrase possesses two functional GyrA-boxes. *The Biochemical Journal*, *455*(3), 285-294. https://doi.org/10.1042/BJ20130430

Bouthier de la Tour, C., Armengaud, J., Dulermo, R., Blanchard, L., Devigne, A., de Groot, A., Ludanyi, M., & Sommer, S. (2015). The abundant and essential HU proteins in Deinococcus deserti and Deinococcus radiodurans are translated from leaderless mRNA. *Microbiology*, *161*(12), 2410-2422. https://doi.org/10.1099/mic.0.000186

Bouthier de la Tour, C., Boisnard, S., Norais, C., Toueille, M., Bentchikou, E., Vannier, F., Cox, M. M., Sommer, S., & Servant, P. (2011). The deinococcal DdrB protein is involved in an early step of DNA double strand break repair and in plasmid transformation through its single-strand annealing activity. *DNA Repair*, *10*(12), 1223-1231. https://doi.org/10.1016/j.dnarep.2011.09.010

Bouthier de la Tour, C., Mathieu, M., Meyer, L., Dupaigne, P., Passot, F., Servant, P., Sommer, S., Le Cam, E., & Confalonieri, F. (2017). In vivo and in vitro characterization of DdrC, a DNA damage response protein in Deinococcus radiodurans bacterium. *PLOS ONE*, *12*(5), e0177751. https://doi.org/10.1371/journal.pone.0177751

Bouthier de la Tour, C., Passot, F. M., Toueille, M., Mirabella, B., Guérin, P., Blanchard, L., Servant, P., de Groot, A., Sommer, S., & Armengaud, J. (2013). Comparative proteomics reveals key proteins recruited at the nucleoid of Deinococcus after irradiation-induced DNA damage. *PROTEOMICS*, *13*(23-24), 3457-3469. https://doi.org/10.1002/pmic.201300249

Bouthier de la Tour, C., Toueille, M., Jolivet, E., Nguyen, H.-H., Servant, P., Vannier, F., & Sommer, S. (2009). The Deinococcus radiodurans SMC protein is dispensable for cell viability yet plays a role in DNA folding. *Extremophiles*, *13*(5), 827-837. https://doi.org/10.1007/s00792-009-0270-2

Bowman, G. R., Comolli, L. R., Zhu, J., Eckart, M., Koenig, M., Downing, K. H., Moerner, W. E., Earnest, T., & Shapiro, L. (2008). A polymeric protein anchors the chromosomal origin/ParB complex at a bacterial cell pole. *Cell*, *134*(6), 945-955. https://doi.org/10.1016/j.cell.2008.07.015

Boyko, K. M., Rakitina, T. V., Korzhenevskiy, D. A., Vlaskina, A. V., Agapova, Y. K., Kamashev, D. E., Kleymenov, S. Y., & Popov, V. O. (2016). Structural basis of the high thermal stability of the histone-like HU protein from the mollicute Spiroplasma melliferum KC3. *Scientific Reports*, *6*(1), 36366. https://doi.org/10.1038/srep36366

Brino, L., Urzhumtsev, A., Mousli, M., Bronner, C., Mitschler, A., Oudet, P., & Moras, D. (2000). Dimerization of Escherichia coli DNA-gyrase B Provides a Structural Mechanism for

Activating the ATPase Catalytic Center. *Journal of Biological Chemistry*, *275*(13), 9468-9475. https://doi.org/10.1074/jbc.275.13.9468

Britton, R. A., Lin, D. C., & Grossman, A. D. (1998). Characterization of a prokaryotic SMC protein involved in chromosome partitioning. *Genes & Development*, *12*(9), 1254-1259. https://doi.org/10.1101/gad.12.9.1254

Broedersz, C. P., Wang, X., Meir, Y., Loparo, J. J., Rudner, D. Z., & Wingreen, N. S. (2014). Condensation and localization of the partitioning protein ParB on the bacterial chromosome. *Proceedings of the National Academy of Sciences*, *111*(24), 8809-8814. https://doi.org/10.1073/pnas.1402529111

Brooks, B. W., & Murray, R. G. E. (1981). Nomenclature for "Micrococcus radiodurans" and Other Radiation-Resistant Cocci : Deinococcaceae fam. Nov. And Deinococcus gen. Nov., Including Five Species. *INT. J. SYST.BACTERIOL.*, 8.

Brown, B. L., Wood, T. K., Peti, W., & Page, R. (2011). Structure of the Escherichia coli antitoxin MqsA (YgiT/b3021) bound to its gene promoter reveals extensive domain rearrangements and the specificity of transcriptional regulation. *The Journal of Biological Chemistry*, *286*(3), 2285-2296. https://doi.org/10.1074/jbc.M110.172643

Browning, D. F., Grainger, D. C., & Busby, S. J. (2010). Effects of nucleoid-associated proteins on bacterial chromosome structure and gene expression. *Current Opinion in Microbiology*, *13*(6), 773-780. https://doi.org/10.1016/j.mib.2010.09.013

Bürmann, F., Shin, H.-C., Basquin, J., Soh, Y.-M., Giménez-Oya, V., Kim, Y.-G., Oh, B.-H., & Gruber, S. (2013). An asymmetric SMC-kleisin bridge in prokaryotic condensin. *Nature Structural & Molecular Biology*, *20*(3), 371-379. https://doi.org/10.1038/nsmb.2488

Bush, N. G., Evans-Roberts, K., & Maxwell, A. (2015). DNA Topoisomerases. *EcoSal Plus*, *6*(2). https://doi.org/10.1128/ecosalplus.ESP-0010-2014

Carabetta, V. J. (2021). Addressing the Possibility of a Histone-Like Code in Bacteria. *Journal of Proteome Research*, *20*(1), 27-37. https://doi.org/10.1021/acs.jproteome.0c00442

Carabetta, V. J., Greco, T. M., Cristea, I. M., & Dubnau, D. (2019). YfmK is an N-lysine acetyltransferase that directly acetylates the histone-like protein HBsu in Bacillus subtilis. *Proceedings of the National Academy of Sciences*, *116*(9), 3752-3757. https://doi.org/10.1073/pnas.1815511116

Carbonneau, M. A., Melin, A. M., Perromat, A., & Clerc, M. (1989). *The Action of Free Radicals on Deinococcus radiodurans Carotenoids*. 8.

Champoux, J. J. (2001). DNA topoisomerases : Structure, function, and mechanism. *Annual Review of Biochemistry*, *70*, 369-413. https://doi.org/10.1146/annurev.biochem.70.1.369

Chan, P. F., Germe, T., Bax, B. D., Huang, J., Thalji, R. K., Bacqué, E., Checchia, A., Chen, D., Cui, H., Ding, X., Ingraham, K., McCloskey, L., Raha, K., Srikannathasan, V., Maxwell, A., & Stavenger, R. A. (2017). Thiophene antibacterials that allosterically stabilize DNA-cleavage complexes with DNA gyrase. *Proceedings of the National Academy of Sciences of the United States of America*, *114*(22), E4492-E4500. https://doi.org/10.1073/pnas.1700721114

Changela, A., DiGate, R. J., & Mondragón, A. (2007). Structural studies of E. coli topoisomerase III-DNA complexes reveal a novel type IA topoisomerase-DNA conformational intermediate. *Journal of Molecular Biology*, *368*(1), 105-118. https://doi.org/10.1016/j.jmb.2007.01.065

Chen, B.-W., Lin, M.-H., Chu, C.-H., Hsu, C.-E., & Sun, Y.-J. (2015). Insights into ParB spreading from the complex structure of Spo0J and parS. *Proceedings of the National Academy of Sciences of the United States of America*, *112*(21), 6613-6618. https://doi.org/10.1073/pnas.1421927112

Chen, C., Ghosh, S., & Grove, A. (2004). Substrate specificity of Helicobacter pylori histone-like HU protein is determined by insufficient stabilization of DNA flexure points. *The Biochemical Journal*, *383*(Pt 2), 343-351. https://doi.org/10.1042/BJ20040938

Chen, S. W., Teulon, J.-M., Godon, C., & Pellequer, J.-L. (2016). Atomic force microscope, molecular imaging, and analysis. *Journal of Molecular Recognition: JMR*, *29*(1), 51-55. https://doi.org/10.1002/jmr.2491

Cho, B.-K., Knight, E. M., Barrett, C. L., & Palsson, B. Ø. (2008). Genome-wide analysis of Fis binding in Escherichia coli indicates a causative role for A-/AT-tracts. *Genome Research*, *18*(6), 900-910. https://doi.org/10.1101/gr.070276.107

Christensen, E. A., & Kristensen, H. (1981). Radiation-resistance of micro-organisms from air in clean premises. *Acta Pathologica Et Microbiologica Scandinavica. Section B, Microbiology*, *89*(5), 293-301. https://doi.org/10.1111/j.1699-0463.1981.tb00192_89b.x

Christodoulou, E., & Vorgias, C. E. (1998). Cloning, overproduction, purification and crystallization of the DNA binding protein HU from the hyperthermophilic eubacterium Thermotoga maritima. *Acta Crystallographica Section D Biological Crystallography*, *54*(5), 1043-1045. https://doi.org/10.1107/S0907444998000341

Chu, C.-H., Yen, C.-Y., Chen, B.-W., Lin, M.-G., Wang, L.-H., Tang, K.-Z., Hsiao, C.-D., & Sun, Y.-J. (2019). Crystal structures of HpSoj–DNA complexes and the nucleoid-adaptor complex formation in chromosome segregation. *Nucleic Acids Research*, *47*(4), 2113-2129. https://doi.org/10.1093/nar/gky1251

Claret, L., & Rouviere-Yaniv, J. (1997). Variation in HU composition during growth of Escherichia coli : The heterodimer is required for long term survival. *Journal of Molecular Biology*, *273*(1), 93-104. https://doi.org/10.1006/jmbi.1997.1310

Cole, S. T., Brosch, R., Parkhill, J., Garnier, T., Churcher, C., Harris, D., Gordon, S. V., Eiglmeier, K., Gas, S., Barry, C. E., Tekaia, F., Badcock, K., Basham, D., Brown, D., Chillingworth, T., Connor, R., Davies, R., Devlin, K., Feltwell, T., … Barrell, B. G. (1998). Deciphering the biology of Mycobacterium tuberculosis from the complete genome sequence. *Nature*, *393*(6685), 537-544. https://doi.org/10.1038/31159

Confalonieri, F., Elie, C., Nadal, M., Forterre, P., & Duguet, M. (1993). Reverse gyrase : A helicase-like domain and a type I topoisomerase in the same polypeptide. *Proc. Natl. Acad. Sci. USA*, 5.

Corbett, K. D., & Berger, J. M. (2003). Structure of the topoisomerase VI-B subunit : Implications for type II topoisomerase mechanism and evolution. *The EMBO Journal*, *22*(1), 151-163. https://doi.org/10.1093/emboj/cdg008

Corbett, K. D., & Berger, J. M. (2005). Structural dissection of ATP turnover in the prototypical GHL ATPase TopoVI. *Structure (London, England: 1993)*, *13*(6), 873-882. https://doi.org/10.1016/j.str.2005.03.013

Corbett, K. D., Schoeffler, A. J., Thomsen, N. D., & Berger, J. M. (2005). The structural basis for substrate specificity in DNA topoisomerase IV. *Journal of Molecular Biology*, *351*(3), 545-561. https://doi.org/10.1016/j.jmb.2005.06.029

Corbett, K. D., Shultzaberger, R. K., & Berger, J. M. (2004). The C-terminal domain of DNA gyrase A adopts a DNA-bending beta-pinwheel fold. *Proceedings of the National Academy of Sciences of the United States of America*, *101*(19), 7293-7298. https://doi.org/10.1073/pnas.0401595101

Cox, M. M., & Battista, J. R. (2005). Deinococcus radiodurans—The consummate survivor. *Nature Reviews Microbiology*, *3*(11), 882-892. https://doi.org/10.1038/nrmicro1264

Cuypers, M. G., Mitchell, E. P., Romão, C. V., & McSweeney, S. M. (2007). The Crystal Structure of the Dps2 from Deinococcus radiodurans Reveals an Unusual Pore Profile with a Non-specific Metal Binding Site. *Journal of Molecular Biology*, *371*(3), 787-799. https://doi.org/10.1016/j.jmb.2006.11.032

Dadinova, L. A., Chesnokov, Y. M., Kamyshinsky, R. A., Orlov, I. A., Petoukhov, M. V., Mozhaev, A. A., Soshinskaya, E. Y., Lazarev, V. N., Manuvera, V. A., Orekhov, A. S., Vasiliev, A. L., & Shtykova, E. V. (2019). Protective Dps-DNA co-crystallization in stressed cells : An in vitro structural study by small-angle X-ray scattering and cryo-electron tomography. *FEBS Letters*, *593*(12), 1360-1371. https://doi.org/10.1002/1873-3468.13439

Daly, M. J., Gaidamakova, E. K., Matrosova, V. Y., Kiang, J. G., Fukumoto, R., Lee, D.-Y., Wehr, N. B., Viteri, G. A., Berlett, B. S., & Levine, R. L. (2010). Small-Molecule Antioxidant Proteome-Shields in Deinococcus radiodurans. *PLoS ONE*, *5*(9), e12570. https://doi.org/10.1371/journal.pone.0012570

Daly, M. J., Gaidamakova, E. K., Matrosova, V. Y., Vasilenko, A., Zhai, M., Venkateswaran, A., Hess, M., Omelchenko, M. V., Kostandarithes, H. M., Makarova, K. S., Wackett, L. P., Fredrickson, J. K., & Ghosal, D. (2004). Accumulation of Mn(II) in Deinococcus radiodurans facilitates gamma-radiation resistance. *Science*, *306*(5698), 1025-1028. https://doi.org/10.1126/science.1103185

Dame, R. T., & Goosen, N. (2002). HU : Promoting or counteracting DNA compaction? *FEBS Letters*, *529*(2-3), 151-156. https://doi.org/10.1016/s0014-5793(02)03363-x

Dame, R. T., Noom, M. C., & Wuite, G. J. L. (2006). Bacterial chromatin organization by H-NS protein unravelled using dual DNA manipulation. *Nature*, *444*(7117), 387-390. https://doi.org/10.1038/nature05283

Dame, R. T., Rashid, F.-Z. M., & Grainger, D. C. (2020). Chromosome organization in bacteria : Mechanistic insights into genome structure and function. *Nature Reviews Genetics*, *21*(4), 227-242. https://doi.org/10.1038/s41576-019-0185-4

Dame, R. T., & Tark-Dame, M. (2016). Bacterial chromatin : Converging views at different scales. *Current Opinion in Cell Biology*, *40*, 60-65. https://doi.org/10.1016/j.ceb.2016.02.015

Dame, R. T., Wyman, C., & Goosen, N. (2000). H-NS mediated compaction of DNA visualised by atomic force microscopy. *Nucleic Acids Research*, *28*(18), 3504-3510. https://doi.org/10.1093/nar/28.18.3504

Danilova, O., Reyes-Lamothe, R., Pinskaya, M., Sherratt, D., & Possoz, C. (2007). MukB colocalizes with the oriC region and is required for organization of the two Escherichia coli chromosome arms into separate cell halves. *Molecular Microbiology*, *65*(6), 1485-1492. https://doi.org/10.1111/j.1365-2958.2007.05881.x

Datta, C., Jha, R. K., Ahmed, W., Ganguly, S., Ghosh, S., & Nagaraja, V. (2019). Physical and functional interaction between nucleoid-associated proteins HU and Lsr2 of Mycobacterium tuberculosis : Altered DNA binding and gene regulation. *Molecular Microbiology*, *111*(4), 981-994. https://doi.org/10.1111/mmi.14202

Déclais, A.-C., Marsault, J., Confalonieri, F., de La Tour, C. B., & Duguet, M. (2000). Reverse Gyrase, the Two Domains Intimately Cooperate to Promote Positive Supercoiling. *Journal of Biological Chemistry*, *275*(26), 19498-19504. https://doi.org/10.1074/jbc.M910091199

de Groot, A., Chapon, V., Servant, P., Christen, R., Saux, M. F.-L., Sommer, S., & Heulin, T. (2005). Deinococcus deserti sp. Nov., a gamma-radiation-tolerant bacterium isolated from the Sahara Desert. *International Journal of Systematic and Evolutionary Microbiology*, *55*(6), 2441-2446. https://doi.org/10.1099/ijs.0.63717-0

de Groot, A., Dulermo, R., Ortet, P., Blanchard, L., Guérin, P., Fernandez, B., Vacherie, B., Dossat, C., Jolivet, E., Siguier, P., Chandler, M., Barakat, M., Dedieu, A., Barbe, V., Heulin, T., Sommer, S., Achouak, W., & Armengaud, J. (2009). Alliance of Proteomics and Genomics to Unravel the Specificities of Sahara Bacterium Deinococcus deserti. *PLoS Genetics*, *5*(3), e1000434. https://doi.org/10.1371/journal.pgen.1000434

de Groot, A., Roche, D., Fernandez, B., Ludanyi, M., Cruveiller, S., Pignol, D., Vallenet, D., Armengaud, J., & Blanchard, L. (2014). RNA Sequencing and Proteogenomics Reveal the Importance of Leaderless mRNAs in the Radiation-Tolerant Bacterium Deinococcus deserti. *Genome Biology and Evolution*, *6*(4), 932-948. https://doi.org/10.1093/gbe/evu069

de Groot, A., Siponen, M. I., Magerand, R., Eugénie, N., Martin-Arevalillo, R., Doloy, J., Lemaire, D., Brandelet, G., Parcy, F., Dumas, R., Roche, P., Servant, P., Confalonieri, F., Arnoux, P., Pignol, D., & Blanchard, L. (2019). Crystal structure of the transcriptional repressor DdrO : Insight into the metalloprotease/repressor-controlled radiation response in Deinococcus. *Nucleic Acids Research*, *47*(21), 11403-11417. https://doi.org/10.1093/nar/gkz883

DeRouchey, J., Hoover, B., & Rau, D. C. (2013). A Comparison of DNA Compaction by Arginine and Lysine Peptides : A Physical Basis for Arginine Rich Protamines. *Biochemistry*, *52*(17), 3000-3009. https://doi.org/10.1021/bi4001408

Devigne, A., Guérin, P., Lisboa, J., Quevillon-Cheruel, S., Armengaud, J., Sommer, S., Bouthier de la Tour, C., & Servant, P. (2016). PprA Protein Is Involved in Chromosome Segregation via Its Physical and Functional Interaction with DNA Gyrase in Irradiated *Deinococcus radiodurans* Bacteria. *MSphere*, *1*(1), e00036-15, /msph/1/1/e00036-15.atom. https://doi.org/10.1128/mSphere.00036-15

Devigne, A., Ithurbide, S., Bouthier de la Tour, C., Passot, F., Mathieu, M., Sommer, S., & Servant, P. (2015). DdrO is an essential protein that regulates the radiation desiccation response and the apoptotic-like cell death in the radioresistant Deinococcus radiodurans bacterium. *Molecular Microbiology*, *96*(5), 1069-1084. https://doi.org/10.1111/mmi.12991

Dey, D., Nagaraja, V., & Ramakumar, S. (2017). Structural and evolutionary analyses reveal determinants of DNA binding specificities of nucleoid-associated proteins HU and IHF. *Molecular Phylogenetics and Evolution*, *107*, 356-366. https://doi.org/10.1016/j.ympev.2016.11.014

D'Imprima, E., Floris, D., Joppe, M., Sánchez, R., Grininger, M., & Kühlbrandt, W. (2019). Protein denaturation at the air-water interface and how to prevent it. *ELife*, *8*, e42747. https://doi.org/10.7554/eLife.42747

Dong, K. C., & Berger, J. M. (2007). Structural basis for gate-DNA recognition and bending by type IIA topoisomerases. *Nature*, *450*(7173), 1201-1205. https://doi.org/10.1038/nature06396

Dorman, C. J. (2014). H-NS-like nucleoid-associated proteins, mobile genetic elements and horizontal gene transfer in bacteria. *Plasmid*, *75*, 1-11. https://doi.org/10.1016/j.plasmid.2014.06.004

Driedger, A. A. (1970). The DNA content of single cells of Micrococcus radiodurans. *Canadian Journal of Microbiology*, *16*(11), 1136-1137. https://doi.org/10.1139/m70-192

Du, J., & Gebicki, J. M. (2004). Proteins are major initial cell targets of hydroxyl free radicals. *The International Journal of Biochemistry & Cell Biology*, *36*(11), 2334-2343. https://doi.org/10.1016/j.biocel.2004.05.012

Dubarry, N., Pasta, F., & Lane, D. (2006). ParABS systems of the four replicons of Burkholderia cenocepacia : New chromosome centromeres confer partition specificity. *Journal of Bacteriology*, *188*(4), 1489-1496. https://doi.org/10.1128/JB.188.4.1489-1496.2006

Dulermo, R., Fochesato, S., Blanchard, L., & de Groot, A. (2009). Mutagenic lesion bypass and two functionally different RecA proteins in Deinococcus deserti. *Molecular Microbiology*, *74*(1), 194-208. https://doi.org/10.1111/j.1365-2958.2009.06861.x

Edwards, G. B., Muthurajan, U. M., Bowerman, S., & Luger, K. (2020). Analytical Ultracentrifugation (AUC) : An Overview of the Application of Fluorescence and Absorbance AUC to the Study of Biological Macromolecules. *Current Protocols in Molecular Biology*, *133*(1). https://doi.org/10.1002/cpmb.131

Eltsov, M., & Dubochet, J. (2005). Fine Structure of the Deinococcus radiodurans Nucleoid Revealed by Cryoelectron Microscopy of Vitreous Sections. *Journal of Bacteriology*, *187*(23), 8047-8054. https://doi.org/10.1128/JB.187.23.8047-8054.2005

Erill, I., Campoy, S., & Barbé, J. (2007). Aeons of distress : An evolutionary perspective on the bacterial SOS response. *FEMS Microbiology Reviews*, *31*(6), 637-656. https://doi.org/10.1111/j.1574-6976.2007.00082.x

Farci, D., Bowler, M. W., Kirkpatrick, J., McSweeney, S., Tramontano, E., & Piano, D. (2014). New features of the cell wall of the radio-resistant bacterium Deinococcus radiodurans. *Biochimica et Biophysica Acta (BBA) - Biomembranes*, *1838*(7), 1978-1984. https://doi.org/10.1016/j.bbamem.2014.02.014

Ferrándiz, M.-J., Carreño, D., Ayora, S., & de la Campa, A. G. (2018). HU of Streptococcus pneumoniae Is Essential for the Preservation of DNA Supercoiling. *Frontiers in Microbiology*, *9*, 493. https://doi.org/10.3389/fmicb.2018.00493

Flint, D. H., Tuminello, J. F., & Emptage, M. H. (1993). The inactivation of Fe-S cluster containing hydro-lyases by superoxide. *The Journal of Biological Chemistry*, *268*(30), 22369-22376.

Floc'h, K., Lacroix, F., Servant, P., Wong, Y.-S., Kleman, J.-P., Bourgeois, D., & Timmins, J. (2019). Cell morphology and nucleoid dynamics in dividing Deinococcus radiodurans. *Nature Communications*, *10*(1), 3815. https://doi.org/10.1038/s41467-019-11725-5

Fraser, C. M., Norris, S. J., Weinstock, G. M., White, O., Sutton, G. G., Dodson, R., Gwinn, M., Hickey, E. K., Clayton, R., Ketchum, K. A., Sodergren, E., Hardham, J. M., McLeod, M. P., Salzberg, S., Peterson, J., Khalak, H., Richardson, D., Howell, J. K., Chidambaram, M., … Venter, J. C. (1998). Complete genome sequence of Treponema pallidum, the syphilis spirochete. *Science (New York, N.Y.)*, *281*(5375), 375-388. https://doi.org/10.1126/science.281.5375.375

Funnell. (1991). The P1 plasmid partition complex at parS. The influence of Escherichia coli integration host factor and of substrate topology. *The Journal of Biological Chemistry*, *266*(22), 14328-14337.

Funnell. (2016). ParB Partition Proteins : Complex Formation and Spreading at Bacterial and Plasmid Centromeres. *Frontiers in Molecular Biosciences*, *3*, 44. https://doi.org/10.3389/fmolb.2016.00044

Ganguly, A., del Toro Duany, Y., & Klostermeier, D. (2013). Reverse Gyrase Transiently Unwinds Double-Stranded DNA in an ATP-Dependent Reaction. *Journal of Molecular Biology*, *425*(1), 32-40. https://doi.org/10.1016/j.jmb.2012.10.016

Gawade, P., Gunjal, G., Sharma, A., & Ghosh, P. (2020). Reconstruction of transcriptional regulatory networks of Fis and H-NS in Escherichia coli from genome-wide data analysis. *Genomics*, *112*(2), 1264-1272. https://doi.org/10.1016/j.ygeno.2019.07.013

Geng, H., & Jiang, R. (2015). cAMP receptor protein (CRP)-mediated resistance/tolerance in bacteria : Mechanism and utilization in biotechnology. *Applied Microbiology and Biotechnology*, *99*(11), 4533-4543. https://doi.org/10.1007/s00253-015-6587-0

Gerdes, K., Møller-Jensen, J., & Bugge Jensen, R. (2000). Plasmid and chromosome partitioning : Surprises from phylogeny. *Molecular Microbiology*, *37*(3), 455-466. https://doi.org/10.1046/j.1365-2958.2000.01975.x

Germe, T., Vörös, J., Jeannot, F., Taillier, T., Stavenger, R. A., Bacqué, E., Maxwell, A., & Bax, B. D. (2018). A new class of antibacterials, the imidazopyrazinones, reveal structural transitions involved in DNA gyrase poisoning and mechanisms of resistance. *Nucleic Acids Research*, *46*(8), 4114-4128. https://doi.org/10.1093/nar/gky181

Ghosh, & Grove, A. (2004). Histone-like Protein HU from Deinococcus radiodurans Binds Preferentially to Four-way DNA Junctions. *Journal of Molecular Biology*, *337*(3), 561-571. https://doi.org/10.1016/j.jmb.2004.02.010

Ghosh, & Grove, A. (2006). The Deinococcus radiodurans Encoded HU Protein Has Two DNA-Binding Domains. *Biochemistry*, *45*(6), 1723-1733. https://doi.org/10.1021/bi0514010

Ghosh, S., Mallick, B., & Nagaraja, V. (2014). Direct regulation of topoisomerase activity by a nucleoid-associated protein. *Nucleic Acids Research*, *42*(17), 11156-11165. https://doi.org/10.1093/nar/gku804

Ghosh, S., Padmanabhan, B., Anand, C., & Nagaraja, V. (2016). Lysine acetylation of the Mycobacterium tuberculosis HU protein modulates its DNA binding and genome organization. *Molecular Microbiology*, *100*(4), 577-588. https://doi.org/10.1111/mmi.13339

Goldfarb, A. R., Saidel, LeoJ., & Mosovich, E. (1951). The ultraviolet absorption spectra of proteins. *Journal of Biological Chemistry*, *193*(1), 397-404. https://doi.org/10.1016/S0021-9258(19)52465-6

Gordon, B. R. G., Li, Y., Cote, A., Weirauch, M. T., Ding, P., Hughes, T. R., Navarre, W. W., Xia, B., & Liu, J. (2011). Structural basis for recognition of AT-rich DNA by unrelated xenogeneic silencing proteins. *Proceedings of the National Academy of Sciences*, *108*(26), 10690-10695. https://doi.org/10.1073/pnas.1102544108

Graham, T. G. W., Wang, X., Song, D., Etson, C. M., van Oijen, A. M., Rudner, D. Z., & Loparo, J. J. (2014). ParB spreading requires DNA bridging. *Genes & Development*, *28*(11), 1228-1238. https://doi.org/10.1101/gad.242206.114

Grainger, D. C. (2016). Structure and function of bacterial H-NS protein. *Biochemical Society*

Transactions, *44*(6), 1561-1569. https://doi.org/10.1042/BST20160190

Grainger, D. C., Goldberg, M. D., Lee, D. J., & Busby, S. J. W. (2008). Selective repression by Fis and H-NS at the Escherichia coli dps promoter. *Molecular Microbiology*, *68*(6), 1366-1377. https://doi.org/10.1111/j.1365-2958.2008.06253.x

Grant, R. A., Filman, D. J., Finkel, S. E., Kolter, R., & Hogle, J. M. (1998). The crystal structure of Dps, a ferritin homolog that binds and protects DNA. *Nature Structural Biology*, *5*(4), 294-303. https://doi.org/10.1038/nsb0498-294

Grove, A., & Lim, L. (2001). High-affinity DNA binding of HU protein from the hyperthermophile Thermotoga maritima. *Journal of Molecular Biology*, *311*(3), 491-502. https://doi.org/10.1006/jmbi.2001.4763

Grove, A. (2011). Functional evolution of bacterial histone-like HU proteins. *Current Issues in Molecular Biology*, *13*(1), 1-12.

Grove, A., & Wilkinson, S. P. (2005). Differential DNA binding and protection by dimeric and dodecameric forms of the ferritin homolog Dps from Deinococcus radiodurans. *Journal of Molecular Biology*, *347*(3), 495-508. https://doi.org/10.1016/j.jmb.2005.01.055

Gruber, S. (2014). Multilayer chromosome organization through DNA bending, bridging and extrusion. *Current Opinion in Microbiology*, *22*, 102-110. https://doi.org/10.1016/j.mib.2014.09.018

Gruber, S., & Errington, J. (2009). Recruitment of condensin to replication origin regions by ParB/SpoOJ promotes chromosome segregation in B. subtilis. *Cell*, *137*(4), 685-696. https://doi.org/10.1016/j.cell.2009.02.035

Guo, F., & Adhya, S. (2007). Spiral structure of Escherichia coli HUalphabeta provides foundation for DNA supercoiling. *Proceedings of the National Academy of Sciences of the United States of America*, *104*(11), 4309-4314. https://doi.org/10.1073/pnas.0611686104

Hales, L. M., Gumport, R. I., & Gardner, J. F. (1994). Determining the DNA sequence elements required for binding integration host factor to two different target sites. *Journal of Bacteriology*, *176*(10), 2999-3006. https://doi.org/10.1128/jb.176.10.2999-3006.1994

Hammel, M., Amlanjyoti, D., Reyes, F. E., Chen, J.-H., Parpana, R., Tang, H. Y. H., Larabell, C. A., Tainer, J. A., & Adhya, S. (2016). HU multimerization shift controls nucleoid compaction. *Science Advances*, *2*(7), e1600650. https://doi.org/10.1126/sciadv.1600650

Hancock, S. P., Stella, S., Cascio, D., & Johnson, R. C. (2016). DNA Sequence Determinants Controlling Affinity, Stability and Shape of DNA Complexes Bound by the Nucleoid Protein Fis. *PloS One*, *11*(3), e0150189. https://doi.org/10.1371/journal.pone.0150189

Hansen, M. T. (1978). Multiplicity of genome equivalents in the radiation-resistant bacterium Micrococcus radiodurans. *Journal of Bacteriology*, *134*(1), 71-75. https://doi.org/10.1128/JB.134.1.71-75.1978

Hariharan, P. P., & Cerutti, P. A. (1971). Repair of gamma-ray-induced thymine damage in Micrococcus radiodurans. *Nature: New Biology*, *229*(8), 247-249. https://doi.org/10.1038/newbio229247a0

Hariharan, P. V., & Cerutti, P. A. (1972). Formation and repair of gamma-ray induced thymine damage in Micrococcus radiodurans. *Journal of Molecular Biology*, *66*(1), 65-81. https://doi.org/10.1016/s0022-2836(72)80006-8

Harris, D. R., Tanaka, M., Saveliev, S. V., Jolivet, E., Earl, A. M., Cox, M. M., & Battista, J. R. (2004). Preserving genome integrity : The DdrA protein of Deinococcus radiodurans R1. *PLoS Biology*, *2*(10), e304. https://doi.org/10.1371/journal.pbio.0020304

Harsojo, H., Kitayama, S., & Matsuyama, A. (1981). Genome multiplicity and radiation resistance in Micrococcus radiodurans. *Journal of Biochemistry*, *90*(3), 877-880. https://doi.org/10.1093/oxfordjournals.jbchem.a133544

Hartmann, S., Gubaev, A., & Klostermeier, D. (2017). Binding and Hydrolysis of a Single ATP Is Sufficient for N-Gate Closure and DNA Supercoiling by Gyrase. *Journal of Molecular Biology*, *429*(23), 3717-3729. https://doi.org/10.1016/j.jmb.2017.10.005

Ho, Y. S., Burden, L. M., & Hurley, J. H. (2000). Structure of the GAF domain, a ubiquitous signaling motif and a new class of cyclic GMP receptor. *The EMBO Journal*, *19*(20), 5288-5299. https://doi.org/10.1093/emboj/19.20.5288

Hognon, C., Garaude, S., Timmins, J., Chipot, C., Dehez, F., & Monari, A. (2019). Molecular Bases of DNA Packaging in Bacteria Revealed by All-Atom Molecular Dynamics Simulations : The Case of Histone-Like Proteins in Borrelia burgdorferi. *The Journal of Physical Chemistry Letters*, *10*(22), 7200-7207. https://doi.org/10.1021/acs.jpclett.9b02978

Holliday, R. (1974). Molecular aspects of genetic exchange and gene conversion. *Genetics*, *78*(1), 273-287.

Hołówka, J., Trojanowski, D., Ginda, K., Wojtaś, B., Gielniewski, B., Jakimowicz, D., & Zakrzewska-Czerwińska, J. (2017). HupB Is a Bacterial Nucleoid-Associated Protein with an Indispensable Eukaryotic-Like Tail. *MBio*, *8*(6), e01272-17, /mbio/8/6/mBio.01272-17.atom. https://doi.org/10.1128/mBio.01272-17

Hołówka, J., Trojanowski, D., Janczak, M., Jakimowicz, D., & Zakrzewska-Czerwińska, J. (2018). The Origin of Chromosomal Replication Is Asymmetrically Positioned on the Mycobacterial Nucleoid, and the Timing of Its Firing Depends on HupB. *Journal of Bacteriology*, *200*(10). https://doi.org/10.1128/JB.00044-18

Hsieh, T.-J., Farh, L., Huang, W. M., & Chan, N.-L. (2004). Structure of the Topoisomerase IV C-terminal Domain. *Journal of Biological Chemistry*, *279*(53), 55587-55593. https://doi.org/10.1074/jbc.M408934200

Hsieh, T.-J., Yen, T.-J., Lin, T.-S., Chang, H.-T., Huang, S.-Y., Hsu, C.-H., Farh, L., & Chan, N.-L. (2010). Twisting of the DNA-binding surface by a beta-strand-bearing proline modulates DNA gyrase activity. *Nucleic Acids Research*, *38*(12), 4173-4181. https://doi.org/10.1093/nar/gkq153

Hu, Hu, Q., Wei, R., Li, R., Zhao, D., Ge, M., Yao, Q., & Yu, X. (2018). The XRE Family Transcriptional Regulator SrtR in Streptococcus suis Is Involved in Oxidant Tolerance and Virulence. *Frontiers in Cellular and Infection Microbiology*, *8*, 452. https://doi.org/10.3389/fcimb.2018.00452

Hu, L., Vecchiarelli, A. G., Mizuuchi, K., Neuman, K. C., & Liu, J. (2015). Directed and persistent movement arises from mechanochemistry of the ParA/ParB system. *Proceedings of the National Academy of Sciences of the United States of America*, *112*(51), E7055-7064. https://doi.org/10.1073/pnas.1505147112

Ilari, Latella, M. C., Ceci, P., Ribacchi, F., Su, M., Giangiacomo, L., Stefanini, S., Chasteen, N. D., & Chiancone, E. (2005). The unusual intersubunit ferroxidase center of Listeria innocua Dps is required for hydrogen peroxide detoxification but not for iron uptake. A study with site-specific mutants. *Biochemistry*, *44*(15), 5579-5587.

https://doi.org/10.1021/bi050005e

Ilari, Stefanini, S., Chiancone, E., & Tsernoglou, D. (2000). The dodecameric ferritin from Listeria innocua contains a novel intersubunit iron-binding site. *Nature Structural Biology*, *7*(1), 38-43. https://doi.org/10.1038/71236

Imlay, J. A. (2006). Iron-sulphur clusters and the problem with oxygen. *Molecular Microbiology*, *59*(4), 1073-1082. https://doi.org/10.1111/j.1365-2958.2006.05028.x

Imlay, J. A. (2008). Cellular Defenses against Superoxide and Hydrogen Peroxide. *Annual Review of Biochemistry*, *77*(1), 755-776. https://doi.org/10.1146/annurev.biochem.77.061606.161055

Ito, H. (1977). Isolation of Micrococcus radiodurans Occurring in Radurized Sawdust Culture Media of Mushroom. *Agricultural and Biological Chemistry*, *41*(1), 35-41. https://doi.org/10.1271/bbb1961.41.35

Jalal, A. S. B., & Le, T. B. K. (2020). Bacterial chromosome segregation by the ParABS system. *Open Biology*, *10*(6), 200097. https://doi.org/10.1098/rsob.200097

Janissen, R., Arens, M. M. A., Vtyurina, N. N., Rivai, Z., Sunday, N. D., Eslami-Mossallam, B., Gritsenko, A. A., Laan, L., de Ridder, D., Artsimovitch, I., Dekker, N. H., Abbondanzieri, E. A., & Meyer, A. S. (2018). Global DNA Compaction in Stationary-Phase Bacteria Does Not Affect Transcription. *Cell*, *174*(5), 1188-1199.e14. https://doi.org/10.1016/j.cell.2018.06.049

Japaridze, A., Muskhelishvili, G., Benedetti, F., Gavriilidou, A. F. M., Zenobi, R., De Los Rios, P., Longo, G., & Dietler, G. (2017). Hyperplectonemes : A Higher Order Compact and Dynamic DNA Self-Organization. *Nano Letters*, *17*(3), 1938-1948. https://doi.org/10.1021/acs.nanolett.6b05294

Jongeneel, C. V., Bouvier, J., & Bairoch, A. (1989). A unique signature identifies a family of zinc-dependent metallopeptidases. *FEBS Letters*, *242*(2), 211-214. https://doi.org/10.1016/0014-5793(89)80471-5

Kamada, K., Miyata, M., & Hirano, T. (2013). Molecular basis of SMC ATPase activation : Role of internal structural changes of the regulatory subcomplex ScpAB. *Structure (London, England: 1993)*, *21*(4), 581-594. https://doi.org/10.1016/j.str.2013.02.016

Kamashev, D., Agapova, Y., Rastorguev, S., Talyzina, A. A., Boyko, K. M., Korzhenevskiy, D. A., Vlaskina, A., Vasilov, R., Timofeev, V. I., & Rakitina, T. V. (2017). Comparison of histone-like HU protein DNA-binding properties and HU/IHF protein sequence alignment. *PLOS ONE*, *12*(11), e0188037. https://doi.org/10.1371/journal.pone.0188037

Kamau, E., Tsihlis, N. D., Simmons, L. A., & Grove, A. (2005). Surface salt bridges modulate the DNA site size of bacterial histone-like HU proteins. *Biochemical Journal*, *390*(1), 49-55. https://doi.org/10.1042/BJ20050274

Karas, V. O., Westerlaken, I., & Meyer, A. S. (2015). The DNA-Binding Protein from Starved Cells (Dps) Utilizes Dual Functions To Defend Cells against Multiple Stresses. *Journal of Bacteriology*, *197*(19), 3206-3215. https://doi.org/10.1128/JB.00475-15

Keegan, R. M., & Winn, M. D. (2008). MrBUMP : An automated pipeline for molecular replacement. *Acta Crystallographica. Section D, Biological Crystallography*, *64*(Pt 1), 119-124. https://doi.org/10.1107/S0907444907037195

Kim, D.-H., Im, H., Jee, J.-G., Jang, S.-B., Yoon, H.-J., Kwon, A.-R., Kang, S.-M., & Lee, B.-J. (2014). β-Arm flexibility of HU from Staphylococcus aureus dictates the DNA-binding

and recognition mechanism. *Acta Crystallographica Section D Biological Crystallography*, *70*(12), 3273-3289. https://doi.org/10.1107/S1399004714023931

Kim, D.-U., Lee, H., Lee, S., Park, S., Yoon, J.-H., Zhao, L., Kim, M.-K., Ahn, J.-H., & Ka, J.-O. (2018). Deinococcus multiflagellatus sp. Nov., isolated from a car air-conditioning system. *Antonie Van Leeuwenhoek*, *111*(4), 619-627. https://doi.org/10.1007/s10482-017-0982-8

Koster, D. A., Croquette, V., Dekker, C., Shuman, S., & Dekker, N. H. (2005). Friction and torque govern the relaxation of DNA supercoils by eukaryotic topoisomerase IB. *Nature*, *434*(7033), 671-674. https://doi.org/10.1038/nature03395

Kota, S., Rajpurohit, Y. S., Charaka, V. K., Satoh, K., Narumi, I., & Misra, H. S. (2016). DNA Gyrase of Deinococcus radiodurans is characterized as Type II bacterial topoisomerase and its activity is differentially regulated by PprA in vitro. *Extremophiles*, *20*(2), 195-205. https://doi.org/10.1007/s00792-016-0814-1

Kotlajich, M. V., Hron, D. R., Boudreau, B. A., Sun, Z., Lyubchenko, Y. L., & Landick, R. (2015). Bridged filaments of histone-like nucleoid structuring protein pause RNA polymerase and aid termination in bacteria. *ELife*, *4*, e04970. https://doi.org/10.7554/eLife.04970

Krabbenhoft, K. L., Anderson, A. W., & Elliker, P. R. (1965). Ecology of Micrococcus radiodurans. *Applied Microbiology*, *13*(6), 1030-1037.

Kramlinger, V. M., & Hiasa, H. (2006). The "GyrA-box" Is Required for the Ability of DNA Gyrase to Wrap DNA and Catalyze the Supercoiling Reaction. *Journal of Biological Chemistry*, *281*(6), 3738-3742. https://doi.org/10.1074/jbc.M511160200

Kristensen, H., & Christensen, E. A. (1981). Radiation-resistant micro-organisms isolated from textiles. *Acta Pathologica Et Microbiologica Scandinavica. Section B, Microbiology*, *89*(5), 303-309. https://doi.org/10.1111/j.1699-0463.1981.tb00193_89b.x

Kundukad, B., Cong, P., van der Maarel, J. R. C., & Doyle, P. S. (2013). Time-dependent bending rigidity and helical twist of DNA by rearrangement of bound HU protein. *Nucleic Acids Research*, *41*(17), 8280-8288. https://doi.org/10.1093/nar/gkt593

Lammens, A., Schele, A., & Hopfner, K.-P. (2004). Structural biochemistry of ATP-driven dimerization and DNA-stimulated activation of SMC ATPases. *Current Biology: CB*, *14*(19), 1778-1782. https://doi.org/10.1016/j.cub.2004.09.044

Lancy, P., & Murray, R. G. (1978). The envelope of Micrococcus radiodurans : Isolation, purification, and preliminary analysis of the wall layers. *Canadian Journal of Microbiology*, *24*(2), 162-176. https://doi.org/10.1139/m78-029

Lanz, M. A., & Klostermeier, D. (2012). The GyrA-box determines the geometry of DNA bound to gyrase and couples DNA binding to the nucleotide cycle. *Nucleic Acids Research*, *40*(21), 10893-10903. https://doi.org/10.1093/nar/gks852

Laponogov, I., Sohi, M. K., Veselkov, D. A., Pan, X.-S., Sawhney, R., Thompson, A. W., McAuley, K. E., Fisher, L. M., & Sanderson, M. R. (2009). Structural insight into the quinolone–DNA cleavage complex of type IIA topoisomerases. *Nature Structural & Molecular Biology*, *16*(6), 667-669. https://doi.org/10.1038/nsmb.1604

Le Gall, A., Cattoni, D. I., Guilhas, B., Mathieu-Demazière, C., Oudjedi, L., Fiche, J.-B., Rech, J., Abrahamsson, S., Murray, H., Bouet, J.-Y., & Nollmann, M. (2016). Bacterial partition complexes segregate within the volume of the nucleoid. *Nature Communications*, *7*, 12107. https://doi.org/10.1038/ncomms12107

Le, T. B. K., Imakaev, M. V., Mirny, L. A., & Laub, M. T. (2013). High-resolution mapping of the spatial organization of a bacterial chromosome. *Science (New York, N.Y.)*, *342*(6159), 731-734. https://doi.org/10.1126/science.1242059

Lee, S. F., Thompson, M. A., Schwartz, M. A., Shapiro, L., & Moerner, W. E. (2011). Super-Resolution Imaging of the Nucleoid-Associated Protein HU in Caulobacter crescentus. *Biophysical Journal*, *100*(7), L31-L33. https://doi.org/10.1016/j.bpj.2011.02.022

Leiros, I., Moe, E., Smalås, A. O., & McSweeney, S. (2005). Structure of the uracil-DNA N-glycosylase (UNG) from Deinococcus radiodurans. *Acta Crystallographica. Section D, Biological Crystallography*, *61*(Pt 8), 1049-1056. https://doi.org/10.1107/S090744490501382X

Leonard, T. A., Butler, P. J. G., & Löwe, J. (2004). Structural analysis of the chromosome segregation protein Spo0J from Thermus thermophilus. *Molecular Microbiology*, *53*(2), 419-432. https://doi.org/10.1111/j.1365-2958.2004.04133.x

Leonard, T. A., Butler, P. J., & Löwe, J. (2005). Bacterial chromosome segregation : Structure and DNA binding of the Soj dimer--a conserved biological switch. *The EMBO Journal*, *24*(2), 270-282. https://doi.org/10.1038/sj.emboj.7600530

Levin-Zaidman, S., Englander, J., Shimoni, E., Sharma, A. K., Minton, K. W., & Minsky, A. (2003). Ringlike structure of the Deinococcus radiodurans genome : A key to radioresistance? *Science (New York, N.Y.)*, *299*(5604), 254-256. https://doi.org/10.1126/science.1077865

Li, Mondragón, A., Hiasa, H., Marians, K. J., & DiGate, R. J. (2000). Identification of a unique domain essential for Escherichia coli DNA topoisomerase III-catalysed decatenation of replication intermediates. *Molecular Microbiology*, *35*(4), 888-895. https://doi.org/10.1046/j.1365-2958.2000.01763.x

Li, Stewart, N. K., Berger, A. J., Vos, S., Schoeffler, A. J., Berger, J. M., Chait, B. T., & Oakley, M. G. (2010). Escherichia coli condensin MukB stimulates topoisomerase IV activity by a direct physical interaction. *Proceedings of the National Academy of Sciences of the United States of America*, *107*(44), 18832-18837. https://doi.org/10.1073/pnas.1008678107

Lim, Jung, J.-H., Blanchard, L., & de Groot, A. (2019). Conservation and diversity of radiation and oxidative stress resistance mechanisms in Deinococcus species. *FEMS Microbiology Reviews*, *43*(1), 19-52. https://doi.org/10.1093/femsre/fuy037

Lim, Surovtsev, I. V., Beltran, B. G., Huang, F., Bewersdorf, J., & Jacobs-Wagner, C. (2014). Evidence for a DNA-relay mechanism in ParABS-mediated chromosome segregation. *ELife*, *3*, e02758. https://doi.org/10.7554/eLife.02758

Lipton, M. S., Pasa-Tolic, L., Anderson, G. A., Anderson, D. J., Auberry, D. L., Battista, J. R., Daly, M. J., Fredrickson, J., Hixson, K. K., Kostandarithes, H., Masselon, C., Markillie, L. M., Moore, R. J., Romine, M. F., Shen, Y., Stritmatter, E., Tolic, N., Udseth, H. R., Venkateswaran, A., … Smith, R. D. (2002). Global analysis of the Deinococcus radiodurans proteome by using accurate mass tags. *Proceedings of the National Academy of Sciences*, *99*(17), 11049-11054. https://doi.org/10.1073/pnas.172170199

Liu, D., Yumoto, H., Murakami, K., Hirota, K., Ono, T., Nagamune, H., Kayama, S., Matsuo, T., & Miyake, Y. (2008). The essentiality and involvement of Streptococcus intermedius histone-like DNA-binding protein in bacterial viability and normal growth. *Molecular Microbiology*, *68*(5), 1268-1282. https://doi.org/10.1111/j.1365-2958.2008.06232.x

Liu, Y., Chen, H., Kenney, L. J., & Yan, J. (2010). A divalent switch drives H-NS/DNA-binding conformations between stiffening and bridging modes. *Genes & Development*, *24*(4),

339-344. https://doi.org/10.1101/gad.1883510

Livny, J., Yamaichi, Y., & Waldor, M. K. (2007). Distribution of centromere-like parS sites in bacteria : Insights from comparative genomics. *Journal of Bacteriology*, *189*(23), 8693-8703. https://doi.org/10.1128/JB.01239-07

Lu, H., Wang, L., Li, S., Pan, C., Cheng, K., Luo, Y., Xu, H., Tian, B., Zhao, Y., & Hua, Y. (2019). Structure and DNA damage-dependent derepression mechanism for the XRE family member DG-DdrO. *Nucleic Acids Research*, *47*(18), 9925-9933. https://doi.org/10.1093/nar/gkz720

Ludanyi, M., Blanchard, L., Dulermo, R., Brandelet, G., Bellanger, L., Pignol, D., Lemaire, D., & de Groot, A. (2014). Radiation response in Deinococcus deserti : IrrE is a metalloprotease that cleaves repressor protein DdrO. *Molecular Microbiology*, *94*(2), 434-449. https://doi.org/10.1111/mmi.12774

Luijsterburg, M. S., White, M. F., van Driel, R., & Dame, R. T. (2008). The major architects of chromatin : Architectural proteins in bacteria, archaea and eukaryotes. *Critical Reviews in Biochemistry and Molecular Biology*, *43*(6), 393-418. https://doi.org/10.1080/10409230802528488

Luscombe, N. M. (2001). Amino acid-base interactions : A three-dimensional analysis of protein-DNA interactions at an atomic level. *Nucleic Acids Research*, *29*(13), 2860-2874. https://doi.org/10.1093/nar/29.13.2860

Macchi, R., Montesissa, L., Murakami, K., Ishihama, A., De Lorenzo, V., & Bertoni, G. (2003). Recruitment of sigma54-RNA polymerase to the Pu promoter of Pseudomonas putida through integration host factor-mediated positioning switch of alpha subunit carboxyl-terminal domain on an UP-like element. *The Journal of Biological Chemistry*, *278*(30), 27695-27702. https://doi.org/10.1074/jbc.M303031200

Magerand, R., Rey, P., Blanchard, L., & de Groot, A. (2021). Redox signaling through zinc activates the radiation response in Deinococcus bacteria. *Scientific Reports*, *11*(1), 4528. https://doi.org/10.1038/s41598-021-84026-x

Makarova, K. S., Aravind, L., Wolf, Y. I., Tatusov, R. L., Minton, K. W., Koonin, E. V., & Daly, M. J. (2001). Genome of the Extremely Radiation-Resistant Bacterium Deinococcus radiodurans Viewed from the Perspective of Comparative Genomics. *Microbiology and Molecular Biology Reviews*, *65*(1), 44-79. https://doi.org/10.1128/MMBR.65.1.44-79.2001

Makarova, K. S., Omelchenko, M. V., Gaidamakova, E. K., Matrosova, V. Y., Vasilenko, A., Zhai, M., Lapidus, A., Copeland, A., Kim, E., Land, M., Mavromatis, K., Pitluck, S., Richardson, P. M., Detter, C., Brettin, T., Saunders, E., Lai, B., Ravel, B., Kemner, K. M., … Daly, M. J. (2007). Deinococcus geothermalis : The Pool of Extreme Radiation Resistance Genes Shrinks. *PLoS ONE*, *9*, 21.

Mangan, M. W., Lucchini, S., Ó Cróinín, T., Fitzgerald, S., Hinton, J. C. D., & Dorman, C. J. (2011). Nucleoid-associated protein HU controls three regulons that coordinate virulence, response to stress and general physiology in Salmonella enterica serovar Typhimurium. *Microbiology (Reading, England)*, *157*(Pt 4), 1075-1087. https://doi.org/10.1099/mic.0.046359-0

Marbouty, M., Le Gall, A., Cattoni, D. I., Cournac, A., Koh, A., Fiche, J.-B., Mozziconacci, J., Murray, H., Koszul, R., & Nollmann, M. (2015). Condensin- and Replication-Mediated Bacterial Chromosome Folding and Origin Condensation Revealed by Hi-C and Super-resolution Imaging. *Molecular Cell*, *59*(4), 588-602.

https://doi.org/10.1016/j.molcel.2015.07.020

Markillie, L. M., Varnum, S. M., Hradecky, P., & Wong, K.-K. (1999). Targeted Mutagenesis by Duplication Insertion in the Radioresistant Bacterium Deinococcus radiodurans : Radiation Sensitivities of Catalase (katA) and Superoxide Dismutase (sodA) Mutants. *Journal of Bacteriology*, *181*(2), 666-669. https://doi.org/10.1128/JB.181.2.666-669.1999

Martínez-Salazar, J. M., Salazar, E., Encarnación, S., Ramírez-Romero, M. A., & Rivera, J. (2009). Role of the extracytoplasmic function sigma factor RpoE4 in oxidative and osmotic stress responses in Rhizobium etli. *Journal of Bacteriology*, *191*(13), 4122-4132. https://doi.org/10.1128/JB.01626-08

Massé, E., & Drolet, M. (1999). Escherichia coli DNA Topoisomerase I Inhibits R-loop Formation by Relaxing Transcription-induced Negative Supercoiling. *Journal of Biological Chemistry*, *274*(23), 16659-16664. https://doi.org/10.1074/jbc.274.23.16659

Maurer, S., Fritz, J., & Muskhelishvili, G. (2009). A Systematic In Vitro Study of Nucleoprotein Complexes Formed by Bacterial Nucleoid-Associated Proteins Revealing Novel Types of DNA Organization. *Journal of Molecular Biology*, *387*(5), 1261-1276. https://doi.org/10.1016/j.jmb.2009.02.050

McCoy, A. J., Grosse-Kunstleve, R. W., Adams, P. D., Winn, M. D., Storoni, L. C., & Read, R. J. (2007). Phaser crystallographic software. *Journal of Applied Crystallography*, *40*(Pt 4), 658-674. https://doi.org/10.1107/S0021889807021206

McKie, S. J., Neuman, K. C., & Maxwell, A. (2021). DNA topoisomerases : Advances in understanding of cellular roles and multi-protein complexes via structure-function analysis. *BioEssays*, 2000286. https://doi.org/10.1002/bies.202000286

Melby, T. E., Ciampaglio, C. N., Briscoe, G., & Erickson, H. P. (1998). The symmetrical structure of structural maintenance of chromosomes (SMC) and MukB proteins : Long, antiparallel coiled coils, folded at a flexible hinge. *The Journal of Cell Biology*, *142*(6), 1595-1604. https://doi.org/10.1083/jcb.142.6.1595

Mitchel, R. E. (1975). Involvement of hydroxyl radicals in the release by ionizing radiation of a cell surface nuclease from Micrococcus radiodurans. *Radiation Research*, *64*(2), 321-330.

Mitchel, R. E. (1976). Ionizing radiation damage in Micrococcus radiodurans cell wall : Release of polysaccharide. *Radiation Research*, *66*(1), 158-169.

Moe, E., Hall, D. R., Leiros, I., Monsen, V. T., Timmins, J., & McSweeney, S. (2012). Structure-function studies of an unusual 3-methyladenine DNA glycosylase II (AlkA) from Deinococcus radiodurans. *Acta Crystallographica. Section D, Biological Crystallography*, *68*(Pt 6), 703-712. https://doi.org/10.1107/S090744491200947X

Mouw, K. W., & Rice, P. A. (2007). Shaping the Borrelia burgdorferi genome : Crystal structure and binding properties of the DNA-bending protein Hbb. *Molecular Microbiology*, *63*(5), 1319-1330. https://doi.org/10.1111/j.1365-2958.2007.05586.x

Mukherjee, A., Bhattacharyya, G., & Grove, A. (2008). The C-terminal domain of HU-related histone-like protein Hlp from Mycobacterium smegmatis mediates DNA end-joining. *Biochemistry*, *47*(33), 8744-8753. https://doi.org/10.1021/bi800010s

Mumm, J. P., Landy, A., & Gelles, J. (2006). Viewing single lambda site-specific recombination events from start to finish. *The EMBO Journal*, *25*(19), 4586-4595. https://doi.org/10.1038/sj.emboj.7601325

Nair, S., & Finkel, S. E. (2004). Dps protects cells against multiple stresses during stationary

phase. *Journal of Bacteriology*, *186*(13), 4192-4198. https://doi.org/10.1128/JB.186.13.4192-4198.2004

Nguyen, & Grove, A. (2012). Metal Binding at the Deinococcus radiodurans Dps-1 N-Terminal Metal Site Controls Dodecameric Assembly and DNA Binding. *Biochemistry*, *51*(33), 6679-6689. https://doi.org/10.1021/bi300703x

Nguyen, H. H., Bouthier de la Tour, C. B., Toueille, M., Vannier, F., Sommer, S., & Servant, P. (2009). The essential histone-like protein HU plays a major role in Deinococcus radiodurans nucleoid compaction. *Molecular Microbiology*, *73*(2), 240-252. https://doi.org/10.1111/j.1365-2958.2009.06766.x

Nicolas, E., Upton, A. L., Uphoff, S., Henry, O., Badrinarayanan, A., & Sherratt, D. (2014). The SMC complex MukBEF recruits topoisomerase IV to the origin of replication region in live Escherichia coli. *MBio*, *5*(1), e01001-01013. https://doi.org/10.1128/mBio.01001-13

Niki, H., Jaffé, A., Imamura, R., Ogura, T., & Hiraga, S. (1991). The new gene mukB codes for a 177 kd protein with coiled-coil domains involved in chromosome partitioning of E. coli. *The EMBO Journal*, *10*(1), 183-193.

Nir, G., Lindner, M., Dietrich, H. R. C., Girshevitz, O., Vorgias, C. E., & Garini, Y. (2011). HU Protein Induces Incoherent DNA Persistence Length. *Biophysical Journal*, *100*(3), 784-790. https://doi.org/10.1016/j.bpj.2010.12.3687

Noom, M. C., Navarre, W. W., Oshima, T., Wuite, G. J. L., & Dame, R. T. (2007). H-NS promotes looped domain formation in the bacterial chromosome. *Current Biology*, *17*(21), R913-R914. https://doi.org/10.1016/j.cub.2007.09.005

Norais, C. A., Chitteni-Pattu, S., Wood, E. A., Inman, R. B., & Cox, M. M. (2009). DdrB Protein, an Alternative Deinococcus radiodurans SSB Induced by Ionizing Radiation. *Journal of Biological Chemistry*, *284*(32), 21402-21411. https://doi.org/10.1074/jbc.M109.010454

Nurse, P., Levine, C., Hassing, H., & Marians, K. J. (2003). Topoisomerase III Can Serve as the Cellular Decatenase in Escherichia coli. *Journal of Biological Chemistry*, *278*(10), 8653-8660. https://doi.org/10.1074/jbc.M211211200

Oberto, J., Nabti, S., Jooste, V., Mignot, H., & Rouviere-Yaniv, J. (2009). The HU regulon is composed of genes responding to anaerobiosis, acid stress, high osmolarity and SOS induction. *PloS One*, *4*(2), e4367. https://doi.org/10.1371/journal.pone.0004367

Ohniwa, R. L., Ushijima, Y., Saito, S., & Morikawa, K. (2011). Proteomic Analyses of Nucleoid-Associated Proteins in Escherichia coli, Pseudomonas aeruginosa, Bacillus subtilis, and Staphylococcus aureus. *PLoS ONE*, *6*(4), e19172. https://doi.org/10.1371/journal.pone.0019172

O'Neil, P., Lovell, S., Mehzabeen, N., Battaile, K., & Biswas, I. (2016). Crystal structure of histone-like protein from Streptococcus mutans refined to 1.9 Å resolution. *Acta Crystallographica Section F Structural Biology Communications*, *72*(4), 257-262. https://doi.org/10.1107/S2053230X1600217X

Ono, S., Goldberg, M. D., Olsson, T., Esposito, D., Hinton, J. C. D., & Ladbury, J. E. (2005). H-NS is a part of a thermally controlled mechanism for bacterial gene regulation. *The Biochemical Journal*, *391*(Pt 2), 203-213. https://doi.org/10.1042/BJ20050453

Opel, M. L., Aeling, K. A., Holmes, W. M., Johnson, R. C., Benham, C. J., & Hatfield, G. W. (2004). Activation of transcription initiation from a stable RNA promoter by a Fis protein-mediated DNA structural transmission mechanism. *Molecular Microbiology*, *53*(2), 665-674.

https://doi.org/10.1111/j.1365-2958.2004.04147.x

Osorio-Valeriano, M., Altegoer, F., Steinchen, W., Urban, S., Liu, Y., Bange, G., & Thanbichler, M. (2019). ParB-type DNA Segregation Proteins Are CTP-Dependent Molecular Switches. *Cell*, *179*(7), 1512-1524.e15. https://doi.org/10.1016/j.cell.2019.11.015

Ott, E., Kawaguchi, Y., Kölbl, D., Rabbow, E., Rettberg, P., Mora, M., Moissl-Eichinger, C., Weckwerth, W., Yamagishi, A., & Milojevic, T. (2020). Molecular repertoire of Deinococcus radiodurans after 1 year of exposure outside the International Space Station within the Tanpopo mission. *Microbiome*, *8*(1), 150. https://doi.org/10.1186/s40168-020-00927-5

Pan, C. Q., Finkel, S. E., Cramton, S. E., Feng, J. A., Sigman, D. S., & Johnson, R. C. (1996). Variable structures of Fis-DNA complexes determined by flanking DNA-protein contacts. *Journal of Molecular Biology*, *264*(4), 675-695. https://doi.org/10.1006/jmbi.1996.0669

Panyakampol, J., Cheevadhanarak, S., Sutheeworapong, S., Chaijaruwanich, J., Senachak, J., Siangdung, W., Jeamton, W., Tanticharoen, M., & Paithoonrangsarid, K. (2015). Physiological and transcriptional responses to high temperature in Arthrospira (Spirulina) platensis C1. *Plant & Cell Physiology*, *56*(3), 481-496. https://doi.org/10.1093/pcp/pcu192

Papageorgiou, A. C., Adam, P. S., Stavros, P., Nounesis, G., Meijers, R., Petratos, K., & Vorgias, C. E. (2016). HU histone-like DNA-binding protein from Thermus thermophilus : Structural and evolutionary analyses. *Extremophiles*, *20*(5), 695-709. https://doi.org/10.1007/s00792-016-0859-1

Papenfort, K., & Vanderpool, C. K. (2015). Target activation by regulatory RNAs in bacteria. *FEMS Microbiology Reviews*, *39*(3), 362-378. https://doi.org/10.1093/femsre/fuv016

Papillon, J., Ménétret, J.-F., Batisse, C., Hélye, R., Schultz, P., Potier, N., & Lamour, V. (2013). Structural insight into negative DNA supercoiling by DNA gyrase, a bacterial type 2A DNA topoisomerase. *Nucleic Acids Research*, *41*(16), 7815-7827. https://doi.org/10.1093/nar/gkt560

Passot, F. M., Nguyen, H. H., Dard-Dascot, C., Thermes, C., Servant, P., Espéli, O., & Sommer, S. (2015). Nucleoid organization in the radioresistant bacterium Deinococcus radiodurans. *Molecular Microbiology*, *97*(4), 759-774. https://doi.org/10.1111/mmi.13064

Pedersen, H. L., Johnson, K. A., McVey, C. E., Leiros, I., & Moe, E. (2015). Structure determination of uracil-DNA N-glycosylase from Deinococcus radiodurans in complex with DNA. *Acta Crystallographica. Section D, Biological Crystallography*, *71*(Pt 10), 2137-2149. https://doi.org/10.1107/S1399004715014157

Pelletier, J., Halvorsen, K., Ha, B.-Y., Paparcone, R., Sandler, S. J., Woldringh, C. L., Wong, W. P., & Jun, S. (2012). Physical manipulation of the Escherichia coli chromosome reveals its soft nature. *Proceedings of the National Academy of Sciences*, *109*(40), E2649-E2656. https://doi.org/10.1073/pnas.1208689109

Petrella, S., Capton, E., Raynal, B., Giffard, C., Thureau, A., Bonneté, F., Alzari, P. M., Aubry, A., & Mayer, C. (2019). Overall Structures of Mycobacterium tuberculosis DNA Gyrase Reveal the Role of a Corynebacteriales GyrB-Specific Insert in ATPase Activity. *Structure*, *27*(4), 579-589.e5. https://doi.org/10.1016/j.str.2019.01.004

Pinson, V., Takahashi, M., & Rouviere-Yaniv, J. (1999). Differential binding of the Escherichia coli HU, homodimeric forms and heterodimeric form to linear, gapped and cruciform DNA. *Journal of Molecular Biology*, *287*(3), 485-497. https://doi.org/10.1006/jmbi.1999.2631

Postow, L., Hardy, C. D., Arsuaga, J., & Cozzarelli, N. R. (2004). Topological domain structure of the Escherichia coli chromosome. *Genes & Development*, *18*(14), 1766-1779. https://doi.org/10.1101/gad.1207504

Quevillon-Cheruel, S., & Servant, P. (2020). Natural Transformation in Deinococcus radiodurans : A Genetic Analysis Reveals the Major Roles of DprA, DdrB, RecA, RecF, and RecO Proteins. *Frontiers in Microbiology*, *11*, 16.

Remesh, S. G., Verma, S. C., Chen, J.-H., Ekman, A. A., Larabell, C. A., Adhya, S., & Hammel, M. (2020). Nucleoid remodeling during environmental adaptation is regulated by HU-dependent DNA bundling. *Nature Communications*, *11*(1), 2905. https://doi.org/10.1038/s41467-020-16724-5

Reon, B. J., Nguyen, K. H., Bhattacharyya, G., & Grove, A. (2012). Functional comparison of Deinococcus radiodurans Dps proteins suggests distinct in vivo roles. *Biochemical Journal*, *447*(3), 381-391. https://doi.org/10.1042/BJ20120902

Requejo, R., Hurd, T. R., Costa, N. J., & Murphy, M. P. (2010). Cysteine residues exposed on protein surfaces are the dominant intramitochondrial thiol and may protect against oxidative damage. *The FEBS Journal*, *277*(6), 1465-1480. https://doi.org/10.1111/j.1742-4658.2010.07576.x

Rice, P. A., Yang, S., Mizuuchi, K., & Nash, H. A. (1996). Crystal structure of an IHF-DNA complex : A protein-induced DNA U-turn. *Cell*, *87*(7), 1295-1306. https://doi.org/10.1016/s0092-8674(00)81824-3

Roque, A., Iloro, I., Ponte, I., Arrondo, J. L. R., & Suau, P. (2005). DNA-induced secondary structure of the carboxyl-terminal domain of histone H1. *The Journal of Biological Chemistry*, *280*(37), 32141-32147. https://doi.org/10.1074/jbc.M505636200

Rothfuss, H., Lara, J. C., Schmid, A. K., & Lidstrom, M. E. (2006). Involvement of the S-layer proteins Hpi and SlpA in the maintenance of cell envelope integrity in Deinococcus radiodurans R1. *Microbiology (Reading, England)*, *152*(Pt 9), 2779-2787. https://doi.org/10.1099/mic.0.28971-0

Rudolph, M. G., del Toro Duany, Y., Jungblut, S. P., Ganguly, A., & Klostermeier, D. (2013). Crystal structures of Thermotoga maritima reverse gyrase : Inferences for the mechanism of positive DNA supercoiling. *Nucleic Acids Research*, *41*(2), 1058-1070. https://doi.org/10.1093/nar/gks1073

Ruthenburg, A. J., Graybosch, D. M., Huetsch, J. C., & Verdine, G. L. (2005). A Superhelical Spiral in the Escherichia coli DNA Gyrase A C-terminal Domain Imparts Unidirectional Supercoiling Bias. *Journal of Biological Chemistry*, *280*(28), 26177-26184. https://doi.org/10.1074/jbc.M502838200

Sachdeva, E., Kaur, G., Tiwari, P., Gupta, D., Singh, T. P., Ethayathulla, A. S., & Kaur, P. (2020). The pivot point arginines identified in the β-pinwheel structure of C-terminal domain from Salmonella Typhi DNA Gyrase A subunit. *Scientific Reports*, *10*(1), 7817. https://doi.org/10.1038/s41598-020-64792-w

Sagi, D., Friedman, N., Vorgias, C., Oppenheim, A. B., & Stavans, J. (2004). Modulation of DNA conformations through the formation of alternative high-order HU-DNA complexes. *Journal of Molecular Biology*, *341*(2), 419-428. https://doi.org/10.1016/j.jmb.2004.06.023

Sanchez, A., Cattoni, D. I., Walter, J.-C., Rech, J., Parmeggiani, A., Nollmann, M., & Bouet, J.-Y. (2015). Stochastic Self-Assembly of ParB Proteins Builds the Bacterial DNA Segregation Apparatus. *Cell Systems*, *1*(2), 163-173.

https://doi.org/10.1016/j.cels.2015.07.013

Santos, S. P., Cuypers, M. G., Round, A., Finet, S., Narayanan, T., Mitchell, E. P., & Romão, C. V. (2017). SAXS Structural Studies of Dps from Deinococcus radiodurans Highlights the Conformation of the Mobile N-Terminal Extensions. *Journal of Molecular Biology*, *429*(5), 667-687. https://doi.org/10.1016/j.jmb.2017.01.008

Santos, S. P., Mitchell, E. P., Franquelim, H. G., Castanho, M. A. R. B., Abreu, I. A., & Romão, C. V. (2015). Dps from Deinococcus radiodurans : Oligomeric forms of Dps1 with distinct cellular functions and Dps2 involved in metal storage. *The FEBS Journal*, *282*(22), 4307-4327. https://doi.org/10.1111/febs.13420

Santos, S. P., Yang, Y., Rosa, M. T. G., Rodrigues, M. A. A., De La Tour, C. B., Sommer, S., Teixeira, M., Carrondo, M. A., Cloetens, P., Abreu, I. A., & Romão, C. V. (2019). The interplay between Mn and Fe in Deinococcus radiodurans triggers cellular protection during paraquat-induced oxidative stress. *Scientific Reports*, *9*(1), 17217. https://doi.org/10.1038/s41598-019-53140-2

Schneider, R., Lurz, R., Lüder, G., Tolksdorf, C., Travers, A., & Muskhelishvili, G. (2001). An architectural role of the Escherichia coli chromatin protein FIS in organising DNA. *Nucleic Acids Research*, *29*(24), 5107-5114. https://doi.org/10.1093/nar/29.24.5107

Schneider, R., Travers, A., Kutateladze, T., & Muskhelishvili, G. (1999). A DNA architectural protein couples cellular physiology and DNA topology in Escherichia coli. *Molecular Microbiology*, *34*(5), 953-964. https://doi.org/10.1046/j.1365-2958.1999.01656.x

Schoeffler, A. J., & Berger, J. M. (2005). Recent advances in understanding structure-function relationships in the type II topoisomerase mechanism. *Biochemical Society Transactions*, *33*(Pt 6), 1465-1470. https://doi.org/10.1042/BST20051465

Schoeffler, A. J., May, A. P., & Berger, J. M. (2010). A domain insertion in Escherichia coli GyrB adopts a novel fold that plays a critical role in gyrase function. *Nucleic Acids Research*, *38*(21), 7830-7844. https://doi.org/10.1093/nar/gkq665

Scholefield, G., Whiting, R., Errington, J., & Murray, H. (2011). Spo0J regulates the oligomeric state of Soj to trigger its switch from an activator to an inhibitor of DNA replication initiation. *Molecular Microbiology*, *79*(4), 1089-1100. https://doi.org/10.1111/j.1365-2958.2010.07507.x

Schumacher, M. A., & Funnell, B. E. (2005). Structures of ParB bound to DNA reveal mechanism of partition complex formation. *Nature*, *438*(7067), 516-519. https://doi.org/10.1038/nature04149

Shendruk, T. N., Bertrand, M., de Haan, H. W., Harden, J. L., & Slater, G. W. (2015). Simulating the Entropic Collapse of Coarse-Grained Chromosomes. *Biophysical Journal*, *108*(4), 810-820. https://doi.org/10.1016/j.bpj.2014.11.3487

Siam, R., Brassinga, A. K. C., & Marczynski, G. T. (2003). A dual binding site for integration host factor and the response regulator CtrA inside the Caulobacter crescentus replication origin. *Journal of Bacteriology*, *185*(18), 5563-5572. https://doi.org/10.1128/jb.185.18.5563-5572.2003

Singh, S. S., Singh, N., Bonocora, R. P., Fitzgerald, D. M., Wade, J. T., & Grainger, D. C. (2014). Widespread suppression of intragenic transcription initiation by H-NS. *Genes & Development*, *28*(3), 214-219. https://doi.org/10.1101/gad.234336.113

Sissi, C., & Palumbo, M. (2009). Effects of magnesium and related divalent metal ions in

topoisomerase structure and function. *Nucleic Acids Research*, *37*(3), 702-711. https://doi.org/10.1093/nar/gkp024

Skoko, D., Wong, B., Johnson, R. C., & Marko, J. F. (2004). Micromechanical analysis of the binding of DNA-bending proteins HMGB1, NHP6A, and HU reveals their ability to form highly stable DNA-protein complexes. *Biochemistry*, *43*(43), 13867-13874. https://doi.org/10.1021/bi048428o

Slade, D., & Radman, M. (2011). Oxidative Stress Resistance in Deinococcus radiodurans. *Microbiology and Molecular Biology Reviews*, *75*(1), 133-191. https://doi.org/10.1128/MMBR.00015-10

Soh, Y.-M., Davidson, I. F., Zamuner, S., Basquin, J., Bock, F. P., Taschner, M., Veening, J.-W., De Los Rios, P., Peters, J.-M., & Gruber, S. (2019). Self-organization of parS centromeres by the ParB CTP hydrolase. *Science (New York, N.Y.)*, *366*(6469), 1129-1133. https://doi.org/10.1126/science.aay3965

Spurio, R., Falconi, M., Brandi, A., Pon, C. L., & Gualerzi, C. O. (1997). The oligomeric structure of nucleoid protein H-NS is necessary for recognition of intrinsically curved DNA and for DNA bending. *The EMBO Journal*, *16*(7), 1795-1805. https://doi.org/10.1093/emboj/16.7.1795

Stein, R. A., Deng, S., & Higgins, N. P. (2005). Measuring chromosome dynamics on different time scales using resolvases with varying half-lives. *Molecular Microbiology*, *56*(4), 1049-1061. https://doi.org/10.1111/j.1365-2958.2005.04588.x

Stella, S., Cascio, D., & Johnson, R. C. (2010). The shape of the DNA minor groove directs binding by the DNA-bending protein Fis. *Genes & Development*, *24*(8), 814-826. https://doi.org/10.1101/gad.1900610

Stelter, M., Acajjaoui, S., McSweeney, S., & Timmins, J. (2013). Structural and Mechanistic Insight into DNA Unwinding by Deinococcus radiodurans UvrD. *PLoS ONE*, *8*(10), e77364. https://doi.org/10.1371/journal.pone.0077364

Stewart, L., Redinbo, M. R., Qiu, X., Hol, W. G., & Champoux, J. J. (1998). A model for the mechanism of human topoisomerase I. *Science (New York, N.Y.)*, *279*(5356), 1534-1541. https://doi.org/10.1126/science.279.5356.1534

Stillman, T. J., Upadhyay, M., Norte, V. A., Sedelnikova, S. E., Carradus, M., Tzokov, S., Bullough, P. A., Shearman, C. A., Gasson, M. J., Williams, C. H., Artymiuk, P. J., & Green, J. (2005). The crystal structures of Lactococcus lactis MG1363 Dps proteins reveal the presence of an N-terminal helix that is required for DNA binding. *Molecular Microbiology*, *57*(4), 1101-1112. https://doi.org/10.1111/j.1365-2958.2005.04757.x

Stivers, J. T., Harris, T. K., & Mildvan, A. S. (1997). Vaccinia DNA topoisomerase I : Evidence supporting a free rotation mechanism for DNA supercoil relaxation. *Biochemistry*, *36*(17), 5212-5222. https://doi.org/10.1021/bi962880t

Sugiman-Marangos, S. N., & Junop, M. S. (2010). The structure of DdrB from Deinococcus : A new fold for single-stranded DNA binding proteins. *Nucleic Acids Research*, *38*(10), 3432-3440. https://doi.org/10.1093/nar/gkq036

Sugiman-Marangos, S. N., Peel, J. K., Weiss, Y. M., Ghirlando, R., & Junop, M. S. (2013). Crystal structure of the DdrB/ssDNA complex from Deinococcus radiodurans reveals a DNA binding surface involving higher-order oligomeric states. *Nucleic Acids Research*, *41*(21), 9934-9944. https://doi.org/10.1093/nar/gkt759

Sugiman-Marangos, S. N., Weiss, Y. M., & Junop, M. S. (2016). Mechanism for accurate, protein-assisted DNA annealing by Deinococcus radiodurans DdrB. *Proceedings of the National Academy of Sciences*, *113*(16), 4308-4313. https://doi.org/10.1073/pnas.1520847113

Sullivan, N. L., Marquis, K. A., & Rudner, D. Z. (2009). Recruitment of SMC by ParB-parS organizes the origin region and promotes efficient chromosome segregation. *Cell*, *137*(4), 697-707. https://doi.org/10.1016/j.cell.2009.04.044

Swinger, K. K., Lemberg, K. M., Zhang, Y., & Rice, P. A. (2003). Flexible DNA bending in HU-DNA cocrystal structures. *EMBO Journal*, *22*(14), 3749-3760. https://doi.org/10.1093/emboj/cdg351

Swinger, K. K., & Rice, P. A. (2004). IHF and HU : Flexible architects of bent DNA. *Current Opinion in Structural Biology*, *14*(1), 28-35. https://doi.org/10.1016/j.sbi.2003.12.003

Talavera, A., Tamman, H., Ainelo, A., Konijnenberg, A., Hadži, S., Sobott, F., Garcia-Pino, A., Hõrak, R., & Loris, R. (2019). A dual role in regulation and toxicity for the disordered N-terminus of the toxin GraT. *Nature Communications*, *10*(1), 972. https://doi.org/10.1038/s41467-019-08865-z

Talukder, A., & Ishihama, A. (2015). Growth phase dependent changes in the structure and protein composition of nucleoid in Escherichia coli. *Science China. Life Sciences*, *58*(9), 902-911. https://doi.org/10.1007/s11427-015-4898-0

Tan, K., Zhou, Q., Cheng, B., Zhang, Z., Joachimiak, A., & Tse-Dinh, Y.-C. (2015). Structural basis for suppression of hypernegative DNA supercoiling by E. coli topoisomerase I. *Nucleic Acids Research*, *43*(22), 11031-11046. https://doi.org/10.1093/nar/gkv1073

Tanaka, M., Earl, A. M., Howell, H. A., Park, M.-J., Eisen, J. A., Peterson, S. N., & Battista, J. R. (2004). Analysis of Deinococcus radiodurans's transcriptional response to ionizing radiation and desiccation reveals novel proteins that contribute to extreme radioresistance. *Genetics*, *168*(1), 21-33. https://doi.org/10.1534/genetics.104.029249

Taneja, B., Patel, A., Slesarev, A., & Mondragón, A. (2006). Structure of the N-terminal fragment of topoisomerase V reveals a new family of topoisomerases. *The EMBO Journal*, *25*(2), 398-408. https://doi.org/10.1038/sj.emboj.7600922

Taniguchi, S., Kasho, K., Ozaki, S., & Katayama, T. (2019). Escherichia coli CrfC Protein, a Nucleoid Partition Factor, Localizes to Nucleoid Poles via the Activities of Specific Nucleoid-Associated Proteins. *Frontiers in Microbiology*, *10*, 72. https://doi.org/10.3389/fmicb.2019.00072

Tay, J. W., Romeo, G., Hughes, Q. W., & Baker, R. I. (2013). Micro-ribonucleic Acid 494 regulation of protein S expression. *Journal of Thrombosis and Haemostasis: JTH*, *11*(8), 1547-1555. https://doi.org/10.1111/jth.12331

Tian, B., Wu, Y., Sheng, D., Zheng, Z., Gao, G., & Hua, Y. (2004). Chemiluminescence assay for reactive oxygen species scavenging activities and inhibition on oxidative damage of DNA inDeinococcus radiodurans. *Luminescence*, *19*(2), 78-84. https://doi.org/10.1002/bio.761

Tian, B., Xu, Z., Sun, Z., Lin, J., & Hua, Y. (2007). Evaluation of the antioxidant effects of carotenoids from Deinococcus radiodurans through targeted mutagenesis, chemiluminescence, and DNA damage analyses. *Biochimica et Biophysica Acta*, 10.

Timmins, J., & Moe, E. (2016). A Decade of Biochemical and Structural Studies of the DNA Repair Machinery of Deinococcus radiodurans : Major Findings, Functional and Mechanistic

Insight and Challenges. *Computational and Structural Biotechnology Journal*, *14*, 168-176. https://doi.org/10.1016/j.csbj.2016.04.001

Tomb, J. F., White, O., Kerlavage, A. R., Clayton, R. A., Sutton, G. G., Fleischmann, R. D., Ketchum, K. A., Klenk, H. P., Gill, S., Dougherty, B. A., Nelson, K., Quackenbush, J., Zhou, L., Kirkness, E. F., Peterson, S., Loftus, B., Richardson, D., Dodson, R., Khalak, H. G., … Venter, J. C. (1997). The complete genome sequence of the gastric pathogen Helicobacter pylori. *Nature*, *388*(6642), 539-547. https://doi.org/10.1038/41483

Toueille, M., Mirabella, B., Guérin, P., Bouthier de la Tour, C., Boisnard, S., Nguyen, H. H., Blanchard, L., Servant, P., de Groot, A., Sommer, S., & Armengaud, J. (2012). A comparative proteomic approach to better define Deinococcus nucleoid specificities. *Journal of Proteomics*, *75*(9), 2588-2600. https://doi.org/10.1016/j.jprot.2012.03.002

Valens, M., Penaud, S., Rossignol, M., Cornet, F., & Boccard, F. (2004). Macrodomain organization of the Escherichia coli chromosome. *The EMBO Journal*, *23*(21), 4330-4341. https://doi.org/10.1038/sj.emboj.7600434

Valkenburg, J. A., & Woldringh, C. L. (1984). Phase separation between nucleoid and cytoplasm in Escherichia coli as defined by immersive refractometry. *Journal of Bacteriology*, *160*(3), 1151-1157. https://doi.org/10.1128/JB.160.3.1151-1157.1984

van der Valk, R. A., Vreede, J., Qin, L., Moolenaar, G. F., Hofmann, A., Goosen, N., & Dame, R. T. (2017). Mechanism of environmentally driven conformational changes that modulate H-NS DNA-bridging activity. *ELife*, *6*. https://doi.org/10.7554/eLife.27369

Vanden Broeck, A., Lotz, C., Ortiz, J., & Lamour, V. (2019). Cryo-EM structure of the complete E. coli DNA gyrase nucleoprotein complex. *Nature Communications*, *10*(1), 4935. https://doi.org/10.1038/s41467-019-12914-y

van Noort, J., Verbrugge, S., Goosen, N., Dekker, C., & Dame, R. T. (2004). Dual architectural roles of HU : Formation of flexible hinges and rigid filaments. *Proceedings of the National Academy of Sciences*, *101*(18), 6969-6974. https://doi.org/10.1073/pnas.0308230101

Vazquez-Anderson, J., & Contreras, L. M. (2013). Regulatory RNAs : Charming gene management styles for synthetic biology applications. *RNA Biology*, *10*(12), 1778-1797. https://doi.org/10.4161/rna.27102

Villa, J. K., Amador, P., Janovsky, J., Bhuyan, A., Saldanha, R., Lamkin, T. J., & Contreras, L. M. (2017). A Genome-Wide Search for Ionizing-Radiation-Responsive Elements in Deinococcus radiodurans Reveals a Regulatory Role for the DNA Gyrase Subunit A Gene's 5′ Untranslated Region in the Radiation and Desiccation Response. *Applied and Environmental Microbiology*, *83*(12), e00039-17, /aem/83/12/e00039-17.atom. https://doi.org/10.1128/AEM.00039-17

Vos, S. M., Lee, I., & Berger, J. M. (2013). Distinct regions of the Escherichia coli ParC C-terminal domain are required for substrate discrimination by topoisomerase IV. *Journal of Molecular Biology*, *425*(17), 3029-3045. https://doi.org/10.1016/j.jmb.2013.04.033

Vos, S. M., Tretter, E. M., Schmidt, B. H., & Berger, J. M. (2011). All tangled up : How cells direct, manage and exploit topoisomerase function. *Nature Reviews. Molecular Cell Biology*, *12*(12), 827-841. https://doi.org/10.1038/nrm3228

Vujičić-Žagar, A., Dulermo, R., Le Gorrec, M., Vannier, F., Servant, P., Sommer, S., de Groot, A., & Serre, L. (2009). Crystal Structure of the IrrE Protein, a Central Regulator of DNA Damage Repair in Deinococcaceae. *Journal of Molecular Biology*, *386*(3), 704-716.

https://doi.org/10.1016/j.jmb.2008.12.062

Vukovic-Nagy, B., Fox, B. W., & Fox, M. (1974). The release of a deoxyribonucleic acid fragment after x-irradiation of Micrococcus radiodurans. *International Journal of Radiation Biology and Related Studies in Physics, Chemistry, and Medicine*, *25*(4), 329-337. https://doi.org/10.1080/09553007414550401

Walker, G. C. (1984). Mutagenesis and inducible responses to deoxyribonucleic acid damage in Escherichia coli. *Microbiological Reviews*, *48*(1), 60-93.

Wang. (1998). Moving one DNA double helix through another by a type II DNA topoisomerase : The story of a simple molecular machine. *Quarterly Reviews of Biophysics*, *31*(2), 107-144. https://doi.org/10.1017/S0033583598003424

Wang, Li, G.-W., Chen, C., Xie, X. S., & Zhuang, X. (2011). Chromosome Organization by a Nucleoid-Associated Protein in Live Bacteria. *Science (New York, N.Y.)*, *333*(6048), 1445-1449. https://doi.org/10.1126/science.1204697

Wang, Reyes-Lamothe, R., & Sherratt, D. J. (2008). Modulation of Escherichia coli sister chromosome cohesion by topoisomerase IV. *Genes & Development*, *22*(17), 2426-2433. https://doi.org/10.1101/gad.487508

Wang, S., Cosstick, R., Gardner, J. F., & Gumport, R. I. (1995). The specific binding of Escherichia coli integration host factor involves both major and minor grooves of DNA. *Biochemistry*, *34*(40), 13082-13090. https://doi.org/10.1021/bi00040a020

Wang, Tang, O. W., Riley, E. P., & Rudner, D. Z. (2014). The SMC condensin complex is required for origin segregation in Bacillus subtilis. *Current Biology: CB*, *24*(3), 287-292. https://doi.org/10.1016/j.cub.2013.11.050

Ward, D., & Newton, A. (1997). Requirement of topoisomerase IV parC and parE genes for cell cycle progression and developmental regulation in Caulobacter crescentus. *Molecular Microbiology*, *26*(5), 897-910. https://doi.org/10.1046/j.1365-2958.1997.6242005.x

Waterhouse, A., Bertoni, M., Bienert, S., Studer, G., Tauriello, G., Gumienny, R., Heer, F. T., de Beer, T. A. P., Rempfer, C., Bordoli, L., Lepore, R., & Schwede, T. (2018). SWISS-MODEL : Homology modelling of protein structures and complexes. *Nucleic Acids Research*, *46*(W1), W296-W303. https://doi.org/10.1093/nar/gky427

Webb, K. M., & DiRuggiero, J. (2012). Role of Mn2+ and compatible solutes in the radiation resistance of thermophilic bacteria and archaea. *Archaea (Vancouver, B.C.)*, *2012*, 845756. https://doi.org/10.1155/2012/845756

Wen, Y., Behiels, E., Felix, J., Elegheert, J., Vergauwen, B., Devreese, B., & Savvides, S. N. (2014). The bacterial antitoxin HipB establishes a ternary complex with operator DNA and phosphorylated toxin HipA to regulate bacterial persistence. *Nucleic Acids Research*, *42*(15), 10134-10147. https://doi.org/10.1093/nar/gku665

White, O., Eisen, J. A., Heidelberg, J. F., Hickey, E. K., Peterson, J. D., Dodson, R. J., Haft, D. H., Gwinn, M. L., Nelson, W. C., Richardson, D. L., Moffat, K. S., Qin, H., Jiang, L., Pamphile, W., Crosby, M., Shen, M., Vamathevan, J. J., Lam, P., McDonald, L., … Fraser, C. M. (1999). Genome sequence of the radioresistant bacterium Deinococcus radiodurans R1. *Science (New York, N.Y.)*, *286*(5444), 1571-1577. https://doi.org/10.1126/science.286.5444.1571

White, S. W., Appelt, K., Wilson, K. S., & Tanaka, I. (1989). A protein structural motif that bends DNA. *Proteins: Structure, Function, and Genetics*, *5*(4), 281-288.

https://doi.org/10.1002/prot.340050405

Wigley, D. B., Davies, G. J., Dodson, E. J., Maxwell, A., & Dodson, G. (1991). Crystal structure of an N-terminal fragment of the DNA gyrase B protein. *Nature*, *351*(6328), 624-629. https://doi.org/10.1038/351624a0

Wolf, S. G., Frenkiel, D., Arad, T., Finkel, S. E., Kolter, R., & Minsky, A. (1999). DNA protection by stress-induced biocrystallization. *Nature*, *400*(6739), 83-85. https://doi.org/10.1038/21918

Work, E., & Griffiths, H. (1968). Morphology and Chemistry of Cell Walls of Micrococcus radiodurans. *Journal of Bacteriology*, *95*(2), 641-657. https://doi.org/10.1128/JB.95.2.641-657.1968

Xin, F., & Radivojac, P. (2012). Post-translational modifications induce significant yet not extreme changes to protein structure. *Bioinformatics*, *28*(22), 2905-2913. https://doi.org/10.1093/bioinformatics/bts541

Xu, G., Lu, H., Wang, L., Chen, H., Xu, Z., Hu, Y., Tian, B., & Hua, Y. (2010). DdrB stimulates single-stranded DNA annealing and facilitates RecA-independent DNA repair in Deinococcus radiodurans. *DNA Repair*, *9*(7), 805-812. https://doi.org/10.1016/j.dnarep.2010.04.006

Xu, Z., Tian, B., Sun, Z., Lin, J., & Hua, Y. (2007). *Identification and functional analysis of a phytoene desaturase gene from the extremely radioresistant bacterium Deinococcus radiodurans*. 11.

Yagüe, P., Gonzalez-Quiñonez, N., Fernández-García, G., Alonso-Fernández, S., & Manteca, A. (2019). Goals and Challenges in Bacterial Phosphoproteomics. *International Journal of Molecular Sciences*, *20*(22), E5678. https://doi.org/10.3390/ijms20225678

Yamamoto, Y., Poole, L. B., Hantgan, R. R., & Kamio, Y. (2002). An iron-binding protein, Dpr, from Streptococcus mutans prevents iron-dependent hydroxyl radical formation in vitro. *Journal of Bacteriology*, *184*(11), 2931-2939. https://doi.org/10.1128/jb.184.11.2931-2939.2002

Yang, S., Xu, H., Wang, J., Liu, C., Lu, H., Liu, M., Zhao, Y., Tian, B., Wang, L., & Hua, Y. (2016). Cyclic AMP Receptor Protein Acts as a Transcription Regulator in Response to Stresses in Deinococcus radiodurans. *PloS One*, *11*(5), e0155010. https://doi.org/10.1371/journal.pone.0155010

Yee, B., Sagulenko, E., & Fuerst, J. A. (2011). Making heads or tails of the HU proteins in the planctomycete Gemmata obscuriglobus. *Microbiology*, *157*(7), 2012-2021. https://doi.org/10.1099/mic.0.047605-0

Zahradka, K., Slade, D., Bailone, A., Sommer, S., Averbeck, D., Petranovic, M., Lindner, A. B., & Radman, M. (2006). Reassembly of shattered chromosomes in Deinococcus radiodurans. *Nature*, *443*(7111), 569-573. https://doi.org/10.1038/nature05160

Zawadzki, P., Stracy, M., Ginda, K., Zawadzka, K., Lesterlin, C., Kapanidis, A. N., & Sherratt, D. J. (2015). The Localization and Action of Topoisomerase IV in Escherichia coli Chromosome Segregation Is Coordinated by the SMC Complex, MukBEF. *Cell Reports*, *13*(11), 2587-2596. https://doi.org/10.1016/j.celrep.2015.11.034

Zhang, L., Yang, Q., Luo, X., Fang, C., Zhang, Q., & Tang, Y. (2007). Knockout of crtB or crtI gene blocks the carotenoid biosynthetic pathway in Deinococcus radiodurans R1 and influences its resistance to oxidative DNA-damaging agents due to change of free radicals

scavenging ability. *Archives of Microbiology*, *188*(4), 411-419. https://doi.org/10.1007/s00203-007-0262-5

Zhang, & Schumacher, M. A. (2017). Structures of partition protein ParA with nonspecific DNA and ParB effector reveal molecular insights into principles governing Walker-box DNA segregation. *Genes & Development*, *31*(5), 481-492. https://doi.org/10.1101/gad.296319.117

Zhao, G., Ceci, P., Ilari, A., Giangiacomo, L., Laue, T. M., Chiancone, E., & Chasteen, N. D. (2002). Iron and hydrogen peroxide detoxification properties of DNA-binding protein from starved cells. A ferritin-like DNA-binding protein of Escherichia coli. *The Journal of Biological Chemistry*, *277*(31), 27689-27696. https://doi.org/10.1074/jbc.M202094200

Zimmerman, J. M., & Battista, J. R. (2005). A ring-like nucleoid is not necessary for radioresistance in the Deinococcaceae. *BMC Microbiology*, *5*(1), 17. https://doi.org/10.1186/1471-2180-5-17

Zimmerman, S. B., & Trach, S. O. (1991). Estimation of macromolecule concentrations and excluded volume effects for the cytoplasm of Escherichia coli. *Journal of Molecular Biology*, *222*(3), 599-620. https://doi.org/10.1016/0022-2836(91)90499-V

Appendices

Table S1. Diversity of the *Deinococcus* genus. Complete list of the validly published species of the genus *Deinococcus* (based on the LSPN database (https://lpsn.dsmz.de/genus/deinococcus) and their physical characteristics.

***Deinococcus* species (reference)**	**(First) Site(s) of Isolation**	**Gram**	**Cell shape**	**Pigmentation**
Deinococcus actinosclerus (Joo et al. 2015)	Soil of a rocky hillside, South Korea	+	coccus or rod	pink
Deinococcus aerius (Yang et al. 2009)	High atmosphere, Japan	+	coccus	orange
Deinococcus aerolatus (Yoo et al. 2010)	Air, South Korea	+	coccus	pink
Deinococcus aerophilus (Yoo et al. 2010)	Air, South Korea	+	coccus	pink
Deinococcus aetherius (Yang et al. 2010)	Stratosphere, Japan	+	coccus	pink to red
Deinococcus alpinitundrae (Callegan et al. 2008)	Alpine environments, Mount Evans, CO, USA	+	coccus	pink
Deinococcus altitudinis (Callegan et al. 2008)	Alpine environments, Mount Evans, CO, USA	+	rod	pink
Deinococcus aluminii (Kim et al. 2018)	Automobile air conditioning system, South Korea	+	coccus	light-pink
Deinococcus antarticus (Dong et al. 2015)	Soil sample collected in the Grove Mountains, Antarctica	+	coccus	pink
Deinococcus apachensis (Rainey and da Costa 2005)	Irradiated Sonoran Desert soil, AZ, USA	+	coccus	pink
Deinococcus aquaticus (Im et al. 2008)	Freshwater, South Korea	-	rod	red
Deinococcus aquatilis (Kämpfer et al. 2008)	Water, Germany	+	rod	light-pink
Deinococcus aquiradiocola (Asker et al. 2009)	Radioactive site, Japan	+	rod	light-pink
Deinococcus arcticus (Wang et al. 2019)	Arctic tundra, Ny-Alesund, Svalbard, Norway	-	rod	red
Deinococcus arenae (Lee et al. 2016)	Sand, South Korea	-	rod	red
Deinococcus budaensis (Makk et al. 2016)	Irradiated biofilm from a hydrothermal spring cave, Hungary	-	coccus	pink
Deinococcus caeni (Im et al. 2008)	Activated sludge, South Korea	-	rod	pink
Deinococcus carri (Kim et al. 2015)	Automobile air conditioning system, South Korea	+	coccus	pink
Deinococcus cellulosilyticus (Weon et al. 2007)	Air sample from Jeju Island, South Korea	+	rod	light-pink
Deinococcus citri (Ahmed et al. 2014)	Citrus canker lesions, Islamabad, Pakistan	+	coccus	pink to red
Deinococcus claudionis (Callegan et al. 2008)	Alpine environments, Pico de Orizaba, Mexico	+	coccus or rod	pink
Deinococcus daejeonensis (Srinivasan et al. 2012)	Sludge in a sewage disposal plant, South Korea	+	coccus	red
Deinococcus depolymerans (Asker et al. 2011)	Radioactive freshwater site, Japan	+	rod	red
Deinococcus deserti (de Groot et al. 2005)	Sahara Desert sand	-	rod	whitish
Deinococcus enclensis (Thorat et al. 2015)	Marine sediment sample, Chorao Island, Goa, India	+	coccus	light-pink
Deinococcus ficus (Lai et al. 2006)	Rhizosphere of Ficus religiosa, Taiwan	+	rod	light-pink
Deinococcus fonticola (Makk et al. 2019)	Radioactive thermal spring, Hungary	-	coccus	light-pink
Deinococcus frigens (Hirsch et al. 2006)	Antarctic soil	+	coccus	pink to orange
Deinococcus geothermalis (Ferreira et al. 1997)	Hot spring, Italy and Portugal	+	coccus	orange
Deinococcus gobiensis (Yuan et al. 2009)	Gobi Desert, China	+	coccus	red
Deinococcus grandis (Rainey et al. 1997)	Freshwater fishes and feces of an elephant, Japan	-	rod	pink
Deinococcus hibisci (Moya et al. 2018)	Rhizosphere of Hibiscus syriacus, South Korea	+	coccus	pink
Deinococcus hohokamensis (Rainey and da Costa 2005)	Irradiated Sonoran Desert soil, AZ, USA	+	coccus	light-pink
Deinococcus hopiensis (Rainey and da Costa 2005)	Irradiated Sonoran Desert soil, AZ, USA	+	coccus	pink
Deinococcus humi (Srinivasan et al. 2012)	Soil, South Korea	+	coccus	red
Deinococcus indicus (Suresh et al. 2004)	Groundwater, India	-	rod	red
Deinococcus irradiatisoli (Kim et al. 2018)	Gamma ray-irradiated soil, Nowongu, South Korea	-	coccus	pink to red
Deinococcus knuensis (Lee et al. 2017)	River water, Han River, South Korea	-	coccus	red
Deinococcus koreensis (Baek et al. 2018)	Freshwater, Seomjin River, South Korea	-	rod	pink
Deinococcus lacus (Park et al. 2018)	Freshwater from an artificial pond, South Korea	-	coccus	pink

Deinococcus malanensis (Zhu et al. 2017)	Radiation-polluted soil, China	-	coccus or rod	pink
Deinococcus maricopensis (Rainey and da Costa 2005)	Irradiated Sonoran Desert soil, AZ, USA	+	rod	pink
Deinococcus marmoris (Hirsch et al. 2006)	Antarctic marble	+	coccus	pink to orange
Deinococcus metalli (Feng et al. 2015)	Lead-zinc ore from an abandoned lead-zinc mine, China	+	rod	orange to red
Deinococcus metallilatus (Kim et al. 2015)	Automobile air-conditioning system, South Korea	+	coccus	light-pink
Deinococcus misasensis (Asker et al. 2008)	Fresh water collected at a radioactive site, Misasa, Japan	+	rod	red
Deinococcus multiflagellatus (Kim et al. 2018)	Automobile air-conditioning system, South Korea	-	rod	pink to red
Deinococcus mumbaiensis (Shashidhar and Bandekar 2006)	Contaminated agar plate, India	-	coccus or rod	red
Deinococcus murrayi (Ferreira et al. 1997)	Hot springs, Portugal	+	coccus	orange
Deinococcus navajonensis (Rainey and da Costa 2005)	Irradiated Sonoran Desert soil, AZ, USA	+	rod	pink
Deinococcus papagonensis (Rainey and da Costa 2005)	Irradiated Sonoran Desert soil, AZ, USA	+	rod	light-pink
Deinococcus peraridilitoris (Rainey et al. 2007)	Coastal desert, Chile	+	coccus or rod	light-pink
Deinococcus persicinus (Jeon et al. 2016)	Irradiated soil, South Korea	-	coccus	pink
Deinococcus petrolearius (Xi et al. 2017)	Crude oil recovery water, China	+	coccus	red
Deinococcus phoenicis (Vaishampayan et al. 2014)	Cleanroom at the Kennedy Space Center, Florida, USA	+	coccus	light-pink
Deinococcus pimensis (Rainey and da Costa 2005)	Irradiated Sonoran Desert soil, AZ, USA	+	rod	pink
Deinococcus piscis (Shashidhar and Bandekar 2009)	Marine fish, India	+	coccus	light-pink
Deinococcus proteolyticus (Kobatake et al. 1973)	Feces of a llama, Japan	+	coccus	orange to red
Deinococcus psychrotolerans (Tian et al. 2019)	Soil from the South Shetland Islands, Antarctica	-	coccus	red
Deinococcus puniceus (Lee et al. 2017)	Irradiated soil, South Korea	+	coccus	dark-red
Deinococcus radiodurans (Anderson et al. 1956)	Gamma-irradiated canned meat, Oregon, USA	+	coccus	red
Deinococcus radiomollis (Callegan et al. 2008)	Alpine environments, Pico de Orizaba, Mexico	+	rod	pink
Deinococcus radiophilus (Lewis 1971)	Irradiated lizardfish (Mumbai duck), India	+	coccus	orange to red
Deinococcus radiopugnans (Brooks and Murray 1981)	Haddock tissue	+	coccus	orange to red
Deinococcus radioresistens (Srinivasan et al. 2016)	Mount Deogyusan, Jeonbuk Province, South Korea	-	rod	orange
Deinococcus radiotolerans (Cha et al. 2014)	Gamma ray-irradiated soil, South Korea	-	rod	pink
Deinococcus reticulitermitis (Chen et al. 2012)	Gut of a wood-feeding termite	-	coccus	red
Deinococcus roseus (Asker et al. 2008)	Fresh water collected at a radioactive site, Misasa, Japan	+	rod	pink
Deinococcus ruber (Kim et al. 2017)	Garden soil, South Korea	+	coccus	red
Deinococcus rufus (Wang et al. 2018)	Soil near an iron factory in Busan, South Korea	-	rod	red
Deinococcus saudiensis (Hussain et al. 2016)	Desert of Yanbu' al Bahr, Saudi Arabia	-	rod	pink
Deinococcus saxicola (Hirsch et al. 2006)	Antarctic sandstone	+	coccus	pink to orange
Deinococcus sedimenti (Lee et al. 2017)	River sediments, Han River, South Korea	+	coccus	pink
Deinococcus seoulensis (Lee et al. 2016)	Irradiated river sediments, Han River, South Korea	+	rod	red
Deinococcus soli (Cha et al. 2014)	Rice field soil, South Korea	-	rod	red
Deinococcus sonorensis (Rainey and da Costa 2005)	Irradiated Sonoran Desert soil, AZ, USA	+	coccus or rod	light-pink
Deinococcus swuensis (Lee et al. 2013)	Mountain soil, South Korea	+	coccus	pink
Deinococcus taklimakanensis (Liu et al. 2017)	Taklimakan Desert in Xinjiang, China	-	rod	light-pink
Deinococcus terrestris (Wang et al. 2020)	Soil, Shandong Province, China	+	coccus	red
Deinococcus terrigena (Ten et al. 2019)	Soil, South Korea.	-	rod	light-pink
Deinococcus wulumuquiensis (Wang et al. 2010)	Radiation-polluted soil, China	+	coccus	orange to red
Deinococcus xibeiensis (Wang et al. 2010)	Radiation-polluted soil, China	+	coccus	pink to red
Deinococcus xinjiangensis (Peng et al. 2009)	Taklimakan Desert in Xinjiang, China	+	coccus	light-pink
Deinococcus yavapaiensis (Rainey and da Costa 2005)	Irradiated Sonoran Desert soil, AZ, USA	+	rod	red
Deinococcus yunweiensis (Zhang et al. 2007)	Contaminant on an agar plate, China	-	rod	red

Figure S1. Alignment of GyrA subunits of *E. coli* (EcGyrA), *D. radiodurans* (DrGyrA) and *T. thermophilus* (TtGyrA). The three-dimensional structure of EcGyrA determined by cryo-EM is indicated on top of the sequence alignment (PDB code 6RKW (Vanden Broeck et al., 2019)).

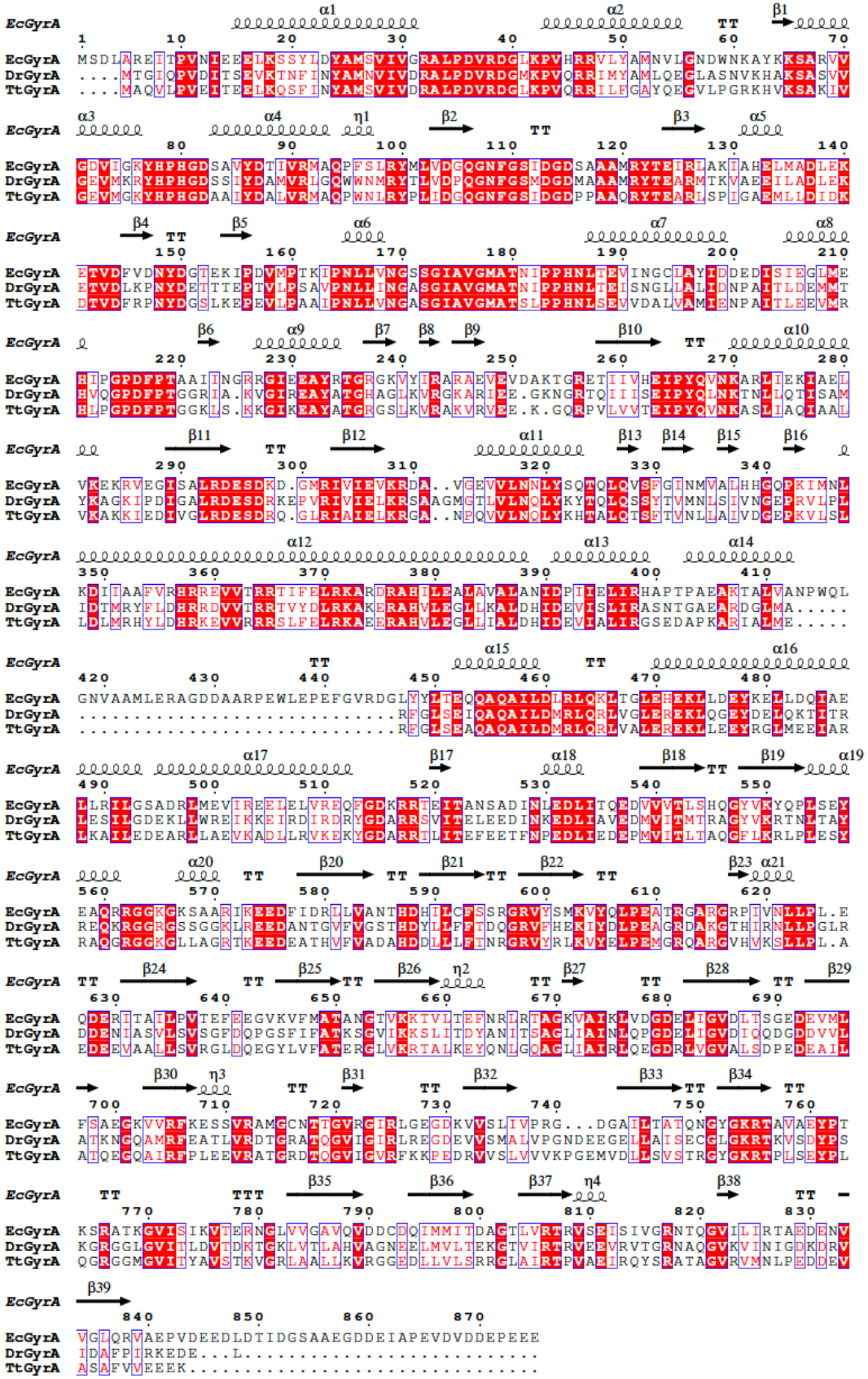

Figure S2. Alignment of GyrB subunits of *E. coli* (EcGyrB), *D. radiodurans* (DrGyrB) and *T. thermophilus* (TtGyrB). The three-dimensional structure of EcGyrB determined by cryo-EM is indicated on top of the sequence alignment (PDB code 6RKW (Vanden Broeck et al., 2019)).

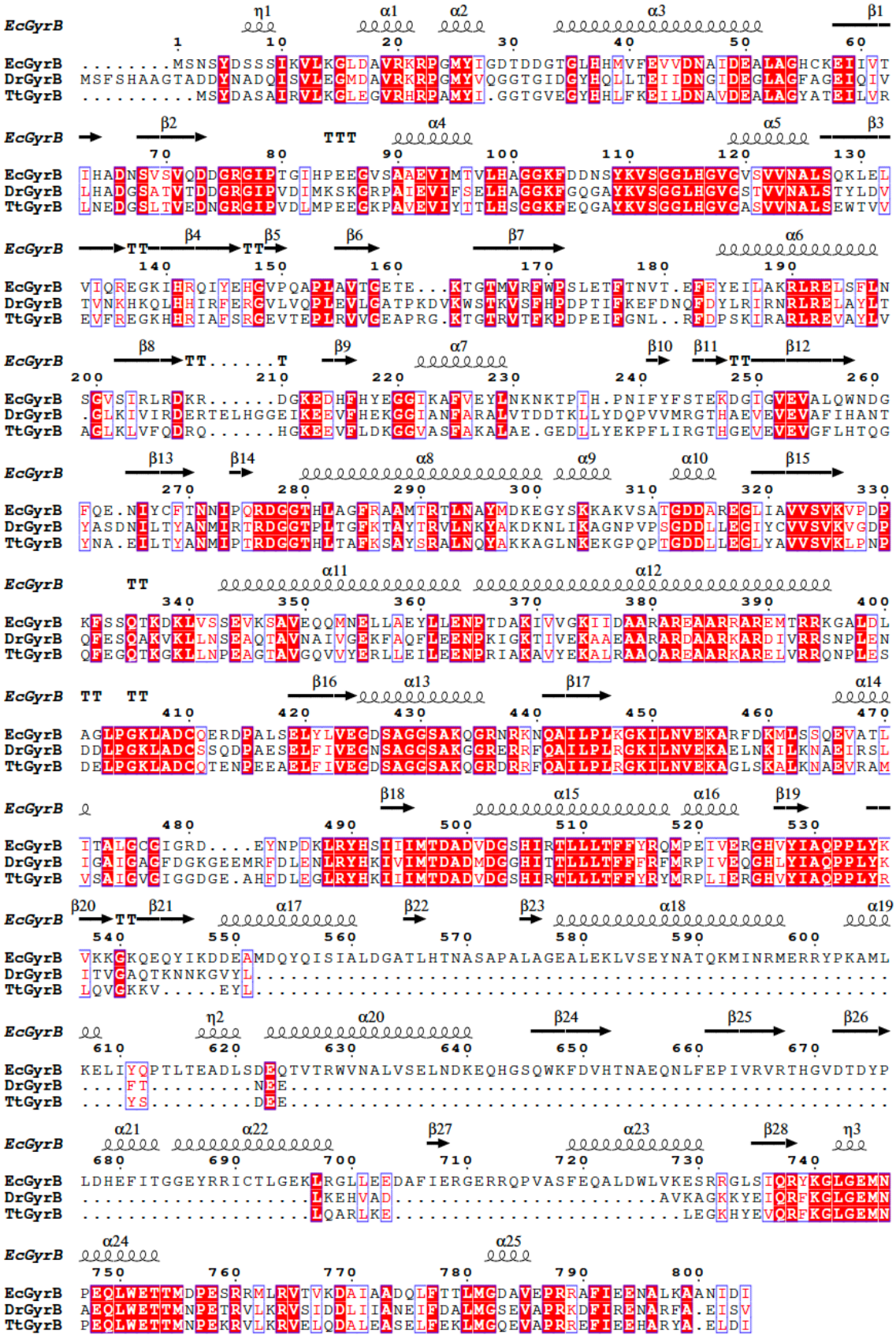

Map of the pET21D plasmid used for expression of DrGyrA

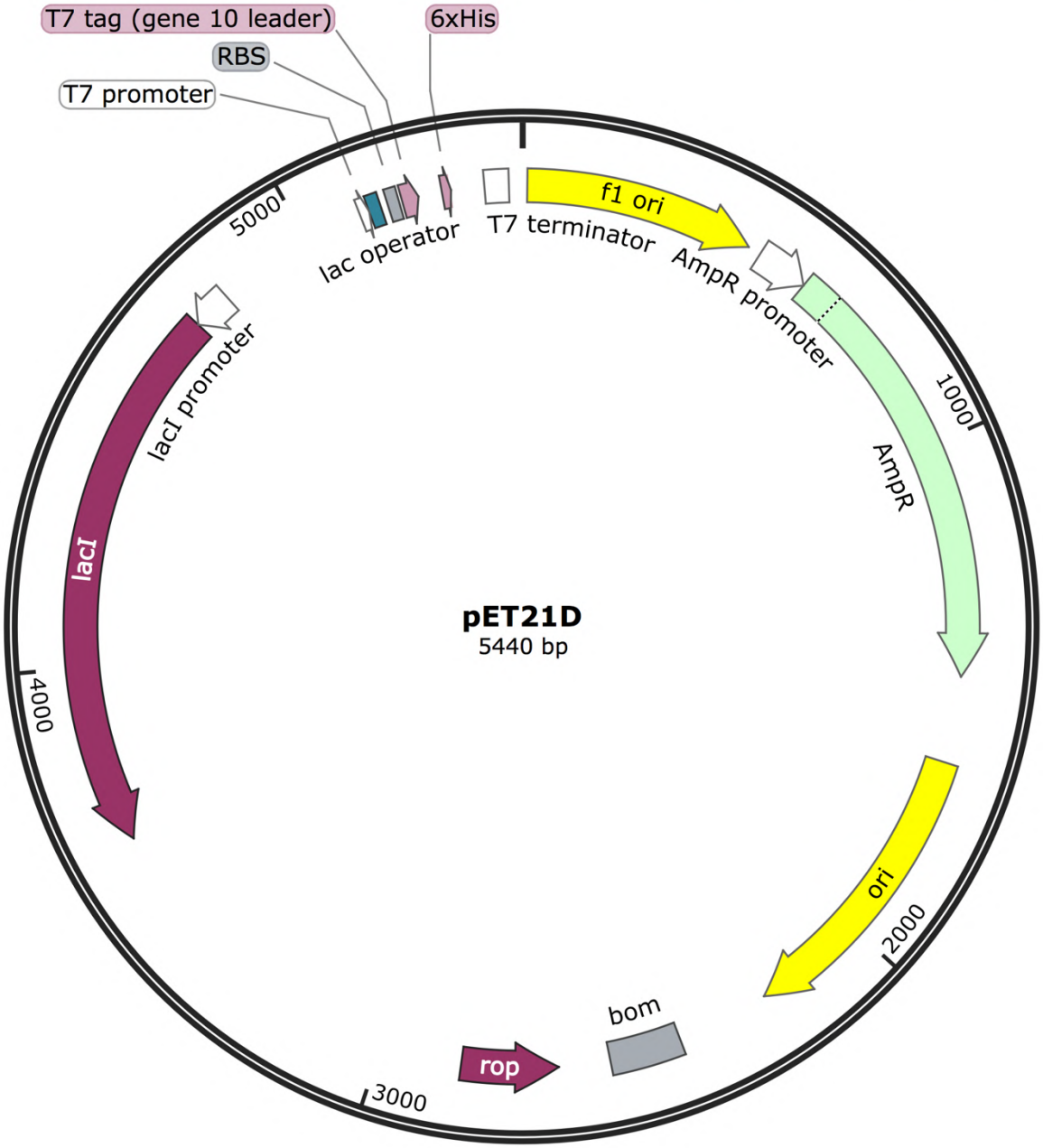

Map of the pProExHTB plasmid used for expression of the HU proteins, DdrC, DrGyrBAfus and DrGyrB

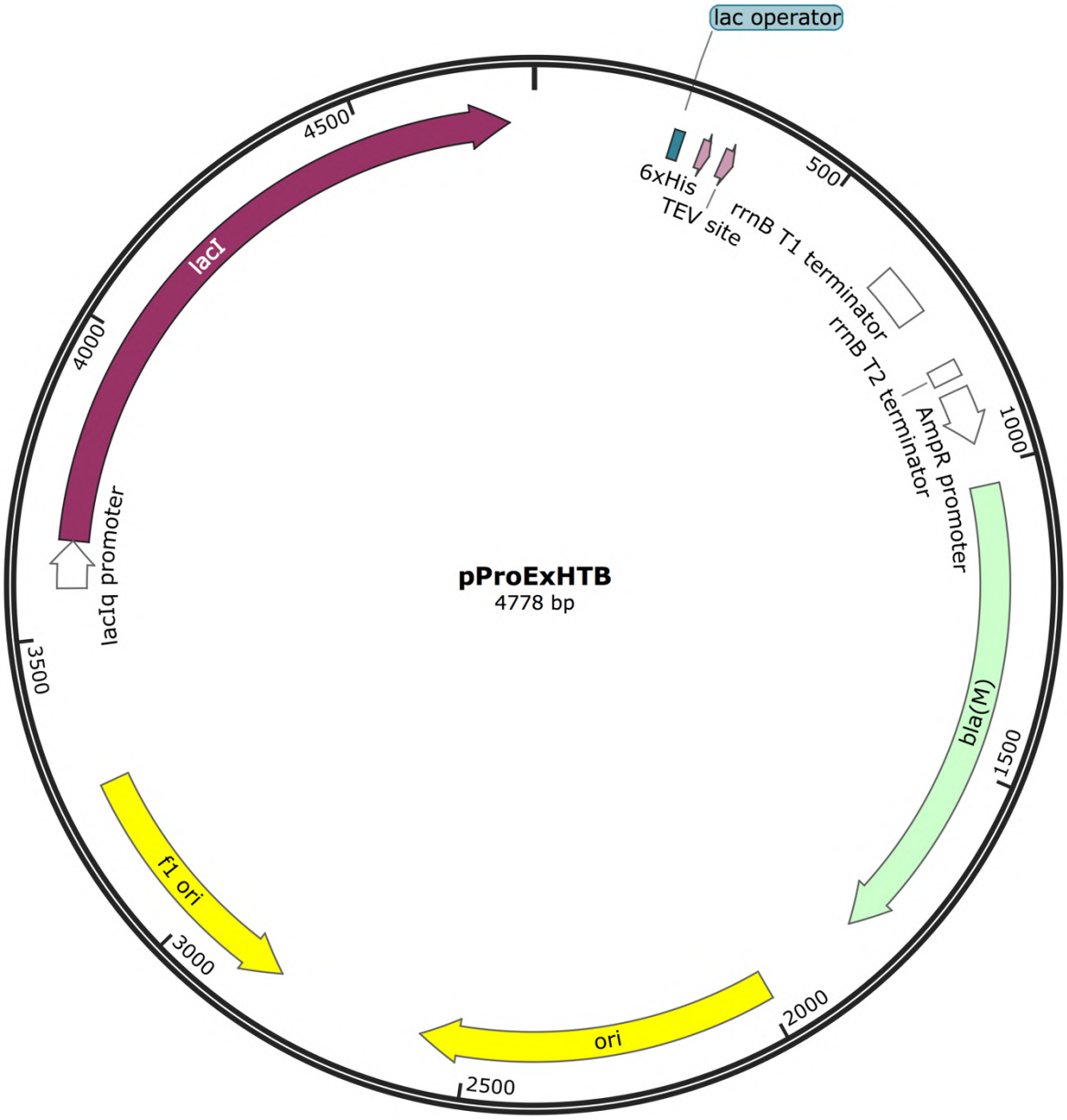

Résumé

La bactérie *Deinococcus radiodurans* est l'un des organismes les plus radio-résistants sur terre. Cette résistance résulte d'un ensemble de mécanismes, dont une structuration particulière de son nucléoïde. Mes travaux de thèse avaient pour but de mieux appréhender l'organisation et la dynamique des nucléoïdes de *D. radiodurans* et de *Deinococcus deserti*, une bactérie isolée dans le désert du Sahara et présentant également une forte résistance aux rayonnements UV et ionisants et à une dessiccation prolongée. Plus précisément, mes études ont porté sur les protéines associées au nucléoïde (ou NAPs) de ces bactéries - les protéines HU et l'ADN gyrase qui sont les plus abondantes - ainsi qu'une NAP spécifique des *Deinococcus*, DdrC. L'objectif était d'élucider la structure tridimensionnelle de ces protéines, de caractériser leurs interactions avec l'ADN, et enfin d'étudier leurs effets sur la conformation et la compaction d'ADN plasmidique.

Par des études biochimiques et des analyses par microscopie à force atomique et par microscopie électronique, nous avons mis en lumière des différences notables dans les mécanismes de compaction et de liaison à l'ADN entre les différents homologues de la protéine HU de *D. radiodurans* (DrHU) et de *D. deserti* (DdHU1, DdHU2 et DdHU3). En particulier, nous avons démontré un double rôle de DrHU dans l'organisation et la compaction de l'ADN plasmidique, qui peut être condensé ou rigidifié en fonction de la concentration de DrHU liée à l'ADN - une double fonction qui n'est pas conservée chez DdHU1, son plus proche homologue. Nous avons également réussi à produire deux formes de l'ADN gyrase, une forme active pouvant être utilisée pour des études fonctionnelles, et une deuxième plus stable, mais moins active, qui est plus adaptée pour des études structurales. Enfin, nos études structurales de DdrC couplées à des analyses biochimiques et de dynamique moléculaire ont révélé la structure tridimensionnelle de DdrC, son état d'oligomérisation et son mode de fixation à l'ADN. Ces résultats suggèrent que DdrC pourrait être une NAP spécifique des *Deinococcus*, jouant un rôle clé dans la compaction du nucléoïde après irradiation et peut-être plus largement dans la réponse de ces bactéries aux dommages de l'ADN. Ensemble, ces études ont permis de mieux comprendre les mécanismes moléculaires mis en œuvre par ces bactéries radio-résistantes pour organiser et structurer leur nucléoïde et répondre de façon efficace à des stress génotoxiques tels que l'irradiation.

Summary

The bacterium *Deinococcus radiodurans* is one of the most radiation resistant organisms on earth. This resistance results from multiple mechanisms, including an unusual nucleoid organization. The aim of my thesis was to better understand the organization and dynamics of the nucleoids of *D. radiodurans* and *Deinococcus deserti*, a bacterium isolated from the Sahara Desert that also exhibits a strong resistance to UV and ionizing radiation and to prolonged desiccation. Specifically, my studies focused on the nucleoid-associated proteins (or NAPs) of these bacteria - the HU proteins and DNA gyrase which are the most abundant - as well as a *Deinococcus*-specific NAP, DdrC. The objective was to elucidate the three-dimensional structure of these proteins, to characterize their interactions with DNA, and finally to study their effects on the conformation and compaction of plasmid DNA.

Through biochemical studies and atomic force microscopy and electron microscopy analyses, we have highlighted significant differences in the mechanisms of compaction and DNA binding used by the different HU protein homologues from *D. radiodurans* (DrHU) and *D. deserti* (DdHU1, DdHU2 and DdHU3). In particular, we have demonstrated a dual role for DrHU in the organization and compaction of plasmid DNA, which can be either condensed or rigidified depending on the concentration of DNA-bound DrHU - a dual function that is not conserved in DdHU1, its closest homolog. We also succeeded in producing two forms of the DNA gyrase, an active form that can be used for functional studies, and a second, more stable, but less active form that is more suitable for structural studies. Finally, our structural studies of DdrC coupled with biochemical and molecular dynamics analyses revealed the three-dimensional structure of DdrC, its oligomerization state, and its mode of binding to DNA. These results suggest that DdrC may be a *Deinococcus*-specific NAP, playing a key role in nucleoid compaction after irradiation and perhaps more broadly in the DNA damage response of these bacteria. Together, these studies have provided a better understanding of the molecular mechanisms used by these radio-resistant bacteria to organize and structure their nucleoid and respond efficiently to genotoxic stresses such as irradiation.